“Have you guessed the riddle yet?” the Hatter said, turning to Alice again.

“No, I give it up,” Alice replied: “what’s the answer?”

“I haven’t the slightest idea,” said the Hatter.

~ Lewis Caroll

Properties and Applications of Hydrogen-Bond Rich Iridium (III) Complexes

by

Trystan Harri Jones

MChem. (1st Class Honours), University of Edinburgh, Scotland, 2021

A Dissertation Submitted in Partial Fulfilment
of the Requirements for the Degree of

Doctor of Philosophy

in the Graduate Academic Unit of Chemistry

Supervisor: Barry A. Blight, PhD, Department of Chemistry

Examining Board: David I. MaGee, PhD, Department of Chemistry
James J. Tait, PhD, Department of Chemistry
Brynle Barrett, PhD, Department of Physics

External Examiner: David E. Herbert, PhD, Department of Chemistry,
University of Manitoba

This dissertation is accepted by the Dean of Graduate Studies

THE UNIVERSITY OF NEW BRUNSWICK

August, 2025

© Trystan Harri Jones, 2025

Abstract

Iridium (III) complexes are used for a wide variety of applications owing to their thermal stability, tuneable electronic properties and strong photoluminescent character. Iridium (III) complexes can be structurally altered to change the wavelengths of light they absorb and emit making them desirable for organic light emitting diodes (OLEDs) and photocatalysis. The structural is altered through changing the ligands in the first sphere of coordination surrounding the iridium metal centre. In this thesis we introduce a wide range of iridium (III) complexes all incorporating a ligand with an incorporated hydrogen-bonding array capable of strong non-covalent interactions. These strong non-covalent interactions provide opportunity for modulation of opto-electronic properties through the second sphere of coordination which allows us to further tune these complexes to specific applications.

Herein we demonstrate the design and synthesis of a large new series of hydrogen-bonding iridium (III) complexes along with a thorough analysis of each new reported complex's opto-electronic properties through spectroscopic and computational techniques. In addition, the new series of hydrogen-bond rich iridium (III) complexes were tested against two main applications: tuneable emissive materials and photoredox catalysis. We found that the complex's dynamic properties with and without hydrogen-bonding compliments demonstrated potential in both applications. Finally, a rudimentary computational screening technique was incorporated to the synthesis of new iridium materials providing improved targeting of new iridium (III) complexes for their opto-electronic properties.

Dedication

To family,

To friends,

To colleagues,

Nothing is possible without you.

Acknowledgements

First, I would like to thank my supervisor Dr Barry Blight for providing me this opportunity and for his strong guidance over the last four years. His enthusiasm to do 'cool science' and discover new systems as 'molecular engineers' is truly inspiring, and I hope to hold that same enthusiasm for my career in the future. Next, I would like to thank all current and former members of the Blight group for their continuing support and tolerance of my incessant jabbering. Sarah, Aroosha, Mason, Robbie, and Declan I wish you all continued success in your endeavours here at UNB and beyond. You are the best team of people I have ever worked with and have made the most stressful time of my life one of the most enjoyable, I love you all. I would also like to thank all those at the University of Liverpool; Dr John Ward, Chris, Lyubomir, and many others for making my brief stay at the Materials Innovation Factory so enjoyable. I thank the members of my advisory committee; Dr Sara Eisler and Dr David MaGee for all their support, advice and input over the years. I would also like to extend my gratitude to the entirety of UNB's faculty in the department of chemistry for giving me so many opportunities in research, teaching and outreach to students. I could not have asked for a better faculty to work under. I have met some amazing people here in New Brunswick, thank you to the friends I've made along the PhD journey, Marta, Steve, Abraham, Jose, Rheya, Nath, and Ethan. I am extremely grateful to have friends back in the UK too who have supported me throughout this journey, Zack, Ece, Sam, Maro, Jack, and all the Bruntsfield flat boys, you guys are amazing. Finally, I would like to thank my family, Mum, Dad, Gwilym, and Martyn thank you for your unwavering support. Your love and encouragement have made this possible, I truly love you all.

Table of Contents

Abstract ii

Dedication iii

Acknowledgements iv

Table of Contents v

List of Tables xi

List of Figures xiv

List of Schemes xl

List of Symbols, Nomenclature, or Abbreviations xlii

Chapter 1 1

Introduction 1

1.1 Thesis Aims 1

1.2 Supramolecular Chemistry 2

1.2.1 Hydrogen-Bonding 6

1.2.2 Quantifying H-Bonding Strength 9

1.3 Guanidine Derivatives 13

1.3.1 Guanidine Derivatives as Ligands 16

1.4 Cyclometalated Iridium (III) Complexes 21

1.4.1 Fluorescence and Phosphorescence 23

1.4.2 Phosphorescence of Ir(III) Complexes 27

1.4.3 Colour Tuning of Iridium (III) Complexes 31

1.5 Density-Functional Theory 38

1.5.1 DFT of Metallic Complexes 43

1.5.2 Time-Dependent Density-Functional Theory 46

1.5.3 TD-DFT of Iridium (III) Complexes 48

1.6 Photoredox Catalysis 49

1.6.1 Homogeneous Photosensitisers 52

1.6.2 Design of Efficient Iridium (III) Photosensitisers 54

1.6.3 Iridium (III) Photosensitisers Applied to Hydrogen Evolution 57

1.7 Automation for Chemistry 64

1.7.1 Automation in Photoredox catalysis 66

1.8 Thesis Objectives 68

1.9 Bibliography 69

Chapter 2 89

Automation Accelerated Screening of Hydrogen-bond-Rich Iridium Photosensitisers for Hydrogen Generation 89

2.1 Abstract 90

2.2 Introduction 90

2.3 Results and Discussion 93

2.3.1 Synthesis and Characterisation 93

2.3.2 Photophysical Properties 93

2.3.3 Electrochemical Properties 95

2.3.4 Computational Investigation 97

2.3.5 Accelerated Hydrogen Screening 99

2.3.6 Quenching kinetics and photo-stability 102

2.3 Conclusions 104

2.4 Bibliography 106

Chapter 3 111

Colour Tuneability of Heteroleptic Iridium Complexes Through Second-Sphere Coordination 111

3.1 Abstract 112

3.2 Introduction 112

3.3 Results 117

3.3.1 Synthesis and Characterisation 117

3.3.2 Photo-Physical Measurements 117

3.3.3 Host Guest Chemistry 121

3.3.4 Electrochemical Studies 122

3.3.5 Computational Studies 123

3.4 Discussion 127

3.4.1 Deep Blue Emission 127
3.4.2 Serendipitous White Light 129
3.4.3 Orange and Red Light 131
3.5 Conclusions 134
3.6 Bibliography 136
Chapter 4 142
Computationally Accelerated Discovery of Efficient Dual Component White Light Emitters 142
4.1 Abstract 143
4.2 Introduction 143
4.3 Results and Discussion 148
4.3.1 Computational Investigation 148
4.3.2 Synthesis and Characterisation 155
4.3.3 Ir(III) Complex Photophysical Investigation 156
4.3.4 Electrochemical Investigation 160
4.3.5 Supramolecular Titrations 162
4.4 Conclusions 167
4.5 Bibliography 169
Chapter 5 174
Conclusions and Future Outlook 174

5.1 Conclusions 174

5.2 Outlook 178

5.3 Bibliography 181

Appendix 1 182

Materials and Experimental Techniques 182

Appendix 2 187

Supplementary Material for Chapter 2 187

A2.1: Synthetic Procedures of Complexes 2.1-2.5 188

A2.2: ^{1}H and ^{13}C NMR Spectra and Mass spectra 197

A2.3: Cyclic Voltammetry 209

A2.4: Excitation and Emission Data 210

A2.5: Stern-Volmer and Photo-Stability 211

A2.6: PLQYs and Decay Lifetimes 219

A2.7: High-Throughput Hydrogen Evolution Condition Screening 224

A2.8: Computational Investigation 226

Appendix 3 229

Supplementary Material for Chapter 3 229

A3.1: Synthetic Procedures of Compounds 3.1-3.5 230

A3.2: ^{1}H and ^{13}C NMR Spectra and Mass spectra 237

A3.3: UV-vis, Excitation and Emission Data 243

A3.4: K_a Binding Studies 247

A3.5: PLQYs and Decay Lifetimes 250

A3.6: PMMA Solid State PLQYs and Decay Lifetimes 259

A3.7: Cyclic Voltammetry 270

A3.8: Computational Investigation 271

Appendix 4 276

Supplementary Material for Chapter 4 276

A4.1: Computational Investigation 277

A4.2: Synthetic Procedures of Complexes 4.1-4.4 294

A4.3: ^{1}H and ^{13}C NMR Spectra and Mass spectra 301

A4.4: UV-vis, Excitation and Emission Data 311

A4.5: K_a Binding Studies 314

A4.6: PLQYs and Decay Lifetimes 317

A4.7: Cyclic Voltammetry 325

Curriculum Vitae

List of Tables

Table 2.1 Photoluminescence data for complexes **2.1-2.5** in argon saturated CH_3CN.... 95

Table 2.2 Electrochemical and photo-redox properties of complexes **2.1-2.5** in argon saturated CH_3CN at 298 K.[a] 96

Table 2.3 Results of quenching studies performed with electron donor [NEt_3] and co-catalyst [$Co(bpy)_3(PF_6)_2$].[a] 103

Table 3.1 Photoluminescence data for complexes **3.1-3.4** and co-complex **3.1•3.5-3.4•3.5**. 120

Table 3.2 Association constants (M^{-1}) and calculated Gibbs free energies (kJ mol^{-1}) for Ir(III) complexes **3.1-3.4** H-bonding to guest molecule **3.5**. 122

Table 3.3 Electrochemical results for complexes **3.1-3.4** and co-complexes **3.1•3.5-3.4•3.5**. 123

Table 4.1 Photoluminescence data for complexes **4.1-4.4** in argon saturated $CHCl_3$ and the data for deep blue emitter compound **4.5** from previous studies.[43] 160

Table 4.2 Electrochemical and photo-redox properties of complexes **4.1-4.4** and co-systems **4.1•4.5-4.4•4.5** in argon saturated CH_3CN at 298 K.[a] Co-complexes are in a 1:1 ratio. 161

Table 4.3 Association constants (M^{-1}) and calculated Gibbs free energies (kJ mol^{-1}) for Ir(III) complexes **4.1-4.4** H-bonding to guest molecule **4.5**. 163

Table 4.4 Photoluminescence data for complexes **4.1-4.5** in argon saturated $CHCl_3$.... 167

Table A.2.1 Screening conditions for photocatalytic hydrogen generation with complex **2**. All variables were changed individually (varying condition highlighted in red), while all other conditions were consistent with the initial conditions. Initial conditions were determined from review of existing literature. Solvents are 5 mL 1:1 ratio unless specified otherwise, all screens were run for 5 hours before hydrogen evolution was measured. Hydrogen generation rate was calculated relative to time mols of H_2 and mass of PS. 224

Table A.2.2 Summary of key findings of TD-DFT predictions for the complexes **2.1-2.5** including energy levels of five highest contributing singlet states and first triplet state. 226

Table A.3.1 a) Significant excitation and emission peaks for Ir(III) complexes **3.1-3.4** in PMMA films at 298 K. **b)** PLQYs for Ir(III) complexes **3.1-3.4**; in PMMA film at 298 K determined using an SC-30 integrating sphere module. **c)** decay lifetimes using TCSPC excited at 365 nm and their corresponding chi-squared values for Ir(III) complexes **3.1-3.4**; in PMMA films at 298 K. All complexes decay biexponentially. **d)** the radiative (k_r) and nonradiative (k_{nr}) rate constants were calculated as $k_r = \phi_{PL}/\tau_{PL}$ and $k_{nr} = (1-\phi_{PL})/\tau_{PL}$. 259

Table A.3.2 Summary of key findings of TD-DFT predictions for the compounds **3.1-3.5** and co-systems **3.1•3.5-3.4•3.5** including energy levels of five highest contributing singlet states and first triplet state. 271

Table A.4.1 Summary of key findings of TD-DFT predictions for the thirty computationally designed complexes **A-AD** (and synthesised complexes **1-4**) including energy levels of five highest contributing singlet states and first triplet state (the predicted peak emission wavelength). 277

Table A.4.2 Summary of key findings of TD-DFT predictions for synthesised complexes **4.1-4.4** in the presence of compound **4.5** energy levels of five highest contributing singlet states and first triplet state (the predicted peak emission wavelength). 291

List of Figures

Figure 1.1 a) H-bonding schematic of compound **1.01** and **1.02** as studied by Balónová *et al.* **b)** Scheme of Commission Internationale de l'Eclairage (CIE) coordinates of photoluminescence titration of compound **1.01** with **1.02**.[1] 1

Figure 1.2 Binding of 18-crown-6 to potassium cations as discovered by Charles J. Pedersen *et al.*[24] 4

Figure 1.3 Stoddart *et al.*'s electrochemically responsive molecular machine. **1.03** is the molecule in its deprotonated form from addition of pyridine. Conversely addition of protons through TFA achieves structure **1.04**.[20] 5

Figure 1.4 a) Schematic of the functional detachment and reattachment of a molecular walker along a thread. **b)** Biomolecule kinesin walking along microtubules, image courtesy of John Lieber ©.[22,29] 6

Figure 1.5 Influences on the strength of hydrogen-bonding. **a)** Electrostatic interactions **b)** Charge-transfer interactions. **c)** Pauli repulsions (sterics). **d)** Dispersion interactions. **e)** π-resonance assistance. **f)** Secondary electrostatic interactions (green arrow = attractive secondary interaction, red arrow = repulsive secondary interaction).[33] 7

Figure 1.6 Hydrogen bonding pairs of Adenine and Thymine (A-T top) and Guanine and Cytosine (G-C bottom). K_a's are also given, demonstrating the much higher triple H-bonding strength of the G-C pair.[36] 8

Figure 1.7 Examples of quadruple H-bond arrays and their H-bonding behaviours. Compounds **1.09-1.10** (ADAD),[43] compounds **1.11-1.12** (AADD),[44] compounds **1.13-1.14** (ADDA-DAAD),[45] compounds **1.15-1.16** (AAAA-DDDD).[42] 9

Figure 1.8 Schematic explaining the relationship between a Host-Guest [HG] complex and K_a in a single Host [H] and Guest [G] system.[46] 11

Figure 1.9 Schematic of a one Host [H] and two Guest [G] system, displaying the relationship between K_1 and K_2.[46] 12

Figure 1.10 Common synthetic routes for the synthesis of guanidine derivatives and examples of mechanisms for routes a), c), e) and f).[54,56,57] 14

Figure 1.11 a) Resonance structures of the protonated form of guanidine (guanidinium) **b)** Acceptor donor behaviour of guanidine (left) and guanidinium salt (right).[54,58] 16

Figure 1.12 Examples of guanidine compounds common in coordination chemistry and their coordination mode.[61] 17

Figure 1.13 Recent examples of metallic complexes incorporating a neutral guanidine.[61] 18

Figure 1.14 Preparation of cyclometalated Pt(II) complexes **1.30** and **1.32** and crystal structures of the corresponding complexes.[67] 19

Figure 1.15 Chemical structures of metformin and structurally similar biguanides commonly used in clinical practice.[63] 20

Figure 1.16 Synthetic route to Ir(III) complexes **1.40-1.42** with a metformin ancillary ligand.[76] 21

Figure 1.17 General synthetic schemes for the synthesis of homo- and heteroleptic Ir(III) complexes based upon phenyl-pyridine ligands (ppy).[82,88] 23

Figure 1.18 Jablonski diagram for the emission of Ir(III) complex **1.45**. S_n are the singlet states, T_n are the triplet states, IC is internal conversion and ISC is the intersystem crossing.[88,94,95] 25

Figure 1.19 Graphical representation of a TCSPC histogram with photon arrival times grouped into channels for fitting.[97] 27

Figure 1.20 CIE 1931 chromaticity diagram.[124] 32

Figure 1.21 The range of Ir(III) complexes used by Banaroff *et al.* to study Hammett correlations and quantifiable structural property relationships.[121] 33

Figure 1.22 Iridium complexes moving towards NIR emission through increasing the efficiency of the cyclometalating ligands.[120,122] 34

Figure 1.23 Energy-harvesting phosphorescence through inter-ligand transfer of complexes **1.60**, **1.61** and **1.62**. ^1L_CC represents the LUMO of the cyclometalating ligand's singlet state, $^1L_{\wedge}C$ represents the LUMO of the ancillary ligands excited singlet state. As the cyclometalating ligand gets larger the $^3L_{\wedge}C$ triplet state's energy decreases, narrowing the HOMO-LUMO gap, leading to a red shift.[95] 36

Figure 1.24 Fe(II) compounds studied by Reiher *et al.* to study exact exchange and spin-state splitting in metallic complexes.[145] 44

Figure 1.25 Schematic of how dispersion forces can occur and affect coordination geometry in a metallic complex.[141] 45

Figure 1.26 TD-DFT modelled global HOMO-LUMO distributions of compound **1.45** and **1.46** (the fac- and mer- isomers of $[Ir(ppy)_3]$). In both cases HOMOs reside on 5dπ orbitals of Ir and phenyl rings, LUMOs are distributed across the phenylpyridines. 49

Figure 1.27 Diagram of the natural process of photosynthesis (inside plant cell chloroplasts). Shows the process to split water giving electrons and protons used to produce carbohydrates using chlorophyll as the light sensitising photocatalyst.[179] 50

Figure 1.28 a) The reaction pathway of a thermal reaction (**R→P**) catalysed by **C** via intermediate **I' b)** Photochemical reaction where **R** is excited to **R'** proceeding to **P** via **I c)** A photocatalytic reaction pathway, where C is excited to C', then colliding with **I** to form **I'** before proceeding to **P**.[177] 51

Figure 1.29 Schemes for reductive and oxidation quenching including photosensitiser (PS), electron donor (ED), and co-catalyst (cat).[179,182] 52

Figure 1.30 Examples of organic dyes and inorganic ruthenium complexes studied as homogeneous photosensitisers.[183,184] 53

Figure 1.31 A selection of the most common Ir(III) photosensitisers in the literature and their respective photoredox potentials.[190] 55

Figure 1.32 a) The percentage by source of where hydrogen is refined from **b)** A flowchart schematic of the steam methane reformation process used to produce 'blue' hydrogen.[199,201,202] 58

Figure 1.33 Examples of the four common types of Ir(III) PS, **1.45** is neutral, **1.47** is cationic, **1.77** is coumarin based, **1.78** and **1.79** are bi- and multi-metallic respectively.[179] 60

Figure 1.34 Photocatalytic cycles of the photo-reductive HER.[205] 61

Figure 1.35 Commercially available automation platforms. **a)** Chemspeed automated synthesis platform[221] **b)** Unchained labs 'Big Kahuna' platform[223] **c)** Mettler-Toledo CHRONECT XPR with GC adaptor.[222] 65

Figure 1.36 Workflow for novel photocatalytic reaction discovery screening. Substrates are combined randomly in the combinatorial reaction screening step. The pools are then irradiated with visible light in the presence of a **PS** and the wells are analysed with GC-MS followed by evaluation.[216,227] 66

Figure 2.1 H-bond rich cyclometalated Ir(III) complexes **2.1-2.5** studied herein as photosensitisers for hydrogen generation. 92

Figure 2.2 a) UV-vis spectra of complexes **2.1-2.5** in CH_3CN (1.0×10^{-5} M, 298 K). **b)** Normalised emission-excitation spectra of complexes **2.1-2.5** in CH_3CN (1.0×10^{-5} M, 298 K), the solid lines represent the emission while the dashed lines represent the absorption. All emission spectra were excited at 300 nm. 94

Figure 2.3 Molecular orbital diagrams, with TD-DFT calculated HOMO-LUMO gap energies for complexes **2.1-2.5**. 99

Figure 2.4 a) Rate of hydrogen evolution determined from volume of hydrogen generated over a 5-hour period, all conditions were kept consistent with initial screen parameters (see appendix A2.7) while pH was varied as specified. **b)** Rate of hydrogen evolution determined from volume of hydrogen generated over a 5-hour period, solvent mixture varied while all other conditions were consistent with initial screen. 101

Figure 2.5 Hydrogen generation rate of complexes **2.1-2.5** in the optimum conditions informed the screening of complex **2.2**. Reaction conditions: 20 μM Ir(III) complex,

[$Co(bpy)_3(PF_6)_2$] 1mM, DMSO:H_2O (1:1, 5 mL), 0.35 M NEt_3, LiCl 0.3 M, and pH 10, samples were irradiated for 5 hr under an oriel solar simulator 1.0 sun. 102

Figure 3.1 Cyclometalated Ir(III) complexes **3.1-3.4** studied herein. 114

Figure 3.2 Proposed triple H-bonded systems, with preorganised arrangement that contributes to the stability of **3.1•3.5** to **3.4•3.5** systems. 116

Figure 3.3 Vials from emission studies of Ir(III) complexes **3.1-3.4** with added aliquots of compound **3.5**. Vials are illuminated with long wave UV-light (365 nm). Values in % corresponding to the molar equivalents of guest content (**3.5**) in solution. 116

Figure 3.4 The normalised Absorption-Emission spectra of complex **3.1**-**3.4**, dashed line representing the excitation of each complex and solid line representing the emission, all spectra were measured in $CHCl_3$ (1.0×10^{-5} M). **b)** The normalised Absorption-Emission spectra of complex **3.1-3.4** with compound **3.5** in a 1:1 molar ratio in $CHCl_3$ (1.0×10^{-5} M)..... 117

Figure 3.5 Overlayed absorption-emission spectra of complex **3.3** with co-system **3.3•3.5** in argon saturated $CHCl_3$ (1×10^{-5}), 298 K, λ_{ex} = 350 nm. 119

Figure 3.6 (left) TD-DFT predicted HOMO and LUMO orbital distributions of complex **3.1**-**3.4** and (right) visualisation of the energy levels of frontier orbitals with computationally obtained HOMO-LUMO gap. 124

Figure 3.7 Comparison of the TD-DFT computationally modelled frontier orbitals of complex **3.3** and assembly **3.3•3.5**. 126

Figure 3.8 Overlaid emission spectra of complex **3.1** (blue), compound **3.5** (grey) and co-complex **3.1•3.5** (purple) from FRET studies in $CHCl_3$ solution. All samples excited at λ_{ex} = 350 nm. 128

Figure 3.9 a) Emission spectra from titration studies of complex **3.2** with additions of compound **3.5** measured in $CHCl_3$ solution. Black line represents emission of Ir(III) complex **3.2** without any additions; blue line represents compound **3.5** with no complex **3.2** present. **b)** (right) CIE diagram from emission titration experiment of host complex **3.2** and guest compound **3.5**. 130

Figure 3.10 Absorption (solid black line) and corrected PL excitation (red dashed line measured at 570 nm) for co-complexes **3.3•3.5** (left) and **3.4•3.5** (right) (1:1 ratio of Ir complex and compound **3.5**). Spectra normalised to absorbance at 440 nm. 132

Figure 4.1 Previously studied yellow Ir(III) complex with complementary deep blue emitting hydrogen-bonder (see chapter 3).[36] 147

Figure 4.2 Yellow emitting Ir(III) complexes **4.1-4.4** and co-complexes **4.1•4.5-4.4•4.5** in their corrected ratios for white light emission. All images taken with samples in argon saturated $CHCl_3$. 148

Figure 4.3 Summation of the predicted peak emissions of the 30 TD-DFT investigated Ir(III) complexes **A-AD**, computations were performed at the B3LYP level of theory with the 6-31G**/LANL2DZ basis sets.[38] 151

Figure 4.4 a) HOMO-LUMO distributions of complexes **4.1-4.4** with computationally predicted bandgaps (ΔE). **b)** HOMO-LUMO distributions of co-systems **4.1•4.5-4.4•4.5**

with key energies and predicted bandgaps of the iridium complexes within the co-systems. 153

Figure 4.5 Yellow emitting Ir(III) complexes **4.1-4.4** chosen to be synthesised based upon their TD-DFT data, high PLQYs of Ir(III) complexes with these ligands in the literature and synthetic feasibility. Blue emitting compound **4.5** is also included to be mixed with yellow iridium emitters to achieve white emission. 155

Figure 4.6 UV-vis absorption spectra of complexes **4.1-4.4** in $CHCl_3$ ($c = 1\times10^{-5}$ M, 298 K). 157

Figure 4.7 Normalised emission-excitation spectra of complexes **4.1-4.4** in argon saturated $CHCl_3$ ($c = 1.0\times10^{-5}$ M, 298 K), solid lines represent the emission while the dashed lines represent the absorption. All emission spectra were excited at 350 nm; the excitation wavelength was chosen for the overlap with compound **4.5**'s excitation profile. 158

Figure 4.8 CIE representations of the results of emission titrations of complexes **4.1-4.4** with deep blue emitter **4.5**. Initial concentration of complexes is ($C_0 = 1\times10^{-5}$ M), 298 K. The emission titrations used to model the CIEs of **4.2•4.5-4.4•4.5** are available in appendix 4 (figure A.4.23) and the titration for **4.1•4.5** is shown in figure 4.9..... 165

Figure 4.9 a) Emission titration of complex **4.1** with deep blue emitter **4.5**. **b)** Emission spectra of compound **4.1**, **4.5** and co-system **4.1•4.5**, all compounds were excited at 350 nm to show evidence of FRET..... 166

Figure 5.1 Proposed Ir(III) complexes for future photocatalytic hydrogen generation incorporating the redox active Légaré ligand (compound **5.1**). 179

Figure 5.2 Proposed organometallic superstrong DDD-AAA H-bonding co-complex incorporating oxidised Légaré ligand and protonated guanidine ligand. 180

Figure A.2.1 ^{1}H NMR spectrum of iridium complex **2.1**, $CDCl_3$, 400 MHz, 298 K..... 197

Figure A.2.2 ^{13}C NMR spectrum of iridium complex **2.1**, $CDCl_3$, 101 MHz, 298 K.... 198

Figure A.2.3 Mass spectrum of iridium complex **2.1**. HMRS [ESI+] ion $[C_{34}H_{29}F_4IrN_7]^+$ m/z calculated: 804.2044 Found: 804.2034 [M+]. 198

Figure A.2.4 ^{1}H NMR spectrum of iridium complex **2.2**, $CDCl_3$, 400 MHz, 298 K..... 199

Figure A.2.5 ^{13}C NMR spectrum of iridium complex **2.2,** $CDCl_3$, 101 MHz, 298 K.... 199

Figure A.2.6 Mass spectrum of complex **2.2**. HMRS [ESI+] ion $[C_{34}H_{33}IrN_7]^+$ m/z calculated: 732.2421 Found: 732.2434 [M+]. 200

Figure A.2.7 ^{1}H NMR spectrum of iridium complex **2.3**, $CDCl_3$, 400 MHz, 298 K..... 200

Figure A.2.8 ^{13}C NMR spectrum of iridium complex **2.3,** $CDCl_3$, 101 MHz, 298 K.... 201

Figure A.2.9 Mass spectrum of iridium complex **2.3**. HMRS [ESI+] ion $[C_{42}H_{37}IrN_7]^+$ m/z calculated: 832.2732. Found: 832.2734 [M+]. 201

Figure A.2.10 ^{1}H NMR spectrum of iridium complex **2.4**, $CDCl_3$, 400 MHz, 298 K... 202

Figure A.2.11 ^{13}C NMR spectrum of iridium complex **2.4,** $CDCl_3$, 101 MHz, 298 K. 202

Figure A.2.12 Mass spectrum of iridium complex **2.4**. HMRS [ESI+] ion $[C_{40}H_{37}IrN_7O_4]^+$ m/z calculated: 872.2546 Found: 872.2546 [M+]. 203

Figure A.2.13 ^{1}H NMR spectrum of iridium complex **2.5**, $CDCl_3$, 400 MHz, 298 K... 203

Figure A.2.14 ^{13}C NMR spectrum of iridium complex **2.5,** $CDCl_3$, 101 MHz, 298 K. 204

Figure A.2.15 Mass spectrum of iridium complex **2.5**. HMRS [ESI+] ion $[C_{58}H_{69}IrN_7O_4]^+$ m/z calculated: 1120.5036 Found: 1120.5036 [M+]. 204

Figure A.2.16 ^{1}H NMR spectrum of ligand **2.6** DMSO-d_6, 400 MHz, 298 K**.**..... 205

Figure A.2.17 ^{13}C NMR spectrum of ligand **2.6** DMSO-d_6, 101 MHz, 298 K**.**..... 205

Figure A.2.18 ^{1}H NMR spectrum of ligand **2.7**, $CDCl_3$, 400 MHz, 298 K. 206

Figure A.2.19 ^{13}C NMR spectrum of ligand **2.7,** $CDCl_3$, 101 MHz, 298 K. 206

Figure A.2.20 Mass spectrum of ligand **2.7**. HMRS [ESI+] ion $[C_{14}H_{11}NO_2Na]^+$ m/z calculated: 248.0688 Found: 248.0682 [M+]. 207

Figure A.2.21 ^{1}H NMR spectrum of ligand **2.8**, $CDCl_3$, 400 MHz, 298 K. 207

Figure A.2.22 ^{13}C NMR spectrum of ligand **2.8,** $CDCl_3$, 101 MHz, 298 K. 208

Figure A.2.23 Mass spectrum of ligand **2.8**. HMRS [ESI+] ion $[C_{23}H_{28}NO_2]^+$ m/z calculated: 350.2115 Found: 350.2115 [M+]. 208

Figure A.2.24 Cyclic voltammetry of complexes **2.1-2.5**, the samples were 5 mM in dry degassed CH_3CN and normalised to a ferrocene standard under inert argon conditions. **a)** Complex **2.1**, **b)** complex **2.2**, c) complex **2.3**, **d)** complex **2.4**, **e)** complex **2.5**. 209

Figure A.2.25 Normalized absorption-emission spectra of iridium complexes **2.1-2.5** ($1x10^{-5}$ M) measured in CH_3CN solution, excited at 300 nm. The dashed lines are the normalised absorption spectra; solid lines are the emission spectra. **a)** Complex **2.1**, **b)** complex **2.2**, c) complex **2.3**, **d)** complex **2.4**, **e)** complex **2.5**..... 210

Figure A.2.26 a-e) Emission titration of iridium complexes **2.1-2.5** ($1x10^{-5}$ M) with $[Co(bpy)_3]^{2+}$ measured in argon degassed CH_3CN solution, excited at 300 nm Number of

molar equivalents added indicated in graph legends. **a)** Complex **2.1**, **b)** complex **2.2**, c) complex **2.3**, **d)** complex **2.4**, **e)** complex **2.5**. **f)** Stern-Volmer plot for emission quenching of complexes **2.1-2.5** with $[Co(bpy)_3]^{2+}$. 211

Figure A.2.27 a-e) Emission titration of iridium complexes **2.1-2.5** ($1x10^{-5}$ M) with NEt_3 measured in argon degassed CH_3CN solution, excited at 300 nm Number of molar equivalents added indicated in graph legends. **A)** Complex **2.1**, **b)** complex **2.2**, c) complex **2.3**, **d)** complex **2.4**, **e)** complex **2.5**. **f)** Stern-Volmer plot for emission quenching of complexes **2.1-2.5** with NEt_3. 212

Figure A.2.28 UV-vis spectra of complex **2.1** in a series of degassed solvents, the mixtures were excited by an array of UV LEDs (365 nm) for 4 hours, UV-vis profile was remeasured at specified time intervals to measure stability to UV light. 213

Figure A.2.29 UV-vis spectra of complex **2.1** in a series of degassed solvents, the mixtures were excited by an array of Blue light LEDs (465 nm) for 4 hours, UV-vis profile was remeasured at specified time intervals to measure stability to intense blue light. 213

Figure A.2.30 UV-vis spectra of complex **2.2** in a series of degassed solvents, the mixtures were excited by an array of UV LEDs (365 nm) for 4 hours, UV-vis profile was remeasured at specified time intervals to measure stability to UV light. 214

Figure A.2.31 UV-vis spectra of complex **2.2** in a series of degassed solvents, the mixtures were excited by an array of Blue light LEDs (465 nm) for 4 hours, UV-vis profile was remeasured at specified time intervals to measure stability to intense blue light. 214

Figure A.2.32 UV-vis spectra of complex **2.3** in a series of degassed solvents, the mixtures were excited by an array of UV LEDs (365 nm) for 4 hours, UV-vis profile was remeasured at specified time intervals to measure stability to UV light. 215

Figure A.2.33 UV-vis spectra of complex **2.3** in a series of degassed solvents, the mixtures were excited by an array of Blue light LEDs (465 nm) for 4 hours, UV-vis profile was remeasured at specified time intervals to measure stability to intense blue light. 215

Figure A.2.34 UV-vis spectra of complex **2.4** in a series of degassed solvents, the mixtures were excited by an array of UV LEDs (365 nm) for 4 hours, UV-vis profile was remeasured at specified time intervals to measure stability to intense blue light. 216

Figure A.2.35 UV-vis spectra of complex **2.4** in a series of degassed solvents, the mixtures were excited by an array of Blue light LEDs (465 nm) for 4 hours, UV-vis profile was remeasured at specified time intervals to measure stability to intense blue light. 216

Figure A.2.36 UV-vis spectra of complex **2.5** in a series of degassed solvents, the mixtures were excited by an array of UV LEDs (365 nm) for 4 hours, UV-vis profile was remeasured at specified time intervals to measure stability to UV light. 217

Figure A.2.37 UV-vis spectra of complex **2.5** in a series of degassed solvents, the mixtures were excited by an array of Blue light LEDs (465 nm) for 4 hours, UV-vis profile was remeasured at specified time intervals to measure stability to intense blue light. 217

Figure A.2.38 UV-vis titration of complex **2.2** in MeCN 1×10^{-5} M with molar additions of TFA in MeCN. The legend indicating how many molar equivalents are present in each scan. 218

Figure A.2.39 UV-vis dilution of complex **2.2** in MeCN 1×10^{-5} M with additions of MeCN without TFA. Volume of MeCN added was equal to the additions in the TFA titration of figure S55. 218

Figure A.2.40 UV-vis spectra of complex **2.2** in DMSO:H_2O (1:1) 1×10^{-5} M in varying Ph conditions. 218

Figure A.2.41 Biexponential lifetime decay of Ir(III) complex **2.1**, ~$1\cdot10^{-5}$ M (Absorbance of 0.065 from UV-Vis) in $CHCl_3$ degassed for 20 mins (Ar) at 298 K after excitation at 365 nm. Data collected at λ_{max} = 470 nm. 219

Figure A.2.42 Fit result of Ir(III) complex **2.1**, ~$1\cdot10^{-5}$ M (Absorbance of 0.065 from UV-Vis) in $CHCl_3$ degassed for 20 mins (Ar) at 298 K after excitation at 365 nm. Data collected at λ_{max} = 470 nm. 219

Figure A.2.43 Monoexponential lifetime decay of Ir(III) complex **2.2**, ~$1\cdot10^{-5}$ M (Absorbance of 0.081 from UV-Vis) in $CHCl_3$ degassed for 20 mins (Ar) at 298 K after excitation at 365 nm. Data collected at λ_{max} = 540 nm. 220

Figure A.2.44 Fit result of Ir(III) complex **2.2**, ~$1\cdot10^{-5}$ M (Absorbance of 0.081 from UV-Vis) in $CHCl_3$ degassed for 20 mins (Ar) at 298 K after excitation at 365 nm. Data collected at λ_{max} = 540 nm. 220

Figure A.2.45 Biexponential lifetime decay of Ir(III) complex **3,** ~$1 \cdot 10^{-5}$ M (Absorbance of 0.079 from UV-Vis) in $CHCl_3$ degassed for 20 mins (Ar) at 298 K after excitation at 365 nm. Data collected at λ_{max} = 540 nm..... 221

Figure A.2.46 Fit result of Ir(III) complex **3**, ~$1 \cdot 10^{-5}$ M (Absorbance of 0.079 from UV-Vis) in $CHCl_3$ degassed for 20 mins (Ar) at 298 K after excitation at 365 nm. Data collected at λ_{max} = 540 nm. 221

Figure A.2.47 Biexponential lifetime decay of Ir(III) complex **2.4,** ~$1 \cdot 10^{-6}$ M (Absorbance of 0.073 from UV-Vis) in $CHCl_3$ degassed for 20 mins (Ar) at 298 K after excitation at 365 nm. Data collected at λ_{max} = 540 nm. 222

Figure A.2.48 Fit result of Ir(III) complex **2.4**, ~$1 \cdot 10^{-6}$ M (Absorbance of 0.073 from UV-Vis) in $CHCl_3$ degassed for 20 mins (Ar) at 298 K after excitation at 365 nm. Data collected at λ_{max} = 540 nm. 222

Figure A.2.49 Biexponential lifetime decay of Ir(III) complex **2.5,** ~$1 \cdot 10^{-6}$ M (Absorbance of 0.080 from UV-Vis) in $CHCl_3$ degassed for 20 mins (Ar) at 298 K after excitation at 365 nm. Data collected at λ_{max} = 540 nm. 223

Figure A.2.50 Fit result of Ir(III) complex **2.5**, ~$1 \cdot 10^{-6}$ M (Absorbance of 0.080 from UV-Vis) in $CHCl_3$ degassed for 20 mins (Ar) at 298 K after excitation at 365 nm. Data collected at λ_{max} = 540 nm. 223

Figure A.3.1 ^{1}H NMR spectrum of orange iridium complex **3.3**, $CDCl_3$, 400 MHz, 298 K..... 237

Figure A.3.2 ^{13}C NMR spectrum of orange iridium complex **3.3**, $CDCl_3$, 101 MHz, 298 K..... 237

Figure A.3.3 Mass spectrum of iridium complex **3.3**. HMRS [ESI+] ion $[C_{48}H_{41}IrN_7S_2]^+$ m/z calculated: 972.2488. Found: 972.2498 [M+]. 238

Figure A.3.4 ^{1}H NMR spectrum of red iridium complex **3.4**, $CDCl_3$, 400 MHz, 298 K. 238

Figure A.3.5 ^{13}C NMR spectrum of red iridium complex **3.4**, $CDCl_3$, 101 MHz, 298 K. 239

Figure A.3.6 Mass spectrum of iridium complex **3.4**. HMRS [ESI+] ion $[C_{48}H_{41}IrN_7S_2]^+$ m/z calculated: 872.2176. Found: 872.2202 [M+]. 239

Figure A.3.7 ^{1}H NMR spectrum of compound **3.5**, DMSO-d_6, 400 MHz, 298 K..... 240

Figure A.3.8 ^{13}C NMR spectrum of compound **3.5**, DMSO-d_6, 101 MHz, 298 K..... 240

Figure A.3.9 Mass spectrum for compound **3.5**. LMRS [ESI+] ion $[C_{11}H_8N_4]^+$..... 241

Figure A.3.10 ^{1}H NMR spectrum of compound **3.7** with inset ^{1}H NMR spectrum expanded into aromatic region, $CDCl_3$, 400 MHz, 298 K. 241

Figure A.3.11 ^{13}C NMR spectrum of compound **3.7**, $CDCl_3$, 101 MHz, 298 K. 242

Figure A.3.12 ^{1}H NMR spectrum of compound **3.8** with inset ^{1}H NMR spectrum expanded into aromatic region, $CDCl_3$, 400 MHz, 298 K. 242

Figure A.3.13 ^{13}C NMR spectrum of compound **3.8**, $CDCl_3$, 101 MHz, 298 K. 243

Figure A.3.14 UV-vis absorption spectra of complexes **3.1** (blue line), **3.2** (yellow line), **3.3** (black line) and **3.4** (red line) in $CHCl_3$, c = 1×10^{-5} M. 243

Figure A.3.15 Normalised emission and excitation spectra of iridium complex **3.1** (c = 1×10^{-5} M) measured in $CHCl_3$ solution. 244

Figure A.3.16 Emission spectra from studies of complex **3.1** with additions of compound **3.5** measured in $CHCl_3$ solution. All samples excited at 350 nm. 244

Figure A.3.17 Normalised emission and excitation spectra of iridium complex **3.2** (c = 1×10^{-5} M) measured in $CHCl_3$ solution. 245

Figure A.3.18 Normalised emission and excitation spectra of iridium complex **3.3** (c = 1×10^{-5} M) measured in $CHCl_3$ solution. 245

Figure A.3.19 Emission spectra from studies of complex **3.3** with additions of compound **3.5** measured in $CHCl_3$ solution. All samples excited at 350 nm. 246

Figure A.3.20 Normalised emission and excitation spectra of iridium complex **3.4** (c = 1×10^{-5} M) measured in $CHCl_3$ solution. 246

Figure A.3.21 Emission spectra from studies of complex **3.4** with additions of compound **3.5** measured in $CHCl_3$ solution. All samples excited at 360 nm. 247

Figure A.3.22 Screengrab of linear regression bindfit calculation data of co-system **3.1•3.5**. Links to open-source calculations of titration runs presented below. 247

Figure A.3.23 Screengrab of linear regression bindfit calculation data of co-system **3.2•3.5**. Links to open-source calculations of titration runs presented below. 248

Figure A.3.24 Screengrab of linear regression bindfit calculation data of co-system **3.3•3.5**. Links to open-source calculations of titration runs presented below. 248

Figure A.3.25 Screengrab of linear regression bindfit calculation data of co-system **3.4•3.5**. Links to open-source calculations of titration runs presented below. 249

Figure A.3.26 Biexponential lifetime decay of Ir(III) complex **3.1**, ~$1 \cdot 10^{-5}$ M (Absorbance of 0.065 from UV-Vis) in $CHCl_3$ degassed for 20 mins (Ar) at 298 K after excitation at 365 nm. Data collected at λ_{max} = 470 nm. 250

Figure A.3.27 Fit result of Ir(III) complex **3.1**, ~$1 \cdot 10^{-5}$ M (Absorbance of 0.065 from UV-Vis) in $CHCl_3$ degassed for 20 mins (Ar) at 298 K after excitation at 365 nm. Data collected at λ_{max} = 470 nm. 250

Figure A.3.28 Monoexponential lifetime decay of Ir(III) complex **3.2**, ~$1 \cdot 10^{-5}$ M (Absorbance of 0.081 from UV-Vis) in $CHCl_3$ degassed for 20 mins (Ar) at 298 K after excitation at 365 nm. Data collected at λ_{max} = 540 nm. 251

Figure A.3.29 Fit result of Ir(III) complex **3.2**, ~$1 \cdot 10^{-5}$ M (Absorbance of 0.081 from UV-Vis) in $CHCl_3$ degassed for 20 mins (Ar) at 298 K after excitation at 365 nm. Data collected at λ_{max} = 540 nm. 251

Figure A.3.30 Biexponential lifetime decay of Ir(III) complex **3.3,** ~$1 \cdot 10^{-6}$ M (Absorbance of 0.079 from UV-Vis) in $CHCl_3$ degassed for 20 mins (Ar) at 298 K after excitation at 365 nm. Data collected at λ_{max} = 570 nm. 252

Figure A.3.31 Fit result of Ir(III) complex **3.3**, ~$1 \cdot 10^{-6}$ M (Absorbance of 0.079 from UV-Vis) in $CHCl_3$ degassed for 20 mins (Ar) at 298 K after excitation at 365 nm. Data collected at λ_{max} = 570 nm. 252

Figure A.3.32 Monoexponential lifetime decay of Ir(III) complex **3.4,** ~$1 \cdot 10^{-6}$ M (Absorbance of 0.076 from UV-Vis) in $CHCl_3$ degassed for 20 mins (Ar) at 298 K after excitation at 365 nm. Data collected at λ_{max} = 590 nm. 253

Figure A.3.33 Fit result of Ir(III) complex **3.4**, ~$1 \cdot 10^{-6}$ M (Absorbance of 0.076 from UV-Vis) in $CHCl_3$ degassed for 20 mins (Ar) at 298 K after excitation at 365 nm. Data collected at λ_{max} = 590 nm. 253

Figure A.3.34 Biexponential lifetime decay of Ir(III) complex **3.1•3.5,** (1:1) ~$1 \cdot 10^{-5}$ M (Absorbance of 0.071 from UV-Vis) in $CHCl_3$ degassed for 20 mins (Ar) at 298 K after excitation at 365 nm. Data collected at λ_{max} = 470 nm. 254

Figure A.3.35 Fit result of Ir(III) complex **3.1•3.5,** (1:1) ~$1 \cdot 10^{-5}$ M (Absorbance of 0.071 from UV-Vis) in $CHCl_3$ degassed for 20 mins (Ar) at 298 K after excitation at 365 nm. Data collected at λ_{max} = 470 nm. 254

Figure A.3.36 Monoexponential lifetime decay of Ir(III) complex **3.2•3.5,** (1:1) ~$1 \cdot 10^{-5}$ M (Absorbance of 0.085 from UV-Vis) in $CHCl_3$ degassed for 20 mins (Ar) at 298 K after excitation at 365 nm. Data collected at λ_{max} = 540 nm. 255

Figure A.3.37 Fit result of Ir(III) complex **3.2•3.5,** (1:1) ~$1 \cdot 10^{-5}$ M (Absorbance of 0.085 from UV-Vis) in $CHCl_3$ degassed for 20 mins (Ar) at 298 K after excitation at 365 nm. Data collected at λ_{max} = 540 nm. 255

Figure A.3.38 Biexponential lifetime decay of Ir(III) complex **3.3•3.5,** (1:1) ~$1 \cdot 10^{-6}$ M (Absorbance of 0.080 from UV-Vis) in $CHCl_3$ degassed for 20 mins (Ar) at 298 K after excitation at 365 nm. Data collected at λ_{max} = 570 nm. 256

Figure A.3.39 Fit result of Ir(III) complex **3.3•3.5,** (1:1) ~$1 \cdot 10^{-6}$ M (Absorbance of 0.080 from UV-Vis) in $CHCl_3$ degassed for 20 mins (Ar) at 298 K after excitation at 365 nm. Data collected at λ_{max} = 570 nm. 256

Figure A.3.40 Biexponential lifetime decay of Ir(III) complex **3.4•3.5,** (1:1) ~$1 \cdot 10^{-6}$ M (Absorbance of 0.085 from UV-Vis) in $CHCl_3$ degassed for 20 mins (Ar) at 298 K after excitation at 365 nm. Data collected at λ_{max} = 590 nm. 257

Figure A.3.41 Fit result of Ir(III) complex **3.4•3.5,** (1:1) ~$1 \cdot 10^{-6}$ M (Absorbance of 0.085 from UV-Vis) in $CHCl_3$ degassed for 20 mins (Ar) at 298 K after excitation at 365 nm. Data collected at λ_{max} = 590 nm. 257

Figure A.3.42 Monoexponential lifetime decay of Ir(III) complex **3.2•3.5,** (1:1.3) ~$1 \cdot 10^{-5}$ M (Absorbance of 0.082 from UV-Vis) in $CHCl_3$ degassed for 20 mins (Ar) at 298 K after excitation at 365 nm. Data collected at λ_{max} = 540 nm. 258

Figure A.3.43 Fit result of Ir(III) complex **3.2•3.5,** (1:1) ~$1 \cdot 10^{-5}$ M (Absorbance of 0.082 from UV-Vis) in $CHCl_3$ degassed for 20 mins (Ar) at 298 K after excitation at 365 nm. Data collected at λ_{max} = 540 nm. 258

Figure A.3.44 Combined normalised emission spectra of complex **1**-**4** obtained through solid state excitation of PMMA thin films. 259

Figure A.3.45 Combined normalised absorption spectra of complex **1**-**4** obtained through solid state analysis of PMMA thin films. 260

Figure A.3.46 Combined normalised emission spectra of co-complex **1**-**4•5** obtained through solid state excitation of PMMA thin films. 260

Figure A.3.47 Combined normalised absorption spectra of co-complex **1**-**4•5** obtained through solid state analysis of PMMA thin films. 261

Figure A.3.48 Biexponential lifetime decay of Ir(III) complex **3.1** in PMMA film at 298 K, excited at 365 nm. Data collected at λ_{max} = 495 nm. 262

Figure A.3.49 Fit result of Ir(III) complex **3.1** in PMMA film at 298 K, excited at 365 nm. Data collected at λ_{max} = 495 nm..... 262

Figure A.3.50 Biexponential lifetime decay of Ir(III) complex **3.2** in PMMA film at 298 K, excited at 365 nm. Data collected at λ_{max} = 580 nm. 263

Figure A.3.51 Fit result of Ir(III) co-system **3.2** in PMMA film at 298 K, excited at 365 nm. Data collected at λ_{max} = 580 nm..... 263

Figure A.3.52 Biexponential lifetime decay of Ir(III) complex **3.3** in PMMA film at 298 K, excited at 365 nm. Data collected at λ_{max} = 598 nm. 264

Figure A.3.53 Fit result of Ir(III) co-system **3.3** in PMMA film at 298 K, excited at 365 nm. Data collected at λ_{max} = 598 nm..... 264

Figure A.3.54 Biexponential lifetime decay of Ir(III) complex **3.4** in PMMA film at 298 K, excited at 365 nm. Data collected at λ_{max} = 595 nm. 265

Figure A.3.55 Fit result of Ir(III) co-system **3.4** in PMMA film at 298 K, excited at 365 nm. Data collected at λ_{max} = 595 nm..... 265

Figure A.3.56 Biexponential lifetime decay of Ir(III) co-system **3.1•3.5** in PMMA film at 298 K, excited at 365 nm. Data collected at λ_{max} = 496 nm. 266

Figure A.3.57 Fit result of Ir(III) co-system **3.1•3.5** in PMMA film at 298 K, excited at 365 nm. Data collected at λ_{max} = 496 nm..... 266

Figure A.3.58 Biexponential lifetime decay of Ir(III) complex **3.2•3.5** in PMMA film at 298 K, excited at 365 nm. Data collected at λ_{max} = 581 nm. 267

Figure A.3.59 Fit result of Ir(III) co-system **3.2•3.5** in PMMA film at 298 K, excited at 365 nm. Data collected at λ_{max} = 581 nm..... 267

Figure A.3.60 Biexponential lifetime decay of Ir(III) complex **3.3•3.5** in PMMA film at 298 K, excited at 365 nm. Data collected at λ_{max} = 599 nm. 268

Figure A.3.61 Fit result of Ir(III) co-system **3.3•3.5** in PMMA film at 298 K, excited at 365 nm. Data collected at λ_{max} = 599 nm..... 268

Figure A.3.62 Biexponential lifetime decay of Ir(III) complex **3.4•3.5** in PMMA film at 298 K, excited at 365 nm. Data collected at λ_{max} = 595 nm. 269

Figure A.3.63 Fit result of Ir(III) co-system **3.4•3.5** in PMMA film at 298 K, excited at 365 nm. Data collected at λ_{max} = 595 nm..... 269

Figure A.3.64 Cyclic voltammetry of complexes **3.1-3.4** and co-systems **3.1•3.5-3.4•3.5** 2 mM in dry degassed $CHCl_3$ normalised to a ferrocene standard. **a)** complex **4.1**, **b)** co-system **3.1•3.5**, **c)** complex **3.2**, **d)** co-system **3.2•3.5**, **e)** complex **3.3**, **f)** co-system **3.3•3.5**, **g)** complex **3.3** and **h)** co-system **3.4•3.5**. 270

Figure A.4.1 ^{1}H NMR spectrum of iridium complex **4.1**, DMSO-*d*$_6$, 400 MHz, 298 K. 301

Figure A.4.2 ^{13}C NMR spectrum of iridium complex **4.1,** DMSO-*d*$_6$, 101 MHz, 298 K. 301

Figure A.4.3 Mass spectrum of iridium complex **4.1**. HMRS [ESI+] ion $[C_{38}H_{33}IrN_7S_2]^+$ m/z calculated: 844.1863 Found: 844.1868 [M+]. 302

Figure A.4.4 ^{1}H NMR spectrum of iridium complex **4.2**, DMSO-*d*$_6$, 400 MHz, 298 K. 302

Figure A.4.5 ^{13}C NMR spectrum of iridium complex **4.2**, DMSO-d_6, 101 MHz, 298 K. 303

Figure A.4.6 Mass spectrum of iridium complex **4.2**. HMRS [ESI+] ion $[C_{42}H_{43}IrN_9S_2]^+$ m/z calculated: 930.2707 Found: 930.2669 [M+]. 303

Figure A.4.7 ^{1}H NMR spectrum of iridium complex **4.3**, DMSO-d_6, 400 MHz, 298 K. 304

Figure A.4.8 ^{13}C NMR spectrum of iridium complex **4.3**, DMSO-d_6, 101 MHz, 298 K. 304

Figure A.4.9 Mass spectrum of iridium complex **4.3**. HMRS [ESI+] ion $[C_{30}H_{29}IrN_7S_2]^+$ m/z calculated: 744.1550. Found: 744.1547 [M+]. 305

Figure A.4.10 ^{1}H NMR spectrum of iridium complex **4.4**, DMSO-d_6, 400 MHz, 298 K. 305

Figure A.4.11 ^{13}C NMR spectrum of iridium complex **4.4**, DMSO-d_6, 101 MHz, 298 K. 306

Figure A.4.12 Mass spectrum of iridium complex **4.4**. HMRS [ESI+] ion $[C_{38}H_{37}IrN_7O_2]^+$ m/z calculated: 816.2633. Found: 816.2633 [M+]. 306

Figure A.4.13 ^{1}H NMR spectrum of ligand **4.7**, DMSO-d_6, 400 MHz, 298 K..... 307

Figure A.4.14 ^{13}C NMR spectrum of ligand **4.7**, DMSO-d_6, 101 MHz, 298 K..... 307

Figure A.4.15 ^{1}H NMR spectrum of ligand **4.8**, $CDCl_3$, 400 MHz, 298 K. 308

Figure A.4.16 ^{13}C NMR spectrum of ligand **4.8**, $CDCl_3$, 101 MHz, 298 K. 308

Figure A.4.17 ^{1}H NMR spectrum of ligand **4.9**, $CDCl_3$, 400 MHz, 298 K. 309

Figure A.4.18 ^{13}C NMR spectrum of ligand **4.9**, $CDCl_3$, 101 MHz, 298 K. 309

Figure A.4.19 ^{1}H NMR spectrum of ligand **4.10**, DMSO-d_6, 400 MHz, 298 K..... 310

Figure A.4.20 ^{13}C NMR spectrum of ligand **4.10**, DMSO-d_6, 101 MHz, 298 K..... 310

Figure A.4.21 Normalised emission and excitation spectra of iridium complexes **4.1-4.4** ($c = 1\times10^{-5}$ M) measured in $CHCl_3$ solution. **a)** Complex **4.1**, **b)** complex **4.2**, **c)** complex **4.3**, **d)** complex **4.4**. 311

Figure A.4.22 Overlaid emission spectra of complexes **4.1** with deep blue emitter compound **4.5** (blue) and co-systems **4.1•4.5-4.1•4.5** from FRET experiments in $CHCl_3$ solution. All samples excited at λ_{ex} = 350 nm. **a)** Complex **4.1** and co-system **4.1•4.5**, **b)** complex **4.2** and co-system **4.2•4.5**, **c)** complex **4.3** and co-system **4.3•4.5**, **d)** complex **4.4** and co-system **4.4•4.5**. 312

Figure A.4.23 Emission titrations of complexes **4.1-4.4** with deep blue emitter **4.5** used to create CIE plots in figure **4.6**. Equivalents added are indicated in the legend of each graph; **a)** complex **4.1** with **4.5**, **b)** complex **4.2** with **4.5**, **c)** complex **4.3** with **4.5** and **d)** complex **4.4** with **4.5**..... 313

Figure A.4.24 UV-vis titration of complexes **4.1-4.4** with additions of compound **4.5** in $CHCl_3$ at 298 K. Initial concentration of complexes **4.1-4.4** is 1×10^{-5} M, the legend indicates molar equivalents of compound **4.5** added. **a)** complex **4.1** with **4.5**, **b)** complex **4.2** with **4.5**, **c)** complex **4.3** with **4.5** and **d)** complex **4.4** with **4.5**. 314

Figure A.4.25 Screengrab of linear regression bindfit calculation data of co-system **4.1•4.5**. Links to open-source calculations of titration runs presented below. 315

Figure A.4.26 Screengrab of linear regression bindfit calculation data of co-system **4.2•4.5**. Links to open-source calculations of titration runs presented below. 315

Figure A.4.27 Screengrab of linear regression bindfit calculation data of co-system **4.3•4.5**. Links to open-source calculations of titration runs presented below. 316

Figure A.4.28 Screengrab of linear regression bindfit calculation data of co-system **4.4•4.5**. Links to open-source calculations of titration runs presented below. 316

Figure A.4.29 Biexponential lifetime decay of Ir(III) complex **4.1**, ~$1 \cdot 10^{-5}$ M in $CHCl_3$ degassed for 20 mins (Ar) at 298 K after excitation at 365 nm. Data collected at λ_{max} = 470 nm. 317

Figure A.4.30 Fit result of Ir(III) complex **4.1**, ~$1 \cdot 10^{-5}$ M in $CHCl_3$ degassed for 20 mins (Ar) at 298 K after excitation at 365 nm. Data collected at λ_{max} = 470 nm. 317

Figure A.4.31 Biexponential lifetime decay of Ir(III) complex **4.1•4.5,** (1:24) ~$1 \cdot 10^{-5}$ M in $CHCl_3$ degassed for 20 mins (Ar) at 298 K after excitation at 365 nm. Data collected at λ_{max} = 540 nm..... 318

Figure A.4.32 Fit result of Ir(III) complex **4.1•4.5,** (1:24) ~$1 \cdot 10^{-5}$ M in $CHCl_3$ degassed for 20 mins (Ar) at 298 K after excitation at 365 nm. Data collected at λ_{max} = 540 nm. 318

Figure A.4.33 Biexponential lifetime decay of Ir(III) complex **4.2**, ~$1 \cdot 10^{-5}$ M in $CHCl_3$ degassed for 20 mins (Ar) at 298 K after excitation at 365 nm. Data collected at λ_{max} = 470 nm. 319

Figure A.4.34 Fit result of Ir(III) complex **4.2**, ~$1 \cdot 10^{-5}$ M in $CHCl_3$ degassed for 20 mins (Ar) at 298 K after excitation at 365 nm. Data collected at λ_{max} = 470 nm. 319

Figure A.4.35 Biexponential lifetime decay of Ir(III) complex **4.2•4.5,** (1:32) ~$1 \cdot 10^{-5}$ M in $CHCl_3$ degassed for 20 mins (Ar) at 298 K after excitation at 365 nm. Data collected at λ_{max} = 540 nm..... 320

Figure A.4.36 Fit result of Ir(III) complex **4.2•4.5,** (1:32) ~$1 \cdot 10^{-5}$ M in $CHCl_3$ degassed for 20 mins (Ar) at 298 K after excitation at 365 nm. Data collected at λ_{max} = 540 nm. 320

Figure A.4.37 Biexponential lifetime decay of Ir(III) complex **4.3**, ~$1 \cdot 10^{-5}$ M in $CHCl_3$ degassed for 20 mins (Ar) at 298 K after excitation at 365 nm. Data collected at λ_{max} = 470 nm. 321

Figure A.4.38 Fit result of Ir(III) complex **4.3**, ~$1 \cdot 10^{-5}$ M in $CHCl_3$ degassed for 20 mins (Ar) at 298 K after excitation at 365 nm. Data collected at λ_{max} = 470 nm. 321

Figure A.4.39 Biexponential lifetime decay of Ir(III) complex **4.3•4.5,** (1:20) ~$1 \cdot 10^{-5}$ M in $CHCl_3$ degassed for 20 mins (Ar) at 298 K after excitation at 365 nm. Data collected at λ_{max} = 540 nm..... 322

Figure A.4.40 Fit result of Ir(III) complex **4.3•4.5,** (1:20) ~$1 \cdot 10^{-5}$ M in $CHCl_3$ degassed for 20 mins (Ar) at 298 K after excitation at 365 nm. Data collected at λ_{max} = 540 nm. 322

Figure A.4.41 Biexponential lifetime decay of Ir(III) complex **4.4**, ~$1 \cdot 10^{-5}$ M in $CHCl_3$ degassed for 20 mins (Ar) at 298 K after excitation at 365 nm. Data collected at λ_{max} = 470 nm. 323

Figure A.4.42 Fit result of Ir(III) complex **4.4**, ~$1 \cdot 10^{-5}$ M in $CHCl_3$ degassed for 20 mins (Ar) at 298 K after excitation at 365 nm. Data collected at λ_{max} = 470 nm. 323

Figure A.4.43 Biexponential lifetime decay of Ir(III) complex **4.4•4.5**, (1:25) ~$1 \cdot 10^{-5}$ M (Absorbance of 0.082 from UV-Vis) in $CHCl_3$ degassed for 20 mins (Ar) at 298 K after excitation at 365 nm. Data collected at λ_{max} = 540 nm. 324

Figure A.4.44 Fit result of Ir(III) complex **4.4•4.5,** (1:25) ~$1 \cdot 10^{-5}$ M (Absorbance of 0.082 from UV-Vis) in $CHCl_3$ degassed for 20 mins (Ar) at 298 K after excitation at 365 nm. Data collected at λ_{max} = 540 nm..... 324

Figure A.4.45 Cyclic voltammetry of complexes **4.1-4.4** and co-systems **4.1•4.5-4.4•4.5** 2 mM in dry degassed $CHCl_3$ normalised to a ferrocene standard. **a)** complex **4.1**, **b)** co-system **4.1•4.5**, **c)** complex **4.2**, **d)** co-system **4.2•4.5**, **e)** complex **4.3**, **f)** co-system **4.3•4.5**, **g)** complex **4.4** and **h)** co-system **4.4•4.5**. 325

List of Schemes

Scheme A.2.1 General procedure for the synthesis of the 1-(1H-benzo[d]imidazole-2-yl)-3-butylguanidine ligand (**2.6**) is as follows. Reagents and conditions: a) MeCN, 50 °C, 20 hours; b) *n*-butyl amine, catalytic DMAP, DMF, 100 °C, 18 hr; c) HgO, (NH_3/MeOH (2 M)), $CHCl_3$, room temperature, 3 hours. 188

Scheme A.2.2 The routes for the preparation of the ligands **2.7** and **2.8**. Reagents and conditions: a) NMP, pyridine, N_2, 202 °C, 5 hr; b) MeCN, K_2CO_3, N_2, 90 °C, 12 hr.... 188

Scheme A.2.3 The general synthetic route of all iridium complexes herein. Reagents and conditions: a) 2- ethoxyethanol: water (3:1), 130 °C, 19 hr; b) K_2CO_3, toluene, N_2, 110 °C, 16 hr. Ligands **2.9-2.11** were all synthesised using previously established procedures in the literature. 189

Scheme A.3.1 Synthesis of ligand **3.7** and **3.8**. Reagents and conditions: 3 mol % $Pd(Ph_3)_4$, 5% solution of Na_2CO_3, dry THF, reflux, 24 hr, N_2 (g)..... 230

Scheme A.3.2 The general synthetic route of all iridium complexes herein. Reagents and conditions: a) 2-ethoxyethanol: water (3:1), reflux, 19 hr; b) 1-(1H-benzo[d]imidazole-2-yl)-3-butylguanidine **3.6**, K_2CO_3, toluene, N_2 (g)..... 230

Scheme A.3.3 The synthetic route of compound **3.5**. Reagents and conditions: a) DMF, 0°C to rt., 3 hr, 88%; b) MW, K_2CO_3, $Pd(PPh_3)_4$, dioxane:water (3:1), 150 °C, 3 hr N_2 (g). 230

Scheme A.4.1 The general synthetic route of all iridium complexes herein. Reagents and conditions: a) 2-ethoxyethanol: water (3:1), 130 °C, 19 hr; b) K_2CO_3, toluene, N_2, 110

°C, 16 hr. Ligands **4.6-4.10** were all synthesised using microwave modified procedures from the literature. 294

List of Symbols, Nomenclature, or Abbreviations

A – Acceptor

A – Adenine

acac – Acetylacetonate

a_i – Relative Brightness

atm – Atmospheres

a.u. – Arbitrary Units

B3LYP – Becke, 3-parameter, Lee-Yang-Parr

bpy – Bipyridine

bt – Benzothiazole

C – Carbon

C – Cytosine

°C – Degrees Celsius

^{13}C NMR – Carbon-13 Nuclear Magnetic Resonance Spectroscopy

C^N – Carbon and Nitrogen Bound Ligand

cat – Photoredox Co-Catalyst

CIE – Commission Internationale d'Eclairage

$CDCl_3$ – Deuterated Chloroform

CD_2Cl_2 – Deuterated Dichloromethane

CH_4 – Methane

$CHCl_3$ – Chloroform

CH_2Cl_2 – Dichloromethane

CH_3CN – Acetonitrile

CHPh – Cycloheptane

Cl – Chloride

Co(II) – Cobalt (II)

CO_2 – Carbon Dioxide

cps – Photon Count per Second

Cr(III) – Chromium (III)

18-crown-6 – 1,4,7,10,13,16-Hexaoxacyclooctadecane

CT – Charge Transfer

Cu(II) – Copper (II)

CV– Cyclic Voltammetry

Cy_3P – Tricyclohexylphosphine

D – Donor

d – Doublet

DFT – Density Functional Theory

DMAP – Dimethyl-aminopyridine

DMF – Dimethyl Formamide

DMSO – Dimethyl Sulfoxide

DMSO-d_6 – Deuterated-Dimethyl Sulfoxide

DNA – Deoxyribonucleic Acid

$E_{(PS+/PS*)}$ – Photochemical Oxidation

$E_{(PS*/PS-)}$ – Photochemical Reduction

$E_{0\text{-}0}$ – Optoelectronic Bandgap

E_{ox} – Oxidation Potential

E_{red} – Reduction Potential

ΔE – Change in Chemistry

EBU – European Broadcasting Union

ECP – Effective Core Potential

ED – Electron Donor

EDG – Electron Donating Group

ESI – Electron-Spray Ionisation

EWG – Electron Withdrawing Group

eV – Electron Volts

F – Fluorine

fac- – Facial

FMO – Frontier Molecular Orbital

FRET – Föster Resonance Energy Transfer

G – Guanine

[G] – Guest

ΔG – Change in Gibbs Free Energy

GC-MS – Gas Chromatography - Mass Spectrometry

GGA – Generalised Gradient Approximation

h – Planck's Constant

H – Hamiltonian

H – Hydrogen

H_2 – Hydrogen

H^+ – Proton

H-bond – Hydrogen-bond

^{1}H NMR – Proton Nuclear Magnetic Resonance Spectroscopy

[H] – Host

HER – Hydrogen Evolution Reaction

[HG] – Host-Guest Assembly

[HG$_2$] – One Host – Two Guest Assembly

HK – Hohenberg-Kohn Theorems

HNC(NH$_2$)$_2$ – Guanidine Molecular Formula

HOMO – Highest Occupied Molecular Orbital

H$_2$O – Water

hr – hour

HRMS – High Resolution Mass Spectrometry

HT – High-Throughput

***H*(t)** – Hamiltonian as a function of Time

I – Emission Intensity

I – Intermediate

IC – Internal Conversion

Ir – Iridium

Ir(III) – Iridium (III)

IrCl$_3$ – Iridium Chloride

IMes – 1,3-Bis(2,4,6-trimethylphenyl)-1,3-dihydro-2*H*-imidazol-2-ylidene

ISC – Inter-System Crossing

IUPAC – International Union of Pure and Applied Chemistry

K – Kelvin

***K*$_a$** – Constant of Association

kcalmol^{-1} – Kilocalorie per Mole

kJmol^{-1} – kilojoules per mole

***k*$_{nr}$** – Non-Radiative Decay

***K*$_q$** – Quenching Constant

***k*$_r$** – Radiative Decay

***K*$_{sv}$** – Stern-Volmer Constant

***K*₁** – First Equilibrium Association Constant

***K*₂** – Second Equilibrium Association Constant

LANL2DZ – Los Alamos National Laboratory 2 double-ξ

^{1}LC – Singlet Ligand-Centred Transitions

^{3}LC – Singlet Ligand-Centred Transitions

LC-MS – Liquid Chromatography - Mass Spectrometry

^{3}LLCT – Ligand to Ligand Charge Transfer

LR – Linear-Response Formalism

LUMO – Lowest Unoccupied Molecular Orbital

M – Molarity

m – Multiplet

Me₂N-bt – 4-(benzothiazolato-N,C2′-2-yl)-N,N-dimethylaniline

mer- – Meridional

MJ/kg – Megajoules per Kilogram

mL – millilitres

ML – Machine Learning

MLCT – Metal to Ligand Charge Transfer

^{1}MLCT – Singlet Metal to Ligand Charge Transfer

^{3}MLCT – Triplet Metal to Ligand Charge Transfer

mm – millimetres

N – Nitrogen

N – Number of Electrons in a Many-Body System

Ni(II) – Nickel (II)

NMP – N-methylpyrrolidone

NMR – Nuclear Magnetic Resonance Spectroscopy

nm – Nanometres

N^N – Dual Nitrogen Bound Ligand

n(r) – Electron Density

ns – Nanosecond

NTSC – National Television System Committee

O – Oxygen

$^1O_2$ – Reactive Oxygen Species

OH^- – Hydroxide

OLED – Organic Light Emitting Diode

O^N – Oxygen and Nitrogen Bound Ligand

O^O – Dual Oxygen Bound Ligand

PC – Photocatalyst

Pd(II) – Palladium (II)

P_F – Fermi Momentum

PF_6 – Hexafluorophosphate

pH – Potential of Hydrogen

PhOLED – Phosphorescent Organic Light Emitting Diode

pK_a – Negative Base-10 Logarithm of the Acid Dissociation Contant

PL – Photoluminescence

PLQY / Φ_{PL} – Photoluminescence Quantum Yield

PMMA – Polymethyl Methacrylate

ppy – Phenyl-Pyridine Ligands

ptz – 2-Phenylthiazolato-N

PS – Photosensitiser

[Q] – Concentration of Quencher

q – Quartet

R – Ideal Gas Constant

R – Reagent

RG – Runge-Gross Theorems

RGB – Red Green Blue Colour Mixing

ROS – Reactive Oxygen Species

$(R_1R_2N)(R_3R_4N)C{=}N\text{-}R_5$ – General Formula of Guanidine Derivatives

s – Seconds

s – Singlet

S_0 – Singlet Ground State

S_1 – Singlet Excited State

SDL – Self-driving Laboratories

SET – Single Electron Transfer

SOC – Spin-Orbit Coupling

T – Temperature

$\boldsymbol{T}$ – *N*-Electron Kinetic Energy

T – Thymine

t – Triplet

$\mathbf{T_1}$ – First Triplet Excited State

$\mathbf{T_2}$ – Second Triplet Excited State

TCSPC – Time Correlated Single Photon Counting

TD-DFT – Time-Dependent Density-Functional Theory

TEA – Triethylamine

$\mathbf{T_{ex}}$ – Excited Triplet State

TFA – Trifluoroacetic Acid

tmg – 1,1,2,(2-)Tetramethylguanidine

TON – Turnover Number

$\boldsymbol{U}$ – Electron-Electron Interaction

UV-vis – Ultraviolet-Visible Spectrophotometry

V – Volts

$\boldsymbol{V}$ – *N*-Electron Potential Energy from an External Field

$\boldsymbol{V_{ext}(t)}$ – *N*-Electron Potential Energy from an External Field as a Function of Time

$\boldsymbol{V_F}$ – Momentum-Space Volume

$\boldsymbol{W}$ – Energy of Spin-Independent Particle-Particle Interaction

WLED – White Light Emitting Diode

WOLED – White Organic Light Emitting Diode

WRC – Water Reduction Catalyst

Zn(II) – Zinc (II)

ε – Molar Absorption Coefficient

χ – Mole Fraction

λ – Wavelength

$\boldsymbol{\lambda_{em}}$ – Emission Wavelength

λ_{ex} – Excitation Wavelength

λ_{max} – Highest Wavelength of Emission

μs – Microseconds

ν – Frequency

ν(r) – External Potential

τ – Photophysical Lifetime

Φ – Quantum Yield

Φ_p – Phosphorescence Quantum Yield

Ψ – Wavefunction

Chapter 1

Introduction

1.1 Thesis Aims

This thesis discusses the properties and applications of a large series of hydrogen-bond (H-bond) rich iridium (III) complexes. This work is inspired by previous efforts to incorporate functional H-bonding arrays into highly photoluminescent Ir(III) complexes.[1–8] It was noted in preceding works that the incorporation of complimentary H-bond arrays (compounds 1.01 with 1.01) could allow for modification of the photoluminescent properties of Ir(III) complexes when a suitable H-bond compliment was introduced.[1] Figure 1.1 illustrates the assembly of H-bonding system of compound 1.01 with 1.02 and the effect adding increasing equivalents of 1.02 has on chromaticity.[1]

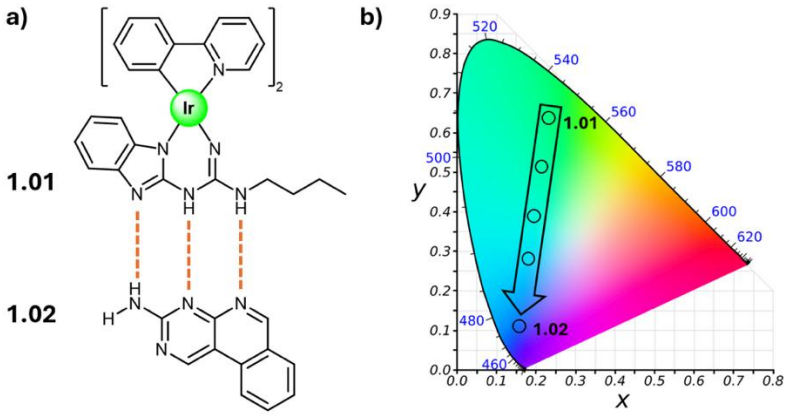


Figure 1.1 a) H-bonding schematic of compound **1.01** and **1.02** as studied by Balónová *et al.* **b)** Scheme of Commission Internationale de l'Eclairage (CIE) coordinates of photoluminescence titration of compound **1.01** with **1.02**.[1]

Further observation revealed energy transfer may have been occurring between the Ir(III) complex (host) and the H-bonding complementary guest facilitated by the H-

bonding arrays. This discovery informs the basis of this thesis: how can the properties of these H-bond rich Ir(III) complexes with and without appropriate guests be applied? This introductory chapter outlines the deeper inspirations for this work and how this thesis fits into the broader fields of inorganic and supramolecular chemistry.

1.2 Supramolecular Chemistry

Chemistry is often referred to as 'the molecular science'.[9] While this description may be appropriate for the characterisation of a unimolecular system, it negates to acknowledge that chemistry almost entirely takes place under dynamic conditions. Supramolecular chemistry is a highly interdisciplinary broad field of chemistry, referring to the study of intermolecular (non-covalent) interactions within dynamic chemical systems.[10] These non-covalent interactions include, but are not limited to π-π interactions, Van der Waals forces, metal coordination, electrostatic interactions and hydrogen-bonding.[4]

The existence of intermolecular forces was first postulated by Johannes Diderik Van der Waals in 1873.[11] While working on the characteristics of gases, he found neutral molecules in the gas phase were attracted to one another. He hypothesised that uneven electron distribution within molecules created 'temporary dipoles' causing weak electrostatic interactions to occur between the uncharged molecules.[12] Van der Waals forces are weak as they rely on temporary dipoles with a typical bond strength lying between 0.4-4 $kJmol^{-1}$, especially weak when compared to H-bonds which range from 2-168.2 $kJmol^{-1}$.[13] Van der Waals interactions are a universal intermolecular force between all molecules, but are sufficiently weak to be dwarfed by other stronger electrostatic

interactions like H-bonds. H-bonds consist of strong electrostatic interactions powered by a sharp difference in electronegativity between the donor atom bearing at least one lone pair of electrons (N, O, F, or Cl) and a hydrogen covalently bound to a separate donor on another molecule.[13] Supramolecular chemistry builds upon the discovery of intermolecular forces by studying the strength of higher order associations that exist between molecules and the intermolecular forces which govern them.[14]

Supramolecular chemistry can trace its philosophical roots to the work of Nobel Laureate Hermann Emil Fischer.[14,15] Fischer proposed that enzyme and substrate interactions resemble a 'lock and key', a concept broadly accepted in biology today.[14,16] This concept is also the basis of molecular recognition and host-guest chemistry, the study of which leads to a greater understanding of biomacromolecules and their processes.[16,17] While studying biological systems and their host-guest chemistry is of great importance, scientists have also worked on developing synthetic structures involving non-covalent interactions including; crown ethers (seen below in figure 1.2), micelles, vesicles, and mechanically interlocked molecules, with some leading to artificial molecular machines.[10,18–22] Development of these artificial systems helps scientists gain a greater understanding of how biological systems interact through their non-covalent interactions,[23] as synthetic systems are often far simpler than their biological counterparts and are therefore easier to monitor in-situ.[19]

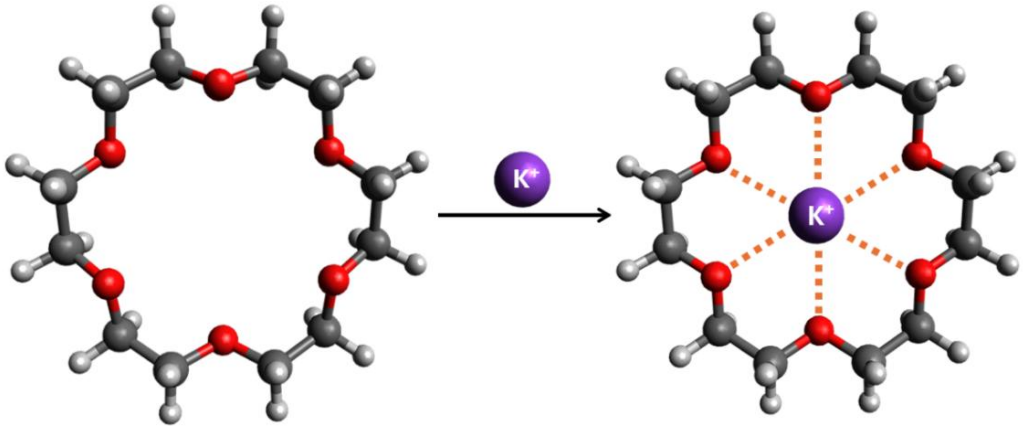


Figure 1.2 Binding of 18-crown-6 to potassium cations as discovered by Charles J. Pedersen *et al.*[24]

In 1987 the Nobel prize in chemistry was awarded to Donald J. Cram, Jean-Maire Lehn and Charles J. Pedersen 'for their development and use of molecules with structure-specific interactions of high selectivity'.[25] Following this award and the establishment of the field of supramolecular chemistry as a promising field of study, developments in the area accelerated.[18] Though the first rotaxane had been published in 1969 by Gottfried Schill and Hubertus Zollenkopf and was the first example of a macrocyclic ring being threaded onto a linear aromatic moiety,[26] it wasn't until the demonstration of stimuli-response behaviour that mechanically interlocked molecules saw broader interest.[19] J. Fraser Stoddart, Angel E. Kaifer and co-workers reported the first non-degenerate 'molecular shuttle' in 1994, incorporating a macrocycle that was able to 'shuttle' in a controlled fashion between 'stations' upon a thread using electrochemical signals to influence motion (shown below in figure 1.3).[20] Dave Leigh and co-workers also published several crucial works in this field, of particular note being the first example of a rotaxane-based molecular machine which had light-based unidirectional rotation attributed to reversible electron transfer.[21]

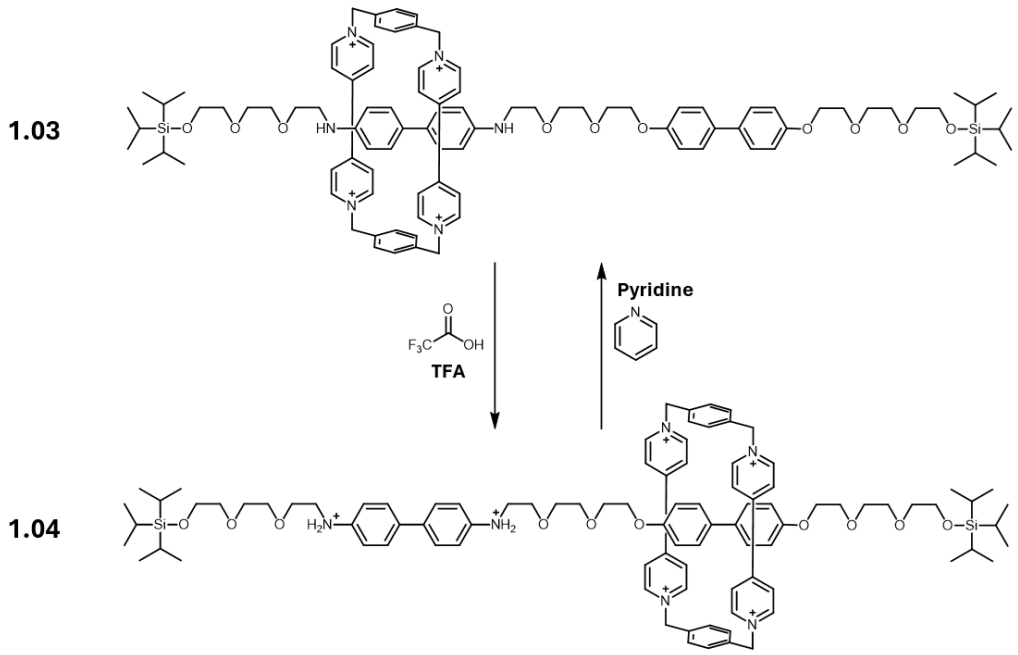


Figure 1.3 Stoddart *et al.*'s electrochemically responsive molecular machine. **1.03** is the molecule in its deprotonated form from addition of pyridine. Conversely addition of protons through TFA achieves structure **1.04**.[20]

These molecular machines and their dynamic switchable behaviours emulate real biological systems, such as shuttles, switches, walkers and propellers/ motors.[27] In biology, molecular machines are assembled from much larger molecules where the non-covalent interactions are far stronger due to the high volume of them.[28] A notable example of these differences between synthetic and biological systems can be found when comparing Leigh and co-workers synthetic walking molecules to kinesin, a biped linear motor protein.[22] In kinesin, several motor proteins are folded together to make one complex dynamic oligomer capable of transversing microtubules,[22] meanwhile synthetic walkers were relatively simple organic molecules made from chemical precursors and capable of limited motion along linear threads.[22]

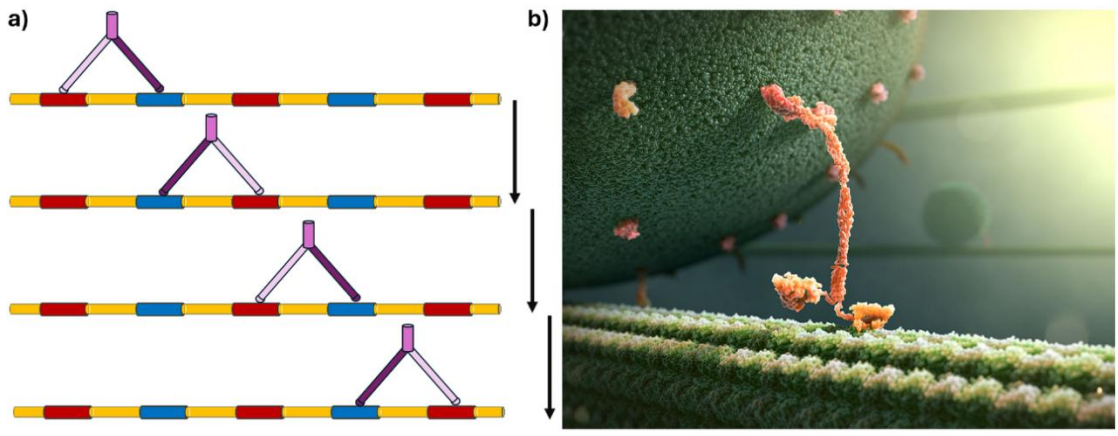


Figure 1.4 a) Schematic of the functional detachment and reattachment of a molecular walker along a thread. **b)** Biomolecule kinesin walking along microtubules, image courtesy of John Lieber ©.[22,29]

The larger biologically abundant molecular machines are held together through strong cumulative intermolecular forces, including H-bonds.[10,18] H-bonds allow these large biological self-assemblies to form and maintain their dynamic behaviour with their structures remaining functionally consistent.[10,18]

1.2.1 Hydrogen-Bonding

Hydrogen-bonding (H-bonding) is an inter-molecular force which exhibits partial covalent character through an especially strong dipole-dipole interaction.[30,31] This occurs when a hydrogen atom is covalently bound to a highly electronegative atom (eg. N, O, F or Cl) and comes in close proximity to another electronegative atom.[30,31] In a H-bonding interaction, the covalently bound H atom is defined as the bond donor (D) and the proximal electronegative atom is the acceptor (A).[32] This IUPAC nomenclature refers to the donor hydrogen as protic and therefore able to behave as a Lewis acid while the lone

pair of the electronegative atom (A) behaves as a Lewis base.[32] H-bonds are generally stronger than other dipole-dipole and dispersion forces due to the explicably large difference in electronegativity,[31] and can vary greatly in strength. Weak H-bonds range from around 1-2 kJmol^{-1} whereas strong H-bonds are as high as 161.5 kJmol^{-1} as is the case for the HF_2^- ion.[13] A summary of the factors which govern the strength of H-bonds is shown below in figure 1.5.[33]

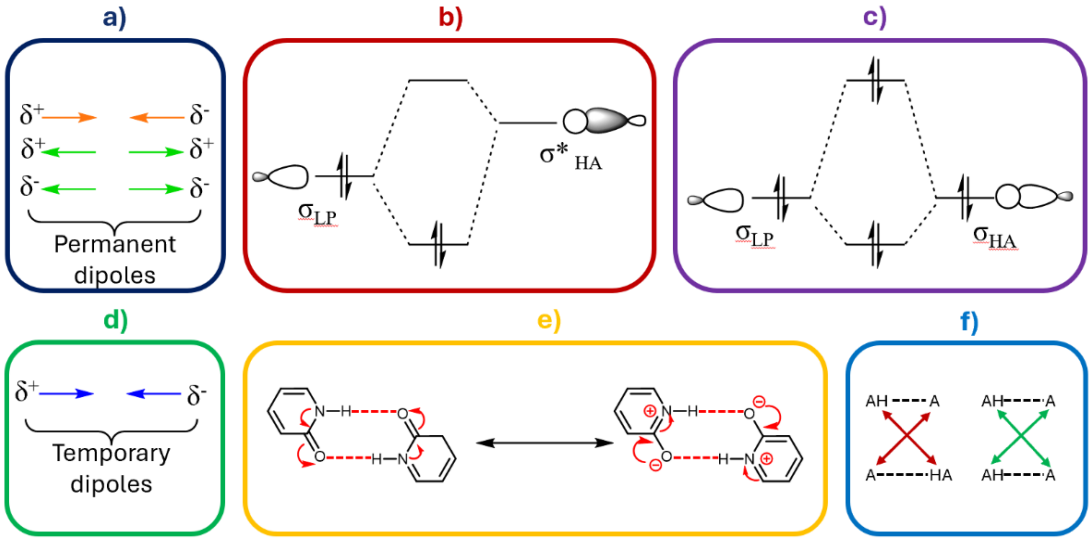


Figure 1.5 Influences on the strength of hydrogen-bonding. **a)** Electrostatic interactions **b)** Charge-transfer interactions. **c)** Pauli repulsions (sterics). **d)** Dispersion interactions. **e)** π-resonance assistance. **f)** Secondary electrostatic interactions (green arrow = attractive secondary interaction, red arrow = repulsive secondary interaction).[33]

H-bonds are the key components of supramolecular assemblies, with artificial and biological systems due to their additive enthalpy of formation and short lifetime that facilitate dynamic behaviour.[34,35] DNA, being a well-known example of this, forms a double helix through double and triple multipoint hydrogen-bonding of complementary base pairs.[36] When measured in chloroform, the double bonded adenine-thymine pair (A-T) has a constant of association (K_a) of 130 M^{-1}, whereas the triple bonding pair of

guanine-cytosine (G-C) has a far higher K_a of between 10^4–10^5 M^{-1}.[36] The far higher K_a observed in the G-C pair is evidence of how the strength of H-bonds is additive and increases exponentially through organisation, through cooperativity, resonance assistance and secondary interactions.[36]

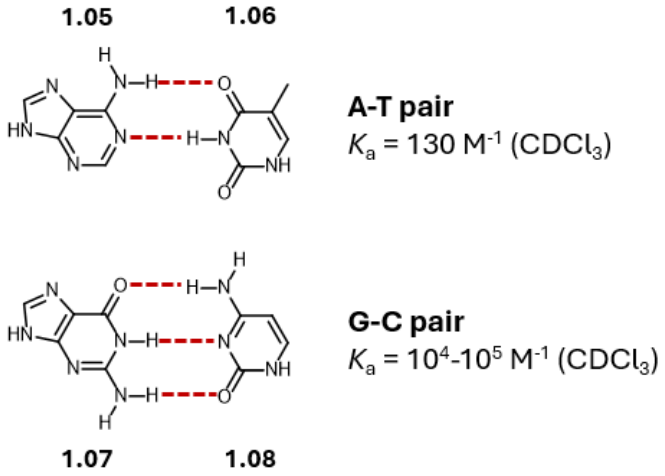


Figure 1.6 Hydrogen bonding pairs of Adenine and Thymine (A-T top) and Guanine and Cytosine (G-C bottom). K_a's are also given, demonstrating the much higher triple H-bonding strength of the G-C pair.[36]

Supramolecular chemists have used this understanding of H-bonding to create synthetic self-recognising non-covalent complexes.[19,21,22] According to Jorgensen, secondary electrostatic interactions play an important role in multipoint H-bonding systems and can dictate stability according to the arrangement of the H-bonds.[37,38] For example, in triple H-bonded systems the strength of complexes proceed in order ADA–DAD<ADD–DAA<AAA–DDD (A is an H-bond acceptor; D is an H-bond donor).[39–41] In the case of quadruple H-bonded systems, there are far fewer examples to determine accurate trends from the literature due to the inherent difficulty in synthesising supramolecular systems capable of such strong non-covalent interactions.[42] Examples in

the literature of ADAD–DADA,[43] AADD–DDAA,[44] ADDA–DAAD,[45] and AAAA-DDDD^{+} are all shown below in figure 1.7. The latter of these synthesised by Blight *et al.* is to this date the strongest multipoint H-bonding system ever recorded with a K_a greater than 10^{12} M^{-1} when measured in CH_2Cl_2.[42]

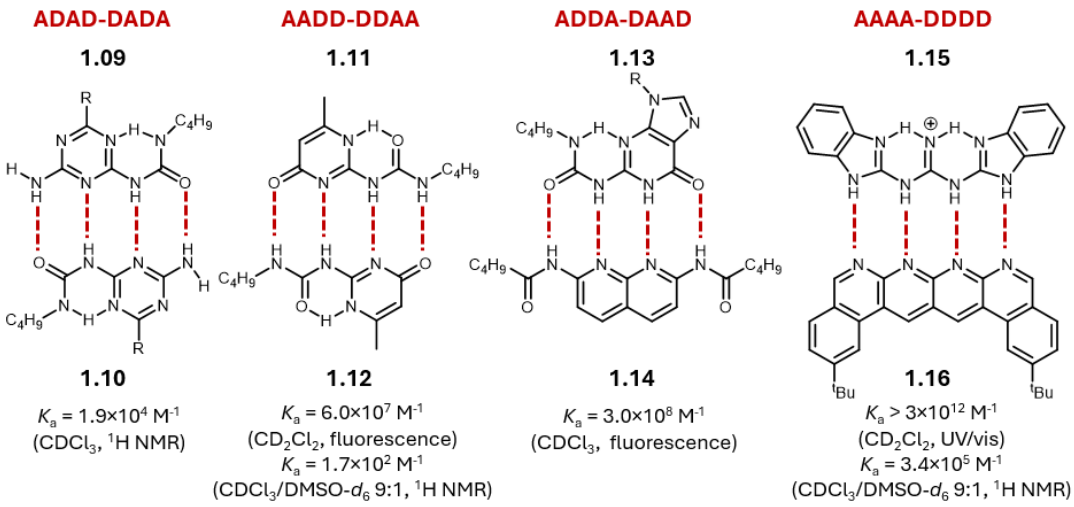


Figure 1.7 Examples of quadruple H-bond arrays and their H-bonding behaviours. Compounds **1.09-1.10** (ADAD),[43] compounds **1.11-1.12** (AADD),[44] compounds **1.13-1.14** (ADDA-DAAD),[45] compounds **1.15-1.16** (AAAA-DDDD).[42]

1.2.2 Quantifying H-Bonding Strength

As referenced in the previous subsection, K_a (association constant) is a measurement of the equilibrium of the association of two supramolecularly interacting components and frequently used to evaluate non-covalent interactions.[46] This equilibrium constant (K_a) can be used to evaluate the strength of the association through calculating the change in Gibbs free energy (ΔG) (see equation 1.02).[46] There are several analytical titration techniques used to determine the K_a of a supramolecular assembly including NMR spectroscopy, UV-vis spectroscopy and photoluminescent emission spectroscopy.[46]

Host-guest titrations are performed by titrating a host with small aliquots of a guest. After every addition the change in physical or optical property is measured and plotted.[47] Plots are then coalesced and the change in signal transduction results in a binding isotherm. The binding isotherm is then fitted to an appropriate mathematical model to obtain the K_a.[46,47] Mathematical models used to obtain K_a are developed from realising that the physical change observed is correlated to the concentration of the self-assembly or in some cases the change in concentration of host and guest. Binding constants are dimensionless and are calculated as reciprocal concentrations giving units of M^{-1}.[46] Association constants are dependent on a number of external factors, which must be kept constant when evaluating and comparing systems, such as temperature, pH, and solvent conditions.[46,47]

A two-component supramolecular system (figure 1.8) forms when a host [H] and a guest [G] self-assemble in solution forming [HG].[46] The simplest systems self-assemble into a stoichiometric 1:1 complex, where $K_a = K_1$ (K_1 referring to the first constant of association) and is mathematically defined in the following equations where:

$$K_a = \frac{[HG]}{[H][G]} \tag{1.01}$$

$$\Delta G = -RTlnK_a \tag{1.02}$$

The strength of this association (ΔG) can then be calculated from the negative natural logarithm of K_a by factoring with the ideal gas constant (R) and the temperature (T).

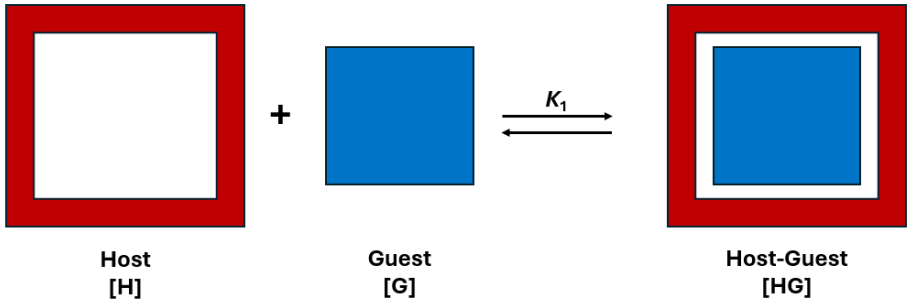


Figure 1.8 Schematic explaining the relationship between a Host-Guest [HG] complex and K_a in a single Host [H] and Guest [G] system.[46]

The concentration of these species in equilibrium cannot always be directly measured, though it is known that the total concentration of host $[H]_0$ and total concentration of guest $[G]_0$ balance in the following equations:

$$[H]_0 = [H] + [HG] \tag{1.03}$$

$$[G]_0 = [G] + [HG] \tag{1.04}$$

Isolating [H] and [G] from these equations and introducing their values into equations 1.05 and 1.06 below can give multiple expressions of K_a. Equation 1.06 shows two potential answers for [HG], though only one is taken forward for experimental purposes (the negative expansion) as the positive product leads to [HG] values larger than initial [H] or [G] concentrations, which is experimentally implausible:

$$K_a = \frac{[HG]}{([H]_0 - [HG])([G]_0 - [HG])} = \frac{[HG]}{[H]_0[G]_0 - [HG]([H]_0 + [G]_0) + [HG]^2} \tag{1.05}$$

$$[HG] = \frac{1}{2}\left\{\left([G]_0 + [H]_0 + \frac{1}{K_a}\right) \mp \sqrt{\left([G]_0 + [H]_0 + \frac{1}{K_a}\right)^2 - 4[H]_0[G]_0}\right\} \tag{1.06}$$

Supramolecular self-assemblies do not exclusively exist as 1:1 models, for instance 1:2 equilibria behave as a stepwise process where two guests interact with one host.[46] In this

case we introduce a term for a second association constant (K_2), the relationship between these stepwise equilibrium constants is described in the equations below.[46]

$$K_1 = \frac{[HG]}{[H][G]} \tag{1.07}$$

$$K_2 = \frac{[HG_2]}{[HG][G]} = \frac{[HG_2]}{K_1[H][G]^2} \tag{1.08}$$

Equations 1.07 and 1.08 show the relationship between K_1 and K_2, in the case of these equilibria. This relationship can also exist for a 2:1 [H]:[G] system whereby the equation's parameters are reversed so:

$$K_2 = \frac{[HG_2]}{[HG][G]} = \frac{[H_2G]}{K_1[H]^2[G]} \tag{1.09}$$

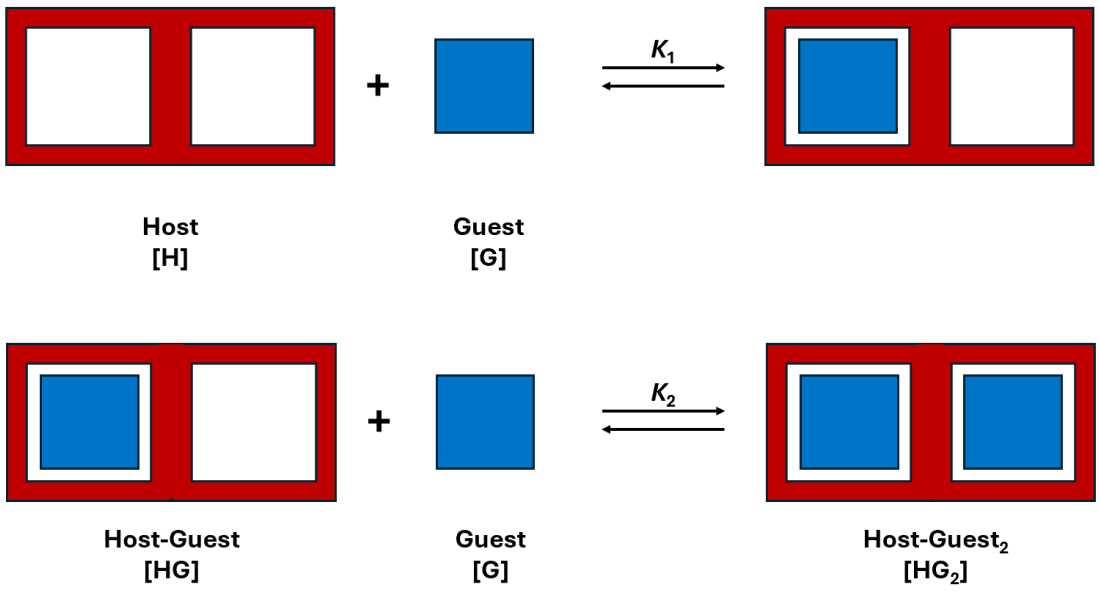


Figure 1.9 Schematic of a one Host [H] and two Guest [G] system, displaying the relationship between K_1 and K_2.[46]

Supramolecular titrations are used to determine the strength of non-covalent interactions. Understanding these interactions is essential for designing drug molecules to

bind non-covalently with biological molecules such as enzymes to promote or inhibit function.[48] Guanidine derivatives are a good example of this and are one of the most common functional groups implemented into drug molecules thanks to their strong non-covalent interactions.[49]

1.3 Guanidine Derivatives

Guanidine is a small nitrogen-rich molecule with the formula $HNC(NH_2)_2$.[50] It is a naturally occurring molecule found in plants and animals and is stable under ambient conditions.[50,51] First isolated in 1861 by Adolph Strecker via oxidative degradation of guanine,[52] the compound is more commonly synthesised through the thermal decomposition of dry ammonium thiocyanate.[53] This functional group, and derivatives of it, are found in essential biological molecules such as the nucleobase guanine in DNA, arginine (the amino acid), agmatine (neurotransmission), and various alkaloids like tetrodotoxin and saxitoxin.[51] For decades guanidine functionalised drug molecules have also been studied in clinical evaluation; several of the world's top selling pharmaceuticals contain a guanidine moiety.[49] The importance of this functional group in drug design is the strong H-bonding abilities and basicity of guanidine derivatives and the strength of their non-covalent interactions.[51,54] Under physiological conditions guanidine derivatives exist almost exclusively as guanidinium cations due to the inherent basicity and high pK_a (12.5 in guanidine) of the guanidine moiety. This allows guanidinium species to promote or inhibit protein function and bind other molecular targets like anions such as phosphates, sulfides or carboxylates through strong ion-dipole interactions.[51,54]

Guanidine derivatives refer to organic compounds incorporating the guanidine functional group with the general formula $(R_1R_2N)(R_3R_4N)C{=}N\text{-}R_5$ (a range of guanidine derivatives and synthetic approaches towards them is shown below in figure 1.10).[54,55] The key bonding functional group within a guanidine derivative is both an aminal and simultaneously an imine. This versatility of function informs both the nucleophilic and electrophilic character of these compounds. The aminal is responsible for the N-nucleophilic character and for alkylation or acylation reactions.[54] Meanwhile, the electrophilic character is determined by the imine function.

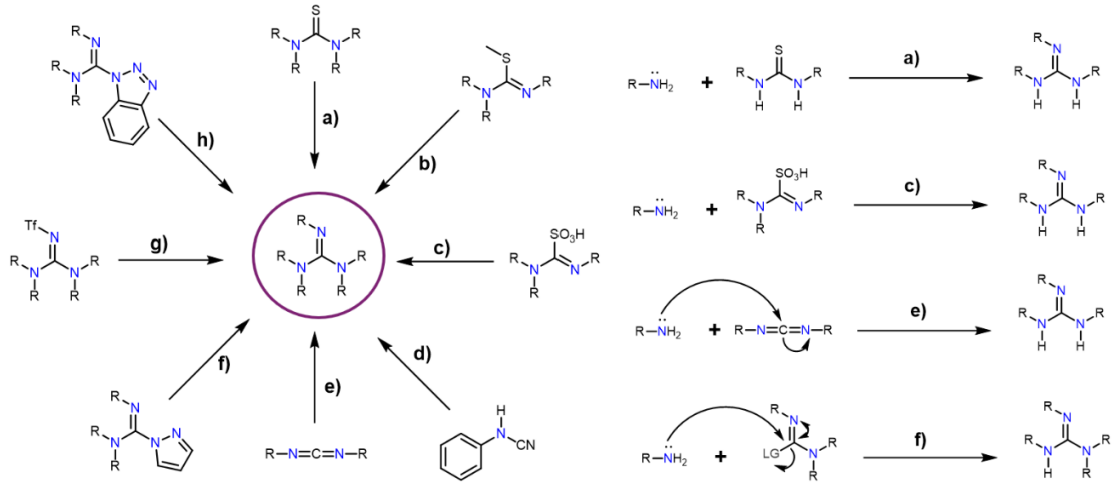


Figure 1.10 Common synthetic routes for the synthesis of guanidine derivatives and examples of mechanisms for routes a), c), e) and f).[54,56,57]

There are several common synthetic routes for guanidine derivatives. These routes can be grouped into two main strategies; the first is based on stoichiometric reactions involving guanylation reagents, its considered 'classical guanidine synthesis'.[50,54] Guanylation reagents are precursors which hold the aminal/ imine functional group core and a leaving group which can be easily removed through substitution. The other is using a catalytic approach to access substituted guanidines.[54] In

the classical synthesis of a guanidine core, an amine reacts with an activated guanidine or carbonyl-like precursor. This strategy avoids synthetic challenges of purification or reactivity, but can limit the scope of products due to the simple nature of these reactions.[54] Guanylation precursors are selected based on the reactivity of the amine and include but aren't limited to thioureas, isothioureas, amidine sulfonic acids, cyanamides, carbodiimides and pyrazole carboximidamides.[56] For aromatic amines, Lewis-acid reactions are preferable, aliphatic amines are more nucleophilic and therefore can react with a wider range of guanidine precursors.[58]

Non-classical guanidine synthesis or 'catalytic synthesis' is implemented when aromatic amines and other less nucleophilic amines are required.[54,56] If following a classical synthetic method, the use of poorly nucleophilic amines will result in low yields and difficult to purify mixtures.[54] The development of less energetic catalytic routes have helped to overcome these limitations of classical guanidine synthesis.[54] Once synthesised, guanidine derivatives tend to be very stable molecules. Protonated guanidinium cations can delocalise positive charge through the resonance forms shown below in figure 1.11. This stability can be explained by the electronics being almost identical to aromatic compounds, with six π-electrons being delocalised across bonding orbitals called the Y-delocalised system.[58] The delocalisation of these electrons, especially the lone pair on the nitrogen makes guanidine derivatives excellent ligands for metal complexation.[58]

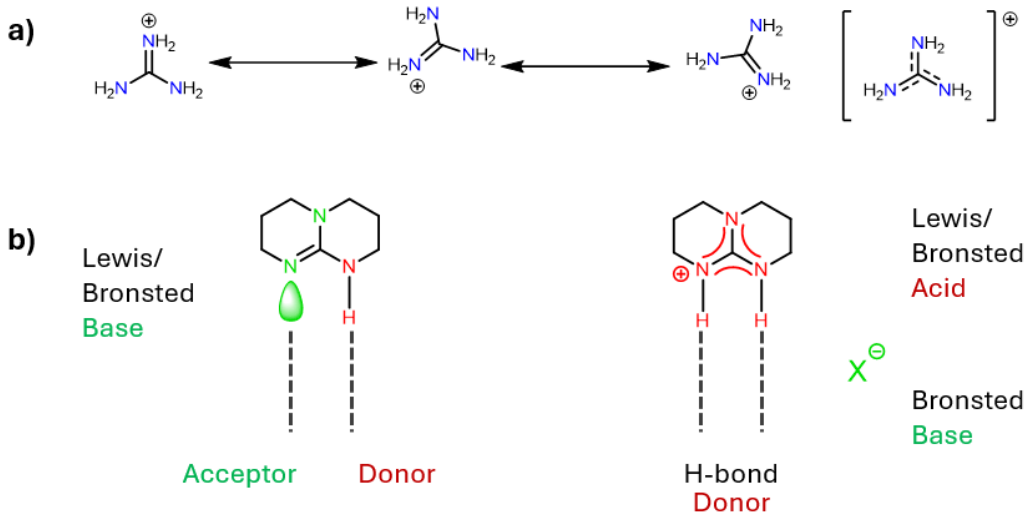


Figure 1.11 a) Resonance structures of the protonated form of guanidine (guanidinium) **b)** Acceptor donor behaviour of guanidine (left) and guanidinium salt (right).[54,58]

1.3.1 Guanidine Derivatives as Ligands

As previously discussed, guanidines are desirable in medicinal chemistry due to their non-covalent interactions with common bio-molecules.[59–66] The coordination chemistry of guanidines has developed slowly when compared to other analogues eg. amindines, amides or ureas.[65] This is likely due to the high basicity of guanidine derivatives and their propensity to form guanidium cations in aqueous media.[65] Once protonated, guanidium species $[C(NR_2)_3]^+$ have little to no ability to behave as Lewis bases and thus an inability to behave as σ-donating ligands in a metal coordinated system.[65] Despite this, there have been significant advances in the understanding and practice of the coordination modes of guanidine-based ligands, mostly in their anionic form which increases their σ-donor characteristics and strengthens their coordination to d-block metals.[61] Neutral guanidines do also have many examples of strong performance as σ-donor ligands with electron rich transition metals such as cobalt, copper and

platinum.[60,66,67] Shown below in figure 1.12 is a range of guanidine compounds commonly applied to coordination chemistry and how they bind to metals.[61]

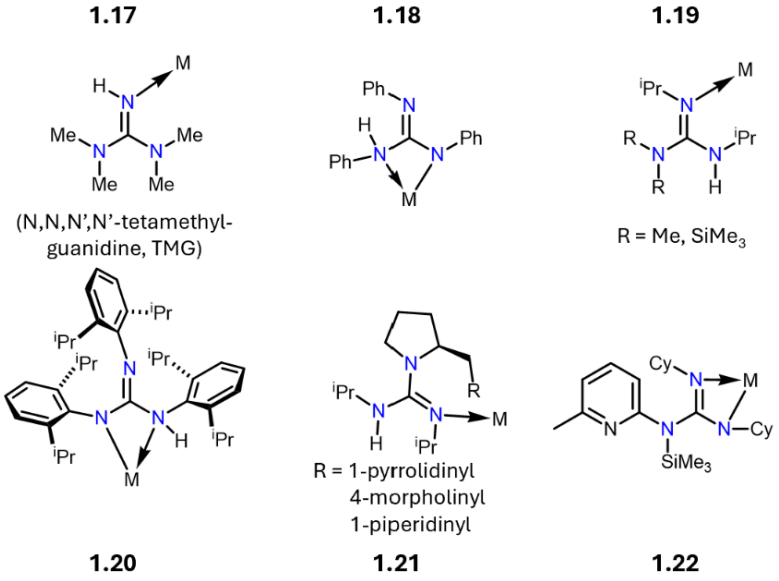


Figure 1.12 Examples of guanidine compounds common in coordination chemistry and their coordination mode.[61]

The earliest complexes of monovalent guanidine ligands came from the formation of adducts with 1,1,2,(2-)tetramethylguanidine (compound 1.17).[68] First reported in 1965 by Drago *et al.* complexes of Co(II), Cu(II), Zn(II), Pd(II), Ni(II) and Cr(III) were prepared from perchlorate precursors.[68] The complexes were characterised through a variety of analytical techniques revealing a general elemental composition of $[M(tmg)_4](ClO_4)_2$, showing four neutral tmg guanidine ligands for every metal centre.[68] Additionally, a υ(C=N) stretch in the IR from 1609-1548 cm^{-1} confirmed coordination through the imine nitrogen in all complexes.[68] In the late 1990s, neutral guanidines in coordination chemistry saw an uptick in discoveries with notable studies on gold and copper.[61] The gold complex shown in figure 1.13 (compound **1.24**) presented a unique

aurophilic reaction between multiple gold centres because of the σ-donor properties of the guanidine's imine lone pair.[69] It is the hard donor characteristics of the aminal/imine ligand that can stabilise the Au(I) cation and prevent rapid irreversible disproportionation to the Au(III) cation which is seen with other donor ligands such as ethers, water, alcohols, and even aqueous ammonia.[69] Furthermore the stability of the guanidine coordinated Au(I) cation provided by the σ-donor character of the aminal/imine group allows for the electrostatic binding with the oppositely charged $AuBr_2^-$ anion observed through X-ray crystallography.[69]

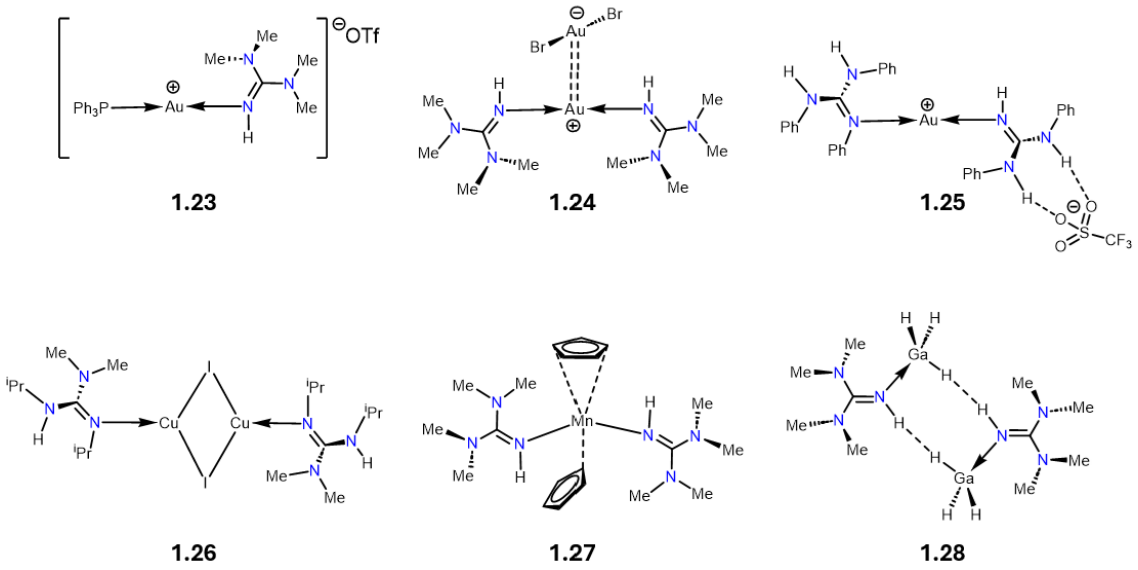


Figure 1.13 Recent examples of metallic complexes incorporating a neutral guanidine.[61]

More recently (2025) in neutral guanidine coordination chemistry Isabel Rozas *et al.* demonstrated a series of Pt(II) complexes with aryl guanidine-like ligands as anti-cancer agents.[67] This is not the first study incorporating cisplatin-inspired guanidines into platinates, which are well established powerful chemotherapeutic drugs for late stage cancer treatments.[67] This study from Rozas *et al.* hypothesised the design of their

platinum complex would be especially effective due to the complex potentially behaving as a DNA minor groove binder (shown in figure 1.14).[67] The complex's cytotoxic potential was assessed based on cyclometalated platinum's ability to create reactive oxygen species (ROS).[70] They found complexes **1.30** and **1.32** had strong cytotoxic effects in the presence of light generating $^1O_2$ (a reactive oxygen species).[67] In control studies, it was shown that the unbound guanidine ligand had no toxicity towards cancer cell lines, demonstrating the importance of metal coordination for this purpose.[67]

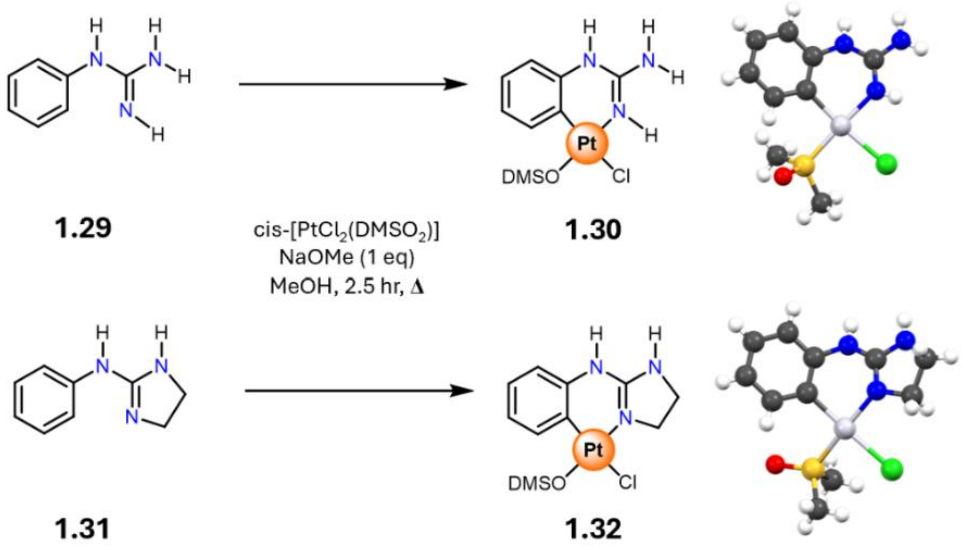


Figure 1.14 Preparation of cyclometalated Pt(II) complexes **1.30** and **1.32** and crystal structures of the corresponding complexes.[67]

Biguanides (two adjacent guanidines working cooperatively) have also been incorporated into metallic complexes for medicinal purposes.[59,61–63] Complexes of Cu(II), Ni(II), Co(II) and Zn(II) with the biguanide known as metformin have all been synthesised, characterised and studied for various drug uses.[63] Metformin itself is a common biguanide used as a drug to manage type 2 diabetes.[71,72] Other biguanides used

in pharmaceuticals, which have been incorporated into early-row transition metal complexes include phenformin, buformin, proguanil etc. (see figure 1.15).[63]

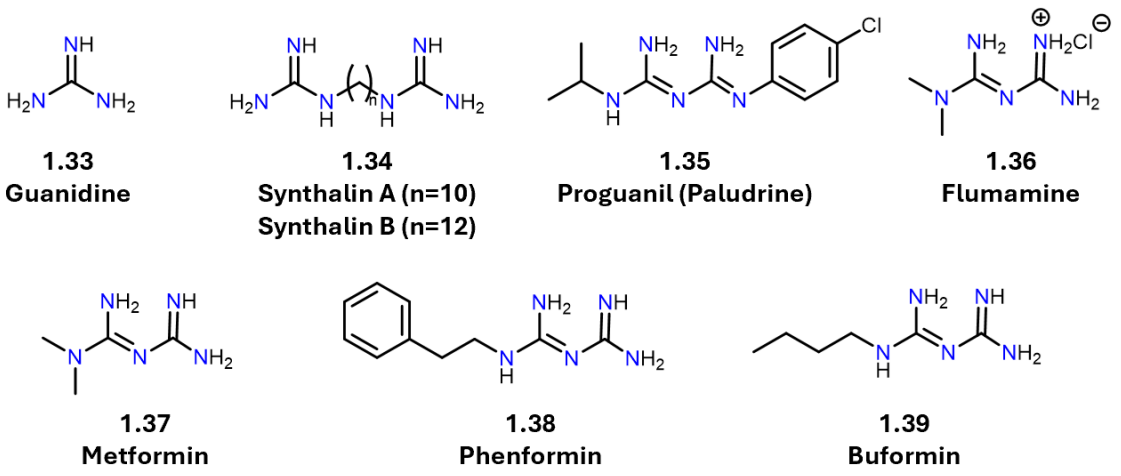


Figure 1.15 Chemical structures of metformin and structurally similar biguanides commonly used in clinical practice.[63]

More recently, researchers have looked to iridium for its anti-cancer properties for patients who have gained resistance towards other platinum chemotherapeutics.[73–75] The research team of Mao *et al.* have recently (2021) prepared a series of iridium complexes (figure 1.16), each incorporating metformin as the ancillary ligand. These complexes were tested against a panel of cancer cells in aerobic and hypoxic conditions showing decreasing cytotoxicity in order **1.42**>**1.43**>**1.44**.[76] The observed decrease in toxicity aligns with a red shift in complex emission with lower energy phosphorescence and a lower lying T_1 state. This results in a smaller energy difference between ground and excited states, therefore less available energy to generate reactive oxygen species through quenching reactions between the T_1 excited state and triplet oxygen to form singlet oxygen. This change in emission profile upon modification of the cyclometalating ligands is a phenomenon which will be explored in the next section.[76,77]

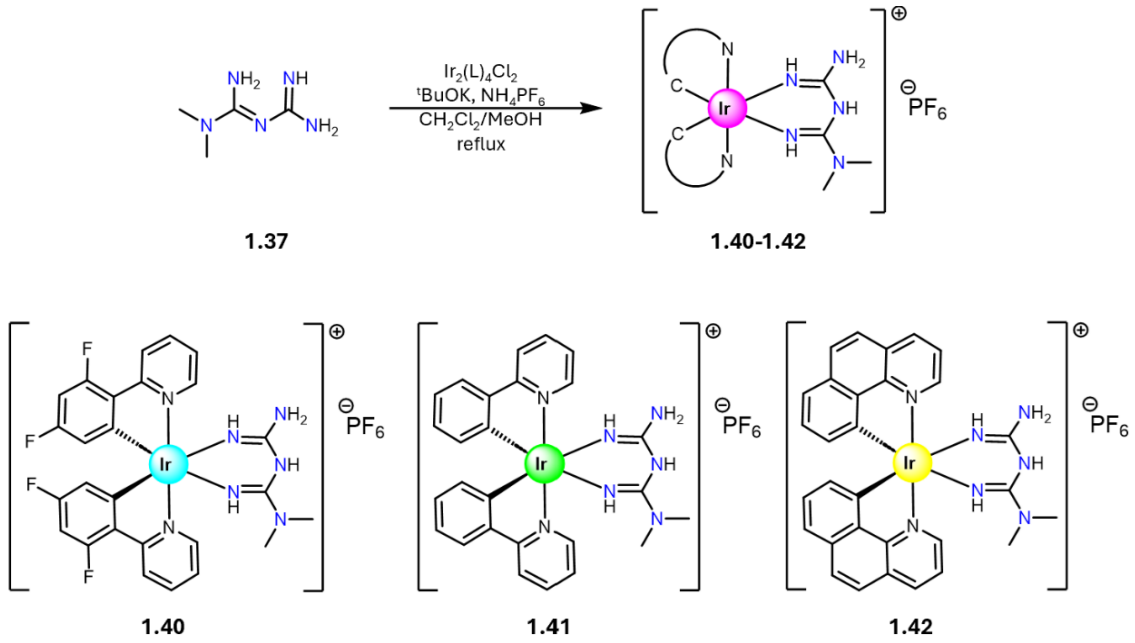


Figure 1.16 Synthetic route to Ir(III) complexes **1.40-1.42** with a metformin ancillary ligand.[76]

1.4 Cyclometalated Iridium (III) Complexes

Iridium is one of the rarest and most expensive metals available in the earth's crust.[78] First discovered in 1803 in acid-insoluble residues from platinum ore by English chemist Smithson Tennant,[78] its etymology is derived from the Greek word *iris* (rainbow), referring to the various colours of iridium compounds.[78] Not only is iridium incredibly rare, but it is also a crucial ingredient in many high performance electrical components,[79] catalysts,[80,81] and OLEDs,[82] due to its high corrosion resistance, density, and high thermal stability.[78] Iridium, like many other transition metals has a variety of common oxidation states ranging between -1 and +6,[78] with some notable less common states of +7, +8 and +9.[83] For this thesis, the primary focus is on complexes of iridium in the +3 oxidation state.

For many years Ir(III) complexes have been the focus of research in opto-electronics.[82,84–86] Ir(III) is able to form iridium-carbon bonds with strong covalent character leading to high thermal stability in its complexed form.[87] Additionally, all Ir(III) complexes are low spin and thus are diamagnetic due to the valence electronic arrangement of $5d^6$.[88,89] This enables structural elucidation by NMR,[89] leading to a greater understanding of structural and electronic effects from the first and second sphere of coordination.[90]

Ir(III) complexes are synthesised from hydrated iridium trichloride, first by forming a chloro-bridged dinuclear Ir(III) dimer with varying C^N cyclometalating ligands.[82] The choice of these ligands can determine many properties of the complex from solubility to the complex's luminescence.[82] Through this chloro-bridged dimer product, a wide range of ancillary ligands can be introduced, giving great structural and property variability.[82,88] From the isolated dimer, synthesis of a cyclometalated complex can be completed in four ways (shown in figure 1.17); route one is adding two equivalents of a third identical C^N ligand to the dimer yielding two homoleptic products: a facial (fac-) and a meridional (mer-) isomer.[88] Route two is the introduction of an N^N datively coordinating ancillary ligand leading to a positively charged iridium complex; these ligands are usually symmetrical and the synthesis often involves a bulky counter anion to stabilise the complex.[88] Route three is the addition of donating exchangeable ligands such as cyanide anions; this is common when labile exchangeable ligands are needed so the iridium metal may be exposed and exploited for organic transformations, e.g. Megger's catalysts.[88,91] The final route is to add an ancillary ligand capable of forming σ- and π-bonds with iridium (commonly O^O^- or N^N^-).[82,88,92] This

produces a charge neutral heteroleptic iridium complex which may be symmetric or asymmetric depending upon the structure of the ancillary ligand applied.[82] We use this approach throughout this thesis in the synthesis of our H-bond rich Ir(III) complexes.

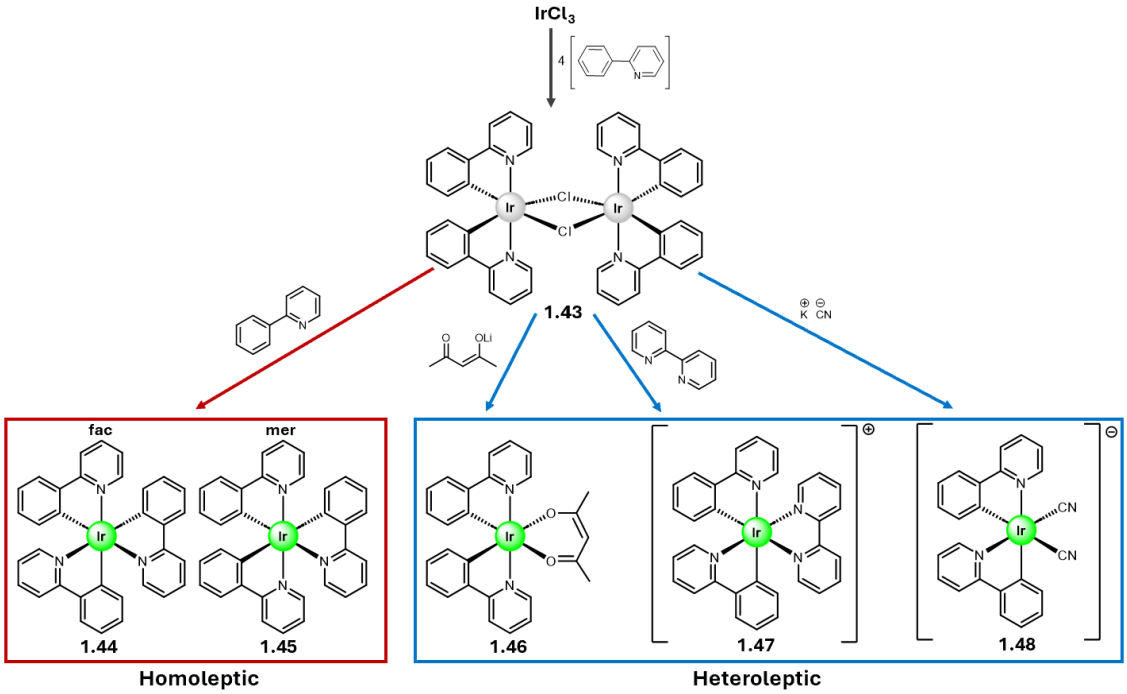


Figure 1.17 General synthetic schemes for the synthesis of homo- and heteroleptic Ir(III) complexes based upon phenyl-pyridine ligands (ppy).[82,88]

1.4.1 Fluorescence and Phosphorescence

Luminescence is the emission of light from substances and occurs when the substance is radiatively, electronically or vibrationally excited.[93] Luminescence can be further divided into two categories, phosphorescence and fluorescence, whether a photophysical event is described as phosphorescence or fluorescence depends on the nature of the excited state.[93] Fluorescence occurs when electrons are excited from a singlet ground state (S_0) to a singlet excited state (S_1, S_2, S_3…..), after excitation the electron rapidly relaxes to the lowest excited state (S_1) through internal conversion (IC).

The electron then decays from the lowest vibrational excited S_1 state to any available vibrational ground state (S_0). The return to a ground state releasing energy in the form of emission of photons known as a radiative decay (see figure 1.18).[93] Fluorescent emission events have a radiative emission rate around 10^8 s^{-1}, meaning the typical timescale for fluorescent lifetime (τ) from excitation to complete emission is ~10 ns.[93] It is also worth noting that fluorescence is not limited to singlet excited to singlet ground state transitions, but can refer to any radiative decay where there is no net spin change.[93]

Phosphorescence is a type of photoluminescent emission observed in larger molecular systems incorporating both organic and inorganic components.[94] Unlike fluorescent emission in which emission occurs almost spontaneously on the timescale of ~10 nanoseconds, phosphors can delay emission of the absorbed energy giving a longer lifetime of radiative decay.[94] This prolonged emission is caused by a phenomenon known as intersystem crossing (ISC). ISC is where an electron that has been excited from the singlet ground state (S_0) to the singlet excited state (S_1), undergoes a 'spin forbidden' non-radiative transition into a triplet state (T_1, T_2….).[94] From here the electron will undergo IC relaxing to the lowest available triplet state (T_1), and following this the electron will undergo another 'spin forbidden transition' and radiatively decay back to a singlet ground state (S_0).[94] The electronically spin forbidden nature of phosphorescent emission leads to the triplet excited states being longer lived. The transition from T_1 to S_0 is also not spin allowed so the electron resides in the excited triplet state for much longer as the radiative decay is less statistically likely to occur.[94] The T_1 state of Ir(III) phosphors tends to lie below S_1 making phosphorescent emission less energetic than emission from the singlet state and subsequently longer wavelengths of light are to be

expected from phosphors.[94] The summary of the mechanisms of fluorescence and phosphorescence are shown in figure 1.18 and equation 1.10 below.

$$S_0 + hv \rightarrow S_1 \rightarrow T_1 \rightarrow S_0 + hv' \qquad (1.10)$$

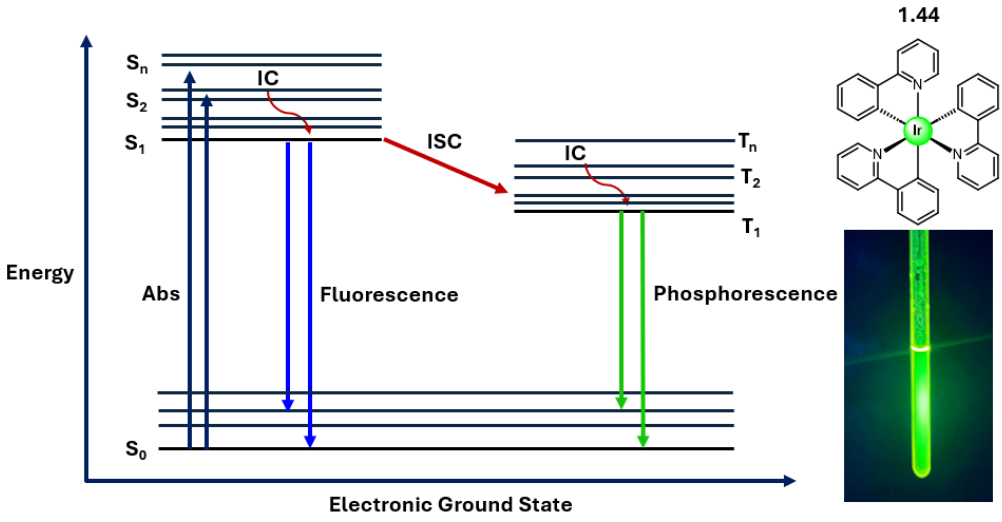


Figure 1.18 Jablonski diagram for the emission of Ir(III) complex **1.45**. S_n are the singlet states, T_n are the triplet states, IC is internal conversion and ISC is the intersystem crossing.[88,94,95]

To measure the intensity of a phosphorescent event several parameters must be defined; quantum yield (Φ), lifetime (τ), radiative decay (k_r) and non-radiative decay (k_{nr}).[88,95] Photoluminescence quantum yield (PLQY, Φ_{PL}) can be measured through two methods, both of which were used in this thesis; the relative method and photon counting. The relative method uses measurements of absorbance and emission and compares them to an accepted PLQY internal standard such as quinine sulfate or rhodamine 6G.[96] The choice of standard depends upon the absorption and emission character of the emitter being studied. Ideally the emitter is matched to a standard of a similar emissive character (colour).[96] The measurements of the standard and the sample are then implemented into equation (1.11) shown below.

$$\phi_s = \phi_r \times \frac{A_r}{A_s} \times \frac{I_s}{I_r} \times \frac{\eta_s^2}{\eta_r^2} \quad (1.11)$$

Here, Φ_s is the relative quantum yield of the sample, Φ_r is the quantum yield of the reference (internal standard), η_s and η_r refer to the refractive indeces of the solvents the standard and sample are dissolved in, A is the absorbance of the reference and I is the intensity of the emission as an integrated function of the area under the corrected emission curves.[96] The second method of calculating PLQY is the photon counting method which uses an integrating sphere to directly measure efficiency by comparing the count of photons entering a system against those exiting. We measure the photons absorbed by the compound against the number emitted by the compound as a function of photon count per second by the detector (see equation 1.12 and 1.13).

$$PLQY = \frac{\#\ emitted\ photons}{\#\ absorbed\ photons} \quad (1.12)$$

$$PLQY = \frac{Em_{sample} - Em_{blank}}{Ex_{blank} - Ex_{sample}} \quad (1.13)$$

A compound's lifetime (τ) is a time measurement of the length of a photophysical event (the amount of time for the sample to relax to the ground state).[97] To measure this we can use the time correlated single photon counting (TCSPC) method.[97] This method relies upon the use of a short pulse laser and a detector capable of measuring precise photon count per unit time on the desired scale. The results of TCSPC studies often resemble a histogram (as shown in figure 1.19) reflecting the decay of the sample, this is then fitted to an equation used to work out the exponential decay of the sample (see equation 1.14).[97]

$$\text{Fit: } B_1 e^{(-t/\tau_1)} + B_2 e^{(-t/\tau_2)} + B_3 e^{(-t/\tau_3)} + B_4 e^{(-t/\tau_4)} \quad (1.14)$$

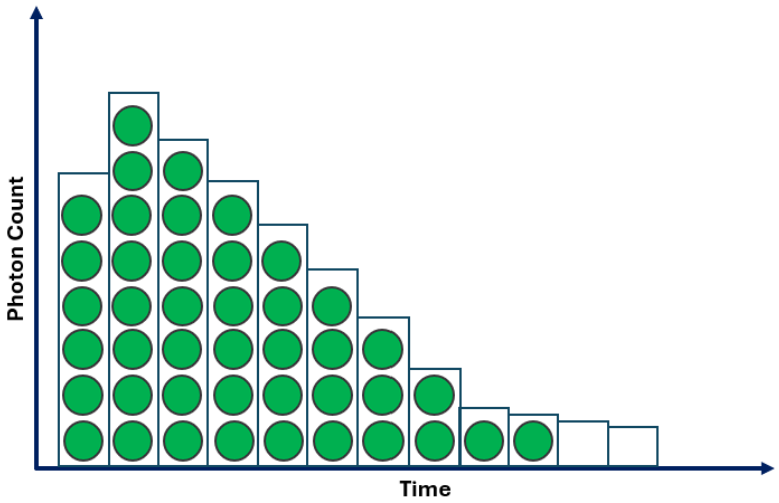


Figure 1.19 Graphical representation of a TCSPC histogram with photon arrival times grouped into channels for fitting.[97]

1.4.2 Phosphorescence of Ir(III) Complexes

Cyclometalated Ir(III) complexes such as compound **1.44** in figure 1.17 have been commercially applied to second generation OLEDs due to their strong phosphorescent properties.[98–102] Ir(III) complexes are strong phosphors due to iridium's larger nuclear charge leading to efficient spin orbit coupling (SOC) which promotes higher rates of inter-system crossing (ISC).[114] To understand the mechanisms of phosphorescence in iridium complexes we must first understand the electronic behaviours upon absorption of photons and subsequent transitions which occur.[95] In theory, four types of transitions should be considered when investigating phosphorescent Ir(III) complexes; singlet and triplet metal-to ligand charge transfers (^{1}MLCT and ^{3}MLCT) and single and triplet ligand-centred transitions (^{1}LC and ^{3}LC).[95] These pathways are available due to two factors; one, the delocalisation of the highest occupied molecular orbital (HOMO) that can span over the iridium metal's valence orbitals and the π-systems of the coordinating

ligands;[95] two, the lowest unoccupied molecular orbital (LUMO) being localised to the ligands, and finally, efficient spin-orbit coupling.[95]

The ^{1}LC transition energy is the highest of all the charge transfers followed by the ^{1}MLCT. Inversely the ^{3}MLCT energies are higher than ^{3}LC due to the exchange energy of the MLCT transition being lower than the LC transition.[103] This leads to an energetic order of $^{3}LC \leq {}^{3}MLCT < {}^{1}MLCT < {}^{1}LC$ which can be observed through UV-vis spectroscopy.[95] Even with UV-vis spectroscopy, ^{3}MLCT and ^{3}LC UV-vis absorption bands are so close together and look so similar that they can rarely be distinguished.[95] In addition to the bands being so similar, the oscillator strengths of the aforementioned transitions tend to be very low and can only be observed in the presence of heavy metals which can also be obscured by broader allowed absorptions.[95,104] According to Kasha's rule 'the emitting level of a given multiplicity is the lowest excited level of that multiplicity', this infers the emission of light from a substance occurs from the lowest available excited singlet or triplet electronic state of a given multiplicity.[105] In the case of Ir(III) complexes the ^{3}LC or ^{3}MLCT transition states are the lowest triplet states and are subsequently responsible for phosphorescence.[95,106] Although we cannot differentiate between these low-lying states through UV-vis, we can distinguish them through solvatochromic behaviours, rigidochromic behaviours, and photoluminescent lifetimes (τ).[81,95] ^{3}MLCT phosphorescence exhibits hypsochromic shifts (blue shifts) in non-polar media (aprotic apolar solvents) and when the medium becomes rigid (frozen solvent or polymer suspended).[95,107,108] These blue shifts infer charge-transfer (CT) is involved in the phosphorescence as CT energy is heavily influenced by the arrangement of dipoles in the media.[95,109] As outlined different complexes have preference of ^{3}LC or ^{3}MLCT

dominated phosphorescence, though it is widely accepted that both phosphor mechanisms are always observed so it is appropriate to describe the mechanism as a mix of ^{3}MLCT and ^{3}LC transition states.[95]

As shown below in equation 1.15 phosphorescent quantum efficiency (Φ_p) can be deduced in relation to the radiative decay constant (k_r) and the sum of the non-radiative decay constants (Σk_{nr}).[95]

$$\Phi_p = k_r/(k_r + \Sigma k_{nr}) \quad (1.15)$$

This equation demonstrates high Φ_p can be achieved through increasing k_r or reducing k_{nr}.[95] k_r in the case of phosphors is highly connected to spin-orbit coupling in the excited states as k_r is proportional to the square of the phosphorescence emission energy but inversely to the difference in energy between two perturbing excited states.[110] k_{nr} meanwhile can be predicted through established band-gap theory, which states ln(k_{nr}) is inversely proportional to the emission energy.[110] This means in order to predict Φ_p, the electronic structure of the ground state, all involved excited states and any photophysical interactions among them must be fully understood.[95]

When designing an Ir(III) complex it is possible to minimise k_{nr} while maximising k_r to achieve high quantum efficiencies through understanding the factors that govern k_{nr}.[95] It is worth noting that the number of synthetic modifications and structural considerations governing Φ_p could be the basis of an entire thesis, and therefore I will only elaborate on a select few in this section. Geometric isomer control in homoleptic Ir (III) complexes is one such method. The *fac*- isomer is accepted to be the thermodynamic product and mostly gives higher Φ_p, and due to this it is preferred to push synthesis to the

fac- form.[111] Restricting molecular motion and increasing rigidity can also increase Φ_p.[112] Freezing media or suspending the complex in polymers can reduce k_{nr} by limiting unwanted vibronic oscillations, and thus non-radiative transitions, leading to a more efficient phosphor.[95] The origin of these unwanted behaviours lies in Ir-ligand stretching vibrations, ring deformation and C-H vibration on the aryl rings.[95] Longer Ir-C bonds can also increase stretching leading to increased vibronic coupling (Herzberg-Teller coupling).[113,114] Therefore, increasing the Ir-C bond strength as well as increasing ligand rigidity can decrease k_{nr} through reducing unwanted vibronic coupling.[115] Confining the phosphorescent region to a single ligand in a heteroleptic iridium complex can also increase Φ_p.[95] There exist several examples where the LUMO is delocalised across the complex leading to mixing with various electronic states and the weakening of Ir-C bonds.[116] Thus it is beneficial to confine the global LUMO within a strongly bound rigid ligand which can promote a high Φ_p.[117] The final design choice to introduce is the control of substituents on the ligands, such as the incorporation of electron donating (EDG) and withdrawing groups (EWG) to various position on the ligands. The effect the introduction of these groups has on Φ_p and τ is not as clear as the other design choices that have been discussed. Further studies are needed to make definitive arguments over the effect of ring modifications.[95] In a 2004 paper by Coppo *et al*., they demonstrated that the introduction of fluorine atoms to the carbon ring weakened the Ir-C bond, weakening the Φ_p and shortening the τ. Introduction of fluorine atoms is also an effective strategy for stabilising the HOMO of Ir(III) complexes and blue shifting the emission.[118,119] Cesno *et al.* later coupled this with the introduction of EDGs onto the pyridine rings which work to destabilise the LUMO, further widening the HOMO-LUMO gap and working to blue-

shift the complexes.[118] This destabilisation of the LUMO also had a negative effect on Φ_p and τ, they hypothesised that low-frequency vibrational motion imposed on the dimethylamino group was responsible for the increase in k_{nr} making the complex less efficient.[118] As mentioned in these examples controlling substituents also has notable effects on the emission wavelengths of the complexes.[95,103,119–122]

1.4.3 Colour Tuning of Iridium (III) Complexes

What is colour? The Commission International de l'Eclairage (CIE) system refines emission intensities into coordinates (x,y) in order to describe the colours perceived by human vision.[123,124] The assignment of these coordinates is based upon the intensity of the RGB colour matching functions denoted as x(λ), y(λ), z(λ), where x is the red, y is the green and z is the blue component.[124] These functions are based on emission intensity in the visible light spectrum. By using them light can be assigned to having any spectral power through the equations 1.16-1.18:

$$X = k \int \phi(\lambda) x(\lambda) d\lambda \quad (1.16)$$

$$Y = k \int \phi(\lambda) y(\lambda) d\lambda \quad (1.17)$$

$$Z = k \int \phi(\lambda) z(\lambda) d\lambda \quad (1.18)$$

In these equations, k is a normalising constant such that X+Y+Z=1, and $\Phi(\lambda)$ is the spectral distribution of light stimulus.[124] The integrated products of $\Phi(\lambda)$ i.e. X, Y, Z(λ) shown in equations 1.16-1.18 are known as the tristimulus values. When tristimulus values are projected on a unit plane where X+Y+Z=1, combining these values using

equation 1.19 converts the values into a 2-dimensional (x,y) CIE coordinate in accordance with the CIE 1931 diagram (Figure 1.20).[124]

$$x = \frac{X}{X+Y+Z}; y = \frac{Y}{X+Y+Z} \tag{1.19}$$

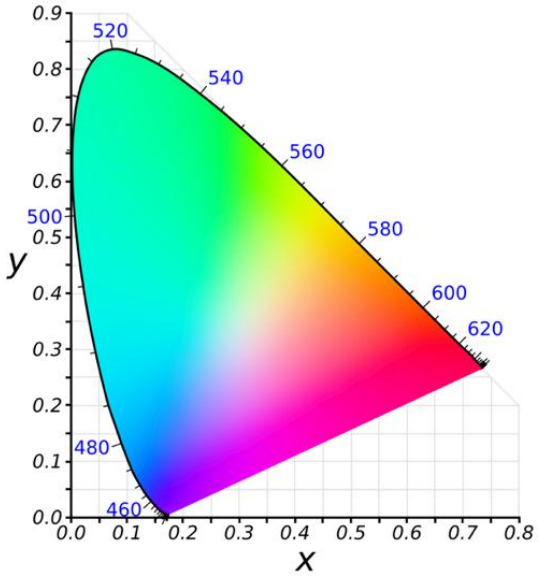


Figure 1.20 CIE 1931 chromaticity diagram.[124]

The 1931 CIE diagram shown above in figure 1.20 shows the projection of the tristimulus values onto a 2-dimensional plane resulting in the curvature and colour distribution.[124] On the top of the colour curve are specific wavelengths of light related to the different regions from deep blue to near infra-red.[124]

Understanding the factors that govern colour in a photophysical event allows us to engineer molecules to emit different colours through structural modification altering orbital energies and HOMO-LUMO distributions. Ir(III) complexes can achieve a vast array of colours, absorption and emission profiles of Ir(III) complexes can be changed by the variation of ligands altering the relative position of the HOMO and LUMO.[95,120–122]

Introduction of electron-donating and electron-withdrawing groups to varying positions on cyclometalating ligands greatly affects the emission wavelengths (λ) of Ir(III) complexes.[120,121] Changing these substituents also impacts Φ_p and τ, although the understanding of the control of substitution on these properties is less understood than the effect on emission.[120,121] Baranoff *et al.* have established quantifiable structure property relationships between opto-electronic properties of Ir(III) complexes and Hammett values (see figure 1.21 for the compounds Baranoff *et al.* studied).[121]

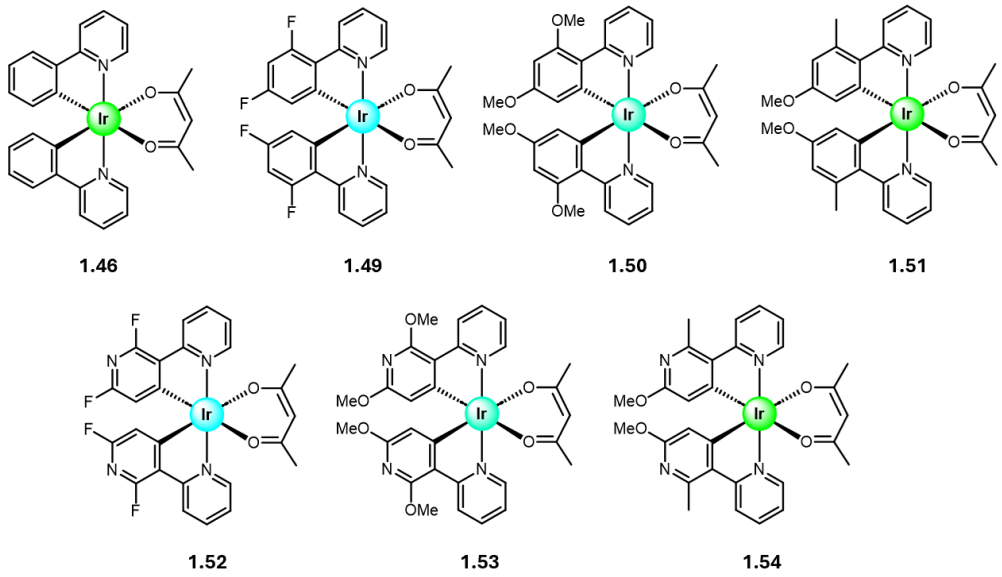


Figure 1.21 The range of Ir(III) complexes used by Banaroff *et al.* to study Hammett correlations and quantifiable structural property relationships.[121]

Due to the different orbital distributions of the HOMOs and LUMOs in different forms of Ir(III) complexes it is important to discuss the effects of structural alteration and substituent substitution on individual areas of a complex.[120] When the cyclometalating ligands are phenylpyridine derivatives, well established Hammett parameters can be used to predict the effects of substituent substitution as demonstrated by Baranoff *et al.*[121]

Incorporating electron-withdrawing groups, such as fluorine atoms onto the aryl ring is an effective method of blue shifting the emission of iridium complexes.[120,121] Other examples of electron-withdrawing groups studied with the goal of causing a blue shift include nitrile,[125] phosphonium,[126] and sulfonyl.[127] Conversely introducing electron-donating groups onto the aryl ring causes a red shift though an even more effective method is extending the ligand π-system, for example by converting the phenyl ring to a naphthyl ring.[120–122]

Substitution of the pyridyl ring with another heterocycle can also be an effective way to modulate electronic induction or withdrawal into the π-system thereby changing the coordination strength of the ligand to the iridium and changing the emission energies.[120] Using smaller 5-membered rings such as pyrazoles can cause a blue shift through HOMO-stabilisation of complexes.[110,120] It has also been shown by Zysman-Colman *et al.* that the alternative introduction of triazoles and tetrazoles can also significantly increase LUMO energies.[120]

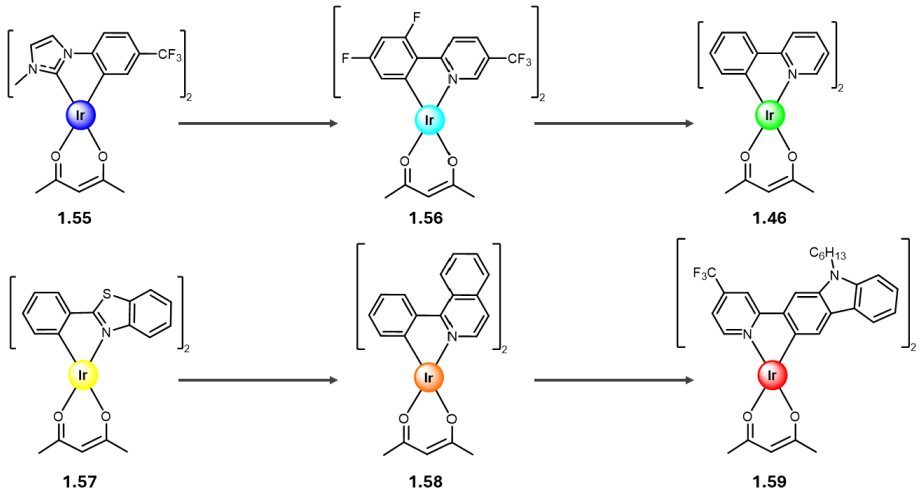


Figure 1.22 Iridium complexes moving towards NIR emission through increasing the efficiency of the cyclometalating ligands.[120,122]

Due to the modular synthetic nature of Ir(III) complexes outlined in section 1.4, we can access structurally diverse ancillary ligands quite different from their cyclometalating counterparts.[82] Charged N^N ligands or introduction of ligands that can form σ- and π- interactions similar to the cyclometalating ligands can have a large impact on photophysical behaviour.[95] For example, the LUMO tends to reside on the N^N ligands in complexes such as **1.47**, therefore strategies around blue or red shifting emissions rely upon modifications which can change the LUMO energies.[95] In this thesis no charged N^N complexes were studied, rather iridium complexes with neutral N^N ligands which are a growing subclass of iridium complexes (e.g. Ir-metformin; compound 1.41) were investigated.[76] In these complexes the HOMO-LUMO distribution was altered due to the electron rich nature of a σ- and π-bound N^N ligand, where the HOMO tends to reside on the ancillary ligand.[128] The subsequent incorporation of EWGs and/or shrinking the π-system then contributed to stabilising the HOMO, blue-shifting the complex's emission.[120] Figure 1.23 shows examples of charge neutral Ir(III) complexes with O^N ancillary ligands which have a similar bonding to complexes studied in this thesis and the effect of extending the π-system on the orbital energies.[95]

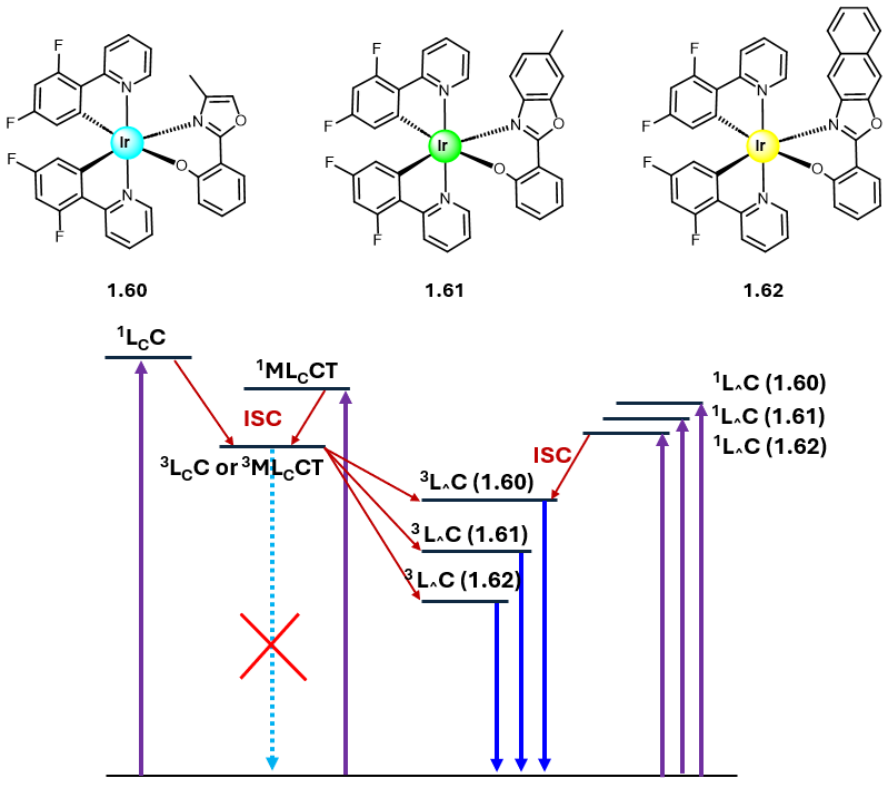


Figure 1.23 Energy-harvesting phosphorescence through inter-ligand transfer of complexes **1.60**, **1.61** and **1.62**. ^1L_CC represents the LUMO of the cyclometalating ligand's singlet state, $^1L_{\wedge}C$ represents the LUMO of the ancillary ligands excited singlet state. As the cyclometalating ligand gets larger the $^3L_{\wedge}C$ triplet state's energy decreases, narrowing the HOMO-LUMO gap, leading to a red shift.[95]

So far, strategies for the colour tuning of iridium complex through structural modification have been discussed. Effects of how modifications can affect HOMO-LUMO energies altering the optical bandgap and therefore the emission profile of the complex have been elaborated upon.[95,120–122] These approaches are only in reference to the first sphere of coordination of the complex, i.e. the coordination of ligands to the metal centre. As discussed in the first paragraph of section 1.2, though chemistry often takes place in a dynamic media (gas phase, solvent, or solid), the nature of this media has drastic effects on the emissive properties of Ir(III) complexes. The second sphere of

coordination, i.e. non-covalent interactions with the ligands of the metal complex, can also bathochromically or hypsochromically shift the emission.[95] Phosphorescence from the lowest triplet state is stronger when the system can remain rigid due to the ISC requirements of a phosphorescent event.[95] Rigidity helps promote phosphorescence, therefore making the solvent non-polar will lead to less disturbance of the structure leading to fewer vibronic events, less non-radiative decay and more efficient phosphorescence phosphors.[95] Freezing solvents or moving to non-polar solvents causes a hypsochromic shift whereas the introduction of strongly H-bonding solvents leads to a bathochromic shift and a weakening in emission intensity.[95]

As established, understanding the HOMO-LUMO distribution across octahedral Ir(III) complexes is essential in predicting the strength of phosphorescent events.[95,112] Experimental techniques to analyse phosphorescence and lifetime have been discussed which provide insight into the photophysical nature of Ir(III) complexes. Computational techniques are also commonly applied in the design of Ir(III) complexes in addition to experimental photophysical characterisation. Density-functional theory (DFT) has been extensively applied to large molecules to give accurate data on the ground state distribution of orbitals within a many-body system.[129] Applying DFT to the design of Ir(III) complexes gives accurate estimations of orbital energies and distributions.[118,130] When these estimations are combined with the rules governing phosphorescence discussed within this section, this information can be used to predict whether a complex will be an efficient phosphor.[118,130]

1.5 Density-Functional Theory

Density Functional Theory (DFT) is a theory of electronic ground state structure based on estimations of the distribution of electron density ($n(\mathbf{r})$) in many-body systems.[131] DFT is mathematically rooted in the Thomas-Fermi model of electronic structure for materials.[131] Introduced in 1927 by Llewellyn Thomas and Enrico Fermi, this quantum mechanical theory uses a statistical model to approximate the electron distribution in an atom or molecule.[132] The basis of the theorem is that within a small phase space-volume element (ΔV) electrons are distributed uniformly in phase space, with two electrons in every h^3 of phase space-volume (where h is Planck's constant). Additionally, for each element occupying momentum-space volume (V_F) the sphere of momentum could be filled up to the Fermi momentum (P_F).[132]

$$V_F = \frac{4}{3}\pi p_F^3(\boldsymbol{r}) \tag{1.20}$$

Equation 1.20 defines V_F where $\boldsymbol{r}$ is the position vector of a point in ΔV. This expression can be expanded to encompass the volume element in phase-space (ΔV_{Ph}):

$$\Delta V_{Ph} = V_F \Delta V = \frac{4}{3}\pi p_F^3(\boldsymbol{r})\Delta V \tag{1.21}$$

The number of electrons (ΔN) in ΔV can be equated with electron density ($n(\mathbf{r})$) as shown in equation 1.22:

$$\Delta N = n(\boldsymbol{r})\Delta V \tag{1.22}$$

If the assumed uniform relationship shown in equation 1.22 is factored, when assuming there are 2 electrons per h^3 in the phase space volume ($\Delta V_{Ph} = h^3$) and this is factored into equation 1.21 then equation 1.23 is obtained, which demonstrates the $n(\mathbf{r})$ in a small element volume.

$$n(\boldsymbol{r}) = \frac{8\pi}{3}\frac{p_F^3}{h^3}(\boldsymbol{r}) \tag{1.23}$$

If this equation is solved for p_F and substitute the value into a classical kinetic energy formula, then the kinetic energy as a function of the electron density is obtained.[132] The accuracy of any further calculations is limited due to the kinetic-energy functional being an approximation based upon the uniform electron distribution and the lack of exchange-energy functionals (does not incorporate exchange forces/ Pauli repulsions).[132] A functional is a mathematical expression that assumes a function as an input (such as electron density) to calculate a new scalar number as an output (like energy). The kinetic energy functional is the input function of electron density denoted as $n(\mathbf{r})$ which defines the electron density distributed in space. $n(\mathbf{r})$ in electronic structure ground theory and DFT are the central quantity, all energies and properties are derived from it. Shown below in equation 1.24 is the integration of $n(\mathbf{r})$ which integrates to the total number of electrons in the many-body system (N).[132]

$$\int n(\boldsymbol{r})d\boldsymbol{r} = N \tag{1.24}$$

The simplest functional we can introduce $n(\mathbf{r})$ to is the Thomas-Fermi kinetic energy functional ($T_{TF}[n]$) which is defined in the absence of orbitals and simplifies the approximation of electron density:[132]

$$T_{TF}[\rho] = C\int n(\boldsymbol{r})^{\frac{5}{3}}d\boldsymbol{r} \tag{1.25}$$

$$\text{Where} \quad C = \frac{3}{10}(3\pi^2)^{2/3}$$

This approach to electron density is rough and only works for uniform electron gases but fails for molecules and atoms.[132] The Thomas-Fermi kinetic-energy functional was

improved by adding the von Weizsäcker correction in 1935,[133] but even with this improvement it was proven definitively by Edward Teller in 1962 that the Thomas-Fermi model could not describe molecular bonding.[134]

DFT was adopted in solid-state physics in the early 1970s after the introduction of the Hohenberg-Kohn (HK) theorems.[131,135,136] The first HK theorem demonstrated that the ground-state properties of many-electron systems can be determined by the electron density distribution.[131,135] This was achieved through the use of functionals of electron density, simplifying the many-body problem of N electrons each with $3N$ spatial variables to just three spatial variables. The second HK theorem defines a system's energy functional in terms of electron density.[136]

DFT entered the field of quantum chemistry in the 1990s once calculations were perceived to be accurate enough to be implemented into larger many body systems.[137] Parallel advancements in computer science allowed for lower computational costs compared to fully classical quantum mechanical methods.[138] Despite its popularity in quantum chemistry, the theory has significant limitations, especially when applied to supramolecular chemistry. The primary limitation of DFT is the same one the Thomas-Fermi electronic ground state theory has; a lack of knowledge of exchange energy correlation functionals and inaccuracies in the implementation of dispersion forces.[131] As a result, DFT struggles to describe intermolecular interactions and non-covalent bonding (the cornerstones of the study of supramolecular chemistry).[139] These issues negatively impact DFT results when used uncorrected, so improved functionals have been introduced to improve external contribution considerations.[139]

DFT is best used when the number of atoms in a many body system is >5-10, mainly because more modest quantum mechanical accuracy is excepted in larger many body systems, and classical methods become computationally challenging, costly and inefficient.[131] Additionally, some classical methods and DFT are complementary due to their shared building blocks of single-electron orbitals (ψ_j) and many-electron wave functions ($\boldsymbol{\psi}$). When defining DFT, the simplest class of system, the nonrelativistic system, must be considered in which electrons (N) are interacting in a nonmagnetic state with the Hamiltonian (H).[131] Below in equation 1.26 the relationship between H, the N-electron kinetic energy (T), the N-electron potential energy from an external field (V), and the energy of electron-electron interaction (U) can be seen.[131]

$$H \equiv T + V + U \tag{1.26}$$

The beginning of DFT relies on the HK theorems.[131,135,136] The ground state $n(\boldsymbol{r})$ determines the external potential ($v(\boldsymbol{r})$), and since $n(\boldsymbol{r})$ also determines N by integration, it determines the full H and therefore all properties defined by H. Through these assumptions it is possible to derive a minimal principle for the energy as a functional of $n(\boldsymbol{r})$ for a given $v(\boldsymbol{r})$:

$$E_{v(\boldsymbol{r})}[n(\boldsymbol{r})] \equiv \int v(\boldsymbol{r})n(\boldsymbol{r})d^3\boldsymbol{r} + F[n(\boldsymbol{r})] \tag{1.27}$$

$$F[n(\boldsymbol{r})] \equiv \langle \boldsymbol{\psi}[n(\boldsymbol{r})], (T+U)\boldsymbol{\psi}[n(\boldsymbol{r})] \rangle \tag{1.28}$$

Where $F[n(r)]$ is also a functional of $n(\boldsymbol{r})$, as $\boldsymbol{\psi}$ is a functional of $n(\boldsymbol{r})$. $\psi[n(\mathbf{r})]$ is the many electron wavefunction we use to assume electron density within a DFT system. V is excluded here from equation 1.28 as this derivation of the base equations of DFT is in its

simplest form where the energy does not depend on an external potential so they (V) are removed.[131]

The minimal principle is when $n(\boldsymbol{r})$ and E are the density and energy of the electronic ground state $n_0(\boldsymbol{r})$. From here $F[n]$'s largest elementary contributions can be extracted

$$F[n(\boldsymbol{r})] = T_S[n(\boldsymbol{r})] + \frac{1}{2}\int \frac{n(\boldsymbol{r})n(\boldsymbol{r'})}{[\boldsymbol{r}-\boldsymbol{r'}]} d\boldsymbol{r}\, d\boldsymbol{r'} + E_{xc}[n(\boldsymbol{r})] \tag{1.29}$$

where $T_s[n(\boldsymbol{r})]$ is the kinetic energy of a non-interacting system with density $n(\boldsymbol{r})$ and E_{xc} is the exchange correlation energy.[131] As mentioned previously, E_{xc} is an approximation and is the greatest source of error in the calculation of the ground state energy of a many-body system; according to W. Kohn's derivations it is the 'only source of error' in this calculation.[131] DFT's base equation for the ground state energy approximation follows, where ϵ_j and n are self-consistent quantities:

$$E = \sum_{j=1}^{v} \in_j - \frac{1}{2}\int \frac{n(\boldsymbol{r})n(\boldsymbol{r'})}{[\boldsymbol{r}-\boldsymbol{r'}]} d\boldsymbol{r}d\boldsymbol{r'} - \int v_{xc}(\boldsymbol{r})n(\boldsymbol{r})d\boldsymbol{r} + E_{xc}[n(\boldsymbol{r})] \tag{1.30}$$

$$\text{Where} \qquad v_{XC}(\boldsymbol{r}) = \frac{\delta E_{XC}[n]}{\delta n(\boldsymbol{r})}$$

ϵ_j is obtained from solving the Kohn-Sham orbital energy equations and depends on effective potential which is dependent on $n(\mathbf{r})$. $v_{xc}(\mathbf{r})$ is the exchange correlation potential which is a functional derivative of exchange-correlation energy (E_{xc}) and depends upon $n(\mathbf{r})$.[131] Self-consistency means that the equation components depend on each other and must be determined through multiple iterations starting with an initial guess of electron density and ending when electron density and potential converge.[131] For simplicity this explanation of DFT fundamentals was limited to the simplest class of electronic system

with no external fields. In practice DFT has always been used to describe larger systems where magnetic, electronic and relativistic corrections must be considered.[138] For this, more accurate orbital energy approximations, bond energies, and exchange correlations are required to optimise our understanding of larger molecules.[131,138,139] These are introduced through implementing modern functionals which have been developed to overcome limitations and increase accuracy of DFT predictions.[131,138,140]

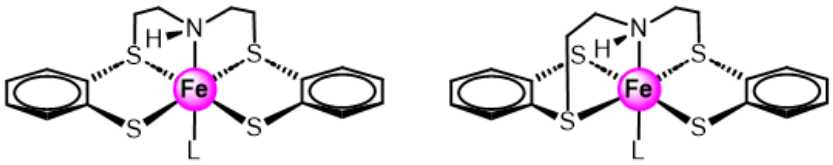
1.5.1 DFT of Metallic Complexes

As computational power grew and cost decreased, new advanced basis sets and functionals for DFT were introduced allowing for larger and larger many body systems to be investigated.[138] Many examples in the literature of large open-shell compounds are known, with most of them adopting the 'high-performing' B3LYP correlation functional (Becke, 3-parameter, Lee-Yang-Parr).[141] This functional is a hybrid-GGA (Generalised Gradient Approximation), meaning it incorporates a portion of exact exchange from Hartree-Fock theory with approximations from a generalised gradient approximation as shown in equation 1.31 where $f(n,|\nabla_n|)$ is a suitably chosen function of its two variables.[131]

$$E_{xc}^{GGA} = \int f(n(\boldsymbol{r}), |\nabla n(\boldsymbol{r})|) d^3r \tag{1.31}$$

Hybrid-GGAs like B3LYP often give good results for spin-state splitting and non-uniform electron distributions, therefore they are ideal for analysing the electronic nature of inorganic covalently bound metallic complexes.[142]

In parallel to the B3LYP functional when modelling transition metal compounds, it is common to use a variant of the 6-31G basis set. A basis set is a set of functions chosen to represent electronic wave functions in a manner suitable for computation. A basis set is chosen based on the atoms present within the structure being modelled, the desired levels of contributing effects, the symmetries within the molecule, the polarity of the bonding, and accepted level of computational cost.[142] For transition metal complexes specifically (such as those shown in figure 1.24), 6-31G basis set variants are applied to all atoms except the metals that the LANL2DZ basis set is applied to.[142–144]



1.63 **1.64**

Figure 1.24 Fe(II) compounds studied by Reiher *et al.* to study exact exchange and spin-state splitting in metallic complexes.[145]

The LANL2DZ (Los Alamos National Laboratory 2 double-ξ) basis set is implemented because the electronic sphere of transition metals is too great, therefore a 'double-ξ People-type' basis set must be applied to model the effective core potential (ECP) of the metal.[142,146] ECPs assume the inner core of electrons of a transition metal to be inactive, allowing one to model only the valence electrons of a metal. This drastically reduces computational costs since cost increases at $\sim N^4$ where N is the number of electrons required to be explicitly treated.[142,147] Of importance in the choice of an ECP, is that they should be paired to work in tandem with a specific basis set and functional in mind.[148] The pairing of 6-31Gs with LANL2DZ under variants of the B3LYP functional

is one such example of this, but also noteworthy is the use of Def-2 basis sets with the Stuttgart-Dresden-Bonn ECPs.[149] Accuracy of the chosen basis sets and functionals is assessed through comparison to experimental data on bond energy, geometry and spectroscopic properties with the data of DFT predictions.[141–143] DFT of transition metal complexes tend to yield good geometries for most traditional coordination compounds, though there are some shortcomings to DFT in investigation of organometallic complexes. Dispersion interactions are weakly accounted for (see figure 1.25), as well as electron self-interaction treatment and inaccuracy of exchange-correlation functionals.[141,143,150]

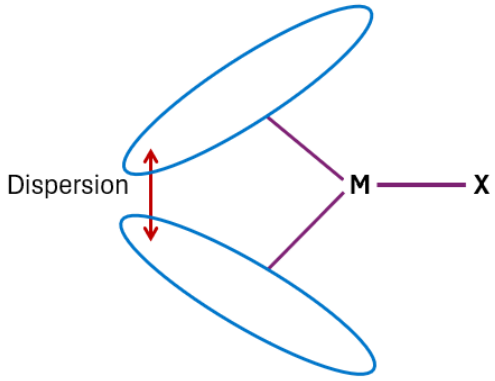


Figure 1.25 Schematic of how dispersion forces can occur and affect coordination geometry in a metallic complex.[141]

Intramolecular dispersion forces are certainly present in transition metal complexes, especially in larger complexes with bulky ligands on a single metal site.[151] DFT calculations on these complexes often fail to correctly reproduce interactions between ligands which can lead to geometric alterations around the metal.[141] A good example of this is Harvey *et al.*'s study of the dispersion in Grubbs catalysts $(Cy_3P)_2Ru(Cl)_2(CHPh)$ and $(Cy_3P)(IMes)Ru(Cl)_2(CHPh)$, where they found that the

CHPh, Cy_3P and IMes had van der Waals contact.[152] They found that introducing forcefields to constrain certain geometries by fixing electrons to certain ligands in the calculation led to more accurate estimates of bond energies. There are several methods for introducing forcefields into calculations including constraining quantum mechanical calculations simply to active sites,[153] adding external potentials,[154] or constraining electron density.[155] Before the forcefield was introduced M-P bond energies were found to be 17.3 and 15.9 $kcalmol^{-1}$ for each complex. After forcefield introduction they found bond energies of 30.7 and 28.5 $kcalmol^{-1}$ showing how much inaccuracy dispersion forces were introducing into their DFT methods.[152]

1.5.2 Time-Dependent Density-Functional Theory

Time-dependent density-functional theory (TD-DFT) is used to investigate the excited-state properties of many-body systems through time-dependent potentials.[156,157] Potentials such as electric or magnetic fields, the effects of which can be studied allowing computational chemists to extract excited state data. TD-DFT results can give accurate predictions of excitation energies, photo-absorption spectra, photoluminescent emission, and photo-electronic bandgap data.[156,157]

The foundation of TD-DFT is the Runge-Gross (RG) theorems shown below in equation 1.32 where the relationship between the Hamiltonian as a function of time (H(t)), the N-electron kinetic energy (T), the N-electron potential energy from an external field as a function of time (V_{ext}(t)), and the energy of spin-independent particle-particle interaction (W) can be seen.[158]

$$\hat{H}(t) = \hat{T} + \hat{V}_{ext}(t) + \hat{W} \tag{1.32}$$

The hats above the components in equation 1.30 are present to represent the external time-dependant field this Hamiltonian experiences. Postulated in 1984, the theorem is analogous to the HK theorems and shows that for an initial given wavefunction there is a relationship between the external time-dependent potential and the time-dependent density.[158] The implication of this is that the many-body wavefunction depends upon 3*N* variables equivalent to the electron density, and furthermore all properties of the system can be predicted from electronic density alone.[156,158,159] These calculations are built upon the linear response function, which shows how electron density can change upon exposure to external potentials, therefore calculations require the derivative of the exchange-correlation functional with respect to external density.[160]

Ten years after the initial RG equations, Casida *et al.* developed an effective linear-response formalism (LR) for TD-DFT, the 'random-phase Casida equations' allow rapid and efficient solutions of TD-DFT approximations for molecules.[161,162] Thanks to his pioneering work TD-DFT has been adopted as a computationally efficient solution to effectively estimate the energy of many body-systems.[163] The Casida equations rely on a matrix formulation of the LR for TD-DFT and were such a landmark moment that in a 2013 review by Laurent and Jacquemin they claimed that more than 1000 papers devoted to TD-DFT had been published in the decade after their introduction (an order of magnitude higher than the first decade).[157]

1.5.3 TD-DFT of Iridium (III) Complexes

In this thesis, computational investigations entirely revolved around the implementation of a B3LYP/6-31G**/LANL2DZ methodology using closed-source Gaussian for file calculations, and the open-source software Avogadro for creating input files and orbital models. The reason these methods were exclusively used for these investigations was driven primarily by the success and extensive studies by computational chemists when studying iridium complexes using these methods.[118,129,130,164–170]

TD-DFT can accurately predict phosphorescent emission energies (λ), the involved orbitals and electronic states for Ir(III) complexes.[118,130,165,166] This accuracy has limitations, as methods often fail to give quantitative information on emission lifetimes (τ) and phosphorescent strength (Φ_p). This is due to TD-DFT's inability to account for spin-orbit coupling effects.[163] This limitation in TD-DFT meant that computational methodologies could not be solely relied upon when considering the design of new complexes. Instead, known experimental and structural parameters must be considered in the design process. TD-DFT can be used to assist in this process though, as established in sections 1.4.1 and 1.4.2 the locations and distributions of HOMOs-LUMOs have a direct effect on the phosphorescent efficiency of an iridium complex.[95,120–122] TD-DFT has been proven to be a very effective computational method to predict the global HOMO and LUMO distributions. As such, these predictions can be used on orbital distribution to make inferences about the potential strength of the phosphorescent emitter.[163]

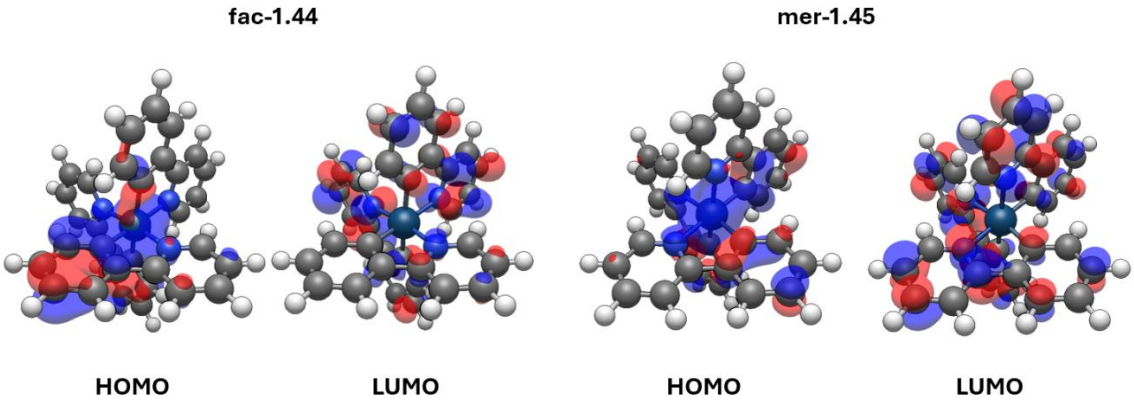


Figure 1.26 TD-DFT modelled global HOMO-LUMO distributions of compound **1.45** and **1.46** (the fac- and mer- isomers of [Ir(ppy)$_3$]). In both cases HOMOs reside on 5dπ orbitals of Ir and phenyl rings, LUMOs are distributed across the phenylpyridines.

Another use of TD-DFT when applied to organometallics, especially iridium and platinum complexes, is the estimation of electronic and optoelectronic bandgaps.[165] When designing efficient photo-catalysts frontier molecular orbitals (FMO) in their ground and excited states must be considered.[164] As the FMOs are what are involved in reductive and oxidative cycles of photoredox catalysis, understanding of their distributions and energies is essential in making informed decisions when tuning catalyst properties to their desired applications.[171–173]

1.6 Photoredox Catalysis

Photoredox is a branch of catalysis that uses light driven single-electron transfer mechanisms to harvest energy for a chemical reaction as an alternative to thermal chemistry.[174–178] The inspiration for photocatalysis lies in nature; plants generate the chemical energy for photosynthesis by capturing light energy from the sun using chlorophyl (figure 1.27).[179] The light energy harvested by chlorophyl is then used to

reduce a chain of electron acceptors to eventually deliver electronic fuel to the Calvin cycle.[180]

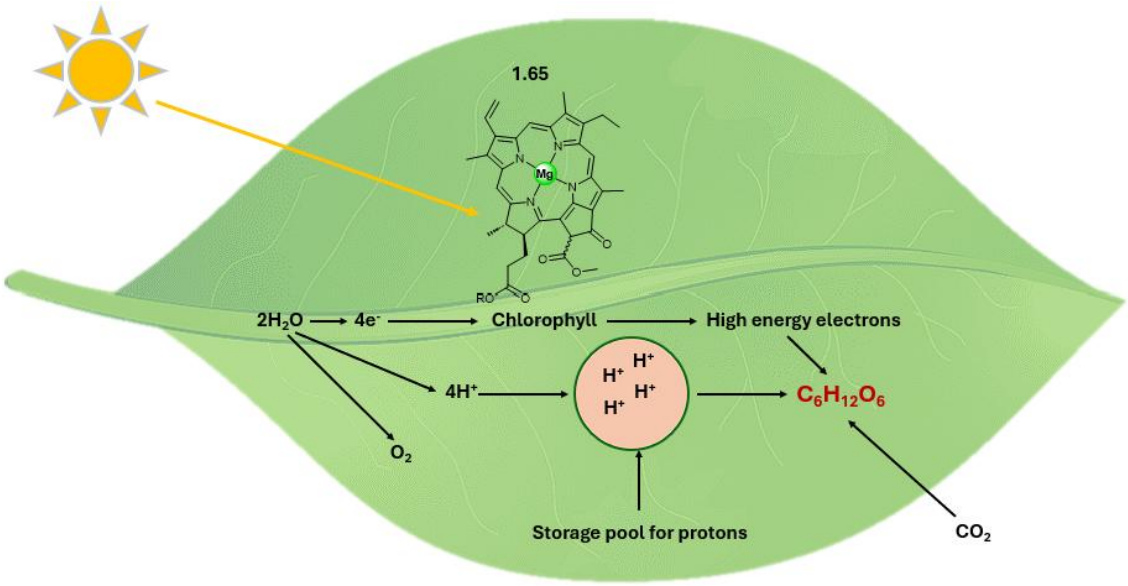


Figure 1.27 Diagram of the natural process of photosynthesis (inside plant cell chloroplasts). Shows the process to split water giving electrons and protons used to produce carbohydrates using chlorophyll as the light sensitising photocatalyst.[179]

Synthetic photoredox processes emulate this same design: incorporating a photosensitiser (PS); an organic dye, transition metal complex, or semiconductor, electron transport catalysts, reductive or oxidative fuels, and a media for processes to occur in.[176,177,179] The complexity of these systems is the fundamental difference between photochemistry and thermal chemistry. The understanding and recognition of this difference was the turning point in the development of photoredox systems.[177] Figure 1.28 shows the reaction pathways of a thermal chemical transformation against photochemical and photocatalytic reactions.[177]

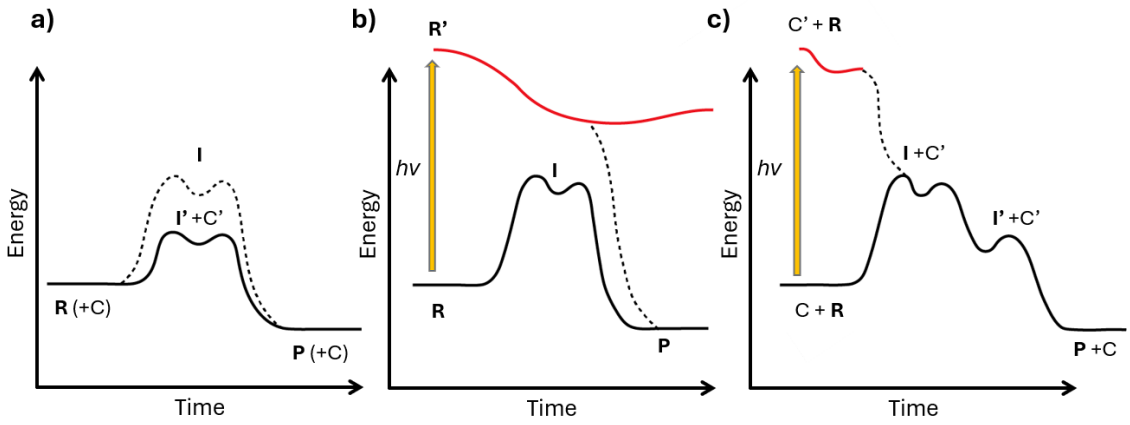


Figure 1.28 a) The reaction pathway of a thermal reaction (**R→P**) catalysed by **C** via intermediate **I' b)** Photochemical reaction where **R** is excited to **R'** proceeding to **P** via **I c)** A photocatalytic reaction pathway, where C is excited to C', then colliding with **I** to form **I'** before proceeding to **P**.[177]

Photoredox catalysis has seen increasing interest since the 1970s, especially since 2008, as a litany of new visible light driven pathways have been discovered.[176,181] These elegant pathways have been developed into practical systems whereby organic dyes, organometallics, and semiconductors can facilitate organic transformations by acting as a PS.[176,177,181] Photoredox catalysis' methodology takes cues from electrochemistry, inorganic chemistry and catalysis, but most importantly lies firmly in the field of green/ sustainable chemistry due to the lower energetic requirements of photocatalytic systems.[177]

$$reagents \xrightarrow{h\nu + PC} products \tag{1.33}$$

Photocatalysts (PC), unlike thermal catalysts, are only effective in their excited state (PC*). The PC* undergoes a chemical reaction with a reagent (R), like a single electron transfer (SET) or the transfer of a small atom such as a proton.[177] From this initial reaction an intermediate (I) is formed, along with a radical or a radical ion and a

reduced or oxidised PC'. The PC' then undergoes oxidative or reductive quenching (shown below in figure 1.29). Whether a PC' undergoes the oxidative or reductive quenching cycle is dependent upon the photochemical energetics of all reagents and catalysts required to undergo organic/inorganic transformation.[177]

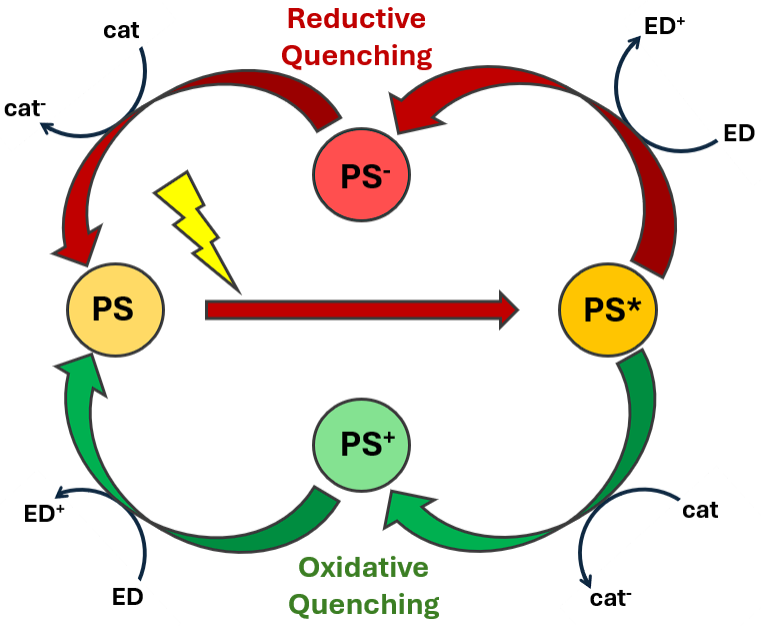


Figure 1.29 Schemes for reductive and oxidation quenching including photosensitiser (PS), electron donor (ED), and co-catalyst (cat).[179,182]

1.6.1 Homogeneous Photosensitisers

Homogeneous photosensitisers are an interesting subset of molecules. In homogeneous catalytic configurations the PS is paired with a co-catalyst and are generally two separate units.[177] The co-catalysts can be strongly hydrogen-bonding co-catalysts for stereospecific organic transformations or redox catalysts capable of oxidation or reduction, but in both cases the chemical energy for the reactions is provided by the PS.[177] A homogeneous PS is defined as any light harvesting material in the same

phase as all other components of the catalytic system. These PSs can range from organic dyes such as methylene blue, to inorganic and organometallic complexes (see figure 1.30).[183]

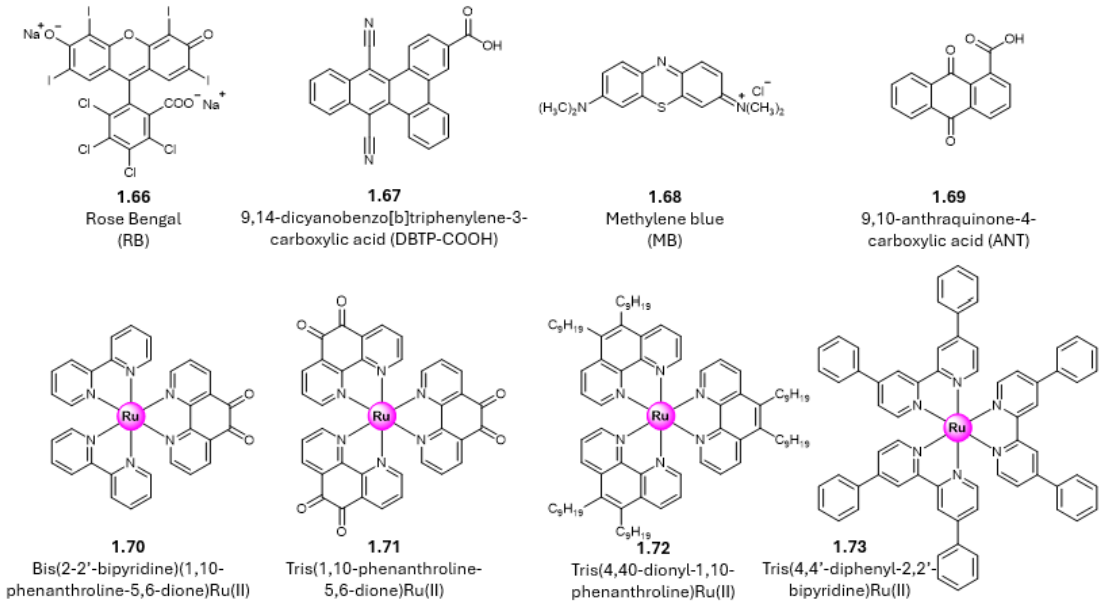


Figure 1.30 Examples of organic dyes and inorganic ruthenium complexes studied as homogeneous photosensitisers.[183,184]

Organic dyes are proven to be cost effective, abundant materials for a variety of photosensitising purposes, and many are naturally occurring in flowers, leaves and fruits.[183] Furthermore, the use of these materials limits our reliance on precious metals such as platinum, iridium, and ruthenium. Unfortunately, unlike their metallic counterparts, organic dyes have far lower light absorption efficiencies (the highest recorded being 1.7% with betalain pigments).[185,186] This inefficiency means far less light energy can be transformed into the chemical energy required for photocatalytic transformations. Ruthenium complexes however, have been heavily studied as PSs dating

back to the late 1970s and are effective PSs due to their photo- and electrochemical properties, excellent photo-stability, strong charge transfer abilities and wide visible absorption ranges.[185] Ruthenium complexes do have several caveats; they are difficult to synthesise, degrade readily in the presence of water, and consequently are harmful to the environment.[185]

1.6.2 Design of Efficient Iridium (III) Photosensitisers

Unlike ruthenium complexes, Ir(III) complexes are easy to synthesise in high yields and many are stable in the presence of water.[187] Their variable oxidation states, high corrosion, and rich electronics, make Ir(III) complexes effective catalysts for a variety of purposes (see figure 1.31 for common examples of Ir(III) photocatalysts).[90,176,179,181,188] Heavy metal complexes such as Ir(III) have several intrinsic advantages as photocatalysts owing to their electronic properties. In particular, heavier atoms increase ISC efficiency through improved spin-orbit coupling.[114,189] With improved ISC comes longer-lived T_1 states and thus it is theorised that the longer lifetimes allow for more favourable kinetics in photochemistry.[179] Another key advantage in using Ir(III) complexes as PSs is the separation of the HOMOs and LUMOs.[95] For example, heteroleptic Ir(III) complexes with general formulae $[Ir(C\hat{}N)_2(N\hat{}N)]^+$ have LUMOs that tend to reside on the N^N ligand, while the HOMOs reside on the C^N cyclometalating ligands and Ir(III) metal itself. Due to this orbital localisation, the electronic and photophysical properties of these complexes are very sensitive to the nature of the ligands,[179] making it easier to introduce EWGs and EDGs to specifically

tune the photochemical behaviour of FOMOs. In addition, localisation of FOMOs has been proven to assist charge transfer in SET mechanisms.[95]

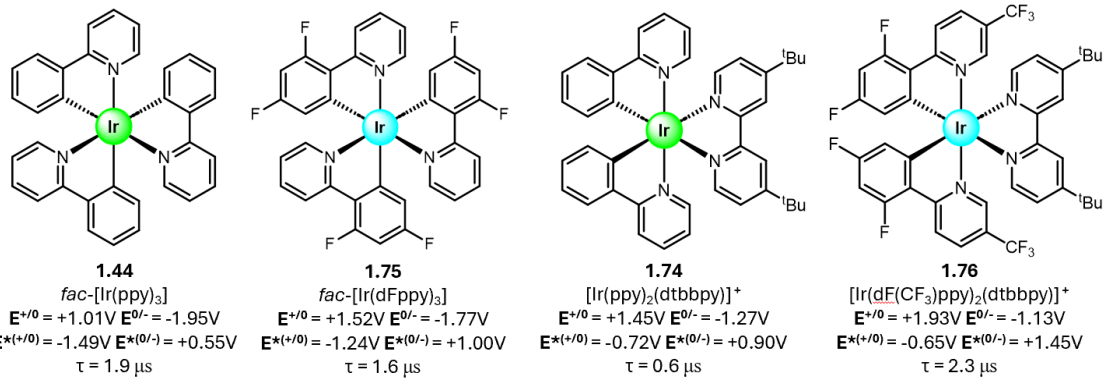


Figure 1.31 A selection of the most common Ir(III) photosensitisers in the literature and their respective photoredox potentials.[190]

Just like in figure 1.31 many of the most studied Ir(III) photosensitisers incorporate variations of substituted 2-phenylpyridines. As established in section 1.4.2, changing the positions and nature of substituted groups can have drastic effects on orbital energies. This approach to colour tuning also applies in optimising the photoredox properties.[190] The most important properties of a high performance PS are: broad light absorption range with a high molar absorption coefficient, suitable photoredox potentials to the intended system, long excited-state lifetimes, high photostability to ensure structural integrity under prolonged irradiation, and good solubility in the reaction media.[179,190] Knowing these desired properties and how efficient prolonged T_1 states for phosphorescence can be designed, all previously discussed design techniques to create new photochemically suitable and efficient PSs can be applied.

How suitability of a photosensitiser to a reaction can be determined is through Rehm–Weller photoredox potentials. They are used to estimate the feasibility of a

favourable SET within a photoredox system.[191,192] Photochemical oxidation ($E_{(PS+/PS*)}$) and photochemical reduction ($E_{(PS*/PS-)}$) can be calculated as shown below in the Rehm–Weller equations 1.34 and 1.35, which require electrochemical data on the oxidation (E_{ox}) and reduction (E_{red}) of the PS along with data of the electronic origin ($E_{0\text{-}0}$).[191,192]

$$E_{(PS^+/PS^*)} = E_{ox} - E_{0-0} \quad (1.34)$$

$$E_{(PS^*/PS^-)} = E_{red} + E_{0-0} \quad (1.35)$$

Oxidation and reduction potentials can be found using cyclic voltammetry (CV) giving knowledge on the ΔE of the system, while the electronic origin ($E_{0\text{-}0}$) is estimated from the intersection of normalised excitation and emission photoluminescence spectra.[128,170,179,187,193] $E_{0\text{-}0}$ (zero-zero transition energy) is the difference between the lowest vibrational level of the ground electronic state (S_0, ν=0) and the lowest vibrational level of the excited state, which in the case of Ir(III) phosphors is T_1, ν=0. There are several ways to gain the estimate of $E_{0\text{-}0}$, the most abundant approach in organic electronics mentioned above is to use the intersection of normalised excitation-emission spectra, however this method has been shown to produce inaccuracies in metallic complexes with strong charge transfer bands.[98,128,170,179,187,193] Another technique for the estimation of $E_{0\text{-}0}$ values is phosphorescence onset which is applied when there is no obvious intersection between absorption and emission spectra.[98,194] Phosphorescent onset is when the $E_{0\text{-}0}$ value is assumed to be equivalent to the first rapid increase in emission intensity, recently Wegner et al. used the 10% of peak emission value on the hypsochromic shoulder of a series of water soluble iridium complexes to estimate the 0-0 transition.[98] A more accurate method for the estimation of $E_{0\text{-}0}$ is to use time-resolved emission spectroscopy at 77 K to help resolved the vibrational structure, this makes the 0-

0 transition peak more visible and allows for more accurate estimations as to the true value of $E_{0\text{-}0}$.[194–197] Computational techniques such as TD-DFT can also be used to estimate $E_{0\text{-}0}$ or verify experimental findings by calculating the optimised geometries in the ground and excited states then computing the adiabatic energy difference between the optimised structures.[198] Using this computational technique enables accurate estimations of excited state orbital energies and therefore aids in the design of efficient PSs.[164] One such use of Ir(III) PSs is in the production of hydrogen through water splitting,[179] of which there are countless studies of this photocatalytic reaction with a wide range of Ir(III) complexes.

1.6.3 Iridium (III) Photosensitisers Applied to Hydrogen Evolution

Hydrogen is one of the most important chemical feedstocks in the world.[199] It is required in a wide range of energy intensive industrial reactions, most notably the Haber-Bosch process (55% of global hydrogen is used in this process) where 3 hydrogen molecules are required to produce every 2 ammonias.[200] Although hydrogen is often touted as a clean energy source, hydrogen has a "dirty little secret".[201] The vast majority of hydrogen (48%) is produced through the steam methane reformation process (shown in figure 1.32).[200] This reaction uses high temperatures and pressures (carbon emitting processes) to combine methane with water vapour and convert them into hydrogen and carbon dioxide.

$$CH_4 + 2H_2O \xrightarrow{\Delta} CO_2 + 4H_2 \qquad (1.36)$$

The balanced equation of the industrial process shown in equation 1.36 demonstrates that even before considering the cost of generating the thermal energy and pressure required for this process, CO_2 is generated as a reaction by-product. This means that even if renewable or nuclear energy could be guaranteed to fuel this reaction, the process itself is still a contributor to the greenhouse effect.[201]

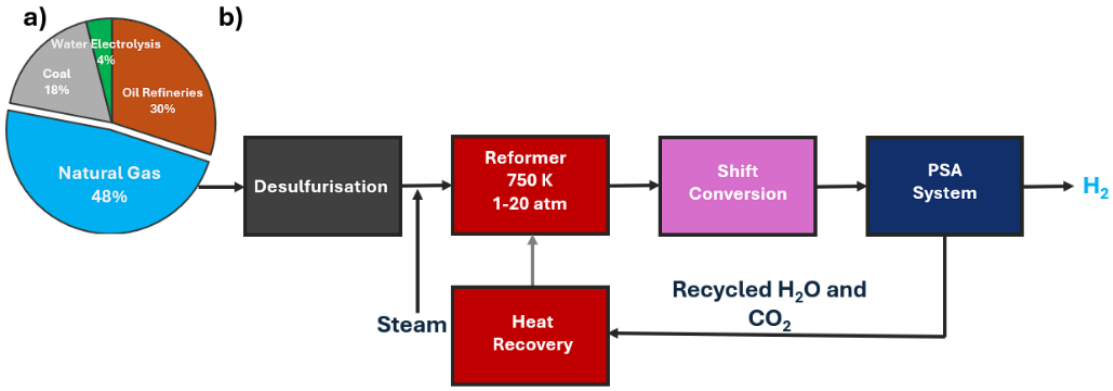


Figure 1.32 a) The percentage by source of where hydrogen is refined from **b)** A flowchart schematic of the steam methane reformation process used to produce 'blue' hydrogen.[199,201,202]

Knowing hydrogen's clandestine backstory makes it evident that alternate methods of generating hydrogen are essential to remove this large source of CO_2 emissions. Currently only 4% of the world's hydrogen production comes from water electrolysis (arguably a green source depending on energy production), but industrial water electrolysis is an incredibly energy intensive process.[200] When performing energy cost analysis on large scale established processes, it is demonstrated that the overall energy demands of producing hydrogen through water electrolysis are higher than steam methane reformation on a per molecule basis: steam methane reformation requiring 165

MJ/kg of hydrogen produced vs water electrolysis requiring 192 MJ/kg of hydrogen produced.[201]

In the past photocatalysis has provided lower energetic pathways for many processes.[178,179,181] In addition, water is split in the biological process of photosynthesis producing the oxygen we breathe and providing evidence from nature that a light driven process to split water is possible.[179] A wide range of synthetic systems incorporating iridium for photocatalytic hydrogen production have been developed over many years,[179] but this thesis will limit the scope of discussion to purely homogenous Ir(III).

There are four types of Ir(III) complexes applied to hydrogen generation: cationic $[Ir(C^N)_2(N^N)]^+$, neutral $[Ir(C^N)_3]$/ $[Ir(C^N)_2(N^N)]$, coumarin co-sensitised, and multimetallic.[179] Each of these systems have enough examples in the literature to warrant individual reviews, but for the relevance of this thesis, examples will be restricted to cationic and neutral Ir(III) complexes. Cationic $[Ir(C^N)_2(N^N)]^+$ (such as compounds **1.74** and **1.76** in figure 1.31) are the most ubiquitous iridium PSs in the hydrogen evolution reaction (HER). Complexes of this nature have particularly high molar extinction coefficients (ε), which means a greater ability to harvest light and therefore are a higher functioning PS.[179] $[Ir(C^N)_2(N^N)]^+$ complexes do suffer from one enormous drawback: the long-term stability of the complex is limited due to the purely dative coordination of the N^N bpy styled ligand to the Ir(III) centre.[179] This lack of stability has led some research groups to favour neutral Ir(III) complexes (both homo- and heteroleptic) for photocatalytic water splitting, but neutral Ir(III) compounds (such as compounds **1.74** and **1.44** in figure 1.75) see far lower catalytic turnover numbers (TON) (calculated from the mols of hydrogen generated to the mols of PS) than their cationic

counterparts.[179] TONs for cationic systems have been shown to be as high as 17,000 whereas the highest TON observed for a charge neutral system is 3704.[179,203]

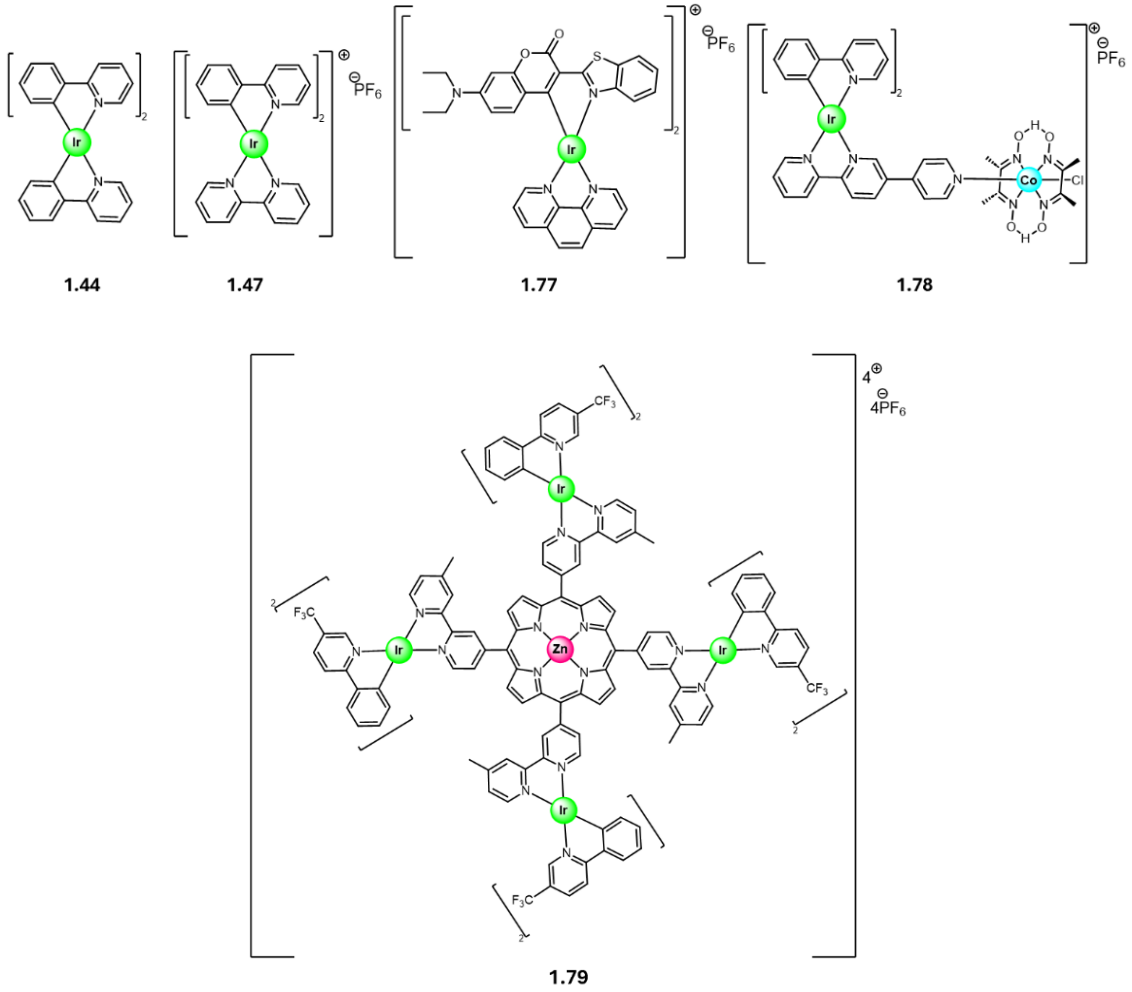


Figure 1.33 Examples of the four common types of Ir(III) PS, **1.45** is neutral, **1.47** is cationic, **1.77** is coumarin based, **1.78** and **1.79** are bi- and multi-metallic respectively.[179]

Both cationic and neutral Ir(III) complexes tend to follow a reductive quenching cycle for the HER.[179] In the reductive quenching cycle, the PS absorbs light energy exciting the complex to be PS*, from here the PS* can accept an electron from a sacrificial electron donor (ED). EDs vary, but one common theme of them is an available

lone pair capable of behaving as a cationic radical. The most common EDs in the literature are triethylamine, triethanolamine, and ascorbic acid/ sodium ascorbate.[179] Next the reduced PS (PS^-) passes the electron to a water reduction catalyst or co-catalyst, common examples are $[Co(bpy)_3]^{2+}(Z^-)_2$ (where Z is an appropriate anion) and $K_2[PtCl_4]$. The water reduction catalyst then reduces protons to hydrogen which evolves from the solution (the mechanism described is depicted below in figure 1.34).[179] Accurately determining the mechanism of reduction to hydrogen at this point is very challenging, especially with the basic nature of many of these catalytic systems (systems must be basic so electron donor lone pairs remain unoccupied).[204]

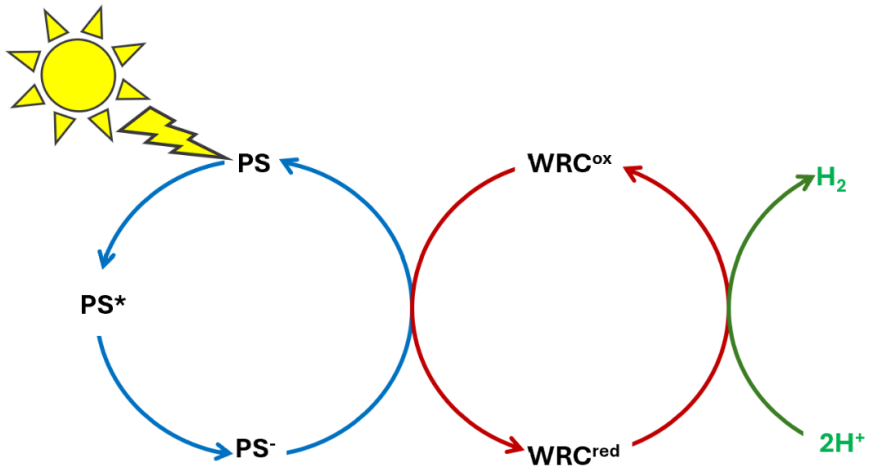


Figure 1.34 Photocatalytic cycles of the photo-reductive HER.[205]

Although the energy requirements for the HER have not been fully established,[179,193] a comprehensive knowledge of the redox potentials and charge transfer abilities of individual components is known. Fully assembled photocatalytic systems are, however, notoriously difficult to characterise.[193] Current methods of mechanistically

characterising a photoredox system rely heavily on PL quenching studies.[193] Quenching studies can establish energy transfer *versus* SET processes by analysing the drop in PL emission of the photosensitiser. The drop in emission as quencher is being added is proportional to energy transference to the quencher and can therefore be used to estimate the increase of non-radiative electronic processes such as SET.[193] Quenching studies for photoredox catalysis rely on the Stern–Volmer equations shown below in equations 1.37 and 1.38. K_{sv} is extracted from the gradient of the fit of I_0/I with increasing molar equivalents of quencher [Q] added to the solution containing the PS. K_q is then calculated by dividing the K_{sv} by the PL lifetime of the PS with no [Q] present, and thus K_q's are reported as a reciprocal of molarity per unit time.[206]

$$I_0/I = 1 + K_{SV}[Q] \tag{1.37}$$

$$K_q = K_{SV}/\tau_0 \tag{1.38}$$

These Stern-Volmer equations apply to the dynamic quenching pathway where the quencher collides with a chromophore after excitation.[207,208] There is another mechanism of quenching known as static quenching whereby pre-association of chromophore and quencher happens before excitation leading to a change in emission intensity and Φ, but no change in the lifetime of the chromophore.[207,208] A combination of these two quenching effects leads to upwardly deviating non-linear curves which can be fit with higher order Stern-Volmer equations reliant on an understanding of the chromophore's K_D (dynamic quenching constant) and K_S (static quenching constant) with the quencher shown below in equation 1.39.[207,208]

$$\frac{I_0}{I} = K_D K_s[Q]^2 + (K_D + K_S)[Q] + 1 \tag{1.39}$$

A comprehensive study by Shih-Chun Lo *et al.* outlined the minimum energetic requirements for Ir(III) photosensitisers in the photo-reductive HER cycle.[193] They synthesised a broad range of Ir(III) complexes and performed extensive Stern-Volmer mechanistic analysis to help explain the variation in H_2 generation when solely changing the photosensitiser. They demonstrated that favourable photoredox potentials were the most important factor in determining suitability of a PS, while lifetime of excited states appeared to be a second order effect.[193]

After photoexcitation there are many electron transfer processes available and so far in this thesis, we have solely focused on the desired SET reaction for a successful catalytic cycle. It is important to also acknowledge cage escape yields (Φ_{CE}) and the potential side reactions which can occur to quench the system.[209,210] Below in equations 1.40-1.42 are general expressions of how photoreduction can lead to loss of energy through unwanted side reactions.[209,210]

$$[PS]^* + Substrate \rightarrow [PS^{\cdot} + Substrate^{\cdot}] \quad (1.40)$$

$$[PS^{\cdot} + Substrate^{\cdot}] \rightarrow PS + Substrate \quad (1.41)$$

$$[PS^{\cdot} + Substrate^{\cdot}] \xrightarrow{diffusion} Free\ Radicals \quad (1.42)$$

Equation 1.40 demonstrates the general scheme for the SET process from a substrate to an excited PS*, equation 1.41 gives the general scheme for cage recombination eg. transferring the electron straight back to reform PS and substrate, and equation 1.42 displays the general scheme of cage escape where $PS^{\cdot}$ and $substrate^{\cdot}$ diffuse and react with other substances forming radicals and undesired side products. Cage escape yields (Φ_{CE}) can be measured through several experimental techniques including transient

absorption spectroscopy,[211–214] photoproduct analysis,[214] and chemical trapping.[214,215] Φ_{CE} vary significantly based on the nature of solvent, redox potentials of catalysts and substrates, and the catalyst structure i.e. is it an organic photosensitiser or inorganic complex.[209,210] Due to the complexity of photocatalytic systems demonstrated by how many factors must be considered when designing reactions, high-throughput techniques are often applied in the discovery of new reactions.[216]

1.7 Automation for Chemistry

Chemistry is a highly labour-intensive practical science. Bench chemists must simultaneously have a comprehensive understanding of complex theories surrounding the planning and design of experimentation, while also performing said complex experimentation. The advent of automation and high-throughput (HT) technologies has enabled a rapid increase in lab productivity and the generation of data.[216] Early lab automation can be ascribed to life sciences looking for more efficient ways to aliquot samples for testing.[217] This took the form of liquid handling automation which could generate consistent arrays of assays with little manual intervention, leading to rapid uptake in clinical sample production across academia and industry.[217]

The early adopters of HT technology in the chemical space were drug discovery and materials scientists.[218–220] Before data driven techniques began to dominate these fields they relied on large scale combinatorial formulations and serendipitous discovery.[216] Using HT techniques allows for an exponential scale up of combinatorial formulations and an increased rate in the discovery of novel materials through sheer volume of experimentation.[216] Platforms allowing these accelerated screening techniques are shown below in figure 1.35 and are all built on the same foundations of adaptable

software and hardware.[216] Hardware must be adaptable to allow for different applications, with exchangeable modules for both formulation and analysis that allow platforms to be used across a variety of fields and industries.[216] Some of the leading vendors of automated chemical platforms include Chemspeed (used in chapter 2 of this thesis), Unchained Labs (originally Symyx Technologies), and Mettler-Toledo.[221–223]



Figure 1.35 Commercially available automation platforms. **a)** Chemspeed automated synthesis platform[221] **b)** Unchained labs 'Big Kahuna' platform[223] **c)** Mettler-Toledo CHRONECT XPR with GC adaptor.[222]

More modern approaches to automation techniques involve the incorporation of self-driving laboratories (SDL).[224] SDLs combine automation experimental workflows with autonomous experimental planning made possible by advances in machine learning (ML) in the chemical space.[224] SDLs use the large volume of data generated through HT techniques and combine it with an automated data-driven decision-making element. This decision-maker allows for experimentation to continue autonomously in a 'closed-loop' manner.[224] The levels of autonomy achieved by different groups vary, but the consensus end goal is an autonomous lab in which all experimentation and laboratory duties would be fully automated and experimentation would be led with a data driven approach capable of self-optimisation in the discovery of novel desirable chemicals and materials.[224]

1.7.1 Automation in Photoredox catalysis

Due to the complex nature of photocatalysis requiring many components working cooperatively for successful chemical transformation, HT techniques are readily applied to the optimisation of photoredox systems.[225] For this purpose, arrayed experimentation is implemented to observe discrete variables such as metal salts, choice of catalysts, ligands, solvents, additives etc.[224,226] This variation leads to rapid determination of viable combinations of substrates for photoredox systems and in an indirect fashion employs the concept of 'accelerated serendipity'.[216] This HT technique for photocatalyst screening made famous by McNally *et al.* combines pools of substrates in a 'random' recombinant fashion to force 'serendipitous discovery' of new reactions or new conditions capable of known processes.[227] The wells of mixed reagents are analysed using GC- or/and LC-MS to identify desirable reaction products through observing masses which indicate new bond formation.[227]

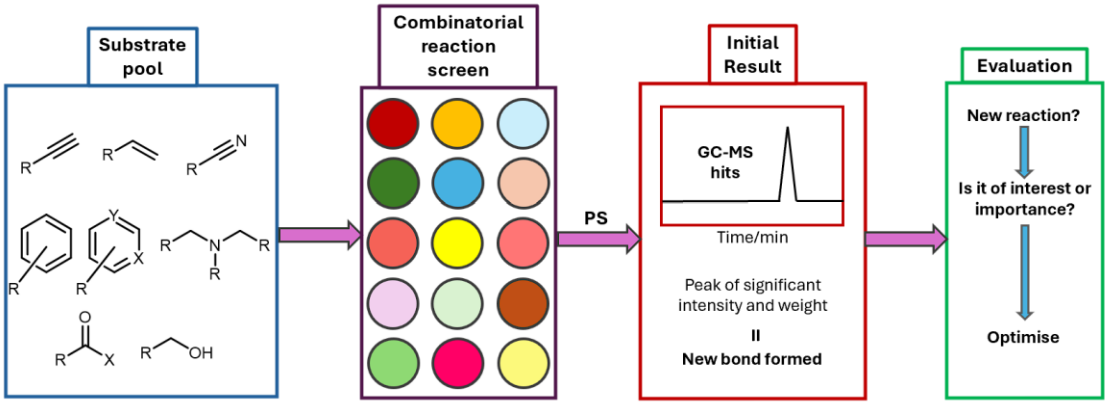


Figure 1.36 Workflow for novel photocatalytic reaction discovery screening. Substrates are combined randomly in the combinatorial reaction screening step. The pools are then irradiated with visible light in the presence of a **PS** and the wells are analysed with GC-MS followed by evaluation.[216,227]

Although many examples of HT techniques applied to combinatorial screenings in photocatalysis exist, there are not many examples of these techniques applied to the conditions of Ir(III) complex catalysed hydrogen production.[216,226,228] The earliest example is from the group of Bernhard *et al.*, who synthesised a library of heteroleptic Ir(III) complexes through combinatorial screening and then evaluated their photoredox hydrogen production.[229] This work focused on discovery of new Ir(III) PS compounds through combinatorial screening and had very little focus on optimising the HER (the conditions of the HER were kept constant).[229] Sixteen years later they followed this combinatorial synthesis paper up with a data driven approach to predict the triplet photophysical properties.[230] They used a similar random combinatorial synthetic approach, followed by lifetime and emission analysis to evaluate the photophysical/photoredox properties of 1440 distinct heteroleptic complexes.[230] Despite few examples of HT techniques being applied to Ir(III) catalysed HER, there exist many examples of Ir(III) complexes used as the PS in combinatorial novel reaction discovery.[226,231–234]

1.8 Thesis Objectives

The preceding literature overview outlines the context of the thesis aims, from phosphorescent hydrogen-bonding Ir(III) emitters to automation accelerated photocatalysis and all appropriate characterisations. Each of the following experimental discussions in chapters 2, 3 and 4 will address the thesis aims fourfold through these objectives:

1. To synthesise a series of hydrogen-bond rich Ir(III) complexes and test their properties.
2. Evaluate the properties of the complexes and test them against an appropriate application.
3. Evaluate the success of testing and the feasibility of the application.
4. Suggest improvements and adjustments to increase success of any future testing.

In fulfilling these objectives, we will demonstrate that hydrogen-bond rich Ir(III) complexes (with and without appropriate guests) have tangible applicability.

1.9 Bibliography

1 B. Balónová, D. R. Martir, E. R. Clark, H. J. Shepherd, E. Zysman-Colman and B. A. Blight, *Inorg. Chem.*, 2018, **57**, 8581–8587.

2 L. Yang, J. R. Adsetts, R. Zhang, B. Balónová, M. T. Piqueras, K. Chu, C. Zhang, E. Zysman-Colman, B. A. Blight and Z. Ding, *J. Electroanal. Chem.*, 2022, **906**, 115891.

3 B. Balónová and B. A. Blight, *Front. Chem.*, 2021, **9**, 712698.

4 F. Biedermann and H.-J. Schneider, *Chem. Rev.*, 2016, **116**, 5216–5300.

5 M. T. Piqueras, H. J. Howe, S. A. Englehart, R. M. Williamson, A. M. Paul and B. A. Blight, *Chem. Commun.*, 2023, **59**, 12727–12730.

6 B. Balónová, Shepherd ,Helena J, Serpell ,Christopher J and B. A. and Blight, *Supramol. Chem.*, 2020, **32**, 1–12.

7 W. Da, T. H. Jones, J.-B. Lin and B. A. Blight, *Can. J. Chem.*, 2023, **101**, 177–185.

8 S. J. Thomas, B. Balónová, J. Cinatl Jr., M. N. Wass, C. J. Serpell, B. A. Blight and M. Michaelis, *ChemMedChem*, 2020, **15**, 349–353.

9 F. Weinhold and R. A. Klein, *Chem. Educ. Res. Pract.*, 2014, **15**, 276–285.

10 J.-M. Lehn, *Science*, 1993, **260**, 1762–1763.

11 J. D. van der Waals, *Over de continuïteit van den gas- en vloeistoftoestand*, Sijthoff, 1873.

12 H. Margenau, *Rev. Mod. Phys.*, 1939, **11**, 1–35.

13 H. P. Dixon, H. D. B. Jenkins and T. C. Waddington, *J. Chem. Phys.*, 1972, **57**, 4388–4397.

14 J. Vicens and Q. Vicens, *J. Incl. Phenom. Macrocycl. Chem.*, 2011, **71**, 251–274.

15 H. Kunz, *Angew. Chem. Int. Ed.*, 2002, **41**, 4439–4451.

16 E. Fischer, *Berichte Dtsch. Chem. Ges.*, 1894, **27**, 2985–2993.

17 D. E. Koshland Jr., *Angew. Chem. Int. Ed. Engl.*, 1995, **33**, 2375–2378.

18 J. W. Steed and J. L. Atwood, *Supramolecular Chemistry*, John Wiley & Sons, 2022.

19 V. Balzani, A. Credi, F. M. Raymo and J. F. Stoddart, *Angew. Chem. Int. Ed.*, 2000, **39**, 3348–3391.

20 R. A. Bissell, E. Córdova, A. E. Kaifer and J. F. Stoddart, *Nature*, 1994, **369**, 133–137.

21 D. A. Leigh, J. K. Y. Wong, F. Dehez and F. Zerbetto, *Nature*, 2003, **424**, 174–179.

22 M. Von Delius and D. A. Leigh, *Chem. Soc. Rev.*, 2011, **40**, 3656.

23 R. F. Ludlow and S. Otto, *Chem Soc Rev*, 2008, **37**, 101–108.

24 C. J. Pedersen, *Science*, 1988, **241**, 536–540.

25 Press release, https://www.nobelprize.org/prizes/chemistry/1987/press-release/, (accessed 3 May 2025).

26 G. Schill and H. Zollenkopf, *Justus Liebigs Ann. Chem.*, 1969, **721**, 53–74.

27 K. Kinbara and T. Aida, *Chem. Rev.*, 2005, **105**, 1377–1400.

28 J.-P. Sauvage and P. Gaspard, *From Non-Covalent Assemblies to Molecular Machines*, John Wiley & Sons, 2011.

29 john liebler, Well, You Can Tell by the Way I Use My Walk... Scientific Illustration, https://www.artofthecell.com/well-you-can-tell-by-the-way-i-use-my-walk/, (accessed 4 June 2025).

30 A. D. Buckingham, J. E. Del Bene and S. A. C. McDowell, *Chem. Phys. Lett.*, 2008, **463**, 1–10.

31 P. A. Kollman and L. C. Allen, *Chem. Rev.*, 1972, **72**, 283–303.

32 E. Arunan, G. R. Desiraju, R. A. Klein, J. Sadlej, S. Scheiner, I. Alkorta, D. C. Clary, R. H. Crabtree, J. J. Dannenberg, P. Hobza, H. G. Kjaergaard, A. C. Legon, B. Mennucci and D. J. Nesbitt, *Pure Appl. Chem.*, 2011, **83**, 1637–1641.

33 S. C. C. van der Lubbe, F. Zaccaria, X. Sun and C. Fonseca Guerra, *J. Am. Chem. Soc.*, 2019, **141**, 4878–4885.

34 S. I. Stupp and L. C. Palmer, *Chem. Mater.*, 2014, **26**, 507–518.

35 L. Yang, X. Tan, Z. Wang and X. Zhang, *Chem. Rev.*, 2015, **115**, 7196–7239.

36 E. T. Kool, *Annu. Rev. Biophys. Biomol. Struct.*, 2001, **30**, 1–22.

37 T. Uchimaru, J. Korchowiec, S. Tsuzuki, K. Matsumura and S. Kawahara, *Chem. Phys. Lett.*, 2000, **318**, 203–209.

38 W. L. Jorgensen and J. Pranata, *J. Am. Chem. Soc.*, 1990, **112**, 2008–2010.

39 S. Djurdjevic, D. A. Leigh, H. McNab, S. Parsons, G. Teobaldi and F. Zerbetto, *J. Am. Chem. Soc.*, 2007, **129**, 476–477.

40 T. J. Murray and S. C. Zimmerman, *J. Am. Chem. Soc.*, 1992, **114**, 4010–4011.

41 J. R. Quinn, S. C. Zimmerman, J. E. Del Bene and I. Shavitt, *J. Am. Chem. Soc.*, 2007, **129**, 934–941.

42 B. A. Blight, C. A. Hunter, D. A. Leigh, H. McNab and P. I. T. Thomson, *Nat. Chem.*, 2011, **3**, 244–248.

43 F. H. Beijer, H. Kooijman, A. L. Spek, R. P. Sijbesma and E. W. Meijer, *Angew. Chem. Int. Ed.*, 1998, **37**, 75–78.

44 R. P. Sijbesma, F. H. Beijer, L. Brunsveld, B. J. B. Folmer, J. H. K. K. Hirschberg, R. F. M. Lange, J. K. L. Lowe and E. W. Meijer, *Science*, 1997, **278**, 1601–1604.

45 P. S. Corbin and S. C. Zimmerman, *J. Am. Chem. Soc.*, 1998, **120**, 9710–9711.

46 P. Thordarson, *Chem Soc Rev*, 2011, **40**, 1305–1323.

47 G. ALBERTI, *Solid-State Supramol. Chem. Two- Three-Dimens. Inorg. Netw.*, 1996, **7**, 425–482.

48 C. Bissantz, B. Kuhn and M. Stahl, *J. Med. Chem.*, 2010, **53**, 5061–5084.

49 The Top 300 of 2022, https://clincalc.com/DrugStats/Top300Drugs.aspx, (accessed 3 May 2025).

50 R. G. S. Berlinck and M. H. Kossuga, *Nat. Prod. Rep.*, 2005, **22**, 516.

51 R. G. S. Berlinck, A. E. Trindade-Silva and M. F. C. Santos, *Nat. Prod. Rep.*, 2012, **29**, 1382.

52 A. Strecker, Justus Liebigs Annalen der Chemie, 1861, **118**, 2, 151-177.

53 T. Güthner, B. Mertschenk and B. Schulz, in *Ullmann's Encyclopedia of Industrial Chemistry*, John Wiley & Sons, Ltd, 2006.

54 A. R. Gomes, C. L. Varela, A. S. Pires, E. J. Tavares-da-Silva and F. M. F. Roleira, *Bioorganic Chem.*, 2023, **138**, 106600.

55 M. Staszewski, D. Nelic, J. Jończyk, M. Dubiel, A. Frank, H. Stark, M. Bajda, J. Jakubik and K. Walczyński, *ACS Chem. Neurosci.*, 2021, **12**, 2503–2519.

56 C. Alonso-Moreno, A. Antiñolo, F. Carrillo-Hermosilla and A. Otero, *Chem Soc Rev*, 2014, **43**, 3406–3425.

57 O. Grytsai, C. Ronco and R. Benhida, *Beilstein J. Org. Chem.*, 2021, **17**, 1001–1040.

58 Enikolopov Institute of Synthetic Polymeric Materials, Russian Academy of Sciences, ul. Profsoyuznaya 70, Moscow, 117393 Russia, F. V. Drozdov, V. M. Kotov, and Nesmeyanov Institute of Organoelement Compounds, Russian Academy of Sciences, 2020, **3** (6), 200–213.

59 S. Herres-Pawlis, A. Neuba, O. Seewald, T. Seshadri, H. Egold, U. Flörke and G. Henkel, *Eur. J. Org. Chem.*, 2005, **2005**, 4879–4890.

60 J. N. Ballı, O. Gungor and M. Kose, *Chem. Biodivers.*, 2024, **21**, e202301434.

61 M. P. Coles, *Dalton Trans.*, 2006, 985–1001.

62 S. Villamizar-Delgado, L. M. Porras-Osorio, O. Piñeros, J. Ellena, N. Balcazar, R. E. Varela-Miranda and R. F. D'Vries, *RSC Adv.*, 2020, **10**, 22856–22863.

63 D. A. Rusanov, J. Zou and M. V. Babak, *Pharmaceuticals*, 2022, **15**, 453.

64 A. Pastrana-Dávila, G. Minotta, J. Ellena, P. H. O. Santiago and R. F. D'Vries, *Crystals*, 2023, **13**, 1176.

65 P. J. Bailey and S. Pace, *Coord. Chem. Rev.*, 2001, **214**, 91–141.

66 S. Herres-Pawlis, U. Flörke and G. Henkel, *Eur. J. Inorg. Chem.*, 2005, **2005**, 3815–3824.

67 P. O'Sullivan, V. Previtali, B. Twamley, C. J. Marmion, A. R. McDonald and I. Rozas, *RSC Adv.*, 2025, **15**, 3427–3438.

68 R. Longhi and R. S. Drago, *Inorg. Chem.*, 1965, **4**, 11–14.

69 W. Schneider, A. Bauer, A. Schier and H. Schmidbaur, *Chem. Ber.*, 1997, **130**, 1417–1422.

70 Singlet Oxygen Quantum Yields of Different Photosensitizers in Polar Solvents and Micellar Solutions | Journal of Porphyrins and Phthalocyanines, https://www.worldscientific.com/doi/abs/10.1002/%28SICI%291099-1409%28199803/04%292%3A2%3C145%3A%3AAID-JPP60%3E3.0.CO%3B2-2, (accessed 5 May 2025).

71 R. Masarwa, V. C. Brunetti, S. Aloe, M. Henderson, R. W. Platt and K. B. Filion, *Pediatrics*, 2021, **147**, e20201610.

72 WHO Model List of Essential Medicines - 22nd list, 2021, https://www.who.int/publications/i/item/WHO-MHP-HPS-EML-2021.02, (accessed 5 May 2025).

73 T. Yang, M. Zhu, M. Jiang, F. Yang and Z. Zhang, *Front. Pharmacol.*, 2022, **13**:1025544.

74 M. G. Ferraro, M. Piccolo, G. Misso, R. Santamaria and C. Irace, *Pharmaceutics*, 2022, **14**, 954.

75 P. Štarha, *Inorg. Chem. Front.*, 2025, **12**, 897–954.

76 J. Yang, H.-J. Fang, Q. Cao and Z.-W. Mao, *Chem. Commun.*, 2021, **57**, 1093–1096.

77 M. Li, Y. Xu, Z. Pu, T. Xiong, H. Huang, S. Long, S. Son, L. Yu, N. Singh, Y. Tong, J. L. Sessler, X. Peng and J. S. Kim, *Proc. Natl. Acad. Sci.*, 2022, **119**, e2210504119.

78 Iridium - Element information, properties and uses | Periodic Table, https://periodic-table.rsc.org/element/77/iridium, (accessed 5 May 2025).

79 Z. Özçelik and N. GültekiN, *Int. J. Energy Appl. Technol.*, 2019, **6**, 44–48.

80 H. Cheung, R. S. Tanke and G. P. Torrence, in *Ullmann's Encyclopedia of Industrial Chemistry*, John Wiley & Sons, Ltd, 2000.

81 S. Lamansky, P. Djurovich, D. Murphy, F. Abdel-Razzaq, H.-E. Lee, C. Adachi, P. E. Burrows, S. R. Forrest and M. E. Thompson, *J. Am. Chem. Soc.*, 2001, **123**, 4304–4312.

82 C. Ulbricht, B. Beyer, C. Friebe, A. Winter and U. S. Schubert, *Adv. Mater.*, 2009, **21**, 4418–4441.

83 G. Wang, M. Zhou, J. T. Goettel, G. J. Schrobilgen, J. Su, J. Li, T. Schlöder and S. Riedel, *Nature*, 2014, **514**, 475–477.

84 E. Zysman-Colman, *Iridium(III) in Optoelectronic and Photonics Applications*, John Wiley & Sons, 2017.

85 H. Yersin, *Highly Efficient OLEDs with Phosphorescent Materials*, John Wiley & Sons, 2008.

86 E. Holder, B. M. W. Langeveld and U. S. Schubert, *Adv. Mater.*, 2005, **17**, 1109–1121.

87 F. Monti, A. Baschieri, L. Sambri and N. Armaroli, *Acc. Chem. Res.*, 2021, **54**, 1492–1505.

88 Y. Zhang and J. Qiao, *iScience*, 2021, **24**, 102858.

89 E. N. Sloth and C. S. Garner, *J. Chem. Phys.*, 1954, **22**, 2064–2066.

90 A. Narath, *Phys. Rev.*, 1968, **165**, 506–511.

91 X. Shen, H. Huo, C. Wang, B. Zhang, K. Harms and E. Meggers, *Chem. – Eur. J.*, 2015, **21**, 9720–9726.

92 A. A. Eremina, M. A. Kinzhalov, E. A. Katlenok, A. S. Smirnov, E. V. Andrusenko, E. A. Pidko, V. V. Suslonov and K. V. Luzyanin, *Inorg. Chem.*, 2020, **59**, 2209–2222.

93 J. R. Lakowicz, in *Principles of Fluorescence Spectroscopy*, ed. J. R. Lakowicz, Springer US, Boston, MA, 1999, pp. 1–23.

94 G. Baryshnikov, B. Minaev and H. Ågren, *Chem. Rev.*, 2017, **117**, 6500–6537.

95 Y. You and S. Y. Park, *Dalton Trans.*, 2009, 1267–1282.

96 A. M. Brouwer, *Pure Appl. Chem.*, 2011, **83**, 2213–2228.

97 P. Kapusta, M. Wahl, A. Benda, M. Hof and J. Enderlein, *J. Fluoresc.*, 2007, **17**, 43–48.

98 M. R. Schreier, X. Guo, B. Pfund, Y. Okamoto, T. R. Ward, C. Kerzig and O. S. Wenger, *Acc. Chem. Res.*, 2022, **55**, 1290–1300.

99 G. Hong, X. Gan, C. Leonhardt, Z. Zhang, J. Seibert, J. M. Busch and S. Bräse, *Adv. Mater.*, 2021, **33**, 2005630.

100 S. Yoon and T. S. Teets, *Chem. Commun.*, 2021, **57**, 1975–1988.

101 J. Yan, Y. Pan, I.-C. Peng, W.-Y. Hung, B. Hu, G. Ni, S.-M. Yiu, Y. Chi and K. C. Lau, *Inorg. Chem. Front.*, 2024, **11**, 2413–2426.

102 C. Wu, K. Shi, S. Li, J. Yan, Z.-Q. Feng, K.-N. Tong, S.-W. Zhang, Y. Zhang, D. Zhang, L.-S. Liao, Y. Chi, G. Wei and F. Kang, *EnergyChem*, 2024, **6**, 100120.

103 J. Li, P. I. Djurovich, B. D. Alleyne, M. Yousufuddin, N. N. Ho, J. C. Thomas, J. C. Peters, R. Bau and M. E. Thompson, *Inorg. Chem.*, 2005, **44**, 1713–1727.

104 A. B. Maurer and G. J. Meyer, *J. Am. Chem. Soc.*, 2020, **142**, 6847–6851.

105 M. Kasha, *Discuss. Faraday Soc.*, 1950, **9**, 14.

106 S. Kappaun, C. Slugovc and E. J. W. List, *Int. J. Mol. Sci.*, 2008, **9**, 1527–1547.

107 K. Dedeian, J. Shi, E. Forsythe, D. C. Morton and P. Y. Zavalij, *Inorg. Chem.*, 2007, **46**, 1603–1611.

108 A. R. Hosseini, C. Y. Koh, J. D. Slinker, S. Flores-Torres, H. D. Abruña and G. G. Malliaras, *Chem. Mater.*, 2005, **17**, 6114–6116.

109 P.-T. Chou, Y.-I. Liu, H.-W. Liu and W.-S. Yu, *J. Am. Chem. Soc.*, 2001, **123**, 12119–12120.

110 A. B. Tamayo, S. Garon, T. Sajoto, P. I. Djurovich, I. M. Tsyba, R. Bau and M. E. Thompson, *Inorg. Chem.*, 2005, **44**, 8723–8732.

111 A. B. Tamayo, B. D. Alleyne, P. I. Djurovich, S. Lamansky, I. Tsyba, N. N. Ho, R. Bau and M. E. Thompson, in *Electrophosphorescent Materials and Devices*, Jenny Stanford Publishing, 2023.

112 R. E. Harding, S.-C. Lo, P. L. Burn and I. D. W. Samuel, *Org. Electron.*, 2008, **9**, 377–384.

113 X.-F. WANG, G.-F. ZUO, Z.-F. LI and H.-X. LI, *Acta Phys.-Chim. Sin.*, 2015, **31**, 1667–1676.

114 A. R. G. Smith, P. L. Burn and B. J. Powell, *ChemPhysChem*, 2011, **12**, 2429–2438.

115 W. J. Finkenzeller and H. Yersin, *Chem. Phys. Lett.*, 2003, **377**, 299–305.

116 C.-J. Chang, C.-H. Yang, K. Chen, Y. Chi, C.-F. Shu, M.-L. Ho, Y.-S. Yeh and P.-T. Chou, *Dalton Trans.*, 2007, 1881.

117 V. Pawlowski, H. Kunkely and A. Vogler, *J. Photochem. Photobiol. Chem.*, 2004, **161**, 95–97.

118 D. Di Censo, S. Fantacci, F. De Angelis, C. Klein, N. Evans, K. Kalyanasundaram, H. J. Bolink, M. Grätzel and M. K. Nazeeruddin, *Inorg. Chem.*, 2008, **47**, 980–989.

119 P. Coppo, E. A. Plummer and L. D. Cola, *Chem. Commun.*, 2004, **0**, 1774–1775.

120 A. F. Henwood and E. Zysman-Colman, *Chem. Commun.*, 2017, **53**, 807–826.

121 J. Frey, B. F. E. Curchod, R. Scopelliti, I. Tavernelli, U. Rothlisberger, M. K. Nazeeruddin and E. Baranoff, *Dalton Trans*, 2014, **43**, 5667–5679.

122 M. Tavasli, T. N. Moore, Y. Zheng, M. R. Bryce, M. A. Fox, G. C. Griffiths, V. Jankus, H. A. Al-Attar and A. P. Monkman, *J. Mater. Chem.*, 2012, **22**, 6419–6428.

123 M. Shaw and M. Fairchild, *Color Res. Appl.*, 2002, **27**, 316–329.

124 Y. Ohno, *NIP Digit. Fabr. Conf.*, 2000, **16**, 540–545.

125 J. H. Lee, G. Sarada, C. Moon, W. Cho, Kwon-Hyeon Kim, Y. G. Park, J. Y. Lee, S. H. Jin, and J. Kim, Advanced Optical Materials, 2015, **3**, 139-269.

126 H. J. Bolink, L. Cappelli, E. Coronado, A. Parham and P. Stössel, *Chem. Mater.*, 2006, **18**, 2778–2780.

127 C. Fan, Y. Li, C. Yang, H. Wu, J. Qin and Y. Cao, *Chem. Mater.*, 2012, **24**, 4581–4587.

128 Y. Zhou, P. He, X.-F. Mo, C. Liu, Z.-L. Gan, H.-X. Tong and X.-Y. Yi, *Inorg. Chem.*, 2021, **60**, 6266–6275.

129 K. H. Hopmann, *Organometallics*, 2016, **35**, 3795–3807.

130 X. Shang, D. Han, Q. Zhan, G. Zhang and D. Li, *Organometallics*, 2014, **33**, 3300–3308.

131 W. Kohn, A. D. Becke and R. G. Parr, *J. Phys. Chem.*, 1996, **100**, 12974–12980.

132 L. H. Thomas, *Math. Proc. Camb. Philos. Soc.*, 1927, **23**, 542–548.

133 C. F. v. Weizsäcker, *Z. Für Phys.*, 1935, **96**, 431–458.

134 E. Teller, *Rev. Mod. Phys.*, 1962, **34**, 627–631.

135 P. Hohenberg and W. Kohn, *Phys. Rev.*, 1964, **136**, B864–B871.

136 W. Kohn and L. J. Sham, *Phys. Rev.*, 1965, **140**, A1133–A1138.

137 Density functional theory across chemistry, physics and biology, https://royalsocietypublishing.org/doi/epdf/10.1098/rsta.2012.0488, (accessed 5 May 2025).

138 L. E. Ratcliff, S. Mohr, G. Huhs, T. Deutsch, M. Masella and L. Genovese, *WIREs Comput. Mol. Sci.*, 2017, **7**, e1290.

139 C. Corminboeuf, *Acc. Chem. Res.*, 2014, **47**, 3217–3224.

140 K. A. Baseden and J. W. Tye, *J. Chem. Educ.*, 2014, **91**, 2116–2123.

141 J. N. Harvey, *Annu. Rep. Sect. C Phys. Chem.*, 2006, **102**, 203–226.

142 Y. Yang, M. N. Weaver and K. M. Jr. Merz, *J. Phys. Chem. A*, 2009, **113**, 9843–9851.

143 J. N. Harvey, in *Principles and Applications of Density Functional Theory in Inorganic Chemistry I*, eds. N. Kaltsoyannis and J. E. McGrady, Springer, Berlin, Heidelberg, 2004, pp. 151–184.

144 S.-C. Qi, J. Hayashi and L. Zhang, *RSC Adv.*, 2016, **6**, 77375–77395.

145 M. Reiher, O. Salomon and B. Artur Hess, *Theor. Chem. Acc.*, 2001, **107**, 48–55.

146 Ab initio effective core potentials for molecular calculations. Potentials for K to Au including the outermost core orbitals | The Journal of Chemical Physics | AIP Publishing, https://pubs.aip.org/aip/jcp/article/82/1/299/218896/Ab-initio-effective-core-potentials-for-molecular, (accessed 5 May 2025).

147 C. C. Lovallo and M. Klobukowski, *J. Comput. Chem.*, 2003, **24**, 1009–1015.

148 P. Matczak, *Comput. Theor. Chem.*, 2012, **983**, 25–30.

149 W. E. I. Minnette, E. P. Hoy and A. M. Sand, *J. Phys. Chem. A*, 2024, **128**, 6555–6565.

150 S. Niu and M. B. Hall, *Chem. Rev.*, 2000, **100**, 353–406.

151 A. D. Becke and E. R. Johnson, *J. Chem. Phys.*, 2005, **123**, 154101.

152 A. C. Tsipis, A. G. Orpen and J. N. Harvey, *Dalton Trans.*, 2005, 2849.

153 H. M. Senn and W. Thiel, *Angew. Chem. Int. Ed.*, 2009, **48**, 1198–1229.

154 J. Behler, *Angew. Chem. Int. Ed.*, 2017, **56**, 12828–12840.

155 B. Kaduk, T. Kowalczyk and T. Van Voorhis, *Chem. Rev.*, 2012, **112**, 321–370.

156 M. A. L. Marques, C. A. Ullrich, F. Nogueira, A. Rubio, K. Burke and E. K. U. Gross, *Time-Dependent Density Functional Theory*, Springer, 2006.

157 A. D. Laurent and D. Jacquemin, *Int. J. Quantum Chem.*, 2013, **113**, 2019–2039.

158 E. Runge and E. K. U. Gross, *Phys. Rev. Lett.*, 1984, **52**, 997–1000.

159 G. Onida, L. Reining and A. Rubio, *Rev. Mod. Phys.*, 2002, **74**, 601–659.

160 J. Jornet-Somoza and I. Lebedeva, *J. Chem. Theory Comput.*, 2019, **15**, 3743–3754.

161 M. E. Casida, in *Recent Advances in Density Functional Methods*, WORLD SCIENTIFIC, 1995, vol. Volume 1, pp. 155–192.

162 M. E. Casida, in *Theoretical and Computational Chemistry*, ed. J. M. Seminario, Elsevier, 1996, vol. 4, pp. 391–439.

163 D. Jacquemin, B. Mennucci and C. Adamo, *Phys. Chem. Chem. Phys.*, 2011, **13**, 16987–16998.

164 Y. Ji, Guo ,Xi-Lian, Yang ,Jia-Yu, Zhang ,Hai-Han, Liu ,Xu-Hui, Song ,Ming-Xing, Qin ,Zheng-Kun, Wang ,Jia and F.-Q. and Bai, *Mol. Phys.*, 2023, **121**, e2217781.

165 G. R. Morello, *J. Mol. Model.*, 2017, **23**, 174.

166 R. Schira and C. Latouche, *Dalton Trans.*, 2021, **50**, 746–753.

167 P. Laha, F. Chandra, A. Husain, A. L. Koner and S. Patra, *Dyes Pigments*, 2022, **197**, 109925.

168 G.-J. Kang, Y.-F. Wu, X.-F. Ren, J.-Q. Mei, S.-J. Lu and X. Zeng, *Phys. Chem. Chem. Phys.*, 2024, **26**, 23910–23919.

169 N. Zulkifli, N. M. Ali, N. H. A. S. Bain, Y. Juahir, S. Mustafar, N. Hashim, M. S. M. Yusof, A. K. El-Sawaf and E. H. Anouar, *Inorganica Chim. Acta*, 2023, **558**, 121757.

170 Z. Li, Z. Ge, X. Tong, L. Guo, J. Huo, D. Li, H. Li, A. Lu and T. Li, *Dyes Pigments*, 2021, **186**, 109016.

171 D. C. Cabanero and T. Rovis, *Nat. Rev. Chem.*, 2025, **9**, 28–45.

172 N. Kandoth, J. Pérez Hernández, E. Palomares and J. Lloret-Fillol, *Sustain. Energy Fuels*, 2021, **5**, 638–665.

173 K. J. Kron, A. Rodriguez-Katakura, R. Elhessen and S. Mallikarjun Sharada, *ACS Omega*, 2021, **6**, 33253–33264.

174 T. P. Yoon, M. A. Ischay and J. Du, *Nat. Chem.*, 2010, **2**, 527–532.

175 J. M. R. Narayanam and C. R. J. Stephenson, *Chem. Soc. Rev.*, 2010, **40**, 102–113.

176 M. H. Shaw, J. Twilton and D. W. C. MacMillan, *J. Org. Chem.*, 2016, **81**, 6898–6926.

177 D. Ravelli, D. Dondi, M. Fagnoni and A. Albini, *Chem. Soc. Rev.*, 2009, **38**, 1999–2011.

178 X. Lang, J. Zhao and X. Chen, *Chem. Soc. Rev.*, 2016, **45**, 3026–3038.

179 D. N. Tritton, F.-K. Tang, G. B. Bodedla, F.-W. Lee, C.-S. Kwan, K. C.-F. Leung, X. Zhu and W.-Y. Wong, *Coord. Chem. Rev.*, 2022, **459**, 214390.

180 C. A. Raines, *Photosynth. Res.*, 2003, **75**, 1–10.

181 J. Xuan and W.-J. Xiao, *Angew. Chem. Int. Ed.*, 2012, **51**, 6828–6838.

182 A. Mazzeo, S. Santalla, C. Gaviglio, F. Doctorovich and J. Pellegrino, *Inorganica Chim. Acta*, 2021, **517**, 119950.

183 M. Thandu, C. Comuzzi and D. Goi, *Int. J. Photoenergy*, 2015, **2015**, 521367.

184 S. Berardi, S. Drouet, L. Francàs, C. Gimbert-Suriñach, M. Guttentag, C. Richmond, T. Stoll and A. Llobet, *Chem Soc Rev*, 2014, **43**, 7501–7519.

185 M. A. M. Al-Alwani, A. B. Mohamad, N. A. Ludin, Abd. A. H. Kadhum and K. Sopian, *Renew. Sustain. Energy Rev.*, 2016, **65**, 183–213.

186 G. Calogero, G. Di Marco, S. Cazzanti, S. Caramori, R. Argazzi, A. Di Carlo and C. A. Bignozzi, *Int. J. Mol. Sci.*, 2010, **11**, 254–267.

187 S. Hansen, M.-M. Pohl, M. Klahn, A. Spannenberg and T. Beweries, *ChemSusChem*, 2013, **6**, 92–101.

188 E. Meggers, *Chem. Commun.*, 2015, **51**, 3290–3301.

189 M.-X. Song, H.-H. Zhang, X.-H. Liu, Y. Ji, X.-L. Guo, J.-Y. Yang, Z.-K. Qin, F.-Q. Bai and H.-J. Zhang, *Appl. Organomet. Chem.*, 2022, **36**, e6875.

190 R. Bevernaegie, S. A. M. Wehlin, B. Elias and L. Troian-Gautier, *ChemPhotoChem*, 2021, **5**, 217–234.

191 S. M. Hubig and J. K. Kochi, *J. Am. Chem. Soc.*, 1999, **121**, 1688–1694.

192 S. Farid, J. P. Dinnocenzo, P. B. Merkel, R. H. Young, D. Shukla and G. Guirado, *J. Am. Chem. Soc.*, 2011, **133**, 11580–11587.

193 S. Fan, X. Zong, P. E. Shaw, X. Wang, Y. Geng, A. R. G. Smith, P. L. Burn, L. Wang and S.-C. Lo, *Phys. Chem. Chem. Phys.*, 2014, **16**, 21577–21585.

194 T. Hofbeck and H. Yersin, *Inorg. Chem.*, 2010, **49**, 9290–9299.

195 S. Guo, C. Guo, Z. Lu, L. Du, M. Gao, S. Liu, Y. Liu and Q. Zhao, *Crystals*, 2021, **11**, 1190.

196 M. Z. Shafikov, A. V. Zaytsev and V. N. Kozhevnikov, *Inorg. Chem.*, 2024, **63**, 1317–1327.

197 A. F. Rausch, M. E. Thompson and H. Yersin, *J. Phys. Chem. A*, 2009, **113**, 5927–5932.

198 P. Loos and D. Jacquemin, *ChemPhotoChem*, 2019, **3**, 684–696.

199 H. M. U. Ayub, S. Y. Alnouri, M. Stijepovic, V. Stijepovic and I. A. Hussein, *Process Saf. Environ. Prot.*, 2024, **186**, 921–932.

200 W. I. Inc, Top Industrial Uses of Hydrogen | Industrial Hydrogen Safety, https://wha-international.com/hydrogen-in-industry/, (accessed 6 May 2025).

201 R. S. Kadam, P. R. Sutar and G. D. Yadav, *Int. J. Hydrog. Energy*, 2025, **106**, 994–1005.

202 D. Tonelli, L. Rosa, P. Gabrielli, K. Caldeira, A. Parente and F. Contino, *Nat. Commun.*, 2023, **14**, 5532.

203 D. R. Whang, K. Sakai and S. Y. Park, *Angew. Chem. Int. Ed.*, 2013, **52**, 11612–11615.

204 S. Fukuzumi, Y. Yamada, T. Suenobu, K. Ohkubo and H. Kotani, *Energy Environ. Sci.*, 2011, **4**, 2754.

205 F. Gärtner, D. Cozzula, S. Losse, A. Boddien, G. Anilkumar, H. Junge, T. Schulz, N. Marquet, A. Spannenberg, S. Gladiali and M. Beller, *Chem. – Eur. J.*, 2011, **17**, 6998–7006.

206 D. A. Olley, E. J. Wren, G. Vamvounis, M. J. Fernee, X. Wang, P. L. Burn, P. Meredith and P. E. Shaw, *Chem. Mater.*, 2011, **23**, 789–794.

207 A. S. Tanwar, R. Parui, R. Garai, M. A. Chanu and P. K. Iyer, *ACS Meas. Sci. Au*, 2022, **2**, 23–30.

208 L. K. Fraiji, D. M. Hayes and T. C. Werner, *J. Chem. Educ.*, 1992, **69**, 424.

209 John. Olmsted and T. J. Meyer, *J. Phys. Chem.*, 1987, **91**, 1649–1655.

210 M. J. Goodwin, J. C. Dickenson, A. Ripak, A. M. Deetz, J. S. McCarthy, G. J. Meyer and L. Troian-Gautier, *Chem. Rev.*, 2024, **124**, 7379–7464.

211 S. De Kreijger, B. Elias and L. Troian-Gautier, *Inorg. Chem.*, 2023, **62**, 16196–16202.

212 A. Aydogan, R. E. Bangle, S. De Kreijger, J. C. Dickenson, M. L. Singleton, E. Cauët, A. Cadranel, G. J. Meyer, B. Elias, R. N. Sampaio and L. Troian-Gautier, *Catal. Sci. Technol.*, 2021, **11**, 8037–8051.

213 A. Ripak, S. De Kreijger, B. Elias and L. Troian-Gautier, *STAR Protoc.*, 2023, **4**, 102312.

214 C. Wang, H. Li, T. H. Bürgin and O. S. Wenger, *Nat. Chem.*, 2024, **16**, 1151–1159.

215 Z. Qiu and C. N. Neumann, *ACS Org. Inorg. Au*, 2024, **4**, 1–25.

216 J. A. Selekman, J. Qiu, K. Tran, J. Stevens, V. Rosso, E. Simmons, Y. Xiao and J. Janey, *Annu. Rev. Chem. Biomol. Eng.*, 2017, **8**, 525–547.

217 R. Macarron, M. N. Banks, D. Bojanic, D. J. Burns, D. A. Cirovic, T. Garyantes, D. V. S. Green, R. P. Hertzberg, W. P. Janzen, J. W. Paslay, U. Schopfer and G. S. Sittampalam, *Nat. Rev. Drug Discov.*, 2011, **10**, 188–195.

218 A. Nadin, C. Hattotuwagama and I. Churcher, *Angew. Chem. Int. Ed.*, 2012, **51**, 1114–1122.

219 B. Jandeleit, D. J. Schaefer, T. S. Powers, H. W. Turner and W. H. Weinberg, *Angew. Chem. Int. Ed.*, 1999, **38**, 2494–2532.

220 J. Wang, Y. Yoo, C. Gao, I. Takeuchi, X. Sun, H. Chang, X.-D. Xiang and P. G. Schultz, *Science*, 1998, **279**, 1712–1714.

221 Chemspeed Swing Platform Review 2024 - Automation Chemistry, https://automationchemistry.com/chemspeed-swing-platform-review/, (accessed 5 May 2025).

222 M.-T. I. I. all rights reserved, CHRONECT XPR Robotic Powder and Liquid Dispensing, https://www.mt.com/us/en/home/products/Laboratory_Weighing_Solutions/mettler-product-collaboration/axel-semrau.html, (accessed 5 May 2025).

223 Specifications, https://www.unchainedlabs.com/specifications/, (accessed 5 May 2025).

224 G. Tom, S. P. Schmid, S. G. Baird, Y. Cao, K. Darvish, H. Hao, S. Lo, S. Pablo-García, E. M. Rajaonson, M. Skreta, N. Yoshikawa, S. Corapi, G. D. Akkoc, F. Strieth-Kalthoff, M. Seifrid and A. Aspuru-Guzik, *Chem. Rev.*, 2024, **124**, 9633–9732.

225 C. D. Sahm, G. M. Ucoski, S. Roy and E. Reisner, *ACS Catal.*, 2021, **11**, 11266–11277.

226 X. Li, P. M. Maffettone, Y. Che, T. Liu, L. Chen and A. I. Cooper, *Chem. Sci.*, 2021, **12**, 10742–10754.

227 A. McNally, C. K. Prier and D. W. C. MacMillan, *Science*, 2011, **334**, 1114–1117.

228 T. Dai, S. Vijayakrishnan, F. T. Szczypiński, J.-F. Ayme, E. Simaei, T. Fellowes, R. Clowes, L. Kotopanov, C. E. Shields, Z. Zhou, J. W. Ward and A. I. Cooper, *Nature*, 2024, **635**, 890–897.

229 J. I. Goldsmith, W. R. Hudson, M. S. Lowry, T. H. Anderson and S. Bernhard, *J. Am. Chem. Soc.*, 2005, **127**, 7502–7510.

230 S. DiLuzio, V. Mdluli, T. U. Connell, J. Lewis, V. VanBenschoten and S. Bernhard, *J. Am. Chem. Soc.*, 2021, **143**, 1179–1194.

231 E. Weis, M. Johansson, P. Korsgren, B. Martín-Matute and M. J. Johansson, *JACS Au*, 2022, **2**, 906–916.

232 J. C. Bawden, P. S. Francis, S. DiLuzio, D. J. Hayne, E. H. Doeven, J. Truong, R. Alexander, L. C. Henderson, D. E. Gómez, M. Massi, B. I. Armstrong, F. A. Draper, S. Bernhard and T. U. Connell, *J. Am. Chem. Soc.*, 2022, **144**, 11189–11202.

233 D. Ebrahimi, D. F. Kennedy, B. A. Messerle and D. B. Hibbert, *The Analyst*, 2008, **133**, 817.

234 J. M. Zakis, R. A. Lipina, S. Bell, S. R. Williams, M. Mathis, M. J. Johansson, J. Wencel-Delord and T. Smejkal, *ACS Catal.*, 2025, **15**, 3525–3534.

Chapter 2

Automation Accelerated Screening of Hydrogen-bond-Rich Iridium Photosensitisers for Hydrogen Generation

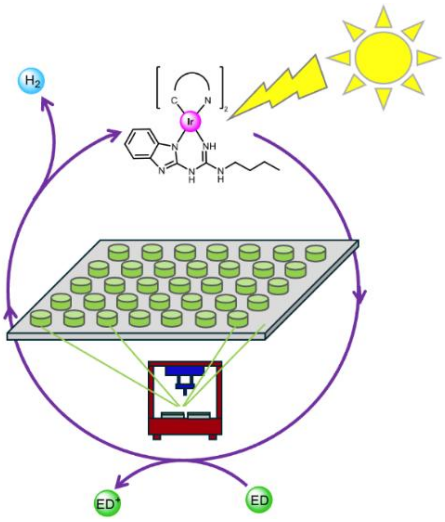
This chapter is based on the following publication:

Automation accelerated screening of H-bond-rich iridium photosensitisers for hydrogen generation

Catal. Sci. Technol., 2025, **15**, 2459-2465

T. Harri Jones, Christopher F. Bradshaw, John W. Ward*, and Barry A. Blight*

T Harri Jones was responsible for the conceptualisation, experimental methodology, computational methodology, investigation, validation, formal analysis and writing of the manuscript. Christopher F. Bradshaw validated and worked to implement experimentation. John W. Ward supervised automation and photocatalysis work and analysed data and results. Barry A. Blight conceptualised, supervised, analysed data and results, and procured funding.



2.1 Abstract

In the pursuit of a stable hydrogen evolution photosensitiser, we demonstrate the incorporation of a series of our H-bond rich guanidine-styled Ir(III) complexes into a catalytic system. Using automation accelerated catalysis screening techniques we optimised our system quickly and effectively to observe how these strongly H-bonding complexes may perform. Proven to be photo-electronically suitable, and with effective electron transfer abilities evidenced by Stern-Volmer mechanistic studies, the complexes showed modest levels of H_2 evolution in comparison to previously investigated photosensitisers with general formula $[Ir(C^N)_2(N^N)]$.

2.2 Introduction

Cyclometalated Ir(III) complexes with the general formula $[Ir(C^N)_2(N^N)]^+$ have been shown to have strong molar extinction coefficients when compared to homoleptic complexes with a similar ligand system.[1–3] This property makes them desirable candidates as photosensitizers (PS) for the photocatalytic hydrogen generation.[4–9] While these catalysts can show turnover numbers (TONs) as high as 17,000, they are typically short-lived,[10] as the catalysts tend to degrade over prolonged periods.[11-12] This is due to metal-ligand bonds rupturing in the presence of unstable radicals and anions, causing the cationic ligand moiety of the complex to dissociate.[12–14]

Previous solutions to this shortcoming came from the replacement of the N^N^+ ligand with a C^N ligand,[15,16] but these complexes show far lower TONs (as high as 3704) than their N^N^+ counterparts.[16] In recent years this issue has been addressed through the development of N^N chelating ligands that can coordinate to the Ir (III)

centre through both π-donor and π*-acceptor bonding interactions,[17-18] maintaining the general formula [Ir(C^N)$_2$(N^N)] around the central metal while removing the positive charge.[17] This type of ligand system increases the long-term cycle stability of the catalysts by strengthening the binding of the ancillary N^N ligand to the iridium metal.[17,19] Increased stability implies more longevity in the catalytic cycle, though they are yet to meet the high turnover numbers and hydrogen evolution activity of the previous generation of cationic Ir (III) catalysts.[17]

In recent years, we have synthesized various cyclometalated complexes with a unique N^N chelating ligand (1-(1H-benzo[d]imidazole-2-yl)-3-butylguanidine).[20–24] This ligand contains a 'guanine nucleobase mimicking' highly donating hydrogen-bonding (H-bonding) array.[22,25] These complexes contain a guanidine chelating ligand and tend to display high quantum efficiency, while also inviting the coordination of various H-bonding guests which in some cases enhance the optoelectronic properties.[23] Based upon this enhancement, we believed the H-bonding array of the complex is capable of efficient energy transfer in the triplet excited state,[23] and therefore can be appropriately introduced as an efficient photosensitiser into existing hydrogen evolution (HER) systems.[26–28]

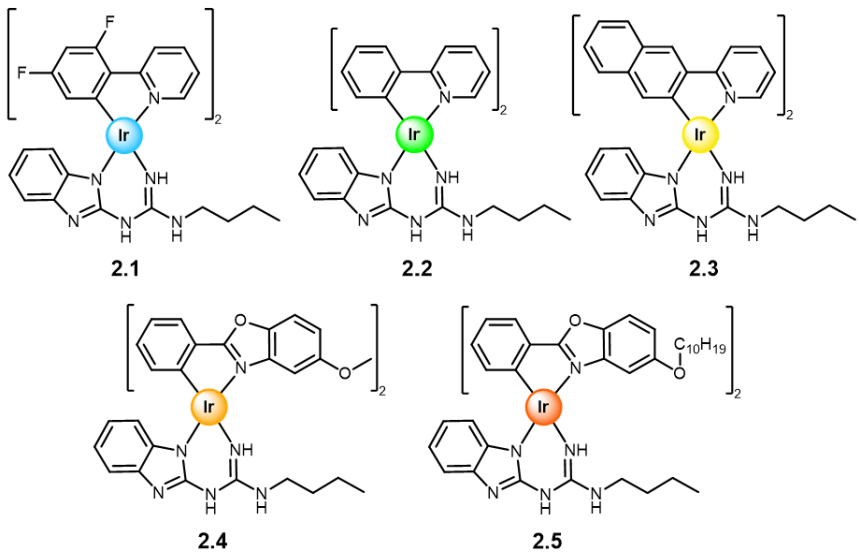


Figure 2.1 H-bond rich cyclometalated Ir(III) complexes **2.1-2.5** studied herein as photosensitisers for hydrogen generation.

In order to accelerate the evaluation of these complexes as PS candidates, an automation accelerated screening approach was introduced, through use of the Chemspeed automated synthesis platform (see supporting information).[29-30] This allowed for high throughput screening of conditions for these catalytic systems to determine optimum parameters for the HER reaction of our complexes.[30] Complexes **2.1-2.3** were previously investigated by our group for potential OLED applications and showed promising $E_{(PS*/PS-)}$ and $E_{(PS+/PS*)}$ values inspiring us to investigate them further as PS'. Complexes **2.4** and **2.5** were included in this study to gauge the effectiveness of the benzoxazole based C^N ligand's effectiveness when included in the Ir(III) PS, as we hope to further functionalise complexes of this nature into larger supramolecular architectures.

2.3 Results and Discussion

2.3.1 Synthesis and Characterisation

The synthesis of complexes **2.1-2.5** and supporting ligands can be found in the appendix, A2.1. All compounds were characterised through a combination of ^{1}H and ^{13}C NMR, ESI^{+}-MS and absorption/emission spectroscopy.

2.3.2 Photophysical Properties

The UV-vis spectra of complexes **2.1-2.5** in CH_3CN are shown in figure 2.2. The absorption spectra share similar bands to those observed in other charge neutral $Ir(C^N)_2(N^N)$ complexes.[17,22,23] Absorptions from 350-450 nm are caused by spin-allowed metal to ligand charge transfer and ligand to ligand charge transfer ^{1}MLCT/^{1}LLCT. The weak bands extending beyond 450 nm can be attributed to the spin forbidden ^{3}MLCT/^{3}LLCT transitions.[31] The sharper absorbances above 350 nm are assigned to ligand centred singlet state (^{1}LC) π-π* transitions.

Complex **2.3** showed the largest absorption above 350 nm, due to the cyclometalating ligands extended π-system producing more efficient (^{1}LC) π-π* transitions. Complex **2.1** and **2.2**, based upon ppy and F_2ppy ligands show very similar absorptions from above 260 nm, though complex **2.1** has a sharper absorbance at wavelengths lower than this due to the electron withdrawing fluorine atoms present on the phenyl moiety of the ligand. Complexes **2.4** and **2.5** have the larger absorbances at wavelengths above 350 nm showing stronger ^{1}MLCT/^{1}LLCT bands and forbidden ^{3}MLCT/^{3}LLCT transitions. Furthermore, UV-vis spectra were taken in a variety of

solvents before and after prolonged excitation by blue (465 nm) and UV light (365 nm), the results of these experiments can be found in appendix A2.5.

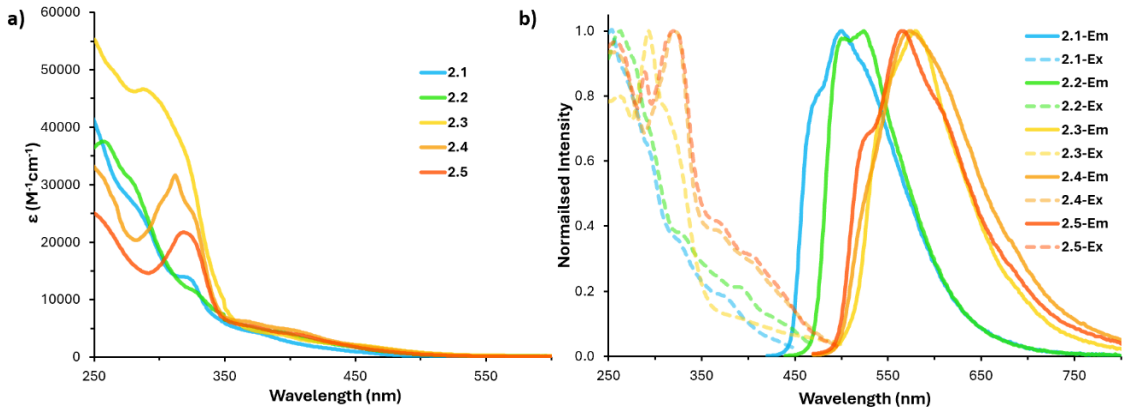


Figure 2.2 a) UV-vis spectra of complexes **2.1-2.5** in CH_3CN (1.0×10^{-5} M, 298 K). **b)** Normalised emission-excitation spectra of complexes **2.1-2.5** in CH_3CN (1.0×10^{-5} M, 298 K), the solid lines represent the emission while the dashed lines represent the absorption. All emission spectra were excited at 300 nm.

The emission and tuneable properties of complexes **2.1-2.3** have been previously characterised in $CHCl_3$ and within PMMA films.[22-23] In this study we wished to investigate the quantum efficiencies and energetics of the complexes in a polar solvent system. This was to observe any possible effects upon the guanidine ligand's hydrogen-bonding array when saturated with an H-bond acceptor species like CH_3CN.[32–34] Fortunately, we saw quantum efficiencies and lifetimes comparable with our previous studies, suggesting minimal quenching by saturation of the H-bond donor ligands.

Complexes **2.4** and **2.5** are reported for the first time, and they both show strong emission peaks in the yellow region with a vibrational structure indicative of ligand-involved emission. This character indicates the phosphorescence comes from a mixture of two excited states a ^{3}LC $^3(\pi\text{-}\pi^*)$ and ^{3}MLCT state.[35] Complex **2.5** exhibits a slightly higher quantum efficiency at 34% compared to complex **2.4**'s 30%, while the lifetimes of

the complexes **2.4** and **2.5** were also very similar (1.92 and 1.75 μs respectively). Most of the complexes we present in this paper have low non-radiative decay showing efficient emissive properties and a high probability of inter-system crossing events, thus high contributions of phosphorescent emission.[35-36] Complex **2.3** is the only candidate we proposed herein with a high non-radiative decay (k_{nr}) which is consistent with previous studies of Ir(III) complexes with similar ligand systems.[23] We attribute the high k_{nr} and k_r, and the short lifetime to the larger naphthalene ring in place of a phenyl ring withdrawing electron density from the Ir-C bond leading to higher levels of k_{nr}.[38]

Table 2.1 Photoluminescence data for complexes **2.1-2.5** in argon saturated CH_3CN.

Complex	λ_{exc} **(nm)**[a]	λ_{em} **(nm)**[a]	Φ_{PL} **(%)**[b]	τ **(μs)**[c]	k_r **($\times 10^5$ s^{-1})**[d]	k_{nr} **($\times 10^5$ s^{-1})**[d]
2.1	266, 320, 368	473, 498	89	1.84	4.8	0.6
2.2	264, 335, 391	500, 522	67	0.68	9.9	4.9
2.3	294, 382, 450	547, 583	12	0.02	60.0	440.0
2.4	316, 363, 401	534, 576	30	1.75	1.7	4.0
2.5	316, 365, 399	530, 568	34	1.92	1.8	3.4

[a] All complexes were prepared and measured in argon saturated CH_3CN at 298 K. [b] PLQYs for Ir(III)complexes, determined using a FS5 SC-30 integrating sphere module. [c] Decay lifetimes measured using TCSPC excited at 365 nm. [d] The radiative (k_r) rate constant was calculated as $k_r = \Phi_{PL} / \tau_{PL}$. [d] The nonradiative ($k_{nr}$) rate constant was calculated as $k_{nr} = (1 - k_r = \Phi_{PL} / \tau_{PL})$.

2.3.3 Electrochemical Properties

Complexes **2.1-2.5** were studied by cyclic voltammetry experiments (see appendix A2.3) and the electrochemical data is reported in table 2.2. Each complex exhibits irreversible reduction peaks between -1.45 and -1.31 V. There is little variation

in these reduction peaks suggesting that these irreversible reduction peaks should be ascribed to the cyclometalating C^N/C^N$^-$ one electron reduction process.[39] The E_{ox} is generally ascribed to the Ir(IV)/Ir(III) one electron oxidation process. E_{ox} values vary significantly from 0.93 V to 0.63 V; the values tend to decrease as either the π-system of ligands extends or electron withdrawing groups are removed.[40] These changes show that the nature of the cyclometalating C^N ligands have significant implications for the ligand field strength of the metal centre.[41–43]

Table 2.2 Electrochemical and photo-redox properties of complexes **2.1-2.5** in argon saturated CH_3CN at 298 K.[a]

Complex	E_{red} **(V)[a]**	E_{ox} **(V)[a]**	ΔE **(V)[a]**	$E_{0\text{-}0}$ **(eV)[a]**	$E_{(PS^*/PS^-)}$ **(V)[b]**	$E_{(PS^+/PS^*)}$ **(V)[b]**
2.1	-1.45	0.93	2.38	2.74	1.29	-1.81
2.2	-1.40	0.75	2.15	2.64	1.24	-1.89
2.3	-1.31	0.63	1.94	2.45	1.14	-1.82
2.4	-1.35	0.77	2.12	2.47	1.12	-1.70
2.5	-1.35	0.75	2.10	2.50	1.15	-1.75

[a]E_{ox} and E_{red} values were measured by CV in argon saturated CH_3CN at 298 K, $E_{0\text{-}0}$ values were estimated from the intersection of the emission-excitation spectra as shown in figure 2.1. [b]Rehm-Weller calculated $E_{(PS^+/PS^*)} = E_{ox} - E_{0\text{-}0}$; $E_{(PS^*/PS^-)} = E_{red} + E_{0\text{-}0}$.

We also calculated the photo-redox excited state oxidation $E_{(PS^+/PS^*)}$ and reduction $E_{(PS^*/PS^-)}$ potentials through the Rehm-Weller equations, estimating the feasibility of electron transfer during an HER cycle.[44] The $E_{(PS^*/PS^-)}$ values range from 1.29-1.12 V w.r.t. a ferrocene standard as (see table 2.2) all of these are more positive than the

triethylamine (TEA) redox couple $E(TEA^{+}/TEA)$ (+0.93 V).[3,8] This difference indicated that all our complexes can accept electrons from the chosen ideal electron donor (TEA). Additionally, the $E_{(red)}$ values for all our complexes are lower than the reduction redox couple of our chosen co-catalyst $[Co(bpy)_3(PF_6)_2]$ (-0.95 V vs NHE).[2,3,17] The data from these redox couples informed us that our complexes should effectively evolve hydrogen when paired with donor TEA and co-catalyst $[Co(bpy)_3(PF_6)_2]$ through the reductive quenching process. This pathway is indicated as the relationship between the PS, ED and catalyst follows the trend; $E_{(PS^*/PS^-)} > E_{(ED^+/ED)}$ and $E_{(PS^-/PS)} < E_{(cat/cat^-)} < E_{(H^+/H2)}$.[3,8,17]

2.3.4 Computational Investigation

For further insight into the photophysical and electronic properties of the complexes, time dependent density functional theory (DFT) calculations were undertaken at the B3LYP level of theory with the (6-31G**/LANL2DZ) basis sets.[45] Butyl chains on the guanidine ligands were truncated to methyl groups to limit computational cost, likewise the decene chains of complex **2.5** were shortened to hexyl chains.

Frontier energies and the HOMO-LUMO distributions are shown in figure 3. In all complexes the HOMO resides on the N^N benzimidazole guanidine ligand's π-orbitals with residuals on the iridium's dπ orbitals. This is due to the high concentration of nitrogen within the guanidine moiety of the ligand.[23] HOMO energies range from -4.75 eV in complex **2.1** to -4.45 eV in complexes **2.4** and **2.5**. Complex **2.1**'s significantly lower HOMO energy can be ascribed to the electron withdrawing effects of the fluorides on the cyclometalating ligands leading to a destabilised LUMO and an increased HOMO-LUMO gap causing a blue shift.[23] Our studies also show the LUMOs of the complexes reside on the cyclometalating ligands. This tends to align with our

previous studies on guanidine type Ir(III) complexes[22-23] along with previous studies on the electronic distribution of the HOMO-LUMO in nitrogen rich $Ir(C^N)_2(N^N)$ complexes.[17-18]

To further investigate the nature of the excited states of the complexes a TD-DFT approach was applied. The first five triplet states were calculated for each complex, estimating major orbital transitions and the electronic nature and energies of the T_1-T_5 states. The first 25 excited singlet states were also simulated to predict absorption properties and plotted into a UV-vis prediction using Gaussum. A full detailed breakdown of major orbital contributions for computationally predicted absorptions and emissions is available in appendix A2.8.

The variation in the cyclometalating ligands and their electronic structure leads to significant differences in the predicted emission profiles. This agrees with our photophysical measurements, larger ligands with extended π-systems tend to lead to a smaller bandgap and a red shift in emission. Despite significant variations there are still common trends, the T1 and T2 excited states tend to involve the HOMO-4, HOMO-3, HOMO-2 and HOMO all contributing to the LUMO and LUMO+1. The HOMOs reside on the iridium dπ orbitals and the π-orbitals of the benzimidazole guanidine ligand.

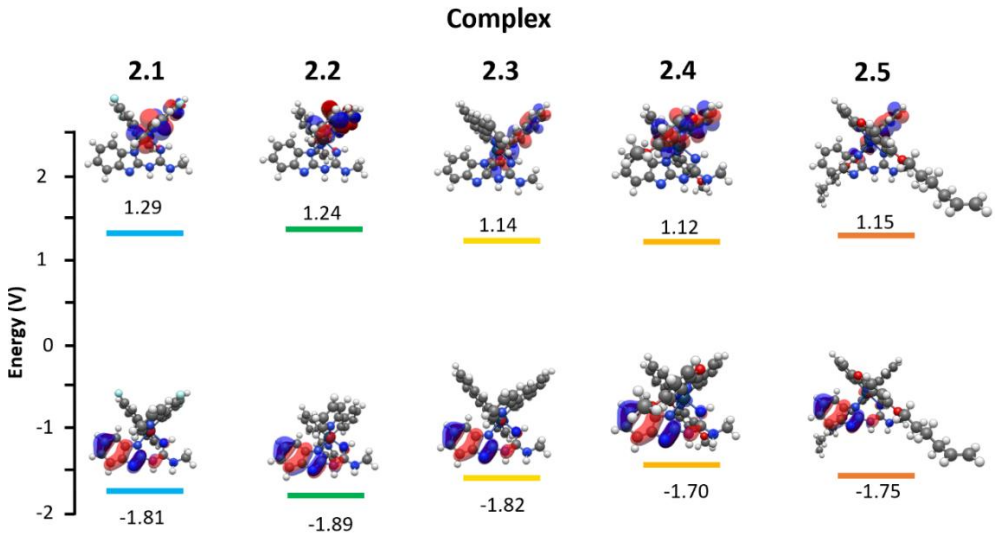


Figure 2.3 Molecular orbital diagrams, with TD-DFT calculated HOMO-LUMO gap energies for complexes **2.1-2.5**.

2.3.5 Accelerated Hydrogen Screening

After probing the photo-redox properties of the complexes, we began investigating the hydrogen generation potential. To accelerate the optimisation of the catalytic systems, we decided to incorporate automation accelerated screening techniques inspired by previous studies in the discovery of Ir(III) catalysts.[2,7,29] Using our automated approach, we performed all 43 screening experiments in 36 hours, including preparation of stock solutions, photolysis, and GC analysis. Each experiment was performed twice, totalling 86 experiments in all, to ensure consistency in the results. Carefully selected condition variations were informed by previous literature and comparable studies into metallic photo-redox systems,[2–5,8,10,17] while the robotic platform was used for the preparation of all samples under an inert atmosphere. A full breakdown of all variations in the condition screening can be found in appendix A2.7.

During the screen, complex **2.2** was chosen as the photosensitiser to develop the optimum conditions to test all our catalysts, additionally there would be no variation in co-catalyst. We chose to focus on complex **2.2** and co-catalyst [$Co(bpy)_3(PF_6)_2$] due to the abundance of literature on similar complexes as photoredox catalysts for hydrogen evolution.[2,3,17] Additionally, we kept our electrolyte of LiCl constant for the same reason, though we did experiment with the concentration of the LiCl electrolyte. Control experiments were also performed during the screening, such as removal of photosensitiser and co-catalyst. All controls gave expected results of negligible, or no hydrogen gas generated when catalysts or electron donors were removed from the system.

Several screened conditions identified clear trends; one notable example is pH. Variation of pH revealed an obvious optimum pH of 10. We hypothesised that this was due to the basic nature of the guanidine moiety of complex **2.2** being proton saturated at low pH and unable to transfer electrons. However, a UV-Vis titrations with the catalyst in both organic solvent and water/DMSO mixtures showed little impact on absorption capacity. Further review of the literature revealed that NEt_3 is not an appropriate electron donor under acidic conditions as shown by Pellegrin *et al.*[46] Solvent variation showed that organic solvents miscible with water are necessary for hydrogen generation. We observed DMF/H_2O to be the best preforming solvent mixture, yet we chose DMSO/H_2O for optimum conditions to reduce the excessive use of hazardous DMF.[47] Select results of screening experiments can be seen in figure 2.4.

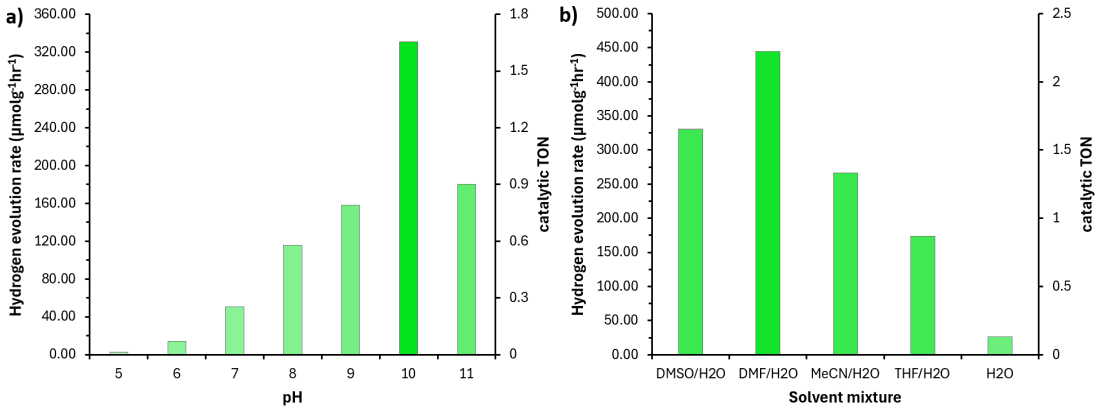


Figure 2.4 a) Rate of hydrogen evolution determined from volume of hydrogen generated over a 5-hour period, all conditions were kept consistent with initial screen parameters (see appendix A2.7) while pH was varied as specified. **b)** Rate of hydrogen evolution determined from volume of hydrogen generated over a 5-hour period, solvent mixture varied while all other conditions were consistent with initial screen.

After the screening optimum conditions were established, and all 5 complexes were tested under these conditions, the results of which (and the nature of the conditions) are shown in figure 2.5. The hydrogen generated in our system was less than anticipated based upon the energetics of our complexes and previously established literature on charge neutral $Ir(C^N)_2(N^N)$ photosensitisers. Although we did not expect turnover numbers comparable to cationic Ir(III) complexes with N^N type ligands, based on our electrochemical and photo-physical studies we anticipated a more efficient photocatalytic performance than we observed.

Complexes **2.1** and **2.2** performed best under the optimum conditions showing the highest rate of hydrogen evolution, due to their $E_{(PS^*/PS^-)}$ values being significantly more positive than the TEA redox couple $E(TEA^+/TEA)$ (+0.93 V).[3,8,10] Complexes **2.3-2.5** all show similar rates of hydrogen generation, consistent with their $E_{(PS^*/PS^-)}$ values being

similar ranging from 1.12-1.15 V. These values are closer to the TEA redox couple making the oxidation of TEA less energetically favourable with these photosensitisers.

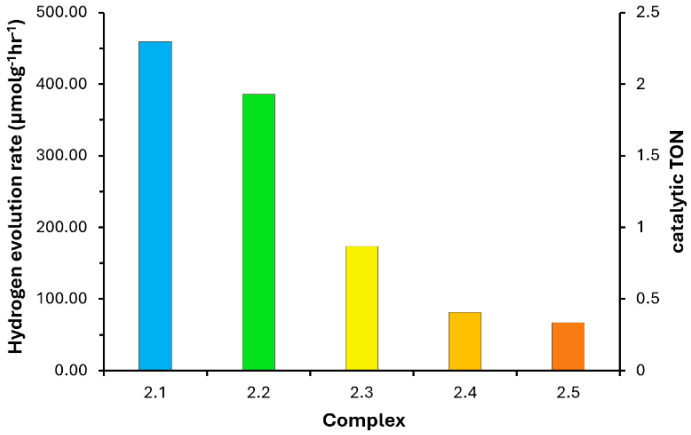


Figure 2.5 Hydrogen generation rate of complexes **2.1-2.5** in the optimum conditions informed the screening of complex **2.2**. Reaction conditions: 20 µM Ir(III) complex, $[Co(bpy)_3(PF_6)_2]$ 1mM, DMSO:H_2O (1:1, 5 mL), 0.35 M NEt_3, LiCl 0.3 M, and pH 10, samples were irradiated for 5 hr under an oriel solar simulator 1.0 sun.

2.3.6 Quenching kinetics and photo-stability

To understand why our hydrogen generation numbers were lower than expected, we performed quenching studies with both our co-catalyst $[Co(bpy)_3(PF_6)_2]$ and sacrificial electron donor NEt_3. Stern-Volmer constants (K_{sv}) were determined from the fit of $PL_0/PL = 1 + K_{sv}[NEt_3]$; k_q's were determined from the resolved Stern-Volmer equation $k_q = K_{sv}/\tau_0$. Table 3 shows the summary of these results.

Table 2.3 Results of quenching studies performed with electron donor [NEt_3] and co-catalyst [$Co(bpy)_3(PF_6)_2$].[a]

Complex	K_{sv}[NEt_3][a] M^{-1}	k_q[NEt_3][b] $M^{-1}s^{-1}$	K_{sv}[$Co(bpy)_3(PF_6)_2$][a] M^{-1}	k_q[$Co(bpy)_3(PF_6)_2$][b] $M^{-1}s^{-1}$
2.1	4×10^3	2×10^9	9×10^4	5×10^{10}
2.2	4×10^3	5×10^9	5×10^4	8×10^{10}
2.3	3×10^3	2×10^{11}	6×10^5	3×10^{13}
2.4	5×10^3	3×10^9	1×10^4	6×10^9
2.5	5×10^3	3×10^9	1×10^4	8×10^9

[a]K_{sv} calculated from the fit of the steady-state Stern-Volmer equation ($PL_0/PL = 1 + K_{sv}[NEt_3]$). [b]$k_q$ Was calculated from $k_q = K_{sv}/\tau_0$.

k_q values tend to stay consistent in the presence of molar additions of electron donor, NEt_3, with little variation and k_q's remaining around 10^9 except for complex **2.3**. Complex **2.3**'s significantly higher quenching constants for both NEt_3 and $[Co(bpy)_3(PF_6)_2]$ may be due to the high non-radiative decay (k_{nr}) of the complex. This higher non-radiative decay may allow for faster electron transfer due to the complex's propensity to relax through non-radiative pathways which we attributed to the large cyclometalating ligands. The shorter lifetime of **2.3** does result in a shorter lived excited state and consequently less time to accept or transfer an electron between substrates which also explains the underperformance of complex **2.3** as a PS. Appropriate k_q values for PS compounds with good Stern-Volmer behaviour tend to lie between 10^8 and 10^{10}.[48] The k_q's for complexes **2.1** and **2.2** being above 10^{10} also may explain the lower activity, as k_q's above this value show potential for static quenching as well as dynamic. This evidences that multiple mechanisms of electron transfer may be involved leading to a

lower efficiency of the proposed catalytic cycle.[48] The k_q's also observe a general trend of shorter lifetime complexes having higher quenching constants, though there is a notable exception to this trend when complex **2.1** is in the presence of NEt_3. Complexes **2.4** and **2.5** have the lowest k_q in the presence of the cobalt co-catalyst and second and third lowest in the presence of NEt_3, where their k_q's were determined to be near identical. These lower k_q's explain the rather modest catalytic activity from these complexes.

2.3 Conclusions

Five Ir(III) complexes have been investigated as photosensitisers for hydrogen production. The optoelectronic and photoredox properties were determined through a mixture of analytical and computational techniques. Electrochemical data showed suitable photoredox properties for use in reductive quenching mechanism for water splitting.[3] Automation accelerated screening techniques were then employed to determine the optimum conditions for hydrogen generation for complexes **2.1-2.5** using complex **2.2** as a basis for the studies.

Upon investigation into the hydrogen generation abilities of all our complexes, we found that although they had the capacity to behave as photosensitisers in the optimised cycle, they showed lower catalytic activity than their optoelectronic and electrochemical profiles would suggest. Quenching studies did confirm that the complexes can accept/donate electrons from co-catalysts and electron donor species but also revealed that some of the compounds may have multiple quenching behaviours (static and dynamic). These quenching studies did show that overall, these Ir(III) complexes are

capable of electron transfer with quencher species. This implies that they may yet have applications in other photocatalytic cycles or with different co-catalysts.

Additionally, we hypothesise that with minor modification this series of complexes may have applications in photoredox/hydrogen-bonding cooperative catalysis, due to the guanidine moiety of our complexes. This moiety may allow our complexes to act as a hybrid photosensitiser and hydrogen-bonding catalyst, imparting stereoselective control through the guanidine ligand.[46-47]

2.4 Bibliography

1 D. N. Tritton, F.-K. Tang, G. B. Bodedla, F.-W. Lee, C.-S. Kwan, K. C.-F. Leung, X. Zhu and W.-Y. Wong, *Coordination Chemistry Reviews*, 2022, **459**, 214390.

2 J. I. Goldsmith, W. R. Hudson, M. S. Lowry, T. H. Anderson and S. Bernhard, *J. Am. Chem. Soc.*, 2005, **127**, 7502–7510.

3 S. Fan, X. Zong, P. E. Shaw, X. Wang, Y. Geng, A. R. G. Smith, P. L. Burn, L. Wang and S.-C. Lo, *Physical Chemistry Chemical Physics*, 2014, **16**, 21577–21585.

4 Y. Wang, Y. Huang, S. Chen, J. Gao, Y. Zhang, Y. Duan and P. Deng, *Inorg. Chem.*, 2023, **62**, 7212–7219.

5 S.-C. Yiu, P.-Y. Ho, Y.-Y. Kwok, X. He, Y. Wang, W.-H. Yu, C.-L. Ho and S. Huang, *Chemistry – A European Journal*, 2022, **28**, e202104575.

6 J.-G. Cai, Z.-T. Yu, Y.-J. Yuan, F. Li and Z.-G. Zou, *ACS Catal.*, 2014, **4**, 1953–1963.

7 S. DiLuzio, V. Mdluli, T. U. Connell, J. Lewis, V. VanBenschoten and S. Bernhard, *J. Am. Chem. Soc.*, 2021, **143**, 1179–1194.

8 G. B. Bodedla, D. N. Tritton, X. Chen, J. Zhao, Z. Guo, K. C.-F. Leung, W.-Y. Wong and X. Zhu, *ACS Appl. Energy Mater.*, 2021, **4**, 3945–3951.

9 F. Gärtner, S. Denurra, S. Losse, A. Neubauer, A. Boddien, A. Gopinathan, A. Spannenberg, H. Junge, S. Lochbrunner, M. Blug, S. Hoch, J. Busse, S. Gladiali and M. Beller, *Chemistry – A European Journal*, 2012, **18**, 3220–3225.

10 D. R. Whang, K. Sakai and S. Y. Park, *Angewandte Chemie International Edition*, 2013, **52**, 11612–11615.

11 L. L. Tinker, N. D. McDaniel, P. N. Curtin, C. K. Smith, M. J. Ireland and S. Bernhard, *Chemistry – A European Journal*, 2007, **13**, 8726–8732.

12 Y.-J. Yuan, Z.-T. Yu, H.-L. Gao, Z.-G. Zou, C. Zheng and W. Huang, *Chemistry – A European Journal*, 2013, **19**, 6340–6349.

13 S. H. Wadman, J. M. Kroon, K. Bakker, R. W. A. Havenith, G. P. M. van Klink and G. van Koten, *Organometallics*, 2010, **29**, 1569–1579.

14 F.-M. Hwang, H.-Y. Chen, P.-S. Chen, C.-S. Liu, Y. Chi, C.-F. Shu, F.-I. Wu, P.-T. Chou, S.-M. Peng and G.-H. Lee, *Inorg. Chem.*, 2005, **44**, 1344–1353.

15 Z.-T. Yu, Y.-J. Yuan, J.-G. Cai and Z.-G. Zou, *Chemistry – A European Journal*, 2013, **19**, 1303–1310.

16 Y.-J. Yuan, Z.-T. Yu, J.-G. Cai, C. Zheng, W. Huang and Z.-G. Zou, *ChemSusChem*, 2013, **6**, 1357–1365.

17 Y. Zhou, P. He, X.-F. Mo, C. Liu, Z.-L. Gan, H.-X. Tong and X.-Y. Yi, *Inorg. Chem.*, 2021, **60**, 6266–6275.

18 Y. Wang, X. Zhao, Y. Zhao, T. Yang, X. Liu, J. Xie, G. Li, D. Zhu, H. Tan and Z. Su, *Dyes and Pigments*, 2019, **170**, 107547.

19 J. A. Flores, J. G. Andino, N. P. Tsvetkov, M. Pink, R. J. Wolfe, A. R. Head, D. L. Lichtenberger, J. Massa and K. G. Caulton, *Inorg. Chem.*, 2011, **50**, 8121–8131.

20 B. Balónová and B. A. Blight, *Front. Chem.*, 2021, **9**, 712698.

21 S. J. Thomas, B. Balónová, J. Cinatl Jr., M. N. Wass, C. J. Serpell, B. A. Blight and M. Michaelis, *ChemMedChem*, 2020, **15**, 349–353.

22 B. Balónová, D. R. Martir, E. R. Clark, H. J. Shepherd, E. Zysman-Colman and B. A. Blight, *Inorg. Chem.*, 2018, **57**, 8581–8587.

23 B. Balónová, T. H. Jones, A. E. True, S. M. Hetherington and B. A. Blight, *RSC Adv.*, 2024, **14**, 34288–34297.

24 W. Da, T. H. Jones, J.-B. Lin and B. A. Blight, *Can. J. Chem.*, 2023, **101**, 177–185.

25 M. Chahkandi, B. Madani Khoshbakht and M. Mirzaei, *Computational and Theoretical Chemistry*, 2016, **1095**, 36–43.

26 S. Sobottka, M. Nößler, A. L. Ostericher, G. Hermann, N. Z. Subat, J. Beerhues, M. Behr-van der Meer, L. Suntrup, U. Albold, S. Hohloch, J. C. Tremblay and B. Sarkar, *Chemistry – A European Journal*, 2020, **26**, 1314–1327.

27 S. Masaoka, Y. Mukawa and K. Sakai, *Dalton Trans.*, 2010, **39**, 5868–5876.

28 D. Kim and T. S. Teets, *Chemical Physics Reviews*, 2022, **3**, 021302.

29 T. F. Jaramillo, A. Ivanovskaya and E. W. McFarland, *J. Comb. Chem.*, 2002, **4**, 17–22.

30 W. Zhang, M. Yu, T. Liu, M. Cong, X. Liu, H. Yang, Y. Bai, Q. Zhu, S. Zhang, H. Gu, X. Wu, Z. Zhang, Y. Wu, H. Tian, X. Li, W.-H. Zhu and A. I. Cooper, *Nat. Synth*, 2024, **3**, 595–605.

31 P.-N. Lai, C. H. Brysacz, M. K. Alam, N. A. Ayoub, T. G. Gray, J. Bao and T. S. Teets, *J. Am. Chem. Soc.*, 2018, **140**, 10198–10207.

32 A. Ganguly, S. Jana, S. Ghosh, S. Dalapati and N. Guchhait, *Spectrochimica Acta Part A: Molecular and Biomolecular Spectroscopy*, 2013, **112**, 237–244.

33 Y. Liu, X. Tao, F. Wang, J. Shi, J. Sun, W. Yu, Y. Ren, D. Zou and M. Jiang, *J. Phys. Chem. C*, 2007, **111**, 6544–6549.

34 Y. Zhou, G. Baryshnikov, X. Li, M. Zhu, H. Ågren and L. Zhu, *Chem. Mater.*, 2018, **30**, 8008–8016.

35 S. Lamansky, P. Djurovich, D. Murphy, F. Abdel-Razzaq, H.-E. Lee, C. Adachi, P. E. Burrows, S. R. Forrest and M. E. Thompson, *J. Am. Chem. Soc.*, 2001, **123**, 4304–4312.

36 Q. Peng, Q. Shi, Y. Niu, Y. Yi, S. Sun, W. Li and Z. Shuai, *Journal of Materials Chemistry C*, 2016, **4**, 6829–6838.

37 R. E. Harding, S.-C. Lo, P. L. Burn and I. D. W. Samuel, *Organic Electronics*, 2008, **9**, 377–384.

38 Y. You and S. Y. Park, *Dalton Trans.*, 2009, 1267–1282.

39 H. J. Bae, J. Chung, H. Kim, J. Park, K. M. Lee, T.-W. Koh, Y. S. Lee, S. Yoo, Y. Do and M. H. Lee, *Inorg. Chem.*, 2014, **53**, 128–138.

40 M. Hebda, G. Stochel, K. Szaciłowski and W. Macyk, *J. Phys. Chem. B*, 2006, **110**, 15275–15283.

41 A. J. Wilkinson, H. Puschmann, J. A. K. Howard, C. E. Foster and J. A. G. Williams, *Inorg. Chem.*, 2006, **45**, 8685–8699.

42 X. Qu, Y. Liu, G. Godefroid, Y. Si, X. Shang, X. Wu and Z. Wu, *European Journal of Inorganic Chemistry*, 2013, **2013**, 3370–3383.

43 H.-R. Tsai, K.-Y. Lu, S.-H. Lai, C.-H. Fan, C.-H. Cheng and I.-C. Chen, *J. Phys. Chem. C*, 2011, **115**, 17163–17174.

44 A. Rosspeintner, D. R. Kattnig, G. Angulo, S. Landgraf and G. Grampp, *Chemistry – A European Journal*, 2008, **14**, 6213–6221.

45 Assessment of the "6-31+G** + LANL2DZ" Mixed Basis Set Coupled with Density Functional Theory Methods and the Effective Core Potential: Prediction of Heats of Formation and Ionization Potentials for First-Row-Transition-Metal Complexes | The Journal of Physical Chemistry A, 2009, 113, 36, 9843–9851

46 Y. Pellegrin and F. Odobel, *Comptes Rendus. Chimie*, 2017, **20**, 283–295.

47 Dimethylformamide [MAK Value Documentation, 2016] - Hartwig - Major Reference Works - Wiley Online Library, https://onlinelibrary.wiley.com/doi/full/10.1002/3527600418.mb6812e6017, (accessed 14 December 2024).

48 X. L. Soto and J. R. Swierk, *ACS Omega*, 2022, **7**, 25532–25536.

49 C. Jiang, W. Chen, W.-H. Zheng and H. Lu, *Org. Biomol. Chem.*, 2019, **17**, 8673–8689.

50 D. Uraguchi, Y. Kimura, F. Ueoka and T. Ooi, *J. Am. Chem. Soc.*, 2020, **142**, 19462–19467.

Chapter 3

Colour Tuneability of Heteroleptic Iridium Complexes Through Second-Sphere Coordination

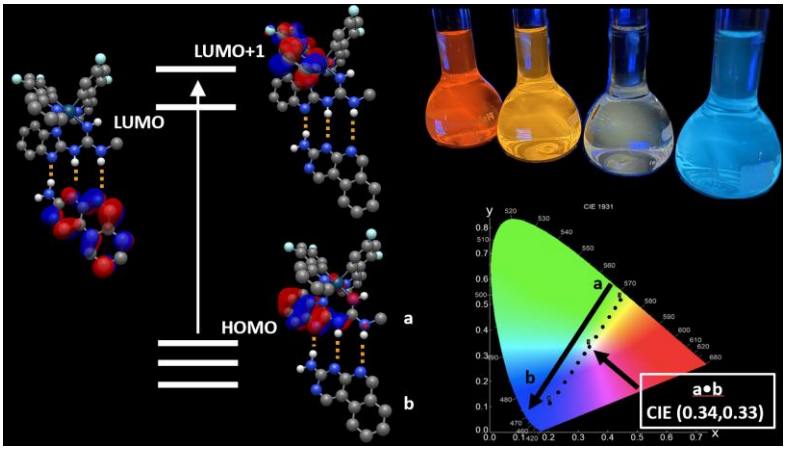
This chapter is based on the following publication:

Colour Tuneability of Heteroleptic Iridium Complexes Through Second-Sphere Coordination

RSC Adv., 2024, **14**, 34288-34297

T. Harri Jones, Barbora Balónová, Allison E. True, Sydney M. Hetherington and Barry A. Blight *

T. Harri Jones was responsible for synthesis, characterisation, experimental studies, computational studies and writing drafts for publication. Barbora Balónová synthesised the original compounds and performed preliminary photophysical investigations, this work also contributed to her thesis, Allison E. True performed UV-vis titrations, Sydney M. Hetherington assisted Balónová in synthesis of the complexes, Barry A. Blight conceptualised, supervised, analysed data and results, and procured funding.



3.1 Abstract

Novel H-bond-rich iridium (III) complexes with different systems of cyclometalating ligands bearing the general formula [Ir(C^N)$_2$(N^N)] were synthesised, characterised and their photophysical properties determined. The incorporated guanidine moieties allow us to introduce a hydrogen-bonding array for the formation of self-assembled iridium-bound hydrogen-bonded systems. Through a series of experimental and computational studies we demonstrated the host-guest chemistry of these systems. These hydrogen-bonding interactions were shown to have significant impacts on chromaticity; quantum yields and lifetimes with emphasis on energy transfer studies based on this second-sphere coordination approach.

3.2 Introduction

Iridium complexes have catalysed significant research interest due to their various applications such as bioimaging,[1-6] organic photovoltaic cells,[7-10] and catalysis.[11-14] Particularly, the implementation of Ir(III) complexes as emitters in phosphorescent organic light-emitting diodes (PhOLEDs) has attracted great attention.[15-17] Cyclometalated Ir(III) complexes have exhibited short lifetimes in excited states and high photoluminescence efficiencies which makes them particularly interesting when exploited in PhOLEDs.[18-20] Phosphorescent Ir(III) emitters can harvest both the generated singlet and triplet excitation pathways which theoretically makes them able to realise a 100 % external quantum efficiency giving them an advantage in comparison to fluorescent systems, which can only reach a maximum of 25 %.[21] To fulfil the requirements of full-colour OLED displays, the colour regulation toward efficient red,

green and blue emissions is highly desirable. Colour tunability is one of the key features of cyclometalated Ir(III) complexes,[22-27] and can be achieved through synthetic modifications of C^N ligands; these modifications change the energy of the frontier orbitals that take part in the photoexcitation process. The major triplet excited states observed in phosphorescent Ir(III) complexes, according to Shakirova *et al.*,[28] are (a) metal perturbed intra-ligand (^{3}IL) transition (or ligand centred transition), (b) metal to ligands charge transfer (^{3}MLCT) and (c) inter-ligand charge transfer (^{3}LLCT). The energy of the excited states can be changed in multiple ways, but the most common approach is the synthetic modification of C^N ligands through incorporation of either donor or acceptor substituents.[29-32] Other methodologies that can shift the emission colour of Ir(III) complexes include size variations with increase of rigidity of the cyclometalating ligands, for instance, dibenzo[f,h]quinoxaline ligands that are able to bathochromically shift the phosphorescence colour.[33]

To date, Ir(III) complexes emitting in green and yellow regions have reported high quantum efficiencies.[34-35] On the other hand, orange and red emitting Ir(III) complexes typically suffer from slightly lower quantum yields since the radiative rate constant (k_r) has a dependence on the excited state energy[10] and it usually decreases with longer emission wavelengths.[36] Blue Ir(III) complexes are still under intense investigation for their application in the display and lighting industry as they also have relatively low efficiencies compared to standard Ir(III) yellow and green devices. According to Pal *et al*.,[37] the criteria for deep blue emitters are: i) possess the required chromaticity standards defined by the National Television System Committee (NTSC) and European Broadcasting Union (EBU) with Commission International de l'Éclairage

(CIE)[38] coordinates of (0.14, 0.08) and (0.15, 0.06), respectively; ii) possess high photoluminescence quantum yields (Φ_{PL}) that translate into high external quantum efficiencies in OLED and iii) exhibit competitive device stabilities to fluorescent systems.[38]

Despite the efforts of various research groups,[39-41] the design and synthesis of stable, efficient, and pure blue Ir(III) complexes remains challenging. This study presents the design and synthesis of neutral Ir(III) complex **3.1** (Figure 3.1), with cyan-blue emission in $CHCl_3$ solution with CIE coordinates: (0.18, 0.31). The chromaticity of complex **3.1** can be modified and reach deep blue emission (CIE coordinates: (0.15, 0.11)) when combined with compound **3.5** (Figure 3.2). Furthermore, we prepared neutral yellow complex **3.2** and red/orange emissive Ir(III) complexes **3.3** and **3.4** (Figure 3.1), which are also desirable for their application in the display industry, but moreover the Ir(III) complexes with red emission are often exploited in bioimaging and anticancer studies.[42-43] The reasoning behind the synthesis of yellow complex **3.2** was to examine if white emission can be achieved by combining it with guest **3.5** (blue fluorescence in solution), as white emission is a crucial component in white OLEDs (WOLEDs).[44-45]

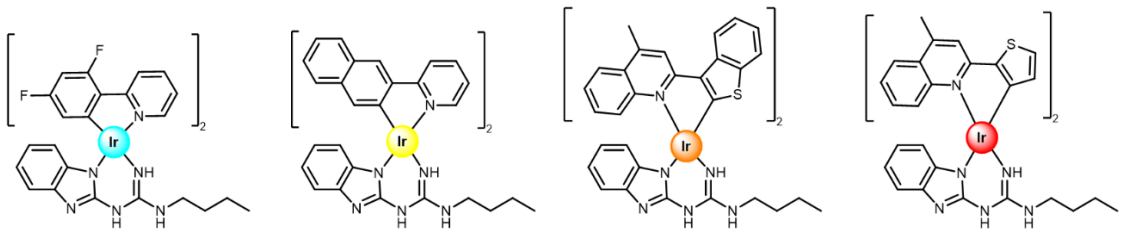


Figure 3.1 Cyclometalated Ir(III) complexes **3.1-3.4** studied herein.

Usually, WOLEDs are made up of the three primary colours (RGB), so there is a broad gap (up to 100 nm) in the white-light spectrum, which means that the emission ranging from 520-620 nm is missing. White emission can be obtained based on the principle of additive colour mixing. Combination of blue and complementary yellow emissions is an attractive approach to reach white emission.[46] Concomitantly, guest molecule **3.5** represents a suitable binding partner for yellow Ir(III) complex **3.2**, creating self-assembled hydrogen bonding systems, with preorganised arrangement that contributes to the stability of the **3.2•3.5** system. As defined by the CIE chromaticity system, an ideal white light has coordinates of x=0.33, y=0.33 and can be realised by additive colour mixing.[47-48] Separately, through the synthesis of heteroleptic Ir(III) complexes **3.3** and **3.4**, based on thiophenephenylquinoline derivatives as C^N ligands, red emission was targeted.

Our team has reported a series of Ir(III) complexes with ancillary ligands based on guanidine and thiourea moieties, i.e., inherently H-bond rich motifs (Figure 3.2).[49] Through second-sphere coordination via H-bonding, we introduced a de novo strategy to alter photophysical properties of emitters, accessing a linear colour scale with a discretely interacting two component system, reaching into colour regions obviating the need of synthetic modifications around the metal centre. We have further demonstrated the effectiveness of this approach through electrochemiluminescence in which this supramolecular system exhibits unique photo-emissive processes upon electrochemical excitation.[50-51]

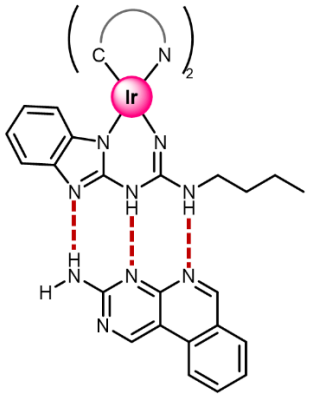


Figure 3.2 Proposed triple H-bonded systems, with preorganised arrangement that contributes to the stability of **3.1•3.5** to **3.4•3.5** systems.

Here, we present the design, synthesis, and both an experimental and computational investigation of the photoluminescent properties of yellow, orange/red and blue Ir(III) complexes **3.1-3.4** (Figure 3.1). This expands the library of H-bond capable emitters towards colour tuning in phosphorescent materials (Figure 3.3). All complexes were examined as single species and as co-complexes in combination with previously reported guest molecule **3.5**.[49] Compound **3.5** represents a suitable binding partner for the guanidine ancillary ligand that was combined with analogues Ir(III) complexes[49,52] due to its ability to form triple H-bonded systems, modifying the photophysical properties of each complex.

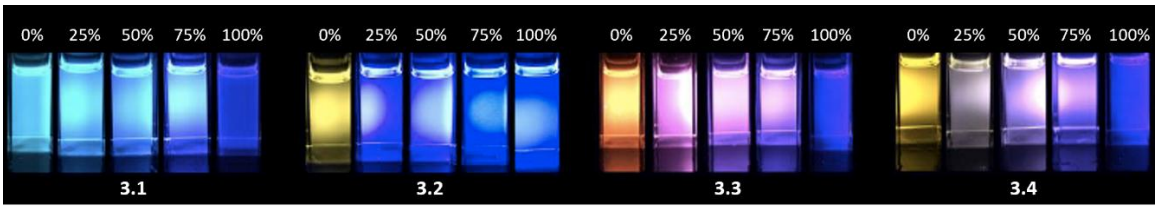


Figure 3.3 Vials from emission studies of Ir(III) complexes **3.1-3.4** with added aliquots of compound **3.5**. Vials are illuminated with long wave UV-light (365 nm). Values in % corresponding to the molar equivalents of guest content (**3.5**) in solution.

3.3 Results

3.3.1 Synthesis and Characterisation

Details for the synthesis of compounds **3.1-3.5** are presented in the appendix A3.1. All compounds were physically characterised through ^{1}H NMR, ^{13}C NMR and HRMS, the results of which are presented in appendix A3.2. In addition, computational, photophysical and electrochemical studies were conducted for further structural dissemination.

3.3.2 Photo-Physical Measurements

Absorption-Emission spectra of Ir(III) complexes **3.1-3.4** were measured in $CHCl_3$ solution at the same concentration (1.0×10^{-5} M).

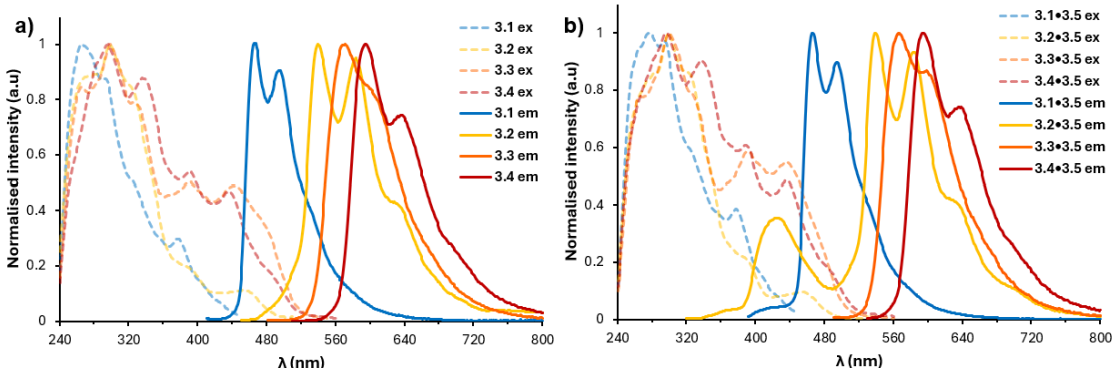


Figure 3.4 The normalised Absorption-Emission spectra of complex **3.1-3.4**, dashed line representing the excitation of each complex and solid line representing the emission, all spectra were measured in $CHCl_3$ (1.0×10^{-5} M). **b)** The normalised Absorption-Emission spectra of complex **3.1-3.4** with compound **3.5** in a 1:1 molar ratio in $CHCl_3$ (1.0×10^{-5} M).

As shown in Figure 4 above, the absorption spectra of the four complexes are mainly comprised of three parts. Complexes **3.1-3.4** show relatively strong bands in the

range of 250 to 350 nm, which can be attributed to spin-allowed singlet state ligand centred (^{1}LC) π - π* transitions. Absorptions from 350 to 450 nm can be ascribed to spin-allowed metal-to-ligand charge transfer singlet state and ligand-to-ligand charge transfer ^{1}MLCT/^{1}LLCT. The lowest energy component, extending beyond 450 nm arises primarily from spin-forbidden ^{3}MLCT/^{3}LLCT transitions.[53] These types of electronic transitions are consistent with pertinent literature.[54-55] The photoluminescence data, including emission maxima, lifetimes and quantum yields of complexes **3.1**-**3.4** are summarised in Table 3.1.

All Ir(III) compounds studied herein exhibit two emission maxima to some extent which is indicative of strong vibronic progressions contributing to phosphorescence from a mixture of ^{3}LC and ^{3}MLCT states. Complex **3.1** emits a cyan-blue colour (467, 493 nm) with a high quantum yield (Φ_{PL} =86.7 %) and a microsecond lifetime (τ =2.3 μs) showing clear phosphorescent character. When in the presence of compound **3.5** forming co-complex **3.1•3.5,** we see a decrease in both quantum yield and lifetime in the co-complex as well as a minor blue shift ~4 nm in the peak of the Ir(III) complex's emission, this 'blue shift' is a common trend of all complexes in this study when compound **3.5** is present in solution.

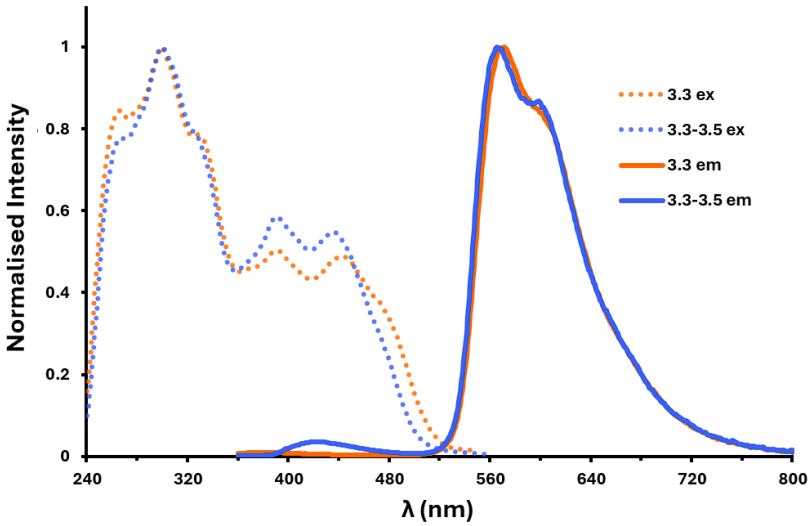


Figure 3.5 Overlayed absorption-emission spectra of complex **3.3** with co-system **3.3•3.5** in argon saturated $CHCl_3$ (1×10^{-5}), 298 K, λ_{ex} = 350 nm.

Complex **3.2** emits yellow (545, 588 nm) with a relatively low quantum yield (Φ_{PL} =8.7 %), lifetime measurements showed an uncharacteristically short lifetime of 19 ns (short for a cyclometalated Ir(III) complex). Upon addition of compound **3.5** an enhancement in the lifetime of up to 36 ns was recorded, it was also possible to achieve near white light emission (CIE coordinates: 0.34, 0.33) when 1.3 molar equivalents of **3.5** were added to **3.2**, as well as an increase to the overall quantum yield of this co-complex. Complexes **3.3** and **3.4** emitted orange and red respectively, both have long lifetimes which could be enhanced through equimolar additions of compound **3.5**. Both compounds also saw enhancement in quantum yields when forming a co-complex with compound **3.5** in solution. The overall blue shifting in the colour of the bimolecular systems can be ascribed to a combination of the presence of the blue emitting compound **3.5** and the H-bonding interactions of compound **3.5** with each of Ir(III) complexes **3.1**-**3.4**.

Table 3.1 Photoluminescence data for complexes **3.1-3.4** and co-complex **3.1•3.5-3.4•3.5**.

System	λ_{exc} (nm)[a]	λ_{em} (nm)[a]	Φ_{PL} [b] (%)	t (µs) [c]	k_r ($\times 10^5$ s^{-1})[d]	k_{nr} ($\times 10^5$ s^{-1})[e]
3.1	264, 378	467, 493	86.7	2.3	3.8	0.6
3.1•3.5 ***(1:1)***	280, 378	462, 489	82.2	2.1	0.4	0.9
3.2	296, 320	545, 588	8.7	0.0019	448.5	4706.2
3.2•3.5 ***(1:1)***	298, 325	538 ,584	15.6	0.0036	430.9	2331.5
3.2•5 ***(1:1.3)***	298, 326	538 ,584	33.2	0.0034	985.2	1982.2
3.3	298, 332	570, 610	23.4	1.7	1.4	4.5
3.3•3.5 ***(1:1)***	297, 340	569, 607	43.3	4.3	1.0	1.3
3.4	296, 338	594, 640	36.1	3.6	1.0	1.8
3.4•3.5 ***(1:1)***	308, 391	593, 635	41.4	3.6	1.2	1.6

[a] All data was collected in $CHCl_3$ and degassed for 1 min (Argon) at 298 K. [b] PLQYs for Ir(III) complexes **3.1-3.4**, determined using the relative method. Further details of standard in the Supporting Information S1 and S5. [c] Decay lifetimes using TCSPC excited at 365 nm and their corresponding chi-squared values for Ir(III) complexes 1-4, in $CHCl_3$ degassed for 20 mins (Ar) at 298 K. Complexes **3.1**, **3.2**, **3.3**, and **3.4** decay biexponentially. [d,e] the radiative (k_r) and nonradiative (k_{nr}) rate constants were calculated as $k_r = f_{PL}/t_{PL}$ and $k_{nr} = (1\text{-}f_{PL})/t_{PL}$.

Solid state photophysical measurements were also collected by preparing polymer films of 2 wt % (calculated based on weight of complex) dispersion in PMMA from argon degassed $CHCl_3$ using a spin coating method. Films with equimolar host-guest complexes were then made and the photophysical properties measured. In PMMA films, the blue shift in emission was weakened compared to solution when one molar equivalent

of compound **3.5** was added to complexes **3.2**, **3.3**, and **3.4**. The emission profile of **3.1** saw a minor red shift of 2 nm when compound **3.5** was added to form the co-complex in film. In all solid-state (PMMA) co-complexes, except **3.2•3.5**, the presence of compound **3.5** also led to a decrease in quantum yield. The table summarising these results can be found in the appendix, A3.6.

3.3.3 Host Guest Chemistry

All complexes were studied as single species in $CHCl_3$ solutions and in combination with guest molecule **3.5**. Stacked emission spectra from the host-guest studies of complexes **3.1-3.4** in combination with **3.5** are presented in appendix A3.4 and their association constants (K_a; M^{-1}) summarised in Table 3.2. Surprisingly, the trend in association constants' relative strengths did not correlate with well-established Hammett parameters, which can be used to benchmark the electron-withdrawing (EWD) or donating (EDG) ability of a substituent or ligand.[56] However, since the H-bonding interactions are occurring between the guest molecule **3.5** and the same ancillary ligand of the Ir(III) complexes, the cyclometalating ligands do exhibit a noteworthy influence on the K_a values of each HG complex.

Molecular recognition imparted by the H-bond sites enacts directed assemblies of the heterodimers with measurable association constants. Further, the stoichiometric addition of **3.5** can tune the colour of the overall visible light emissions of our host guest systems. These effects on the photophysical properties by equimolar additions of compound **3.5** are summarised in Table 3.1.

Table 3.2 Association constants (M^{-1}) and calculated Gibbs free energies (kJ mol^{-1}) for Ir(III) complexes **3.1**-**3.4** H-bonding to guest molecule **3.5**.

System	$K_a \pm \sigma$ (M^{-1})[a]	ΔG_a (kJ mol^{-1})
3.1•3.5	$6.8 \times 10^3 \pm 0.13$ %	-21.9
3.2•3.5	$6.1 \times 10^2 \pm 0.30$ %	-15.9
3.3•3.5	$6.5 \times 10^3 \pm 0.30$ %	-21.8
3.4•3.5	$1.1 \times 10^4 \pm 0.24$ %	-23.1

[a] K_a and error determined by non-linear regression (*via* BindFit)[41] of UV-Vis absorption data ($CHCl_3$:DMSO/99:1) at 298 K.

3.3.4 Electrochemical Studies

The electrochemical properties of our Ir-complexes and co-systems were investigated using cyclic voltammetry. Relevant data is summarised in Table 3.3 below, and all potentials reported are referenced to a ferrocene standard. Complexes **3.1**-**3.4** all exhibit irreversible reductions between (-1.52 to -1.48 V), these irreversible reductions are consistent with other cyclometalated Ir(III) complexes in the literature.[57] Upon additions of one molar equivalent of compound **3.5**, no consistent trends were seen in the irreversible reduction peaks; from this and previous literature, we can infer these reduction peaks are centred on the various C^N ligands.[57] Each complex also has a reversible oxidation, the values of which vary significantly from 1.17 V in complex **3.1** to 0.54 V in complex **3.4** with a clear decreasing trend of the E_{ox} value with the red shifting of the Ir(III) complex. These reversible oxidations are often ascribed to the Ir(III)/ Ir(IV) redox couple with contributions from an N^N^- ligand.[49, 58] Upon addition of compound **3.5** to complexes **3.1**-**3.4** forming their respective assemblies in solution, the E_{ox} values anodically shift by a range of values (0.10 to 0.03 V). The largest change is complex **3.1**

in **3.1•3.5** where the anode shift is 0.1 V, leading to a *ΔE* value increase of 0.11V. Overall, these anode shifts in the presence of compound **3.5** agree with our previous study into the H-bonding properties of the benzimidazolyl-guanidine ligands H-bonding interactions with compound **3.5** as well as electrochemical studies into frontier orbitals.[49,59]

Table 3.3 Electrochemical results for complexes **3.1**-**3.4** and co-complexes **3.1•3.5**-**3.4•3.5**.

System	E_{ox} (V)[a]	E_{red} (V)[a]	ΔE (V)[a]	*(com)*$E_{0\text{-}0}$ (eV)[b]	$E_{0\text{-}0}$ (eV)[c]	$E_{(PS^*/PS^-)}$ (V)[d]	$E_{(PS^*/PS^+)}$ (V)[e]
3.1	1.17	-1.51	2.68	3.16	2.81	1.30	-1.64
3.1•3.5	1.27	-1.50	2.77	3.26	2.84	1.34	-1.57
3.2	0.82	-1.49	2.31	2.95	2.58	1.09	-1.76
3.2•3.5	0.85	-1.51	2.36	3.07	2.59	1.08	-1.74
3.3	0.67	-1.52	2.19	2.83	2.36	0.84	-1.69
3.3•3.5	0.71	-1.50	2.21	2.96	2.39	0.89	-1.68
3.4	0.54	-1.51	2.05	2.79	2.26	0.75	-1.72
3.4•3.5	0.61	-1.48	2.09	2.84	2.28	0.80	-1.67

[a] All samples were studied in an argon flushed glove box in degassed, dry $CHCl_3$. Further details of electrodes and apparatus can be found in the appendix; [b] *(com)*$E_{0\text{-}0}$ calculated from the computationally obtained HOMO-LUMO gap; [c] $E_{0\text{-}0}$ was calculated from the crossover of normalised absorption and emission spectra; [d] $E_{(PS^*/PS^-)} = E_{red} + E_{0\text{-}0}$; [e] $E_{(PS^*/PS^+)} = E_{ox} - E_{0\text{-}0}$. All co-complexes were measured in a 1:1 ratio.

3.3.5 Computational Studies

To further understand the findings of the photophysical and electrochemical data, DFT and TD-DFT studies were performed at the B3LYP/ (6-31G**/LANL2DZ) level on complexes **3.1**-**3.4** and their respective assemblies with **3.5**. Information on software

packages used, structural inputs, specific orbital energies, and visualisations of molecular orbitals can be found in appendix A3.8.

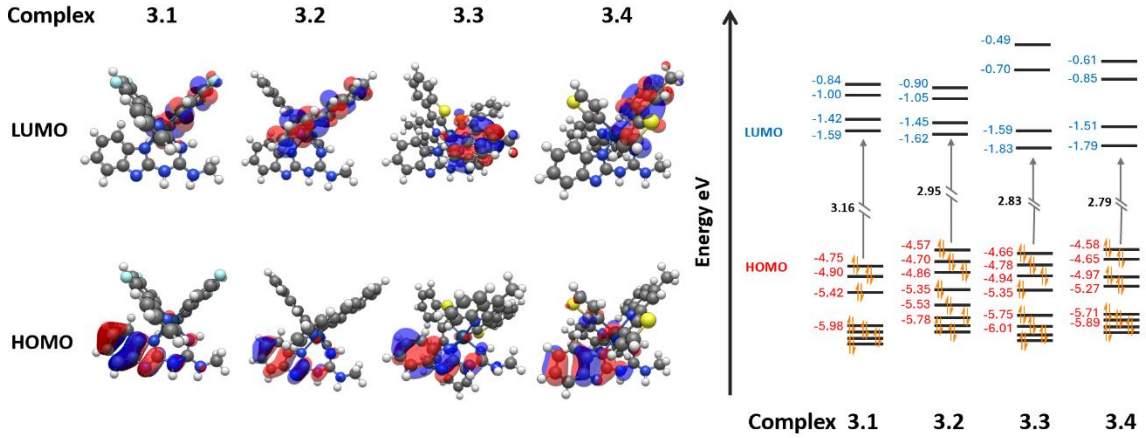


Figure 3.6 (left) TD-DFT predicted HOMO and LUMO orbital distributions of complex **3.1**-**3.4** and (right) visualisation of the energy levels of frontier orbitals with computationally obtained HOMO-LUMO gap.

In complexes **3.1**-**3.4** (Figure 3.5), the HOMO resides upon the ancillary ligand's π-orbitals along with partial residuals on the iridium metal's d and π-orbitals. This is due to the large concentration of nitrogen within the ancillary benzimidazoyl-linked guanidine ligand. The HOMO energies of the complexes range between -4.75 and -4.57 eV. Although the HOMOs in complexes **3.1**-**3.4** reside mostly on the guanidine ligand, there is still variation in these energies. As there are residuals upon the Ir(III) centre, the variation in the HOMO energies between **3.1**-**3.4** can be attributed to the changes in the other two cyclometalating ligands of the complex.

When compound **3.5** is modelled in the presence of complexes **3.1**-**3.4**, a change in the HOMO level is observed in the co-complex. The HOMO continues to reside on the guanidine ligand of the Ir(III) complex, but the HOMOs of the assemblies see an increase

in energy, with the HOMO energies now ranging from -4.65 to -4.48 eV. This increased HOMO stability is due to frontier HOMO-LUMO interactions between the HOMO on the guanidine ligand of the complexes and the LUMO residing on compound **3.5**.[59]

Studies show LUMO levels are affected by the introduction of compound **3.5** differently. In complexes **3.1**-**3.4** the LUMO resides on the π-orbitals of one of the two varying C^N cyclometalating ligands depending on the compound. Rather predictably, the LUMO energies tend to decrease from complex **3.1**-**3.4** from a peak of -1.59 eV in complex **3.1** to the lowest of -1.79 eV in complex **3.4**. This lowering of the LUMO energy is due to the introduction of extended π-conjugation in the C^N cyclometalating ligands and the removal of electron withdrawing fluoride groups, leading to increased LUMO stability.[60] When compound **3.5** is introduced to form their co-complexes, the LUMO of each assembly resides on compound **3.5**. This artificially lowers the HOMO-LUMO gap of the co-complex, and the former LUMO of the Ir(III) complex becomes the LUMO+1 of the new HG complex. In every case despite the stabilisation of the HOMO, this reassignment of the LUMO leads to an increased HOMO-LUMO+1 (formerly HOMO-LUMO) gap of orbitals residing on the Ir(III) complexes. For example, in the case of complex **3.3** and assembly **3.3•3.5** the LUMO energy of complex **3.3** is -1.83 eV, but the LUMO+1 energy of **3.3•3.5** is -1.64 eV leading to a large increase in the Ir-centred HOMO-LUMO+1 gap and a calculated blue shift in the emission profile of the complex.

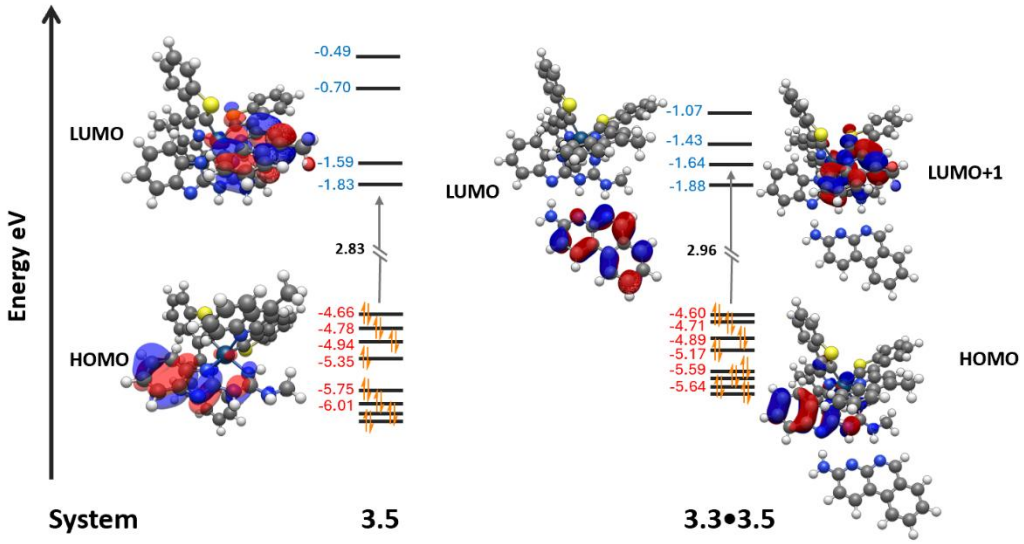


Figure 3.7 Comparison of the TD-DFT computationally modelled frontier orbitals of complex **3.3** and assembly **3.3•3.5**.

Continuing to use the example of complex **3.3** and HG assembly **3.3•3.5**; during the first emission T_1 excited state of complex **3.3**, the transition contributions typically follow HOMO-1/ HOMO-2/ HOMO-3 to the LUMO, resulting in the predicted emission of 566 nm. Major contributions during the first T_1 excited state in the co-system **3.3•3.5** are from HOMO-1/ HOMO-2/ HOMO-3 to LUMO+1, indicating the LUMO+1 is supplanting the position of the LUMO (located on **3.5**) in triplet state excitations within the Ir(III) complexes. Furthermore, the predicted T_1 emission of **3.3•3.5** has blue-shifted by 1 nm to 565 nm indicating the increase in the HOMO→LUMO+1 gap from the introduction of **3.5** has resulted in a change in the emission profile of the complex.

3.4 Discussion

3.4.1 Deep Blue Emission

The cyan-blue emission of complex **3.1** can be ascribed to the introduction of fluorine atoms on the C^N ligand, which generally stabilises the HOMO orbital and leads to an increased HOMO-LUMO gap.[30] In this case, computational investigations revealed that the LUMO resides on the C^N ligand while the HOMO is residing on the guanidine ligand, due to the large electron density of the benzimidazole moiety of the ligand. It may then be assumed that the electron withdrawing fluorine atoms are destabilising the LUMO on the C^N ligands, therefore increasing the HOMO-LUMO gap as evidenced by the largest LUMO value of the complex (-1.59 eV). Upon excitation, emission of cyan-blue complex **3.1** (CIE coordinates: (0.18, 0.31) and (0.16, 0.32), respectively) was modified by adding aliquots of **3.5** dissolved in a solvent system of $CHCl_3$ with 1% DMSO accessing a linear colour change reaching into deep blue region for 1:1 systems (CIE coordinates: (0.15, 0.11)) without the need to synthetically modify the structure of complex **3.1**. Additionally, changes in Φ_{PL} and lifetime values for **3.1•3.5** in a 1:1 ratio in $CHCl_3$ would also serve as a preliminary proof of a mutual communication between the two species (host and guest) that are designed to form stable self-assembled H-bonded systems. For the co-system **3.1•3.5**, a decrease in quantum yield was observed (**1•5** in $CHCl_3$ solution Φ_{PL} =82.2 %) when compared with compound **3.1** (Φ_{PL} =86.7 %). The lifetime decay of complex **3.1** was measured to be 2.3 ms for the major component and decreased upon introduction of complement **3.5**. From the study of the **3.1•3.5** system in $CHCl_3$ solution, the longer lifetime component with value 2.1 ms was ascribed to the photoexcitation of complex **3.1** as the major component with a 97 % contribution. In addition, a fluorescence resonance energy transfer (FRET) experiment was conducted for

3.1•3.5 system in $CHCl_3$ solution.[61] As presented in Figure **7**, the emission intensity of compound **3.5** decreased and the emission intensity of complex **3.1** slightly increased after these two components were combined in 1:1 solution mixture. This study illustrates that compound **3.5** represents a donor molecule that can modestly transfer its energy to complex **3.1** in the excited state.

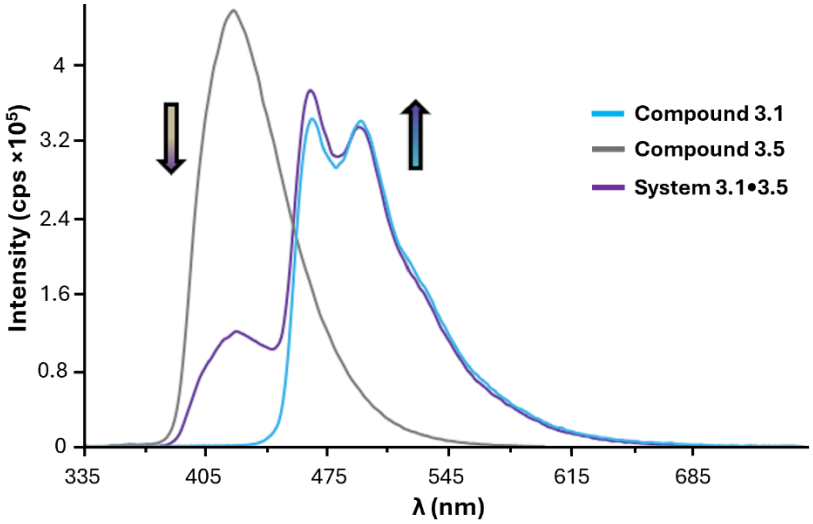


Figure 3.8 Overlaid emission spectra of complex **3.1** (blue), compound **3.5** (grey) and co-complex **3.1•3.5** (purple) from FRET studies in $CHCl_3$ solution. All samples excited at λ_{ex} = 350 nm.

The blue shift of the complex was further investigated using through TD-DFT studies where we identified that the HOMO-LUMO gap of complex **3.1** had been increased by the presence of compound **3.5** by almost 10 eV. Here, H-bonding with compound **3.5** stabilises the HOMO localised on the benzimidazole moiety, increasing it by almost 10 eV. Due to the HOMO-LUMO frontier orbital interaction between **3.1** and **3.5**, the LUMO+1 in the co-complex (residing on the C^N ligand; the LUMO of the complex) was subsequently destabilised by 20 eV. Electrochemical studies confirmed that introducing **3.5** to complex **3.1** increases the ΔE by 0.11 eV, with the E_{ox} value

anodically shifting and the E_{red} value having little change. We posit that H-bonding between compound **3.5** and the benzimidazolyl-guanidine ligand of the complex leads to increased HOMO stability as the HOMO-LUMO interaction between frontier HOMO orbitals of complex **3.1** and the LUMO of compound **3.5** share the electron density residing in complex **3.1**'s HOMO.[59]

3.4.2 Serendipitous White Light

Ir(III) complex **3.2** emits yellow light (at much lower relative intensity) while exhibiting a very low quantum yield (Φ_{PL}=3.4 %) and a short lifetime (τ = 1.94 ns), especially in solution. When complex **3.2** is dispersed in a 2 wt % load in PMMA films there is a dramatic increase in the quantum yield (Φ_{PL}=15.1 %) despite maintaining a short lifetime. Upon adding aliquots of compound **3.5** to **3.2** in solution, we see a gradual increase in quantum yield while maintaining its relatively short lifetimes leading to very high k_r and k_{nr} values for **3.2•3.5**. Though these photophysical properties are not particularly noteworthy, addition of 1.3 equivalents of compound **3.5** to complex **3.2** during an emission titration resulted in white emission with CIE coordinates: (0.34, 0.33) (Figure 8). Since ideal white light has coordinates of (0.33, 0.33),[34] this was an exciting result. The titration with compound **3.5** also improved complex **3.2**'s uncharacteristically low quantum yield, and lifetime. The new quantum yield of the 1:1 co-complex **3.2•3.5** increased to Φ_{PL}=15.6 % in $CHCl_3$ solution. Increasing the ratio of **3.2•3.5** slightly to 1:1.3, produced pure white light emission with an observable doubling in quantum yield (Φ_{PL}=33.2 %). We mainly ascribed this increase to the blue emitting compound **3.5**, as compound **3.5** is known to have efficient fluorescent emission properties (Φ_{PL}=40 %, τ =

3 ns).[49] This ideal ratio of host-guest for white light was also determined through a recently reported theoretical calculation (Equation 1) to estimate the overall contributions of **3.2** and **3.5** in the co-system.

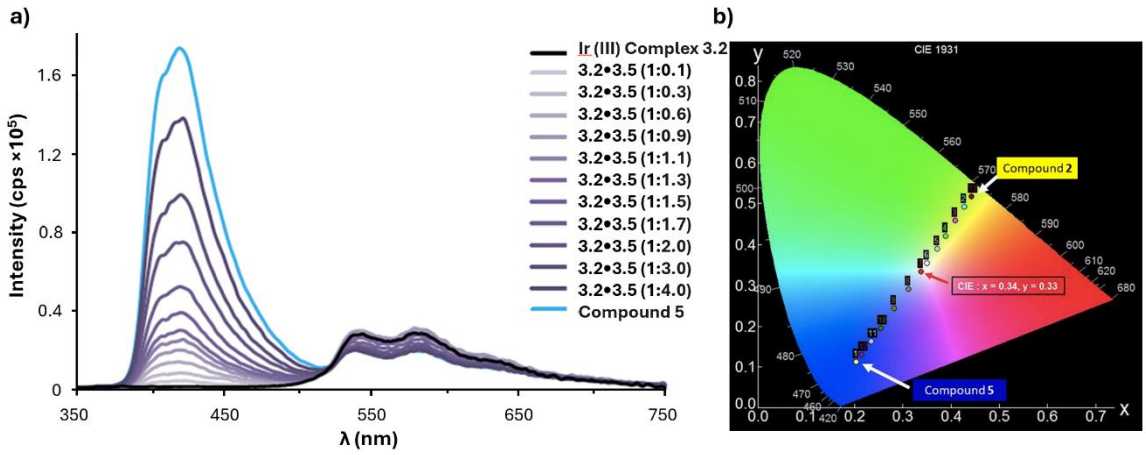


Figure 3.9 a) Emission spectra from titration studies of complex **3.2** with additions of compound **3.5** measured in $CHCl_3$ solution. Black line represents emission of Ir(III) complex **3.2** without any additions; blue line represents compound **3.5** with no complex **3.2** present. **b)** (right) CIE diagram from emission titration experiment of host complex **3.2** and guest compound **3.5**.

$$\left(x_{(mix)}, y_{(mix)}\right) = a_1(x_1 + y_1) + a_2(x_2, y_2) + \cdots + a_i(x_i + y_i) \tag{3.1}$$

$$a_i = \frac{\chi_i \phi_i I_{ex,i}(\lambda_{ex})}{\sum_{i=1}^{n} \chi_i \phi_i I_{ex,i}(\lambda_{ex})} \tag{3.2}$$

Equations 3.1 and 3.2, developed by Price *et al.*,[62] allows for the molar equivalents required in specific colour tuned emissions to be estimated to a high degree of accuracy. The equation considers the PL contributions of the multiple components into a linear combination *or relative brightness* (a_i) as the product of the *i*th components mole fraction (χ_i), photoluminescent quantum yield (Φ_i), and excitation intensity ($I_{ex,i}$) at a common wavelength.

In this instance, the equation can only be used to give a close estimation of the correct constituent ratio of the co-complex for white light emission because the equation does not account for energy transfer within assemblies such as those presented herein. Upon use of the equation, we determined the theoretical molar ratio for white light emission was 1:1.41, which is notably different from our obtained molar ratio of 1:1.3, further indicating energy transfer exists within co-complex **3.2•3.5**. When attempting this 'ideal' white light ratio in PMMA films, the system did not achieve near white light emission, rather a more efficient yellow system, leading us to believe that the hydrogen bond association in the solution phase is necessary to achieve the white light emission.

The computational data for **3.2•3.5** again shows increased HOMO stability in the presence of compound **3.5** due to the frontier orbital HOMO-LUMO interactions as well as the destabilisation of the LUMO+1 residing on the iridium explaining the blue shift of the emission of the complex. This is further supported by the electrochemical data that shows also shows an anode shift of 0.03 V in the E_{ox}. This value is the smallest shift of all E_{ox} values reported herein, showing the weakest H-bonding and frontier HOMO-LUMO interactions between Ir(III) complex and its complement. This weaker frontier orbital interaction aligns with our UV-vis titration studies where it was found that complex **3.2** had the lowest ΔG_a value of -15.9 kJmol^{-1} and a K_a with compound **3.5** of only 6.1×10^2, proving that complex **3.2** had the weakest affinity for compound **3.5**.

3.4.3 Orange and Red Light

Ir(III) complexes **3.3** and **3.4** were synthesised to study orange/red emissive complexes and their communication with compound **3.5** via energy transfer. The energy

transfer (ET) values were calculated from the ratio between the corrected excitation spectrum of host-guest pairs and their absorption spectra. This calculation for ET efficiency works through estimating how much emission is gained by the host in the presence of a guest per unit of absorbed light by the host-guest complex (see equation 3.3 below).[63] This experiment could only be carried out with complexes **3.3** and **3.4** due to their ability to absorb longer wavelengths of light compared to **3.5**. Complexes **3.1** and **3.2**'s excitation spectra overlap too much with compound **3.5**, the guest's excitation spectrum must have minimal overlap with the host to ensure only ET is measured and not direct absorption by the guest.[63]

$$ET\ efficiency \propto \frac{I_{exc}(\lambda)}{A(\lambda)} \tag{3.3}$$

Emission spectra of systems **3.3•3.5** and **3.4•3.5** in $CHCl_3$ solution were collected at a higher wavelength λ_{ex} = 640 nm, which is beyond the emission window of guest compound **3.5**. We observed that the ET efficiency for **3.3•3.5** was approximately 36 % from the ratio between the corrected excitation spectrum of **3.3•3.5** (Figure 3.9).

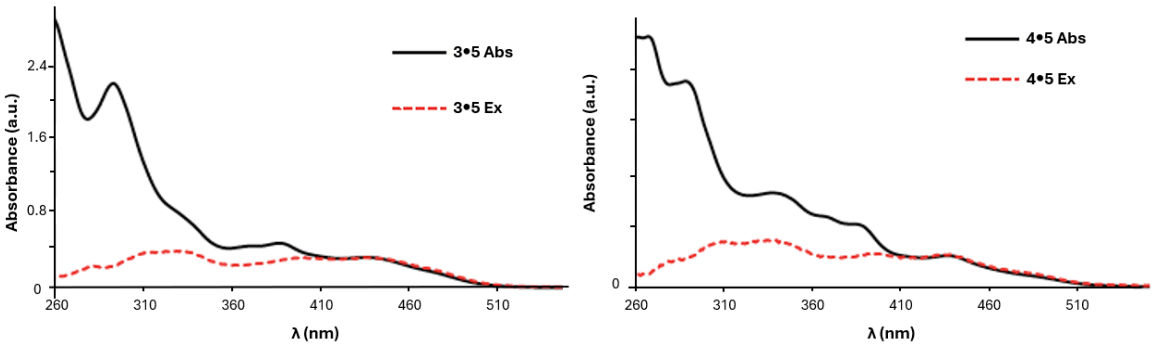


Figure 3.10 Absorption (solid black line) and corrected PL excitation (red dashed line measured at 570 nm) for co-complexes **3.3•3.5** (left) and **3.4•3.5** (right) (1:1 ratio of Ir complex and compound **3.5**). Spectra normalised to absorbance at 440 nm.

The ET efficiency for **3.4•3.5** was calculated to be 35 % which represents an almost identical value to system **3.3•3.5**. From this study, it can be concluded that even if the emission properties of complexes **3.3** and **3.4** were slightly different (shift in emission maxima ~ 20 nm), their energy transfer efficiency values when combined with compound **3.5** are comparable. Furthermore, these experiments demonstrated that there is a sufficient distance for "communication" between complexes **3.3**/**3.4** and guest compound **3.5** in 1:1 solution. To further examine the interaction of complexes **3.3**/**3.4** with **3.5**, emission spectra of 1:1 mixture in $CHCl_3$ solutions were collected for both systems **3.3•3.5** and **3.4•3.5**.

As shown in Table 3.1 there was an increase in the photoluminescence quantum yields measured for assemblies **3.3•3.5** and **3.4•3.5** when compared to the values of the complexes **3.3** and **3.4**. Complex **3.3** had a more significant change when introduced to compound **3.5** with the quantum yield increasing from Φ_{PL}=23.4 % to 43.3 %. As presented in Table 1, the lifetime decays for both **3.3•3.5** and **3.4•3.5** increased when compared to their respective parent Ir-complexes. The longer lifetimes (4.3 μs and 3.6 μs), which are ascribed to the direct photoexcitation of the complexes **3.3** and **3.4**, represent the major components with contributions of 90 % and 99 %, respectively.

Both complexes **3.3** and **3.4** were also investigated electrochemically. Anodic shifts of 0.04 and 0.07 V, respectively, were observed when bound to compound **3.5**. These shifts are consistent with the interactions observed for the other studied complexes and further supported by K_a values established in the UV-Vis binding studies. Similarly, as for complexes **3.1** and **3.2**, the TD-DFT studies exhibited large changes in the HOMO-LUMO gap with the introduction of compound **3.5** to both **3.3** and **3.4.** Computational

studies of both **3.3•3.5** and **3.4•3.5** demonstrate increased HOMO stability through HOMO-LUMO interactions, and the LUMO+1 being subsequently destabilised leading to an increased HOMO-LUMO+1 gap and a minor blue shift in the Ir(III) complex's emission. What is not reflected in the computational or electrochemical data is the enhancement in the quantum yields. Complex **3.1** saw a minor quenching when introduced to compound **3.5**. Complex **3.2** demonstrated an increase in the co-system quantum yield when **3.5** is introduced, which has a significantly higher quantum yield than complex **3.2** itself.[49] Complexes **3.3** and **3.4** in combination with **3.5** exceed all their respective unimolecular quantum yields, the major components of the emission within **3.3•3.5** and **3.4•3.5** are ascribed to the Ir(III) complexes directly (both computationally and experimentally). These results along with the efficient ET leads us to hypothesise that the presence of compound **3.5** directly led to an enhancement of the emission properties of complexes **3.3** and **3.4** through their H-bonding interactions.

3.5 Conclusions

In conclusion, we have demonstrated the design, synthesis and characterisation of four novel heteroleptic Ir(III) complexes all incorporating a benzimidazole-linked guanidine ligand allowing for a high degree of colour tuneability. Each Ir(III) complex (**3.1**-**3.4**) was further studied to demonstrate a unique property when combined with compound **3.5**. Emission of cyan-blue complex **3.1** can be modified to access a deep blue emission[39] through addition of compound **3.5**. Electrochemical and computational data of **3.1** also revealed the complex has an appropriate energetic profile to act as a photosensitiser for photocatalytic water splitting; an area we are currently exploring.[64]

Yellow complex **3.2** demonstrated white light emission, CIE coordinates: (0.33, 0.34), after controlled addition of compound **3.5** in solution along with an increased quantum yield. Future studies into more yellow emitting Ir(III) complexes integrating our benzimidazolyl-guanidine ligand along with compound **3.5** could lead to highly efficient white light emission assuming the yellow Ir(III) components efficiency can be increased. Complexes **3.3** and **3.4** showed tuneable orange/ red emission, a desirable property for PhOLED applications as well as bio-imaging.[43-44] Complex **3.4** showed red emission with λ_{em} = 593 nm and a shoulder peak at 640 nm in $CHCl_3$ solution. Energy transfer efficiency was calculated for complexes **3.3** and **3.4** when mixed with compound **3.5** in a 1:1 ratio in $CHCl_3$ (35% for system **3.3•3.5** and 36% for system **3.4•3.5**). Complexes **3.3** and **3.4** would be suitable for further studies on biological applications due to the biologically active guanidine moieties, which represent an available binding site for appropriate guest molecules in supramolecular hydrogen bonded systems.

3.6 Bibliography

1 Z. Lu, M. Shangguan, X. Jiang, P. Xu, L. Hou and T. Wang. *Dye Pigment.*, 2019, **171**, 107715.

2 K. Y. Zhang, P. Gao, G. Sun, T. Zhang, X. Li, S. Liu, Q. Zhao, K. K.-W. Lo and W. Huang. *J. Am. Chem. Soc*., 2018, **140**, 7827-7834.

3 K. Fan, S.-S. Bao, W.-X. Nie, C.-H. Liao and L.-M. Zheng. *Inorg. Chem.*, 2018, **57**, 1079-1089.

4 J. Shen, T. W. Rees, L. Ji and H. Chao, *Coordination Chemistry Reviews*, 2021, **443**, 214016.d

5 S. Abbas, I. Din, A. Raheel and A. Tameez ud Din, *Applied Organometallic Chemistry*, 2019, **34**, e5413.

6 Lawrence Cho-Cheung Lee and Kenneth Kam-Wing Lo, *Chemistry-an Asian Journal*, 2022, **17**, e202200840.

7 T. Yang, X. Gao, Y. He, H. Wang and Y. Tao, *Journal of materials chemistry. C*, 2020, **8**, 5761–5768.

8 T. Yang, B. Wang, Y. He, A. Zhou, Z. Yao, G. Xing and Y. Tao, *Inorganic chemistry*, 2023, **62**, 5920–5930.

9 Q. Wu, Y. Cheng, Z. Xue, X. Gao, M. Wang, W. Yuan, S. Huettner, S. Wan, X. Cao, Y. Tao and W. Huang. *Chem. Commun.*, 2019, **55**, 2640-2643.

10 E. Baranoff, P. Kumar, in Iridium (III) in Optoelectronic and Photonics Applications, John Wiley & Sons, Ltd, Chichester, UK, 2017, pp. 655-681.

11 X.-S. Gu, N. Yu, X.-H. Yang, A.-T. Zhu, J.-H. Xie and Q.-L. Zhou. *Org. Lett.*, 2019, **21**, 4111-4115.

12 S.-M. Lu, Z. Wang, J. Wang, J. Li, and C. Li. *Green Chem*., 2018, **20**, 1835-1840.

13 H. Wu, Y. Wang, Z. Shi, X. Wang, J. Yang, M. Xiao, J. Ge, W. Xing and C. Liu, *Journal of Materials Chemistry A*, 2022, **10**, 13170–13189.

14 W. J. Kerr, G. J. Knox and L. C. Paterson, *Journal of Labelled Compounds and Radiopharmaceuticals*, 2020, **63**, 281–295.

15 a) I. Omae. *Coord. Chem. Rev.*, 2016, **310**, 154-169. b) T.-Y. Li, J. Wu, Z.-G. Wu, Y.-X. Zheng, J.-L. Zuo and Y. Pan. *Coord. Chem. Rev.*, 2018, **374**, 55-92.

16 J. Kang, K.-M. Park, Kyung Hyung Lee, Jun Yeob Lee and Y. Kang, *Dyes and pigments*, 2021, **190**, 109334–109334.

17 J. Jayabharathi, V. Thanikachalam and S. Thilagavathy, *Coordination Chemistry Reviews*, 2023, **483**, 215100.

18 S. Guo, T. Huang, S. Liu, K. Y. Zhang, H. Yang, J. Han, Q. Zhao and W. Huang. *Chem. Sci.*, 2017, **8**, 348-360.

19 X. Liu, B. Yao, Z. Zhang, X. Zhao, B. Zhang, W.-Y. Wong, Y. Cheng and Z. Xie. *J. Mater. Chem. C*., 2016, **4**, 5787-5794.

20 H. Benjamin, M. A. Fox, A. S. Batsanov, H. A. Al-Attar, C. Li, Z. Ren, A. P. Monkman and M. R. Bryce. *Dalt. Trans*., 2017, **46**, 10996-11007.

21 S. Y. Lee, T. Yasuda, Y. S. Yang, Q. Zhang, C. Adachi. *Angew. Chem. Int. Ed.*, 2014, **53**, 6402-6406.

22 Y. You and S. Y. Park. *Dalt. Trans*., 2009, 1267-1282.

23 N.-Y. Chau, P.-Y. Ho, C.-L. Ho, D. Ma, W.-Y. Wong. *J. Organomet. Chem*., 2017, **829**, 92-100.

24 A. F. Henwood and E. Zysman-Colman. *Chem. Commun.*, 2017, **53**, 807-826.

25 C. Hierlinger, D. B. Cordes, A. M. Z. Slawin, D. Jacquemin, V. Guerchais, E. Zysman-Colman. *Dalt. Trans*., 2018, **47**, 10569-10577.

26 K.-R. Kim, J. Oh and J.-I. Hong, *Analyst (London. 1877. Online)/Analyst*, 2023, **148**, 5619–5626.

27 Y. Liu, Y. Li, T. Pu, Y. Pei, Y. Fan, C. Xu and F. Li, *New journal of chemistry*, 2023, **47**, 16794–16798.

28 J. R. Shakirova, O. A. Tomashenko, E. E. Galenko, A. F. Khlebnikov, P. Hirva, G. L. Starova, S.-H. Su, P.-T. Chou, S. P. Tunik. *Inorg. Chem.*, 2018, **57**, 6853-6864.

29 I. R. Laskar, T.-M. Chen. *Chem. Mater*., 2004, **16**, 111-117.

30 S. Takizawa, J. Nishida, T. Tsuzuki, S. Tokito, Y. Yamashita. *Inorg. Chem.*, 2007, **46**, 4308-4319.

31 Y. Wang, N. Sun, B. F. E. Curchod, L. Male, D. Ma, J. Fan, Y. Liu, W. Zhu, E. Baranoff. *J. Mater. Chem. C*., 2016, **4**, 3738-3746.

32 C.-J. Li, S.-Y. Yin, H.-P. Wang, Z.-W. Wei, M. Pan. *J. Photochem. Photobiol. A Chem*., 2019, **379**, 99-104.

33 a) F.-M. Hwang, H.-Y. Chen, P.-S. Chen, C.-S. Liu, Y. Chi, C.-F. Shu, F.-I. Wu, P.-T. Chou, S.-M. Peng, G.-H. Lee. *Inorg. Chem*., 2005, **44**, 1344-1353. b) G. Li, D. G. Congrave, D. Zhu, Z. Su, M. R. Bryce. *Polyhedron*, 2018, **140**, 146-157.

34 W.-K. Hu, S.-H. Li, X.-F. Ma, S.-X. Zhou, Q. Zhang, J.-Y. Xu, P. Shi, B.-H. Tong, M.-K. Fung and L. Fu. *Dye. Pigment*., 2018, **150**, 284-292. b) J. Yao, S. Ying, Q. Sun, Y. Dai, X. Qiao, D. Yang, J. Chen and D. Ma. *J. Mater. Chem. C*, 2019, **7**, 11293-11302.

35 Z. Chen, H. Zhang, D. Wen, W. Wu, Q. Zeng, S. Chen and Wai Yeung Wong, *Chemical science*, 2020, **11**, 2342–2349.

36 J. V. Caspar, and T. J. Meyer, *The Journal of Physical Chemistry*, 1983, **87**, 952–957

37 A. K. Pal, S. Krotkus, M. Fontani, C. F. R. Mackenzie, D. B. Cordes, A. M. Z. Slawin, I. D. W. Samuel, E. Zysman-Colman. *Adv. Mater*., 2018, **30**, 1804231.

38 R. Bai, X. Meng, X. Wang and L. He, *Advanced Functional Materials*, 2020, **30**, 1907169–1907169.

39 T. Smith, J. Guild. *Trans. Opt. Soc*., 1931, **33**, 73-134.

40 X. Yang, X. Xu, G. Zhou. *J. Mat. Chem. C.*, 2015, **3**, 913-944.

41 J.-H. Lee, G. Sarada, C.-K. Moon, W. Cho, K.-H. Kim, Y. G. Park, J. Y. Lee, S.-H. Jin and J.-J. Kim. *Adv. Opt. Mater*., 2015, **3**, 211-220.

42 Y. Miao, P. Tao, L. Gao, X. Li, L. Wei, S. Liu, H. Wang, B. Xu and Q. Zhao. *J. Mater. Chem. C*., 2018, **6**, 6656-6665.

43 J. Zhu, B. Z. Tang and K. K. Lo. *Chem.: A Eur. J.*, 2019, **25**, 10633-10641.

44 V. Venkatesh, R. Berrocal-Martin, C. J. Wedge, I. Romero-Canelon, C. Sanchez-Cano, J.-I. Song, J. P. C. Coverdale, P. Zhang, G. J. Clarkson, A. Habtemariam, S. W. Magennis, R. J. Deeth, P. J. Sadler. *Chem. Sci*., 2017, **8**, 8271-8278.

45 S. Wang, Q. Yang, B. Zhang, L. Zhao, D. Xia, J. Ding, Z. Xie, L. Wang. *Adv. Opt. Mater*., 2017, **5**, 1700514.

46 H. Wu, L. Ying, W. Yang, Y. Cao. *Chem. Soc. Rev*., 2009, **38**, 3391-3400.

47 P. Tao, W.-L. Li, J. Zhang, S. Guo, Q. Zhao, H. Wang, B. Wei, S.-J. Liu, X.-H. Zhou, Q. Yu, B.-S. Xu and W. Huang. *Adv. Funct. Mater*., 2016, **26**, 881-894.

48 K. T. Kamtekar, A. P. Monkman, M. R. Bryce. *Adv. Mater*., 2010, **22**, 572-582.

49 B. Balónová, D. Rota Martir, E. R. Clark. H. J. Shepherd, E. Zysman-Colman and B. A. Blight. *Inorg. Chem*., 2018, **57(14)**, 8581-8587.

50 L. Yang, J. R. Adsetts, R. Zhang, B. Balónová, M. T. Piqueras, K. Chu, C. Zhang, E. Zysman-Colman, B. A. Blight and Z. Ding, *Journal of Electroanalytical Chemistry*, 2022, **906**, 115891.

51 L. Yang, R. Zhang, B. Balónová, A. E. True, K. Chu, J. R. Adsetts, C. Zhang, X. Qin, E. Zysman-Colman, B. A. Blight and Z. Ding, *Journal of Electroanalytical Chemistry*, 2022, **920**, 116594.

52 B. Balónová and B. A. Blight, *Frontiers in chemistry*, 2021, **9**, 712698.

53 a) P.-N. Lai, C. H. Brysacz, M. K. Alam, N. A. Ayoub, T. G. Gray, J. Bao, T. S. Teets. *J. Am. Chem. Soc*., 2018, **140**, 10198-10207. b) Y.-J. Cho, S.-Y. Kim, C. M. Choi, N. J. Kim, C. H. Kim, D. W. Cho, H.-J. Son, C. Pac, S. O. Kang. *Inorg. Chem*., 2017, **56**, 5305-5315.

54 H. Zhen, C. Luo, W. Yang, W. Song, B. Du, J. Jiang, Y. Zhang and Y. Cao. *Macromolecules*, 2016, **39**, 1693-1700.

55 L. Zhao, S. Wang, L. Lu, J. Ding and L. Wang. *J. Mater. Chem. C.*, 2017, **5**, 9753-9760.

56 Hollingsworth, C. A.; Seybold, P. G.; Hadad, C. M. *International Journal of Quantum Chemistry* 2002, **90** (4-5), 1396–1403.

57 H. J. Bae, J. Chung, H. Kim, J. Park, K. M. Lee, T.-W. Koh, Y. S. Lee, S. Yoo, Y. Do and M. H. Lee, *Inorg. Chem.*, 2014, **53**, 128–138.

58 M. Hebda, G. Stochel, K. Szaciłowski and W. Macyk, *J. Phys. Chem. B*, 2006, **110**, 15275–15283.

59 T. Polat, F. Bulut, I. Arıcan, F. Kandemirli and G. Yildirim, *Journal of Molecular Structure*, 2015, **1101**, 189–211.

60 C. You, D. Liu, M. Zhu, J. Yu, B. Zhang, Y. Liu, Y. Wang and W. Zhu, *Journal of Materials Chemistry C*, 2020, **8**, 7079–7088.

61 P. Thordarson. *Chem. Soc. Rev*., 2011, **40(3)**, 1305-1323.

62 Price, J.; Balónová, B; Blight, B. A.; Eisler, S. *Chemical Science* 2021, **12** (36), 12092–12097.

63 D. Li, X. Liu, L. Yang, H. Li, G. Guo, X. Li and C. He, Chemical Science, 2023, **14**, 2237–2244.

64 Y. Zhou, P. He, X.-F. Mo, C. Liu, Z.-L. Gan, H.-X. Tong and X.-Y. Yi, *Inorg. Chem.*, 2021, **60**, 6266–6275.

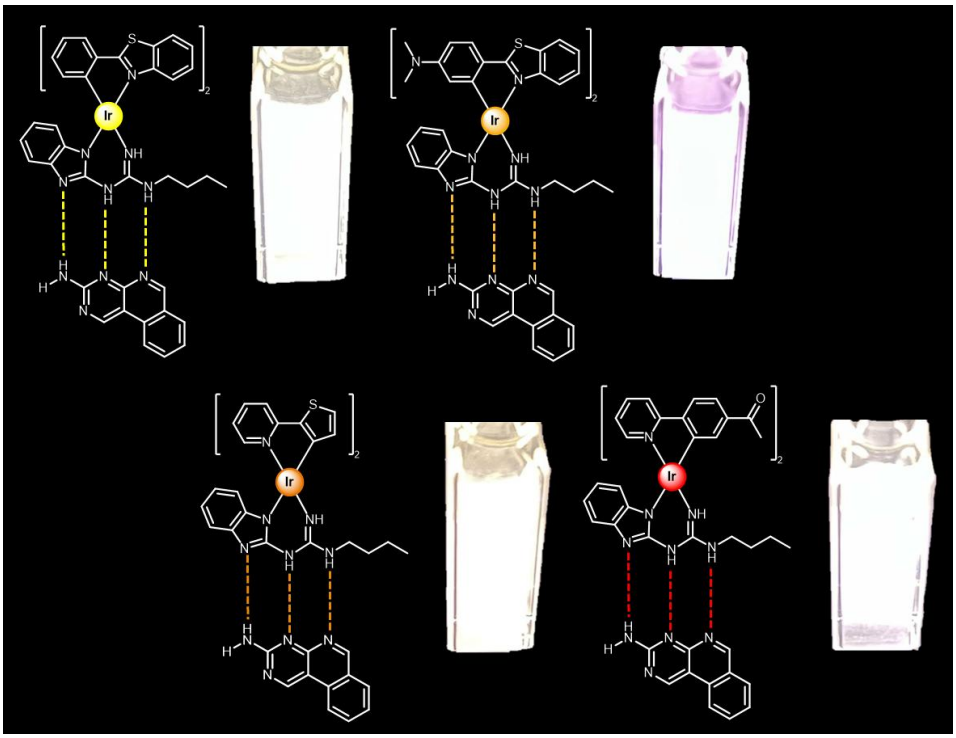
Chapter 4

Computationally Accelerated Discovery of Efficient Dual Component White Light Emitters

T. Harri Jones, Robert S. Horne, and Barry A. Blight *

The following chapter is based on a manuscript intended for publication:

T. Harri Jones was responsible for the design of the project, synthesis, characterisation, computational and experimental studies of the complexes studied herein. Robert Horne was also responsible for the synthesis and characterisation of the complexes. Barry A. Blight assisted in conceptualisation, supervised, analysed data and results, and procured funding.



4.1 Abstract

This chapter presents a computationally guided approach to formulating solution-based white light emission from a series of H-bonded iridium phosphors and a complementary H-bonding fluorophore. Thirty new Ir(III) complexes all incorporating a previously studied H-bond rich guanidine functionalised ligand were computationally investigated. The results of the computational screening based on TD-DFT peak emission data and established lifetime and quantum efficiency data in the literature indicated seven Ir(III) candidates suitable for synthesis and further investigation. Of the seven Ir(III) complexes, four were chosen based on their synthetic feasibility and their suitability to further study based on the parameters of the screen. Photophysical investigations of these four candidates with a deep blue emitter showed how three out of four of the complexes could achieve near ideal white light in the appropriate ratio of the complementary H-bonding fluorophore.

4.2 Introduction

Iridium research centres around a plethora of applications including catalysis,[1–4] bio-imaging,[5–7] and high-performance electrical components.[8,9] Of particular interest is the application of iridium complexes as emitters in PhOLEDs (phosphorescent light emitting diodes).[10–12] Heavy elements such as iridium have good electron spin-orbit coupling (SOC) and therefore can readily achieve highly efficient inter-system crossing (ISC).[13–15] Efficient ISC allows Ir(III) complexes to transfer a large percentage of singlet excited state (S_1) electrons to excited triplet states (T_{ex}) which in theory allows Ir(III) complexes to achieve a close to 100% external quantum efficiency.[15]

The strong phosphorescence of Ir(III) complexes occurs from two major triplet transitions, metal to ligand charge transfer (^{3}MLCT) between the iridium metal's 5dπ orbitals and the π-orbitals of the coordinated ligand,[16] and ligand centred charge transfer (^{3}LC) involving $^3(\pi - \pi)^*$. The ^{3}LC transition in most cases is higher in energy than ^{3}MLCT and according to Kasha's rule the lowest triplet state (T_1) is usually favoured for phosphors which is why the ^{3}MLCT transition typically results in radiative decay in the form of phosphorescence.[13,17,18] The coordinated ligands can be modified to change the strength of Ir-C bonds and the orbital configuration which results in changes to the intensity, lifetime (τ), efficiency (Φ) and colour of the emission.[18–20] Ligand modification can be done through the introduction of electron withdrawing groups (EWGs) or electron donating groups (EDGs),[18,21,22] the shrinking or extension of π-systems of ligands (this can also effect the rigidity of ligands), or the introduction of heteroatoms into the organic ligands such as sulfur or oxygen.[21,23] These modifications perturb the distribution and energies of the frontier molecular orbitals (FMOs) involved in the excitation and emission of phosphorescent complexes.[18,20]

Colour tunability is one of the key advantages of Ir(III) complexes and why they are so often used in OLED materials. Highly efficient Ir(III) complexes in the yellow and green emission regions are well-documented and there have been significant advances in orange and red complexes in recent years for biomedical research.[24–26] Deep blue Ir(III) complexes with high quantum efficiencies still prove difficult for researchers to synthesise regardless of extensive efforts due to the nature of phosphorescence being a lower energy process.[27–29] To achieve efficient phosphorescent emission the bandgap must be narrowed and the complex stabilised, which is antithetical to the structural

modifications required for deep blue emission, to achieve blue emission bandgaps must be increased.[30]

Commercial WLEDs (white light emitting diodes) are produced by combining three colours (red, green and blue) in a ratio to achieve an emission profile which is perceived to human vision as white in a process known as RGB colour mixing. White light was defined over eight decades ago by the Commission Internationale d'Éclairage (CIE) as coordinates in the 1931 colorimetric system. Ideal white light is represented by x,y coordinates (0.33,0.33) on the CIE 1931 system's colour plot which represents the colour perceived by human vision.[31] In traditional WLEDs RGB components are all excited at the same energy, therefore finding the correct ratio of components is the key to achieving white light through RGB mixing.[31] This approach has significant limitations when applied to WLED materials due to the rapid reabsorption of blue light by the green and red emitting components which lowers the efficiency of devices.[32] This limitation is further exacerbated by the blue emitting component being the first emitter to degrade because of the higher energetics of blue luminescence. As the reabsorption of blue light can cause additional emission of red and green components, the loss of the blue emitter can also rapidly result in loss of overall brightness through reduced energy inputs to the red and green components. Fluorescence Resonance Energy Transfer (FRET) must also be considered in RGB single phase systems as phosphors always tend to attain the lowest possible vibrational states. Higher energy components in phase with lower energy components will transfer energy which results in enhanced emission from the lower energy components.[17,31]

RGB mixing is not the only method for achieving white light. Mixing two complementary components by transecting the white region has been done through the mixing of blue and yellow-orange iridium phosphors.[31,33] In 2007 Ho *et al.* attempted doping a series of yellow-orange Ir(III) complexes with blue Ir(III) complexes. They achieved a CIE of (0.36, 0.42) which although in the white region is far removed from the ideal white emission of (0.33, 0.33).[33] More recently Xia *et al.* managed to achieve "near ideal" white light (0.33, 0.36) through supramolecular self-assembly of macrocyclic hosts encapsulating organic dyes allowing a lower vibrational state of the organic emitter to be achieved.[34] They noted an interesting phenomenon, the encapsulation of the organic dyes with appropriate hosts could increase the absolute quantum yield of the fluorophore through restricting vibrational motion thereby reducing non-radiative decay (k_{nr}).[34] Despite the increase in absolute quantum yield the efficiency of their system was still not particularly high at around 8.6% which was not ideal for device implementation.[34,35]

Recently our group achieved near perfect white light emission in the solution state through mixing a yellow and a blue emitter with complementary H-bond arrays, forming a white emitting self-assembly with CIE coordinates (0.34, 0.33).[36] Serendipitously we discovered this while studying the impact of introducing a H-bond rich ligand with an incorporated biguanide to a series of differently coloured Ir(III) complexes. As ideal white light has coordinates (0.33, 0.33) which is only 0.01 in the x value removed from our initial co-complex's CIE emission we decided to see if improvement upon the previous system was achievable. Our previous white light system had a major limitation, low PLQY from the Ir(III) emitter. The complex had an extremely high non-radiative

decay ascribed to vibronic behaviour in the C^N ligands from the extended π-array (see figure 4.1).[36]

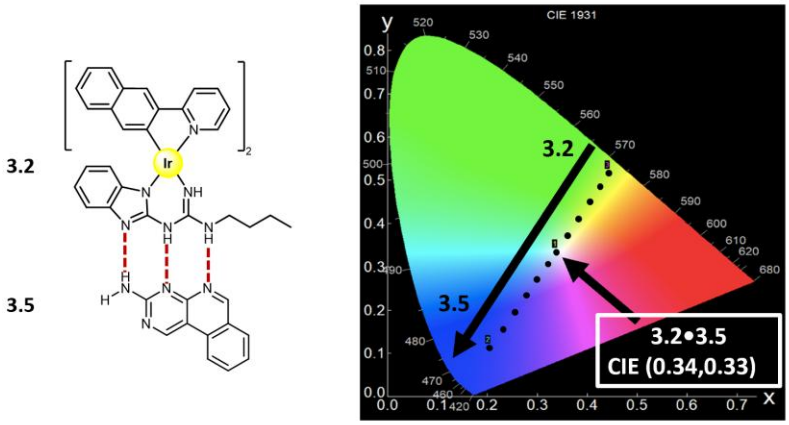


Figure 4.1 Previously studied yellow Ir(III) complex with complementary deep blue emitting hydrogen-bonder (see chapter 3).[36]

In our previous study, computations were used to explain a secondary photophysical effect observed in these complexes. Upon addition of complementary H-bonding blue emitter we observed a widening of the HOMO-LUMO gap and a blue shift in the peak emission of the Ir(III) complex.[36] These computations defined the HOMO-LUMO distributions on the complexes and aided in the description of our theory that frontier HOMO-LUMO interactions through complementary H-bonding could change the emissive properties of the complexes.[36] We also observed that through TD-DFT highly accurate predictions of peak emission wavelengths of these isolated Ir(III) complexes could be achieved. These observations form the basis of this study, herein we demonstrate the computational screening of a large series of Ir(III) complexes informed by previously studied yellow emitting Ir(III) complexes. Appropriate complexes were synthesised and further studied for their photophysical properties to ascertain whether

white light emission through an H-bonding dual-component approach is reproducible and improvable, and whether the computational methodology can provide an accurate starting point to the development of future H-bond rich dual component systems. Yellow emitting Ir(III) complexes **4.1-4.4** have high PLQYs (64-94%) as predicted based on known factors governing phosphorescence and previously demonstrated ligand efficiency. The introduction of deep blue emitting compound **4.5** resulted in quenching of overall phosphorescent quantum efficiency as strong FRET effects were evident between the hydrogen-bonded self-assemblies of fluorophores and phosphors. The quenched PLQYs of co-systems ranged from 28-36% demonstrating an improvement over the previously reported system. In addition, three out of four of the self-assemblies were able to achieve near ideal white light emission with the fourth system still lying within the white region demonstrating the accuracy of a computationally led design philosophy for phosphorescent iridium complexes.

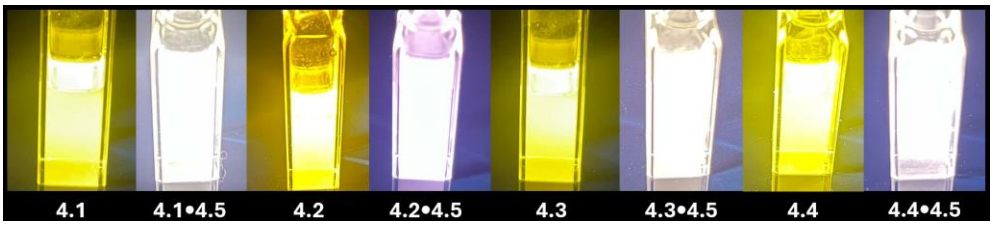


Figure 4.2 Yellow emitting Ir(III) complexes **4.1-4.4** and co-complexes **4.1•4.5-4.4•4.5** in their corrected ratios for white light emission. All images taken with samples in argon saturated $CHCl_3$.

4.3 Results and Discussion

4.3.1 Computational Investigation

This investigation began with the computational design of 30 new Ir(III) complexes all incorporating the previously studied H-bond rich N^N ancillary ligand 1-

(1H-benzo[d]imidazole-2-yl)-3-butylguanidine (see figure 4.3). For the computational investigation we chose the B3LYP level of theory with the 6-31G**/LANL2DZ basis sets because of the accuracy of previous TD-DFT studies of Ir(III) complexes and the abundance of this methodology applied to organo-metallic materials.[14,37–41] Additionally, the butyl chain of the aforementioned guanidine was truncated to a methyl group to simplify the structures for DFT inputs. Full details on the software package used can be found in appendix 1 and a summary of the key singlet states, HOMO-LUMOs and T_1 states can be found in appendix 4 A4.1.

The computational design philosophy was focused under three constraints: firstly, the choice of bidentate cyclometalating ligands would be limited to previously reported Ir(III) complexes with the ancillary ligand acetylacetonate (acac). This ensured that any bathochromic or hypsochromic shifts observed in the literature would be due to the character of the cyclometalating ligands and not a variation of the ancillary ligand. Secondly, all complexes chosen must have a reported external quantum efficiency over 10% or a photoluminescent quantum efficiency above 40% removing any candidates which have similar limitations to previously reported system of a high non-radiative decay (k_{nr}) and low PLQY. We had to account for this limitation before computationally studying the complexes as although TD-DFT can give accurate predictions of the energy of the excited T_1 state, it cannot predict the intensity of phosphorescent emissions owing to its inability to account for SOC effects.[42] Thirdly, the choice of ligands implemented into the computationally modelled complexes was also governed by the emission observed in previous experimental studies. The scope was limited to complexes which had a peak emission (λ_{max}) within 20 nm of our previously studied yellow emitter.

Combining these three constraints to the investigation narrowed the pool of complexes within the literature appropriate for our dual component systems. Figure 4.3 shows the simplified structures of the computationally designed octahedral cyclometalated Ir(III) complexes incorporating our H-bond rich guanidine ligand. The predicted λ_{max} of the T_1 emissions is included in the figure, those highlighted are the emissions deemed close enough to our previous yellow emitting iridium complex to consider for synthesis, the complexes highlighted in blue were the candidates chosen for synthesis.

In previous computational studies on Ir(III) complexes incorporating the guanidine ligand, the large concentration of nitrogen on the H-bond rich ligand heavily localises the HOMOs of the complexes to it. Modelled complexes **A-AD** continue this trend with the HOMOs residing on the π-orbitals of the benzimidazoyl-guanidinyl moiety of the ligand with residuals on the metal's 5dπ orbitals.[1,36,43] The amount of residuals on the iridium depends on the electronics of the cyclometalating ligands applied. More electron rich ligands with more efficient predicted absorptions (higher oscillator strength shown in table A.4.1) tended to have more residuals on the iridium. Increased electron density on the iridium signals a preference for ^{3}MLCT phosphorescence over ^{3}LC phosphorescence from the T_1 state which can also be noted through the increased % contribution of HOMO→LUMO transitions in many of these systems. HOMO energies range from -4.84 in complex **Y** to -4.39 in complex **S**. As all the HOMOs reside on the guanidine ligand and iridium metal, these changes in HOMO energies can be ascribed to the changes in the C^N cyclometalating ligands.

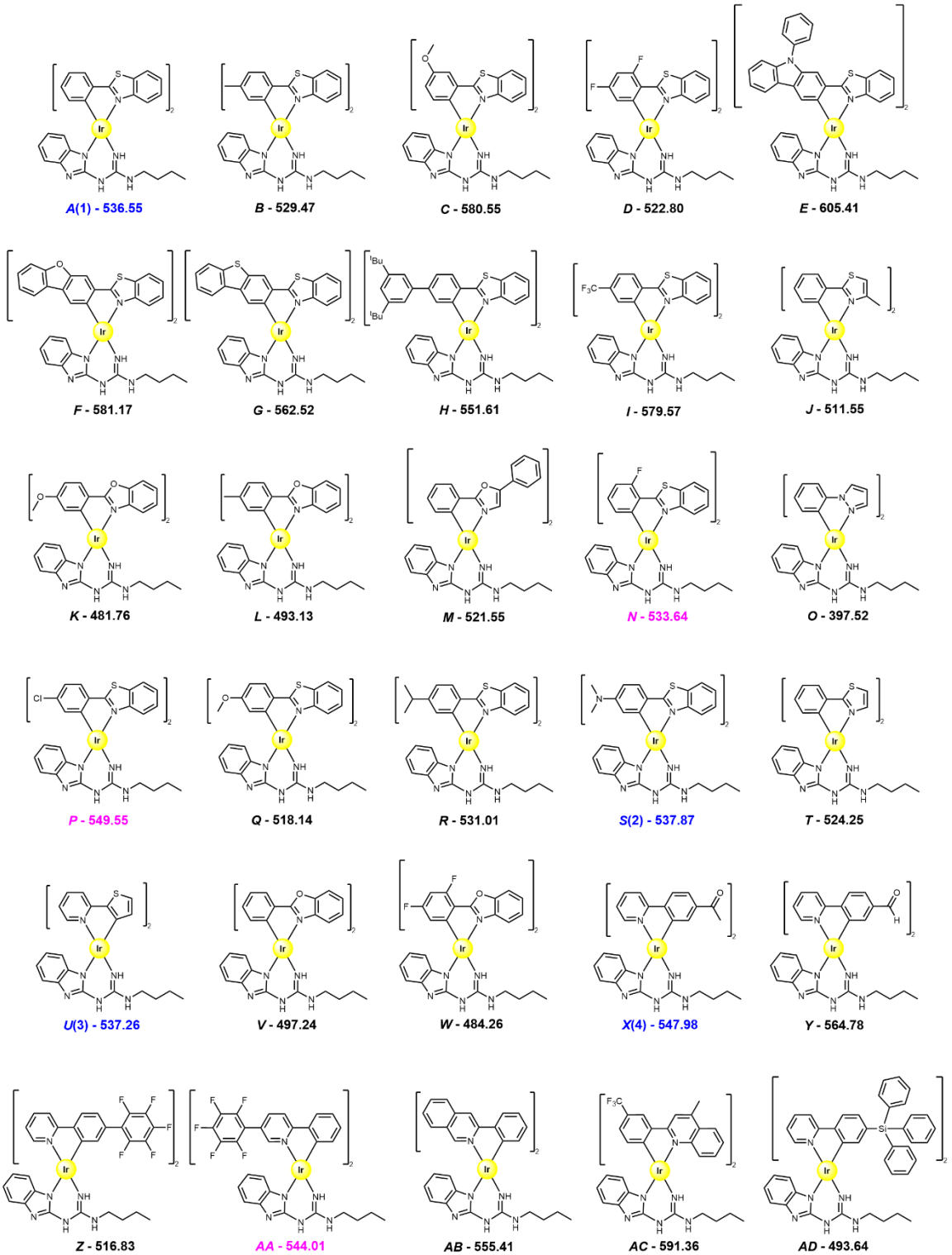


Figure 4.3 Summation of the predicted peak emissions of the 30 TD-DFT investigated Ir(III) complexes **A-AD**, computations were performed at the B3LYP level of theory with the 6-31G**/LANL2DZ basis sets.[38]

The LUMOs on all complexes **A-AD** are localised on the π-orbitals of one of the two cyclometalating ligands with some residuals on the iridium. The structural diversity of the ligands results in great variation in the distribution of the LUMOs and consequently a large variation in the LUMO energies from –2.17 in complexes **I** and **Y** to -0.79 in complex **O**. There are some general observable trends which align with previous computational and experimental studies of Ir(III) complexes. Extending the π-system of ligands tends to stabilise HOMO-LUMO gaps decreasing the T_1 energies leading to a red shift in peak emission. Additionally, the incorporation of EWGs onto the phenyl rings of proposed complexes results in a blue shift caused by the weakening of Ir-C bonds destabilising the LUMOs residing on the C^N ligands and consequently increasing the HOMO-LUMO gap.

Computational screening focused on the T_1 state energy of the complexes. From the thirty candidates screened, seven were identified to have appropriate T_1 energies for yellow emission; candidates **A**, **N**, **P**, **S**, **U**, **X** and **AA** were all shown to have λ_{max} of 537, 534, 550, 538, 537, 548 and 544 nm respectively. These values were very close to our desired λ_{max} of 542 nm with **AA** being the closest. Although **AA** was calculated to be the most appropriate candidate based on λ_{max}, **A**, **S**, **U** and **X** were chosen for synthesis due to their synthetic accessibility and high PLQYs of previous studies in the literature as well as being the complexes with the next most appropriate T_1 energies. Candidates **A**, **S**, **U** and **X** were therefore assigned as complexes **4.1-4.4** and further computational studies were performed on the effects of the addition of deep blue emitter compound **4.5** to each complex. The effects of addition are visualised in figure 4.4 which shows the HOMO-LUMO distributions of complexes **4.1-4.4** and co-systems **4.1•4.5-4.4•4.5**.

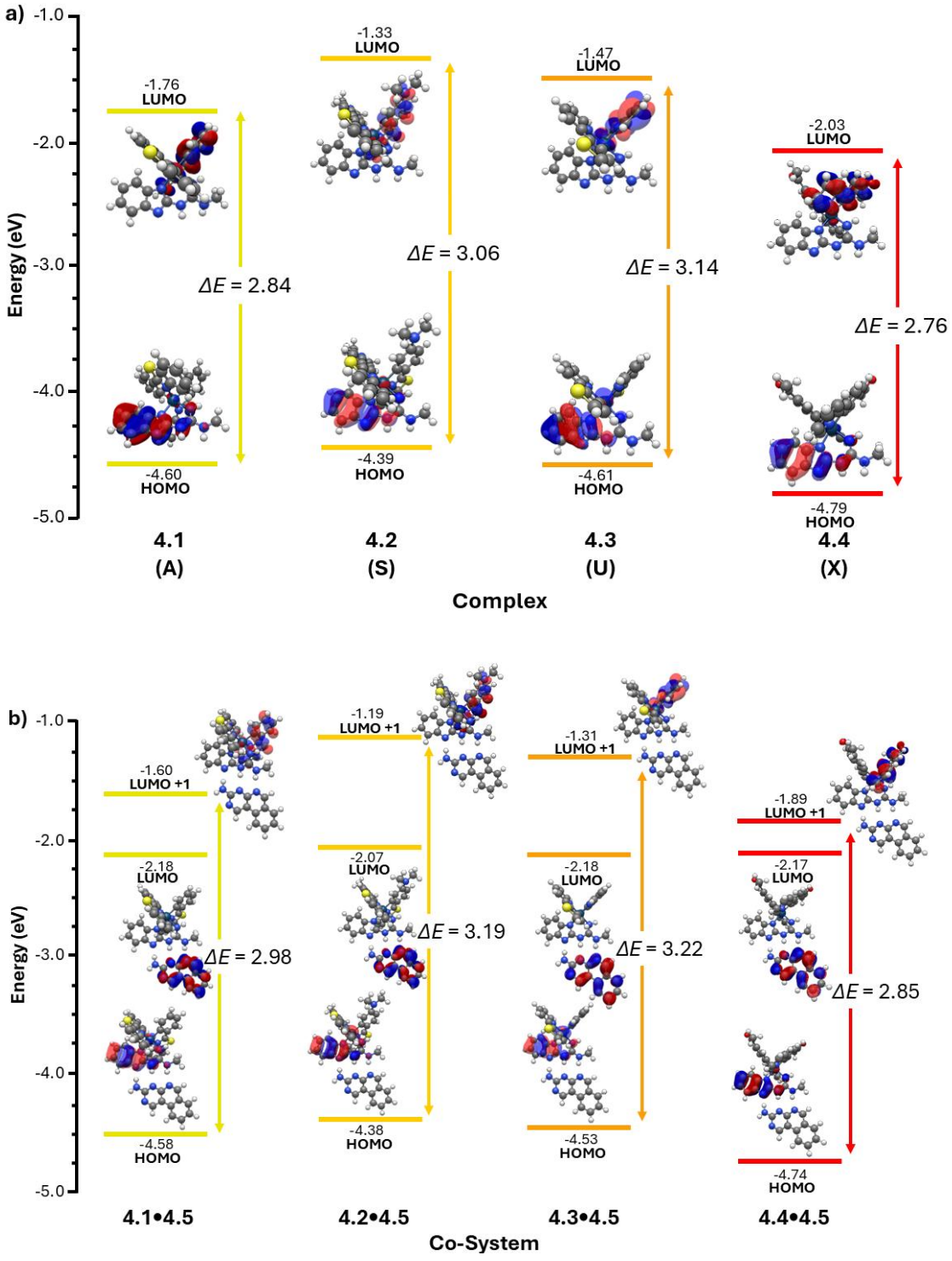


Figure 4.4 a) HOMO-LUMO distributions of complexes **4.1-4.4** with computationally predicted bandgaps (*ΔE*). **b)** HOMO-LUMO distributions of co-systems **4.1•4.5-4.4•4.5** with key energies and predicted bandgaps of the iridium complexes within the co-systems.

The self-assembly of systems **4.1•4.5-4.4•4.5** results in an increase in the HOMO energies through frontier HOMO-LUMO interactions between the LUMOs residing on compound **4.5** and the HOMOs located on the H-bonding guanidine ligand of the Ir(III) complexes. As the LUMO of the co-system now resides on compound **4.5** the HOMO-LUMO gap of the Ir(III) emitter is now the HOMO→LUMO+1 transition. The estimated HOMO-LUMO gap of complexes **4.1-4.4** ranged from 2.76-3.14 eV which increased to range from 2.85-3.22 eV when self-assembled into their respective co-system. Additionally, the estimated T_1 energies of complexes **4.1**, **4.3** and **4.4** increased when **4.5** was introduced aligning with previous computational studies into H-bonding self-assembled co-systems such as these. For example, co-system **4.1•4.5** sees an increase from 2.31 to 2.36 eV with the major contributing states shifting from HOMO→LUMO to HOMO→LUMO+1. Complex **4.2** diverged from trends observed in previous investigations and saw a decrease in the T_1 energy despite the increase in the HOMO-LUMO gap.

When comparing the experimental λ_{max} values (which are specifically discussed in the next section) of the four synthesised complexes, we observed predicted T_1 emissions had varying degrees of accuracy which can be attributed to structural eccentricities and unconsidered contribution effects. Complex **4.2**'s computational prediction was poor with a predicted λ_{max} of 538 nm against the experimental value of 556 nm, a difference of 28 nm. The other two thiazole complexes **4.1** and **4.3** had modest predictions with a difference of 10 nm and 11 nm from their computationally modelled λ_{max} against experimental values respectively. Complex **4.4** was the most accurate with an estimation of 548 nm, a difference of 3 nm from the observed peak emission. We

ascribe the inaccuracy of the thiazole complexes to the increased electronic activity of the sulfur atom incorporated to the cyclometalating ligands resulting in unforeseen contribution effects that the computational methods failed to factor.

4.3.2 Synthesis and Characterisation

The synthesis of complexes **4.1**-**4.4** and the supporting ligands can be found in the appendix (see appendix 4 A4.2). Compound **4.5** is identical to the deep blue emitter compound **3.5** used in colour modulating in the previous chapter. All compounds were structurally characterised with a combination of ^{1}H NMR, ^{13}C NMR and ESI^{+}-HRMS in addition to photoluminescence spectroscopy. Apart from the guanidine ligand referenced in previous chapters, all ligands synthesised for this chapter were made using microwave procedures further accelerating the synthesis and discovery of the new emitters while reducing solvent consumption.

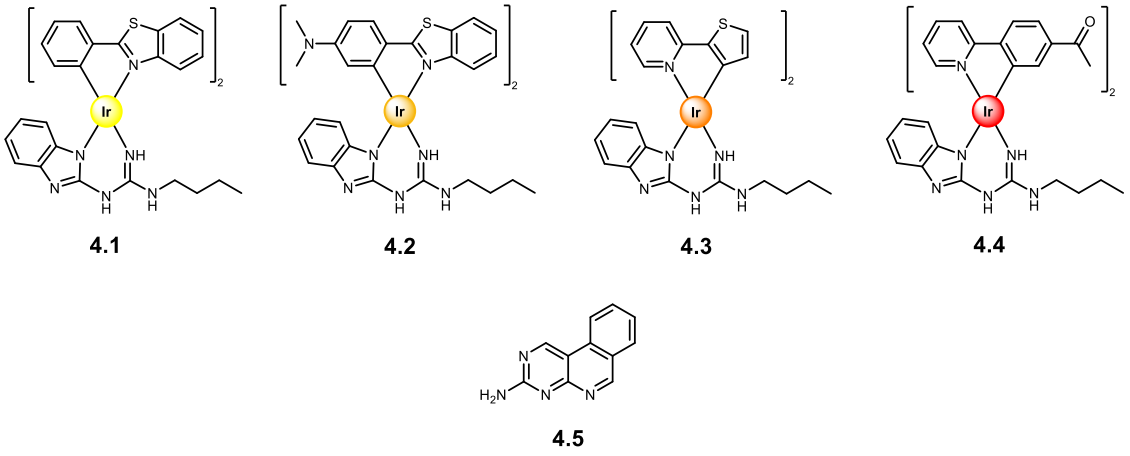


Figure 4.5 Yellow emitting Ir(III) complexes **4.1**-**4.4** chosen to be synthesised based upon their TD-DFT data, high PLQYs of Ir(III) complexes with these ligands in the literature and synthetic feasibility. Blue emitting compound **4.5** is also included to be mixed with yellow iridium emitters to achieve white emission.

4.3.3 Ir(III) Complex Photophysical Investigation

Figure 4.6 shows the UV-vis absorption spectra of complexes **4.1-4.4**. The complexes all show the three main characteristic bands of phosphorescent Ir(III) complexes.[18,44,45] All complexes show strong absorption bands from 250 nm to 350 nm typical of those seen in ^{1}LC π-π* transitions with complex **4.4** having an especially large ^{1}LC transition more typical of phenylpyridine based Ir(III) complexes which absorb at high frequencies. The next significant band is between 350 nm and 450 nm which we ascribe to spin-allowed ^{1}MLCT/^{1}LLCT, complex **4.2** has an especially intense absorption in this region due to the inclusion of the dimethylamino EDG on the phenyl ring leading to a large red shift in the absorption band.[46] The final and weakest absorption bands are beyond 450 nm which occur because of the spin-forbidden ^{3}MLCT/^{3}MLCT. These results imply that apart from complex **4.2** the complex's absorbance are dominated by high energy ^{1}LC π-π* transitions centred on the C^N and N^N ligands. Complex **4.2** on the other hand is dominated by lower energy ^{1}LLCT transitions thanks to the inclusion of the dimethylamine and the ability of this group to promote inter-ligand charge transfer through its π-orbital.[46]

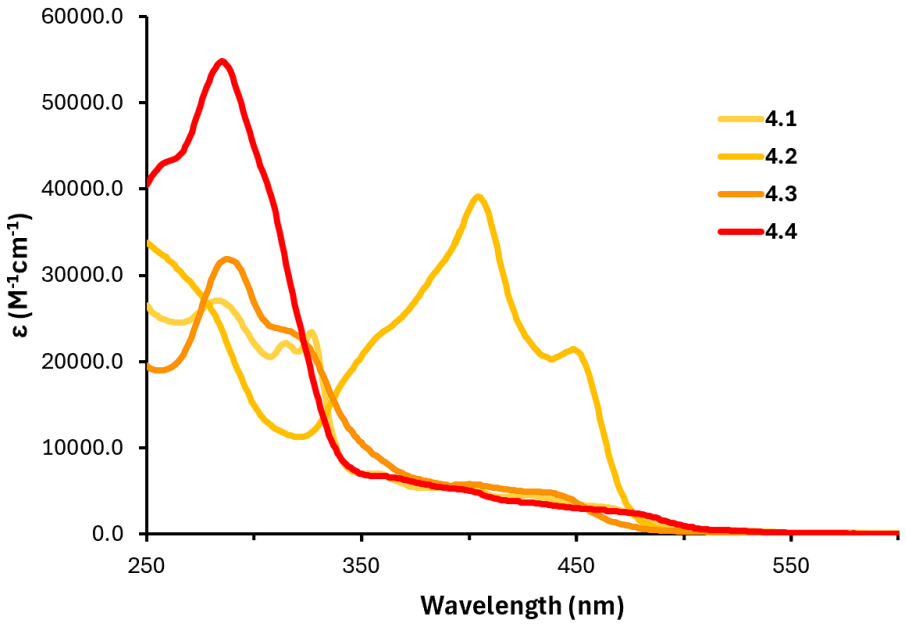


Figure 4.6 UV-vis absorption spectra of complexes **4.1-4.4** in $CHCl_3$ (c = 1×10^{-5} M, 298 K).

Emission spectra were taken of complexes **4.1-4.4** in $CHCl_3$ at 298 K. The spectra are presented in figure 4.7 with a summary of the key results presented in table 4.1, additional spectra figures are available in appendix 4 A4.4. All complexes studied herein exhibit multiple strong vibronic progressions typical to heteroleptic Ir(III) complexes with varying degrees of oscillator strengths. Complex **4.4** has the least pronounced secondary vibronic emission states with a λ_{max} of 551 nm and a subtle shoulder peak at 578 nm. Complex **4.4** also has the 2nd highest PLQY of 86% and the 3rd highest τ of 2.2 µs leading to a low k_{nr} (6×10^{-4} s^{-1}) indicating an efficient phosphorescent emitter. Just like complex **4.4** all the complexes studied have low k_{nr} values ranging between 3-8×10^{-4} s^{-1}. This can be ascribed to the literature screening applied to establish the computational candidates that removed any cyclometalating ligands shown to contribute to low PLQY and high k_{nr} as the structural rules which govern k_{nr} are well established.[18,20,21] Complex

4.3 sees the sharpest, most defined differences in vibronic emission bands with two sharp peaks at 548 nm and 592 nm. The peak at 548 nm is more intense than the peak at 592 nm leading to the overall yellow emission indicated by CIE (0.49,0.51). The sharp dual emission of complex **4.3** is an interesting result especially when compared to the structurally similar complex **4.1** which has a far less pronounced dual emission and a more yellow emission profile than complex **4.3**. Complex **4.1**'s coordinates are shifted by 0.02 in the x value towards the green colour component moving it away from the warmer orange/yellow emission of complex **4.3** and **4.2**.

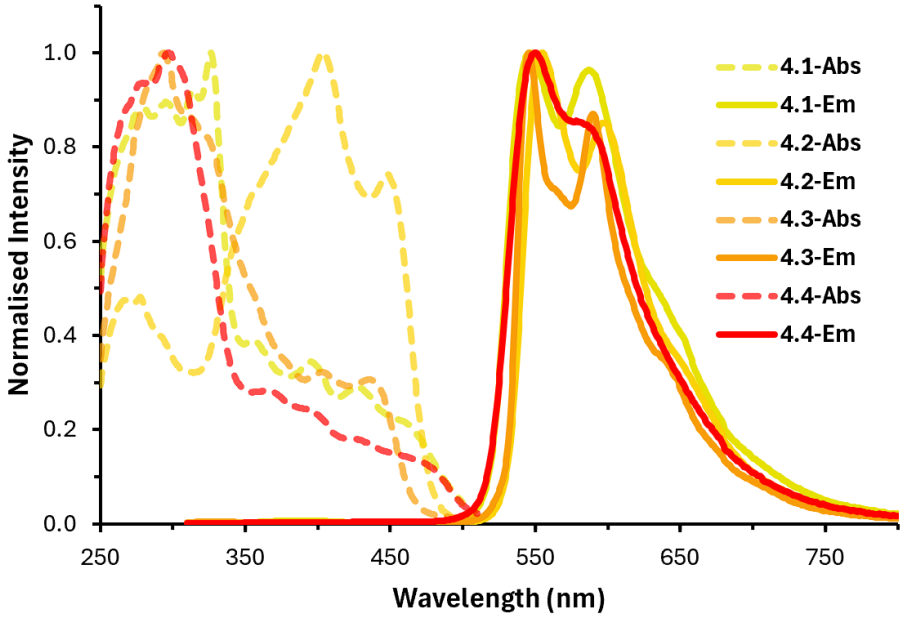


Figure 4.7 Normalised emission-excitation spectra of complexes **4.1-4.4** in argon saturated $CHCl_3$ ($c = 1.0\times10^{-5}$ M, 298 K), solid lines represent the emission while the dashed lines represent the absorption. All emission spectra were excited at 350 nm; the excitation wavelength was chosen for the overlap with compound **4.5**'s excitation profile.

The computational predictions showed that **4.1** and **4.3** would have similar λ_{max} with complex **4.1** being slightly blue shifted in comparison to **4.3**, but the study which inspired the choice of these ligands showed the opposite. $Ir(bt)_2(acac)$ (bt=benzothiazole,

ligand **4.7**) has a λ_{max} of 556 nm whereas Ir(ptz)$_2$(acac) (ptz= 2-phenylthiazolato-N, ligand **4.9**) has a λ_{max} of 547 nm.[47] The reversal of emission trends demonstrates the interesting electronic contributions of the highly electron rich guanidine ligand and how the computations were essential in informing the choice of yellow Ir(III) emitters. According to established rules governing efficient Ir(III) emitter design complex **4.1** should have a more efficient ^{3}LC and ^{3}MLCT owing to its extended π-system leading to a narrower HOMO-LUMO gap and a red-shifted emission. It is possible that due to the bulky nature of the ancillary guanidine ligand the introduction of bulkier cyclometalating ligands to the complex like in complexes **4.1** and **4.2** result in intramolecular dispersion interactions between ligands which has been shown to destabilise octahedral complexes causing blue shift. This theory is further corroborated by complex **4.2** having a peak emission of 556 nm which is 8 nm hypsochromically shifted compared to the peak emission of Ir(Me$_2$N-bt)$_2$(acac) (Me$_2$N-bt = 4-(benzothiazolato-N,C2′-2-yl)-N,N-dimethylaniline, ligand **4.8**) that has a peak emission of 563 nm.[48]

PLQY's of the complexes range from 64-94% with τ ranging from 2.0-4.8 μs. These values all far exceed our previous yellow emitter which had a PLQY of 8% and a lifetime <10 ns showing an immediate improvement in efficiency of the yellow phosphor components. The improved series of Ir(III) complexes studied herein show no clear correlation between their τ and Φ_{PL} despite the significant improvement in both values. When excited at 350 nm all complexes presented CIE coordinates in the yellow emission region meaning all complexes were suitable for further studies in the presence of compound **4.5** to determine whether white light emission is attainable through these new dual component systems.

Table 4.1 Photoluminescence data for complexes **4.1-4.4** in argon saturated $CHCl_3$ and the data for deep blue emitter compound **4.5** from previous studies.[43]

Compound	λ_{exc} (nm)[a]	λ_{em} (nm)[a]	Φ_{PL} (%)[b]	τ (µs)[c]	*CIE (x,y)*	k_r ($\times 10^5$ s^{-1})[d]	k_{nr} ($\times 10^5$ s^{-1})[d]
4.1	290, 320, 350	547, 590	94	2.0	0.47,0.51	4.7	0.3
4.2	351, 404, 443	556, 599	83	4.5	0.49,0.48	1.8	0.4
4.3	294, 325, 352	548, 592	64	4.8	0.49,0.51	1.3	0.8
4.4	268, 278, 297	551, 578	86	2.2	0.47,0.52	3.9	0.6
4.5[43]	265, 360	409, 426	43	0.003	0.16,0.05	2100	2900

[a] All complexes were prepared and measured in argon saturated $CHCl_3$ at 298 K.[b] PLQYs for Ir(III)complexes, determined using a FS5 SC-30 integrating sphere module.[c] Decay lifetimes measured using TCSPC excited at 365 nm.[d] The radiative (k_r) rate constant was calculated as $k_r = \Phi_{PL} / \tau_{PL}$.[d] The nonradiative ($k_{nr}$) rate constant was calculated as $k_{nr} = (1 - k_r = \Phi_{PL} / \tau_{PL})$.

4.3.4 Electrochemical Investigation

After establishing complexes **4.1-4.4** were suitable for further testing in dual component white light emission with compound **4.5** we investigated their electrochemical properties using cyclic voltammetry (CV), the results of which are summarised below in table 4.2.

Consistent with charge neutral [Ir(C^N)$_2$(N^N)] complexes we see irreversible reduction peaks that range from -1.25 to -1.41 V when complexes **4.1-4.4** were measured in isolation in $CHCl_3$.[50] According to previous studies this peak can be ascribed to the cyclometalating C^N/C^N$^-$ one electron reduction process indicated by the consistency of the thiazole complexes **4.1-4.3** reduction peak values compared to complex **4.4** incorporating phenyl pyridine based ligands.[50] Upon addition of compound **4.5** to complexes **4.1-4.4** as in previous studies there were no observable trends on the

irreversible reduction peaks further providing evidence that these peaks should be ascribed to the one electron reduction process. The Ir(IV)/Ir(III) one electron process is responsible for the E_{ox} values of complexes **4.1-4.4** which range from 0.72-1.02 V. Complex **4.4** has the highest E_{ox} value of 1.02 V while the benzothiazole complexes **4.1**, **4.2** and **4.3** all have similar values of 0.83 V, 0.73 V and 0.79 V respectively, because of the similar nature of their cyclometalating ligands. These changes in E_{ox} values dependent on the cyclometalating ligands demonstrates how the nature of the coordinated ligand has drastic implications on the ligand field strength of the metal centre.[51,52]

Table 4.2 Electrochemical and photo-redox properties of complexes **4.1-4.4** and co-systems **4.1•4.5-4.4•4.5** in argon saturated CH_3CN at 298 K.[a] Co-complexes are in a 1:1 ratio.

System	E_{red} (V)[a]	E_{ox} (V)[a]	ΔE (V)[a]	$E_{0\text{-}0}$ (eV)[a]	$E_{(PS^*/PS^-)}$ (V)[b]	$E_{(PS^+/PS^*)}$ (V)[b]
4.1	-1.41	0.83	2.24	2.45	1.04	-1.62
4.1•4.5	-1.39	0.90	2.29	2.46	1.07	-1.56
4.2	-1.36	0.72	2.08	2.43	1.07	-1.71
4.2•4.5	-1.42	0.68	2.10	2.43	1.01	-1.75
4.3	-1.36	0.79	2.15	2.43	1.07	-1.64
4.3•4.5	-1.36	0.85	2.21	2.44	1.08	-1.59
4.4	-1.25	0.97	2.22	2.46	1.21	-1.49
4.4•4.5	-1.29	1.02	2.31	2.47	1.18	-1.45

[a] E_{ox} and E_{red} values were measured by CV in argon saturated CH_3CN at 298 K, $E_{0\text{-}0}$ values were estimated from the intersection of the emission-excitation spectra as shown in figure 2.1. [b] Rehm-Weller calculated $E(PS^+/PS^*) = E_{ox} - E_{0\text{-}0}$; $E(PS^*/PS^-) = E_{red} + E_{0\text{-}0}$.

Previous studies on H-bond rich Ir(III) complexes in apolar media such as $CHCl_3$ revealed that in the presence of complementary H-bonding molecules E_{ox} values tend to

shift anodically due to frontier HOMO-LUMO interactions between the guanidine moiety and the H-bonding compliment.[36,43,49] Complexes **4.1**, **4.3** and **4.4** were consistent with previous studies with anode shifts ranging from 0.04-0.07 V, the largest change occurring when complex **4.1** was in the presence of compound **4.5**. Complex **4.2** does not obey the established trend, conversely, we see a cathodic shift of 0.04 V agreeing with the computational prediction for co-system **4.2•4.5** where we observed a lower T_1 energy than complex **4.2** neat. The diversion from the established trend is not supported by the blue shift in peak emission or the optical bandgap staying consistent in the presence of compound **4.5**. The likely source of the perturbing of the established trend is the dimethylamine group. The electron donating nature of dimethylamine increases the electronic activity of the phenyl ring bound to the iridium, strengthening the Ir-C bonds and decreasing the electronic contributions of the N^N guanidine ligands. This implies that complex **4.2** is less susceptible to the frontier HOMO-LUMO interactions which have been shown to alter the opto-electronic properties of the iridium complexes.

4.3.5 Supramolecular Titrations

The binding strength of complexes **4.1-4.4** with compound **4.5** was determined through host-guest titration. The K_a's and associated ΔG_a values calculated through these studies are summarised in table 4.3 with titration plots and Bindfit study results shown in appendix 4 A4.5. UV-vis host-guest titration revealed all complexes could selectively bind compound **4.5** to varying degrees. Complex **4.4** had the strongest K_a of 829 M^{-1} giving a Gibbs free binding strength of -16.6 $kJmol^{-1}$. Complexes **4.1** and **4.2** have much lower K_a's of 239 and 292 M^{-1} respectively while complex **4.3** has a slightly higher K_a of

406 M^{-1}. This is consistent with the structural nature of complexes **4.1-4.3** incorporating a thiazole moiety, the variation in these values is caused by the modulation in ligand size and EDG incorporation. We believe that complex **4.3**'s higher K_a is due to the size of the ligand as there is evidence that the larger ligands incorporated into complexes **4.1** and **4.2** caused mild dispersion effects weakening the coordination of the N^N ligand to the iridium. Complex **4.3**'s cyclometalating ligand is significantly smaller reducing any intramolecular dispersion effects from ligand spatial overlap and allowing easier access for compound **4.5** to the H-bond array of the ancillary guanidine ligand.

Table 4.3 Association constants (M^{-1}) and calculated Gibbs free energies (kJ mol^{-1}) for Ir(III) complexes **4.1-4.4** H-bonding to guest molecule **4.5**.

System	$K_a \pm \sigma$ (M^{-1})[a]	ΔG_a (kJ mol^{-1})[b]
4.1•4.5	$2.39 \times 10^2 \pm 0.05$ %	-13.6
4.2•4.5	$2.92 \times 10^2 \pm 0.06$ %	-14.1
4.3•4.5	$4.06 \times 10^2 \pm 0.06$ %	-14.9
4.4•4.5	$8.29 \times 10^2 \pm 0.09$ %	-16.6

[a] K_a and error determined by non-linear regression (*via* BindFit)[41] of UV-Vis absorption data ($CHCl_3$:DMSO/99:1) at 298 K. [b] Gibbs free energy of association calculated from $\Delta G = -RT\ln K_a$.

After determining the strength of association, investigation began into the correct ratio of blue and yellow emitter for white emission. We used equations 4.1 and 4.2 developed by Price *et al.* to estimate the molar ratio of blue to yellow emitter to achieve the desired white emission.[53] These equations consider a linear combination or relative brightness (a_i) as the product of the *i*th components mole fraction (χ_i), photoluminescent quantum yield (Φ_i), and excitation intensity ($I_{ex,i}$) at a common wavelength.

$$\left(x_{(mix)}, y_{(mix)}\right) = a_1(x_1 + y_1) + a_2(x_2, y_2) + \cdots + a_i(x_i + y_i) \quad (4.1)$$

$$a_i = \frac{\chi_i \phi_i I_{ex,i}(\lambda_{ex})}{\sum_{i=1}^{n} \chi_i \phi_i I_{ex,i}(\lambda_{ex})} \quad (4.2)$$

The equations give an accurate starting point to the photophysical investigation into white light but are limited by the nature of the investigation that informs them. They are designed to measure very dilute non-cooperative emissive species ~10^{-7} M with minimal intermolecular interactions, therefore they do not account for Förster resonance energy transfer (FRET) or any other photophysical effects. Our white light emitting systems were designed as a cooperative supramolecular self-assembly where emitters will interact in any non-polar media they are measured in. Additionally, with one component being an efficient phosphor and the other being an H-bound fluorophore significant levels of FRET were expected as evidenced by previous studies on similar co-systems which have shown enhancement in PLQY upon addition of compound **4.5**.[36,43]

Figure 4.8 shows the results of the emission titrations of complexes **4.1-4.4** with compound **4.5** to determine white light emission represented as CIE coordinates while table 4.4 shows accompanying photophysical data for the coordinates closest to white light. Complexes **4.1**, **4.3** and **4.4** are all within 0.01 in the x/y coordinates to the ideal white light coordinates of (0.33, 0.33) while complex **4.2** lay in the further white region with CIE coordinates (0.35, 0.31). As emission is preferred from lower energy states, the mixture of our fluorophores in the same phase as phosphors result in efficient FRET. The fluorophore **4.5** transfers its excited state energy to the Ir(III) complex which then undergoes a phosphorescent radiative decay from its lower lying triplet states. The complementary H-bond arrays of compound **4.5** and complexes **4.1-4.4** allow for

efficient FRET demonstrated by the enhancement in the emission profile of the Ir(III) complexes in the presence of compound **4.5** (see figure 4.9 and appendix A.4.22). The enhancement leads to significant errors in the ratios estimated from equations 4.1 and 4.2, for example the ideal ratio of compounds **4.1**:**4.5** was calculated to be 1:19 whereas the actual ratio was 1:24.

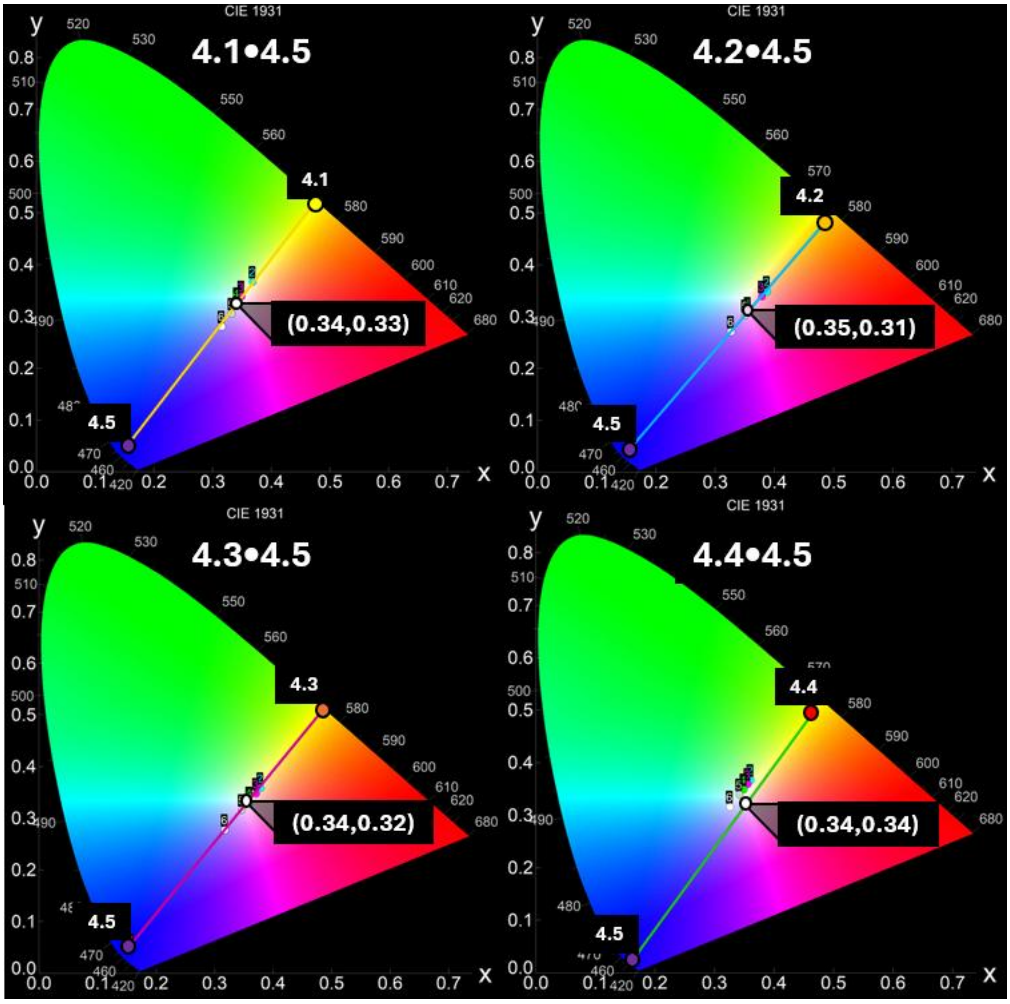


Figure 4.8 CIE representations of the results of emission titrations of complexes **4.1-4.4** with deep blue emitter **4.5**. Initial concentration of complexes is ($C_0 = 1\times10^{-5}$ M), 298 K. The emission titrations used to model the CIEs of **4.2•4.5-4.4•4.5** are available in appendix 4 (figure A.4.23) and the titration for **4.1•4.5** is shown in figure 4.9.

Figure 4.9 shows a FRET study of complex **4.1** and co-system **4.1•4.5**, there are more available in the appendix (figure A.4.22) which display the same trend. When compound **4.5** is added to an Ir(III) complex the emission intensity of the complex increases while the intensity of compound **4.5** decreases. The level of FRET observed varies with the most significant enhancement occurring from the addition of compound **4.5** to complex **4.3** resulting in a 24% increase in the intensity of the peak emission while the least significant FRET is observed in complex **4.2** which sees a 2% increase.

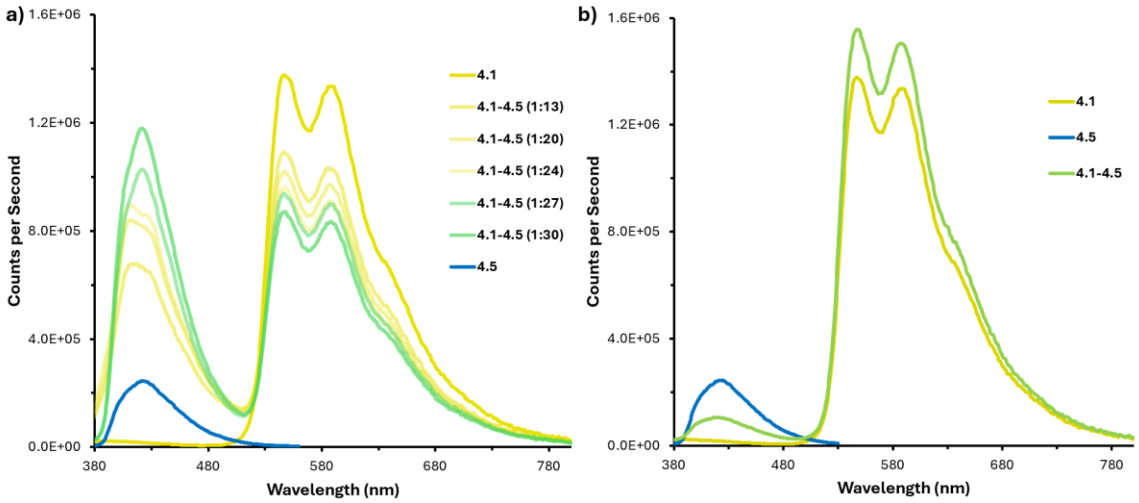


Figure 4.9 a) Emission titration of complex **4.1** with deep blue emitter **4.5**. **b)** Emission spectra of compound **4.1**, **4.5** and co-system **4.1•4.5**, all compounds were excited at 350 nm to show evidence of FRET.

FRET enhanced the emission of the Ir(III) complexes making the predicted ratios of phosphor to fluorophore too low as evidenced by the obtained ratios requiring at least 6 more equivalents of compound **4.5** than the predicted. An unfortunate side effect of having to overwhelm the Ir(III) emitter with compound **4.5** to achieve white light was the subsequent quenching of the emission of the Ir(III) complexes. When in its supramolecular self-assembly with compound **4.5** complex **4.1** saw the worst decrease in

PLQY from 94% to 28% with all other complexes maintaining PLQYs between 35-36%, still significantly lower than when compound **4.5** is absent. Despite the quenching three out of four of these co-systems were able to achieve near ideal white light in the ratios indicated in table 4.4 with co-system **4.4•4.5** showing the most promise due to the lowest level of PLQY quenching (36%) and CIE coordinates of (0.34,0.34).

Table 4.4 Photoluminescence data for complexes **4.1-4.5** in argon saturated $CHCl_3$.

Co-system	λ_{exc} (nm)[a]	λ_{em} (nm)[a]	Φ_{PL} (%)[b]	τ (µs)[c]	*CIE (x,y)*	k_r ($\times 10^5$ s^{-1})[d]	k_{nr} ($\times 10^5$ s^{-1})[d]
4.1•4.5 (1:24)	290, 320, 350	547, 587	28	2.3	0.34,0.33	1.2	3.1
4.2•4.5 (1:32)	351, 404, 443	555, 597	36	4.9	0.35,0.31	0.7	1.3
4.3•4.5 (1:20)	294, 325, 352	547, 591	35	4.9	0.34,0.32	0.7	1.3
4.4•4.5 (1:25)	268, 278, 297	549, 578	36	2.2	0.34,0.34	1.6	2.9

[a] All complexes were prepared and measured in argon saturated $CHCl_3$ at 298 K. [b] PLQYs for Ir(III)complexes, determined using a FS5 SC-30 integrating sphere module. [c] Decay lifetimes measured using TCSPC excited at 365 nm. [d] The radiative (k_r) rate constant was calculated as $k_r = \Phi_{PL} / \tau_{PL}$. [d] The nonradiative ($k_{nr}$) rate constant was calculated as $k_{nr} = (k_r = (1-\Phi_{PL}) / \tau_{PL})$.

4.4 Conclusions

The limitations of our previous studies into dual-component white light emission inspired the implementation of a computational screening methodology to determine appropriate yellow Ir(III) emitters to improve upon our system. Through the computational screening of thirty candidates, we established the four most appropriate complexes to be investigated as yellow emitters for our dual component white light emission. The suitability was based on a combination of their TD-DFT T_1 calculations, literature Φ and synthetic accessibility. After synthesis the initial photophysical

investigation revealed all four candidates showed CIE coordinates, PLQYs and τ appropriate for further investigation into white light emission. Upon titration with deep blue emitting compound **4.5** we found complexes **4.1**, **4.3** and **4.4** were all capable of near ideal white light emission with CIE coordinates of (0.34, 0.33), (0.34, 0.32) and (0.34, 0.34) respectively, with complex **4.2** achieving near white light (0.35, 0.31). Due to significant FRET effects a large excess of **4.5** was required to achieve the near ideal white light for each complex. As a result of this large excess of compound **4.5**, significant quenching in the emission of the Ir(III) complexes was observed with the largest incident occurring from complex **4.1** to co-system **4.1•4.5** showing a precipitous decrease in PLQY of 94% to 28%. The decrease in PLQY means the limitation of the original investigation of a low PLQY persists and future work should aim to increase the efficiency of the blue emitter, perhaps by creating a complementary H-bonding blue Ir(III) emitter. Regardless of the limitation of low PLQYs persisting we believe the use of computational methods to accelerate the new iridium material's discovery a success and future work into H-bonding emissive systems will incorporate further refined computational methodologies.

4.5 Bibliography

1 T. H. Jones, C. F. Bradshaw, J. W. Ward and B. A. Blight, *Catal. Sci. Technol.*, 2025, **15**, 2459–2465.

2 D. Ebrahimi, D. F. Kennedy, B. A. Messerle and D. B. Hibbert, *Analyst*, 2008, **133**, 817.

3 J. M. Zakis, R. A. Lipina, S. Bell, S. R. Williams, M. Mathis, M. J. Johansson, J. Wencel-Delord and T. Smejkal, *ACS Catal.*, 2025, **15**, 3525–3534.

4 D. N. Tritton, F.-K. Tang, G. B. Bodedla, F.-W. Lee, C.-S. Kwan, K. C.-F. Leung, X. Zhu and W.-Y. Wong, *Coord. Chem. Rev*, 2022, **459**, 214390.

5 S. Abbas, I.D. Din, A. Raheel, A. T. Din, Applied Organometallic Chemistry, 2019, 34, e5413.

6 J. Shen, T. W. Rees, L. Ji and H. Chao, *Coord. Chem. Rev*, 2021, **443**, 214016.

7 Z. Lu, M. Shangguan, X. Jiang, P. Xu, L. Hou and T. Wang, *Dyes Pigm*, 2019, **171**, 107715.

8 Z. Özçelik and N. GültekiN, *International Journal of Energy Applications and Technologies*, 2019, **6**, 44–48.

9 Q. Jia, Q. Sun, F. Yang, I. Anderson, A. P. Soleymani, J. Jankovic and C. Mittelsteadt, *Meet. Abstr.*, 2023, **MA2023-02**, 2100.

10 J. Kang, K.-M. Park, K. H. Lee, J. Y. Lee and Y. Kang, *Dyes Pigm*, 2021, **190**, 109334.

11 J. Jayabharathi, V. Thanikachalam and S. Thilagavathy, *Coord. Chem. Rev*, 2023, **483**, 215100.

12 G. Hong, X. Gan, C. Leonhardt, Z. Zhang, J. Seibert, J. M. Busch and S. Bräse, *Adv. Mater.*, 2021, **33**, 2005630.

13 A. R. G. Smith, P. L. Burn and B. J. Powell, *ChemPhysChem*, 2011, **12**, 2429–2438.

14 M.-X. Song, H.-H. Zhang, X.-H. Liu, Y. Ji, X.-L. Guo, J.-Y. Yang, Z.-K. Qin, F.-Q. Bai and H.-J. Zhang, *Appl. Organomet. Chem.*, 2022, **36**, e6875.

15 H. Yersin, A. F. Rausch, R. Czerwieniec, T. Hofbeck and T. Fischer, *Coord. Chem. Rev*, 2011, **255**, 2622–2652.

16 S. Kanti Seth, P. Gupta and P. Purkayastha, *New J. Chem.*, 2017, **41**, 6540–6545.

17 J. C. Del Valle and J. Catalán, *Phys. Chem. Chem. Phys.*, 2019, **21**, 10061–10069.

18 Y. You and S. Y. Park, *Dalton Trans.*, 2009, 1267–1282.

19 C. Ulbricht, B. Beyer, C. Friebe, A. Winter and U. S. Schubert, *Adv. Mater.*, 2009, **21**, 4418–4441.

20 A. F. Henwood and E. Zysman-Colman, *ChemComm*, 2017, **53**, 807–826.

21 M. Tavasli, T. N. Moore, Y. Zheng, M. R. Bryce, M. A. Fox, G. C. Griffiths, V. Jankus, H. A. Al-Attar and A. P. Monkman, *J. Mat. Chem.*, 2012, **22**, 6419–6428.

22 J. Frey, B. F. E. Curchod, R. Scopelliti, I. Tavernelli, U. Rothlisberger, M. K. Nazeeruddin and E. Baranoff, *Dalton Trans.*, 2014, **43**, 5667–5679.

23 C. You, D. Liu, M. Zhu, J. Yu, B. Zhang, Y. Liu, Y. Wang and W. Zhu, *J. Mater. Chem. C*, 2020, **8**, 7079–7088.

24 P. L. Dos Santos, P. Stachelek, Y. Takeda and P. Pander, *Mater. Chem. Front.*, 2024, **8**, 1731–1766.

25 Y.-P. Han, J.-M. Zhang, Y.-C. Duan, L.-L. Wen, G.-Y. Ding, K.-Z. Shao, G.-G. Shan, W.-F. Xie and Z.-M. Su, *J. Mater. Chem. C*, 2022, **10**, 14202–14210.

26 P. S. Chelushkin, J. R. Shakirova, I. S. Kritchenkov, V. A. Baigildin and S. P. Tunik, *Dalton Trans.*, 2022, **51**, 1257–1280.

27 M. Kim, I.-S. H. Lee, J.-Y. Lee, S. H. Han, K.-M. Park and Y. Kang, Ind. Eng. Chem, 2018, **58**, 386–390.

28 I. Siddiqui, S. Kumar, Y.-F. Tsai, P. Gautam, Shahnawaz, K. Kesavan, J.-T. Lin, L. Khai, K.-H. Chou, A. Choudhury, S. Grigalevicius and J.-H. Jou, *Nanomaterials*, 2023, **13**, 2521.

29 J. Yuan, H. Jiang, Q. Yang, Y. Xiang, Y. Zhang, Y. Dai, P. Li, C. Zheng, G. Xie and R. Chen, *J. Mater. Chem. C*, 2021, **9**, 687–692.

30 Q.-Y. Meng, X.-L. Wen and J. Qiao, *J. Phys. Chem. Lett.*, 2024, **15**, 12571–12583.

31 S. Mukherjee and P. Thilagar, *Dyes Pigm*, 2014, **110**, 2–27.

32 J. Li, Q. Liang, J.-Y. Hong, J. Yan, L. Dolgov, Y. Meng, Y. Xu, J. Shi and M. Wu, *ACS Appl. Mater. Interfaces*, 2018, **10**, 18066–18072.

33 C.-L. Ho, W.-Y. Wong, G.-J. Zhou, B. Yao, Z. Xie and L. Wang, *Adv. Funct. Mater.*, 2007, **17**, 2925–2936.

34 Y. Xia, S. Chen and X.-L. Ni, *ACS Appl. Mater. Interfaces*, 2018, **10**, 13048–13052.

35 J. Bauri, R. B. Choudhary and G. Mandal, *J Mater Sci*, 2021, **56**, 18837–18866.

36 B. Balónová, T. H. Jones, A. E. True, S. M. Hetherington and B. A. Blight, *RSC Adv.*, 2024, **14**, 34288–34297.

37 K. H. Hopmann, *Organometallics*, 2016, **35**, 3795–3807.

38 Y. Yang, M. N. Weaver and K. M. Jr. Merz, *J. Phys. Chem. A*, 2009, **113**, 9843–9851.

39 R. Schira and C. Latouche, *Dalton Trans*, 2021, **50**, 746–753.

40 A. K. Rao, A. Kumar, K. Jain and A. Kaur, *Mater. Today Commun.*, 2023, **34**, 104973.

41 V. Cherpak, P. Stakhira, B. Minaev, G. Baryshnikov, E. Stromylo, I. Helzhynskyy, M. Chapran, D. Volyniuk, D. Tomkuté-Lukšiené, T. Malinauskas, V. Getautis, A. Tomkeviciene, J. Simokaitiene and J. V. Grazulevicius, *J. Phys. Chem. C*, 2014, **118**, 11271–11278.

42 D. Jacquemin, B. Mennucci and C. Adamo, *Phys. Chem. Chem. Phys.*, 2011, **13**, 16987–16998.

43 B. Balónová, D. R. Martir, E. R. Clark, H. J. Shepherd, E. Zysman-Colman and B. A. Blight, *Inorg. Chem.*, 2018, **57**, 8581–8587.

44 P.-N. Lai, C. H. Brysacz, M. K. Alam, N. A. Ayoub, T. G. Gray, J. Bao and T. S. Teets, *J. Am. Chem. Soc.*, 2018, **140**, 10198–10207.

45 Y.-J. Cho, S.-Y. Kim, C. M. Choi, N. J. Kim, C. H. Kim, D. W. Cho, H.-J. Son, C. Pac and S. O. Kang, *Inorg. Chem.*, 2017, **56**, 5305–5315.

46 Y.-J. Yuan, J.-Y. Zhang, Z.-T. Yu, J.-Y. Feng, W.-J. Luo, J.-H. Ye and Z.-G. Zou, *Inorg. Chem.*, 2012, **51**, 4123–4133.

47 M. Xu, R. Zhou, G. Wang and J. Yu, *Inorganica Chimica Acta*, 2009, **362**, 515–518.

48 P. Ivanov, P. Petrova, S. Stanimirov and R. Tomova, *J. Phys.: Conf. Ser.*, 2017, **794**, 012021.

49 B. Balónová and B. A. Blight, *Front. Chem.*, 2021, **9**, 712698.

50 H. J. Bae, J. Chung, H. Kim, J. Park, K. M. Lee, T.-W. Koh, Y. S. Lee, S. Yoo, Y. Do and M. H. Lee, *Inorg. Chem.*, 2014, **53**, 128–138.

51 A. J. Wilkinson, H. Puschmann, J. A. K. Howard, C. E. Foster and J. A. G. Williams, *Inorg. Chem.*, 2006, **45**, 8685–8699.

52 X. Qu, Y. Liu, G. Godefroid, Y. Si, X. Shang, X. Wu and Z. Wu, *Eur. J. Inorg. Chem*, 2013, **2013**, 3370–3383.

53 J. Price, B. Balónová, B. A. Blight and S. Eisler, *Chem. Sci.*, 2021, **12**, 12092–12097.

Chapter 5

Conclusions and Future Outlook

5.1 Conclusions

The aims and objectives of each chapter of this thesis are outlined as:

- Chapter 2: Synthesise and test a series of H-bond rich Ir(III) complexes as photosensitisers for photoredox hydrogen generation and evaluate their efficiency and efficacy as photosensitisers.[1]
- Chapter 3: Synthesise a series of H-bond rich Ir(III) emitters and test their colour modulation abilities through H-bonding and evaluate their potential application as emitters.[2]
- Chapter 4: Computationally design a series of Ir(III) emitters, pick the most desirable candidates, synthesise them and evaluate their potential as efficient white light emitters.

In general, we can conclude that H-bond rich Ir(III) complexes have application potential with and without appropriate guests, though the level of success of these applications varies greatly. In chapter 2 we demonstrated the potential of complexes **2.1-2.5** in the HER. First, the complexes were analysed photo-physically and electrochemically to calculate their Rehm-Weller photoredox potentials.[3] $E_{(PS*/PS-)}$ ranged from 1.29-1.12 V while $E_{(PS+/PS*)}$ lay between -1.89V and -1.70V, these values were all in the appropriate ranges for photoredox hydrogen generation with co-catalyst $[Co(bpy)_3]^{2+}$ and electron donor TEA.[4] With the aid of our collaborators in the Ward group at the University of Liverpool's materials innovation factory, we leveraged automated synthesis

platforms to rapidly optimise the catalytic system using complex **2.2** for the basis of condition modulation. After screening we tested complexes **2.1-2.5** under the optimised conditions and found complexes **2.1** and **2.2** to be the best performing PSs for hydrogen evolution. Even though complex **2.1** and **2.2** performed best, they still performed lower than expected based on their Rehm-Weller values. We then performed Stern-Volmer quenching studies and photostability studies to explain this underperformance. Photostability showed all complexes had relatively good stability under prolonged irradiation under intense UV and blue light proving that complex stability was not the issue. Stern-Volmer studies demonstrated the complexes have high k_q's (between 2×10^9-3×10^{13}) when titrated against electron donor TEA and co-catalyst which indicated that the complexes may have multiple quenching behaviours through their strong H-bonding interactions leading to reduced activity as a PS.[5]

Chapter 3 presented the synthesis and photophysical studies of another series of Ir(III) complexes **3.1-3.4** with and without the complementary H-bonding deep blue emitter **3.5**. Complexes **3.1**, **3.3** and **3.4** had PL lifetimes over 1.7 μs and PLQYs above 23.4%, these values demonstrated strong emissions with further evidence provided by the low k_{nr} values between 0.6-4.5×10^5 s^{-1}.[6] Complex **3.2** had a much higher calculated k_{nr} of 4.7×10^8 s^{-1} due to the short lifetime (1.9 ns) and low PLQY (8.7%) which was ascribed to unwanted vibronic decays caused by the nature of complex **3.2**'s cyclometalating ligands extended π-system.[7] On addition of the complementary H-bonding compound **3.5** we see significant changes in the electrochemical and emissive properties of the iridium emitters. E_{ox} values increase between 0.04-0.1V indicating an increase in electrochemical bandgap, this was corroborated by the blue shift of peak emissions and the blue shift of the opto-

electronic bandgap.[8] Each complex also had an eccentricity in the presence of compound **3.5**, complex **3.1** was able to achieve deep blue emission through titration with compound **3.5** CIE (0.15,0.11). Complexes **3.3** and **3.4** saw an enhancement in their PLQY values through addition of compound **3.5** of 23.4-43.3% and 36.1-41.4% respectively. We attributed this increase in PLQY to the energy transfer demonstrated in our FRET studies which showed clear communication between emitters in the co-system. Complex **3.2** in the presence of compound **3.5** was able to achieve white light emission in the ratio of 1:1.3 with an enhanced PLQY of 33.2%, largely due to the high PLQY of organic emitter **3.5**.

TD-DFT studies further validated this blue shifting hypothesis by calculating the orbital distributions and energies of complexes **3.1-3.4** with and without compound **3.5**. HOMOs all reside on the guanidine ligand with partial residues on the iridium metal while LUMOs were localised on one of the two cyclometalating ligands of complexes **3.1-3.4**. When the complexes are modelled with the complementary H-bonding compound **3.5** we observed that the LUMO of the co-system moves to **3.5** and the HOMO energies have been stabilised through frontier HOMO-LUMO interactions. Further, the lowest unoccupied orbital on the iridium complex (LUMO+1 of co-system) now had increased energy, widening the optoelectronic bandgap of the iridium complex and causing a small blue shift in the emission profile of the iridium complex. Through this computational investigation we also noticed how accurately the TD-DFT methods were in modelling the peak emission energy of **3.1-3.4** from the T_1 state.[9]

The final experimental chapter was inspired by the accuracy of previous TD-DFT calculations and the serendipitous discovery of white light emission in the dual

component system with CIE coordinates (0.34, 0.33). We designed a series of thirty new iridium complexes incorporating the H-bonding rich guanidine ligand. The new complexes were inspired by previously synthesised yellow emitters selected from the literature based on certain constraints including peak emission, reported quantum yield and a fixed ancillary ligand of acetylacetonate. From this computational screen we identified seven potential candidates for further study, four complexes were synthesised based on accessibility and the proximity of their predicted peak emission (T_1 state energy) to our previous yellow emitter.[2] The four synthesised complexes were then analysed photo-physically and the data sets were compared to the computational predictions. We found complexes incorporating sulfur atoms had less accuracy in our computational predictions due to the increased electronic effects of the larger orbital configuration of 3p atoms, but despite this inaccuracy all complexes **4.1-4.4** did emit in the yellow region.

The complexes were also studied in the presence of the deep blue emitter compound **4.5**. We performed a similar series of investigations to those shown in chapter 3 to show the effects of complementary H-bonding on emissive and electrochemical properties. In addition to this we performed emission titrations of all complexes with compound **4.5** to determine whether the co-systems were capable of white light emission. These titrations revealed that complexes **4.1**, **4.3** and **4.4** were all capable of near white emission with CIEs of (0.34, 0.33), (0.34, 0.32) and (0.34, 0.34) respectively. Complex **4.2** achieved CIE of (0.35, 0.31) in the white region, but not as accurate or close as the other three complexes. Although all complexes achieved some degree of white light a large excess of compound **4.5** was required to overcome FRET effects. This means the

increased PLQYs provided by these new yellow emitters are diminished with complex **4.1** seeing the worst quenching from 94% to 28% when in the white emitting co-system. Even with the low PLQY issue persisting the success of the computationally led designs cannot be ignored and is responsible for the accelerated discovery of new white emitting supramolecular self-assembly materials.

5.2 Outlook

This thesis began the investigations into the applications of H-bond rich Ir(III) complexes. In chapters **2-4** we studied potential applications as photosensitisers for photocatalysis and emitters for variable chromaticity and accessing challenging colours. Success in these applications varied as chapter 2 showed low TONs not suitable for long term cycling, but we greatly expanded the library of H-bond rich Ir(III) complexes incorporating (1-(1H-benzo[d]imidazole-2-yl)-3-butylguanidine) both theoretically and experimentally. Chapter **4** also challenges our group's previous experimentally led design philosophy by showing how implementing computational screening can provide semi-empirical data into a theorised molecule's properties that could inform and influence how we attempt to apply them.

Chapters **2-4** focused solely on the H-bond rich guanidine ligand as the functional ancillary ligand. Future studies on H-bond rich precious metal complexes should move towards other H-bond rich ligands as through this thesis and separate studies into the bioactive nature of these complexes we have exhausted potential avenues of application for this guanidine functionalised ligand. I believe we have demonstrated that H-bond rich materials of this nature can have functional applicability, but design refinements to

improve the H-bonding ligand are necessary to further tune complexes to specific applications. Through a collaboration with the Légaré group at McGill University our group has recently been provided with a new ligand, compound **5.1** shown below in figure 5.1. Incorporating this molecule as the ancillary ligand to the library of known iridium complexes may open a new wave of application testing, especially in photoredox hydrogen generation due to the variable redox profile of the ligand. If Rehm-Weller investigations reveal suitability to the HER, then additional photocatalytic investigations may be warranted with a new range of complexes with collaborators at the University of Liverpool.

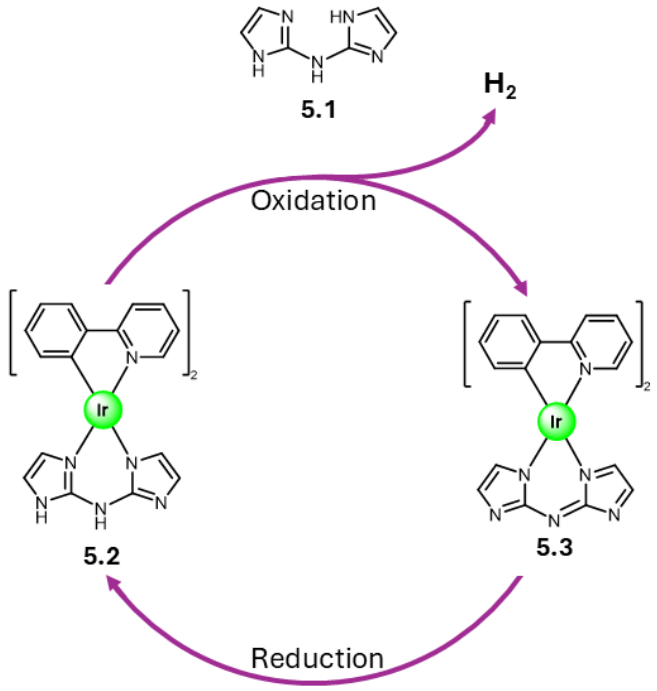


Figure 5.1 Proposed Ir(III) complexes for future photocatalytic hydrogen generation incorporating the redox active Légaré ligand (compound **5.1**).

This new ligand (**5.1**) may also open new avenues in H-bonded emissive system designs. The major limitation of white light generation across chapters 3 and 4 was the

lowering of the PLQY due to the choice of deep blue emitter. The Zysman-Colman group have previously designed a deep blue emitting Ir(III) complex with relatively high quantum yields.[10] Assuming ligand **5.1** doesn't hinder the quantum yield, the oxidised version of **5.1** could be introduced as the ancillary ligand and combined with a protonated form of our yellow emitting guanidine complexes. This combination could create an ion-dipole assisted super strong organometallic H-bonding AAA-DDD self-assembly capable of white light through second-sphere coordination shown below in figure 5.2.[11]

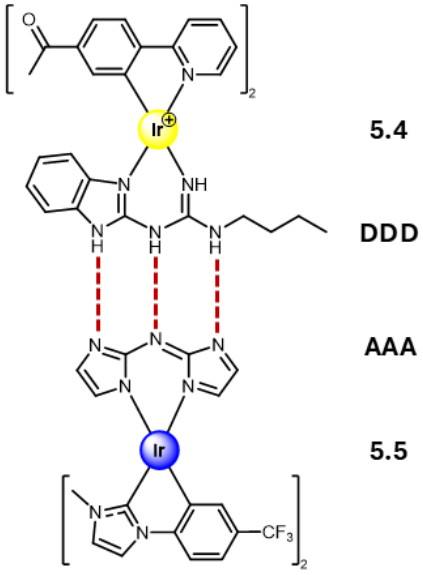


Figure 5.2 Proposed organometallic superstrong DDD-AAA H-bonding co-complex incorporating oxidised Légaré ligand and protonated guanidine ligand.

This work provides the investigative toolbox necessary for future work into studying the applications of functional H-bond rich molecular organometallic materials. My hope is that the findings of these studies may inform future design philosophy of precious metal complexes with strong non-covalent interactions incorporated into their structure.

5.3 Bibliography

1 T. H. Jones, C. F. Bradshaw, J. W. Ward and B. A. Blight, *Catal. Sci. Technol.*, 2025, **15**, 2459–2465.

2 B. Balónová, T. H. Jones, A. E. True, S. M. Hetherington and B. A. Blight, *RSC Adv.*, 2024, **14**, 34288–34297.

3 S. Farid, J. P. Dinnocenzo, P. B. Merkel, R. H. Young, D. Shukla and G. Guirado, *J. Am. Chem. Soc.*, 2011, **133**, 11580–11587.

4 S. Fan, X. Zong, P. E. Shaw, X. Wang, Y. Geng, A. R. G. Smith, P. L. Burn, L. Wang and S.-C. Lo, *Phys Chem Chem Phys*, 2014, **16**, 21577–21585.

5 N. Kandoth, J. Pérez Hernández, E. Palomares and J. Lloret-Fillol, *Sustain. Energy Fuels*, 2021, **5**, 638–665.

6 R. E. Harding, S.-C. Lo, P. L. Burn and I. D. W. Samuel, *Org. Electron.*, 2008, **9**, 377–384.

7 Y. You and S. Y. Park, *Dalton Trans.*, 2009, 1267–1282.

8 L. Yang, R. Zhang, B. Balónová, A. E. True, K. Chu, J. R. Adsetts, C. Zhang, X. Qin, E. Zysman-Colman, B. A. Blight and Z. Ding, *J. Electroanal. Chem.*, 2022, **920**, 116594.

9 D. Di Censo, S. Fantacci, F. De Angelis, C. Klein, N. Evans, K. Kalyanasundaram, H. J. Bolink, M. Grätzel and M. K. Nazeeruddin, *Inorg. Chem.*, 2008, **47**, 980–989.

10 A. F. Henwood and E. Zysman-Colman, *Chem Commun*, 2017, **53**, 807–826.

11 B. Balónová and B. A. Blight, *Front. Chem.*, 2021, **9**, 712698.

Appendix 1

Materials and Experimental Techniques

Materials. All starting materials were purchased from commercial sources (Sigma Aldrich, Fisher Scientific and TCI) and used without further purification. Analytical thin layer chromatography (TLC) was carried out on precoated TLC plates Alugram Sil G/ UV254. Column chromatography purifications were done with silica gel (ultrapure, 60-200 μm (60 Å)). Experiments were performed as follows:

(i) A conventional hotplate (IKA™ RCT Basic magnetic hot plate stirrer (Stirring range: 50 to 1500 rpm; Size: 5.3 in. dia; Supplier: IKA™ 3810001) – fume hood), under a dry N_2 atmosphere using standard Schlenk Line techniques when specified.

(ii) Microwave reactor – Anton Paar-Monowave 400 (max. temp. 300 °C, power 850 W and pressure of 30 bar) with 10- and 30-mL borosilicate glass vials with a cap material of PEEK. The seal material is made from Teflon-coated silicone. Supplier: Anton Paar.

Nuclear Magnetic Resonance (NMR). ^{1}H (400 MHz) and ^{13}C (101 MHz) NMR spectra were recorded on a Bruker 400 NMR spectrometer in deuterated solvents, namely chloroform-*d* ($CDCl_3$) and dimethyl sulfoxide-d_6 (DMSO-d_6), which were purchased from Fisher Scientific. All chemical shifts are reported in δ (ppm) referenced to tetramethylsilane ($Si(CH_3)_4$) or residual protonated solvent and the peak multiplicities are referred to as singlet (s), doublet (d), triplet(t), quartet (q), multiplet (m). Spin-spin coupling effect is quantify with the coupling constants, which is abbreviated with the capital letter J.

Mass Spectrometry. High-resolution mass spectral data measurements were performed by Xiao Feng at the Mass Spectrometry Laboratory (Dalhousie University, Halifax, Canada). High-resolution mass spectra were recorded on Bruker Daltonics MicrOTOF instrument. The ionization method used for low/high-resolution analysis was positive electrospray ionization (ESI+). The sample was introduced by a syringe pump at a flow rate of 2 μL/min and the spray voltage applied to the ESI needle was 4.5 kV. The dry gas flow rate was 4 L/min with a pressure of 1 Bar and a temperature of 180 °C. For the analysis, samples sizes were between 1.0-2.5 mg and the experiment was replicated 2-3 times to ensure the viability of the results (sample sizes of ~5 mg were sent).

UV-Vis Spectroscopy. UV-Vis spectra for the cyclometalated Ir(III) complexes were recorded with a Cary Series UV-Vis Spectrophotometer (Agilent Technologies). Chloroform – HPLC grade (C606-1, LOT 214513) was used as the blank solution and the solvent to prepare the solutions of the several Ir(III) complexes. Two standard Q macro cuvettes with an optical path length of 10 millimetres which are made of fused quartz glass were used to measure the absorbance of these compounds. UV-Vis spectra were collected with a concentration of the cyclometalated Ir(III) complexes of 1.10^{-5} M.

Photoluminescence Emission Spectroscopy. Emission and excitation spectra, PLQY, and decay lifetime measurements were recorded with a FS5 Spectrofluorometer (Edinburgh Instruments).

- Excitation and emission spectra for the cyclometalated Ir(III) complexes were recorded with a FS5 Spectrofluorometer (Edinburgh Instruments) and a SC-05 (Standard Cuvette Holder) at 298 K. A Hellma Fluorescence Cuvette (Suprasil 6 Quartz, spectral range 200-2,500 nm, pathlength 10×4 mm and chamber volume 3,500 μL) was used to measure the

excitation and emission spectra. The sample solutions were prepared in chloroform – HPLC grade (C606-1, LOT 214513), which was used as a blank solution and the solvent to prepare the solutions.

- Measurements of the quantum yield were carried out with use of an FS5 SC-30 integrating sphere module and a Xenon lamp at 298 K in argon degassed $CHCl_3$. Excitation wavelengths will be specified with figures as compounds have significant variation in excitation.

$$PLQY = \frac{\#\ emitted\ photons}{\#\ absorbed\ photons}$$

Number of absorbed photons was inferred by comparing the difference in the excitation light scattering of the blank and the sample (Ex_{blank} and Ex_{sample}) – whereas the number of emitted photons can be inferred by comparing the difference between the sample and the blank (Em_{sample} and Em_{blank})

$$PLQY = \frac{Em_{sample} - Em_{blank}}{Ex_{blank} - Ex_{sample}}$$

- Decay lifetime measurements were recorded with a FS5 Spectrofluorometer (Edinburgh Instruments) and a SC-05 (Standard Cuvette Holder). All solutions were prepared to a concentration of ~$1 \cdot 10^{-5}$ M using chloroform – HPLC grade (C606-1, LOT 214513) that was degassed in a cuvette for 20 minutes (Ar) before each measurement at 298 K. A QF2001 – 10 mm Lightpath Spectrophotometer Screw Cap Cuvette (Threaded – Quartz 3.5 mL) was used to measure the excitation spectra of each Ir(III) complex. The excited state lifetimes were measured by the time correlated single photon counting spectra (TCSPC) technique using an EPLED-365 (Edinburgh Instruments) laser with emission

detection at 520 nm for all complexes. Each lifetime measurement was calculated through an Exponential Fit Time Scan that follows the formula:

Fit: $B_1 e^{(-t/\tau_1)} + B_2 e^{(-t/\tau_2)} + B_3 e^{(-t/\tau_3)} + B_4 e^{(-t/\tau_4)}$

A chi-squared (χ^2) of values between 1-1.3 were found suitable. These complexes showed either monoexponential decay or biexponential decay.

Hydrogen Evolution Studies. The accelerated screening hydrogen studies were conducted using a Chemspeed Technologies Sweigher platform, operating with a constant N_2 purge at the University of Liverpool. Samples were prepped in vials and thoroughly degassed with N_2. From here vials were moved to the Chemspeed platform to perform a further degas and cap operation. From the degas and cap, sample vials were transferred to an Oriel Solar Simulator 94123A (IEC/JIS/ASTM, 1600 W Xenon) for high energy photo-irradiation rated at 1.0 sun. After a reaction specific amount of time (between 0-5 hours) samples were removed and placed on the carousel of a Shimadzu GC-2010 Plus GC with HS-20 Headspace Sampler. From here an aliquot of the gasses in the vials were taken up and relative volumes of the gasses calculated from the data.

Cyclic Voltammetry. CV was carried out in an argon filled glovebox using a potentiostat/galvanostat (BioLogic SP-150) with a cell consisting of a working electrode (platinum disk, 0.07 cm^2), counter electrode (platinum wire, 5 cm) and Ag/Ag^+ reference electrode (0.01M $AgNO_3$ in 0.1 M NBu_4PF_6 in anhydrous chloroform). All E_{ox} and E_{red} values were referenced to a ferrocene standard. The electrode was washed thoroughly with the electrolyte solution before each sample run. Each sample concentration was measured to be 2 mM.

DFT methodology. DFT calculations were performed using the Gaussian16 revision c.01 software package provided by the University of Waterloo (University of Waterloo) through the Digital Research Alliance of Canada (alliancecan.ca). The ground state geometries were optimised at the B3LYP level using LANL2DZ basis set for iridium and the 6-31G** basis set for all other atoms. The energy minima were confirmed using frequency analysis and the absence of any imaginary frequencies. The butyl chains on the 'guanidine' ligand were truncated to methyl groups to reduce disorder and computational costs. Time-dependant DFT (TD-DFT) was also undertaken to calculate the singlet and triplet excited energetic states. All relevant orbital and geometries are given in section S8.

All initial input structures were created using and optimised Avogadro2 1.91.0

Orbital plots were generated using Avogadro2 1.91.0

UV-vis plots were generated using GaussSum 3.0.2

Appendix 2

Supplementary Material for Chapter 2

Table of Contents

A2.1: Synthetic Procedures of Complexes 2.1-2.5 **224**

A2.2: ^{1}H and ^{13}C NMR Spectra and Mass spectra **233**

A2.3: Cyclic Voltammetry **245**

A2.4: Excitation and Emission Data **246**

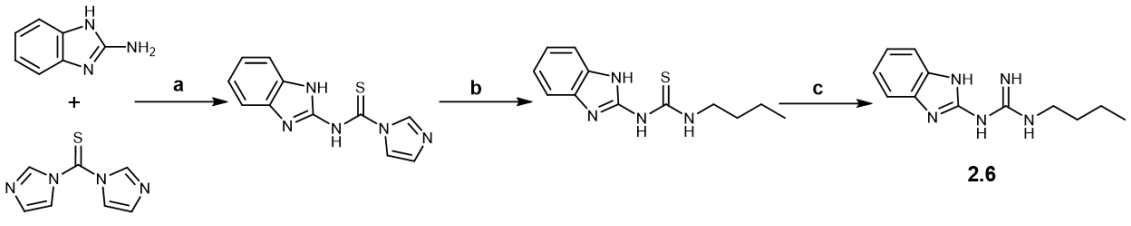
A2.5: Stern-Volmer and Photo-Stability **247**

A2.6: PLQYs and Decay Lifetimes **255**

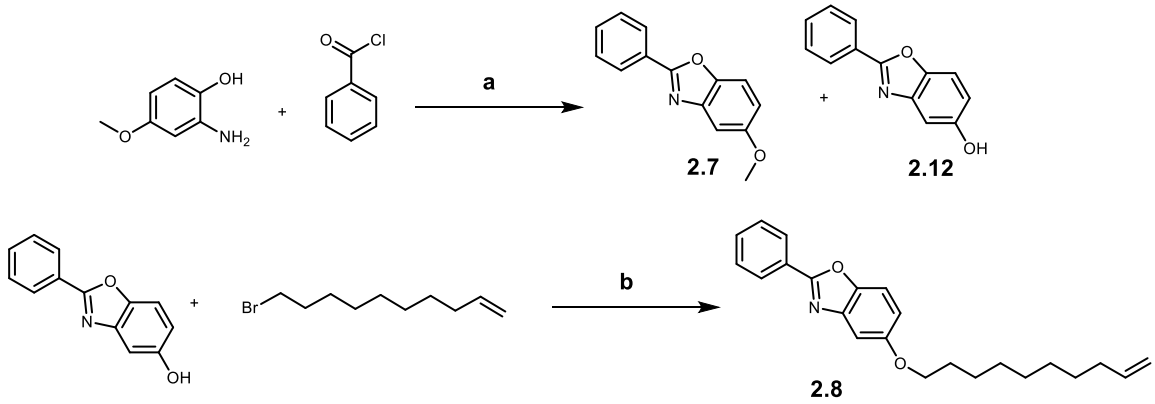
A2.7: High-Throughput Hydrogen Evolution Screening **260**

A2.8: Computational Investigation **262**

A2.1: Synthetic Procedures of Complexes 2.1-2.5



Scheme A.2.1 General procedure for the synthesis of the 1-(1H-benzo[d]imidazole-2-yl)-3-butylguanidine ligand (**2.6**) is as follows. Reagents and conditions: a) MeCN, 50 °C, 20 hours; b) *n*-butyl amine, catalytic DMAP, DMF, 100 °C, 18 hr; c) HgO, (NH_3/MeOH (2 M)), $CHCl_3$, room temperature, 3 hours.

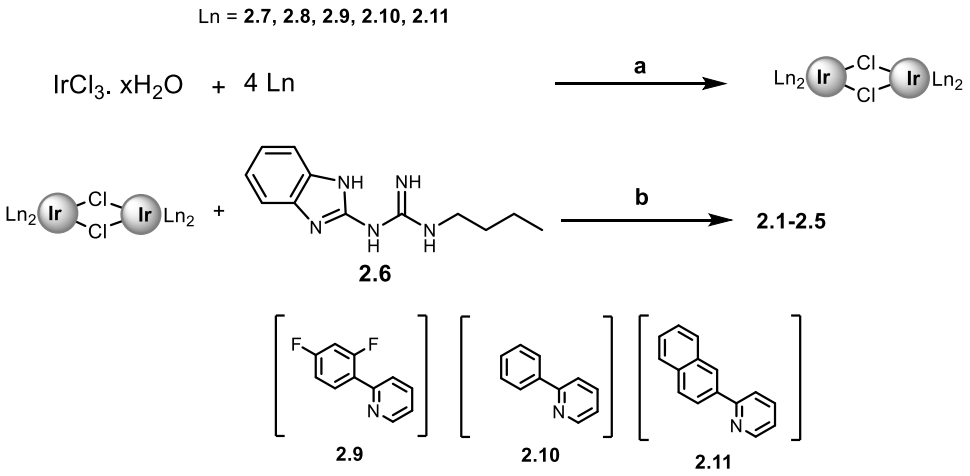


Scheme A.2.2 The routes for the preparation of the ligands **2.7** and **2.8**. Reagents and conditions: a) NMP, pyridine, N_2, 202 °C, 5 hr; b) MeCN, K_2CO_3, N_2, 90 °C, 12 hr.

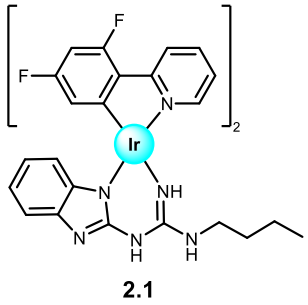
Iridium dimers

All iridium μ-chloro bridged dimers were synthesized following Nonoyama's procedure. Iridium chloride hydrate (1 equivalent) and 2 equivalents of appropriate ligand were added into a mixture of 2-ethoxyethanol: water (3:1) and refluxed for 19-24 hours under nitrogen atmosphere. After cooling to room temperature, a precipitate was formed and

filtered. The solid was washed with water (5 mL), ethanol (5 mL) and acetone (5 mL) and dried on Schlenk line for 48 hours.



Scheme A.2.3 The general synthetic route of all iridium complexes herein. Reagents and conditions: a) 2- ethoxyethanol: water (3:1), 130 °C, 19 hr; b) K_2CO_3, toluene, N_2, 110 °C, 16 hr. Ligands **2.9-2.11** were all synthesised using previously established procedures in the literature.

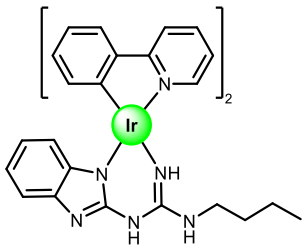


2.1

Iridium complex 2.1 – Combine $[Ir(dFppy)_2Cl]_2$ chloro-bridged dimer (100 mg, 0.08 mmol, 1.0 eq) with 2 equivalents of ligand **2.6** (38 mg, 0.16 mmol) and 10 equivalents of potassium carbonate (72 mg, 0.82 mmol), then add to 10 mL of dry degassed toluene and reflux under nitrogen atmosphere for 16 hours. Next the reaction was cooled to room temperature and solvent was removed under reduced pressure. The solid was then redissolved in DCM and extracted with water, the organic phase was dried again and was

then purified by silica gel column chromatography (DCM: MeOH, 10: 0.5). Product was obtained in 80% yield (132 mg).

^{1}H NMR (400 MHz, $CDCl_3$, 298 K) δ 8.64 (dd, *J* = 5.9, 0.9 Hz, 1H), 8.30 (d, *J* = 8.4 Hz, 1H), 8.21 (d, *J* = 8.4 Hz, 1H), 8.09 (d, *J* = 5.8 Hz, 1H), 7.80 (td, *J* = 7.6, 1.7 Hz, 1H), 7.73 (td, *J* = 7.7, 1.8 Hz, 1H), 7.22 (d, *J* = 7.9 Hz, 1H), 7.13 (ddd, *J* = 7.4, 5.8, 1.4 Hz, 1H), 7.02 (q, *J* = 7.3 Hz, 2H), 6.76 (t, *J* = 7.8 Hz, 1H), 6.47 (dddd, *J* = 15.0, 12.5, 9.1, 2.4 Hz, 2H), 6.19 (d, *J* = 8.3 Hz, 1H), 5.84 (dd, *J* = 8.6, 2.4 Hz, 1H), 5.61 (dd, *J* = 8.5, 2.4 Hz, 1H), 4.85 (s, 2H), 4.45 (s, 1H), 3.08 – 2.91 (m, 2H), 1.47 – 1.39 (m, 2H), 1.25 (h, *J* = 7.6 Hz, 2H), 0.81 (t, *J* = 7.4 Hz, 3H). ^{13}C NMR (101 MHz, $CDCl_3$) δ 165.64, 164.68, 156.93, 156.10, 154.45, 151.24, 149.91, 148.80, 145.86, 140.20, 138.13, 138.04, 128.64, 128.22, 123.29, 123.07, 122.74, 122.33, 120.57, 116.57, 114.90, 114.76, 114.19, 113.99, 111.13, 98.47, 98.22, 97.83, 41.07, 30.70, 20.07, 13.75. HMRS [ESI+] ion $[C_{34}H_{29}F_4IrN_7]^+$ m/z calculated: 804.2044 Found: 804.2034 [M+].

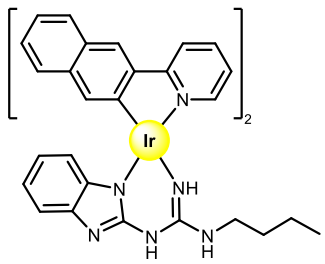


2.2

Iridium complex 2.2 – Iridium chloro-bridged dimer $[Ir(ppy)_2Cl]_2$ made from ligand **2.10** (500 mg, 0.68 mmol) was combined with ligand **2.6** (316 mg, 1.37 mmol) and 10 equivalents of K_2CO_3 (945 mg, 6.84 mmol), the mixture then had 20 mL of dry toluene added and was heated to reflux under nitrogen. After 16 hours, the reaction was cooled to r.t, toluene was removed under reduced pressure and the crude was extracted between

DCM and water. DCM was removed under reduced pressure and the product was columned between DCM and methanol (1:99). 850 mg of the final product was obtained, an 85% yield.

^{1}H NMR (400 MHz, $CDCl_3$, 298 K) δ 11.87 (s, 1H), 11.14 (s, 1H), 8.66 (dd, *J* = 5.8, 0.8 Hz, 1H), 8.09 (dd, *J* = 5.8, 0.8 Hz, 1H), 7.89 (d, *J* = 7.9 Hz, 1H), 7.82 – 7.71 (m, 2H), 7.68 (td, *J* = 7.8, 1.6 Hz, 1H), 7.60 (dd, *J* = 7.8, 1.3 Hz, 2H), 7.23 (d, *J* = 7.8 Hz, 1H), 7.11 (ddd, *J* = 7.4, 5.8, 1.4 Hz, 1H), 7.05 – 6.88 (m, 5H), 6.82 (td, *J* = 7.4, 1.4 Hz, 2H), 6.77 (td, *J* = 7.4, 1.4 Hz, 1H), 6.68 (ddd, *J* = 8.5, 7.4, 1.3 Hz, 1H), 6.45 – 6.36 (m, 2H), 6.21 (dd, *J* = 7.6, 1.4 Hz, 1H), 6.10 (d, *J* = 8.3 Hz, 1H), 4.60 (s, 1H), 3.03 – 2.83 (m, 2H), 1.44 (pd, *J* = 7.4, 3.1 Hz, 2H), 1.22 (dq, *J* = 14.9, 7.4 Hz, 2H), 0.79 (t, *J* = 7.3 Hz, 3H). ^{13}C NMR (101 MHz, $CDCl_3$) δ 169.08, 168.11, 152.35, 150.43, 150.20, 149.89, 148.73, 145.03, 144.61, 144.35, 140.19, 137.15, 137.04, 133.02, 132.01, 131.43, 129.90, 124.65, 124.15, 122.81, 122.72, 122.32, 122.08, 121.92, 121.42, 118.97, 117.42, 110.64, 41.01, 30.68, 20.04, 13.78. HMRS [ESI+] ion $[C_{34}H_{33}IrN_7]^+$ m/z calculated: 732.2421 Found: 732.2434 [M+].

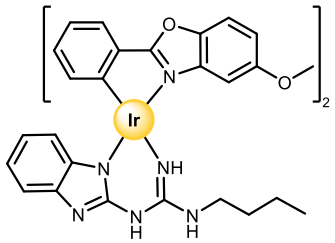


2.3

Iridium complex 2.3 – Iridium chloro-bridged dimer made from ligand **2.11** (120 mg, 0.09 mmol) was combined with ligand **2.6** (44 mg, 0.19 mmol) and 10 equivalents of potassium carbonate (125 mg, 0.94 mmol), this was added to 10 mL of dry toluene and

refluxed under nitrogen atmosphere for 16 hours. After the reaction was completed, it was cooled to room temperature and solvent was removed under reduced pressure. The solid was re-dissolved in dichloromethane and extracted with water, combined organic phases were then purified through column chromatography (DCM: MeOH, 10:0.5). The product was dried in vacuo (Schlenk line) for 48 hr. The final product was obtained as a dark yellow powder in 70 % yield (110 mg).

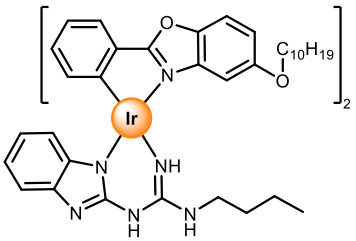
^{1}H NMR (400 MHz, $CDCl_3$, 298 K) δ 11.84 (s, 1H), 11.29 (s, 1H), 8.79 (d, *J* = 5.9 Hz, 1H), 8.26 (d, *J* = 5.9 Hz, 1H), 8.15 (d, *J* = 4.0 Hz, 2H), 8.13 – 8.06 (m, 3H), 7.89 (t, *J* = 7.8 Hz, 1H), 7.82 (t, *J* = 7.8 Hz, 1H), 7.70 (t, *J* = 6.8 Hz, 2H), 7.21 (t, *J* = 7.3 Hz, 7H), 7.13 (t, *J* = 6.6 Hz, 2H), 6.93 (t, *J* = 7.8 Hz, 1H), 6.73 (s, 1H), 6.52 (s, 1H), 6.47 (t, *J* = 7.9 Hz, 1H), 6.41 (s, 1H), 6.15 (d, *J* = 8.4 Hz, 1H), 4.69 (s, 1H), 2.86 (ddd, *J* = 50.9, 12.9, 6.3 Hz, 3H), 1.46 – 1.36 (m, 2H), 1.17 (q, *J* = 7.7 Hz, 2H), 0.75 (t, *J* = 7.3 Hz, 3H). ^{13}C NMR (101 MHz, CD_2Cl_2) δ 168.31, 167.33, 150.59, 150.20, 149.05, 145.53, 145.44, 145.07, 144.57, 144.09, 143.78, 140.46, 137.16, 137.00, 135.25, 131.45, 131.32, 130.20, 129.91, 129.75, 129.00, 128.93, 128.78, 126.74, 126.66, 125.96, 124.17, 123.63, 123.55, 123.14, 123.01, 122.70, 122.35, 119.85, 117.41, 110.66, 41.05, 30.63, 20.00, 13.77. HMRS [ESI+] ion $[C_{42}H_{37}IrN_7]^+$ m/z calculated: 832.2732. Found: 832.2734 [M+].



2.4

Iridium complex 2.4 – Iridium chloro-bridged dimer made from ligand **2.7** (200 mg, 0.15 mmol) was combined with ligand **2.6** (68 mg, 0.30 mmol) and 10 equivalents of potassium carbonate (205 mg, 1.48 mmol). This solid mixture was degassed and, 15 mL of dry toluene was added, this solution was then refluxed at 110 °C for 16 hours. The mixture was then cooled to room temperature, solvent was removed under reduced pressure and the crude was redissolved in DCM, then extracted with water. The combined organic phases were then purified through column chromatography (DCM: MeOH, 99:1). The final product was a dark yellow powder 63 % yield (162 mg).

^{1}H NMR (400 MHz, $CDCl_3$) δ 12.04 (br, 1H), δ 11.44 (br, 1H), δ 7.74 – 7.67 (m, 2H), 7.50 (dd, *J* = 8.9, 1.3 Hz, 2H), 7.23 (d, *J* = 7.6 Hz, 1H), 7.05 – 6.97 (m, 5H), 6.93 – 6.84 (m, 3H), 6.73 (ddd, *J* = 8.5, 7.4, 1.3 Hz, 1H), 6.67 (d, *J* = 7.5 Hz, 1H), 6.53 (d, *J* = 7.4 Hz, 2H), 6.26 (d, *J* = 8.4 Hz, 1H), 5.70 (d, *J* = 2.5 Hz, 1H), 4.76 (s, 1H), 3.84 (s, 3H), 3.13 – 2.93 (m, 2H), 2.85 (s, 3H), 1.60 – 1.48 (m, 2H), 1.37 – 1.26 (m, 3H), 0.84 (t, *J* = 7.4 Hz, 3H). ^{13}C NMR (101 MHz, $CDCl_3$) δ 178.86, 177.88, 158.59, 151.02, 150.89, 148.64, 145.55, 144.77, 144.54, 141.60, 139.64, 139.00, 134.18, 133.43, 132.08, 131.29, 130.23, 130.15, 126.44, 125.78, 123.01, 122.56, 122.43, 121.89, 118.19, 115.14, 113.10, 112.19, 110.67, 99.70, 98.02, 55.99, 54. 73, 41.24, 30.76, 20.16, 13.73. HMRS [ESI+] ion $[C_{40}H_{37}IrN_7O_4]^+$ m/z calculated: 872.2546 Found: 872.2546 [M+].



2.5

Iridium complex 2.5 – Iridium chloro-bridged dimer made from ligand **2.8** (250 mg, 0.14 mmol), ligand **2.6** (31 mg, 0.27 mmol) and 10 equivalents of potassium carbonate (187 mg, 1.35 mmol) was degassed and dissolved in dry toluene (15 mL). The mixture was refluxed for 16 hours at 110 °C, after this it was cooled, the solvent was removed under reduced pressure and the crude was redissolved in DCM before being extracted with water. The combined organic phases were then purified by column chromatography (DCM), the final product was an orange-yellow solid (50 %, 151 mg).

^{1}H NMR (400 MHz, $CDCl_3$, 298K) δ 7.70 (dd, *J* = 6.4, 4.5 Hz, 2H), 7.48 (dd, *J* = 9.3, 2.4 Hz, 2H), 7.20 (d, *J* = 7.6 Hz, 1H), 7.04 – 6.94 (m, 5H), 6.93 – 6.82 (m, 3H), 6.73 – 6.64 (m, 2H), 6.53 (d, *J* = 7.5 Hz, 1H), 6.21 (d, *J* = 8.3 Hz, 1H), 6.16 (s, 1H), 5.70 (s, 1H), 5.51 – 5.28 (m, 4H), 4.70 (s, 1H), 3.95 (dd, *J* = 36.6, 6.8 Hz, 2H), 3.10 – 2.90 (m, 2H), 2.57 – 2.46 (m, 2H), 1.98 (m, 7H), 1.32 (dd, *J* = 30.3, 21.4 Hz, 21H), 0.93 – 0.79 (m, 7H). ^{13}C NMR (101 MHz, $CDCl_3$) δ 178.80, 177.77, 158.07, 144.66, 144.38, 141.99, 139.70, 139.05, 134.28, 133.45, 131.89, 130.29, 126.35, 125.63, 124.78, 122.23, 122.09, 121.68, 119.74, 117.92, 115.38, 113.47, 112.00, 110.42, 105.88, 100.37, 98.62, 91.62, 68.76, 67.51, 62.02, 52.93, 48.93, 41.26, 34.85, 32.62, 31.91, 31.52, 30.92, 29.39, 29.13, 25.74, 22.88, 22.35, 20.22, 18.07, 14.11, 13.79. HMRS [ESI+] ion $[C_{58}H_{69}IrN_7O_4]^+$ m/z calculated: 1120.5036 Found: 1120.5036 [M+].

1-(1H-benzo[d]imidazole-2-yl)-3-butylguanidine (Ligand 6)– From a modified procedure, 1-(1H-benzo[d]imidazole-2-yl)-3-butylthiourea (270 mg, 1.08 mmol) was suspended in 15 mL of $CHCl_3$ and to this were added HgO (320 mg, 1.51 mmol) and 2 M methanolic NH_3 (6 mL). The reaction mixture was stirred at room temperature for 3 h and a colour change from wine red to brown was observed. The reaction was then filtered through celite and concentrated under reduced pressure. The resulting solid was dissolved in 2 M acetic acid (~ 8 mL) and stirred for 1 h, then filtered through celite. The pH was adjusted to 8 by addition of a 10 M solution of NaOH. The formed precipitate was filtered, washed with water and dried. The product was dissolved in chloroform and extracted 3 times with saturated solution of $NaHCO_3$. The organic phase was separated and dried over $MgSO_4$ and the solvent removed under reduced pressure. The final product was dried overnight in a vacuum oven at 40 °C. Compound **7** was obtained as white powder in (31 mg, 50%) yield.

^{1}H NMR (400 MHz, 298 K, DMSO-*d*$_6$): δ 11.00 (s, 1H), 7.20 (d, 1H, *J* = 7.3 Hz), 7.07 (d, 1H, *J* = 7.1 Hz), 6.98 – 6.78 (m, 2H), 3.21 (dd, 2H, *J* = 12.7, 6.9 Hz), 1.48 (dd, 2H, *J* = 14.8, 7.3 Hz), 1.36 (dt, 2H, *J* = 14.7, 7.2 Hz), 0.92 (t, 3H, *J* = 7.3 Hz). ^{13}C NMR (100 MHz, 298K, DMSO-*d*$_6$): δ 159.05, 157.66, 142.59, 132.21, 119.65, 118.99, 114.94, 108.48, 40.07, 39.52, 31.49, 19.66, 13.80. M.p. 190-208°C. EI-MS m/z calculated: 231.15 found: 232.16 [M+]. Anal. calcd. for $C_{12}H_{17}N_5$: C, 62.31; H, 7.41; N, 30.28. Found: C, 62.12; H, 7.55; N, 30.06.

Ligand 2.7 – 2-Amino-4-methoxyphenol (5.00 g, 36 mmol) was dissolved in the minimum amount of degassed, dry NMP (40 mL) and cooled to 0 °C. The cooled mixture

then had dropwise addition of benzoyl chloride (4.17 mL, 36 mmol) over 30 minutes before being allowed to warm to room temperature over an hour. Next 12 mL of pyridine was added, and the mixture was heated to reflux at 202°C under nitrogen. After 5 hours, the mixture was cooled to room temperature and extracted between DCM (6x30mL) and water 50 mL. Combined organic phases were dried over $MgSO_4$, filtered then dry loaded onto silica for purification by column chromatography (gradient, Hexanes:EtOAc, 95:5 → 80:20). The column yielded two products ligand **2.7** 35%, 2.83 g (crystalline white solid) and compound **2.12** 37 %, 2.81 g (an off-white powder).

^{1}H NMR (400 MHz, $CDCl_3$, 298 K) δ 8.22 (dd, J = 6.9, 2.9 Hz, 2H), 7.51 (dd, J = 5.2, 1.8 Hz, 3H), 7.45 (d, J = 8.9 Hz, 1H), 7.25 (s, 1H), 6.95 (s, 1H), 3.86 (s, 3H). ^{13}C NMR (101 MHz, $CDCl_3$) δ 163.84, 157.43, 145.44, 142.92, 133.68, 131.44, 130.20, 128.92, 127.52, 127.27, 113.76, 110.74, 102.91, 55.97. HMRS [ESI+] ion $[C_{14}H_{11}NO_2Na]^+$ m/z calculated: 248.0688 Found: 248.0682 [M+].

Ligand 2.8 – 647 mg, 3.06 mmol of compound **2.12** [2-Phenyl-5-benzoxazolol] was added to a 50 mL Schlenk flask with 1 eq. of 10-bromodecene (0.63 mL, 3.06 mmol) and 5 eq. potassium carbonate (2.00 g, 6.12 mmol). The flask was degassed, then 15 mL of dry acetonitrile was added, and the mixture was refluxed at 90°C under nitrogen. After 12 hours the solvent was removed under reduced pressure, the mixture was redissolved in DCM (20 mL), extracted with water and dried over $MgSO_4$. The product was then purified by column chromatography, (EtOAc:Hexanes, 5:95). The final pure product was a very pale-yellow oil and was acquired in a 75 % yield (800 mg).

^{1}H NMR (400 MHz, $CDCl_3$, 298 K) δ 8.23 (dd, *J* = 6.8, 3.0 Hz, 2H), 7.54 – 7.49 (m, 3H), 7.45 (d, *J* = 8.8 Hz, 1H), 7.25 (d, *J* = 2.4 Hz, 1H), 6.95 (dd, *J* = 8.9, 2.5 Hz, 1H), 5.82 (ddt, *J* = 16.9, 10.2, 6.7 Hz, 1H), 5.05 – 4.89 (m, 2H), 4.01 (t, *J* = 6.6 Hz, 2H), 2.05 (qt, *J* = 6.7, 1.5 Hz, 2H), 1.82 (dq, *J* = 8.0, 6.6 Hz, 2H), 1.55 – 1.25 (m, 11H). ^{13}C NMR (101 MHz, $CDCl_3$) δ 163.73, 156.91, 145.35, 142.93, 139.21, 131.37, 128.90, 127.49, 127.35, 114.32, 114.17, 110.66, 103.69, 68.87, 33.81, 29.43, 29.38, 29.28, 29.08, 28.93, 26.08. HMRS [ESI+] ion $[C_{23}H_{28}NO_2]^+$ m/z calculated: 350.2115 Found: 350.2115 [M+].

A2.2: ^{1}H and ^{13}C NMR Spectra and Mass spectra

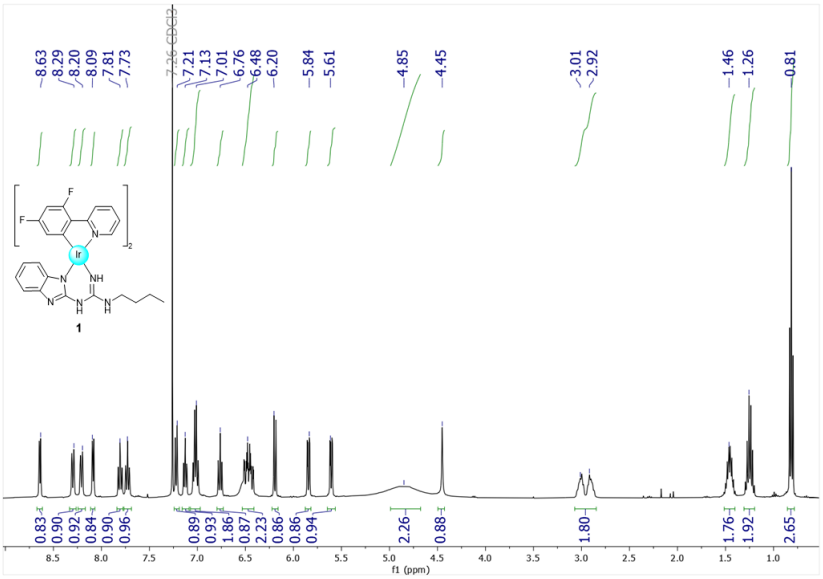


Figure A.2.1 ^{1}H NMR spectrum of iridium complex **2.1**, $CDCl_3$, 400 MHz, 298 K.

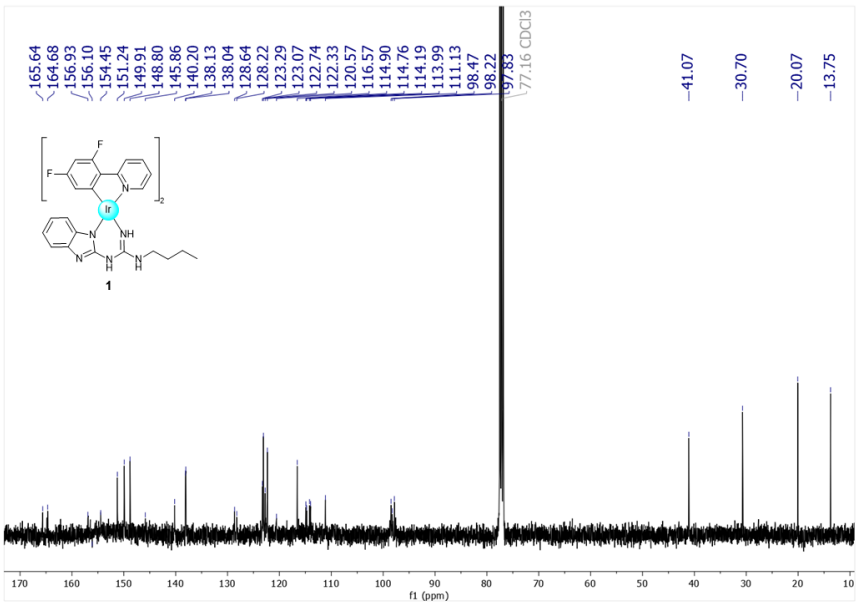


Figure A.2.2 ^{13}C NMR spectrum of iridium complex **2.1**, $CDCl_3$, 101 MHz, 298 K.

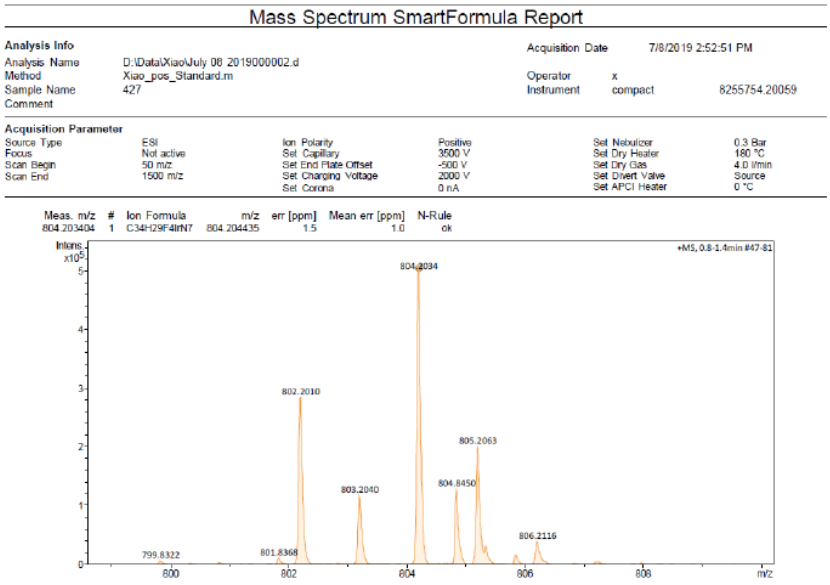


Figure A.2.3 Mass spectrum of iridium complex **2.1**. HMRS [ESI+] ion $[C_{34}H_{29}F_4IrN_7]^+$ m/z calculated: 804.2044 Found: 804.2034 [M+].

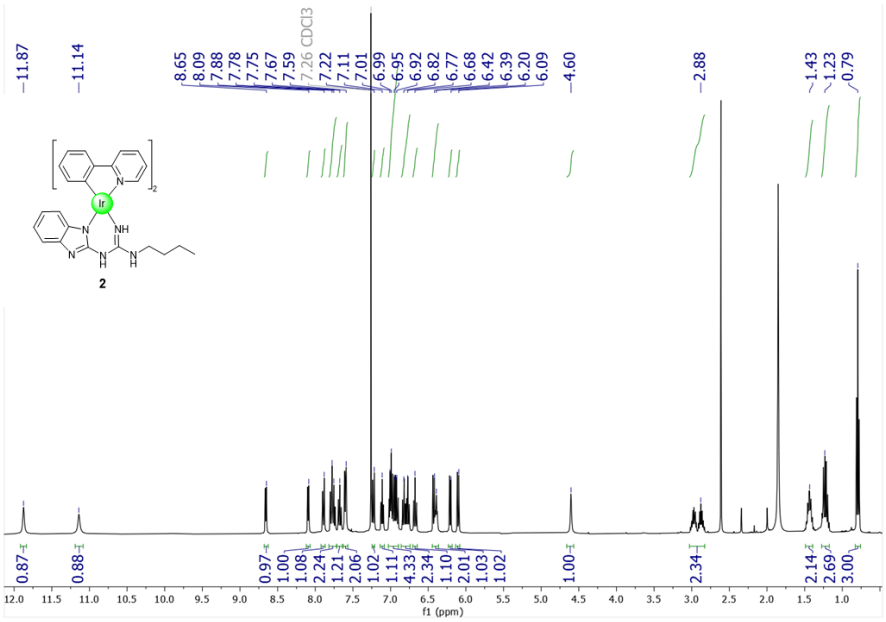


Figure A.2.4 ^{1}H NMR spectrum of iridium complex **2.2**, $CDCl_3$, 400 MHz, 298 K.

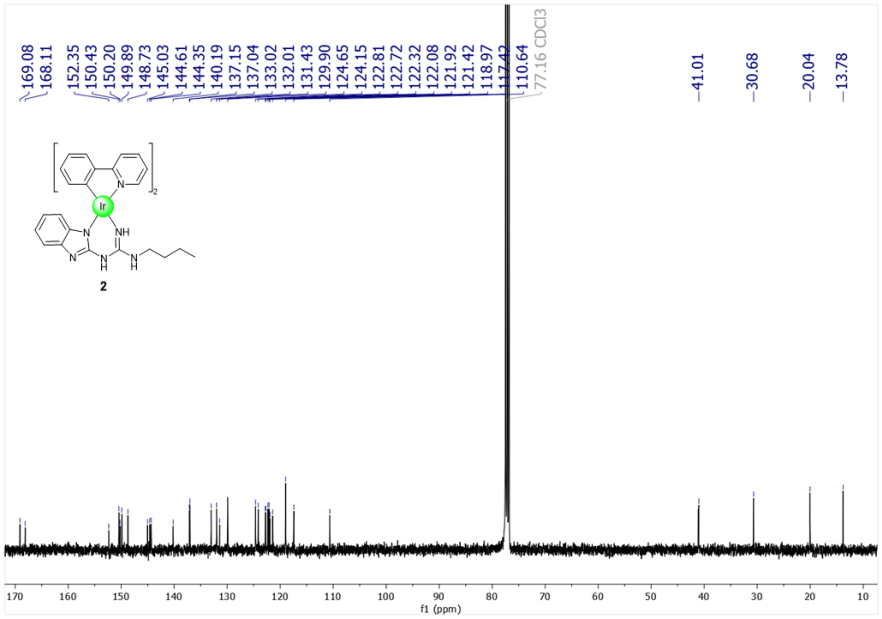


Figure A.2.5 ^{13}C NMR spectrum of iridium complex **2.2,** $CDCl_3$, 101 MHz, 298 K.

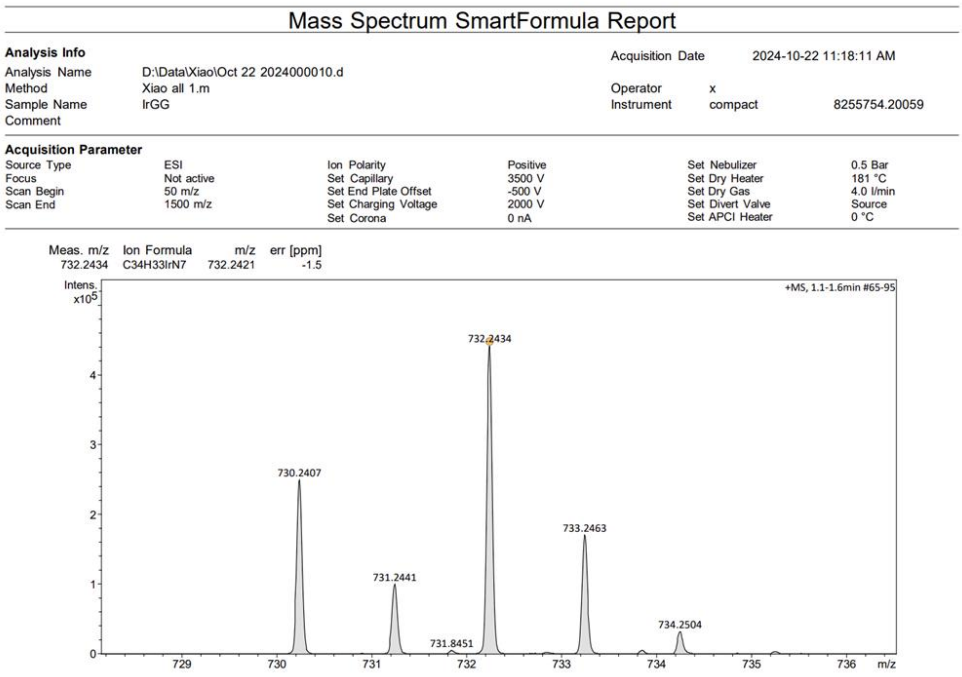


Figure A.2.6 Mass spectrum of complex **2.2**. HMRS [ESI+] ion $[C_{34}H_{33}IrN_7]^+$ m/z calculated: 732.2421 Found: 732.2434 [M+].

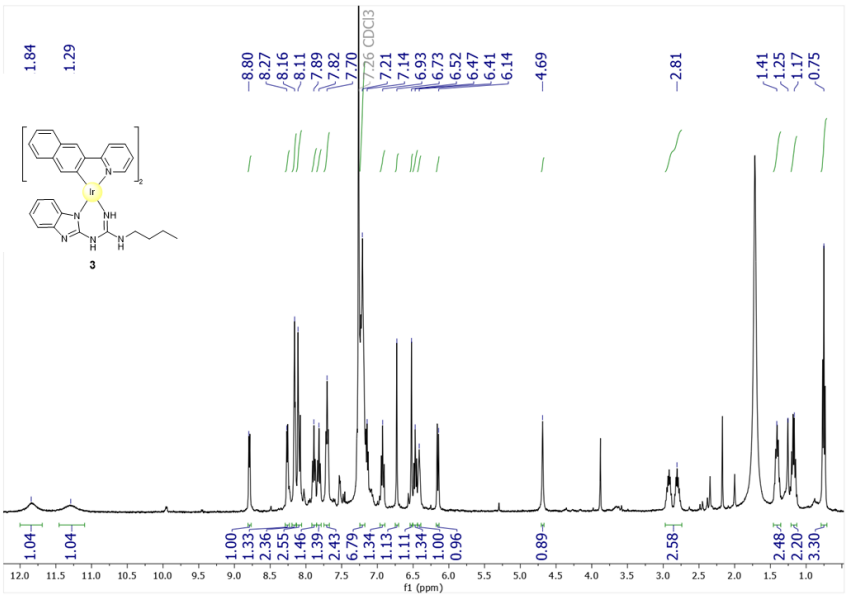


Figure A.2.7 ^{1}H NMR spectrum of iridium complex **2.3**, $CDCl_3$, 400 MHz, 298 K.

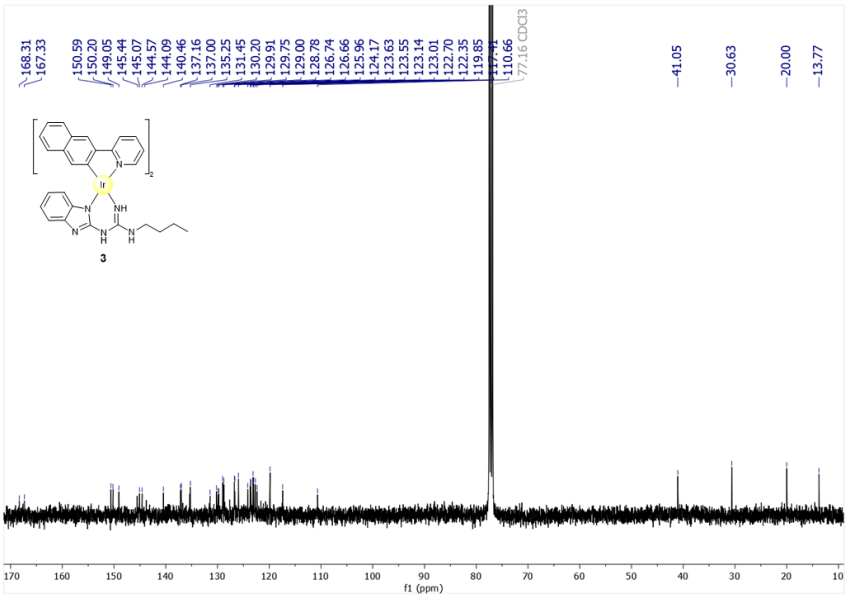


Figure A.2.8 ^{13}C NMR spectrum of iridium complex **2.3,** $CDCl_3$, 101 MHz, 298 K.

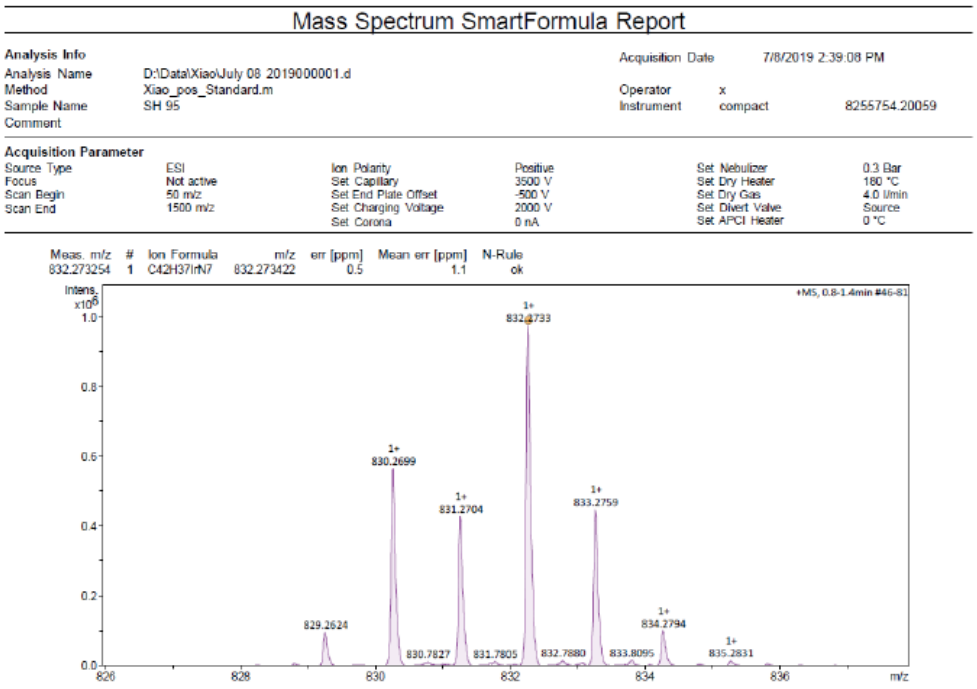


Figure A.2.9 Mass spectrum of iridium complex **2.3**. HMRS [ESI+] ion $[C_{42}H_{37}IrN_7]^+$ m/z calculated: 832.2732. Found: 832.2734 [M+].

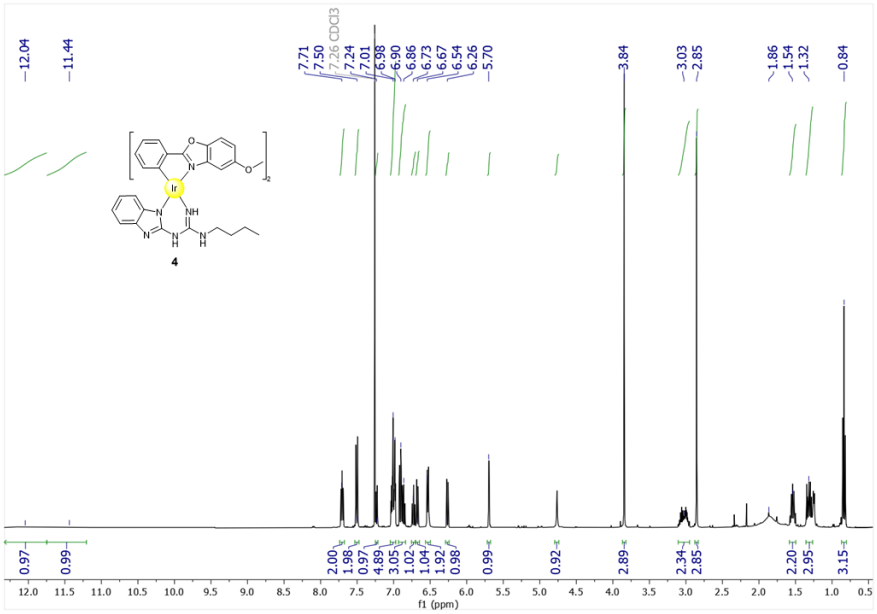


Figure A.2.10 ^{1}H NMR spectrum of iridium complex **2.4**, $CDCl_3$, 400 MHz, 298 K.

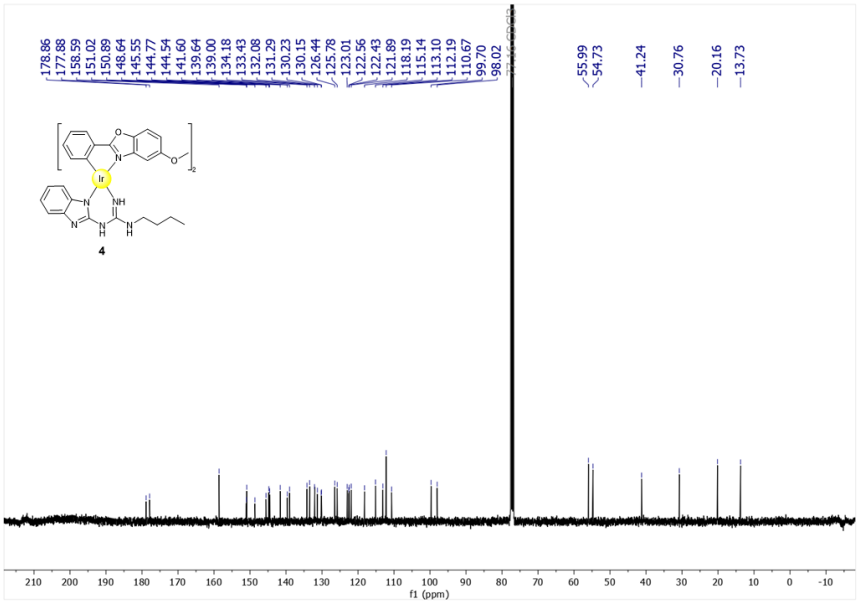


Figure A.2.11 ^{13}C NMR spectrum of iridium complex **2.4,** $CDCl_3$, 101 MHz, 298 K.

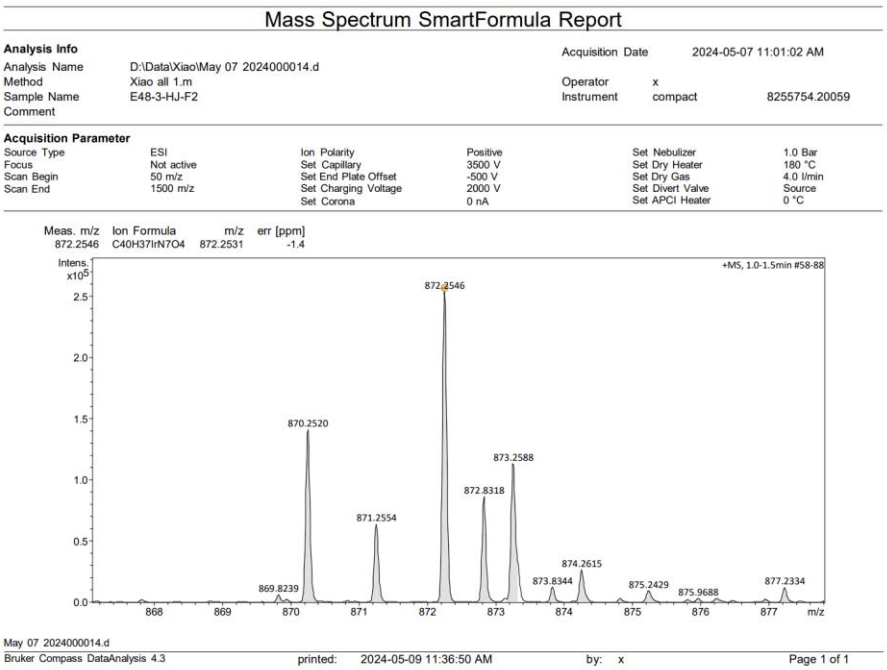


Figure A.2.12 Mass spectrum of iridium complex **2.4**. HMRS [ESI+] ion $[C_{40}H_{37}IrN_7O_4]^+$ m/z calculated: 872.2546 Found: 872.2546 [M+].

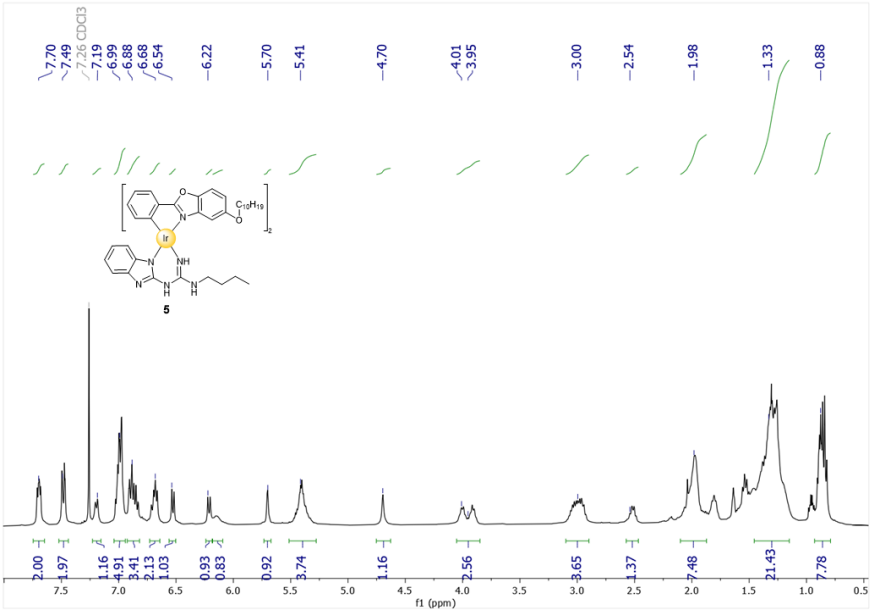


Figure A.2.13 ^{1}H NMR spectrum of iridium complex **2.5**, $CDCl_3$, 400 MHz, 298 K.

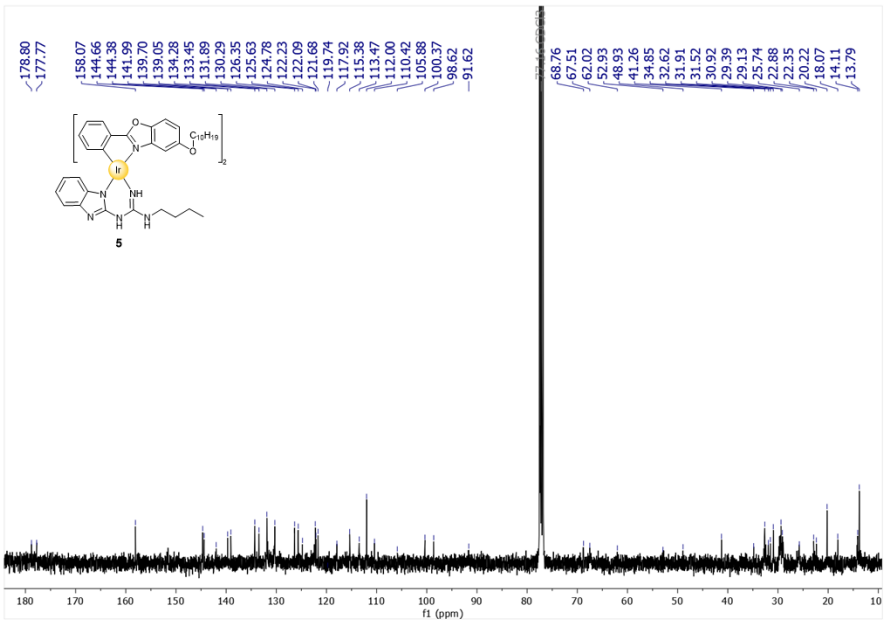


Figure A.2.14 ^{13}C NMR spectrum of iridium complex **2.5,** $CDCl_3$, 101 MHz, 298 K.

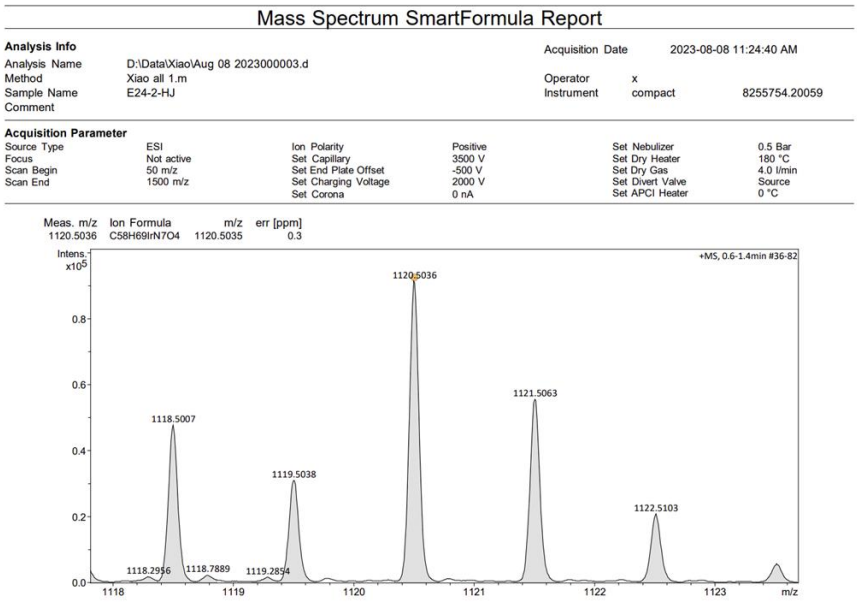


Figure A.2.15 Mass spectrum of iridium complex **2.5**. HMRS [ESI+] ion $[C_{58}H_{69}IrN_7O_4]^+$ m/z calculated: 1120.5036 Found: 1120.5036 [M+].

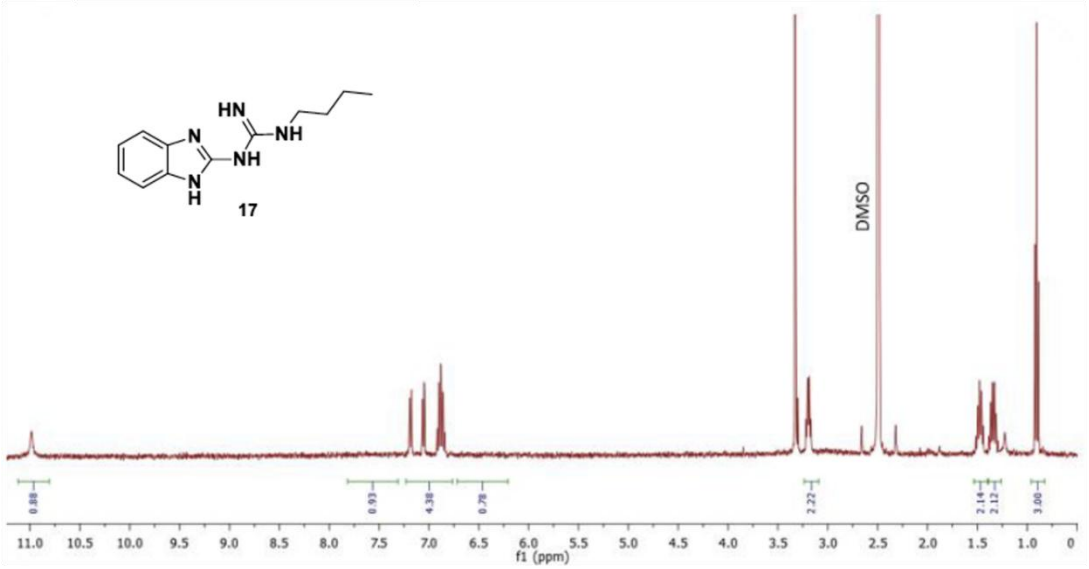


Figure A.2.16 ^{1}H NMR spectrum of ligand **2.6** DMSO-d_6, 400 MHz, 298 K**.**

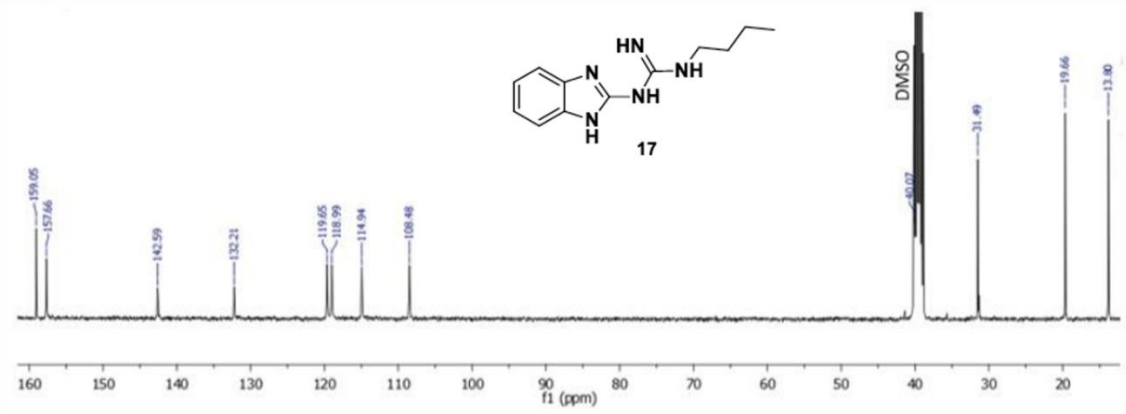


Figure A.2.17 ^{13}C NMR spectrum of ligand **2.6** DMSO-d_6, 101 MHz, 298 K**.**

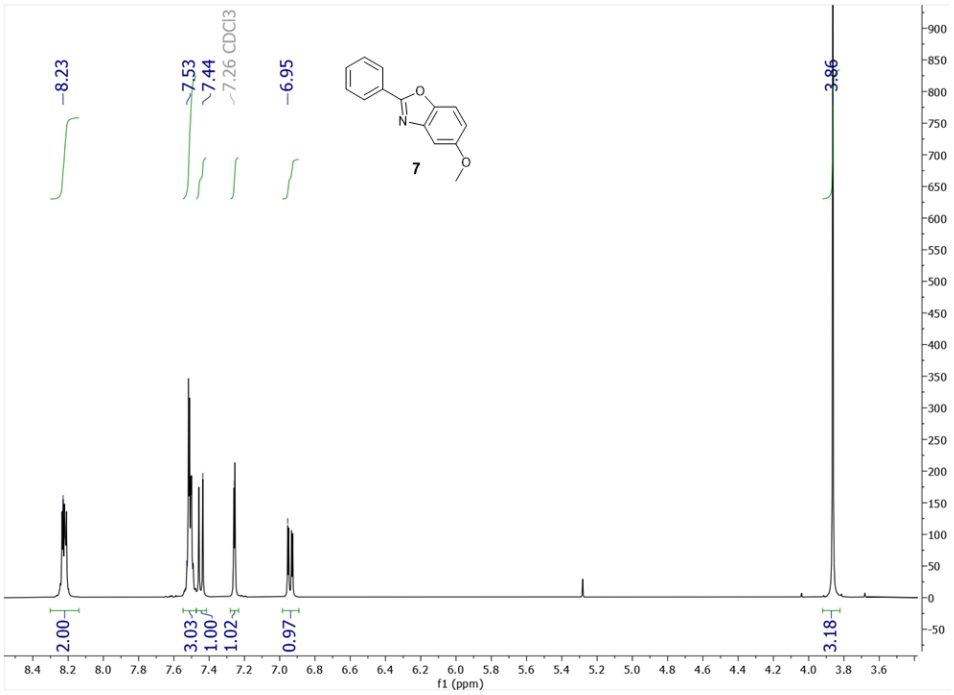


Figure A.2.18 ^{1}H NMR spectrum of ligand **2.7**, $CDCl_3$, 400 MHz, 298 K.

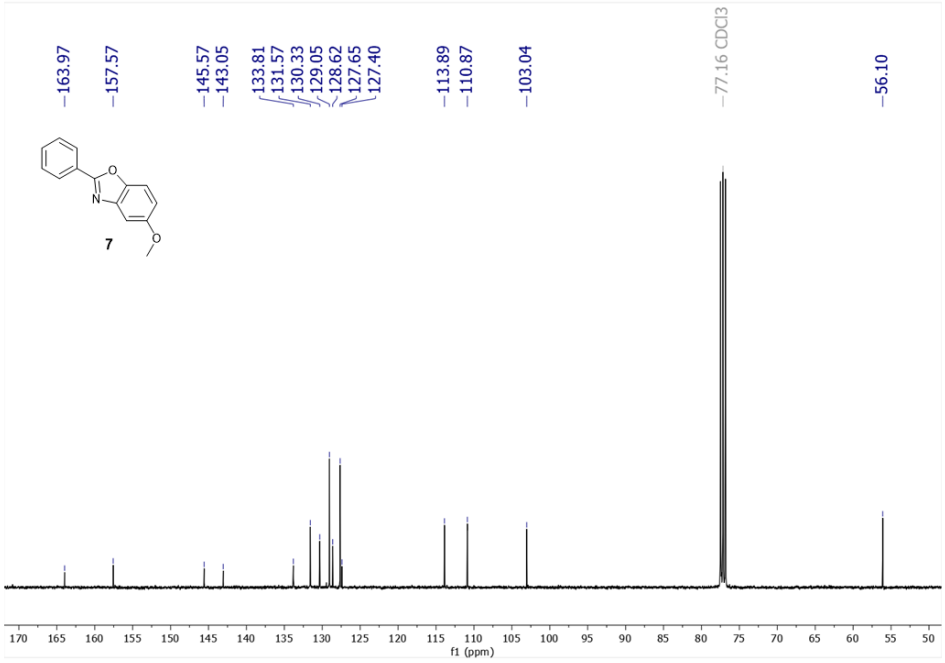


Figure A.2.19 ^{13}C NMR spectrum of ligand **2.7,** $CDCl_3$, 101 MHz, 298 K.

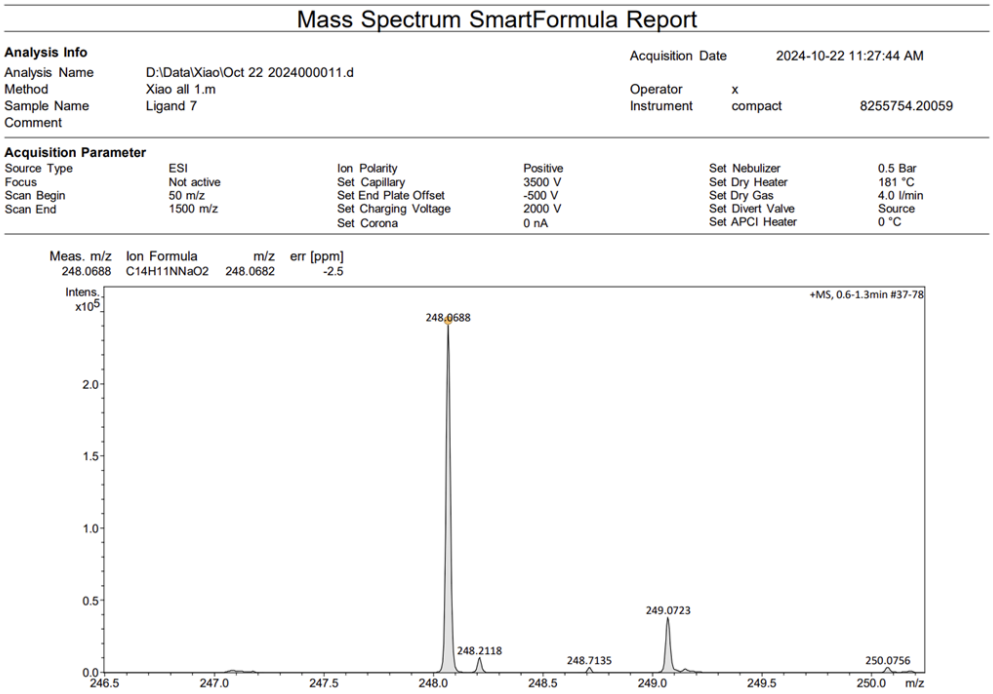


Figure A.2.20 Mass spectrum of ligand **2.7**. HMRS [ESI+] ion $[C_{14}H_{11}NO_2Na]^+$ m/z calculated: 248.0688 Found: 248.0682 [M+].

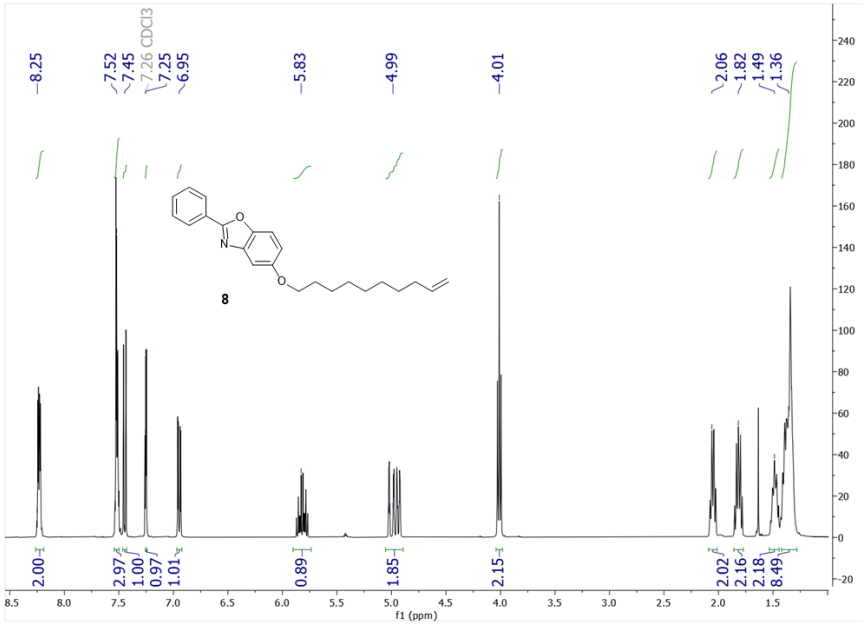


Figure A.2.21 ^{1}H NMR spectrum of ligand **2.8**, $CDCl_3$, 400 MHz, 298 K.

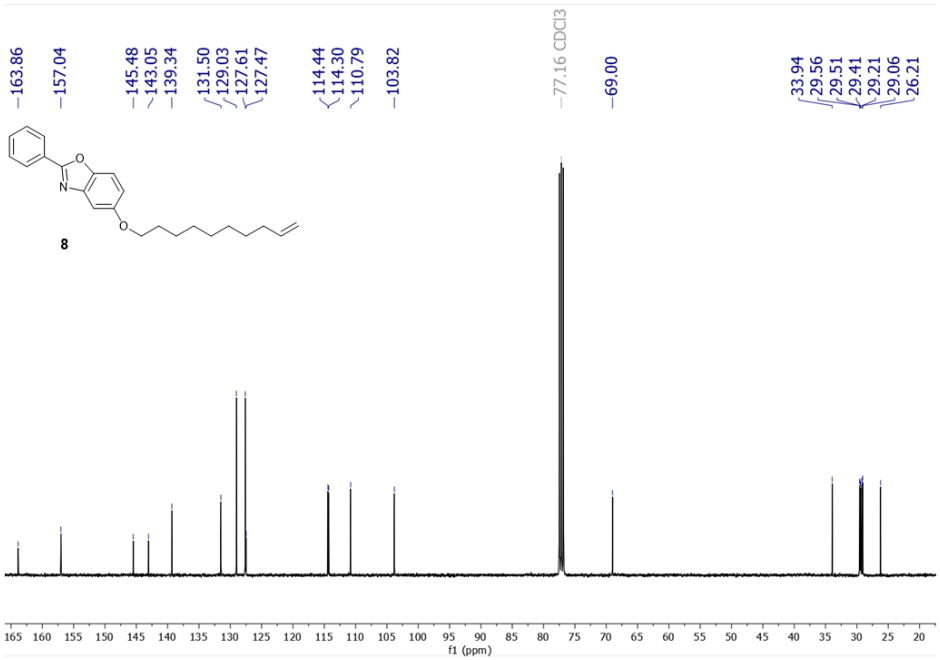


Figure A.2.22 ^{13}C NMR spectrum of ligand **2.8,** $CDCl_3$, 101 MHz, 298 K.

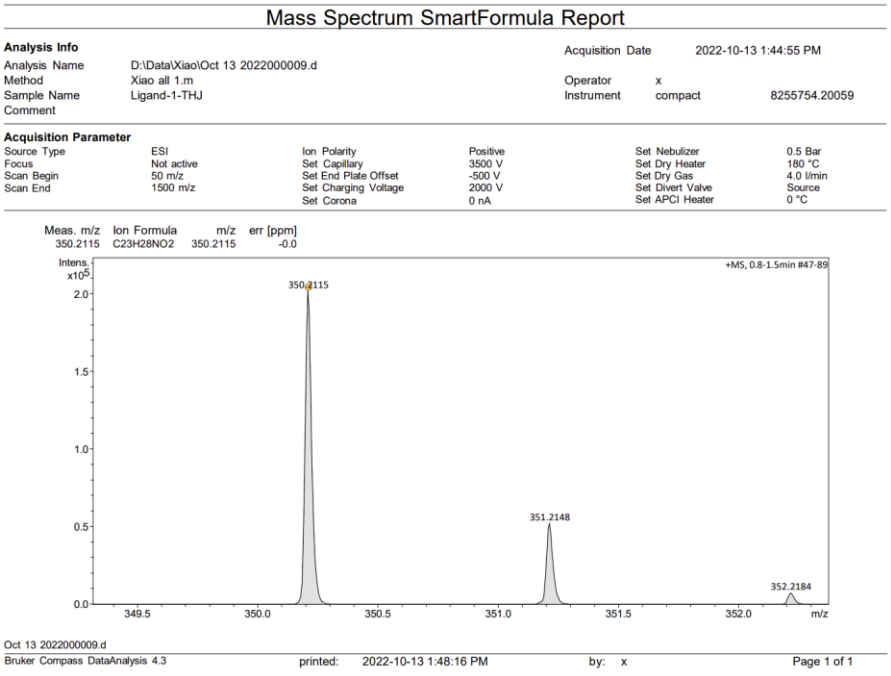


Figure A.2.23 Mass spectrum of ligand **2.8**. HMRS [ESI+] ion $[C_{23}H_{28}NO_2]^+$ m/z calculated: 350.2115 Found: 350.2115 [M+].

A2.3: Cyclic Voltammetry

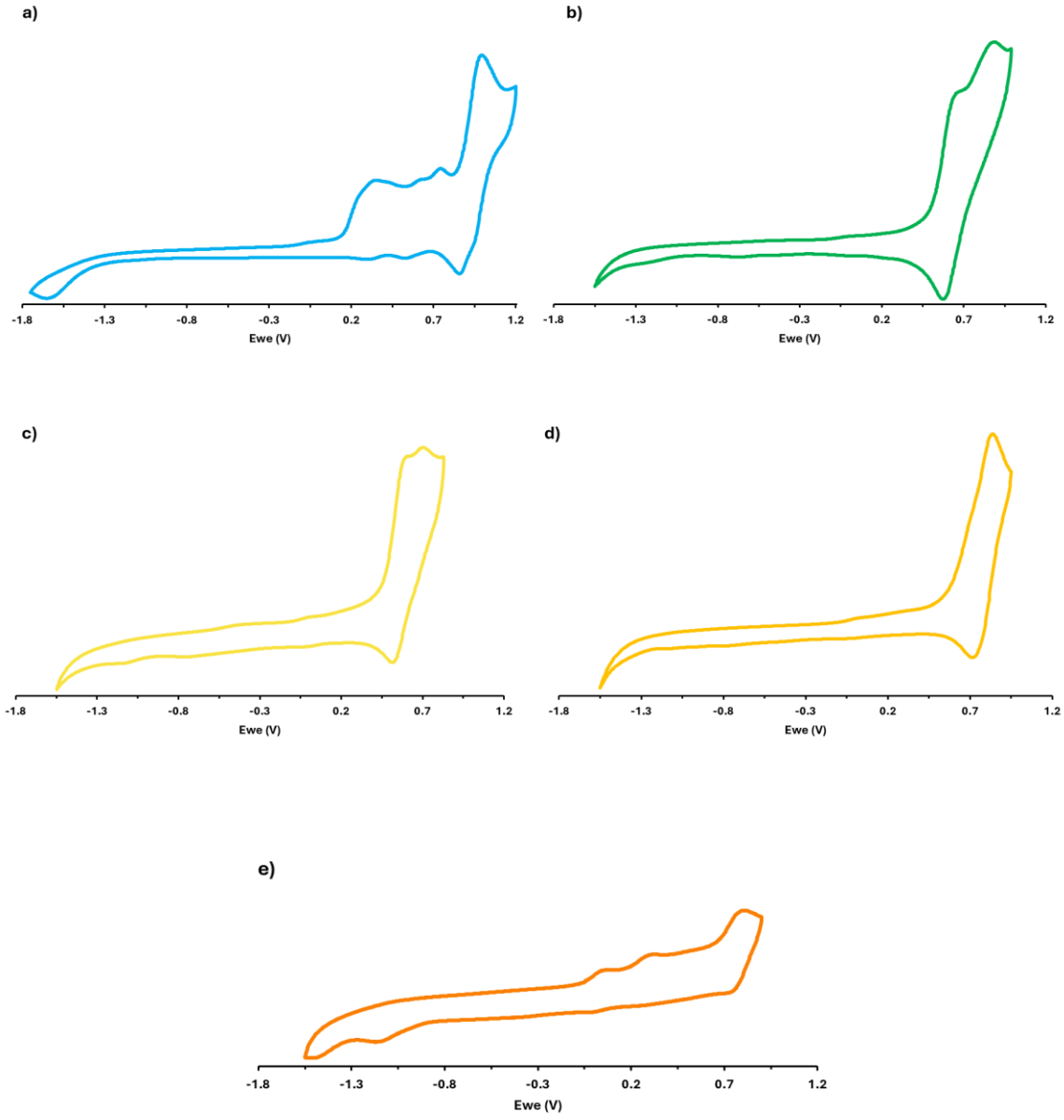


Figure A.2.24 Cyclic voltammetry of complexes **2.1-2.5**, the samples were 5 mM in dry degassed CH_3CN and normalised to a ferrocene standard under inert argon conditions. **a)** Complex **2.1**, **b)** complex **2.2**, c) complex **2.3**, **d)** complex **2.4**, **e)** complex **2.5**.

A2.4: Excitation and Emission Data

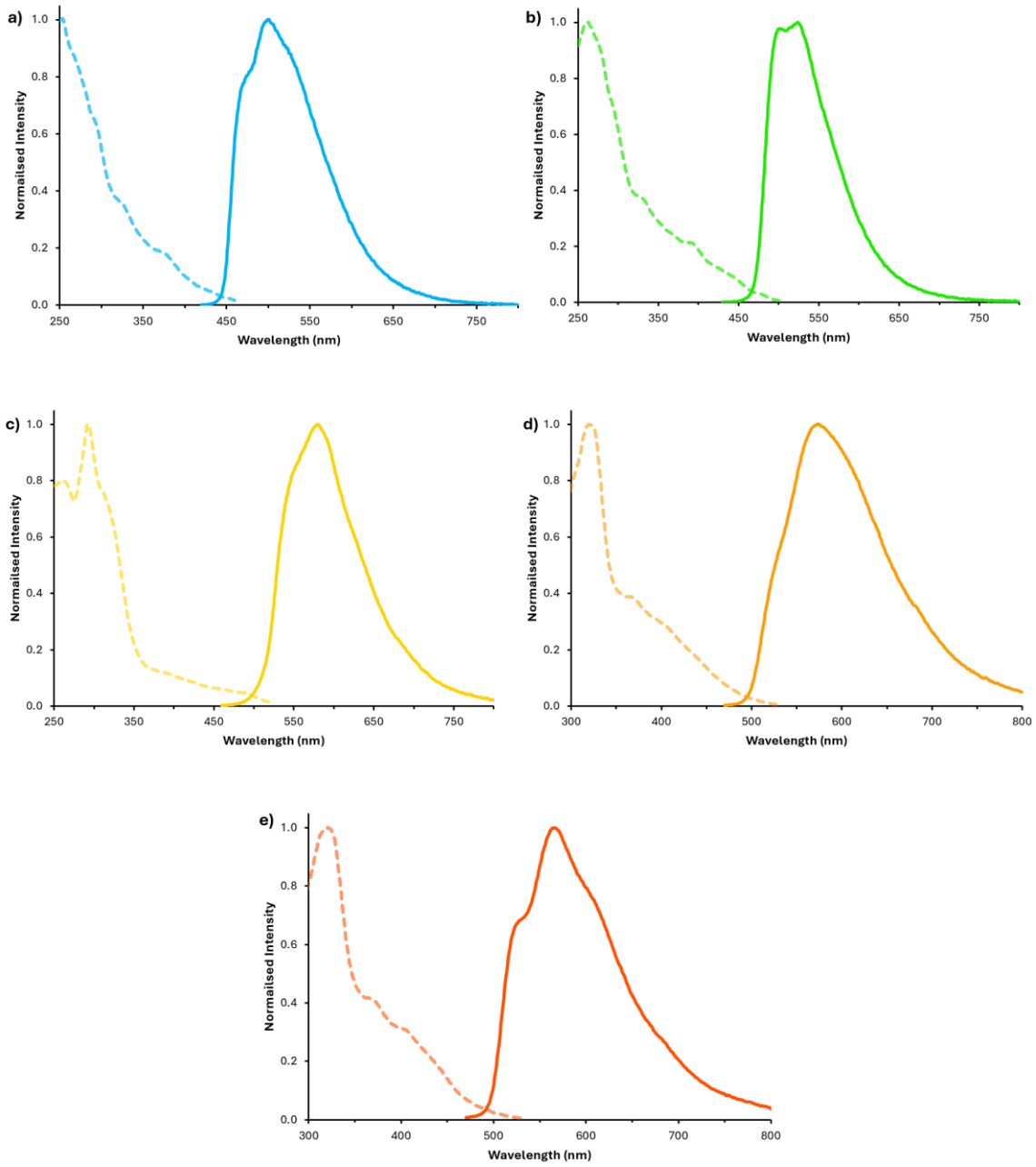


Figure A.2.25 Normalized absorption-emission spectra of iridium complexes **2.1-2.5** ($1x10^{-5}$ M) measured in CH_3CN solution, excited at 300 nm. The dashed lines are the normalised absorption spectra; solid lines are the emission spectra. **a)** Complex **2.1**, **b)** complex **2.2**, c) complex **2.3**, **d)** complex **2.4**, **e)** complex **2.5**.

A2.5: Stern-Volmer and Photo-Stability

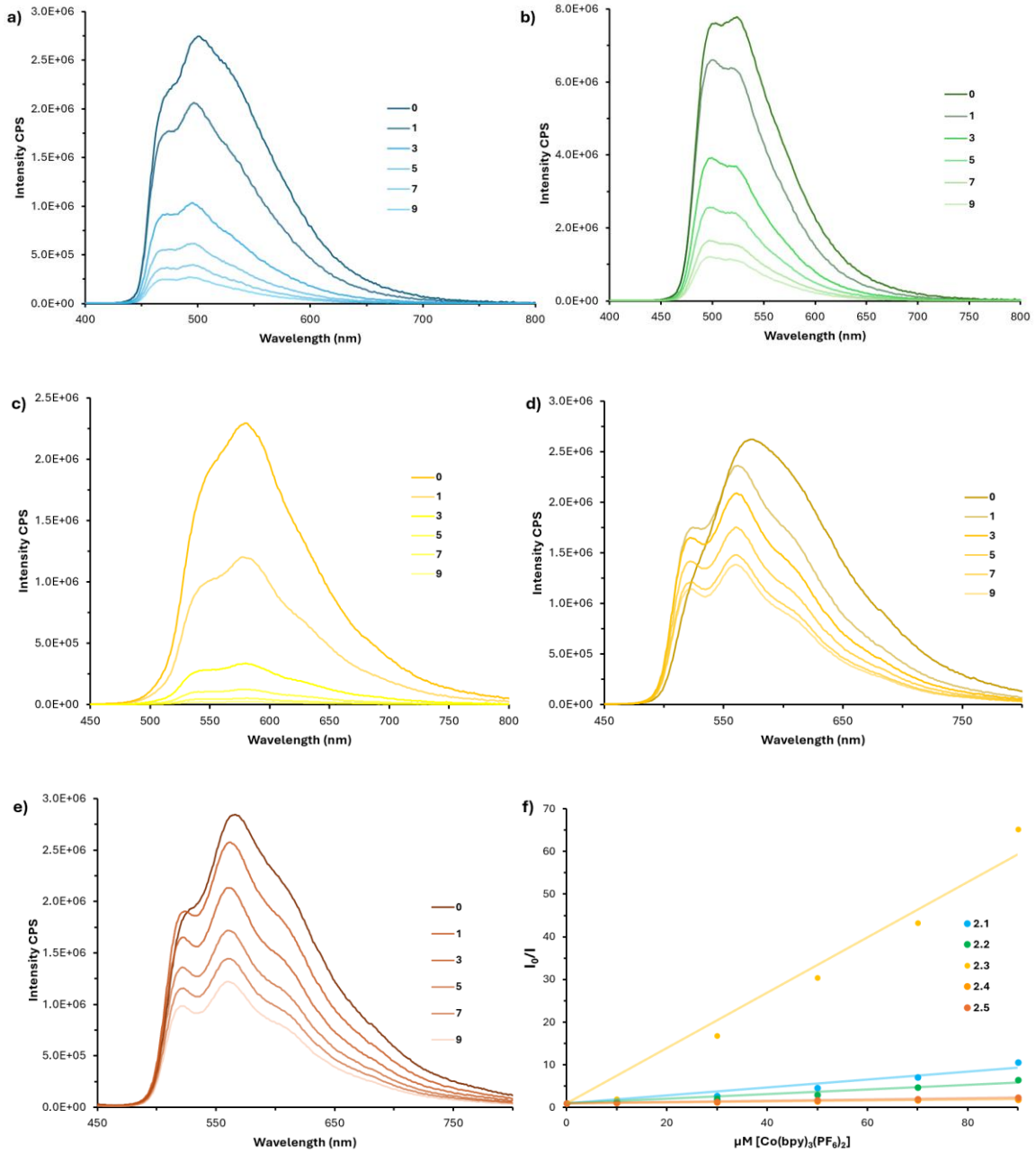


Figure A.2.26 a-e) Emission titration of iridium complexes **2.1-2.5** ($1x10^{-5}$ M) with $[Co(bpy)_3]^{2+}$ measured in argon degassed CH_3CN solution, excited at 300 nm Number of molar equivalents added indicated in graph legends. **a)** Complex **2.1**, **b)** complex **2.2**, c) complex **2.3**, **d)** complex **2.4**, **e)** complex **2.5**. **f)** Stern-Volmer plot for emission quenching of complexes **2.1-2.5** with $[Co(bpy)_3]^{2+}$.

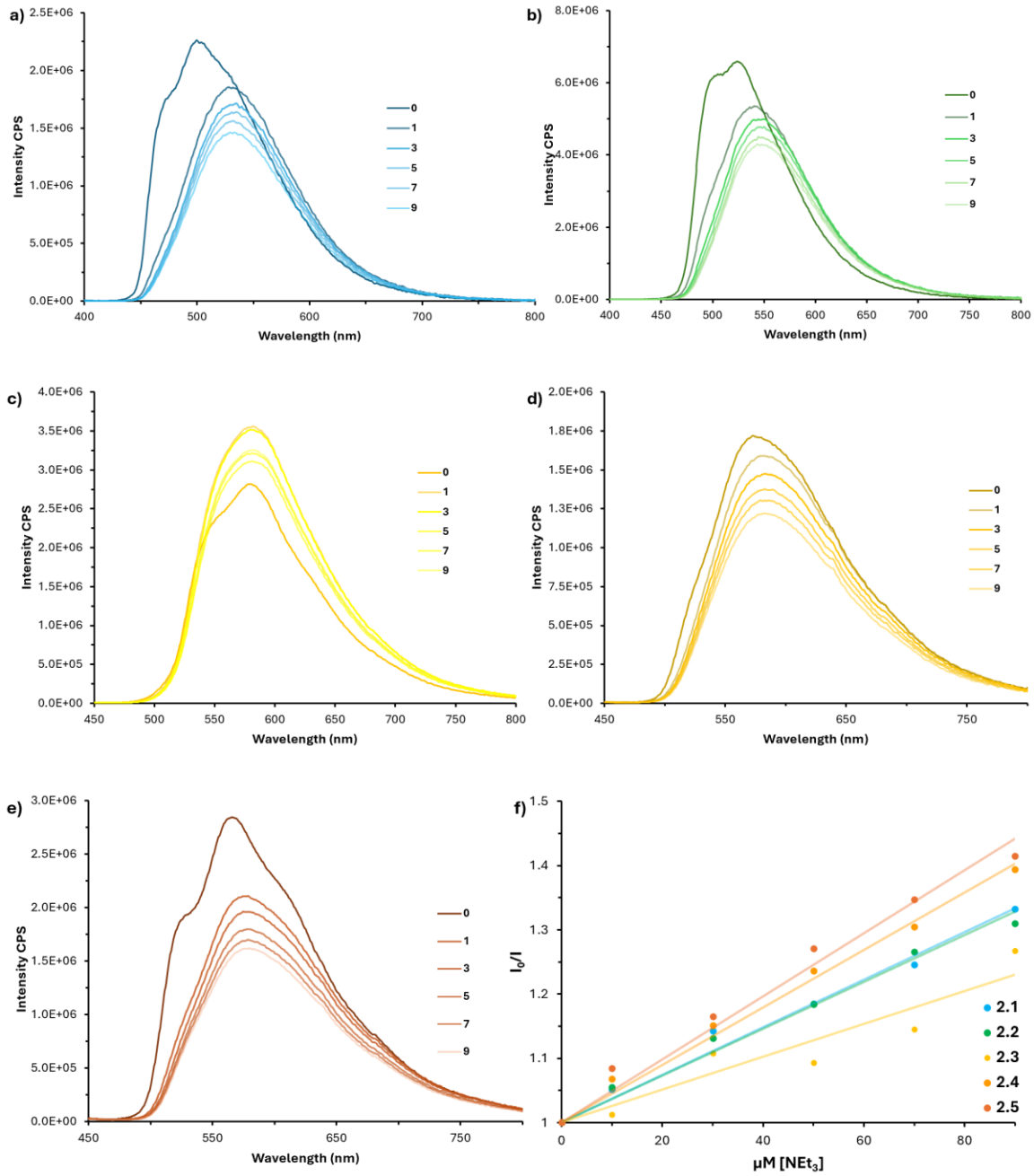


Figure A.2.27 a-e) Emission titration of iridium complexes **2.1-2.5** ($1x10^{-5}$ M) with NEt_3 measured in argon degassed CH_3CN solution, excited at 300 nm Number of molar equivalents added indicated in graph legends. **A)** Complex **2.1**, **b)** complex **2.2**, c) complex **2.3**, **d)** complex **2.4**, **e)** complex **2.5**. **f)** Stern-Volmer plot for emission quenching of complexes **2.1-2.5** with NEt_3.

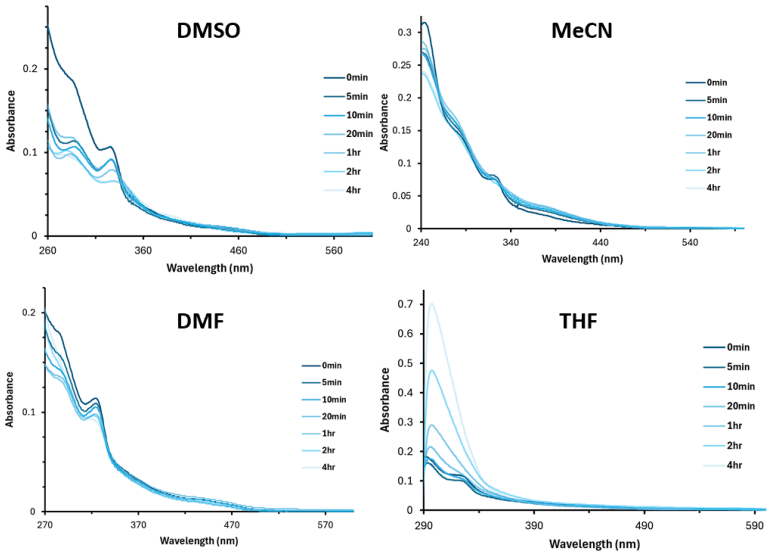


Figure A.2.28 UV-vis spectra of complex **2.1** in a series of degassed solvents, the mixtures were excited by an array of UV LEDs (365 nm) for 4 hours, UV-vis profile was remeasured at specified time intervals to measure stability to UV light.

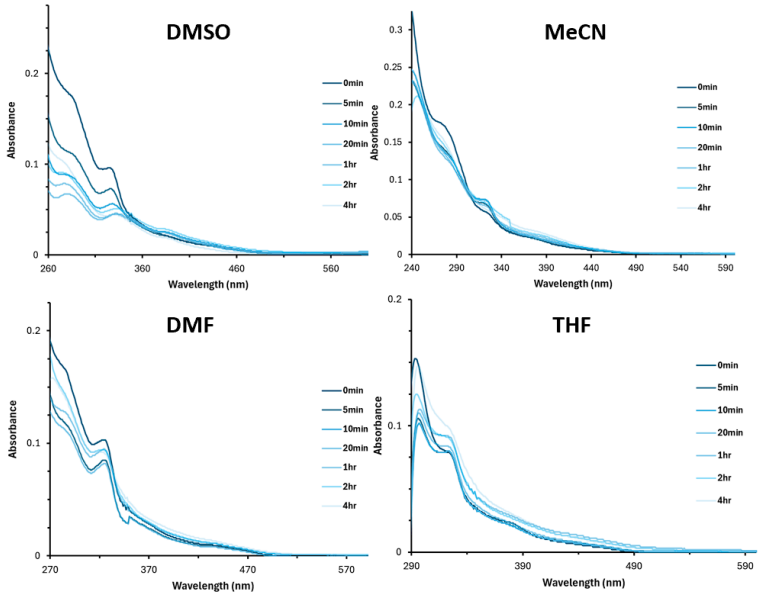


Figure A.2.29 UV-vis spectra of complex **2.1** in a series of degassed solvents, the mixtures were excited by an array of Blue light LEDs (465 nm) for 4 hours, UV-vis profile was remeasured at specified time intervals to measure stability to intense blue light.

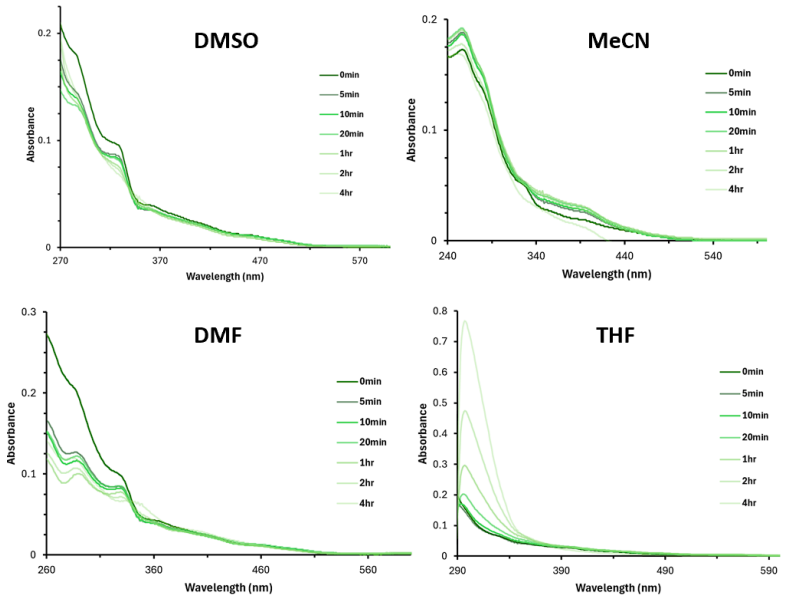


Figure A.2.30 UV-vis spectra of complex **2.2** in a series of degassed solvents, the mixtures were excited by an array of UV LEDs (365 nm) for 4 hours, UV-vis profile was remeasured at specified time intervals to measure stability to UV light.

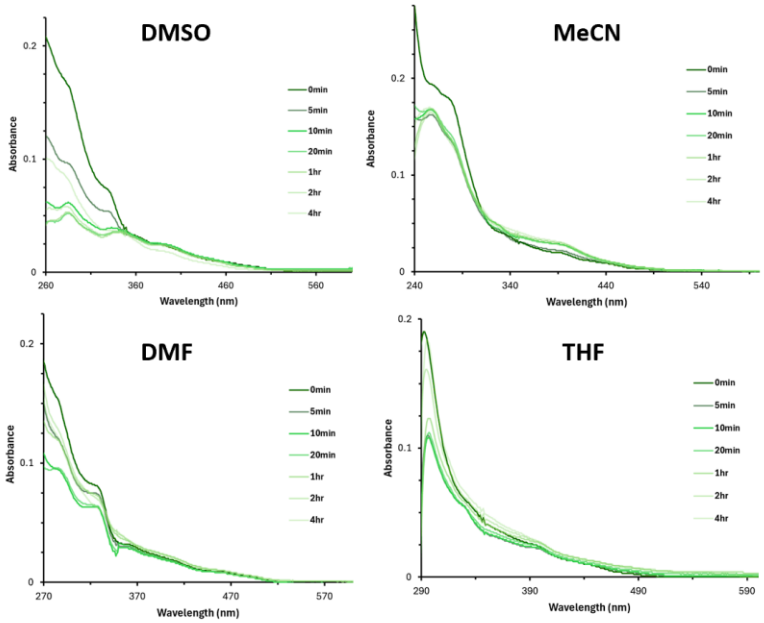


Figure A.2.31 UV-vis spectra of complex **2.2** in a series of degassed solvents, the mixtures were excited by an array of Blue light LEDs (465 nm) for 4 hours, UV-vis profile was remeasured at specified time intervals to measure stability to intense blue light.

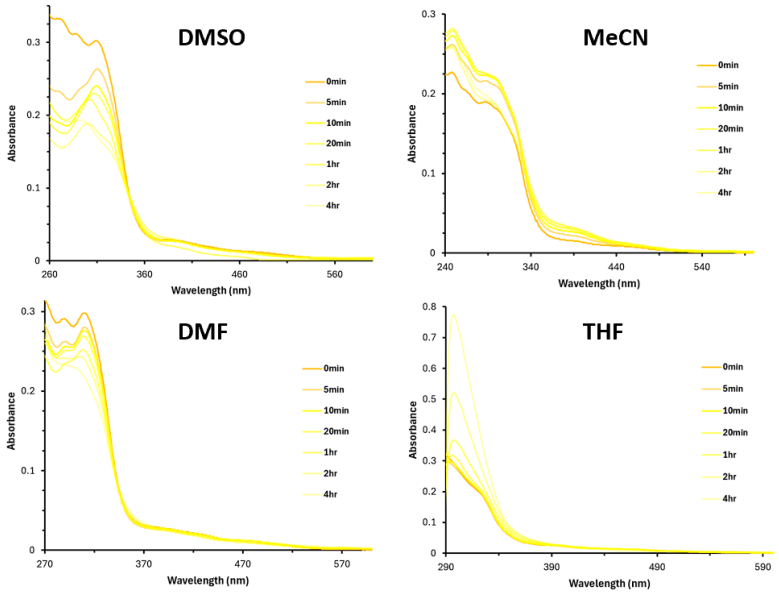


Figure A.2.32 UV-vis spectra of complex **2.3** in a series of degassed solvents, the mixtures were excited by an array of UV LEDs (365 nm) for 4 hours, UV-vis profile was remeasured at specified time intervals to measure stability to UV light.

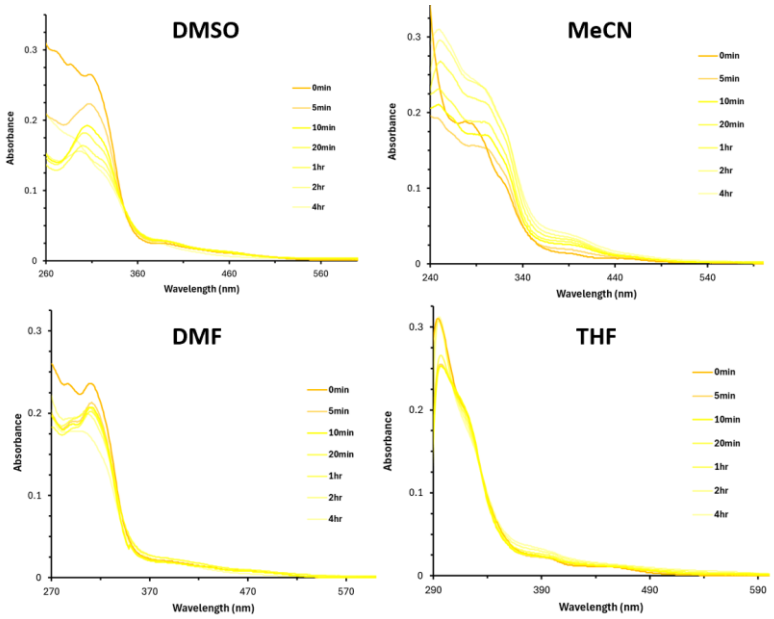


Figure A.2.33 UV-vis spectra of complex **2.3** in a series of degassed solvents, the mixtures were excited by an array of Blue light LEDs (465 nm) for 4 hours, UV-vis profile was remeasured at specified time intervals to measure stability to intense blue light.

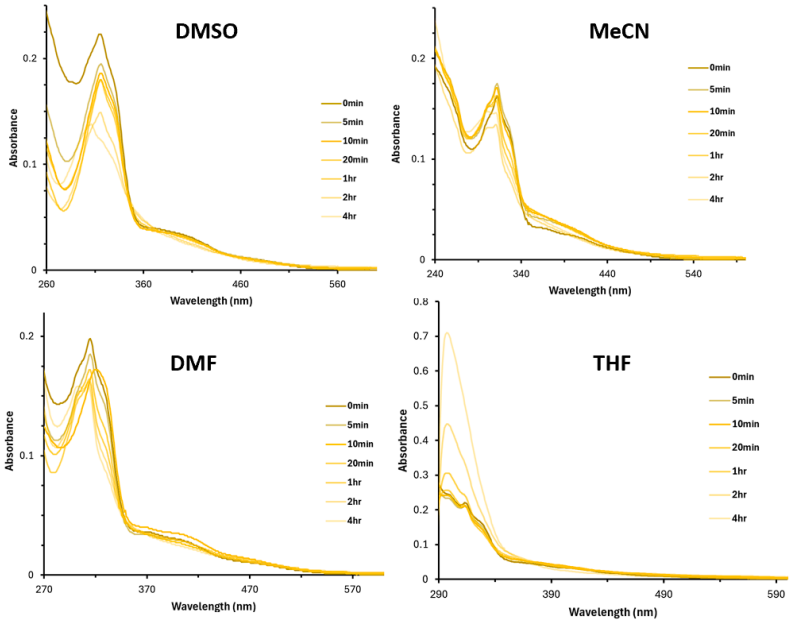


Figure A.2.34 UV-vis spectra of complex **2.4** in a series of degassed solvents, the mixtures were excited by an array of UV LEDs (365 nm) for 4 hours, UV-vis profile was remeasured at specified time intervals to measure stability to intense blue light.

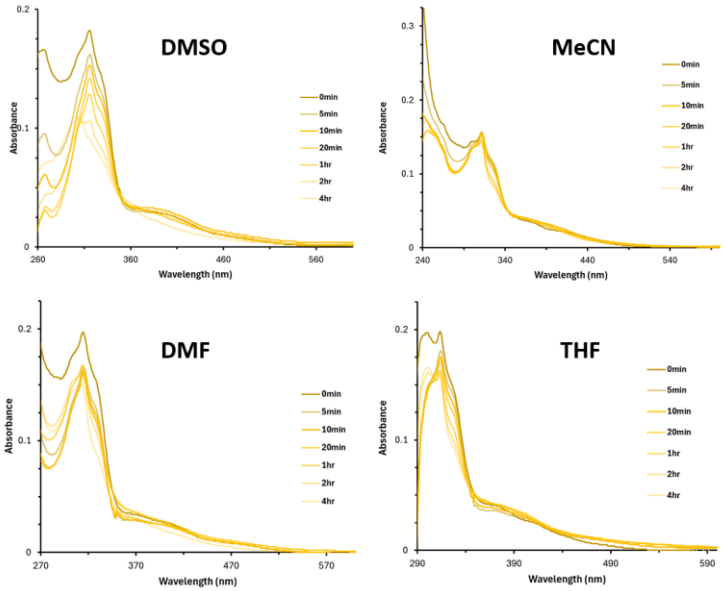


Figure A.2.35 UV-vis spectra of complex **2.4** in a series of degassed solvents, the mixtures were excited by an array of Blue light LEDs (465 nm) for 4 hours, UV-vis profile was remeasured at specified time intervals to measure stability to intense blue light.

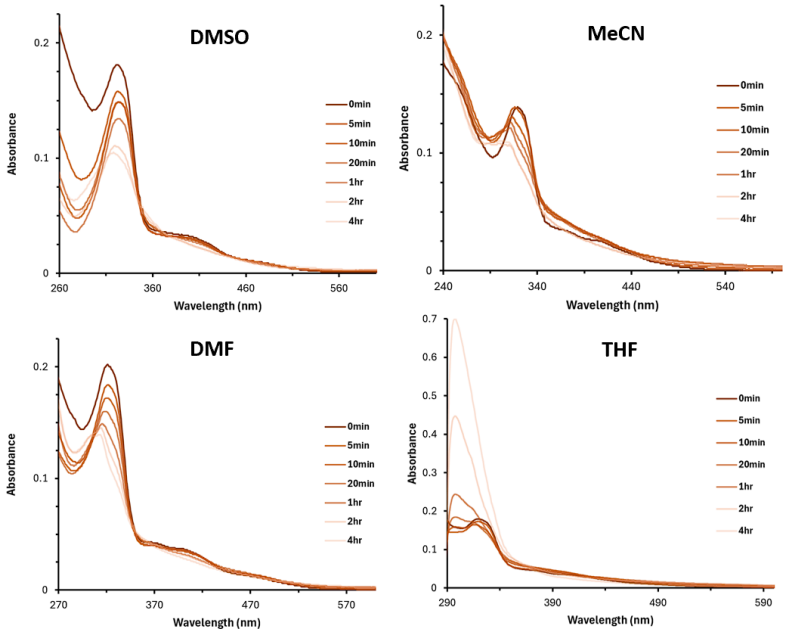


Figure A.2.36 UV-vis spectra of complex **2.5** in a series of degassed solvents, the mixtures were excited by an array of UV LEDs (365 nm) for 4 hours, UV-vis profile was remeasured at specified time intervals to measure stability to UV light.

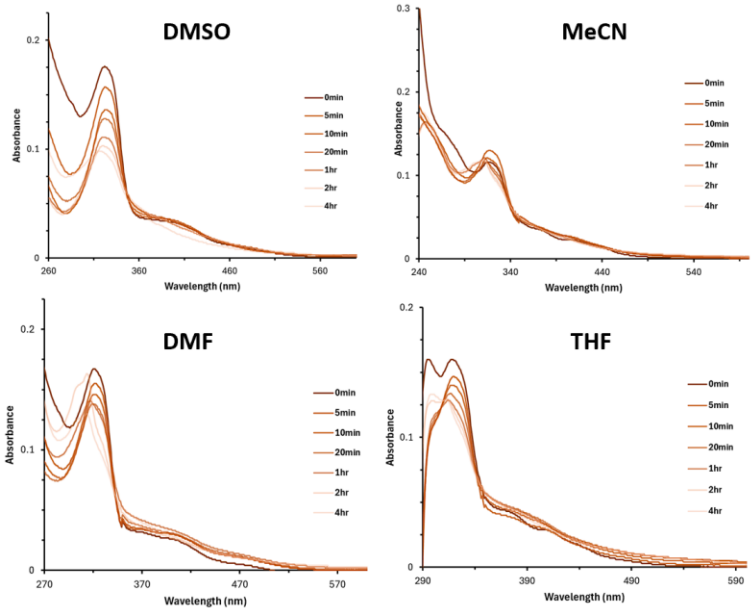


Figure A.2.37 UV-vis spectra of complex **2.5** in a series of degassed solvents, the mixtures were excited by an array of Blue light LEDs (465 nm) for 4 hours, UV-vis profile was remeasured at specified time intervals to measure stability to intense blue light.

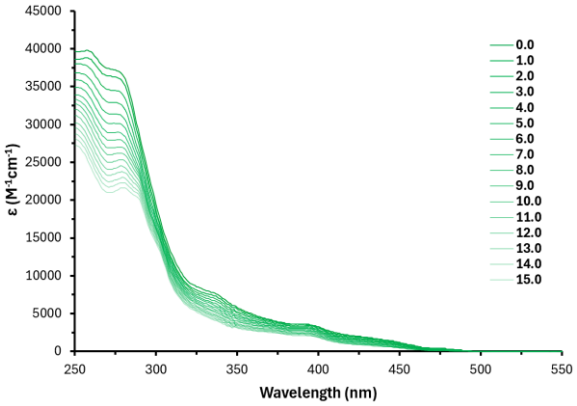


Figure A.2.38 UV-vis titration of complex **2.2** in MeCN 1×10^{-5} M with molar additions of TFA in MeCN. The legend indicating how many molar equivalents are present in each scan.

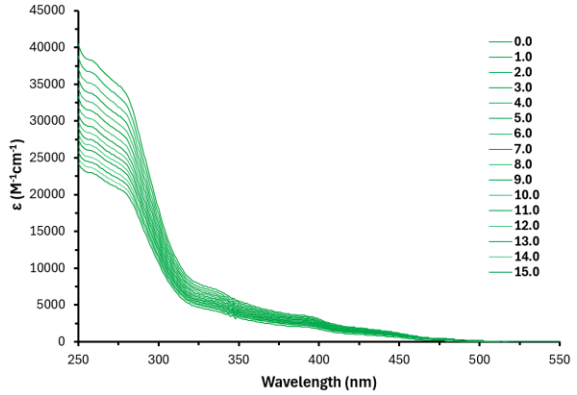


Figure A.2.39 UV-vis dilution of complex **2.2** in MeCN 1×10^{-5} M with additions of MeCN without TFA. Volume of MeCN added was equal to the additions in the TFA titration of figure S55.

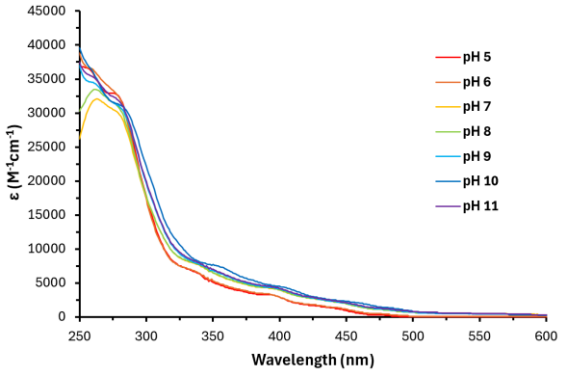


Figure A.2.40 UV-vis spectra of complex **2.2** in DMSO:H_2O (1:1) 1×10^{-5} M in varying Ph conditions.

A2.6: PLQYs and Decay Lifetimes

Decay Lifetime Measurement of Ir(III) complex 2.1

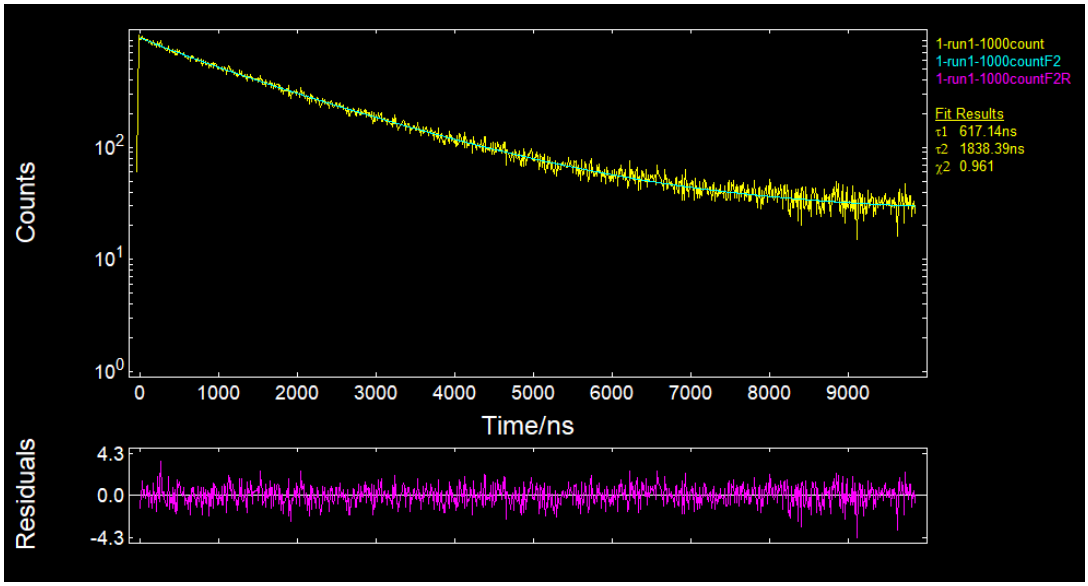


Figure A.2.41 Biexponential lifetime decay of Ir(III) complex **2.1**, ~$1 \cdot 10^{-5}$ M (Absorbance of 0.065 from UV-Vis) in $CHCl_3$ degassed for 20 mins (Ar) at 298 K after excitation at 365 nm. Data collected at λ_{max} = 470 nm.

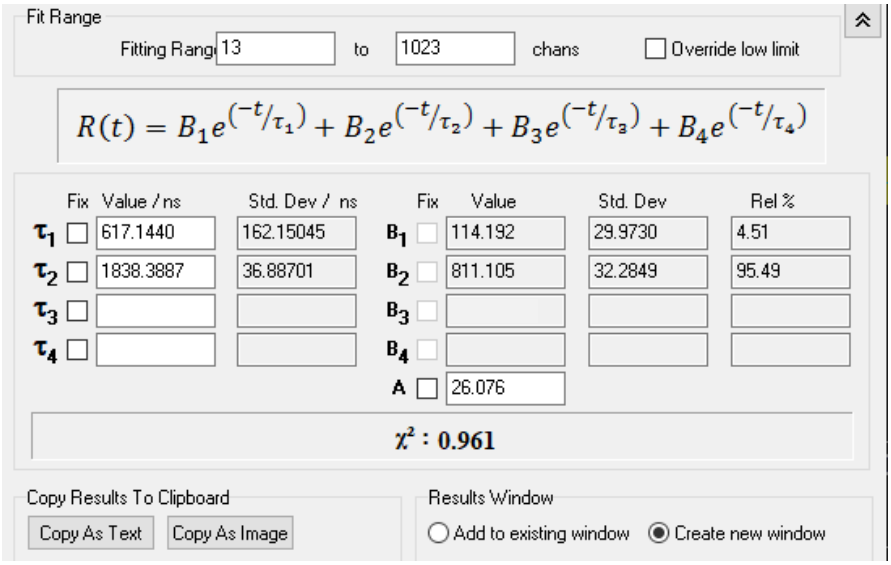


Figure A.2.42 Fit result of Ir(III) complex **2.1**, ~$1 \cdot 10^{-5}$ M (Absorbance of 0.065 from UV-Vis) in $CHCl_3$ degassed for 20 mins (Ar) at 298 K after excitation at 365 nm. Data collected at λ_{max} = 470 nm.

Decay Lifetime Measurement of Ir(III) complex 2.2

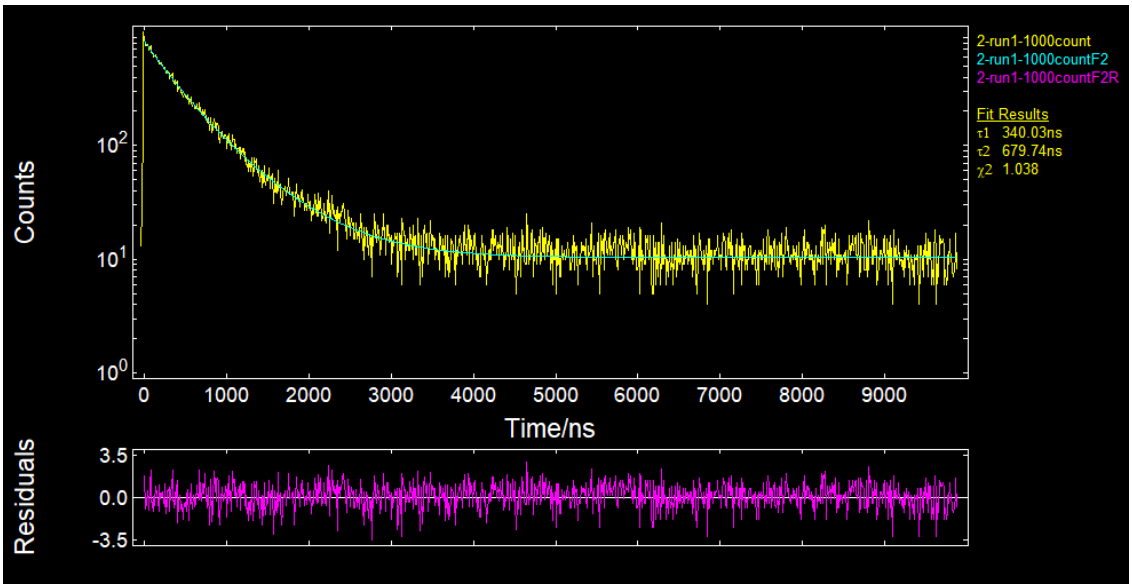


Figure A.2.43 Monoexponential lifetime decay of Ir(III) complex **2.2**, ~$1 \cdot 10^{-5}$ M (Absorbance of 0.081 from UV-Vis) in $CHCl_3$ degassed for 20 mins (Ar) at 298 K after excitation at 365 nm. Data collected at λ_{max} = 540 nm.

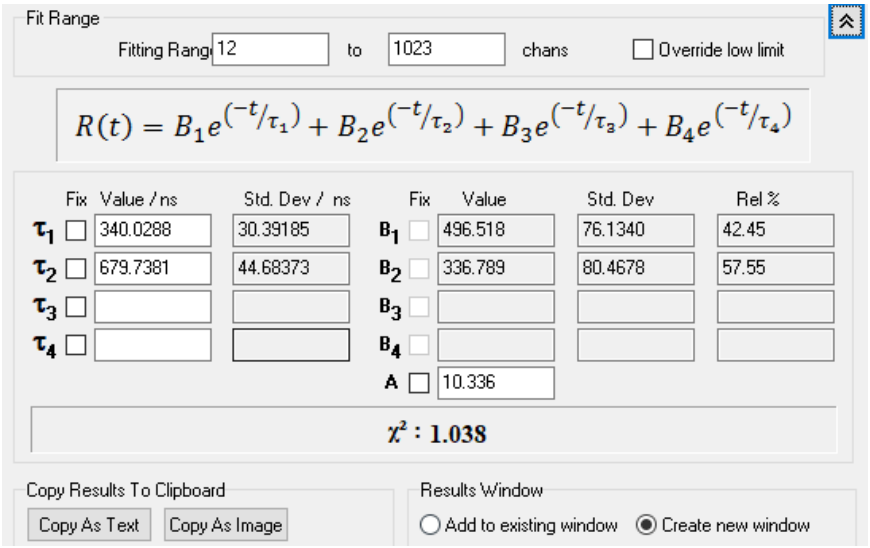


Figure A.2.44 Fit result of Ir(III) complex **2.2**, ~$1 \cdot 10^{-5}$ M (Absorbance of 0.081 from UV-Vis) in $CHCl_3$ degassed for 20 mins (Ar) at 298 K after excitation at 365 nm. Data collected at λ_{max} = 540 nm.

Decay Lifetime Measurement of Ir(III) complex 2.3

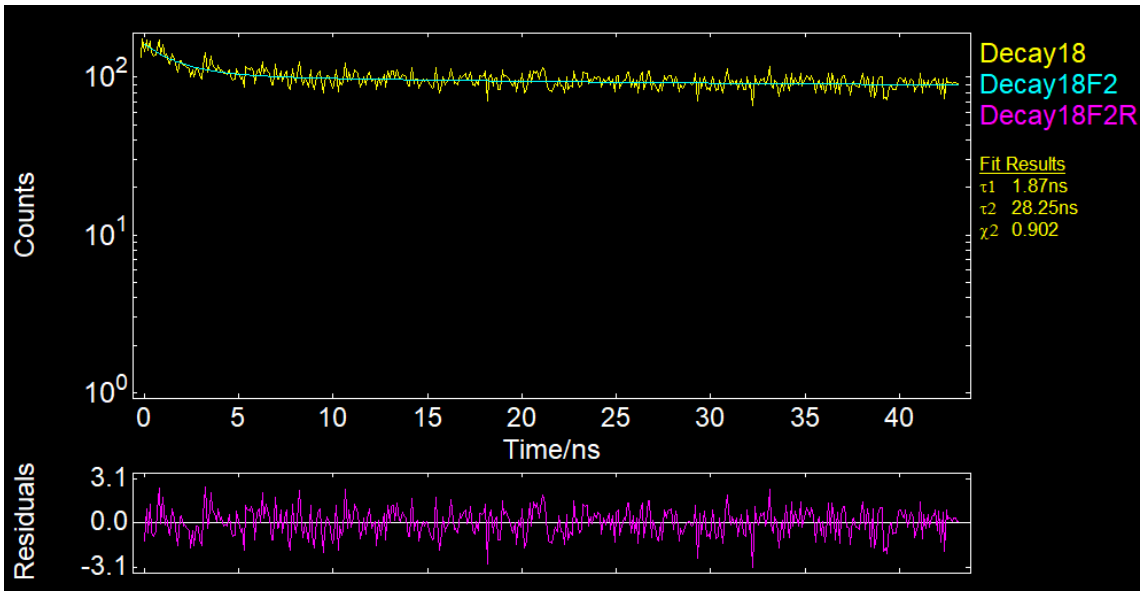


Figure A.2.45 Biexponential lifetime decay of Ir(III) complex **3,** ~$1 \cdot 10^{-5}$ M (Absorbance of 0.079 from UV-Vis) in $CHCl_3$ degassed for 20 mins (Ar) at 298 K after excitation at 365 nm. Data collected at λ_{max} = 540 nm.

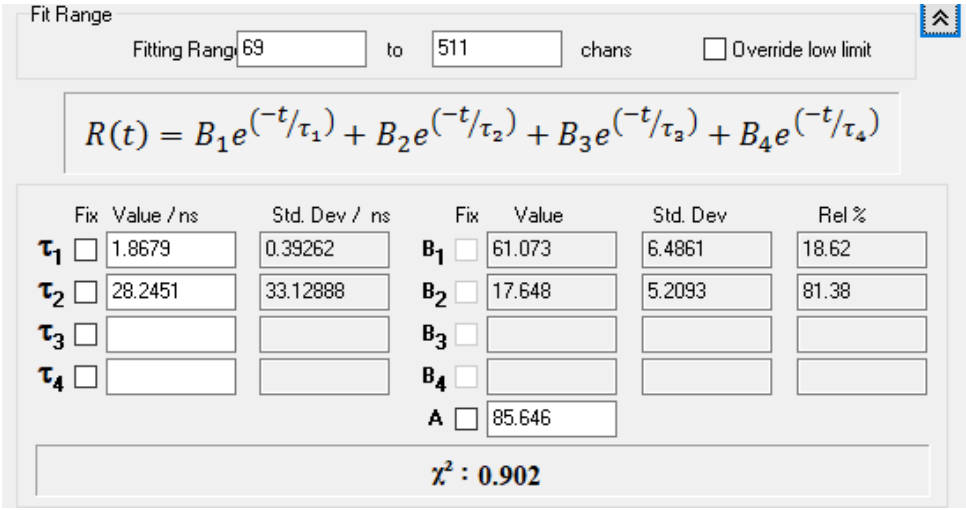


Figure A.2.46 Fit result of Ir(III) complex **3**, ~$1 \cdot 10^{-5}$ M (Absorbance of 0.079 from UV-Vis) in $CHCl_3$ degassed for 20 mins (Ar) at 298 K after excitation at 365 nm. Data collected at λ_{max} = 540 nm.

Decay Lifetime Measurement of Ir(III) complex 2.4

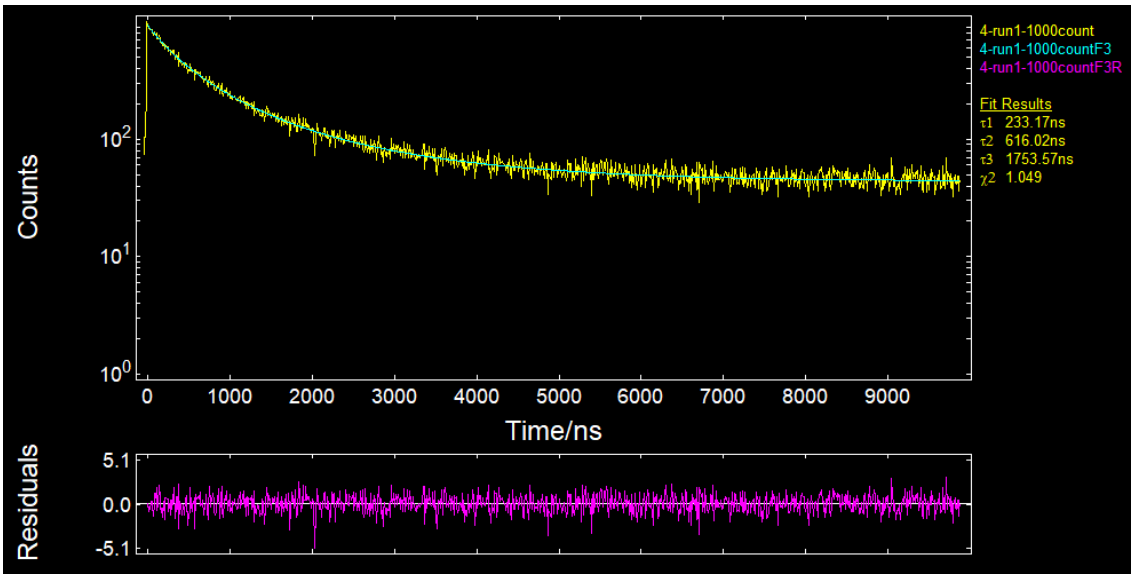


Figure A.2.47 Biexponential lifetime decay of Ir(III) complex **2.4,** ~$1 \cdot 10^{-6}$ M (Absorbance of 0.073 from UV-Vis) in $CHCl_3$ degassed for 20 mins (Ar) at 298 K after excitation at 365 nm. Data collected at λ_{max} = 540 nm.

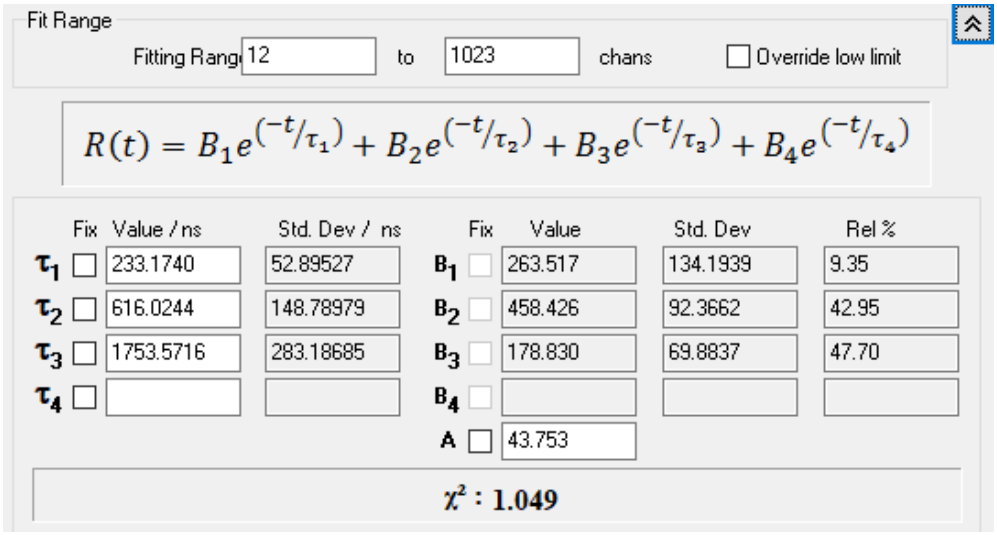


Figure A.2.48 Fit result of Ir(III) complex **2.4**, ~$1 \cdot 10^{-6}$ M (Absorbance of 0.073 from UV-Vis) in $CHCl_3$ degassed for 20 mins (Ar) at 298 K after excitation at 365 nm. Data collected at λ_{max} = 540 nm.

Decay Lifetime Measurement of Ir(III) complex 2.5

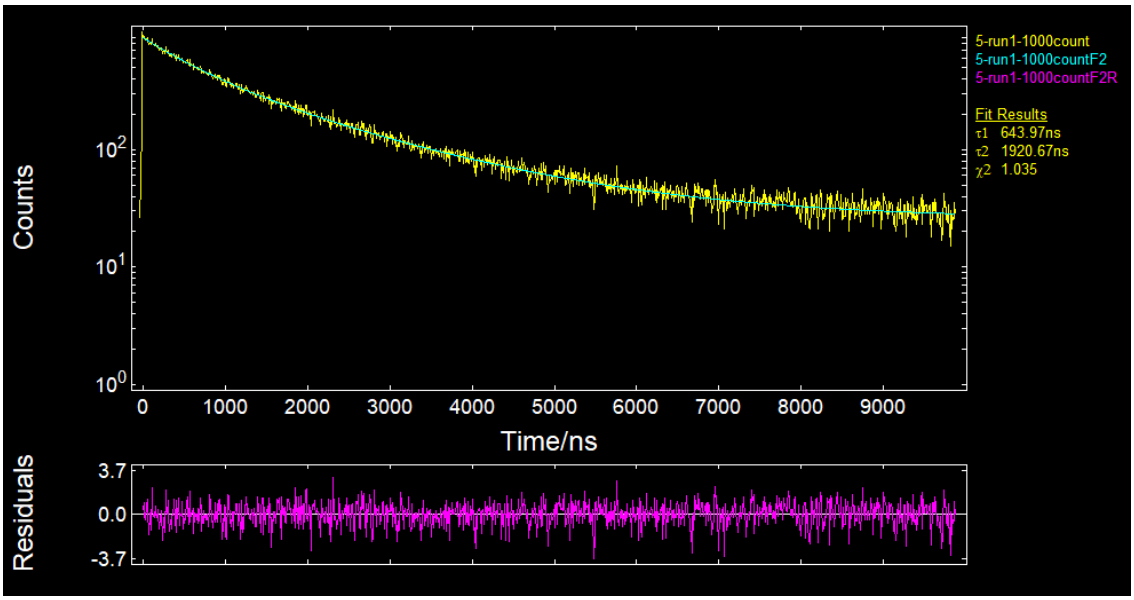


Figure A.2.49 Biexponential lifetime decay of Ir(III) complex **2.5,** ~$1 \cdot 10^{-6}$ M (Absorbance of 0.080 from UV-Vis) in $CHCl_3$ degassed for 20 mins (Ar) at 298 K after excitation at 365 nm. Data collected at λ_{max} = 540 nm.

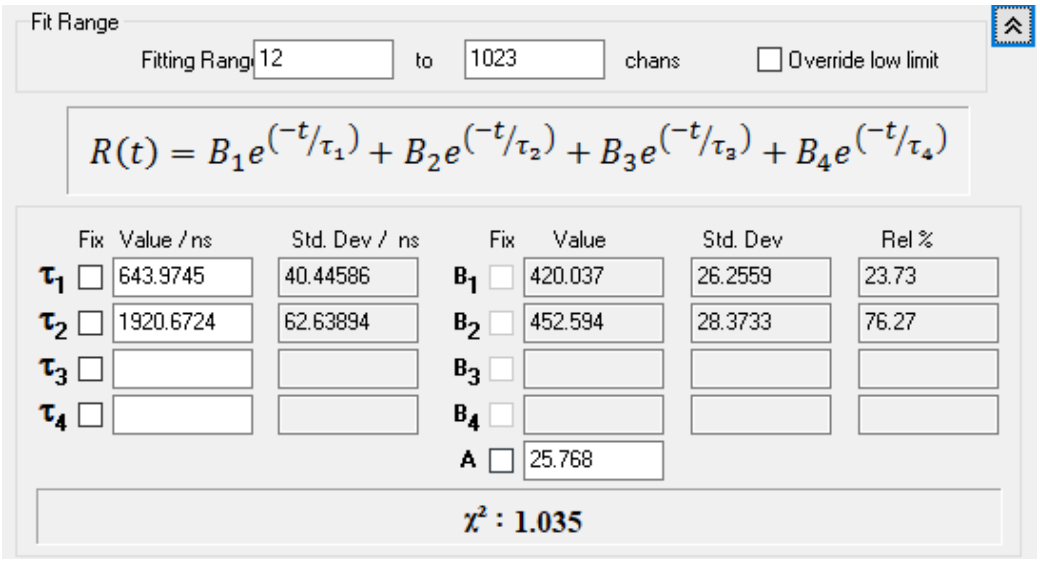


Figure A.2.50 Fit result of Ir(III) complex **2.5**, ~$1 \cdot 10^{-6}$ M (Absorbance of 0.080 from UV-Vis) in $CHCl_3$ degassed for 20 mins (Ar) at 298 K after excitation at 365 nm. Data collected at λ_{max} = 540 nm.

A2.7: High-Throughput Hydrogen Evolution Condition Screening

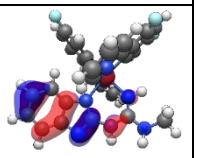
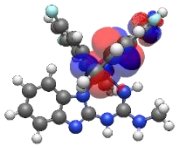
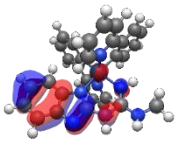
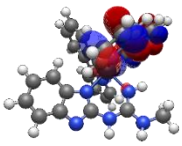
Table A.2.1 Screening conditions for photocatalytic hydrogen generation with complex **2**. All variables were changed individually (varying condition highlighted in red), while all other conditions were consistent with the initial conditions. Initial conditions were determined from review of existing literature. Solvents are 5 mL 1:1 ratio unless specified otherwise, all screens were run for 5 hours before hydrogen evolution was measured. Hydrogen generation rate was calculated relative to time mols of H_2 and mass of PS.

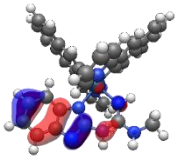
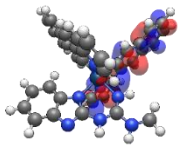
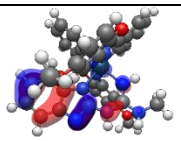
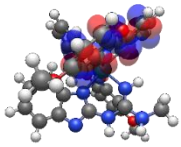
Trial	**PS** (μmol)	**Co-Cat.** (Mm)	**Solvent**	**LiCl** (M)	**Ph**	**Electron donor** (M)	**Rate of H_2** ($\mu molg^{-1}hr^{-1}$) **Run 1**	**Rate of H_2** ($\mu molg^{-1}hr^{-1}$) **Run 2**
Initial	0.10	0.50	DMSO/H_2O	0.2	10	NEt_3 (0.3)	340.7	330.6
1	0.00	0.50	DMSO/H_2O	0.2	10	NEt_3 (0.3)	0	0
2	0.01	0.50	DMSO/H_2O	0.2	10	NEt_3 (0.3)	126.5	145.7
3	0.20	0.50	DMSO/H_2O	0.2	10	NEt_3 (0.3)	43.5	60.3
4	0.50	0.50	DMSO/H_2O	0.2	10	NEt_3 (0.3)	58.8	44.8
5	1.0	0.50	DMSO/H_2O	0.2	10	NEt_3 (0.3)	20.5	22.5
6	2.0	0.50	DMSO/H_2O	0.2	10	NEt_3 (0.3)	11.4	8.1
7	0.10	0.00	DMSO/H_2O	0.2	10	NEt_3 (0.3)	3.5	2.0
8	0.10	0.1	DMSO/H_2O	0.2	10	NEt_3 (0.3)	5.0	7.5
9	0.10	0.25	DMSO/H_2O	0.2	10	NEt_3 (0.3)	122.7	159.3
10	0.10	1.0	DMSO/H_2O	0.2	10	NEt_3 (0.3)	173.4	191.1
11	0.10	2.5	DMSO/H_2O	0.2	10	NEt_3 (0.3)	117.0	127.0
12	0.10	5.00	DMSO/H_2O	0.2	10	NEt_3 (0.3)	81.5	113.9
13	0.10	0.50	DMSO/H_2O 1:4	0.2	10	NEt_3 (0.3)	203.4	207.1
14	0.10	0.50	DMSO/H_2O 1:2	0.2	10	NEt_3 (0.3)	112.1	127.6
15	0.10	0.50	DMSO/H_2O 2:1	0.2	10	NEt_3 (0.3)	73.1	60.0
16	0.10	0.50	DMSO/H_2O 4:1	0.2	10	NEt_3 (0.3)	31.3	41.9
17	0.10	0.50	THF/H_2O	0.2	10	NEt_3 (0.3)	174.1	170.6

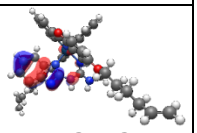
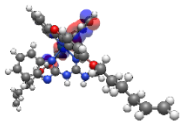
18	0.10	0.50	DMF/H_2O	0.2	10	NEt_3 (0.3)	450.2	444.4
19	0.10	0.50	MeCN/H_2O	0.2	10	NEt_3 (0.3)	279.5	298.7
20	0.10	0.50	H_2O	0.2	10	NEt_3 (0.3)	16.6	20.5
21	0.10	0.50	DMSO/H_2O	0.0	10	NEt_3 (0.3)	13.8	10.3
22	0.10	0.50	DMSO/H_2O	0.02	10	NEt_3 (0.3)	17.8	14.9
23	0.10	0.50	DMSO/H_2O	0.08	10	NEt_3 (0.3)	30.4	37.3
24	0.10	0.50	DMSO/H_2O	0.16	10	NEt_3 (0.3)	99.0	127.6
25	0.10	0.50	DMSO/H_2O	0.40	10	NEt_3 (0.3)	266.5	279.5
26	0.10	0.50	DMSO/H_2O	0.6	10	NEt_3 (0.3)	148.2	158.0
27	0.10	0.50	DMSO/H_2O	0.2	11	NEt_3 (0.3)	162.8	180.4
28	0.10	0.50	DMSO/H_2O	0.2	9	NEt_3 (0.3)	112.7	125.4
29	0.10	0.50	DMSO/H_2O	0.2	8	NEt_3 (0.3)	113.0	115.7
30	0.10	0.50	DMSO/H_2O	0.2	7	NEt_3 (0.3)	17.6	13.8
31	0.10	0.50	DMSO/H_2O	0.2	6	NEt_3 (0.3)	2.6	1.9
32	0.10	0.50	DMSO/H_2O	0.2	5	NEt_3 (0.3)	0	0
33	0.10	0.50	DMSO/H_2O	0.2	10	EDTA (0.3)	14.6	12.5
34	0.10	0.50	DMSO/H_2O	0.2	10	Na^+ ascorbate (0.3)	238.1	250.8
35	0.10	0.50	DMSO/H_2O	0.2	10	DMA (0.3)	5.8	11.5
36	0.10	0.50	DMSO/H_2O	0.2	10	TEOA (0.3)	40.5	13.2
37	0.10	0.50	DMSO/H_2O	0.2	10	MeOH (0.3)	0	0
38	0.10	0.50	DMSO/H_2O	0.2	10	NEt_3 (0.00)	0	0
39	0.10	0.50	DMSO/H_2O	0.2	10	NEt_3 (0.03)	7.9	11.4
40	0.10	0.50	DMSO/H_2O	0.2	10	NEt_3 (0.06)	15.5	18.5
41	0.10	0.50	DMSO/H_2O	0.2	10	NEt_3 (0.10)	152.1	160.3
42	0.10	0.50	DMSO/H_2O	0.2	10	NEt_3 (0.40)	190.7	200.1
43	0.10	0.50	DMSO/H_2O	0.2	10	NEt_3 (0.60)	165.2	157.9

A2.8: Computational Investigation

Table A.2.2 Summary of key findings of TD-DFT predictions for the complexes **2.1-2.5** including energy levels of five highest contributing singlet states and first triplet state.

Complex	Spin State	Transition configurations	Excitation energy (eV, nm)	Oscillator strength	HOMO-LUMO (eV)
2.1	S_7	HOMO-2→LUMO+1 (72.5%) HOMO→LUMO+2 (22.9%)	3.2440, 382.19	0.0107	 **HOMO (-4.75)**
	S_{13}	HOMO-4→LUMO (45.5%) HOMO-4→LUMO+1 (12.4%) HOMO-3→LUMO (8.9%) HOMO-2→LUMO+2 (27.2%)	3.7690, 328.96	0.0627	
	S_{16}	HOMO-5→LUMO (5.2%) HOMO-5→LUMO+1 (2.9%) HOMO-4→LUMO+1 (3.9%) HOMO-3→LUMO (3.3%) HOMO-3→LUMO+1 (68.6%) HOMO-2→LUMO+3 (7.9%)	3.9595, 313.13	0.0568	 **LUMO (-1.59)**
	S_{19}	HOMO-6→LUMO+1 (4.4%) HOMO-5→LUMO+1 (61.2%) HOMO-3→LUMO+1 (5.0%) HOMO-3→LUMO+2 (4.4%) HOMO-3→LUMO+3 (15.7%) HOMO-2→LUMO+3 (2.3%)	4.1691, 297.39	0.0590	
	S_{22}	HOMO-1→LUMO+4 (25.2%) HOMO→LUMO+4 (63.2%)	4.2957, 288.63	0.1574	
	T_1	HOMO-4→LUMO (3.5%) HOMO-2→LUMO (6.5%) HOMO-1→LUMO (13.2%) HOMO→LUMO (72.5%)	2.6327, 470.94		
2.2	S_5	HOMO-2→LUMO (90.7%) HOMO→LUMO (4.6%)	2.8732, 531.51	0.0141	 **HOMO (-4.55)**
	S_{12}	HOMO-4→LUMO (2.3%) HOMO-3→LUMO (19.5%) HOMO-2→LUMO+3 (73.2%)	3.5871, 345.63	0.0269	
	S_{14}	HOMO-4→LUMO (46.4%) HOMO-3→LUMO (25.7%) HOMO-3→LUMO+1 (18.5%) HOMO-2→LUMO+3 (2.0%)	3.6541, 339.30	0.0212	 **LUMO (-1.39)**
	S_{17}	HOMO-6→LUMO+1 (2.1%) HOMO-4→LUMO+1 (84.4%)	3.8864, 319.02	0.0409	
	S_{24}	HOMO-7→LUMO (3.6%) HOMO-5→LUMO+2 (3.2%) HOMO-1→LUMO+4 (27.9%)	4.2862, 289.26	0.1142	
	T_1	HOMO-5→LUMO (3.6%) HOMO-3→LUMO (5.0%) HOMO-2→LUMO (34.0%) HOMO-1→LUMO (13.8%)	2.5568, 484.91		

		HOMO→LUMO (36.0%)			
2.3	S_6	HOMO-2→LUMO+1 (94.7%)	2.7698, 447.64	0.0090	 **HOMO (-4.57)**
	S_{14}	HOMO-6→LUMO (6.6%) HOMO-5→LUMO (5.3%) HOMO-4→LUMO (73.1%) HOMO-3→LUMO (4.0%) HOMO-2→LUMO+3 (3.4%)	3.3556, 369.48	0.0733	
	S_{18}	HOMO-7→LUMO+1 (3.4%) HOMO-6→LUMO (15.3%) HOMO-6→LUMO+1 (5.9%) HOMO-5→LUMO (3.7%) HOMO-5→LUMO+1 (50.7%) HOMO-4→LUMO (2.3%) HOMO-4→LUMO+1 (10.1%) HOMO-2→LUMO+5 (2.5%)	3.6696, 337.86	0.0545	 **LUMO (-1.62)**
	S_{21}	HOMO-7→LUMO (35.4%) HOMO-6→LUMO (2.2%) HOMO-5→LUMO+2 (7.8%) HOMO-4→LUMO+2 (34.3%) HOMO-3→LUMO+2 (4.6%) HOMO-2→LUMO+4 (7.1%)	3.7832, 327.72	0.0355	
	S_{31}	HOMO-7→LUMO (3.9%) HOMO-7→LUMO+1 (19.4%) HOMO-5→LUMO+3 (7.1%) HOMO-2→LUMO+4 (37.7%) HOMO-1→LUMO+5 (15.3%)	4.0659, 304.93	0.1486	
	T_1	HOMO-4→LUMO+1 (5.6%) HOMO-3→LUMO+1 (18.1%) HOMO-3→LUMO+3 (2.6%) HOMO-3→LUMO+5 (2.6%) HOMO-2→LUMO (9.5%) HOMO-2→LUMO+1 (36.6%) HOMO-2→LUMO+3 (3.0%) HOMO-2→LUMO+5 (5.3%) HOMO-1→LUMO+1 (4.8%)	2.2827, 543.14		
2.4	S_5	HOMO-2→LUMO (96.5%)	2.9249, 423.89	0.0482	 **HOMO (-4.45)**
	S_{10}	HOMO-6→LUMO+1 (3.6%) HOMO-4→LUMO+1 (61.6%) HOMO-3→LUMO+1 (25.9%)	3.7378, 331.70	0.0523	
	S_{11}	HOMO-7→LUMO (2.9%) HOMO-6→LUMO (2.1%) HOMO-5→LUMO (83.4%) HOMO-3→LUMO (5.3%)	3.8599, 321.21	0.1458	
	S_{17}	HOMO-7→LUMO (33.2%) HOMO-6→LUMO (2.3%) HOMO-6→LUMO+1 (49.7%) HOMO-5→LUMO+1 (6.3%)	4.1274, 300.39	0.0855	 **LUMO (-1.45)**
	S_{20}	HOMO-7→LUMO+1 (2.5%) HOMO-1→LUMO+4 (10.2%) HOMO-1→LUMO+5 (6.8%) HOMO-1→LUMO+10 (2.1%) HOMO→LUMO+4 (47.2%)	4.2750, 290.02	0.0602	

	T_1	HOMO→LUMO+5 (16.7%) HOMO-3→LUMO (7.5%) HOMO-2→LUMO (11.5%) HOMO-1→LUMO (12.5%) HOMO→LUMO (63.4%)	2.4595, 504.11		
2.5	S_6	HOMO-2→LUMO+1 (96.3%)	3.1042, 399.41	0.0478	 **HOMO (-4.45)**
	S_{11}	HOMO-7→LUMO (2.6%) HOMO-5→LUMO (83.6%) HOMO-3→LUMO (5.7%)	3.8519, 321.88	0.1596	
	S_{14}	HOMO-7→LUMO+1 (4.2%) HOMO-6→LUMO (5.6%) HOMO-6→LUMO+1 (9.4%) HOMO-5→LUMO+1 (60.7%) HOMO-3→LUMO+1 (6.1%) HOMO→LUMO+2 (10.0%)	4.0043, 309.63	0.0990	 **LUMO (-1.44)**
	S_{17}	HOMO-7→LUMO (20.1%) HOMO-6→LUMO+1 (60.1%) HOMO-5→LUMO+1 (9.9%)	4.1182, 301.06	0.1011	
	S_{23}	HOMO-3→LUMO+12 (2.4%) HOMO-1→LUMO+4 (38.2%) HOMO-1→LUMO+11 (2.5%) HOMO-1→LUMO+12 (9.7%) HOMO→LUMO+4 (4.1%) HOMO→LUMO+5 (23.1%)	4.3591, 284.42	0.0531	
	T_1	HOMO-3→LUMO (8.6%) HOMO-2→LUMO (12.4%) HOMO-1→LUMO (11.5%) HOMO→LUMO (62.0%)	2.4707, 501.82		

Appendix 3

Supplementary Material for Chapter 3

Table of Contents

A3.1: Synthetic Procedures of Compounds 3.1-3.5 **266**

A.3.2: ^{1}H and ^{13}C NMR Spectra and Mass spectra **273**

A.3.3: UV-vis, Excitation and Emission Data **279**

A3.4: K_a Binding Studies **283**

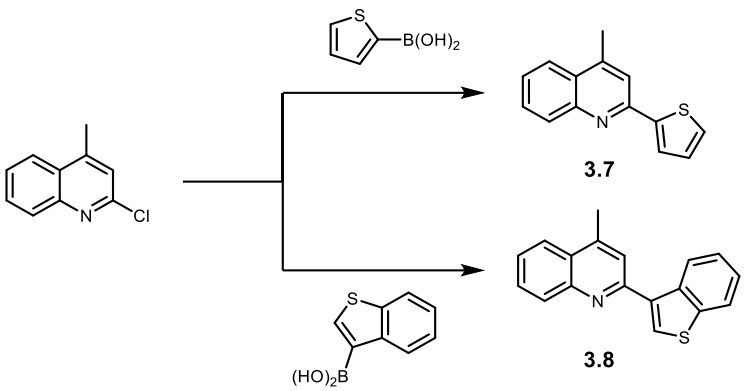
A3.5: PLQYs and Decay Lifetimes **286**

A3.6: PMMA Solid State PLQYs and Decay Lifetimes **295**

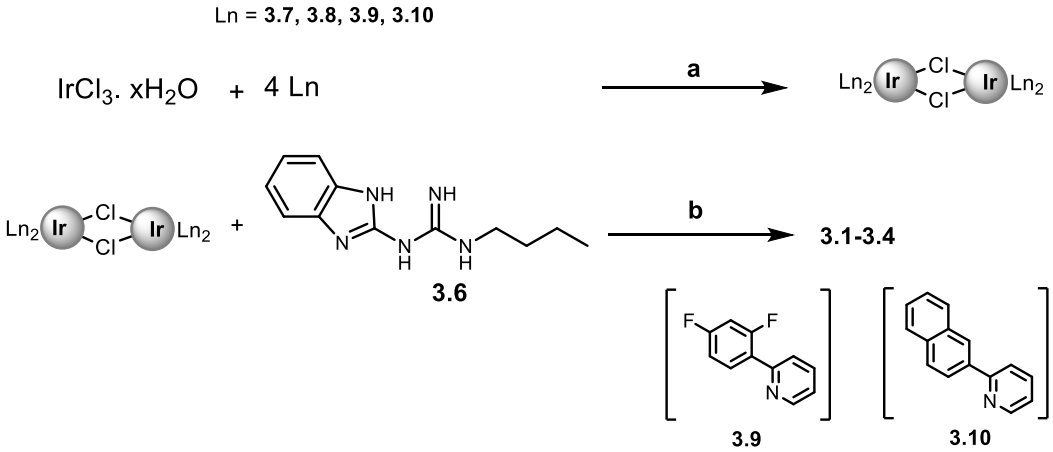
A3.7: Cyclic Voltammetry **306**

A3.8: Computational Investigation **307**

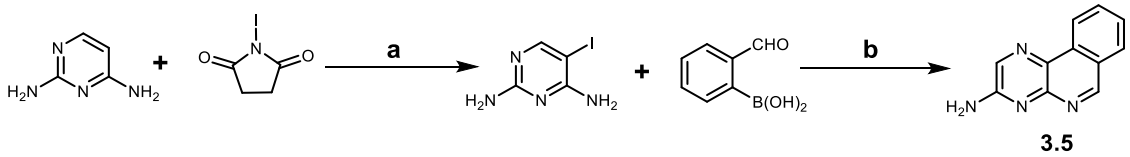
A3.1: Synthetic Procedures of Compounds 3.1-3.5



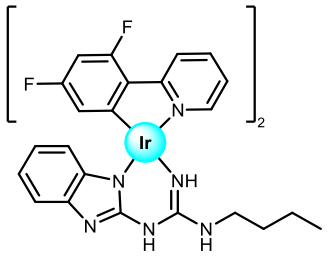
Scheme A.3.1 Synthesis of ligand **3.7** and **3.8**. Reagents and conditions: 3 mol % $Pd(Ph_3)_4$, 5% solution of Na_2CO_3, dry THF, reflux, 24 hr, N_2 (g).



Scheme A.3.2 The general synthetic route of all iridium complexes herein. Reagents and conditions: a) 2-ethoxyethanol: water (3:1), reflux, 19 hr; b) 1-(1H-benzo[d]imidazole-2-yl)-3-butylguanidine **3.6**, K_2CO_3, toluene, N_2 (g).

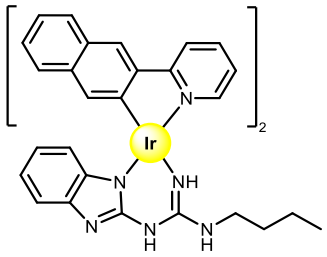


Scheme A.3.3 The synthetic route of compound **3.5**. Reagents and conditions: a) DMF, 0°C to rt., 3 hr, 88%; b) MW, K_2CO_3, $Pd(PPh_3)_4$, dioxane:water (3:1), 150 °C, 3 hr N_2 (g).



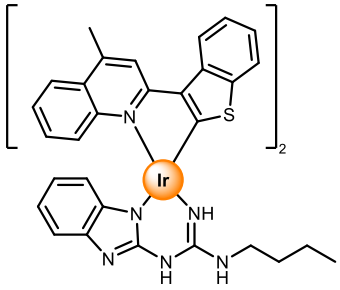
3.1

Iridium complex 3.1 – Complex **3.1** has the same preparation and spectral data as complex **2.1** in appendix 2.



3.2

Iridium complex 3.2 – Complex **3.2** has the same preparation and spectral data as complex **2.3** in appendix 2.

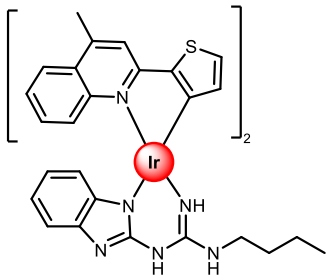


3.3

Iridium complex 3 – Iridium chloro-bridged dimer made from ligand **3.7** (47 mg, 0.03 mmol), (1-(1H-benzo[d]imidazole-2-yl)-3-butylguanidine) ligand **3.6** (20 mg, 0.09 mmol), and potassium carbonate (48 mg, 0.35 mmol) were added to 5 mL of dry toluene and refluxed under nitrogen atmosphere for 18 hours. After the reaction was completed, it

was cooled to room temperature and solvent was removed under reduced pressure. The solid was re-dissolved in dichloromethane and extracted with water, organic phases were combined, and dried over magnesium sulphate and solvent was removed under reduced pressure. The sample was dried and subjected to purification via column chromatography (neutral alumina as stationary phase, DCM: MeOH 10:0.5 as mobile phase). Fractions were collected (R_f = 0.18, DCM: MeOH, 10:0.5), and solvent was removed under reduced pressure. The product was dried in vacuo (Schlenk line) for 48 hr. The final product was obtained in (18 mg, 60%) yield as a dark red powder.

^{1}H NMR (400 MHz, $CDCl_3$, 298 K) δ 8.64 (d, *J* = 8.9 Hz, 1H), 8.28 (dd, *J* = 11.1, 7.3 Hz, 2H), 8.22 (d, *J* = 8.3 Hz, 1H), 8.01 (t, *J* = 8.5 Hz, 1H), 7.84 – 7.79 (m, 1H), 7.52 (d, *J* = 7.8 Hz, 1H), 7.45 – 7.35 (m, 2H), 7.34 – 7.28 (m, 1H), 7.21 (dd, *J* = 11.5, 7.6 Hz, 1H), 7.02 (ddd, *J* = 23.2, 14.7, 7.8 Hz, 3H), 6.88 – 6.79 (m, 1H), 6.44 – 6.37 (m, 1H), 5.71 (d, *J* = 8.3 Hz, 1H), 3.95 (br s, 1H), 2.97 (d, *J* = 9.6 Hz, 6H), 1.25 (s, 2H), 1.25 – 1.19 (m, 2H), 1.09 (dd, *J* = 15.2, 7.6 Hz, 2H), 0.71 (t, *J* = 7.3 Hz, 3H). ^{13}C NMR (400 MHz, $CDCl_3$, 298 K) δ: 167.50, 165.89, 150.33, 148.95, 148.32, 148.14, 144.29, 143.60, 140.46, 139.32, 138.37, 138.34, 137.89, 130.65, 130.58, 126.11, 125.75, 125.70, 125.58, 125.30, 124.97, 124.75, 124.63, 124.54, 124.45, 122.80, 122.64, 121.54, 121.30, 118.80, 118.31, 118.00, 116.30, 110.79, 40.94, 30.85, 30.76, 19.91, 19.72, 19.69, 13.64, 13.61. HRMS m/z calculated: 972.2488. Found: 972.2498 [M+].



3.4

Iridium complex 4 – Iridium chloro-bridged dimer made from ligand **3.8** (118 mg, 0.09 mmol) was combined with 2.5 equivalents of (1-(1H-benzo[d]imidazole-2-yl)-3-butylguanidine) ligand **3.6** (51 mg, 0.22 mmol) and 10 equivalents of potassium carbonate (120 mg, 0.88 mmol) were added to 20 mL of dry toluene and refluxed under nitrogen atmosphere for 20 hours. After the reaction was completed, it was cooled to room temperature and solvent was removed under reduced pressure. The solid was re-dissolved in dichloromethane and extracted with water, organic phases were combined, and solvent was removed under reduced pressure. The sample was dried and subjected to purification via column chromatography (neutral alumina as stationary phase, DCM: MeOH 10:0.5 as mobile phase). Fractions were collected (R_f = 0.28, DCM: MeOH, 10:0.5), and solvent was removed under reduced pressure. The product was dried in vacuo (Schlenk line) for 48 h. The final product was obtained in (41 mg, 54%) yield as a red powder.

^{1}H NMR (400 MHz, $CDCl_3$, 298 K) δ: 8.38 (d, *J* = 8.5 Hz, 1H), 7.97 (d, *J* = 8.2 Hz, 1H), 7.90 (d, *J* = 8.6 Hz, 1H), 7.78 (dd, *J* = 8.2, 1.2 Hz, 1H), 7.64 (s, 1H), 7.55 (s, 1H), 7.47 (d, *J* = 4.7 Hz, 1H), 7.40 (t, *J* = 7.6 Hz, 1H), 7.22 (dd, *J* = 9.6, 4.4 Hz, 2H), 7.08 (d, *J* = 4.8 Hz, 1H), 7.02 (d, *J* = 4.7 Hz, 1H), 7.00 (s, 1H), 6.95 (dd, *J* = 15.0, 7.2 Hz, 1H), 6.82 – 6.75 (m, 1H), 6.49(t, *J* = 7.8, Hz 1H), 6.36 (s, 1H), 6.07 (d, *J* = 4.8 Hz, 1H), 5.81 (d, *J* =

8.3 Hz, 1H), 4.21 (br s, 2H), 2.87 (s, 3H), 2.82 (s, 3H), 1.25 (br s, 1H), 1.23 – 1.16 (m, 2H), 1.07-1.02 (m, *J* = 14.9, 7.4 Hz, 2H), 0.72 (t, *J* = 7.3 Hz, 3H). ^{13}C NMR (101 MHz, $CDCl_3$, 298 K) δ: 165.97, 160.42, 155.06, 153.11, 149.93, 149.59, 147.78, 147.12, 146.90, 144.62, 140.39, 140.18, 139.11, 134.71, 132.07, 131.58, 131.04, 130.38, 130.09, 128.66, 127.39, 126.74, 126.51, 125.64, 125.44, 125.09, 124.70, 124.37, 122.56, 122.26, 118.88, 118.02, 115.58, 111.00, 40.85, 30.55, 19.96, 19.25, 19.02, 13.63. HRMS m/z calculated: 872.2176. Found: 872.2202 [M+].

Pyrimido[4,5-c]isoquinolin-3-amine (Compound 3.5) – 5-iodopyrimidine-2,4-diamine (197 mg, 0.83 mmol), 2-formylphenylboronic acid (182 mg, 1.20 mmol), potassium carbonate (461 mg, 3.30 mmol) and tetrakis(triphenylphosphine)palladium(0) (0.5 mol%) were added to a mixture of dioxane and water (3:1, 9 mL of dioxane, 3 mL of water). The reaction mixture was heated under reflux for 3 h, then cooled to room temperature and placed in a cold bath. The precipitate was filtered and washed with water (2 × 30 mL), three times suspended and sonicated in water and filtered, then finally dried in a vacuum oven (24 hr, 40 °C). Product was obtained as a fine bright yellow powder in (82 mg, 50%) yield.

^{1}H NMR (400 MHz, 298K, DMSO-*d*$_6$): δ 9.88 (s, 1H), 9.50 (s, 1H), 8.72 (d, 1H, *J* = 8.1 Hz), 8.17 (d, 1H, *J* = 7.5 Hz), 7.92 (ddd, 1H, *J* = 8.4, 7.3, 1.3 Hz), 7.70 – 7.63 (m, 1H), 7.18 (s, 2H).^{13}C NMR (100 MHz, 298 K, DMSO-*d*$_6$): δ 163.68, 161.43, 158.80, 158.50, 132.58, 132.22, 129.33, 126.43, 124.43, 124.41, 120.35, 107.00. EI-MS m/z calcd.: 196.07 found: 197.08 [M+]. M.p. > 280°C. Anal. Calcd. For $C_{11}H_8N_4$: C, 67.34; H, 4.11; N, 28.55. Found: C, 67.19; H, 4.25; N, 28.35.

4-methyl-2-thiophen-2-yl-quinoline (Compound 3.7) – Thiophen-2-yl-boronic acid (0.73 g, 5.34 mmol), 2-chloro-4-methylquinoline (0.85 g, 4.71 mmol) and $Pd(PPh_3)_4$ (3 mol %) was added to 20 mL of THF and 2 M aqueous Na_2CO_3 solution (9 mL). Nitrogen was bubbled through the reaction mixture before the reflux started. After 24 hr, the reaction mixture was cooled to room temperature (the colour of the solution was very dark- almost black). The mixture was filtered through celite before extraction with water/EtOAc. The organic phases were combined and dried over magnesium sulfate and solvent was removed under reduced pressure. TLC control of the crude mixture revealed only one spot but from the ^{1}H NMR minor impurities were present. The crude mixture was subjected to column chromatography (silica, DCM) and fractions were collected. Fractions containing the desired product (R_f = 0.78, DCM) were combined and solvent was removed under reduced pressure. The final product was obtained in (741 mg, 70%) yield as a clear oil with a little hint of yellow. Characterization data matched those reported in literature.

^{1}H NMR (400 MHz, $CDCl_3$, 298 K) δ: 8.09 (d, *J* = 9.0 Hz, 1H), 7.95 (dd, *J* = 8.3, 1.0 Hz, 1H), 7.73 (dd, *J* = 3.7, 1.1 Hz, 1H), 7.68 (ddd, *J* = 8.4, 6.9, 1.4 Hz, 1H), 7.65 (d, *J* = 0.8 Hz, 1H), 7.50 (ddd, *J* = 8.2, 6.9, 1.3 Hz, 1H), 7.45 (dd, *J* = 5.0, 1.1 Hz, 1H), 7.16 (dd, *J* = 5.0, 3.7 Hz, 1H), 2.74 (s, 3H). ^{13}C NMR (101 MHz, $CDCl_3$, 298 K) δ: 152.16, 148.11, 144.83, 129.98, 129.61, 128.47, 128.15, 127.48, 126.00, 125.78, 123.76, 118.44, 19.08.

Benzo-thiophen-2-yl-4-methylquinoline (Compound 3.8) – To one equivalent of 2-chloro-4-methylquinoline (1.28 g, 7.25 mmol) with 1.2 equivalents of benzo[b]thiophene-2-boronic acid in 30 mL of dry THF, 6 mol % of $Pd(PPh_3)_4$ was

added. A 5% solution of Na_2CO_3 (~ 10 mL) was added to the mixture and nitrogen was bubbled through (15 min) prior to the reaction start. The reaction was refluxed for 25 hr, under nitrogen atmosphere. After cooling down, the mixture was poured into water, and the organic part was extracted with ethyl acetate. The organic layers were combined, dried over magnesium sulphate, and solvent was removed under reduced pressure. The crude mixture was dark red/brown with an oily texture. The product was further purified with column chromatography (R_f = 0.6, EtOAc: hexane, 2:8) and solvent removed under reduced pressure. The product was then recrystallised from diethyl ether. The final product was obtained in 1.5 g, 74% yield as off-white crystals.

^{1}H NMR (400 MHz, $CDCl_3$, 298 K) δ: 8.80 (d, *J* = 8.1 Hz, 1H), 8.23 (d, *J* = 8.4 Hz, 1H), 8.02 (d, *J* = 8.7 Hz, 1H), 7.93 (d, *J* = 5.9 Hz, 2H), 7.75 (t, *J* = 7.6 Hz, 1H), 7.67 (s, 1H), 7.58 (t, *J* = 7.6 Hz, 1H), 7.50 (t, *J* = 7.6 Hz, 1H), 7.43 (t, *J* = 7.5 Hz, 1H), 2.78 (s, 3H). ^{13}C NMR (101 MHz, $CDCl_3$, 298 K) δ: 154.38, 148.10, 144.79, 141.03, 137.70, 136.94, 130.30, 129.53, 127.39, 127.27, 126.27, 125.04, 124.90, 124.84, 123.78, 122.73, 121.64, 77.48, 77.16, 77.16, 76.84, 19.06. HRMS m/z calculated: 276.0841. Found: 276.0840 [M+]. Calcd for $C_{18}H_{13}NS$: C, 78.51; H, 4.76; N, 5.09. Found: C, 78.28; H, 4.63; N, 5.08.

A3.2: ^{1}H and ^{13}C NMR Spectra and Mass spectra

Complexes **3.1** and **3.2** were defined in appendix 2 as complexes **2.1** and **2.3**.

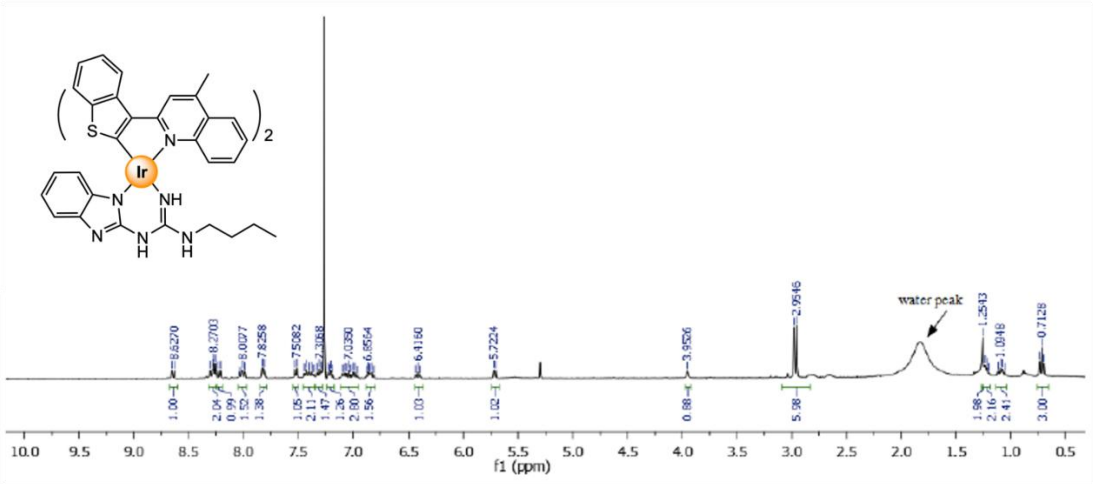


Figure A.3.1 ^{1}H NMR spectrum of orange iridium complex **3.3**, $CDCl_3$, 400 MHz, 298 K.

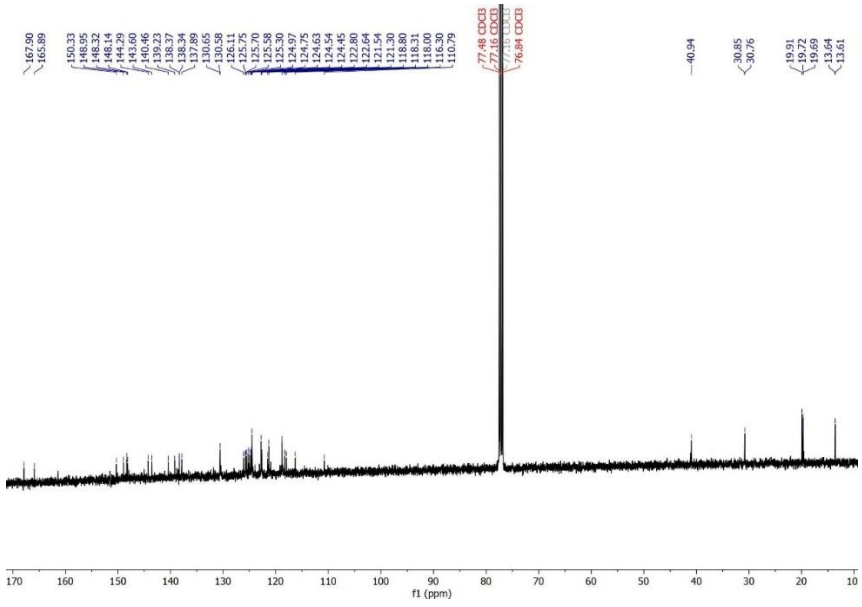


Figure A.3.2 ^{13}C NMR spectrum of orange iridium complex **3.3**, $CDCl_3$, 101 MHz, 298 K.

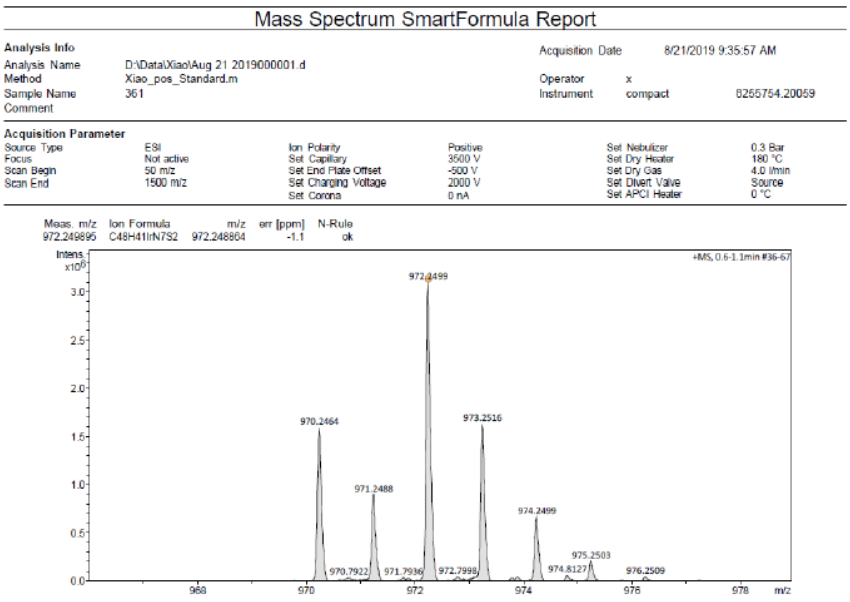


Figure A.3.3 Mass spectrum of iridium complex **3.3**. HMRS [ESI+] ion $[C_{48}H_{41}IrN_7S_2]^+$ m/z calculated: 972.2488. Found: 972.2498 [M+].

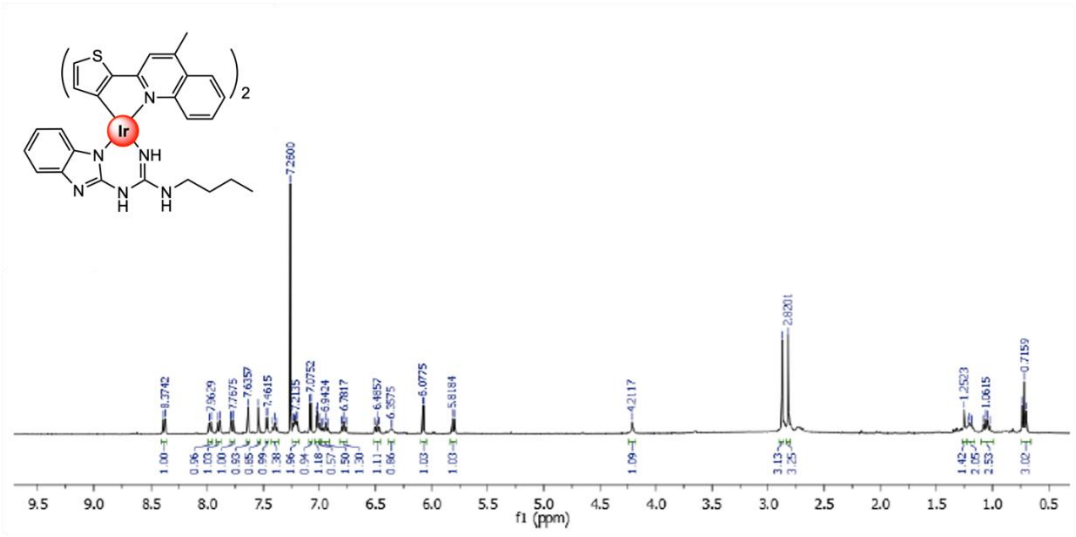


Figure A.3.4 ^{1}H NMR spectrum of red iridium complex **3.4**, $CDCl_3$, 400 MHz, 298 K.

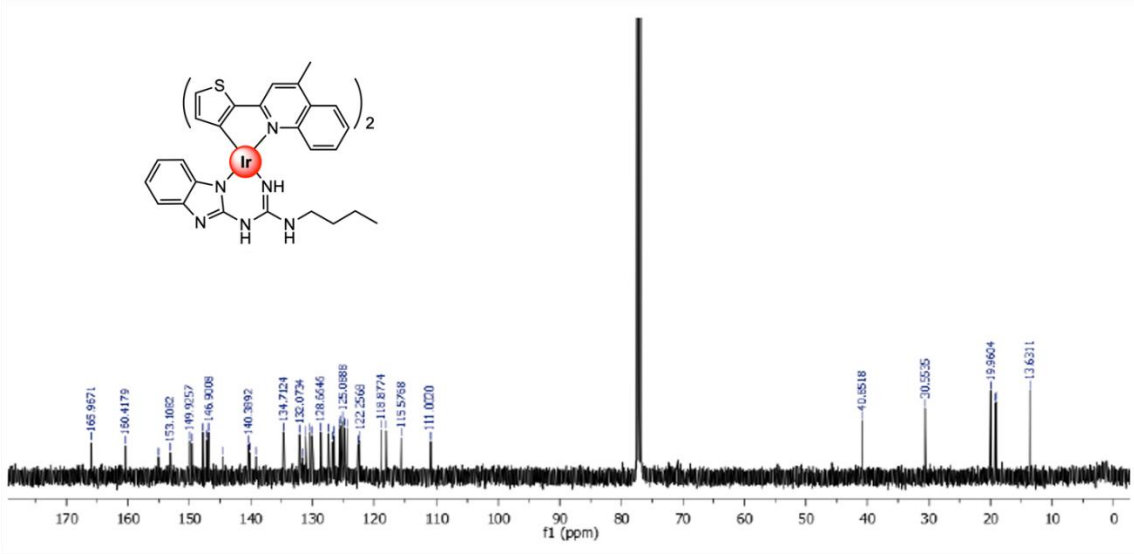


Figure A.3.5 ^{13}C NMR spectrum of red iridium complex **3.4**, $CDCl_3$, 101 MHz, 298 K.

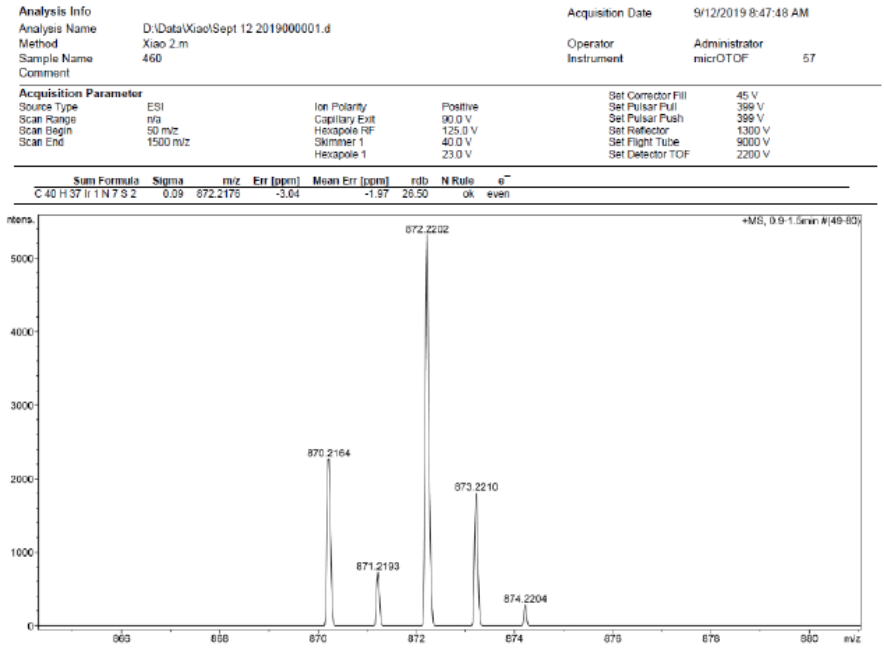


Figure A.3.6 Mass spectrum of iridium complex **3.4**. HMRS [ESI+] ion $[C_{48}H_{41}IrN_7S_2]^+$ m/z calculated: 872.2176. Found: 872.2202 [M+].

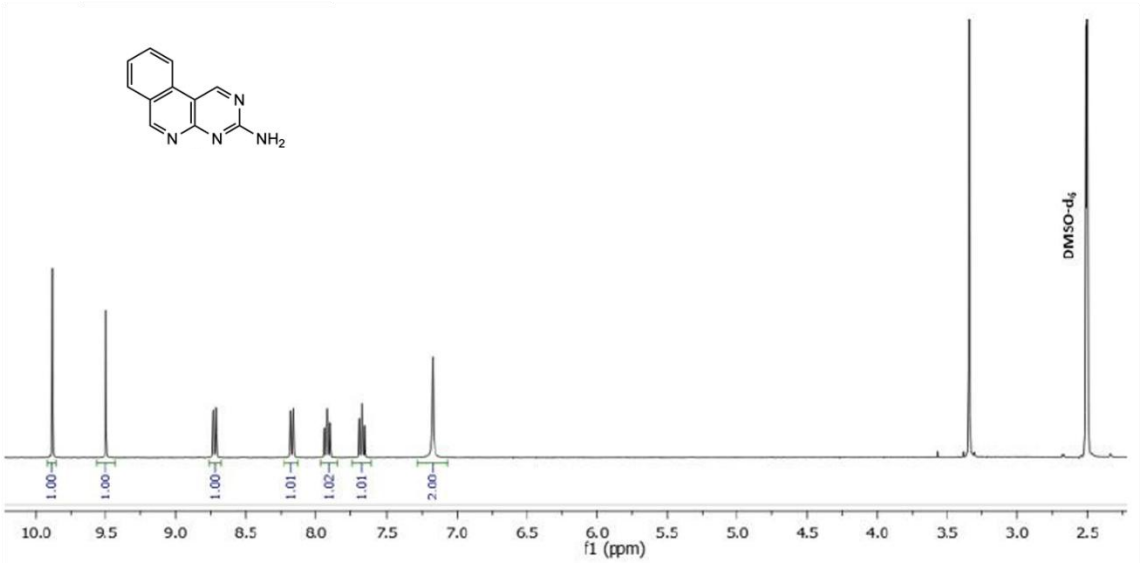


Figure A.3.7 ^{1}H NMR spectrum of compound **3.5**, DMSO-d_6, 400 MHz, 298 K.

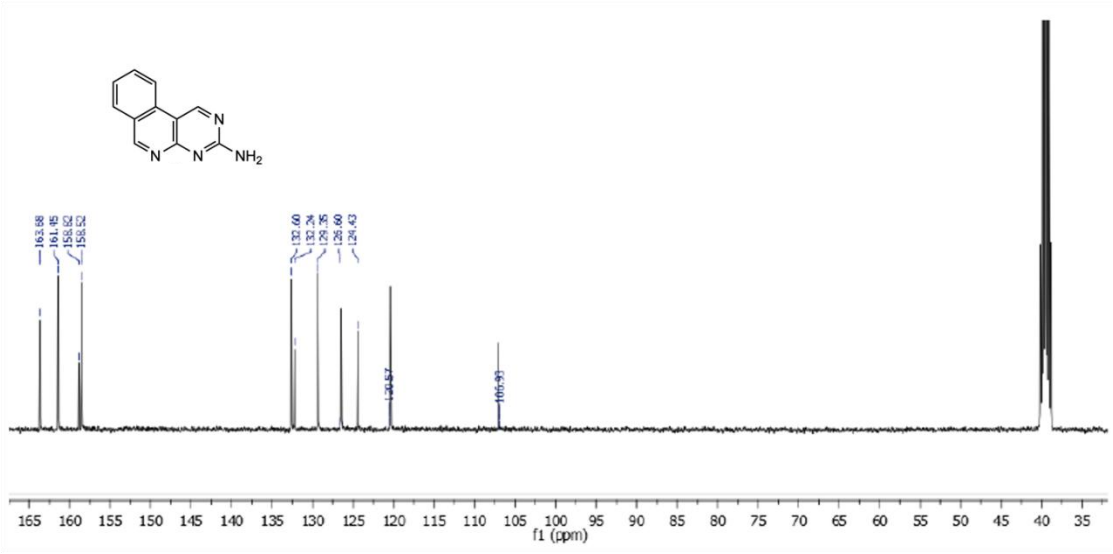


Figure A.3.8 ^{13}C NMR spectrum of compound **3.5**, DMSO-d_6, 101 MHz, 298 K.

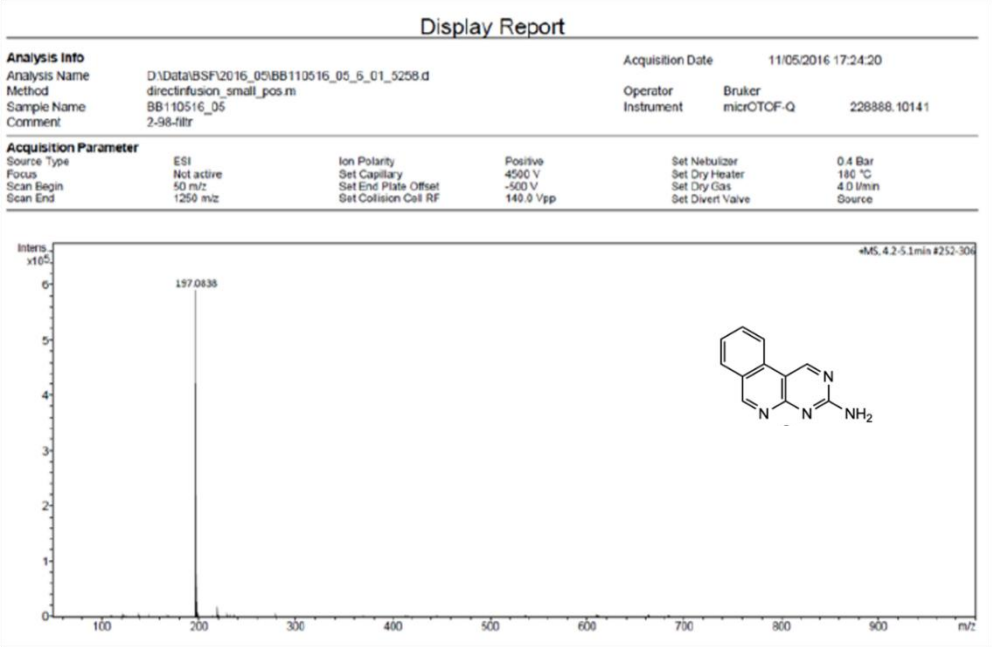


Figure A.3.9 Mass spectrum for compound **3.5**. LMRS [ESI+] ion $[C_{11}H_8N_4]^+$

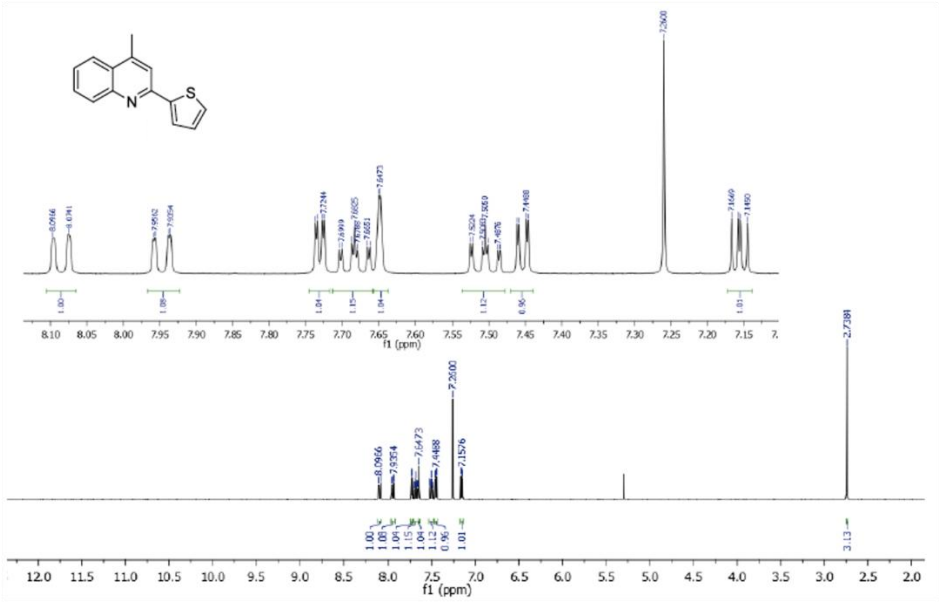


Figure A.3.10 ^{1}H NMR spectrum of compound **3.7** with inset ^{1}H NMR spectrum expanded into aromatic region, $CDCl_3$, 400 MHz, 298 K.

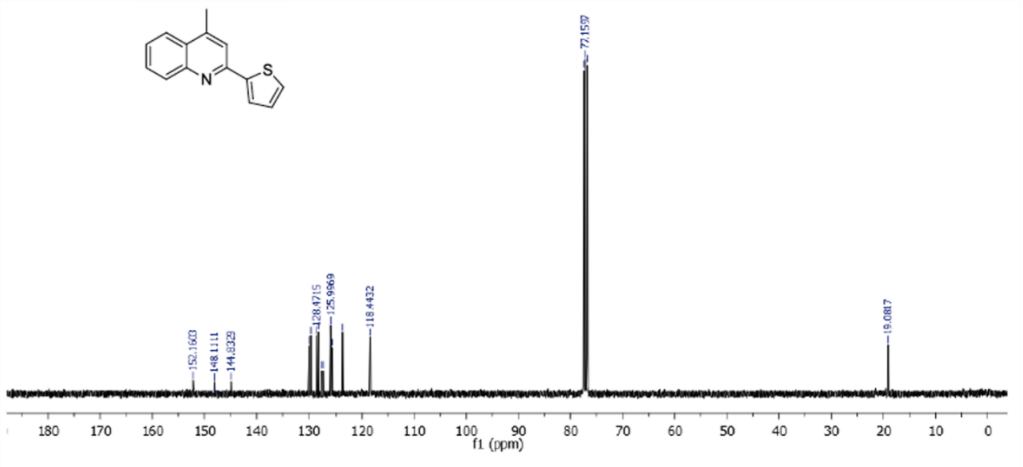


Figure A.3.11 ^{13}C NMR spectrum of compound **3.7**, $CDCl_3$, 101 MHz, 298 K.

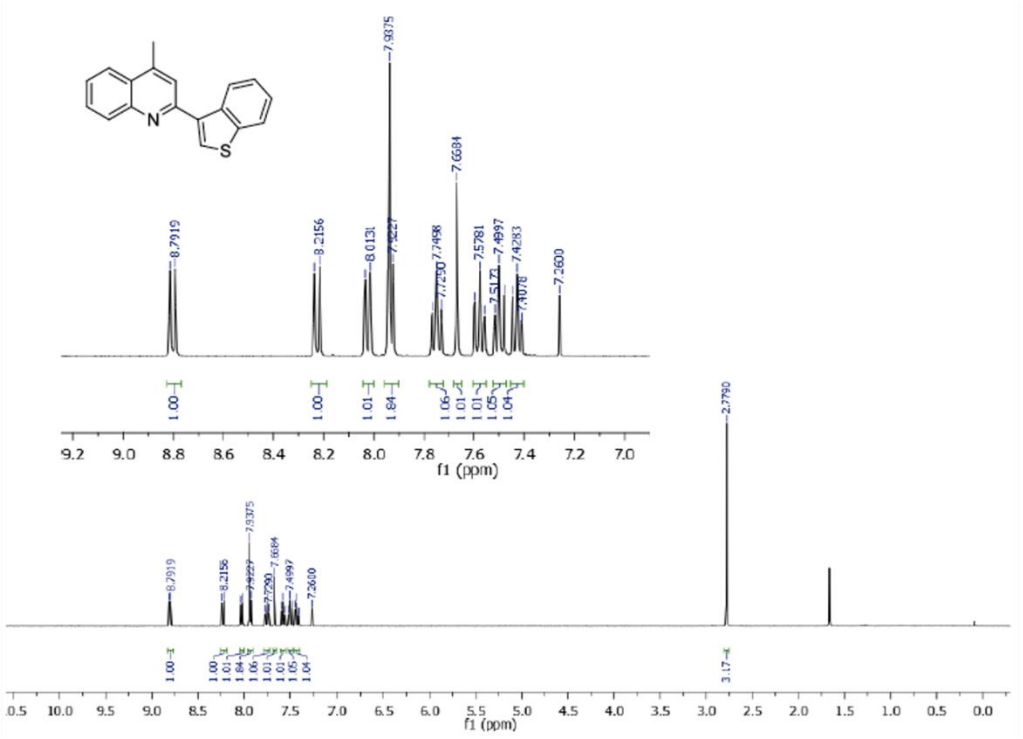


Figure A.3.12 ^{1}H NMR spectrum of compound **3.8** with inset ^{1}H NMR spectrum expanded into aromatic region, $CDCl_3$, 400 MHz, 298 K.

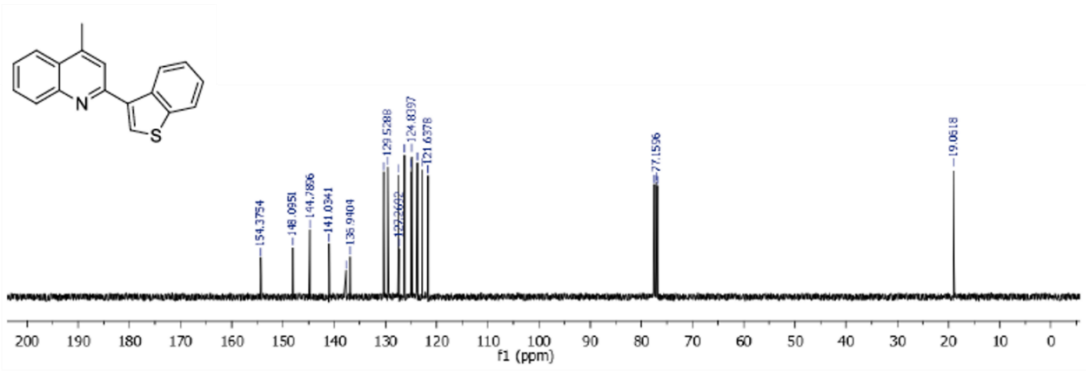


Figure A.3.13 ^{13}C NMR spectrum of compound **3.8**, $CDCl_3$, 101 MHz, 298 K.

A3.3: UV-vis, Excitation and Emission Data

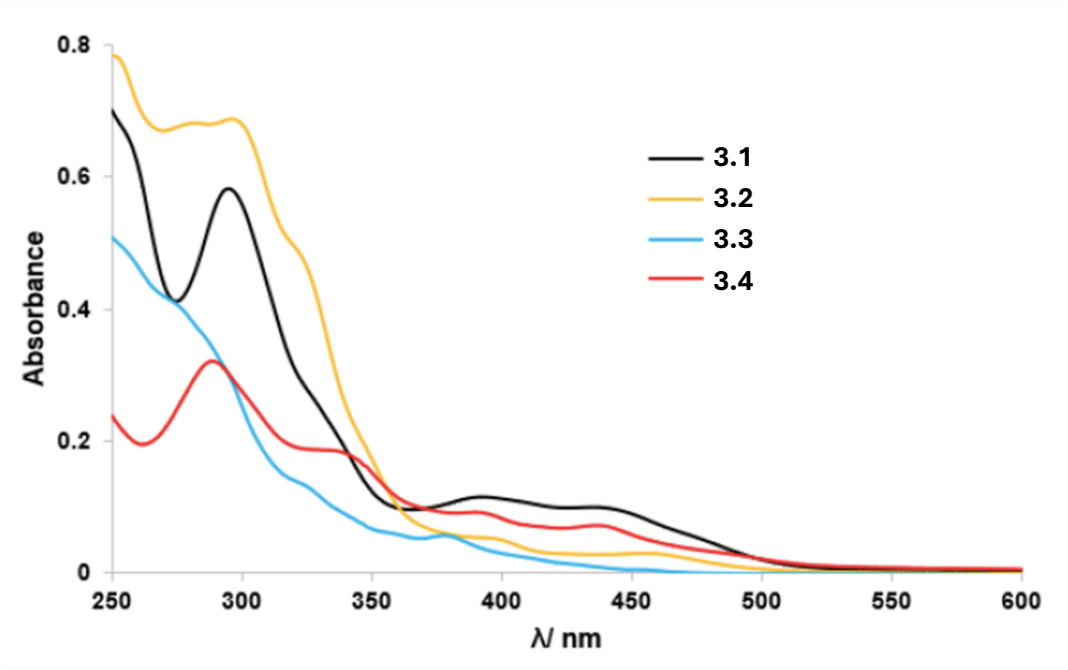


Figure A.3.14 UV-vis absorption spectra of complexes **3.1** (blue line), **3.2** (yellow line), **3.3** (black line) and **3.4** (red line) in $CHCl_3$, c = 1×10^{-5} M.

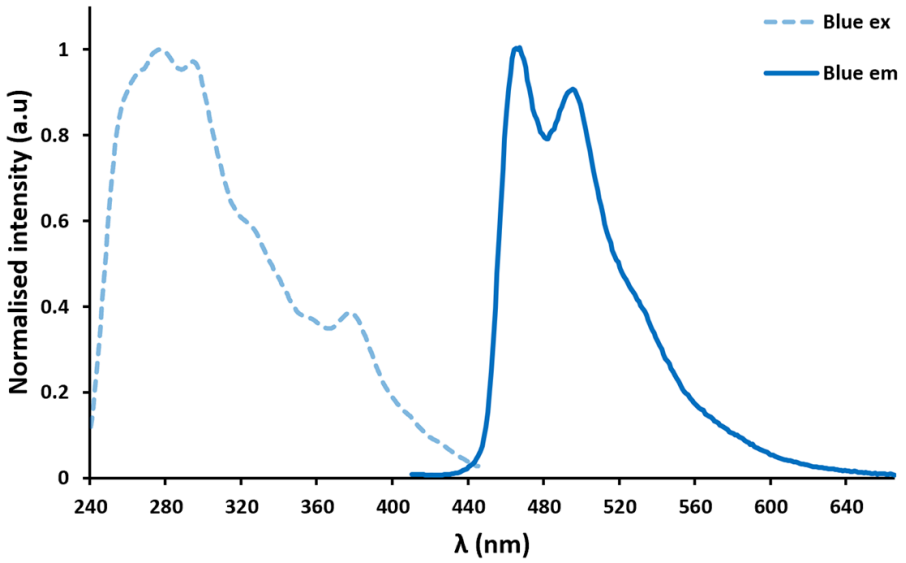


Figure A.3.15 Normalised emission and excitation spectra of iridium complex **3.1** (c = 1×10^{-5} M) measured in $CHCl_3$ solution.

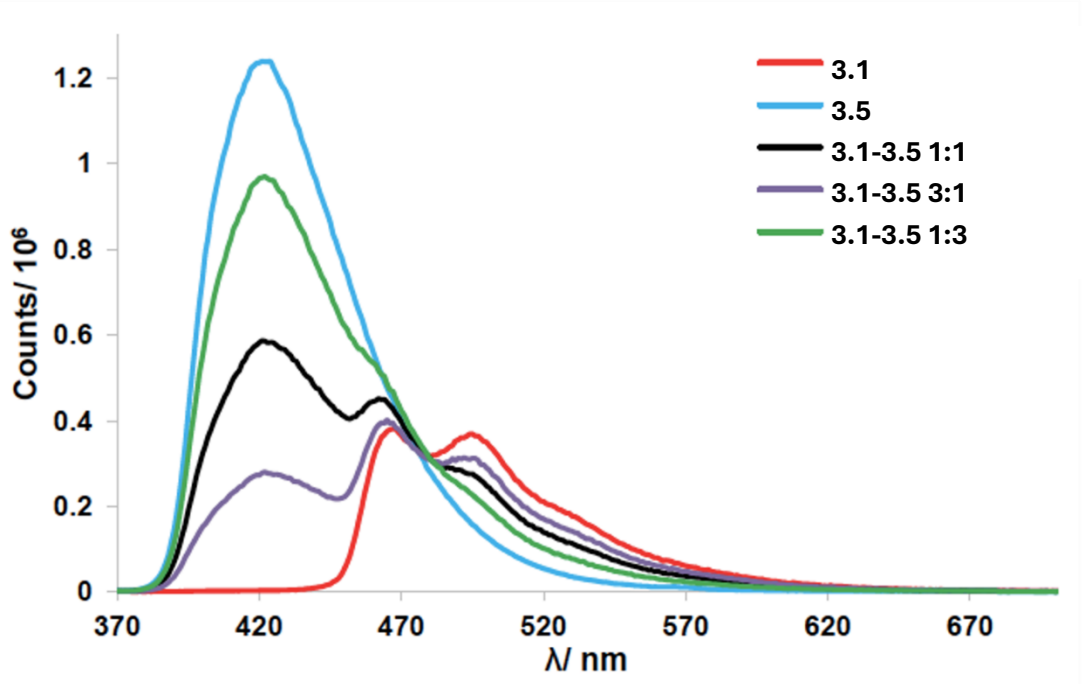


Figure A.3.16 Emission spectra from studies of complex **3.1** with additions of compound **3.5** measured in $CHCl_3$ solution. All samples excited at 350 nm.

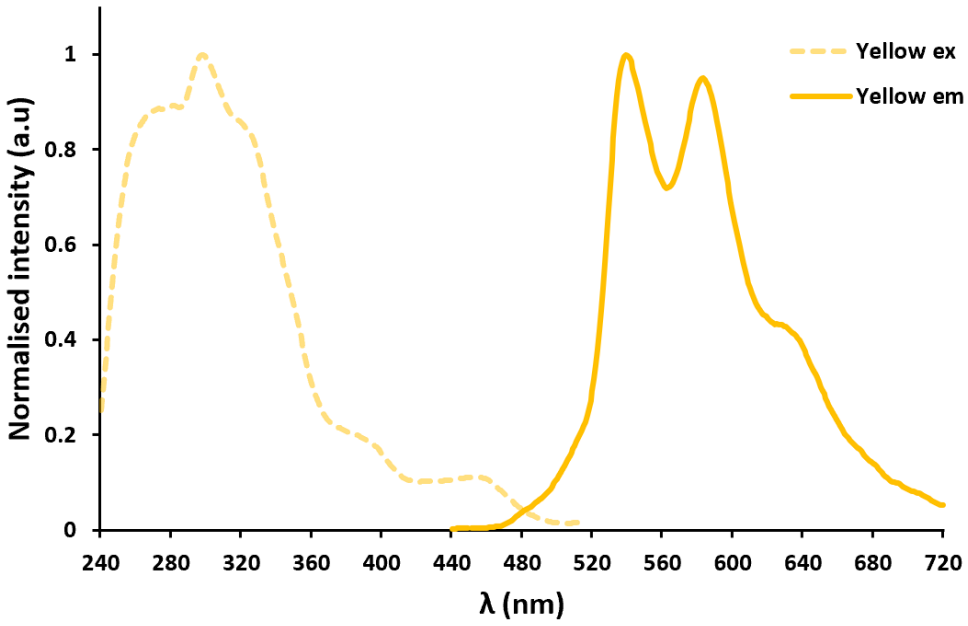


Figure A.3.17 Normalised emission and excitation spectra of iridium complex **3.2** (c = 1×10^{-5} M) measured in $CHCl_3$ solution.

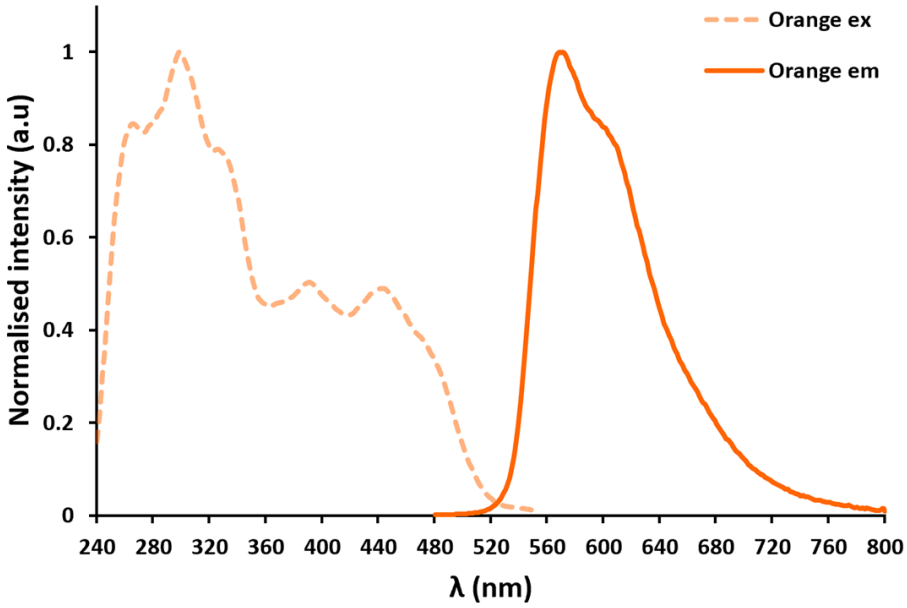


Figure A.3.18 Normalised emission and excitation spectra of iridium complex **3.3** (c = 1×10^{-5} M) measured in $CHCl_3$ solution.

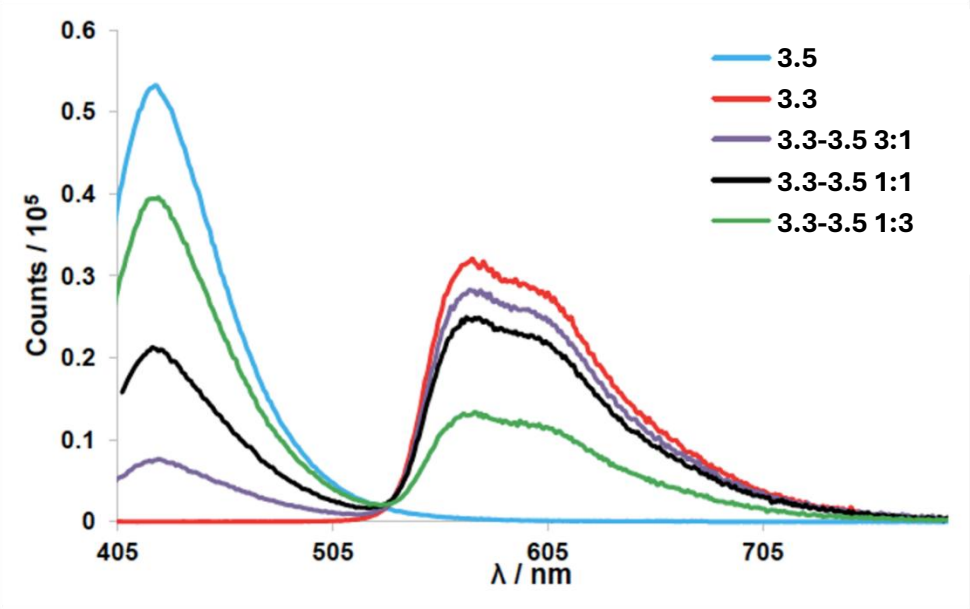


Figure A.3.19 Emission spectra from studies of complex **3.3** with additions of compound **3.5** measured in $CHCl_3$ solution. All samples excited at 350 nm.

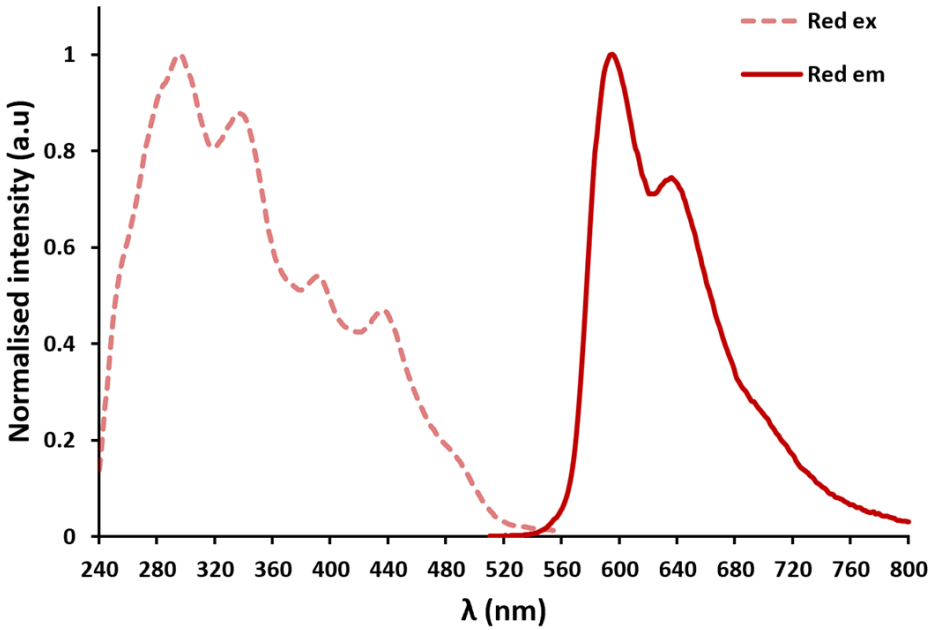


Figure A.3.20 Normalised emission and excitation spectra of iridium complex **3.4** (c = 1×10^{-5} M) measured in $CHCl_3$ solution.

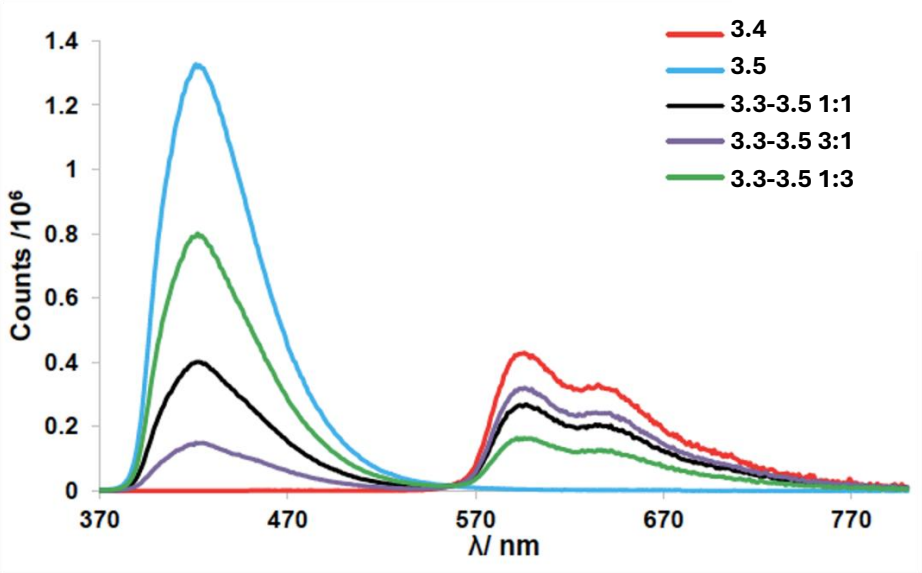


Figure A.3.21 Emission spectra from studies of complex **3.4** with additions of compound **3.5** measured in $CHCl_3$ solution. All samples excited at 360 nm.

A3.4: K_a Binding Studies

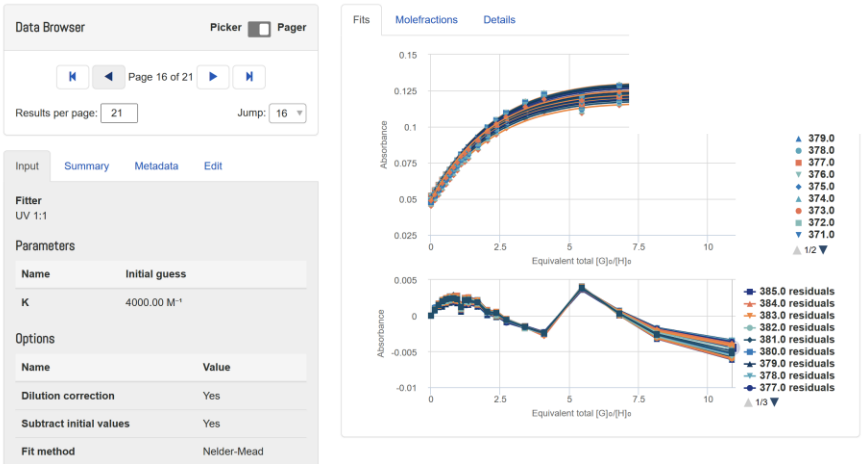


Figure A.3.22 Screengrab of linear regression bindfit calculation data of co-system **3.1•3.5**. Links to open-source calculations of titration runs presented below.

1: http://app.supramolecular.org/bindfit/view/6ff69500-3339-4738-9efd-23f07acd5d88

2: http://app.supramolecular.org/bindfit/view/89e37f52-eea5-43b1-8af7-c9bf5eba4444

3: http://app.supramolecular.org/bindfit/view/c55ba47e-2dc6-4f59-9c9b-fab6a62341fd

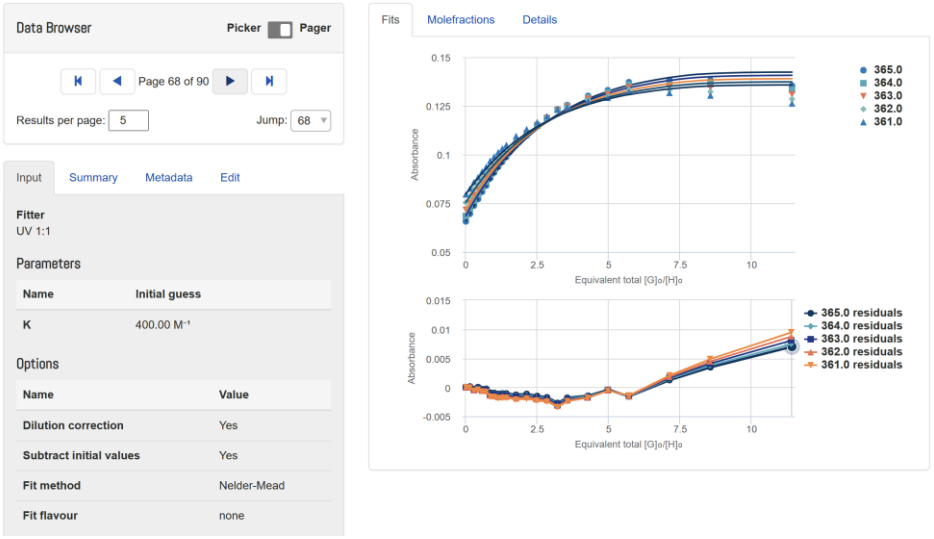


Figure A.3.23 Screengrab of linear regression bindfit calculation data of co-system **3.2•3.5**. Links to open-source calculations of titration runs presented below.

1: http://app.supramolecular.org/bindfit/view/392ca8d9-acb3-474b-af2c-86083be9da51

2: http://app.supramolecular.org/bindfit/view/6b743661-c2e6-404b-a8b9-cf56a2b4afde

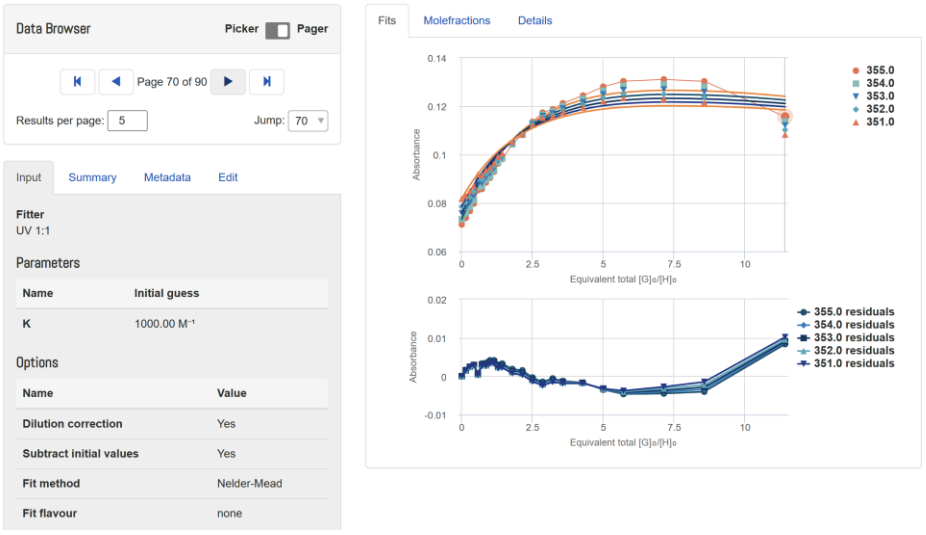


Figure A.3.24 Screengrab of linear regression bindfit calculation data of co-system **3.3•3.5**. Links to open-source calculations of titration runs presented below.

1: http://app.supramolecular.org/bindfit/view/ee837607-e4fb-4ad8-b225-3b3304dbbf66

2: http://app.supramolecular.org/bindfit/view/8c71c12c-8169-433c-b70f-168e0cdb444f

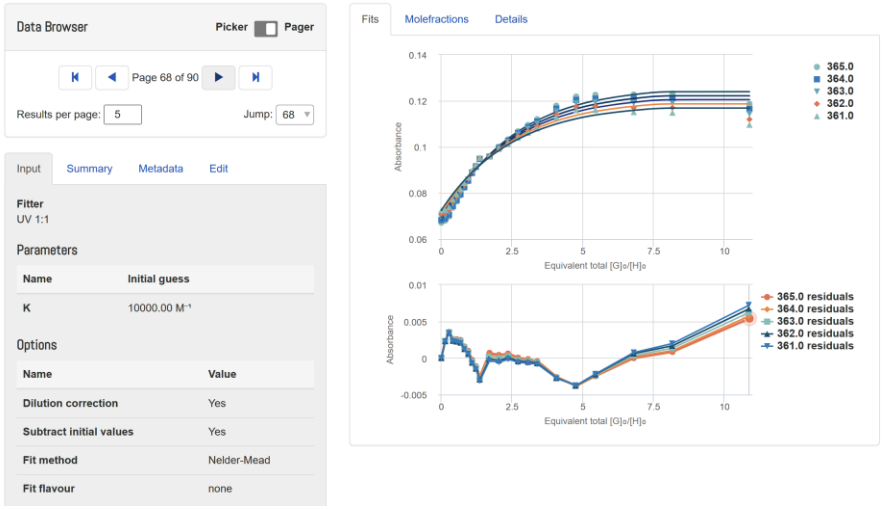


Figure A.3.25 Screengrab of linear regression bindfit calculation data of co-system **3.4•3.5**. Links to open-source calculations of titration runs presented below.

1: http://app.supramolecular.org/bindfit/view/f065cb38-22f6-49af-9fdf-05343806e3b9

2: http://app.supramolecular.org/bindfit/view/39e932ce-5180-4a64-b925-cb0ea5f36c70

3: http://app.supramolecular.org/bindfit/view/715e6a14-22b3-4f98-8c13-8129e238e812

A3.5: PLQYs and Decay Lifetimes

Decay Lifetime Measurement of Ir(III) complex 3.1

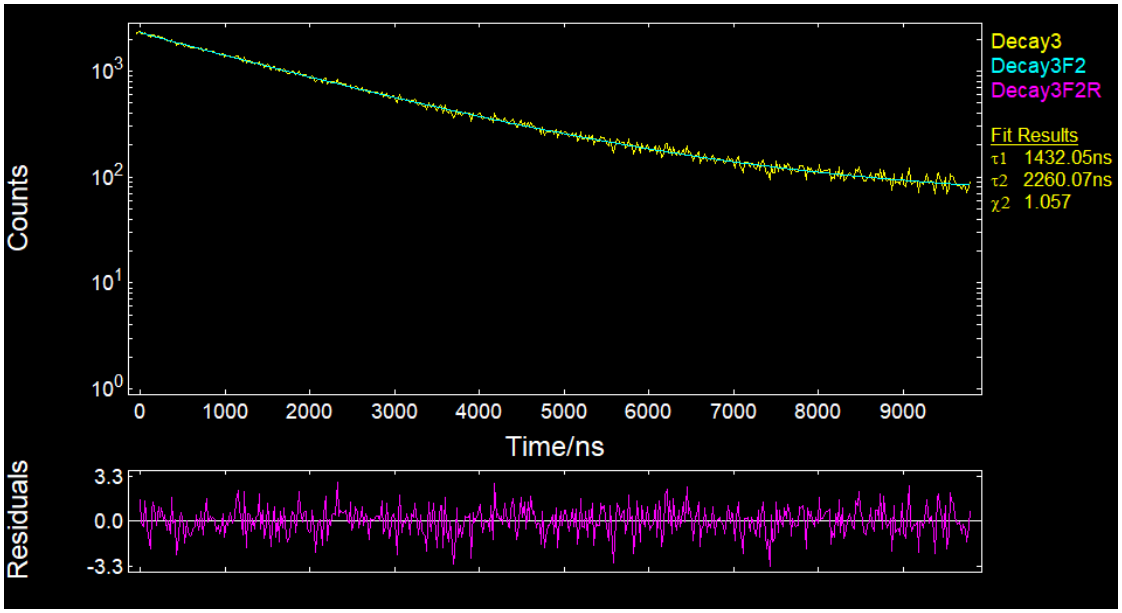


Figure A.3.26 Biexponential lifetime decay of Ir(III) complex **3.1**, ~$1 \cdot 10^{-5}$ M (Absorbance of 0.065 from UV-Vis) in $CHCl_3$ degassed for 20 mins (Ar) at 298 K after excitation at 365 nm. Data collected at λ_{max} = 470 nm.

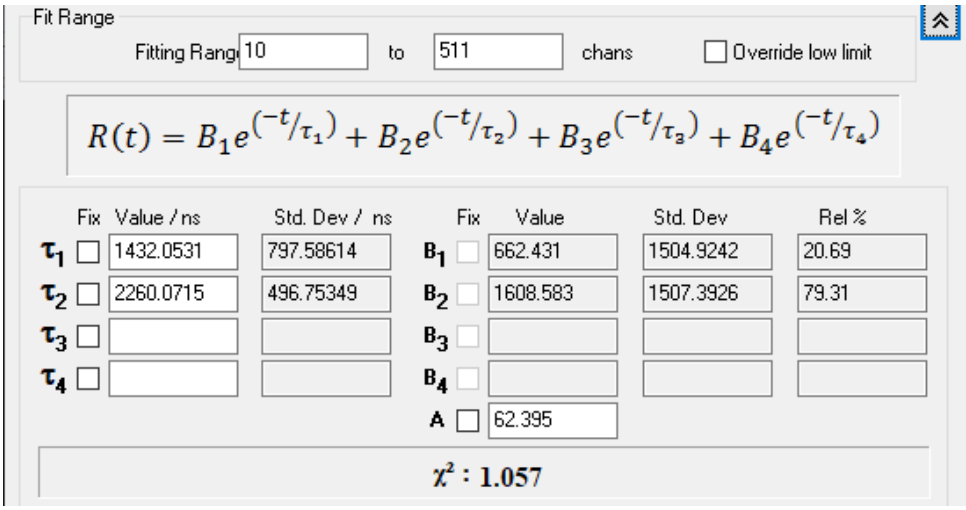


Figure A.3.27 Fit result of Ir(III) complex **3.1**, ~$1 \cdot 10^{-5}$ M (Absorbance of 0.065 from UV-Vis) in $CHCl_3$ degassed for 20 mins (Ar) at 298 K after excitation at 365 nm. Data collected at λ_{max} = 470 nm.

Decay Lifetime Measurement of Ir(III) complex 3.2

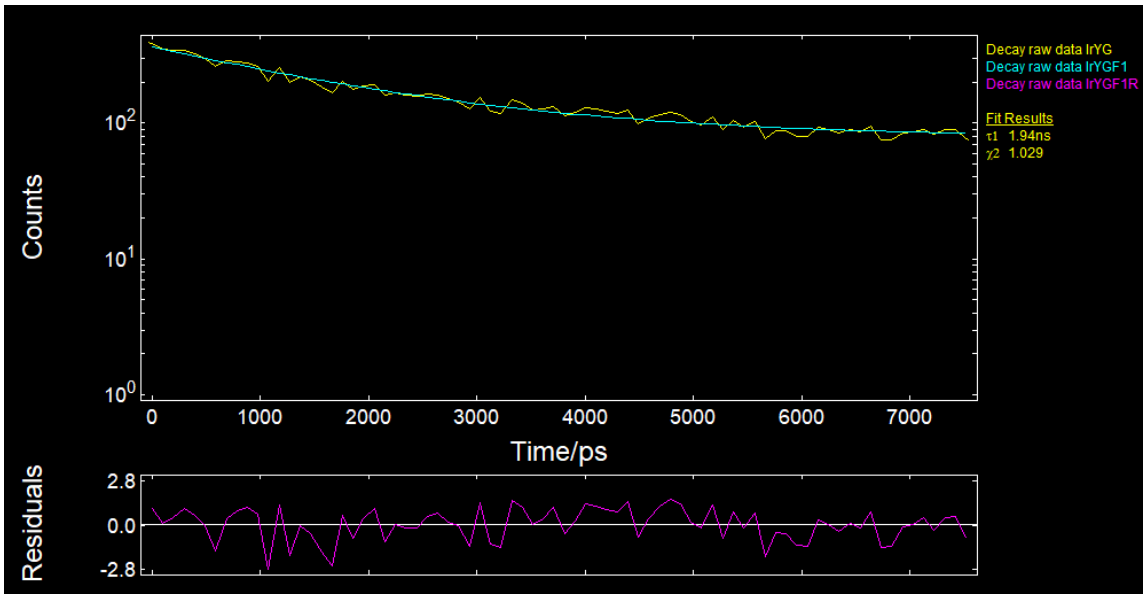


Figure A.3.28 Monoexponential lifetime decay of Ir(III) complex **3.2**, ~$1 \cdot 10^{-5}$ M (Absorbance of 0.081 from UV-Vis) in $CHCl_3$ degassed for 20 mins (Ar) at 298 K after excitation at 365 nm. Data collected at λ_{max} = 540 nm.

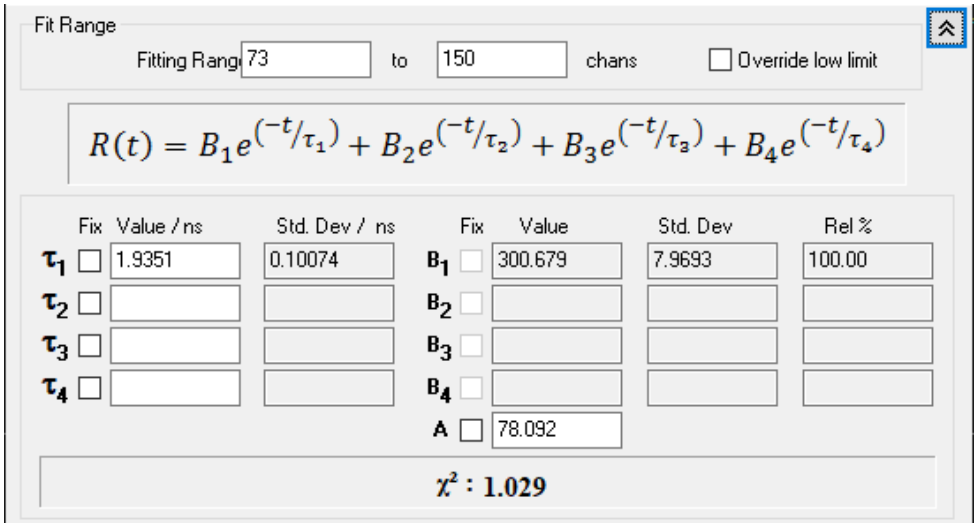


Figure A.3.29 Fit result of Ir(III) complex **3.2**, ~$1 \cdot 10^{-5}$ M (Absorbance of 0.081 from UV-Vis) in $CHCl_3$ degassed for 20 mins (Ar) at 298 K after excitation at 365 nm. Data collected at λ_{max} = 540 nm.

Decay Lifetime Measurement of Ir(III) complex 3.3

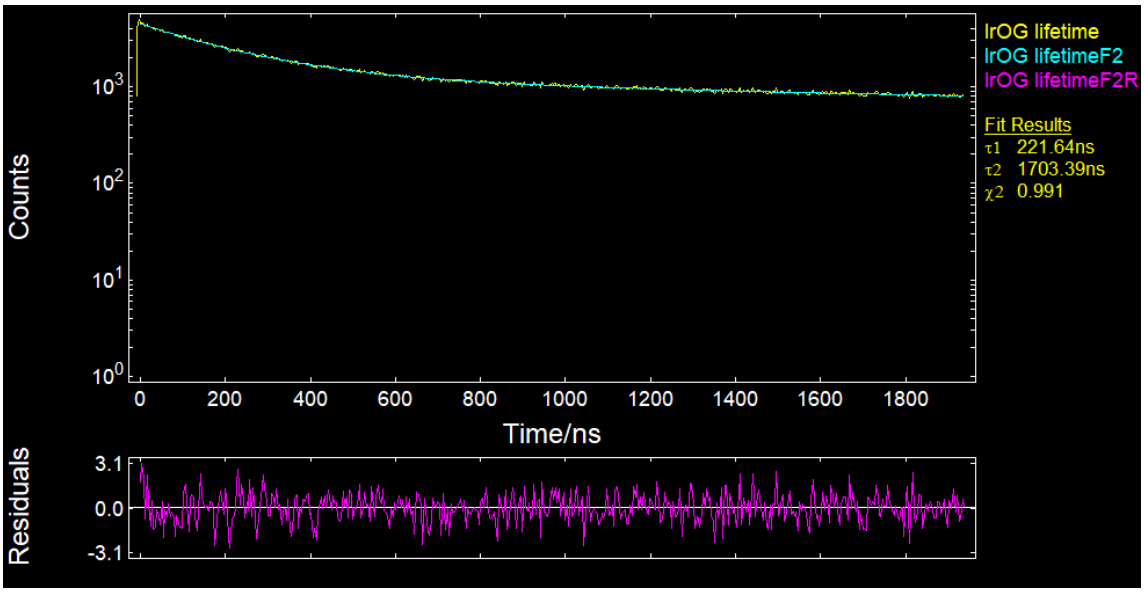


Figure A.3.30 Biexponential lifetime decay of Ir(III) complex **3.3,** ~$1 \cdot 10^{-6}$ M (Absorbance of 0.079 from UV-Vis) in $CHCl_3$ degassed for 20 mins (Ar) at 298 K after excitation at 365 nm. Data collected at λ_{max} = 570 nm.

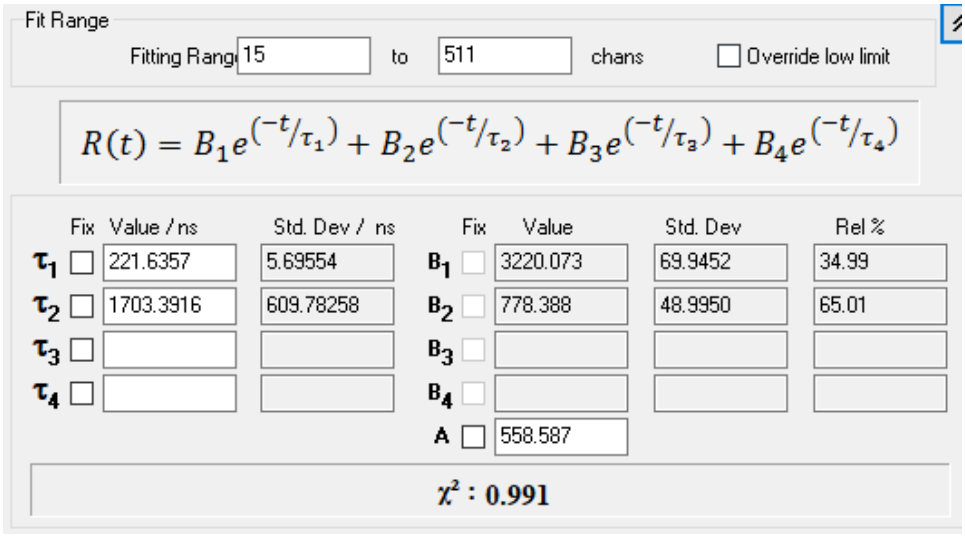


Figure A.3.31 Fit result of Ir(III) complex **3.3**, ~$1 \cdot 10^{-6}$ M (Absorbance of 0.079 from UV-Vis) in $CHCl_3$ degassed for 20 mins (Ar) at 298 K after excitation at 365 nm. Data collected at λ_{max} = 570 nm.

Decay Lifetime Measurement of Ir(III) complex 3.4

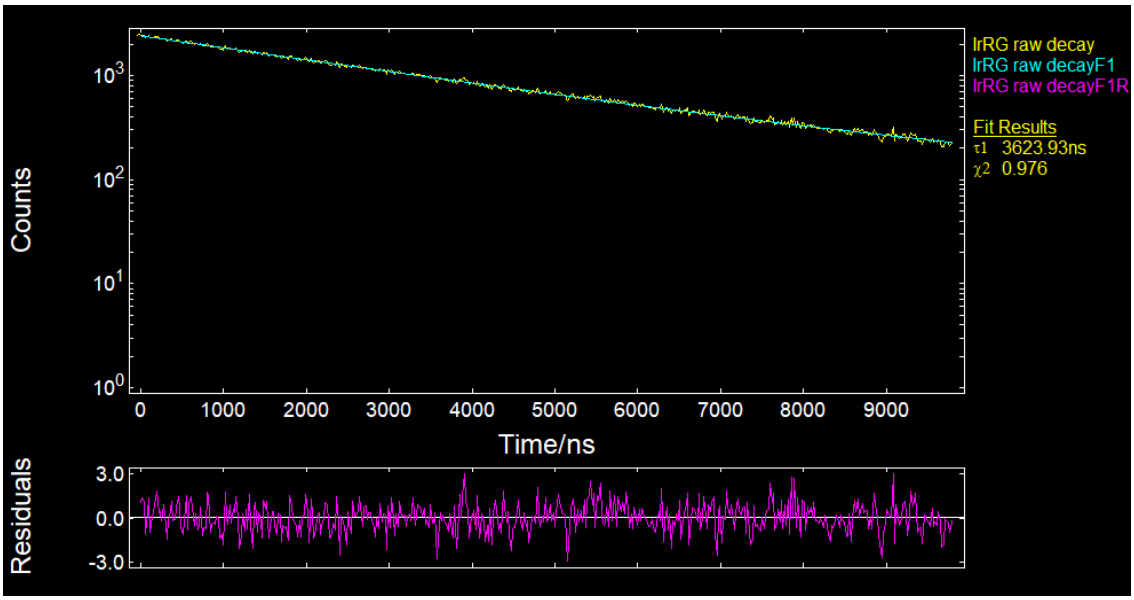


Figure A.3.32 Monoexponential lifetime decay of Ir(III) complex **3.4,** ~$1 \cdot 10^{-6}$ M (Absorbance of 0.076 from UV-Vis) in $CHCl_3$ degassed for 20 mins (Ar) at 298 K after excitation at 365 nm. Data collected at λ_{max} = 590 nm.

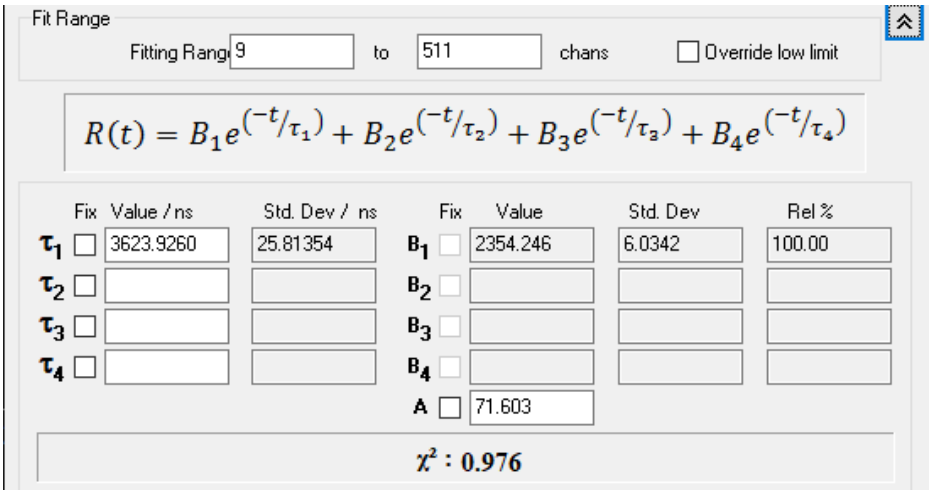


Figure A.3.33 Fit result of Ir(III) complex **3.4**, ~$1 \cdot 10^{-6}$ M (Absorbance of 0.076 from UV-Vis) in $CHCl_3$ degassed for 20 mins (Ar) at 298 K after excitation at 365 nm. Data collected at λ_{max} = 590 nm.

Decay Lifetime Measurement of Ir(III) complex 3.1•3.5

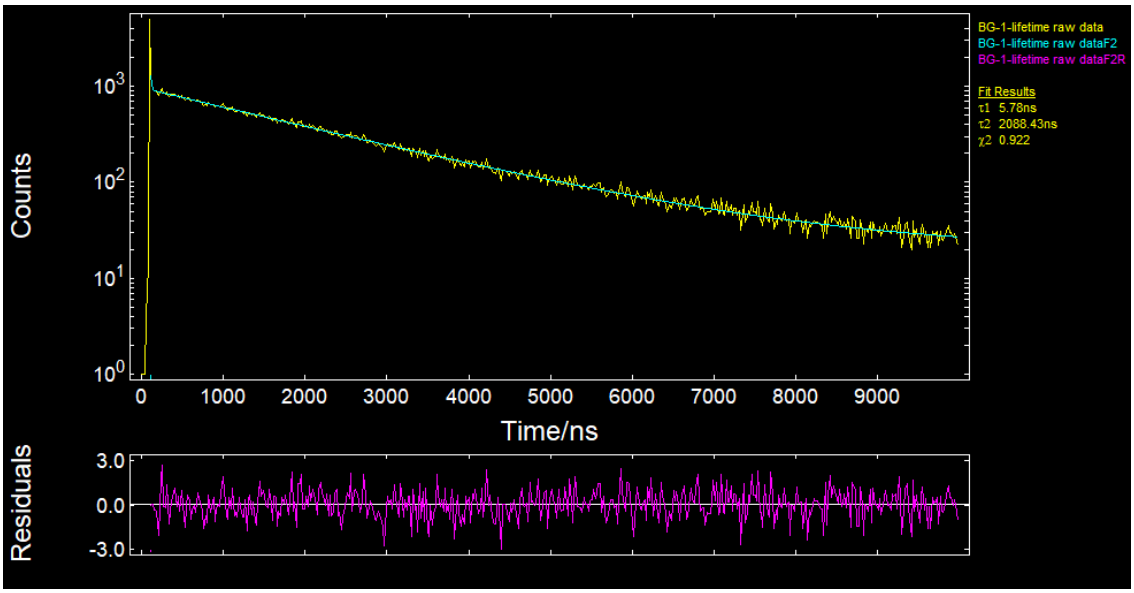


Figure A.3.34 Biexponential lifetime decay of Ir(III) complex **3.1•3.5,** (1:1) ~$1 \cdot 10^{-5}$ M (Absorbance of 0.071 from UV-Vis) in $CHCl_3$ degassed for 20 mins (Ar) at 298 K after excitation at 365 nm. Data collected at λ_{max} = 470 nm.

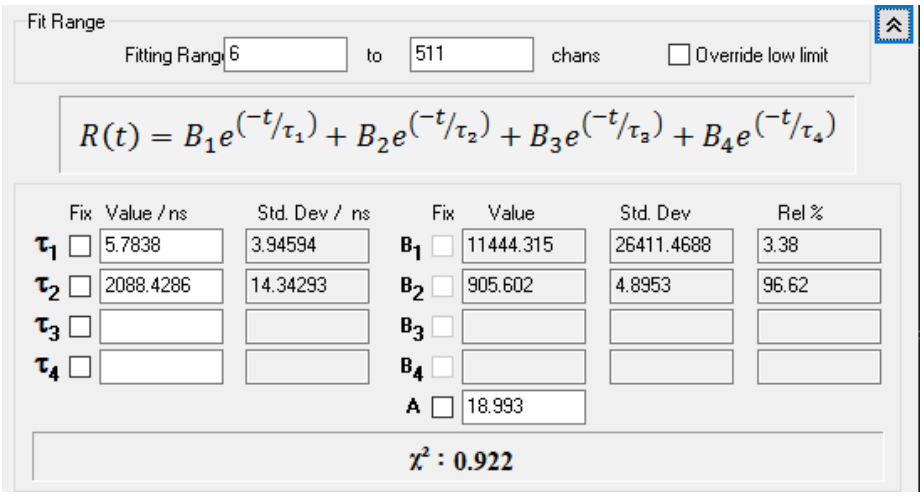


Figure A.3.35 Fit result of Ir(III) complex **3.1•3.5,** (1:1) ~$1 \cdot 10^{-5}$ M (Absorbance of 0.071 from UV-Vis) in $CHCl_3$ degassed for 20 mins (Ar) at 298 K after excitation at 365 nm. Data collected at λ_{max} = 470 nm.

Decay Lifetime Measurement of Ir(III) complex 3.2•3.5

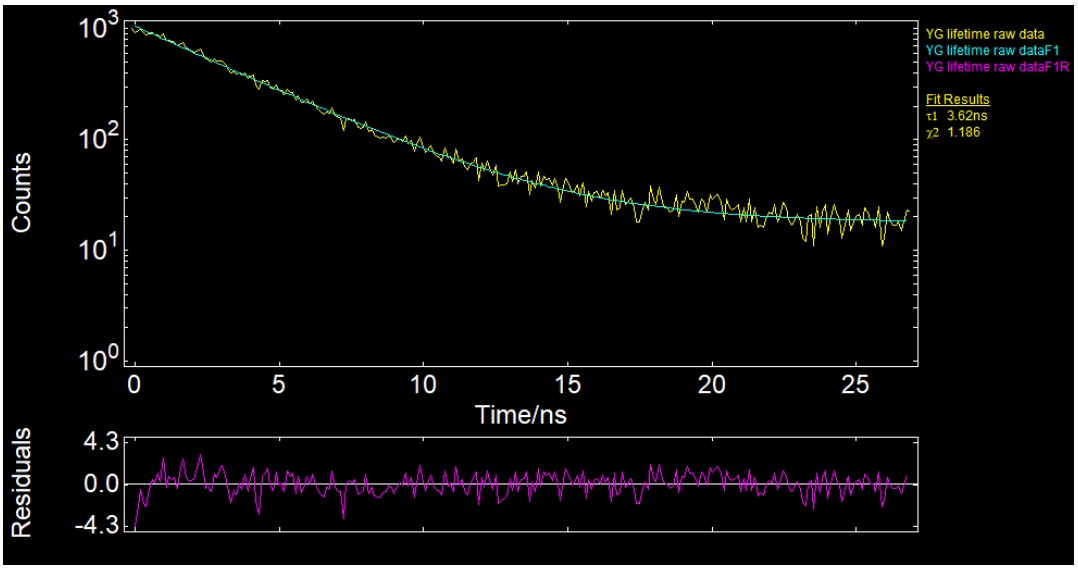


Figure A.3.36 Monoexponential lifetime decay of Ir(III) complex **3.2•3.5,** (1:1) ~$1 \cdot 10^{-5}$ M (Absorbance of 0.085 from UV-Vis) in $CHCl_3$ degassed for 20 mins (Ar) at 298 K after excitation at 365 nm. Data collected at λ_{max} = 540 nm.

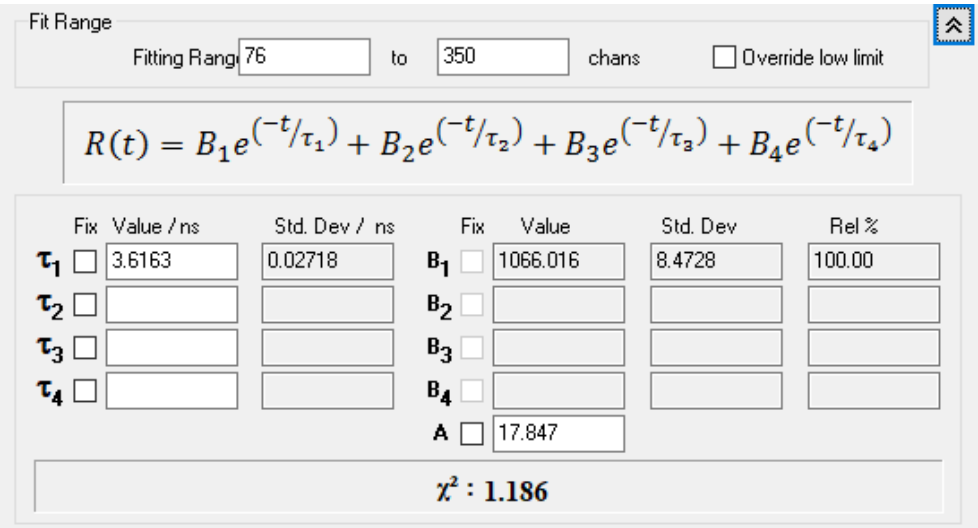


Figure A.3.37 Fit result of Ir(III) complex **3.2•3.5,** (1:1) ~$1 \cdot 10^{-5}$ M (Absorbance of 0.085 from UV-Vis) in $CHCl_3$ degassed for 20 mins (Ar) at 298 K after excitation at 365 nm. Data collected at λ_{max} = 540 nm.

Decay Lifetime Measurement of Ir(III) complex 3.3•3.5

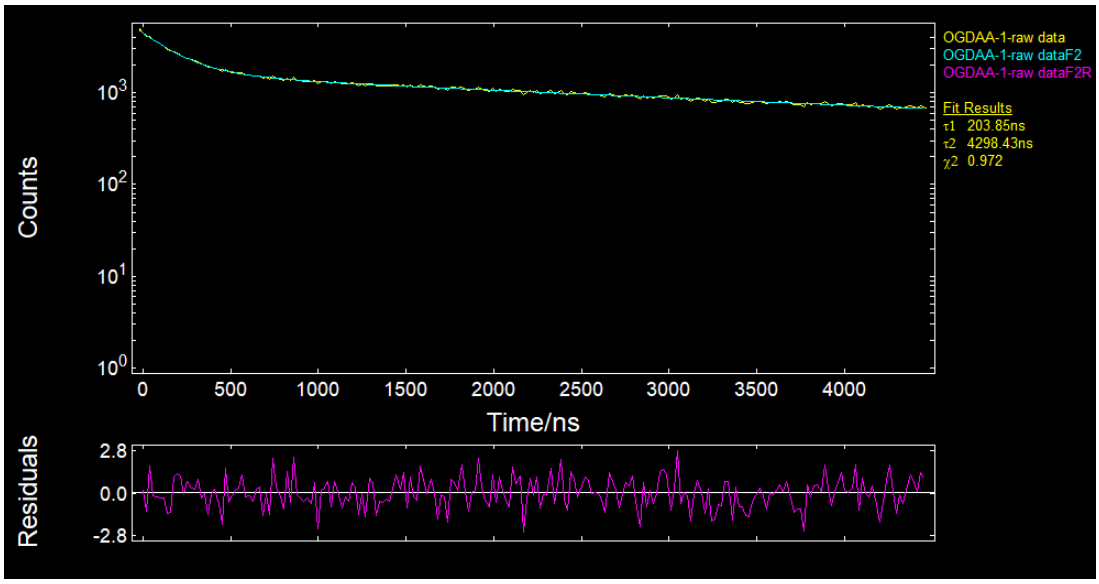


Figure A.3.38 Biexponential lifetime decay of Ir(III) complex **3.3•3.5,** (1:1) ~$1 \cdot 10^{-6}$ M (Absorbance of 0.080 from UV-Vis) in $CHCl_3$ degassed for 20 mins (Ar) at 298 K after excitation at 365 nm. Data collected at λ_{max} = 570 nm.

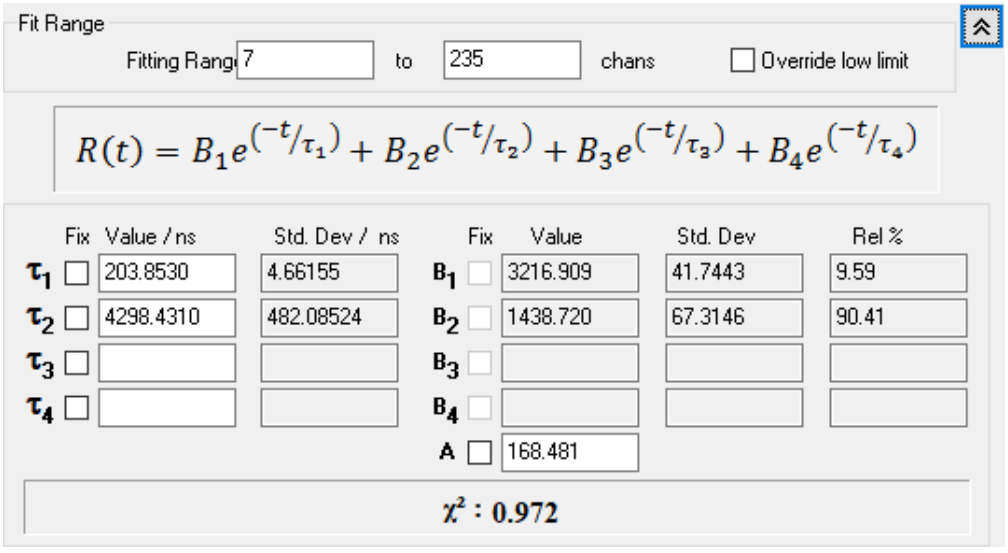


Figure A.3.39 Fit result of Ir(III) complex **3.3•3.5,** (1:1) ~$1 \cdot 10^{-6}$ M (Absorbance of 0.080 from UV-Vis) in $CHCl_3$ degassed for 20 mins (Ar) at 298 K after excitation at 365 nm. Data collected at λ_{max} = 570 nm.

Decay Lifetime Measurement of Ir(III) complex 3.4•3.5

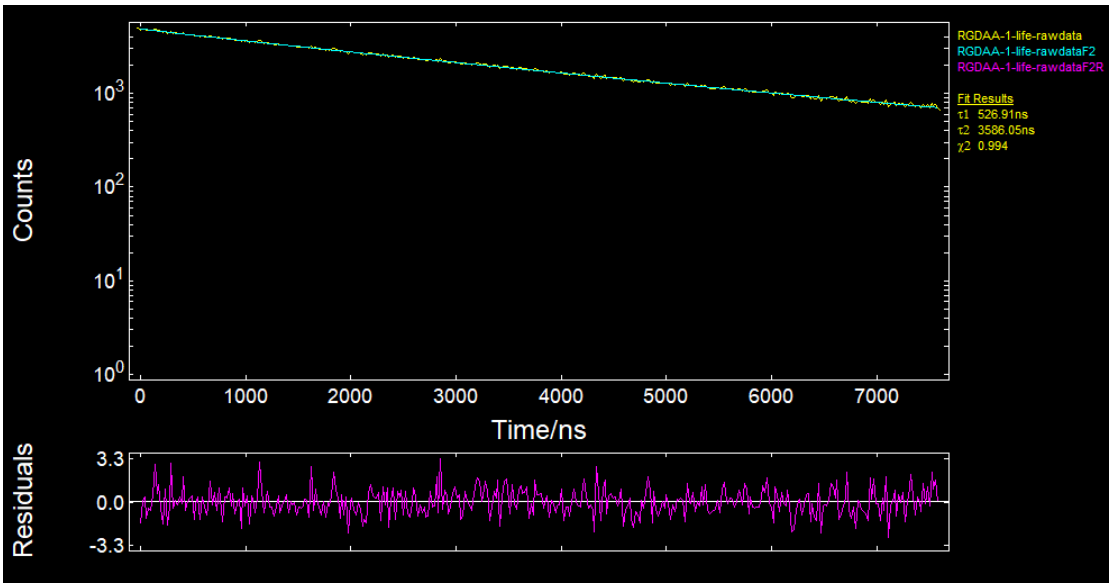


Figure A.3.40 Biexponential lifetime decay of Ir(III) complex **3.4•3.5,** (1:1) ~$1 \cdot 10^{-6}$ M (Absorbance of 0.085 from UV-Vis) in $CHCl_3$ degassed for 20 mins (Ar) at 298 K after excitation at 365 nm. Data collected at λ_{max} = 590 nm.

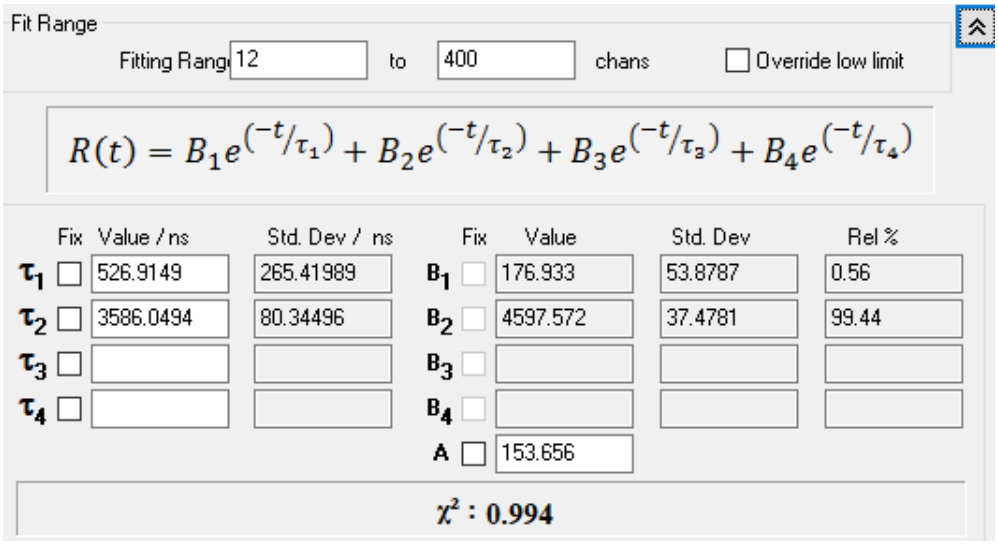


Figure A.3.41 Fit result of Ir(III) complex **3.4•3.5,** (1:1) ~$1 \cdot 10^{-6}$ M (Absorbance of 0.085 from UV-Vis) in $CHCl_3$ degassed for 20 mins (Ar) at 298 K after excitation at 365 nm. Data collected at λ_{max} = 590 nm.

Decay Lifetime Measurement of Ir(III) complex 3.2•3.5 (white light)

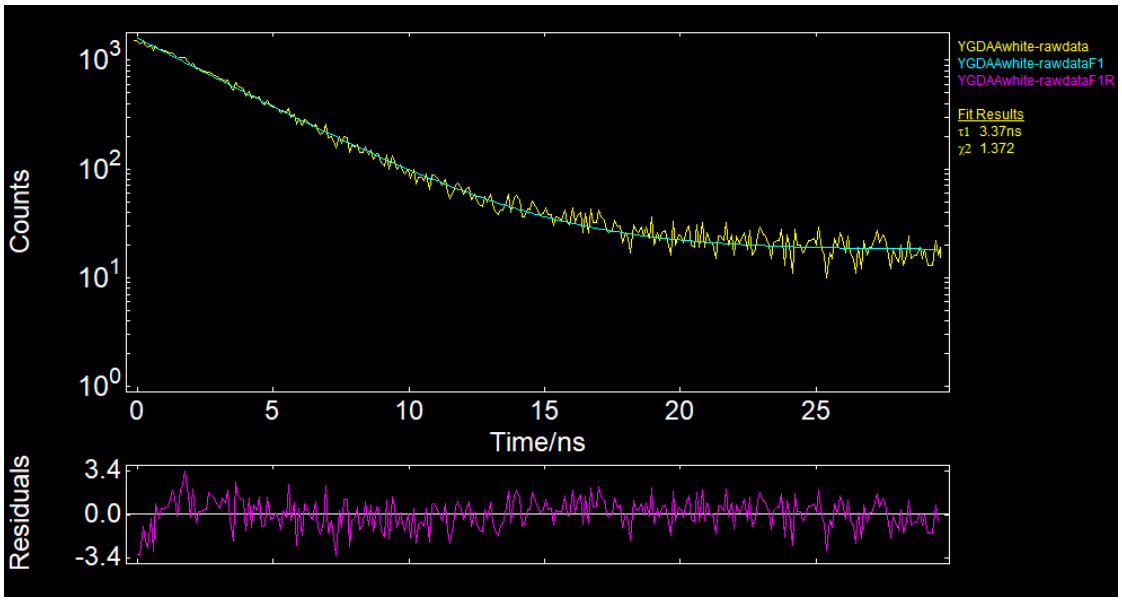


Figure A.3.42 Monoexponential lifetime decay of Ir(III) complex **3.2•3.5,** (1:1.3) ~$1 \cdot 10^{-5}$ M (Absorbance of 0.082 from UV-Vis) in $CHCl_3$ degassed for 20 mins (Ar) at 298 K after excitation at 365 nm. Data collected at λ_{max} = 540 nm.

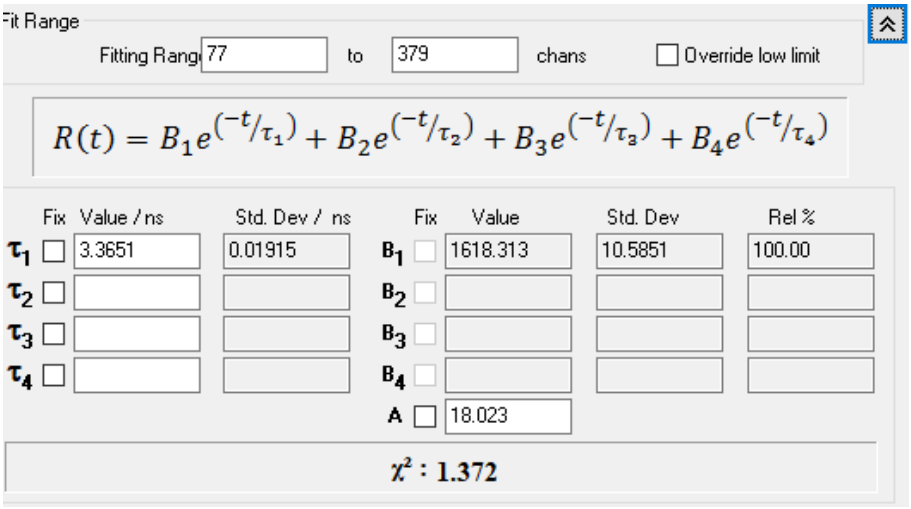


Figure A.3.43 Fit result of Ir(III) complex **3.2•3.5,** (1:1) ~$1 \cdot 10^{-5}$ M (Absorbance of 0.082 from UV-Vis) in $CHCl_3$ degassed for 20 mins (Ar) at 298 K after excitation at 365 nm. Data collected at λ_{max} = 540 nm.

A3.6: PMMA Solid State PLQYs and Decay Lifetimes

Table A.3.1 a) Significant excitation and emission peaks for Ir(III) complexes **3.1-3.4** in PMMA films at 298 K. **b)** PLQYs for Ir(III) complexes **3.1-3.4**; in PMMA film at 298 K determined using an SC-30 integrating sphere module. **c)** decay lifetimes using TCSPC excited at 365 nm and their corresponding chi-squared values for Ir(III) complexes **3.1-3.4**; in PMMA films at 298 K. All complexes decay biexponentially. **d)** the radiative (k_r) and nonradiative (k_{nr}) rate constants were calculated as $k_r = \phi_{PL}/\tau_{PL}$ and $k_{nr} = (1-\phi_{PL})/\tau_{PL}$.

Ir(III) Complex	Excitation (nm)[a]	Emission (nm)[a]	PLQY (%)[b]	Lifetime (ns) (τ_{PL}, χ^2)[c]	k_r ($\times 10^5$ s^{-1})[d]	k_{nr} ($\times 10^5$ s^{-1})[d]
1	250, 295	473, 495	91.3	(1932.14, 0.959) 92%	4.7	0.5
2	302, 328	540, 581	15.1	(0.5778, 1.199) 71.5%	2613.4	14693.7
3	298, 390	565, 597	70.1	(1155.79, 1.092) 95%	6.1	2.6
4	342, 440	595, 634	74.0	(3830.21, 0.979) 95%	1.9	0.7
1•5 (1:1)	261, 329	473, 497	83.4	(2079.96, 1.113) 86%	4.0	0.8
2•5 (1:1)	326, 456	537, 581	15.7	(3.2596, 1.114) 51%	481.7	2586.2
3•5 (1:1)	299, 388	561, 599	65.1	(4042.90, 1.079) 90%	1.6	0.9
4•5 (1:1)	340, 440	595, 693	71.3	(4177.25, 0.989) 80%	1.7	0.7

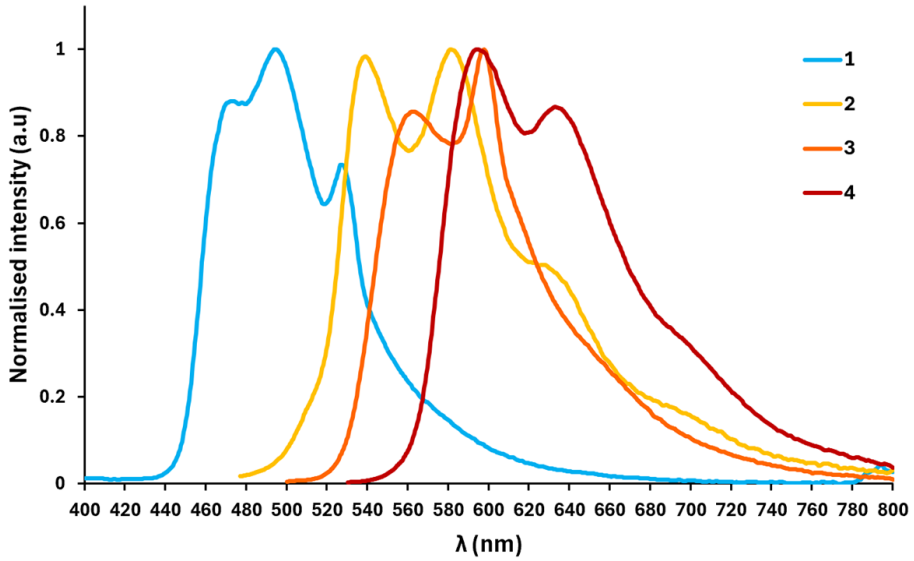


Figure A.3.44 Combined normalised emission spectra of complex **1-4** obtained through solid state excitation of PMMA thin films.

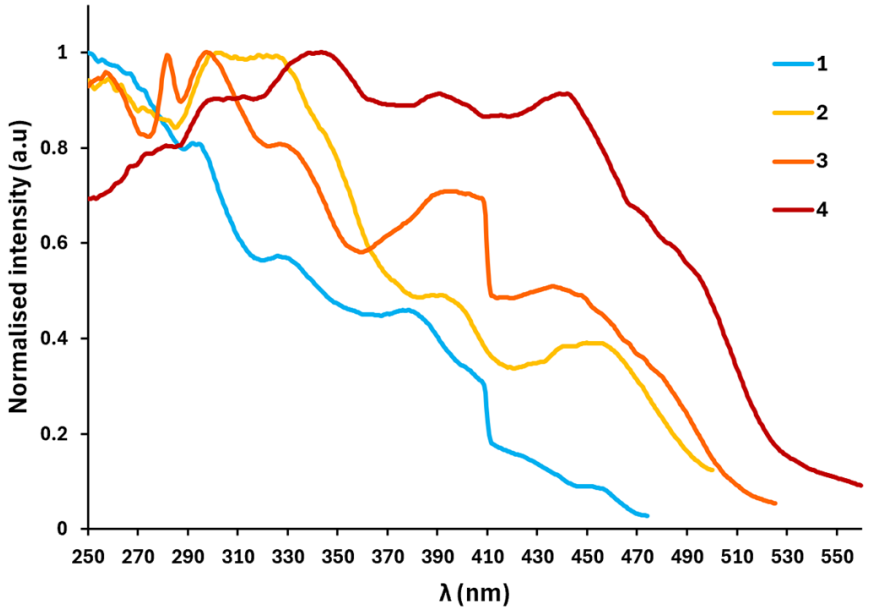


Figure A.3.45 Combined normalised absorption spectra of complex **1**-**4** obtained through solid state analysis of PMMA thin films.

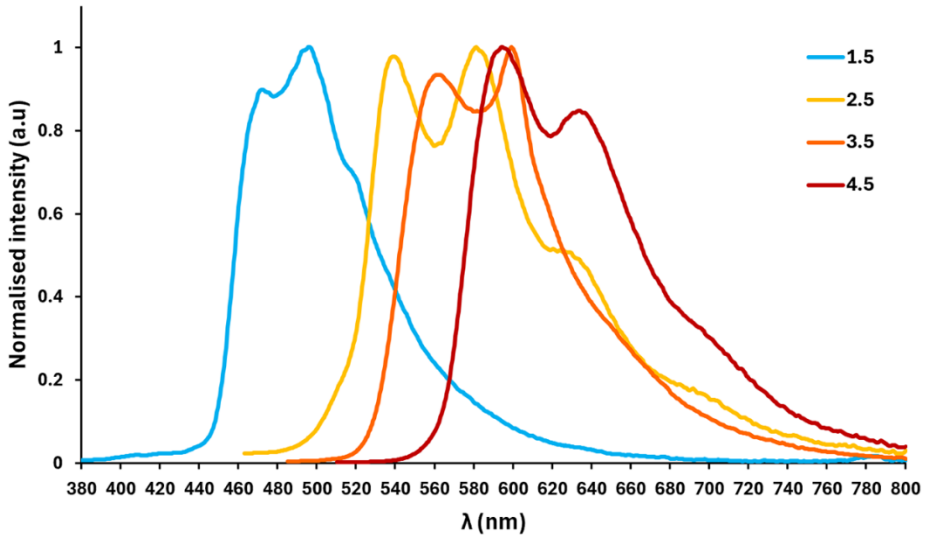


Figure A.3.46 Combined normalised emission spectra of co-complex **1**-**4•5** obtained through solid state excitation of PMMA thin films.

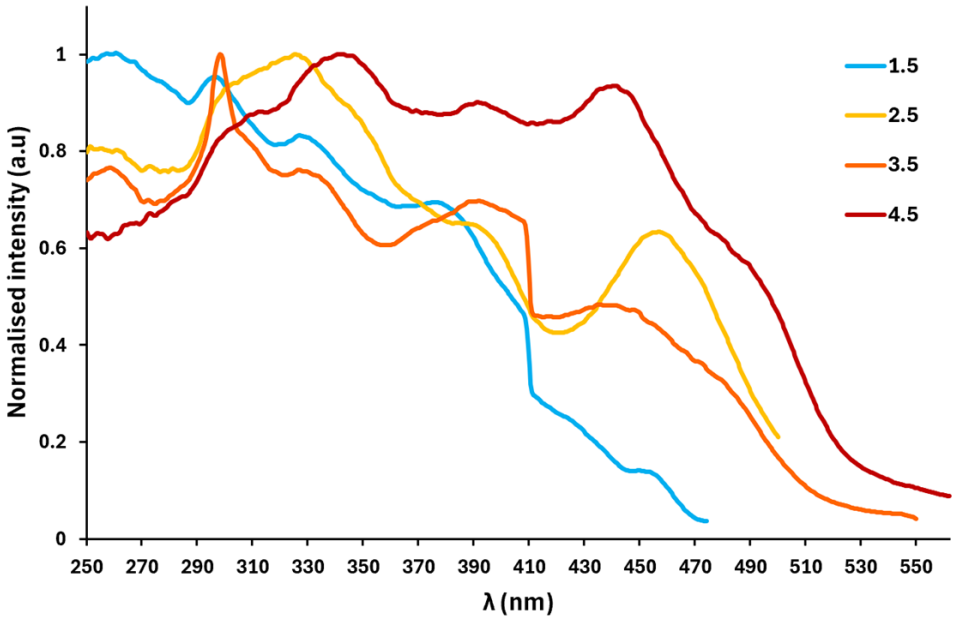


Figure A.3.47 Combined normalised absorption spectra of co-complex **1**-**4**•**5** obtained through solid state analysis of PMMA thin films.

Solid State Decay Lifetime Measurement of Ir(III) complex 3.1

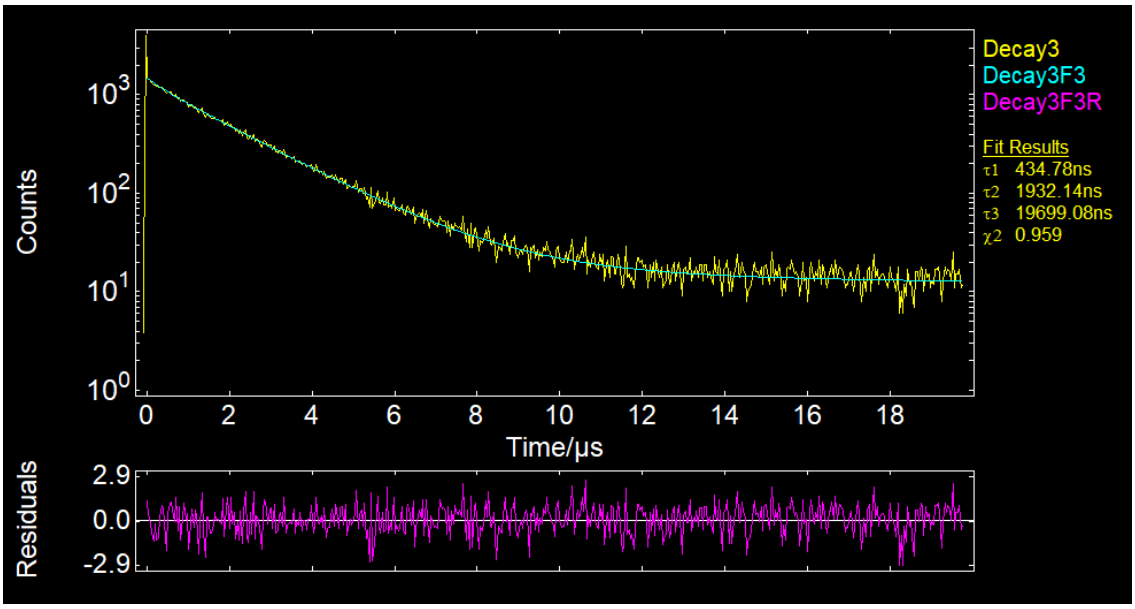


Figure A.3.48 Biexponential lifetime decay of Ir(III) complex **3.1** in PMMA film at 298 K, excited at 365 nm. Data collected at λ_{max} = 495 nm.

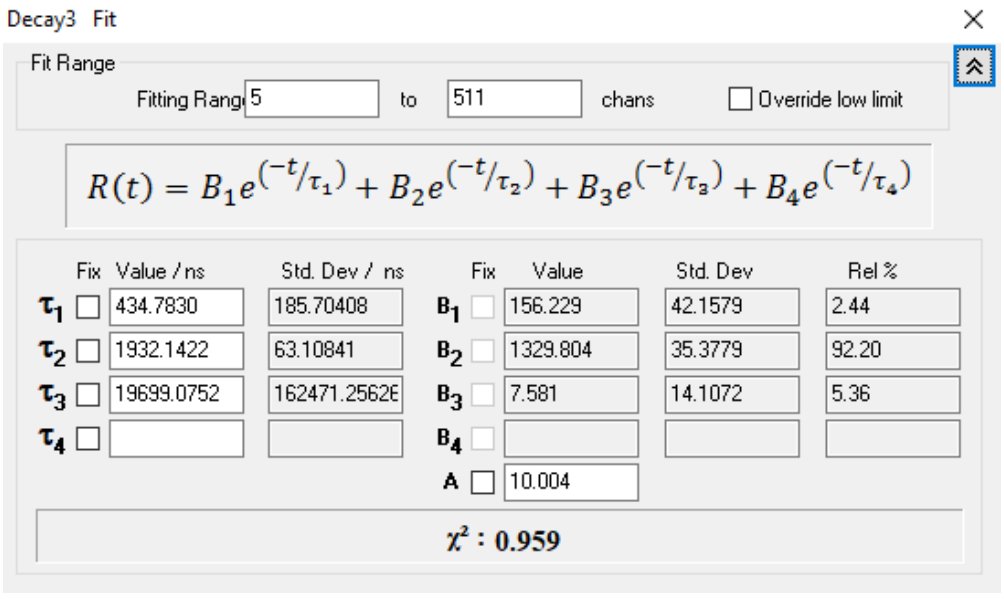


Figure A.3.49 Fit result of Ir(III) complex **3.1** in PMMA film at 298 K, excited at 365 nm. Data collected at λ_{max} = 495 nm.

Solid State Decay Lifetime Measurement of Ir(III) complex 3.2

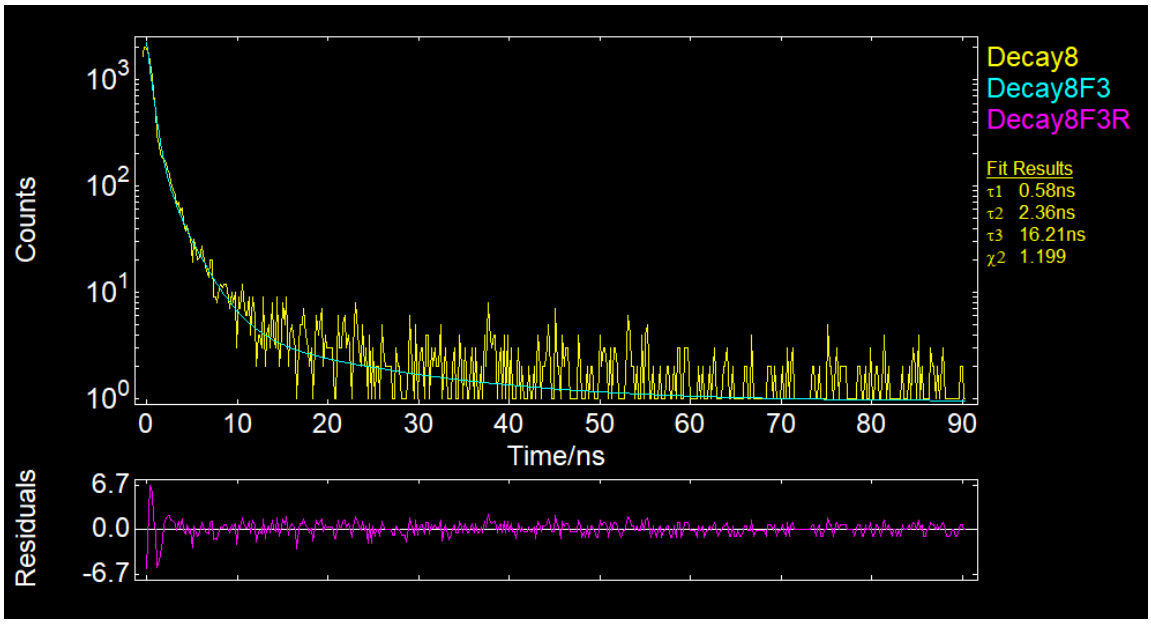


Figure A.3.50 Biexponential lifetime decay of Ir(III) complex **3.2** in PMMA film at 298 K, excited at 365 nm. Data collected at λ_{max} = 580 nm.

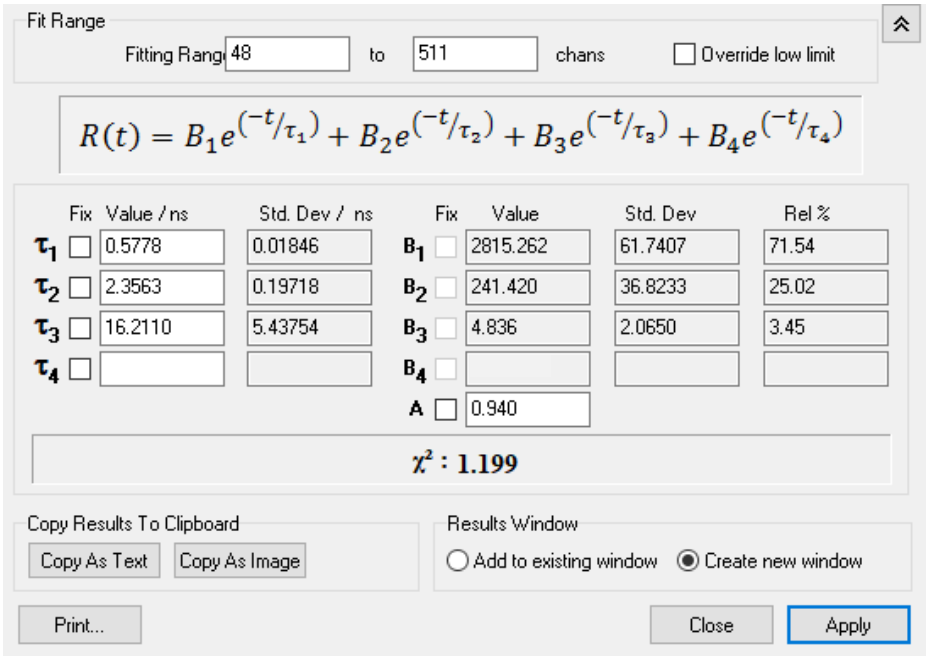


Figure A.3.51 Fit result of Ir(III) co-system **3.2** in PMMA film at 298 K, excited at 365 nm. Data collected at λ_{max} = 580 nm.

Solid State Decay Lifetime Measurement of Ir(III) complex 3.3

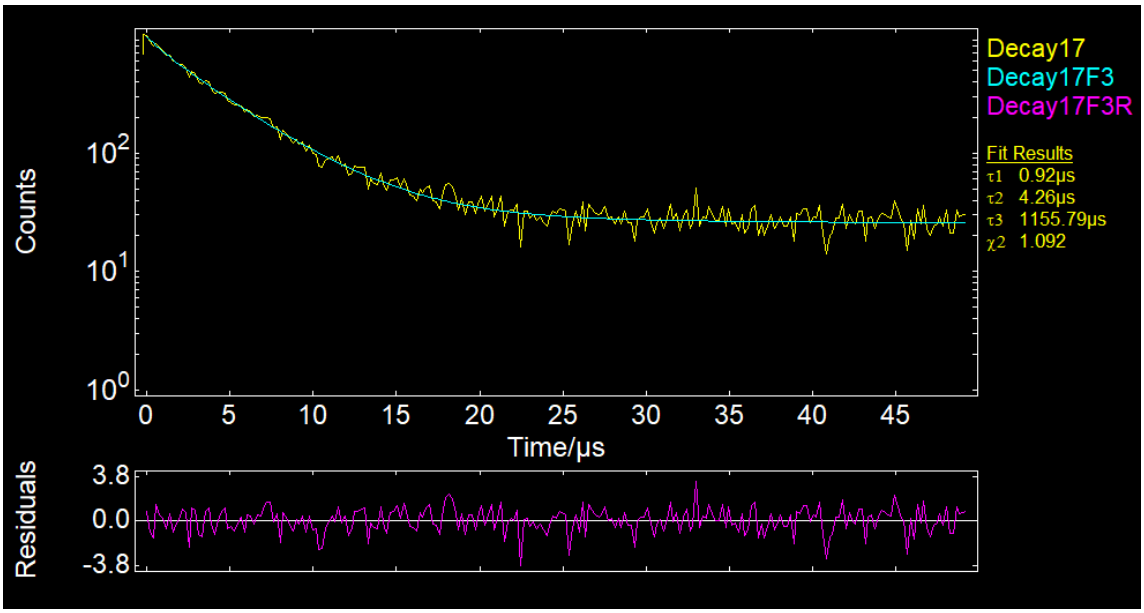


Figure A.3.52 Biexponential lifetime decay of Ir(III) complex **3.3** in PMMA film at 298 K, excited at 365 nm. Data collected at λ_{max} = 598 nm.

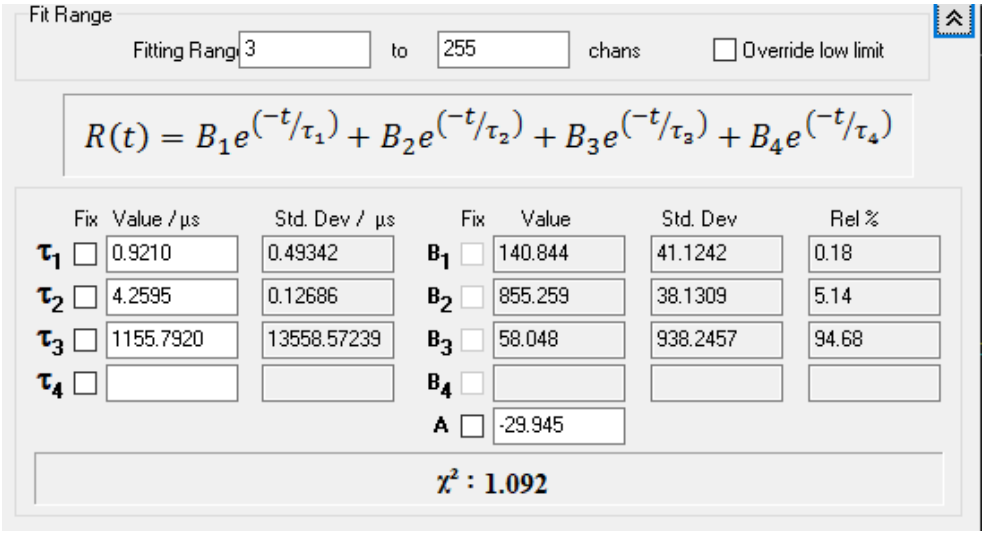


Figure A.3.53 Fit result of Ir(III) co-system **3.3** in PMMA film at 298 K, excited at 365 nm. Data collected at λ_{max} = 598 nm.

Solid State Decay Lifetime Measurement of Ir(III) complex 3.4

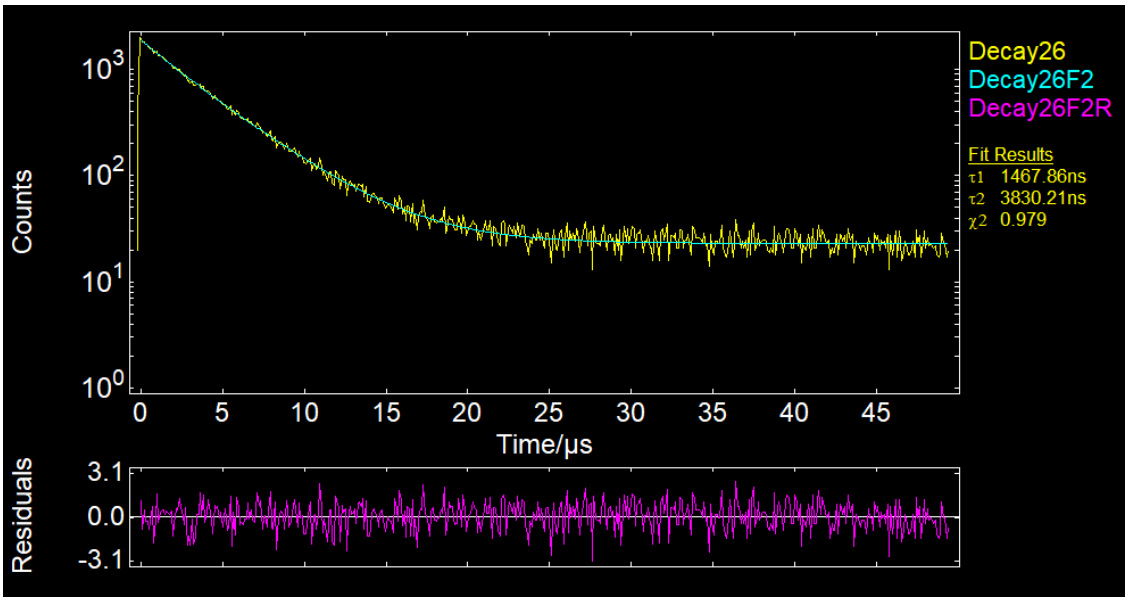


Figure A.3.54 Biexponential lifetime decay of Ir(III) complex **3.4** in PMMA film at 298 K, excited at 365 nm. Data collected at λ_{max} = 595 nm.

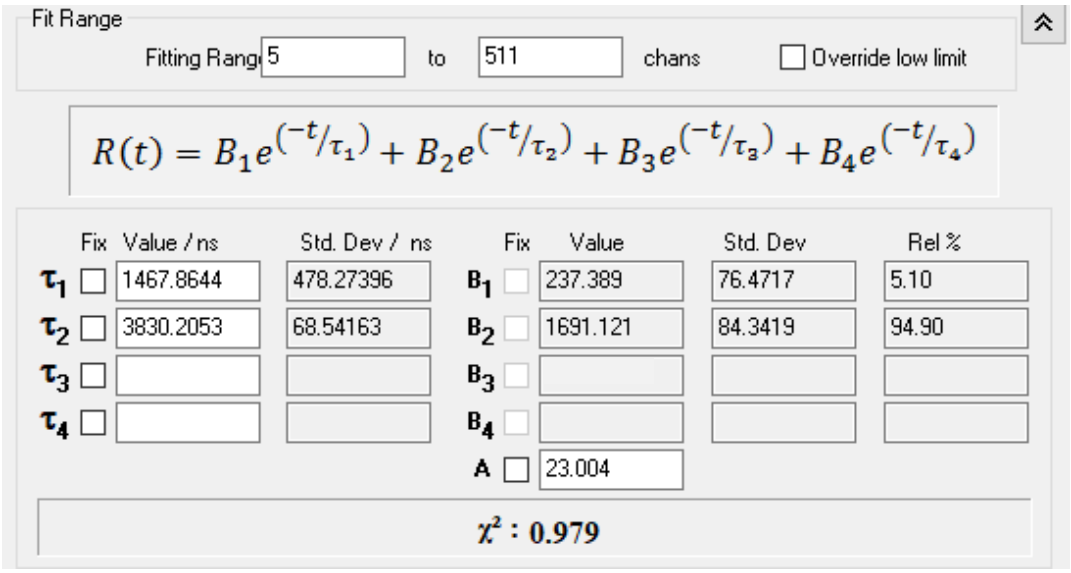


Figure A.3.55 Fit result of Ir(III) co-system **3.4** in PMMA film at 298 K, excited at 365 nm. Data collected at λ_{max} = 595 nm.

Solid State Decay Lifetime Measurement of Ir(III) complex 3.1•3.5

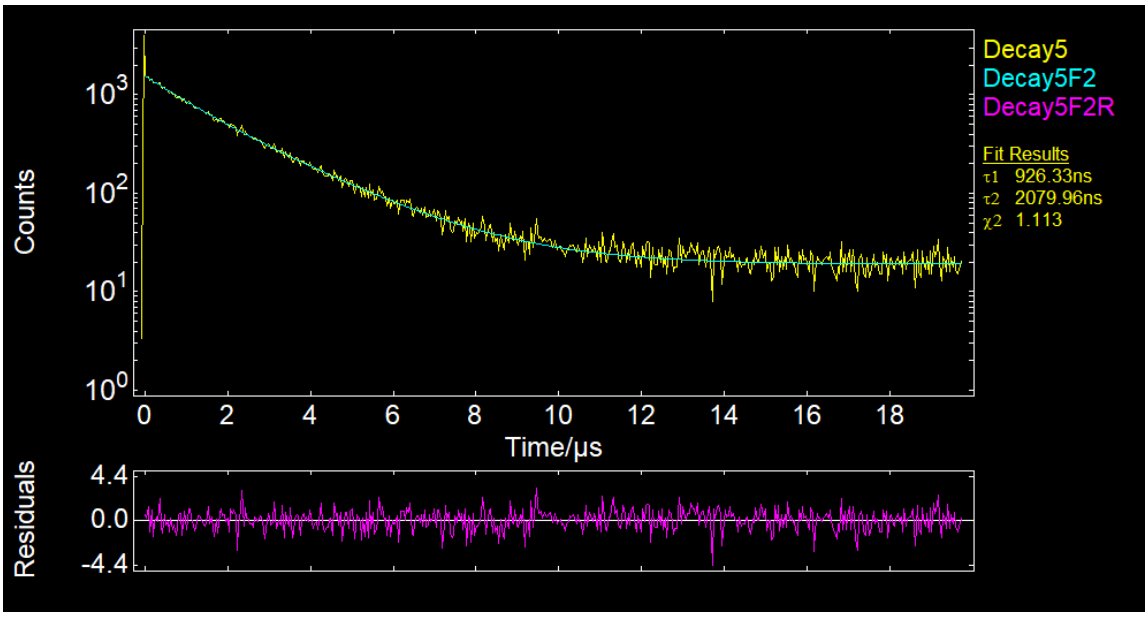


Figure A.3.56 Biexponential lifetime decay of Ir(III) co-system **3.1•3.5** in PMMA film at 298 K, excited at 365 nm. Data collected at λ_{max} = 496 nm.

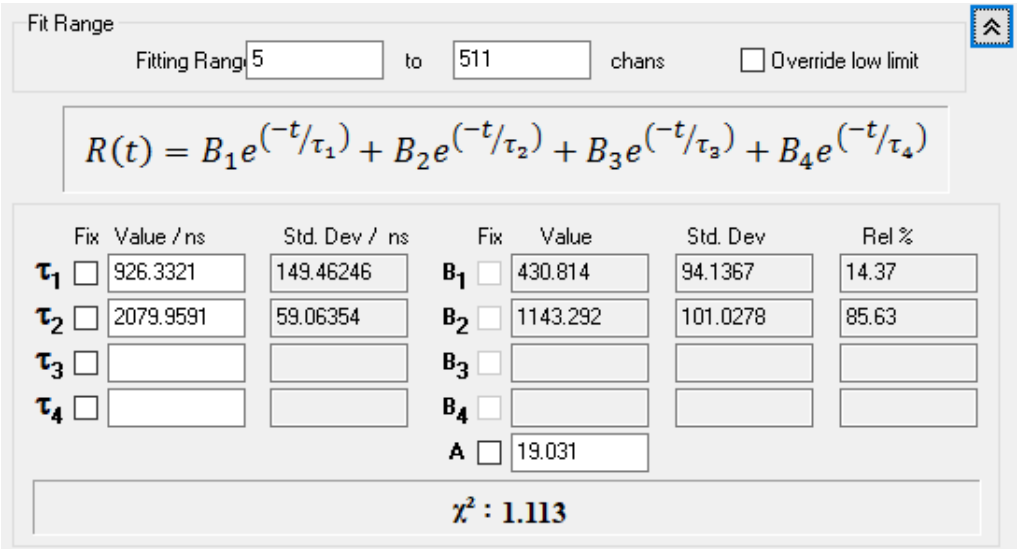


Figure A.3.57 Fit result of Ir(III) co-system **3.1•3.5** in PMMA film at 298 K, excited at 365 nm. Data collected at λ_{max} = 496 nm.

Solid State Decay Lifetime Measurement of Ir(III) complex 3.2•3.5

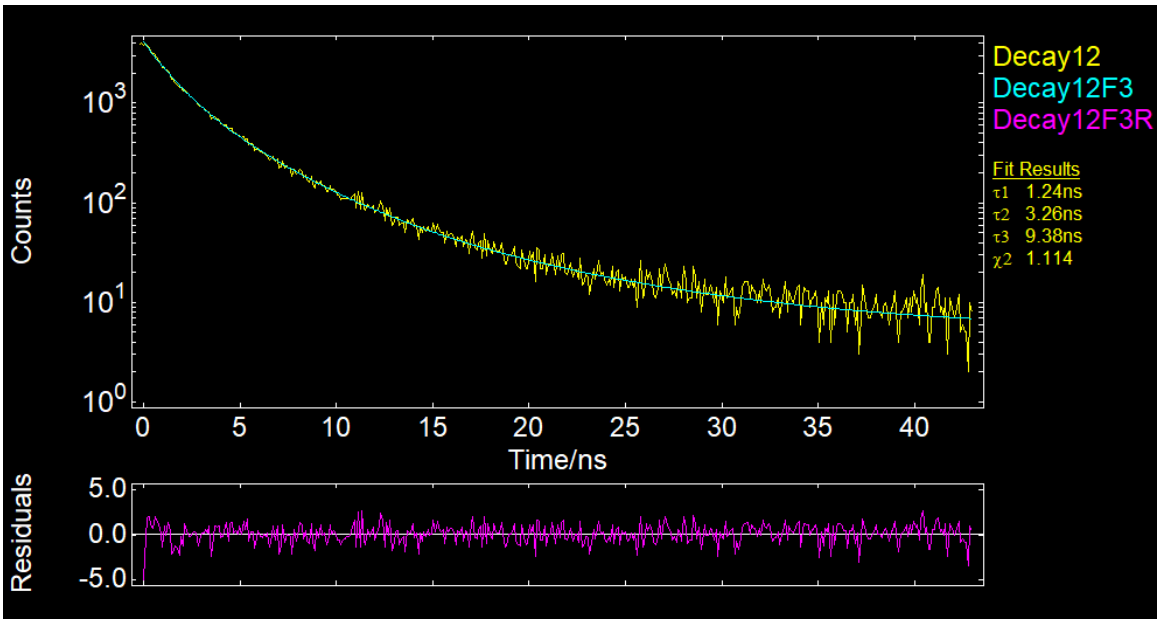


Figure A.3.58 Biexponential lifetime decay of Ir(III) complex **3.2•3.5** in PMMA film at 298 K, excited at 365 nm. Data collected at λ_{max} = 581 nm.

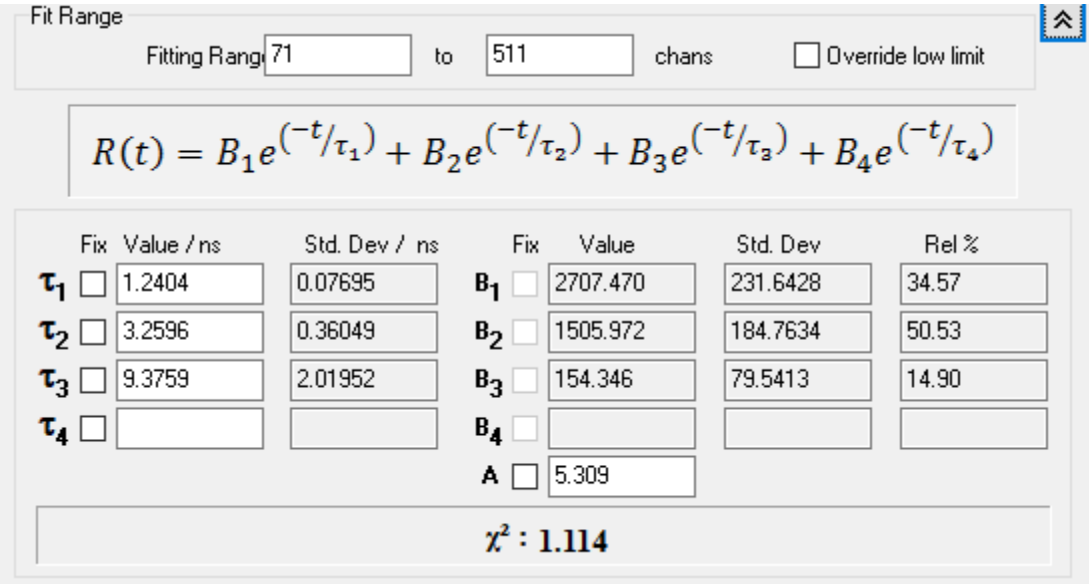


Figure A.3.59 Fit result of Ir(III) co-system **3.2•3.5** in PMMA film at 298 K, excited at 365 nm. Data collected at λ_{max} = 581 nm.

Solid State Decay Lifetime Measurement of Ir(III) complex 3.3•3.5

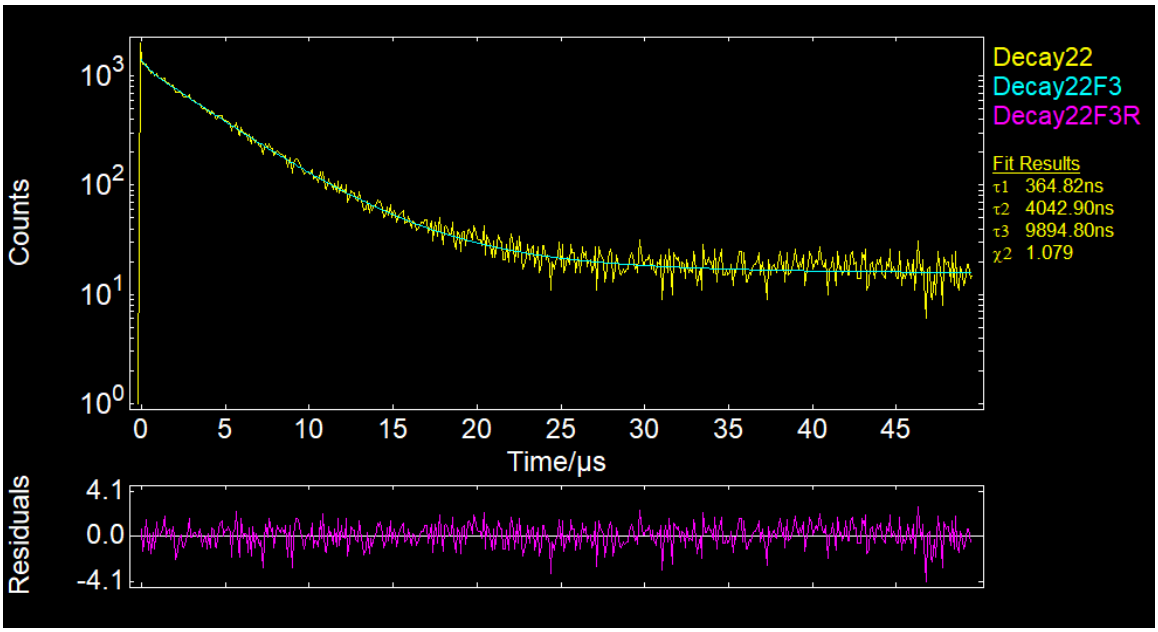


Figure A.3.60 Biexponential lifetime decay of Ir(III) complex **3.3•3.5** in PMMA film at 298 K, excited at 365 nm. Data collected at λ_{max} = 599 nm.

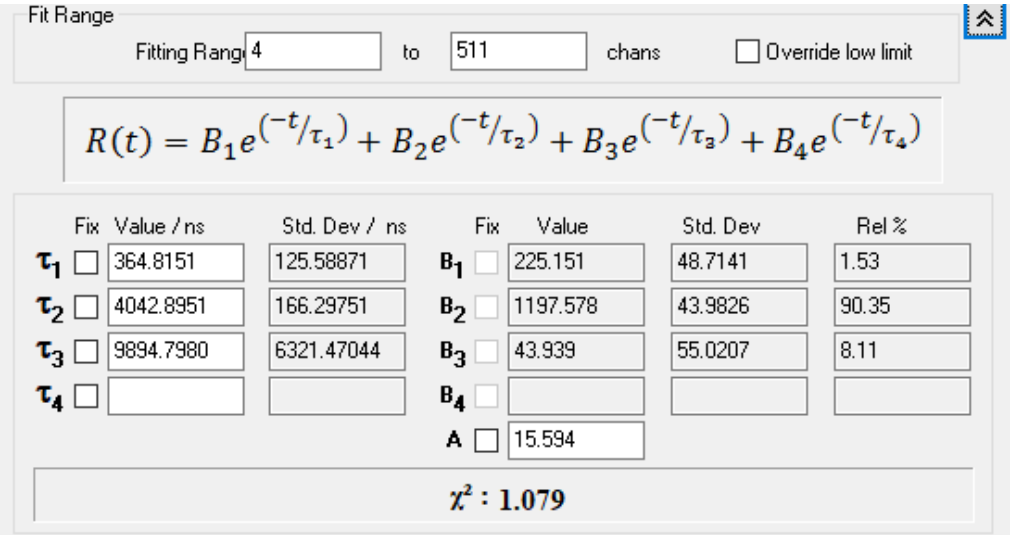


Figure A.3.61 Fit result of Ir(III) co-system **3.3•3.5** in PMMA film at 298 K, excited at 365 nm. Data collected at λ_{max} = 599 nm.

Solid State Decay Lifetime Measurement of Ir(III) complex 3.4•3.5

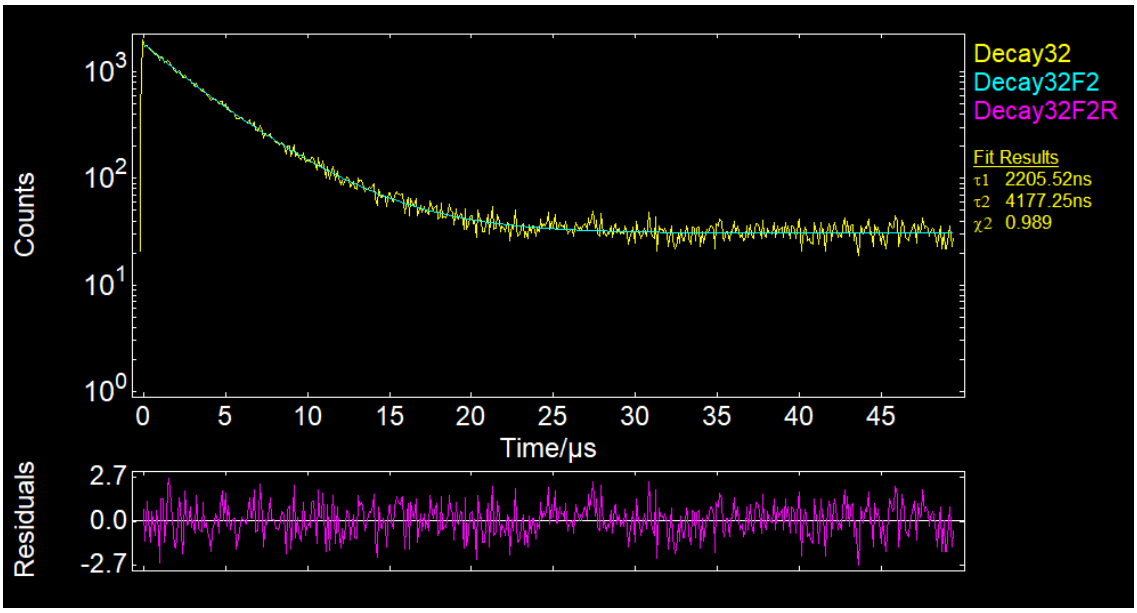


Figure A.3.62 Biexponential lifetime decay of Ir(III) complex **3.4•3.5** in PMMA film at 298 K, excited at 365 nm. Data collected at λ_{max} = 595 nm.

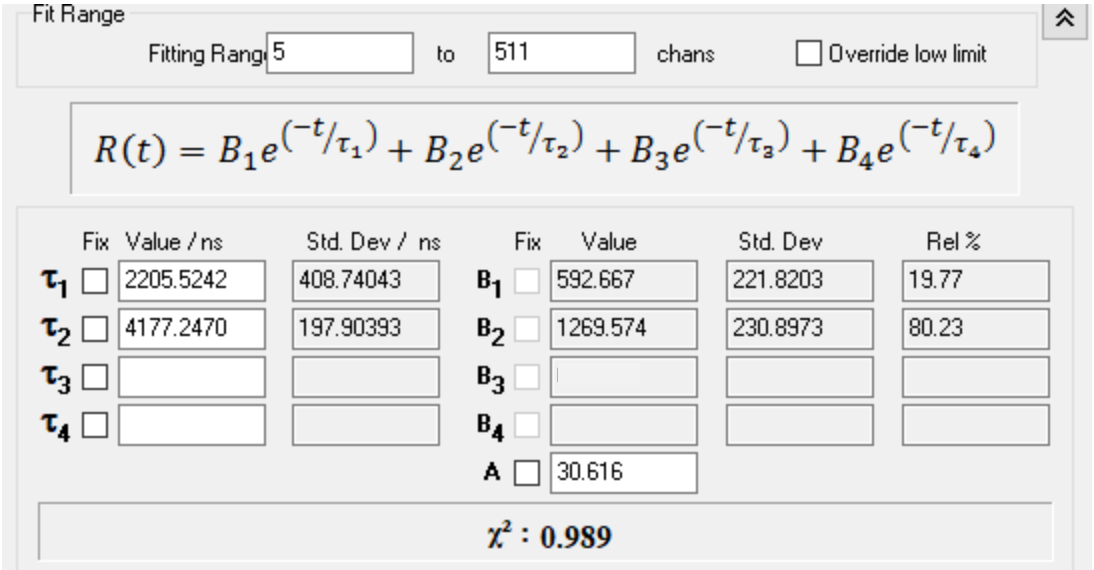


Figure A.3.63 Fit result of Ir(III) co-system **3.4•3.5** in PMMA film at 298 K, excited at 365 nm. Data collected at λ_{max} = 595 nm.

A3.7: Cyclic Voltammetry

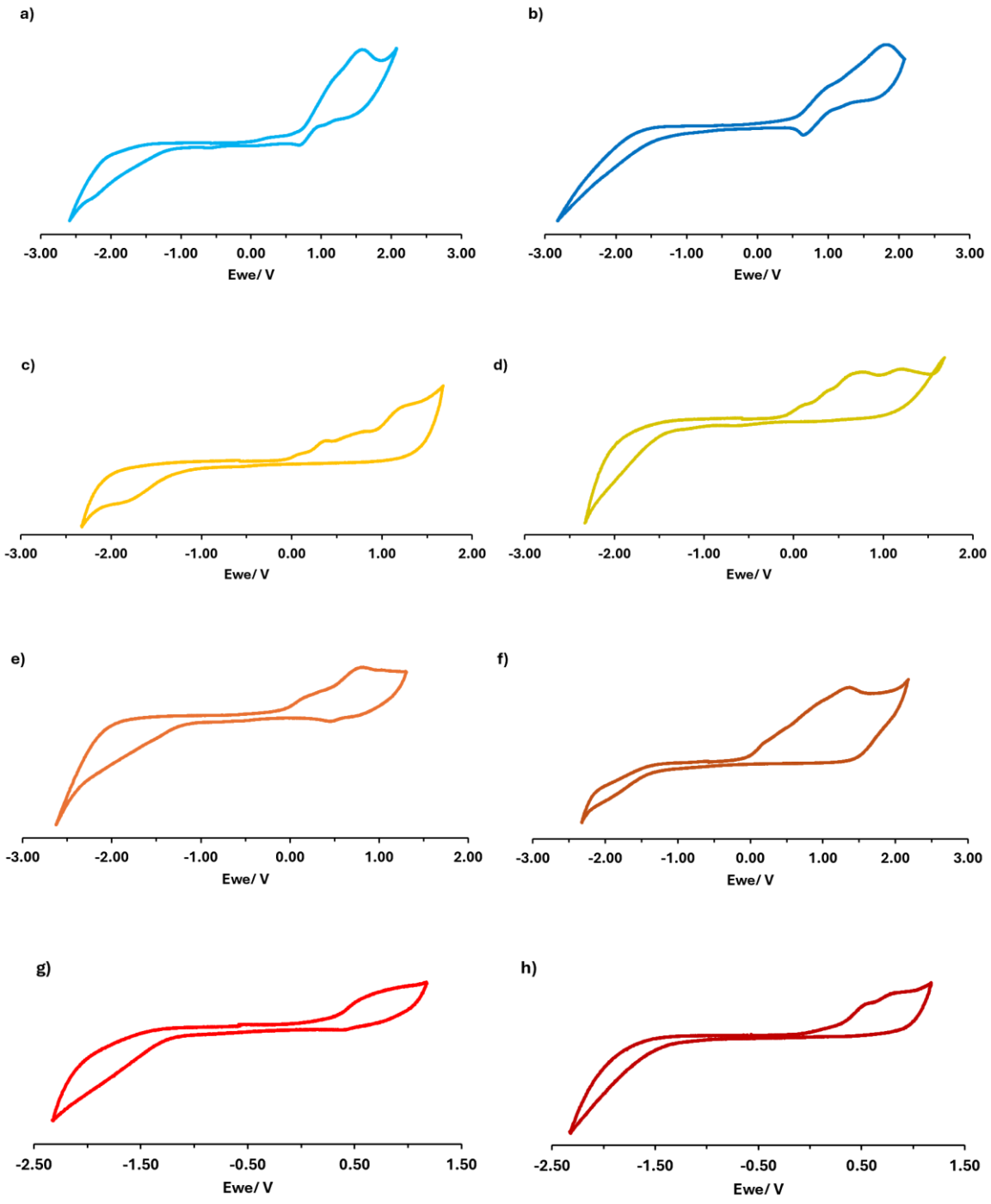
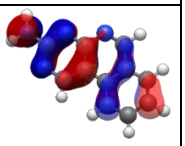
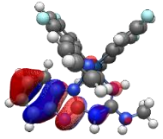
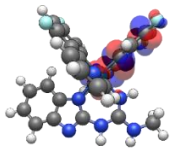
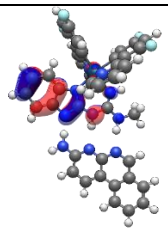
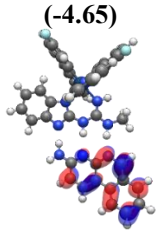
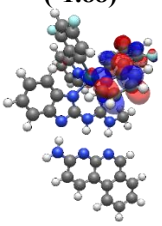
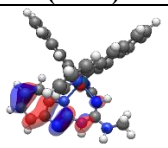
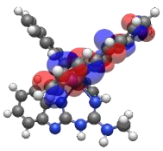


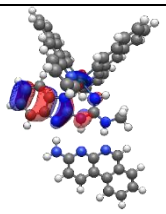
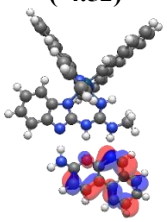
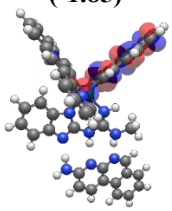
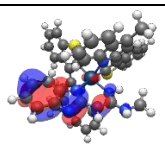
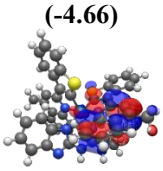
Figure A.3.64 Cyclic voltammetry of complexes **3.1-3.4** and co-systems **3.1•3.5-3.4•3.5** 2 mM in dry degassed $CHCl_3$ normalised to a ferrocene standard. **a)** complex **4.1**, **b)** co-system **3.1•3.5**, **c)** complex **3.2**, **d)** co-system **3.2•3.5**, **e)** complex **3.3**, **f)** co-system **3.3•3.5**, **g)** complex **3.3** and **h)** co-system **3.4•3.5**.

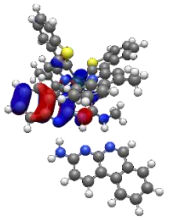
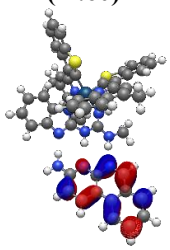
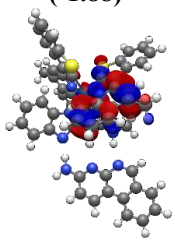
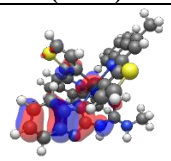
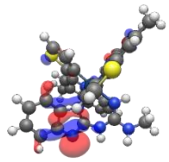
A3.8: Computational Investigation

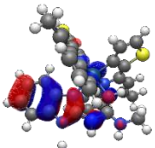
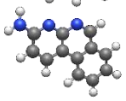
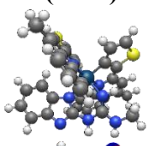
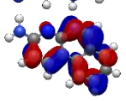
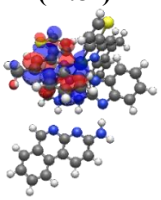
Table A.3.2 Summary of key findings of TD-DFT predictions for the compounds **3.1-3.5** and co-systems **3.1•3.5-3.4•3.5** including energy levels of five highest contributing singlet states and first triplet state.

Complex	Spin State	Transition configurations	Excitation energy (eV, nm)	Oscillator strength	HOMO-LUMO (eV)
3.5	S_1	HOMO→LUMO (95.5%) HOMO-2→LUMO+1 (2.63%)	3.5413, 350.11	0.0500	
	S_6	HOMO→LUMO+2 (39.6%) HOMO-2→LUMO (31.3%) HOMO→LUMO+1 (25.3%)	4.6841, 264.69	0.2127	**HOMO (-5.89)**
	S_7	HOMO-4→LUMO (42.1%) HOMO-2→LUMO+1 (20.3%) HOMO-2→LUMO (6.1%) HOMO→LUMO+1 (5.2%) HOMO→LUMO+2 (22.7%)	4.8494, 255.67	0.0941	
	S_9	HOMO→LUMO+2 (31.1%) HOMO-4→LUMO (21.1%) HOMO→LUMO+1 (10.6%) HOMO-2→LUMO+1 (10.3%) HOMO-2→LUMO+2 (4.0%) HOMO-5→LUMO (4.6%) HOMO-2→LUMO (12.7%)	5.2321, 236.97	0.6581	**LUMO (-1.82)**
	S_{10}	HOMO-3→LUMO+1 (84.2%) HOMO-6→LUMO (2.1%) HOMO-1→LUMO+2 (8.1%)	5.2798, 234.83	0.0112	
	T_1	HOMO→LUMO (91.1%) HOMO-2→LUMO (3.9%)	2.8435, 436.02		
3.1	S_{13}	HOMO-4→LUMO (45.6%) HOMO-4→LUMO+1 (12.3%) HOMO-3→LUMO (8.7%) HOMO-2→LUMO+2 (27.1%)	2.8435, 436.02	0.0628	
	S_{16}	HOMO-5→LUMO (5.2%) HOMO-5→LUMO+1 (2.9%) HOMO-4→LUMO+1 (3.9%) HOMO-3→LUMO (3.3%) HOMO-3→LUMO+1 (68.6%) HOMO-2→LUMO+3 (7.9%)	3.9595, 313.13	0.0568	**HOMO (-4.75)**
	S_{22}	HOMO-1→LUMO+4 (25.2%) HOMO→LUMO+4 (63.2%)	4.2953, 288.65	0.1574	
	S_{29}	HOMO-6→LUMO (4.2%) HOMO-5→LUMO+2 (5.0%) HOMO-4→LUMO+2 (9.4%) HOMO-4→LUMO+3 (36.9%) HOMO-1→LUMO+5 (26.7%) HOMO-1→LUMO+6 (2.2%)	4.4833, 276.55	0.0607	**LUMO (-1.59)**
	S_{33}	HOMO-8→LUMO+1 (2.6%) HOMO-6→LUMO+1 (4.8%)	4.6138, 268.72	0.1575	

		HOMO-5→LUMO+1 (6.2%) HOMO-5→LUMO+2 (16.3%) HOMO-5→LUMO+3 (10.0%) HOMO-3→LUMO+3 (40.5%) HOMO-2→LUMO+5 (5.1%)			
	T_1	HOMO→LUMO (72.5%) HOMO-1→LUMO (13.2%) HOMO-2→LUMO (6.5%) HOMO-4→LUMO (3.5%)	2.6327, 470.95		
3.1•3.5	S_6	HOMO-3→LUMO (97.0%)	2.8418, 436.29	0.0579	
	S_{12}	HOMO-2→LUMO+2 (89.9%) HOMO-1→LUMO+2 (5.8%)	3.2696, 379.21	0.0224	
	S_{18}	HOMO-4→LUMO+1 (78.4%) HOMO-4→LUMO+2 (13.1%)	3.5288, 351.35	0.0451	
	S_{25}	HOMO-2→LUMO+4 (50.0%) HOMO-5→LUMO+1 (36.1%) HOMO-7→LUMO+1 (4.0%) HOMO-4→LUMO+1 (2.6%)	3.7632, 329.46	0.0099	**HOMO (-4.65)**
	S_{32}	HOMO-5→LUMO+2 (66.3%) HOMO-6→LUMO+2 (4.9%) HOMO-7→LUMO+2 (2.9%) HOMO-5→LUMO+1 (3.1%) HOMO-2→LUMO+5 (5.3%) HOMO-3→LUMO+2 (10.4%)	3.9754, 311.88	0.0625	 **LUMO (-1.88)**
	T_1	HOMO-1→LUMO+1 (77.8%) HOMO-2→LUMO+1 (5.0%) HOMO-1→LUMO+1 (3.2%) HOMO-4→LUMO+1 (7.5%)	2.6881, 461.23		 **LUMO+1 (-1.39)**
3.2	S_{14}	HOMO-4→LUMO (73.0%) HOMO-6→LUMO (6.6%) HOMO-5→LUMO (5.3%) HOMO-4→LUMO (4.0%) HOMO-2→LUMO+3 (3.5%)	3.3556, 369.49	0.0733	 **HOMO (-4.57)**
	S_{16}	HOMO-4→LUMO+1 (56.7%) HOMO-5→LUMO+1 (16.8%) HOMO-6→LUMO+1 (5.2%) HOMO-5→LUMO (2.1%) HOMO-3→LUMO+1 (9.3%)	3.4764, 356.65	0.0403	
	S_{23}	HOMO→LUMO+4 (78.6%) HOMO-1→LUMO+4 (6.0%) HOMO-3→LUMO+3 (4.7%) HOMO-6→LUMO+1 (2.9%)	3.8565, 321.49	0.0094	 **LUMO (-1.62)**
	S_{30}	HOMO-1→LUMO+5 (66.7%) HOMO-2→LUMO+4 (19.0%) HOMO-5→LUMO+2 (2.6%) HOMO-2→LUMO+5 (2.4%) HOMO-7→LUMO (2.7%)	4.0581, 305.52	0.0492	

	S_{31}	HOMO-2→LUMO+4 (37.8%) HOMO-7→LUMO+1 (19.4%) HOMO-7→LUMO (3.9%) HOMO-5→LUMO+3 (7.1%) HOMO-1→LUMO+5 (15.2%)	4.0660, 304.93	0.1488	
	T_1	HOMO-2→LUMO+1 (36.6%) HOMO-2→LUMO (9.5%) HOMO-4→LUMO+1 (5.6%) HOMO-3→LUMO+5 (2.6%) HOMO-3→LUMO+3 (2.6%) HOMO-2→LUMO+3 (3.0%) HOMO-1→LUMO+1 (4.8%) HOMO-2→LUMO+5 (5.3%) HOMO+3→LUMO+1 (18.1%)	2.2828, 543.13		
3.2•3.5	S_3	HOMO→LUMO+1 (57.3%) HOMO-1→LUMO+1 (38.1%)	2.5489, 486.43	0.0088	
	S_9	HOMO-2→LUMO+2 (91.7%) HOMO-1→LUMO+2 (5.0%)	2.9039, 426.95	0.0141	
	S_{18}	HOMO-6→LUMO (96.6%)	3.2772, 378.33	0.0602	**HOMO (-4.52)**
	S_{24}	HOMO-3→LUMO+2 (74.6%) HOMO-1→LUMO+5 (2.5%) HOMO-5→LUMO+2 (5.0%) HOMO-4→LUMO+2 (11.6%)	3.4238, 362.12	0.0355	
	S_{29}	HOMO-5→LUMO+2 (68.0%) HOMO-1→LUMO+8 (2.6%) HOMO-4→LUMO+2 (6.1%) HOMO-8→LUMO+2 (7.5%) HOMO-7→LUMO+2 (7.5%)	3.6637, 338.41	0.0852	**LUMO (-1.85)**
	T_1	HOMO-7→LUMO+1 (3.5%) HOMO-5→LUMO+1 (2.1%) HOMO-4→LUMO+1 (5.1%) HOMO-4→LUMO+2 (3.0%) HOMO-3→LUMO+1 (28.6%) HOMO-3→LUMO+4 (3.0%) HOMO-3→LUMO+7 (3.7%) HOMO-2→LUMO+2 (6.1%) HOMO-1→LUMO+1 (11.0%) HOMO-1→LUMO+2 (8.8%) HOMO→LUMO+1 (7.2%)	2.3181, 534.86		
					LUMO+1 (-1.45)
3.3	S_6	HOMO-2→LUMO+1 (97.1%)	2.8022, 442.45	0.0727	
	S_9	HOMO-4→LUMO (94.8%)	3.3909, 365.63	0.0382	
	S_{14}	HOMO-4→LUMO+1 (83.2%) HOMO-2→LUMO+2 (3.4%) HOMO-6→LUMO+1 (3.7%) HOMO→LUMO+3 (5.3%)	3.6200, 342.50	0.0240	**HOMO (-4.66)**
	S_{19}	HOMO-2→LUMO+2 (56.9%) HOMO-7→LUMO (11.0%) HOMO-5→LUMO (10.9%) HOMO-6→LUMO (6.2%) HOMO-1→LUMO+3 (4.0%)	3.7200, 333.29	0.0668	
	S_{32}	HOMO-1→LUMO+5 (45.7%)	4.2029, 295.00	0.0189	**LUMO (-1.83)**

		HOMO-2→LUMO+4 (10.7%) HOMO-2→LUMO+7 (11.7%) HOMO→LUMO+7 (15.8%)			
	T_1	HOMO-2→LUMO (49.0%) HOMO-3→LUMO (28.3%) HOMO-1→LUMO (6.4%) HOMO-2→LUMO+1 (2.0%) HOMO-3→LUMO+1 (2.01%)	2.1906, 565.99		
3.3•3.5	S_3	HOMO-1→LUMO+1 (87.0%) HOMO-2→LUMO+1 (4.0%)	2.5312, 493.32	0.0251	
	S_9	HOMO-2→LUMO+2 (95.5%)	2.9009, 427.39	0.0463	
	S_{10}	HOMO-3→LUMO+1 (93.2%) HOMO-3→LUMO (3.2%)	2.9998, 413.31	0.0355	
	S_{13}	HOMO-3→LUMO+2 (95.0%)	3.2333, 383.46	0.0604	**HOMO (-4.60)**
	S_{18}	HOMO-4→LUMO+1 (49.9%) HOMO-6→LUMO+1 (41.6%)	3.4396, 360.46	0.0603	
	T_1	HOMO-8→LUMO+2 (2.2%) HOMO-3→LUMO+1 (13.1%) HOMO-3→LUMO+2 (4.9%) HOMO-2→LUMO+1 (2.4%) HOMO-2→LUMO+2 (7.6%) HOMO-1→LUMO+2 (41.2%) HOMO→LUMO+2 (18.9%)	2.2312, 555.67		**LUMO (-1.88)**
					
					LUMO+1 (-1.64)
3.4	S_6	HOMO-2→LUMO+1 (89.2%) HOMO-3→LUMO (6.5%)	2.8577, 433.86	0.0379	
	S_8	HOMO-3→LUMO+1 (85.8%) HOMO→LUMO+2 (5.1%) HOMO-4→LUMO+1 (2.4%)	3.2213, 384.89	0.0397	**HOMO (-4.58)**
	S_{16}	HOMO-5→LUMO (60.8%) HOMO-4→LUMO+1 (17.0%) HOMO-2→LUMO+2 (14.9%)	3.6430, 340.33	0.1335	
	S_{21}	HOMO-6→LUMO+1 (34.5%) HOMO-5→LUMO+1 (32.2%) HOMO-3→LUMO+3 (3.0%) HOMO-2→LUMO+3 (2.7%)	3.8616, 321.07	0.0979	**LUMO (-1.79)**
	S_{33}	HOMO-9→LUMO (3.1%) HOMO-2→LUMO+5 (2.2%) HOMO-2→LUMO+7 (2.3%) HOMO-1→LUMO+4 (44.2%) HOMO-1→LUMO+5 (22.5%)	4.3183, 287.11	0.0913	

		HOMO→LUMO+4 (4.2%)			
	T_1	HOMO-5→LUMO (3.6%) HOMO-3→LUMO (17.6%) HOMO-2→LUMO (26.5%) HOMO-1→LUMO (3.8%) HOMO→LUMO (42.2%)	1.9932, 622.03		
3.4•3.5	S_2	HOMO→LUMO+1 (97.2%) HOMO-1→LUMO+1 (2.1%)	2.4140, 513.61	0.0302	
	S_9	HOMO-3→LUMO+2 (2.7%) HOMO-2→LUMO+2 (92.8%)	2.8261, 438.72	0.0430	
	S_{13}	HOMO-4→LUMO+1 (39.2%) HOMO-4→LUMO+2 (10.4%) HOMO-3→LUMO+1 (12.2%) HOMO-3→LUMO+2 (30.8%)	3.1799, 389.90	0.0522	 **HOMO (-4.48)**
	S_{21}	HOMO-7→LUMO+1 (4.6%) HOMO-6→LUMO+1 (29.6%) HOMO-4→LUMO+2 (38.5%) HOMO-3→LUMO+2 (14.8%) HOMO-2→LUMO+4 (2.2%)	3.4394, 360.49	0.0488	
	S_{29}	HOMO-7→LUMO+1 (14.7%) HOMO-7→LUMO+2 (4.4%) HOMO-6→LUMO+1 (2.7%) HOMO-6→LUMO+2 (42.3%) HOMO-2→LUMO+4 (4.7%) HOMO-2→LUMO+5 (9.0%) HOMO-1→LUMO+5 (15.3%)	3.7191, 333.37	0.1632	 **LUMO (-1.82)**
	T_1	HOMO-4→LUMO+2 (2.0%) HOMO-3→LUMO+1 (5.8%) HOMO-3→LUMO+2 (7.1%) HOMO-2→LUMO+1 (18.7%) HOMO-2→LUMO+2 (7.2%) HOMO-1→LUMO+1 (17.3%) HOMO-1→LUMO+2 (14.3%) HOMO→LUMO+1 (6.7%) HOMO→LUMO+2 (12.6%)	2.0528, 603.99		 **LUMO+1 (-1.64)**

Appendix 4

Supplementary Material for Chapter 4

Table of Contents

A4.1: Computational Investigation **313**

A4.2: Synthetic Procedures of Complexes 4.1-4.4 **330**

A4.3: ^{1}H and ^{13}C NMR Spectra and Mass spectra **337**

A4.4: UV-vis, Excitation and Emission Data **347**

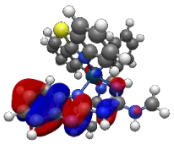
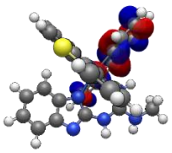
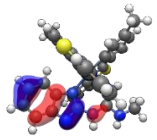
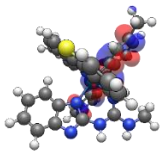
A4.5: K_a Binding Studies **350**

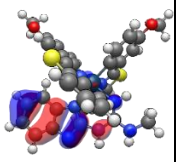
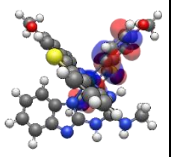
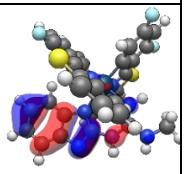
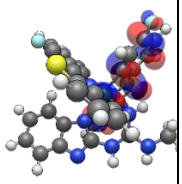
A4.6: PLQYs and Decay Lifetimes **353**

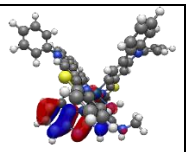
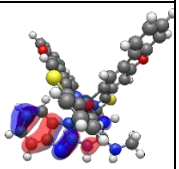
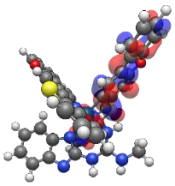
A4.7: Cyclic Voltammetry **361**

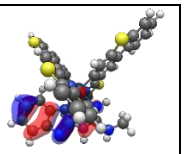
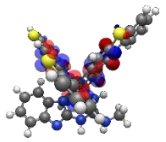
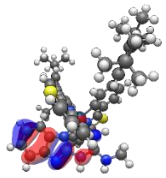
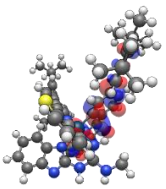
A4.1: Computational Investigation

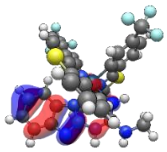
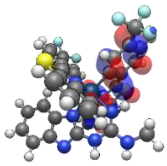
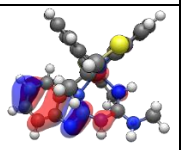
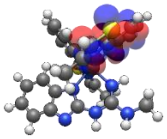
Table A.4.1 Summary of key findings of TD-DFT predictions for the thirty computationally designed complexes **A-AD** (and synthesised complexes **1-4**) including energy levels of five highest contributing singlet states and first triplet state (the predicted peak emission wavelength).

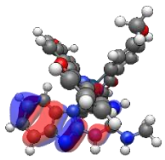
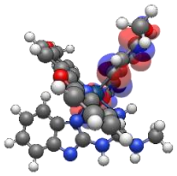
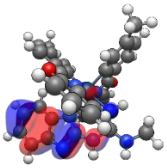
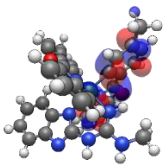
Complex	Spin State	Transition configurations	Excitation energy (eV, nm)	Oscillator strength	HOMO-LUMO (eV)
A/4.1	S_6	HOMO-2→LUMO+1 (96.2%)	2.9518, 420.03	0.0435	
	S_{10}	HOMO-6→LUMO+1 (3.4%) HOMO-5→LUMO+1 (2.8%) HOMO-4→LUMO+1 (66.6%) HOMO-3→LUMO+1 (20.1%)	3.6509, 339.60	0.0614	**HOMO (-4.60)**
	S_{16}	HOMO-7→LUMO (6.3%) HOMO-6→LUMO (48.5%) HOMO-5→LUMO+1 (10.4%) HOMO-1→LUMO+3 (26.4%)	3.9436, 314.40	0.0879	
	S_{20}	HOMO-7→LUMO (71.7%) HOMO-6→LUMO (8.9%)	4.1092, 301.72	0.1756	
	S_{21}	HOMO-6→LUMO+1 (82.0%) HOMO-4→LUMO+1 (2.8%)	4.1390, 299.55	0.1370	**LUMO (-1.76)**
	T_1	HOMO-3→LUMO (8.0%) HOMO-2→LUMO (6.0%) HOMO-1→LUMO (14.9%) HOMO→LUMO (67.4%)	2.3108, 536.55		
B	S_6	HOMO-2→LUMO+1 (95.7%)	2.9759, 416.63	0.0477	
	S_{10}	HOMO-5→LUMO+1 (4.3%) HOMO-4→LUMO (2.6%) HOMO-5→LUMO+1 (2.5%) HOMO-4→LUMO+1 (60.4%) HOMO-3→LUMO+1 (24.4%)	3.6549, 339.23	0.0804	**HOMO (-4.57)**
	S_{16}	HOMO-7→LUMO (4.1%) HOMO-6→LUMO (21.1%) HOMO-5→LUMO+1 (59.2%) HOMO-3→LUMO+1 (5.4%) HOMO-1→LUMO+3	3.9252, 315.87	0.2121	
	S_{20}	HOMO-7→LUMO (59.6%) HOMO-6→LUMO (6.7%) HOMO-6→LUMO+1 (16.1%) HOMO→LUMO+4 (2.5%)	4.0796, 303.91	0.2052	**LUMO (-1.68)**
	S_{21}	HOMO-7→LUMO (15.5%) HOMO-6→LUMO+1 (70.0%) HOMO-4→LUMO+1 (3.0%)	4.0884, 303.26	0.1331	
	T_1	HOMO-4→LUMO (2.5%) HOMO-3→LUMO (11.9%) HOMO-2→LUMO (11.0%) HOMO-1→LUMO (12.6%)	2.3417, 529.47		

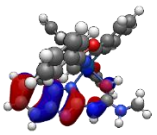
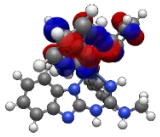
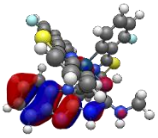
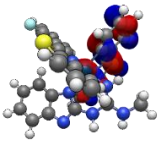
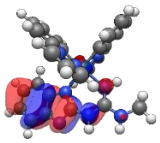
		HOMO→LUMO (58.1%)			
C	S_7	HOMO-5→LUMO (4.6%) HOMO-4→LUMO (3.1%) HOMO-3→LUMO (88.6%)	3.1526, 393.27	0.0407	 **HOMO** **(-4.55)**
	S_{12}	HOMO-6→LUMO+1 (4.1%) HOMO-5→LUMO+1 (33.1%) HOMO-5→LUMO+1 (56.9%)	3.6156, 342.92	0.0497	
	S_{21}	HOMO-7→LUMO (22.5%) HOMO-6→LUMO+1 (37.6%) HOMO-2→LUMO+3 (25.6%)	4.0921, 302.98	0.0961	
	S_{22}	HOMO-7→LUMO (37.8%) HOMO-7→LUMO+1 (12.2%) HOMO-2→LUMO+2 (7.6%) HOMO-2→LUMO+3 (9.1%) HOMO-2→LUMO+4 (10.5%) HOMO→LUMO+4 (9.8%)	4.0966, 302.65	0.1696	 **LUMO** **(-1.73)**
	S_{24}	HOMO-6→LUMO+1 (35.0%) HOMO-2→LUMO+3 (56.6%)	4.1388, 299.56	0.1091	
	T_1	HOMO-3→LUMO (18.5%) HOMO-2→LUMO (60.9%) HOMO-1→LUMO (10.5%) HOMO→LUMO (5.2%)	2.1356, 580.55		
D	S_8	HOMO-6→LUMO (4.4%) HOMO-4→LUMO (80.8%) HOMO-4→LUMO+1 (2.4%) HOMO-3→LUMO (5.4%) HOMO-3→LUMO+1 (2.6%)	3.5077, 353.46	0.0449	 **HOMO** **(-4.78)**
	S_{10}	HOMO-6→LUMO+1 (3.0%) HOMO-5→LUMO+1 (4.2%) HOMO-4→LUMO+1 (53.7%) HOMO-3→LUMO+1 (32.0%)	3.7528, 330.38	0.0748	
	S_{15}	HOMO-6→LUMO (39.3%) HOMO-5→LUMO (6.2%) HOMO-1→LUMO+2 (27.8%) HOMO-1→LUMO+4 (2.0%) HOMO-1→LUMO+5 (5.6%)	4.0009, 309.89	0.1109	 **LUMO** **(-1.90)**
	S_{18}	HOMO-6→LUMO+1 (6.0%) HOMO-5→LUMO+1 (62.9%) HOMO-3→LUMO+1 (7.0%) HOMO-1→LUMO+3 (14.3%)	4.0677, 304.80	0.1599	
	S_{20}	HOMO-6→LUMO+1 (81.3%) HOMO-5→LUMO+1 (2.7%) HOMO-4→LUMO+1 (3.5%)	4.1331, 299.98	0.1178	
	T_1	HOMO-4→LUMO (2.1%) HOMO-3→LUMO (3.9%) HOMO-2→LUMO (2.1%) HOMO-1→LUMO (13.1%) HOMO→LUMO (77.5%)	2.3715, 522.80		

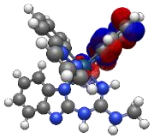
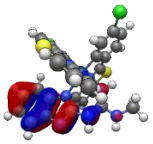
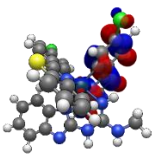
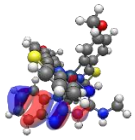
E	S_{10}	HOMO-6→LUMO (11.5%) HOMO-5→LUMO (79.4%) HOMO-3→LUMO+1 (2.1%)	3.1174, 397.72	0.2120	
	S_{12}	HOMO-7→LUMO+1 (3.7%) HOMO-5→LUMO+1 (3.1%) HOMO-4→LUMO+1 (86.3%)	3.2630, 379.98	0.4424	**HOMO (-4.51)**
	S_{14}	HOMO-8→LUMO (4.7%) HOMO-7→LUMO (29.6%) HOMO-6→LUMO (53.1%) HOMO-5→LUMO (7.6%)	3.4987, 354.37	0.2940	
	S_{16}	HOMO-8→LUMO (36.4%) HOMO-7→LUMO+1 (54.0%)	3.6582, 338.92	0.0777	
	S_{17}	HOMO-8→LUMO (52.9%) HOMO-7→LUMO+1 (36.1%) HOMO-6→LUMO (2.3%)	3.6944, 335.60	0.2500	**LUMO (-1.80)**
	T_1	HOMO-5→LUMO (3.0%) HOMO-3→LUMO (12.1%) HOMO-2→LUMO (42.5%) HOMO-2→LUMO+1 (3.8%) HOMO-1→LUMO (26.8%) HOMO-1→LUMO+1 (3.3%) HOMO→LUMO (3.3%)	2.0479, 605.41		
F	S_8	HOMO-6→LUMO (13.7%) HOMO-4→LUMO (81.5%)	3.1150, 398.02	0.1005	
	S_{10}	HOMO-7→LUMO+1 (2.7%) HOMO-6→LUMO+1 (3.1%) HOMO-5→LUMO (39.3%) HOMO-4→LUMO+1 (17.6%) HOMO-3→LUMO+1 (32.2%)	3.3430, 370.88	0.2052	**HOMO (-4.63)**
	S_{11}	HOMO-7→LUMO (3.3%) HOMO-6→LUMO+1 (2.5%) HOMO-5→LUMO (52.5%) HOMO-4→LUMO+1 (15.1%) HOMO-3→LUMO+1 (21.1%)	3.3894, 365.80	0.1778	
	S_{14}	HOMO-7→LUMO (20.9%) HOMO-6→LUMO (54.1%) HOMO-5→LUMO+1 (8.1%) HOMO-4→LUMO (6.4%) HOMO-3→LUMO (2.4%)	3.5777, 346.55	0.5457	**LUMO (-2.00)**
	S_{16}	HOMO-7→LUMO+1 (80.1%) HOMO-6→LUMO+1 (4.9%) HOMO-5→LUMO+1 (3.1%) HOMO-3→LUMO+1 (4.9%) HOMO→LUMO+2 (2.2%)	3.7078, 334.39	0.1744	
	T_1	HOMO-4→LUMO (7.0%) HOMO-3→LUMO (5.5%) HOMO-2→LUMO (14.2%) HOMO-1→LUMO (3.5%) HOMO→LUMO (67.5%)	2.1334, 581.17		

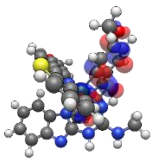
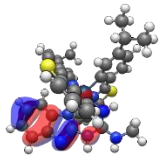
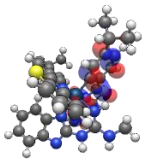
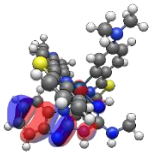
G	S_7	HOMO-6→LUMO (10.7%) HOMO-4→LUMO (64.4%) HOMO-4→LUMO+1 (4.9%) HOMO-3→LUMO (15.4%)	3.1685, 391.31	0.0468	 **HOMO (-4.65)**
	S_{10}	HOMO-7→LUMO+1 (3.2%) HOMO-5→LUMO (15.9%) HOMO-5→LUMO+1 (8.8%) HOMO-3→LUMO (11.6%) HOMO-3→LUMO+1 (51.9%)	3.3249, 372.90	0.2242	
	S_{11}	HOMO-6→LUMO (5.1%) HOMO-5→LUMO (68.6%) HOMO-5→LUMO+1 (2.4%) HOMO-4→LUMO+1 (4.8%) HOMO-3→LUMO+1 (12.3%)	3.4130, 363.27	0.1100	 **LUMO (-1.89)**
	S_{18}	HOMO-7→LUMO (8.0%) HOMO-7→LUMO+1 (76.3%) HOMO-3→LUMO+1 (4.6%) HOMO-2→LUMO+2 (3.4%)	3.6994, 335.15	0.2471	
	S_{21}	HOMO-7→LUMO+1 (2.5%) HOMO-2→LUMO+2 (84.5%)	3.8185, 324.69	0.2681	
	T_1	HOMO-3→LUMO (3.4%) HOMO-3→LUMO+1 (5.5%) HOMO-2→LUMO (14.3%) HOMO-2→LUMO+1 (17.6%) HOMO-1→LUMO (29.0%) HOMO-1→LUMO+1 (22.0%)	2.2041, 562.52		
H	S_6	HOMO-2→LUMO+1 (94.8%)	2.8965, 428.05	0.0541	
	S_9	HOMO-6→LUMO+1 (4.6%) HOMO-5→LUMO+1 (4.9%) HOMO-4→LUMO (3.6%) HOMO-4→LUMO+1 (21.8%) HOMO-3→LUMO+1 (60.0%)	3.3255, 372.83	0.1273	 **HOMO (-4.59)**
	S_{10}	HOMO-6→LUMO (7.5%) HOMO-5→LUMO+1 (10.9%) HOMO-4→LUMO+1 (50.6%) HOMO-3→LUMO+1 (24.7%)	3.4892, 355.34	0.2169	
	S_{12}	HOMO-6→LUMO (29.1%) HOMO-6→LUMO+1 (2.1%) HOMO-5→LUMO (52.8%) HOMO-4→LUMO (7.3%) HOMO-3→LUMO (2.9%)	3.6143, 343.04	0.4650	 **LUMO (-1.82)**
	S_{15}	HOMO-6→LUMO+1 (78.4%) HOMO-5→LUMO (2.2%) HOMO-3→LUMO+1 (5.7%) HOMO→LUMO+2 (7.2%)	3.7700, 328.87	0.3607	
	T_1	HOMO-4→LUMO (4.9%) HOMO-3→LUMO (8.5%) HOMO-2→LUMO (5.3%) HOMO-1→LUMO (20.5%) HOMO→LUMO (57.6%)	2.2477, 551.61		

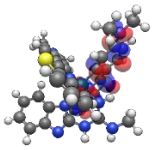
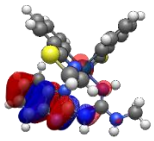
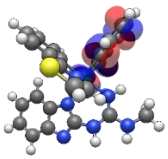
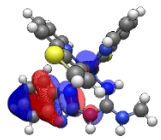
I	S_6	HOMO-2→LUMO+1 (96.6%)	2.9172, 425.02	0.0418	 **HOMO (-4.80)**
	S_{11}	HOMO-8→LUMO (2.1%) HOMO-5→LUMO (90.0%)	3.7022, 334.89	0.0654	
	S_{15}	HOMO-6→LUMO (17.6%) HOMO-5→LUMO+1 (70.0%) HOMO-3→LUMO+1 (3.0%) HOMO-1→LUMO+2 (2.1%)	3.8939, 318.40	0.0540	
	S_{20}	HOMO-7→LUMO (84.0%) HOMO-6→LUMO (8.7%)	4.0297, 307.68	0.2471	 **LUMO (-2.17)**
	S_{22}	HOMO-9→LUMO (14.5%) HOMO-8→LUMO (4.8%) HOMO-6→LUMO+1 (65.5%)	4.1045, 302.07	0.2681	
	T_1	HOMO-3→LUMO (2.8%) HOMO-1→LUMO (11.2%) HOMO→LUMO (83.7%)	2.1392, 579.57		
J	S_7	HOMO-4→LUMO (12.7%) HOMO-3→LUMO (80.2%)	3.4341, 361.04	0.0215	 **HOMO (-4.59)**
	S_{10}	HOMO-6→LUMO+1 (5.6%) HOMO-5→LUMO (26.4%) HOMO-5→LUMO+1 (2.4%) HOMO-4→LUMO+1 (42.6%) HOMO-3→LUMO (2.3%) HOMO-3→LUMO+1 (13.2%)	3.8133, 325.13	0.0437	
	S_{14}	HOMO-7→LUMO (2.2%) HOMO-6→LUMO (2.8%) HOMO-5→LUMO+1 (80.5%) HOMO-4→LUMO+1 (5.9%)	4.0649, 305.01	0.0815	 **LUMO (-1.58)**
	S_{16}	HOMO-7→LUMO (63.8%) HOMO-6→LUMO (9.4%) HOMO-6→LUMO+1 (2.4%) HOMO-5→LUMO (2.4%) HOMO-2→LUMO+3 (2.5%) HOMO-2→LUMO+4 (2.1%) HOMO-1→LUMO+3 (3.9%) HOMO→LUMO+2 (3.7%)	4.2112, 294.42	0.1264	
	S_{18}	HOMO-7→LUMO (4.4%) HOMO-6→LUMO+1 (71.1%) HOMO-4→LUMO+1 (4.4%) HOMO-1→LUMO+3 (4.0%) HOMO→LUMO+3 (4.6%)	4.2652, 290.69	0.0861	
	T_1	HOMO-6→LUMO (3.3%) HOMO-5→LUMO (4.7%) HOMO-3→LUMO (13.4%) HOMO-3→LUMO+1 (4.5%) HOMO-2→LUMO (49.0%) HOMO-1→LUMO (11.6%) HOMO→LUMO (3.3%)	2.4237, 511.55		

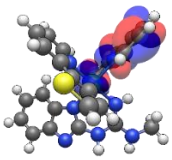
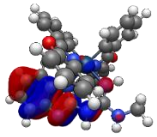
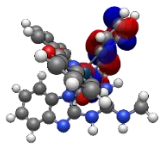
K	S_6	HOMO-3→LUMO+1 (2.0%) HOMO-2→LUMO+1 (92.7%)	3.2448, 382.11	0.0687	
	S_8	HOMO-5→LUMO+1 (4.6%) HOMO-4→LUMO (5.7%) HOMO-4→LUMO+1 (13.3%) HOMO-3→LUMO+1 (70.0%)	3.6385, 340.76	0.0853	**HOMO (-4.57)**
	S_{10}	HOMO-6→LUMO+1 (3.5%) HOMO-5→LUMO+1 (3.8%) HOMO-4→LUMO+1 (73.4%) HOMO-3→LUMO+1 (13.8%)	3.8515, 321.91	0.0956	
	S_{14}	HOMO-6→LUMO (16.8%) HOMO-6→LUMO+1 (3.1%) HOMO-5→LUMO (41.4%) HOMO-5→LUMO+1 (16.7%) HOMO-4→LUMO (5.1%) HOMO-1→LUMO+2 (3.2%) HOMO→LUMO+2 (2.6%)	4.0807, 303.83	0.1359	**LUMO (-1.36)**
	S_{19}	HOMO-6→LUMO+1 (44.7%) HOMO-1→LUMO+4 (3.0%) HOMO→LUMO+4 (34.4%)	4.2454, 292.05	0.1668	
	T_1	HOMO-4→LUMO (5.1%) HOMO-3→LUMO (28.6%) HOMO-1→LUMO (27.3%) HOMO-1→LUMO (8.3%) HOMO→LUMO (23.9%)	2.5735, 481.76		
L	S_5	HOMO-2→LUMO (95.9%)	2.9719, 417.19	0.0438	
	S_{10}	HOMO-6→LUMO+1 (4.1%) HOMO-4→LUMO+1 (62.2%) HOMO-3→LUMO+1 (28.0%)	3.7855, 327.53	0.0814	
	S_{21}	HOMO-7→LUMO (14.0%) HOMO-6→LUMO (2.8%) HOMO-6→LUMO+1 (28.8%) HOMO→LUMO+5 (21.4%) HOMO→LUMO+6 (17.0%)	4.327, 286.54	0.1131	**HOMO (-4.56)**
	S_{22}	HOMO-7→LUMO (55.7%) HOMO-6→LUMO (3.5%) HOMO-6→LUMO+1 (12.4%) HOMO-5→LUMO (2.2%) HOMO-2→LUMO+4 (3.5%) HOMO-1→LUMO+5 (2.9%) HOMO-1→LUMO+6 (2.2%) HOMO→LUMO+6 (2.3%) HOMO→LUMO+7 (2.3%)	4.3398, 285.69	0.1565	
	S_{23}	HOMO-6→LUMO+1 (29.3%) HOMO-1→LUMO+6 (6.6%) HOMO→LUMO+6 (45.5%) HOMO→LUMO+7 (2.8%)	4.3518, 284.90	0.1884	**LUMO (-1.46)**
	T_1	HOMO-4→LUMO (3.5%) HOMO-3→LUMO (14.7%) HOMO-2→LUMO (21.7%) HOMO-1→LUMO (11.8%) HOMO→LUMO (41.2%)	2.5143, 493.13		

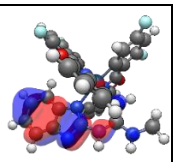
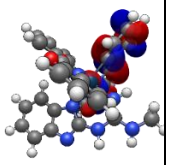
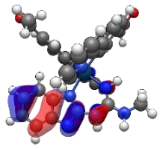
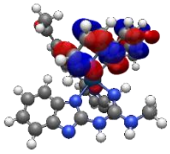
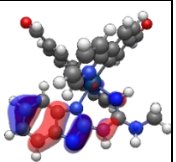
M	S_1	HOMO-1→LUMO (26.1%) HOMO→LUMO (71.4%)	2.6181, 473.56	0.0187	
	S_5	HOMO-3→LUMO (94.4%)	2.9635, 418.38	0.0865	
	S_{14}	HOMO-6→LUMO+1 (3.6%) HOMO-4→LUMO+1 (72.1%) HOMO-3→LUMO+1 (16.5%) HOMO→LUMO+3 (2.5%)	3.7304, 332.36	0.1191	**HOMO (-4.61)**
	S_{15}	HOMO-6→LUMO (3.0%) HOMO-5→LUMO (77.7%) HOMO-3→LUMO (2.2%) HOMO-2→LUMO+2 (11.4%)	3.8678, 320.56	0.1302	
	S_{20}	HOMO-6→LUMO (84.6%) HOMO-4→LUMO (4.9%)	4.0524, 305.95	0.2297	**LUMO (-1.51)**
	T_1	HOMO-5→LUMO (3.2%) HOMO-4→LUMO (8.4%) HOMO-3→LUMO (25.6%) HOMO-3→LUMO+1 (2.1%) HOMO-2→LUMO (23.9%) HOMO-1→LUMO (13.0%) HOMO→LUMO (13.9%)	2.3772, 521.55		
N	S_6	HOMO-2→LUMO+1 (96.3%)	3.0513, 406.34	0.0379	
	S_8	HOMO-4→LUMO (30.4%) HOMO-3→LUMO (59.8%)	3.3949, 365.21	0.0368	
	S_{17}	HOMO-7→LUMO (4.2%) HOMO-7→LUMO+1 (5.3%) HOMO-6→LUMO+1 (9.9%) HOMO-5→LUMO+1 (65.4%) HOMO-3→LUMO+1 (3.2%) HOMO-1→LUMO+3 (4.9%)	4.0243, 308.09	0.0699	**HOMO (-4.68)**
	S_{19}	HOMO-7→LUMO (45.8%) HOMO-6→LUMO (21.3%) HOMO-5→LUMO+1 (4.0%) HOMO-2→LUMO+4 (2.4%) HOMO-1→LUMO+4 (5.2%) HOMO-1→LUMO+5 (3.4%)	4.0644, 305.05	0.2583	
	S_{20}	HOMO-7→LUMO+1 (6.4%) HOMO-6→LUMO+1 (62.1%) HOMO-5→LUMO+1 (11.4%) HOMO-4→LUMO+1 (2.5%) HOMO→LUMO+4 (4.9%)	4.1189, 301.01	0.1574	**LUMO (-1.84)**
	T_1	HOMO-3→LUMO (4.3%) HOMO-1→LUMO (18.4%) HOMO→LUMO (72.3%)	2.3234, 533.64		
O	S_7	HOMO-4→LUMO (31.4%) HOMO-3→LUMO (52.0%) HOMO-3→LUMO+1 (3.2%) HOMO→LUMO+3 (2.9%)	4.1911, 295.83	0.0468	
	S_{10}	HOMO-5→LUMO (6.8%) HOMO-3→LUMO (4.6%) HOMO-1→LUMO+3 (34.3%) HOMO→LUMO+3 (45.7%)	4.2918, 288.89	0.0745	**HOMO (-4.56)**

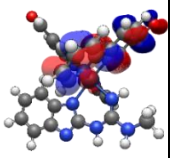
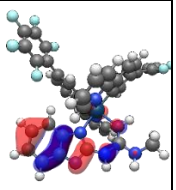
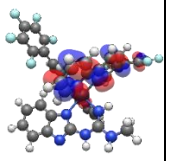
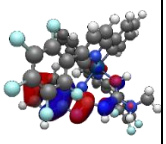
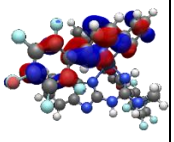
	S_{13}	HOMO-5→LUMO (7.1%) HOMO-1→LUMO+2 (4.6%) HOMO-1→LUMO+3 (51.0%) HOMO→LUMO+3 (29.4%)	4.4121, 281.01	0.0607	
	S_{14}	HOMO-7→LUMO (2.9%) HOMO-5→LUMO (55.6%) HOMO-4→LUMO (9.7%) HOMO-3→LUMO (17.2%) HOMO→LUMO+3 (5.4%)	4.4326, 279.71	0.0849	**LUMO (-0.79)**
	S_{18}	HOMO-6→LUMO+1 (2.7%) HOMO-5→LUMO+1 (43.4%) HOMO-4→LUMO+1 (33.7%) HOMO-2→LUMO+2 (9.9%)	4.6190, 268.42	0.0665	
	T_1	HOMO-6→LUMO+1 (3.5%) HOMO-5→LUMO+1 (5.8%) HOMO-4→LUMO+1 (5.1%) HOMO-2→LUMO (5.4%) HOMO-2→LUMO+1 (26.9%) HOMO1→LUMO (7.5%) HOMO-1→LUMO+1 (24.4%) HOMO→LUMO (4.5%) HOMO→LUMO+1 (8.0%)	3.1159, 397.91		
P	S_6	HOMO-2→LUMO+1 (95.8%)	3.0102, 411.88	0.0503	
	S_{11}	HOMO-6→LUMO (5.7%) HOMO-5→LUMO (81.2%) HOMO-4→LUMO+1 (2.2%) HOMO-3→LUMO (3.9%)	3.7097, 334.22	0.0408	
	S_{14}	HOMO-6→LUMO (60.4%) HOMO-5→LUMO (4.4%) HOMO-5→LUMO+1 (9.6%) HOMO-1→LUMO+2 (10.1%) HOMO-1→LUMO+4 (2.4%)	3.8712, 320.27	0.1101	**HOMO (-4.75)**
	S_{17}	HOMO-6→LUMO (17.1%) HOMO-6→LUMO+1 (2.2%) HOMO-5→LUMO+1 (41.0%) HOMO-3→LUMO+1 (6.1%) HOMO-1→LUMO+2 (2.5%) HOMO-1→LUMO+4 (14.5%) HOMO→LUMO+4 (3.9%)	3.9196, 316.32	0.2519	
	S_{20}	HOMO-6→LUMO+1 (86.2%) HOMO-4→LUMO+1 (3.6%)	4.0469, 306.37	0.1760	**LUMO (-1.99)**
	T_1	HOMO-3→LUMO (4.4%) HOMO-2→LUMO (2.3%) HOMO-1→LUMO (12.8%) HOMO→LUMO (77.8%)	2.2561, 549.55		
Q	S_6	HOMO-3→LUMO+1 (3.1%) HOMO-2→LUMO+1 (91.6%)	3.0691, 403.98	0.0688	
	S_8	HOMO-5→LUMO (3.3%) HOMO-5→LUMO+1 (3.6%) HOMO-4→LUMO (39.4%) HOMO-4→LUMO+1 (8.2%) HOMO-3→LUMO+1 (38.2%)	3.4646, 357.86	0.0599	 **HOMO (-4.58)**

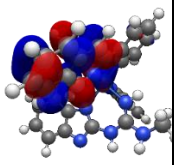
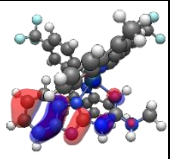
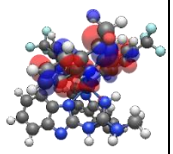
	S_{10}	HOMO-6→LUMO (5.1%) HOMO-6→LUMO+1 (5.0%) HOMO-5→LUMO (4.4%) HOMO-5→LUMO+1 (6.3%) HOMO-4→LUMO+1 (59.7%) HOMO-3→LUMO+1 (13.8%)	3.6918, 335.84	0.0913	 **LUMO (-1.60)**
	S_{13}	HOMO-6→LUMO (11.4%) HOMO-6→LUMO+1 (2.9%) HOMO-5→LUMO (57.5%) HOMO-4→LUMO (9.1%) HOMO-3→LUMO (3.9%) HOMO-1→LUMO+2 (2.1%) HOMO→LUMO+2 (5.2%)	3.8252, 324.13	0.2514	
	S_{19}	HOMO-6→LUMO+1 (68.2%) HOMO-4→LUMO+1 (4.0%) HOMO-3→LUMO+1 (2.3%) HOMO-2→LUMO+1 (2.5%) HOMO-1→LUMO+3 (13.5%)	3.9922, 310.57	0.2436	
	T_1	HOMO-4→LUMO (5.6%) HOMO-3→LUMO (29.3%) HOMO-2→LUMO (24.4%) HOMO-1→LUMO (5.1%) HOMO→LUMO (30.7%)	2.3929, 518.14		
R	S_6	HOMO-2→LUMO+1 (96.1%)	2.957, 419.29	0.0450	
	S_{10}	HOMO-5→LUMO+1 (4.5%) HOMO-4→LUMO+1 (2.2%) HOMO-4→LUMO+1 (57.8%) HOMO-3→LUMO+1 (28.0%)	3.6296, 341.60	0.0868	 **HOMO (-4.57)**
	S_{16}	HOMO-7→LUMO (2.8%) HOMO-6→LUMO (11.2%) HOMO-5→LUMO+1 (71.8%) HOMO-3→LUMO+1 (5.7%)	3.9063, 317.39	0.1963	
	S_{20}	HOMO-7→LUMO (8.5%) HOMO-6→LUMO (2.3%) HOMO-6→LUMO+1 (72.6%) HOMO-4→LUMO+1 (3.0%)	4.0592, 305.44	0.2363	 **LUMO (-1.70)**
	S_{21}	HOMO-7→LUMO (64.1%) HOMO-6→LUMO (4.6%) HOMO-6→LUMO+1 (7.7%) HOMO→LUMO+4 (10.0%)	4.0677, 304.80	0.1490	
	T_1	HOMO-4→LUMO (2.8%) HOMO-3→LUMO (10.4%) HOMO-2→LUMO (10.2%) HOMO-1→LUMO (13.4%) HOMO→LUMO (59.5%)	2.3349, 531.01		
S/4.2	S_7	HOMO-4→LUMO+1 (11.3%) HOMO-3→LUMO+1 (32.6%) HOMO-2→LUMO+1 (50.5%)	3.0690, 403.99	0.0776	 **HOMO (-4.39)**
	S_8	HOMO-4→LUMO (9.0%) HOMO-4→LUMO+1 (10.0%) HOMO-3→LUMO (5.7%) HOMO-3→LUMO+1 (54.8%)	3.2720, 378.93	0.1506	

		HOMO-2→LUMO+1 (17.3%)			
	S_{10}	HOMO-4→LUMO+1 (75.9%) HOMO-2→LUMO+1 (18.6%)	3.4249, 362.01	0.1818	
	S_{11}	HOMO-6→LUMO (16.9%) HOMO-5→LUMO (68.2%) HOMO-4→LUMO (3.6%) HOMO-3→LUMO (4.8%)	3.6164, 342.84	0.1670	**LUMO (-1.33)**
	S_{17}	HOMO-6→LUMO+1 (79.8%) HOMO-2→LUMO+3 (3.9%) HOMO-1→LUMO+3 (3.7%) HOMO→LUMO+3 (2.7%)	3.9116, 316.96	0.1200	
	T_1	HOMO-4→LUMO (3.5%) HOMO-3→LUMO (71.8%) HOMO-2→LUMO (8.8%) HOMO-1→LUMO (2.1%) HOMO→LUMO (7.8%)	2.3051, 537.87		
T	S_8	HOMO-4→LUMO (60.9%) HOMO-4→LUMO+1 (2.7%) HOMO-3→LUMO (31.0%)	3.4933, 354.92	0.0458	
	S_{11}	HOMO-7→LUMO (3.0%) HOMO-5→LUMO (86.2%) HOMO-3→LUMO (4.6%)	3.8115, 325.29	0.0455	**HOMO (-4.62)**
	S_{17}	HOMO-7→LUMO (5.3%) HOMO-6→LUMO+1 (2.4%) HOMO-2→LUMO+3 (2.3%) HOMO-1→LUMO+2 (2.7%) HOMO-1→LUMO+3 (23.1%) HOMO-1→LUMO+5 (2.0%) HOMO→LUMO+2 (2.2%) HOMO→LUMO+3 (49.1%)	4.2793, 289.73	0.1387	
					LUMO (-1.59)
	S_{18}	HOMO-7→LUMO (11.0%) HOMO-6→LUMO+1 (75.4%) HOMO-3→LUMO+1 (2.1%)	4.3073, 287.85	0.0818	
	S_{21}	HOMO-7→LUMO+1 (29.4%) HOMO-1→LUMO+2 (2.4%) HOMO-1→LUMO+3 (43.6%) HOMO→LUMO+3 (12.5%) HOMO→LUMO+4 (2.4%)	4.3941, 282.16	0.0708	
	T_1	HOMO-5→LUMO (3.4%) HOMO-4→LUMO (3.4%) HOMO-3→LUMO (11.7%) HOMO-2→LUMO (29.0%) HOMO-1→LUMO (21.1%) HOMO→LUMO (24.2%)	2.3650, 524.25		
U/4.3	S_8	HOMO-3→LUMO (76.9%) HOMO-2→LUMO (2.6%) HOMO-1→LUMO+2 (4.2%) HOMO→LUMO+2 (4.0%) HOMO→LUMO+3 (3.9%)	3.2337, 383.42	0.0245	
	S_{11}	HOMO-3→LUMO+1 (79.3%) HOMO-2→LUMO+1 (6.3%) HOMO-2→LUMO+3 (2.9%)	3.3964, 365.05	0.0275	**HOMO (-4.61)**

	S_{19}	HOMO-7→LUMO (7.3%) HOMO-7→LUMO+1 (10.2%) HOMO-6→LUMO (49.3%) HOMO-5→LUMO+1 (4.9%) HOMO-4→LUMO (3.4%) HOMO-3→LUMO+3 (14.3%)	3.9325, 315.28	0.0689	 **LUMO (-1.47)**
	S_{22}	HOMO-7→LUMO (25.1%) HOMO-5→LUMO (11.6%) HOMO-5→LUMO+1 (3.3%) HOMO-5→LUMO+2 (3.8%) HOMO-4→LUMO (5.7%) HOMO-4→LUMO+2 (2.3%) HOMO-3→LUMO+2 (3.3%) HOMO-3→LUMO+3 (28.3%) HOMO→LUMO+5 (3.1%)	4.0205, 308.38	0.0723	
	S_{23}	HOMO-7→LUMO (5.2%) HOMO-7→LUMO+1 (8.6%) HOMO-6→LUMO (7.7%) HOMO-5→LUMO+1 (46.0%) HOMO-4→LUMO+1 (16.2%) HOMO→LUMO+4 (5.6%)	4.0675, 304.82	0.0859	
	T_1	HOMO-5→LUMO (2.8%) HOMO-4→LUMO (3.3%) HOMO-3→LUMO (37.6%) HOMO-3→LUMO+2 (2.5%) HOMO-2→LUMO (24.5%) HOMO→LUMO (20.5%)	2.3077, 537.26		
V	S_5	HOMO-2→LUMO (96.5%)	2.9508, 420.17	0.0407	
	S_{10}	HOMO-6→LUMO+1 (3.5%) HOMO-4→LUMO+1 (62.9%) HOMO-3→LUMO+1 (27.3%)	3.7787, 328.11	0.0591	
	S_{12}	HOMO-5→LUMO (65.0%) HOMO→LUMO+2 (27.0%)	3.9782, 311.66	0.0590	**HOMO (-4.59)**
	S_{19}	HOMO-7→LUMO (3.4%) HOMO-6→LUMO (2.2%) HOMO-1→LUMO+5 (10.3%) HOMO-1→LUMO+6 (5.1%) HOMO→LUMO+5 (59.8%) HOMO→LUMO+6 (5.9%)	4.2818, 289.56	0.0677	
	S_{23}	HOMO-7→LUMO (53.9%) HOMO-6→LUMO (10.3%) HOMO-2→LUMO+4 (4.6%) HOMO-1→LUMO+6 (4.3%) HOMO→LUMO+6 (4.2%) HOMO→LUMO+7 (4.7%)	4.3652, 284.03	0.2348	**LUMO (-1.54)**
	T_1	HOMO-4→LUMO (2.2%) HOMO-3→LUMO (10.8%) HOMO-2→LUMO (16.6%) HOMO-1→LUMO (13.4%) HOMO→LUMO (51.5%)	2.4934, 497.24		

W	S_6	HOMO-2→LUMO+1 (96.0%)	3.3303, 372.29	0.0394	
	S_{10}	HOMO-6→LUMO+1 (5.4%) HOMO-4→LUMO+1 (53.0%) HOMO-3→LUMO+1 (35.8%)	3.8755, 319.91	0.0791	
	S_{17}	HOMO-7→LUMO (5.6%) HOMO-6→LUMO (35.7%) HOMO-5→LUMO (26.4%) HOMO-4→LUMO (3.8%) HOMO-1→LUMO+2 (2.4%) HOMO-1→LUMO+3 (7.4%) HOMO-1→LUMO+4 (7.0%) HOMO→LUMO+5 (2.7%)	4.2115, 297.87	0.1215	**HOMO (-4.79)**
	S_{20}	HOMO-5→LUMO+1 (81.8%) HOMO-3→LUMO+1 (3.2%) HOMO-1→LUMO+4 (3.5%)	4.2818, 289.56	0.0644	 **LUMO (-1.70)**
	S_{24}	HOMO-6→LUMO+1 (61.6%) HOMO-4→LUMO+1 (2.0%) HOMO-3→LUMO+1 (2.1%) HOMO→LUMO+6 (22.9%)	4.3520, 283.70	0.2554	
	T_1	HOMO-4→LUMO (3.7%) HOMO-3→LUMO (5.7%) HOMO-2→LUMO (7.6%) HOMO-1→LUMO (12.1%) HOMO→LUMO (68.2%)	2.5603, 484.26		
X/4.4	S_5	HOMO-2→LUMO (95.5%)	2.6405, 469.55	0.0154	
	S_{11}	HOMO-8→LUMO (4.4%) HOMO-5→LUMO (2.7%) HOMO-4→LUMO (40.1%) HOMO-3→LUMO (43.3%)	3.2914, 376.69	0.0125	 **HOMO (-4.79)**
	S_{14}	HOMO-6→LUMO+1 (5.7%) HOMO-4→LUMO (10.4%) HOMO-3→LUMO (23.5%) HOMO-3→LUMO+1 (40.8%) HOMO-2→LUMO+2 (8.4%)	3.3782, 367.02	0.0151	
	S_{18}	HOMO-5→LUMO (9.1%) HOMO-4→LUMO+1 (79.6%) HOMO-2→LUMO+3 (2.5%)	3.6031, 344.10	0.0545	 **LUMO (-2.03)**
	S_{20}	HOMO-7→LUMO+1 (4.1%) HOMO-5→LUMO+1 (88.6%)	3.7959, 326.62	0.0458	
	T_1	HOMO-5→LUMO (2.9%) HOMO-2→LUMO (17.9%) HOMO-1→LUMO (12.2%) HOMO→LUMO (61.8%)	2.2626, 547.98		
Y	S_6	HOMO-2→LUMO+1 (94.8%)	2.8205, 439.58	0.0237	
	S_{12}	HOMO-10→LUMO (2.3%) HOMO-4→LUMO (41.6%) HOMO-3→LUMO (41.9%) HOMO-3→LUMO+1 (5.9%)	3.3076, 374.84	0.0206	
	S_{18}	HOMO-4→LUMO+1 (54.6%) HOMO-2→LUMO+3 (36.4%)	3.5677, 347.51	0.0353	**HOMO (-4.84)**

	S_{20}	HOMO-7→LUMO+1 (3.8%) HOMO-6→LUMO+1 (2.0%) HOMO-5→LUMO+1 (87.3%)	3.7938, 326.81	0.0441	
	S_{22}	HOMO-9→LUMO (2.1%) HOMO-8→LUMO (5.5%) HOMO-7→LUMO (8.6%) HOMO-6→LUMO (78.3%)	3.8928, 318.50	0.0181	**LUMO (-2.17)**
	T_1	HOMO-2→LUMO (10.4%) HOMO-1→LUMO (11.1%) HOMO→LUMO (73.1%)	2.1953, 564.78		
Z	S_6	HOMO-2→LUMO+1 (94.2%)	2.9678, 417.77	0.0245	
	S_{12}	HOMO-6→LUMO (2.4%) HOMO-5→LUMO (3.7%) HOMO-4→LUMO (86.0%)	3.4779, 356.50	0.0276	
	S_{13}	HOMO-6→LUMO (2.3%) HOMO-5→LUMO (5.9%) HOMO-3→LUMO (82.4%) HOMO-2→LUMO+2 (2.6%)	3.4901, 355.24	0.0249	**HOMO (-4.73)**
	S_{16}	HOMO-6→LUMO+1 (3.3%) HOMO-5→LUMO (20.3%) HOMO-5→LUMO+1 (3.5%) HOMO-4→LUMO+1 (31.8%) HOMO-3→LUMO (6.8%) HOMO-3→LUMO+1 (25.9%)	3.7160, 333.65	0.0793	
	S_{22}	HOMO-6→LUMO (9.3%) HOMO-5→LUMO+1 (67.8%) HOMO-4→LUMO+2 (2.4%) HOMO-3→LUMO+1 (7.7%)	3.9068, 317.35	0.1319	**LUMO (-1.82)**
	T_1	HOMO-3→LUMO (3.3%) HOMO-2→LUMO (15.1%) HOMO-1→LUMO (20.7%) HOMO→LUMO (55.0%)	2.3989, 516.83		
AA	S_5	HOMO-2→LUMO (94.5%)	2.6582, 466.42	0.0394	
	S_6	HOMO-2→LUMO+1 (94.0%)	2.7500, 450.86	0.0453	
	S_{15}	HOMO-5→LUMO (6.0%) HOMO-4→LUMO (35.4%) HOMO-4→LUMO+1 (3.5%) HOMO-3→LUMO (38.7%) HOMO-3→LUMO+1 (5.0%) HOMO-2→LUMO+3 (2.3%)	3.4157, 362.98	0.0206	**HOMO (-4.66)**
	S_{17}	HOMO-5→LUMO (73.5%) HOMO-4→LUMO (12.3%) HOMO-4→LUMO+1 (3.0%) HOMO-3→LUMO+2 (2.6%)	3.5861, 345.74	0.1011	
	S_{20}	HOMO-5→LUMO (3.0%) HOMO-5→LUMO+1 (73.6%) HOMO-4→LUMO+1 (15.5%)	3.6633, 338.45	0.1111	**LUMO (-1.88)**
	T_1	HOMO-2→LUMO (6.6%) HOMO-1→LUMO (10.1%)	2.2041, 562.52		

		HOMO→LUMO (77.4%)			
AB	S_{10}	HOMO-1→LUMO+3 (94.2%) HOMO→LUMO+3 (3.0%)	3.0140, 411.36	0.0106	
	S_{12}	HOMO-5→LUMO+1 (4.5%) HOMO-2→LUMO+3 (88.6%)	3.1532, 393.20	0.0394	
	S_{18}	HOMO-5→LUMO+1 (73.4%) HOMO-4→LUMO+3 (2.5%) HOMO-3→LUMO+1 (3.7%) HOMO-3→LUMO+2 (3.1%) HOMO-3→LUMO+3 (4.3%) HOMO-2→LUMO+3 (3.3%)	3.5545, 348.81	0.0829	**HOMO (-4.55)**
	S_{21}	HOMO-7→LUMO (6.7%) HOMO-6→LUMO (6.6%) HOMO-5→LUMO+2 (13.7%) HOMO-4→LUMO+2 (66.1%)	3.7442, 331.14	0.0375	 **LUMO (-1.69)**
	S_{25}	HOMO-7→LUMO (15.8%) HOMO-7→LUMO+2 (4.0%) HOMO-6→LUMO (5.7%) HOMO-5→LUMO+2 (7.0%) HOMO-3→LUMO+2 (55.4%) HOMO-3→LUMO+3 (2.5%)	3.8835, 319.26	0.2055	
	T_1	HOMO-9→LUMO+1 (3.0%) HOMO-6→LUMO+1 (7.2%) HOMO-4→LUMO+1 (5.6%) HOMO-3→LUMO+1 (12.5%) HOMO-2→LUMO (2.3%) HOMO-2→LUMO+1 (26.3%) HOMO-1→LUMO (2.2%) HOMO-1→LUMO+1 (23.9%) HOMO→LUMO+1 (4.4%)	2.2323, 555.41		
AC	S_6	HOMO-2→LUMO+1 (96.8%)	2.7435, 451.92	0.0330	
	S_{12}	HOMO-4→LUMO (68.7%) HOMO-4→LUMO+1 (7.4%) HOMO-3→LUMO (2.6%) HOMO-3→LUMO+1 (12.3%)	3.3181, 373.66	0.0326	 **HOMO (-4.72)**
	S_{18}	HOMO-7→LUMO (6.2%) HOMO-6→LUMO (81.0%)	3.8106, 325.37	0.0363	
	S_{20}	HOMO-8→LUMO (10.7%) HOMO-7→LUMO (68.1%) HOMO-6→LUMO (6.0%)	3.9149, 316.70	0.0515	
	S_{22}	HOMO-7→LUMO+1 (2.7%) HOMO-6→LUMO+1 (76.2%) HOMO-3→LUMO+3 (4.2%) HOMO-2→LUMO+3 (3.5%) HOMO→LUMO+4 (2.6%)	3.9579, 313.25	0.0581	**LUMO (-2.11)**
	T_1	HOMO-3→LUMO (2.3%) HOMO-1→LUMO (15.3%) HOMO→LUMO (78.8%)	2.0966, 591.36		

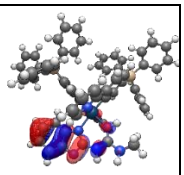
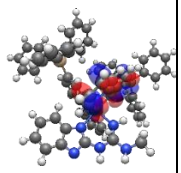
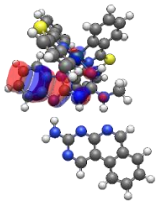
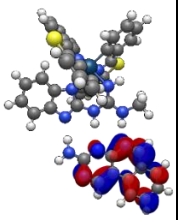
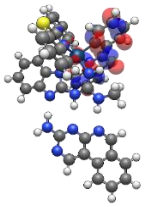
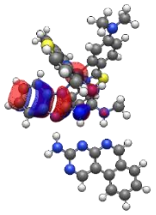
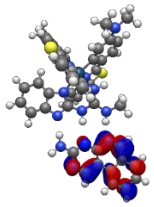
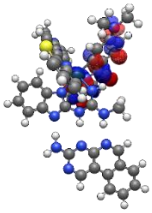
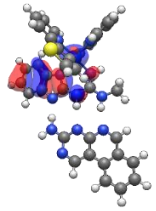
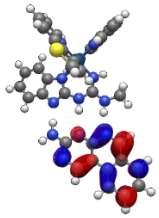
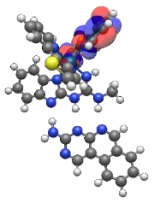
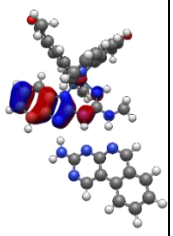
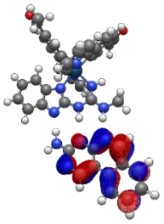
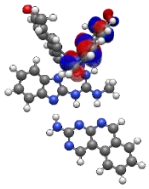
AD	S_6	HOMO-2→LUMO+1 (93.3%)	2.9874, 415.03	0.0190	
	S_{12}	HOMO-5→LUMO (2.0%) HOMO-4→LUMO (18.0%) HOMO-3→LUMO (67.1%) HOMO-3→LUMO+1 (6.2%)	3.5179, 352.44	0.0253	
	S_{16}	HOMO-5→LUMO (29.5%) HOMO-4→LUMO (3.2%) HOMO-4→LUMO+1 (59.1%)	3.7831, 327.73	0.0651	**HOMO (-4.58)**
	S_{20}	HOMO-5→LUMO+1 (89.5%) HOMO-4→LUMO+3 (2.1%)	3.9417, 314.54	0.0495	
	S_{24}	HOMO-6→LUMO (61.0%) HOMO-3→LUMO+2 (30.3%)	4.0531, 305.90	0.0277	
	T_1	HOMO-5→LUMO (4.4%) HOMO-3→LUMO (3.9%) HOMO-2→LUMO (35.2%) HOMO-1→LUMO (12.1%) HOMO→LUMO (37.2%)	2.5116, 493.64		**LUMO (-1.49)**

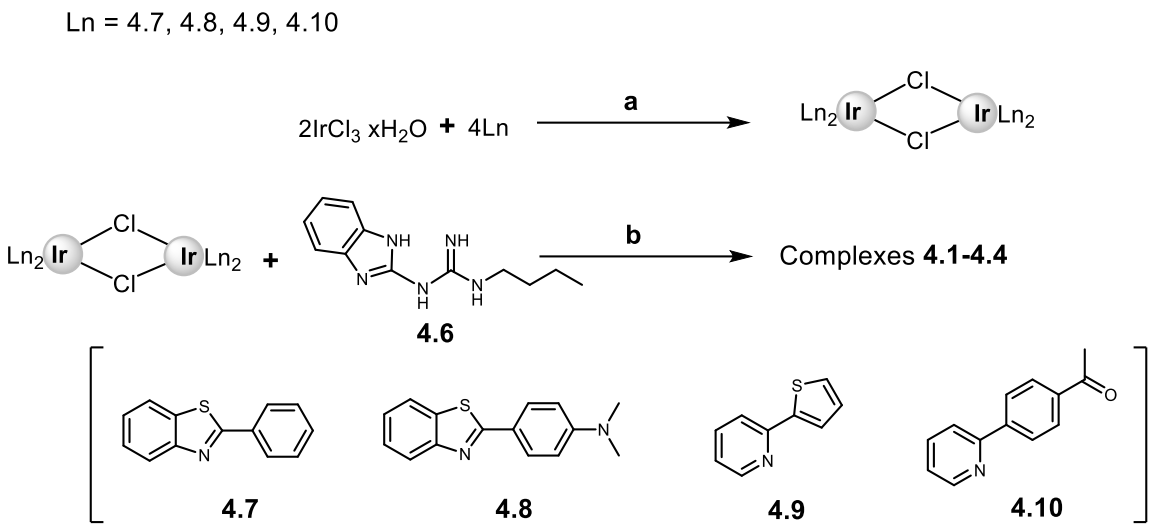
Table A.4.2 Summary of key findings of TD-DFT predictions for synthesised complexes **4.1-4.4** in the presence of compound **4.5** energy levels of five highest contributing singlet states and first triplet state (the predicted peak emission wavelength).

Complex	Spin State	Transition configurations	Excitation energy (eV, nm)	Oscillator strength	HOMO-LUMO (eV)
4.1•4.5	S_8	HOMO-2→LUMO+1 (86.7%) HOMO-1→LUMO+1 (8.9%)	2.8022, 442.45	0.0280	
	S_{12}	HOMO-5→LUMO (97.3%)	3.1642, 391.83	0.0416	
	S_{14}	HOMO-4→LUMO+1 (5.1%) HOMO-3→LUMO+1 (87.7%) HOMO-3→LUMO+2 (2.1%)	3.1992, 387.55	0.0284	**HOMO (-4.58)**
	S_{22}	HOMO-7→LUMO+2 (3.6%) HOMO-6→LUMO+2 (5.4%) HOMO-4→LUMO+2 (82.6%)	3.6617, 338.60	0.0730	
	S_{24}	HOMO-8→LUMO+1 (2.3%) HOMO-7→LUMO+1 (2.0%) HOMO-6→LUMO+1 (81.5%) HOMO-4→LUMO+1 (4.0%) HOMO-1→LUMO+4 (4.1%)	3.7415, 331.37	0.0515	
	T_1	HOMO-4→LUMO+2 (4.9%) HOMO-3→LUMO+1 (3.7%) HOMO-2→LUMO+2 (6.2%) HOMO-1→LUMO+1 (17.7%) HOMO-1→LUMO+2 (10.1%) HOMO→LUMO+1 (47.0%) HOMO→LUMO+2 (5.3%)	2.3593, 525.51		**LUMO (-2.18)**

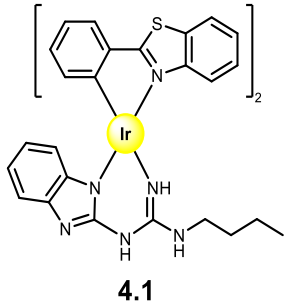
					 **LUMO+1 (-1.60)**
4.2•4.5	S_{12}	HOMO-4→LUMO+1 (7.5%) HOMO-3→LUMO+1 (6.5%) HOMO-2→LUMO+1 (75.6%) HOMO-1→LUMO+1 (5.1%)	2.9735, 416.96	0.0542	
	S_{16}	HOMO-7→LUMO (97.7%)	3.1560, 392.86	0.0430	
	S_{20}	HOMO-5→LUMO+1 (14.6%) HOMO-4→LUMO+1 (20.1%) HOMO-4→LUMO+3 (4.5%) HOMO-3→LUMO+1 (2.6%) HOMO-3→LUMO+3 (31.2%) HOMO-2→LUMO+3 (21.5%)	3.3236, 373.04	0.2942	**HOMO (-4.38)**
	S_{22}	HOMO-4→LUMO+3 (74.7%) HOMO-2→LUMO+3 (12.9%) HOMO-1→LUMO+3 (3.1%)	3.4089, 363.71	0.1731	
	S_{25}	HOMO-5→LUMO+1 (6.2%) HOMO-5→LUMO+3 (83.2%) HOMO-3→LUMO+3 (3.2%)	3.5823, 346.10	0.0410	**LUMO (-2.07)**
	T_1	HOMO-3→LUMO (3.8%) HOMO-2→LUMO (91.6%) HOMO-1→LUMO (4.1%)	2.3028, 538.40		 **LUMO+1 (-1.19)**
4.3•4.5	S_6	HOMO→LUMO+3 (95.4%)	2.7521, 450.51	0.0165	
	S_{14}	HOMO-6→LUMO (92.1%) HOMO-2→LUMO+3 (2.9%)	3.1578, 392.63	0.0415	
	S_{17}	HOMO-3→LUMO+1 (81.8%) HOMO→LUMO+4 (5.3%) HOMO→LUMO+6 (6.6%)	3.2790, 378.12	0.0197	
	S_{19}	HOMO-3→LUMO+1 (5.7%) HOMO-3→LUMO+3 (4.3%) HOMO-1→LUMO+4 (4.2%) HOMO-1→LUMO+6 (3.3%) HOMO→LUMO+4 (2.5%) HOMO→LUMO+6 (75.7%)	3.3723, 367.66	0.0128	**HOMO (-4.53)**
	S_{21}	HOMO-3→LUMO+3 (69.6%) HOMO-1→LUMO+4 (10.6%) HOMO→LUMO+6 (7.2%)	3.4169, 362.86	0.0289	
	T_1	HOMO-4→LUMO+1 (9.4%)	2.3597, 543.22		**LUMO (-2.18)**

		HOMO-3→LUMO+1 (14.7%) HOMO-2→LUMO+1 (39.9%) HOMO→LUMO+1 (25.3%)			 **LUMO+1 (-1.31)**
4.4•4.5	S_8	HOMO-2→LUMO+1 (40.5%) HOMO-1→LUMO+1 (8.1%) HOMO-1→LUMO+2 (43.6%) HOMO→LUMO+2 (2.5%)	2.6559, 466.82	0.0076	
	S_9	HOMO-2→LUMO+2 (89.1%) HOMO-1→LUMO+2 (5.5%)	2.8522, 434.69	0.0263	
	S_{13}	HOMO-3→LUMO+1 (83.8%) HOMO-3→LUMO+2 (5.0%) HOMO→LUMO+4 (2.1%) HOMO→LUMO+5 (3.8%)	3.1378, 395.14	0.0261	**HOMO (-4.74)**
	S_{14}	HOMO-5→LUMO (90.4%) HOMO-4→LUMO (7.1%)	3.1688, 391.26	0.0425	
	S_{21}	HOMO-4→LUMO+1 (5.1%) HOMO-2→LUMO+4 (72.7%) HOMO-1→LUMO+4 (4.1%) HOMO-1→LUMO+5 (10.7%)	3.3794, 366.88	0.0072	**LUMO (-2.17)**
	T_1	HOMO-6→LUMO (6.9%) HOMO-6→LUMO (2.3%) HOMO-3→LUMO (2.1%) HOMO-2→LUMO (57.5%) HOMO-2→LUMO (2.4%) HOMO-1→LUMO (3.1%) HOMO→LUMO+1 (18.4%)	2.3331, 531.42		 **LUMO+1 (-1.89)**

A4.2: Synthetic Procedures of Complexes 4.1-4.4



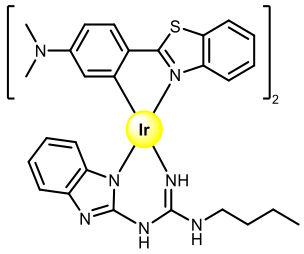
Scheme A.4.1 The general synthetic route of all iridium complexes herein. Reagents and conditions: a) 2-ethoxyethanol: water (3:1), 130 °C, 19 hr; b) K_2CO_3, toluene, N_2, 110 °C, 16 hr. Ligands **4.6-4.10** were all synthesised using microwave modified procedures from the literature.



4.1

Iridium complex 4.1 – Iridium chloro-bridged dimer made from Ligand **4.7** (2-phenylbenzothiazole) (0.34 g, 0.26 mmol) was added to a Schlenk flask with 1-(1H-benzo[d]imidazole-2-yl)-3-butylguanidine) (**4.6**), (0.12 g, 0.52 mmol) and 10 equivalents of potassium carbonate (0.36 g, 2.58 mmol) was degassed and dissolved in dry toluene (20 mL). The mixture was refluxed for 16 hours at 110 °C, after this it was cooled, the solvent was removed under reduced pressure, and the crude was redissolved in DCM

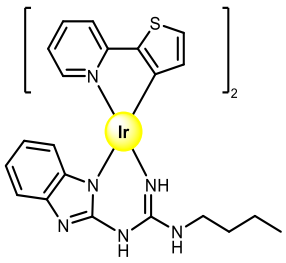
before being extracted with water. The combined organic phases were then purified by column chromatography (DCM/MeOH, 95:5), the final product was a yellow solid (0.28 g, 63%). ^{1}H NMR (400 MHz, DMSO-d_6) δ 12.45 (s, 1H), 10.91 (s, 1H), 8.28 (d, J = 7.0 Hz, 1H), 8.19 (dd, J = 5.5, 2.4 Hz, 1H), 7.86 (dd, J = 24.6, 8.4 Hz, 2H), 7.54 – 7.48 (m, 2H), 7.45 (t, J = 7.7 Hz, 1H), 7.35 (d, J = 7.9 Hz, 1H), 7.15 (t, J = 8.4 Hz, 2H), 7.04 – 6.92 (m, 3H), 6.83 – 6.72 (m, 3H), 6.60 (t, J = 8.4 Hz, 1H), 6.43 (d, J = 7.1 Hz, 1H), 6.20 (d, J = 7.0 Hz, 1H), 5.94 (d, J = 8.3 Hz, 1H), 5.66 (s, 1H), 3.25 – 3.01 (m, 2H), 1.27 – 1.18 (m, 2H), 1.15 – 1.05 (m, 2H), 0.74 (t, J = 7.3 Hz, 3H). ^{13}C NMR (101 MHz, DMSO-d_6) δ 181.21, 180.38, 150.34, 149.74, 141.49, 140.90, 140.09, 133.83, 132.35, 131.77, 131.23, 130.93, 130.74, 127.68, 127.57, 126.69, 125.95, 125.70, 125.57, 124.11, 123.92, 122.39, 122.04, 121.67, 121.53, 119.45, 118.09, 115.89, 111.39, 54.92, 30.64, 19.10, 13.47. HMRS [ESI+] ion $[C_{38}H_{33}IrN_7S_2]^+$ m/z calculated: 844.1863 Found: 844.1868 [M+].



4.2

Iridium complex 4.2 – Iridium chloro-bridged dimer made from Ligand **4.8** (2-(4-dimethylaminophenyl)benzothiazole) (0.39 g, 0.26 mmol) was added to a Schlenk flask with 1-(1H-benzo[d]imidazole-2-yl)-3-butylguanidine) (**4.6**), (0.12 g, 0.53 mmol) and 10 equivalents of potassium carbonate (0.37 g, 2.64 mmol). The mixture was degassed and dissolved in dry toluene (20 mL). The mixture was refluxed for 16 hours at 110 °C, after

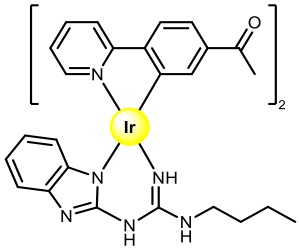
this it was cooled, the solvent was removed under reduced pressure and the crude was redissolved in DCM before being extracted with water. The combined organic phases were then purified by column chromatography (DCM/MeOH, 90:10), the final product was an orange-yellow solid (48 %, 240 mg). ^{1}H NMR (400 MHz, DMSO-d_6) δ 12.54 (s, 1H), 10.65 (s, 1H), 8.09 (d, J = 7.8 Hz, 1H), 8.02 (d, J = 8.8 Hz, 2H), 7.68 (d, J = 8.6 Hz, 1H), 7.55 (d, J = 8.6 Hz, 1H), 7.42 – 7.24 (m, 4H), 7.03 (dt, J = 24.8, 7.9 Hz, 3H), 6.65 (t, J = 8.4 Hz, 2H), 6.41 (dd, J = 8.8, 2.5 Hz, 1H), 6.34 (dd, J = 8.7, 2.6 Hz, 1H), 6.26 (d, J = 8.4 Hz, 1H), 5.66 (d, J = 2.5 Hz, 1H), 5.57 (s, 1H), 5.41 (d, J = 2.5 Hz, 1H), 3.18 – 2.97 (m, 2H), 2.59 (s, 4H), 2.51 (s, 5H), 1.20 (d, J = 6.6 Hz, 1H), 1.15 – 1.04 (m, 2H), 0.76 (t, J = 7.3 Hz, 3H). ^{13}C NMR (101 MHz, DMSO-d_6) δ 179.85, 179.00, 155.47, 152.98, 151.42, 151.08, 150.89, 150.12, 144.99, 140.39, 131.66, 130.27, 130.20, 129.34, 128.68, 127.79, 127.08, 124.12, 123.96, 123.37, 123.17, 122.43, 121.81, 118.39, 116.89, 116.41, 115.02, 13.53, 111.33, 106.37, 106.02, 54.91, 30.55, 19.15, 13.50. HMRS [ESI+] ion $[C_{42}H_{43}IrN_9S_2]^+$ m/z calculated: 930.2707 Found: 930.2669 [M+].



4.3

Iridium complex 4.3 – Iridium chloro-bridged dimer made from Ligand **4.9** (2-(2-thienyl)pyridine) (0.47 g, 0.43 mmol) was added to a Schlenk flask with 1-(1H-benzo[d]imidazole-2-yl)-3-butylguanidine) (**4.6**), (0.20 g, 0.86 mmol) and 10 equivalents of potassium carbonate (0.60 g, 4.33 mmol) was degassed and dissolved in dry toluene

(20 mL). The mixture was refluxed for 16 hours at 110 °C, after this it was cooled, the solvent was removed under reduced pressure and the crude was redissolved in DCM before being extracted with water. The combined organic phases were then purified by column chromatography (DCM/MeOH, 20:80), the final product was a yellow solid (0.46 g, 72%). ^{1}H NMR (400 MHz, DMSO-d_6) δ 11.17 (s, 1H), 8.64 (d, J = 5.6 Hz, 1H), 7.93 (d, J = 5.8 Hz, 1H), 7.79 (td, J = 7.4, 1.6 Hz, 1H), 7.75 – 7.69 (m, 1H), 7.69 – 7.65 (m, 1H), 7.59 (d, J = 7.8 Hz, 1H), 7.50 (d, J = 4.6 Hz, 1H), 7.39 (d, J = 4.8 Hz, 1H), 7.27 (d, J = 7.1 Hz, 1H), 7.09 (ddd, J = 7.4, 5.9, 1.5 Hz, 1H), 7.01 (ddd, J = 7.4, 5.9, 1.5 Hz, 1H), 6.94 (t, J = 7.6 Hz, 1H), 6.63 (t, J = 7.6 Hz, 1H), 6.17 (d, J = 4.6 Hz, 1H), 6.01 – 5.94 (m, 1H), 5.32 (s, 1H), 3.09 (hept, J = 6.8 Hz, 2H), 1.32 – 1.22 (m, 2H), 1.13 (h, J = 7.2 Hz, 2H), 0.77 (t, J = 7.3 Hz, 3H). ^{13}C NMR (101 MHz, DMSO-d_6) δ 166.59, 164.87, 164.00, 159.82, 155.80, 154.93, 152.51, 149.74, 149.00, 142.39, 137.39, 135.89, 135.11, 134.57, 132.74, 131.00, 128.94, 128.40, 119.46, 119.05, 118.54, 117.09, 116.71, 114.12, 109.06, 40.72, 31.48, 19.52, 13.74. HMRS [ESI+] ion $[C_{30}H_{29}IrN_7S_2]^+$ m/z calculated: 744.1550. Found: 744.1547 [M+].



4.4

Iridium complex 4.4: Iridium chloro-bridged dimer made from Ligand **4.10** (1-[4-(2-pyridinyl)phenyl]ethanone) (0.53 g, 0.43 mmol) was added to a Schlenk flask with 1-(1H-benzo[d]imidazole-2-yl)-3-butylguanidine) (**4.6**), (0.20 g, 0.86 mmol) and 10

equivalents of potassium carbonate (0.60 g, 4.33 mmol) was degassed and dissolved in dry toluene (20 mL). The mixture was refluxed for 16 hours at 110 °C, after this it was cooled, the solvent was removed under reduced pressure and the crude was redissolved in DCM before being extracted with water. The combined organic phases were then purified by column chromatography (DCM/MeOH, 10:90), the final product was a red solid (0.53 g, 76%). ^{1}H NMR (400 MHz, DMSO-*d*$_6$) δ 12.44 (s, 1H), 10.33 (s, 1H), 8.87 (d, *J* = 5.1 Hz, 1H), 8.37 (d, *J* = 8.1 Hz, 1H), 8.31 (d, *J* = 7.8 Hz, 1H), 8.21 (d, *J* = 4.4 Hz, 1H), 8.05 (t, *J* = 7.9 Hz, 1H), 7.99 (t, *J* = 8.2 Hz, 2H), 7.93 (d, *J* = 8.3 Hz, 1H), 7.54 – 7.42 (m, 3H), 7.38 (t, *J* = 6.7 Hz, 1H), 6.93 (s, 1H), 5.90 (d, *J* = 7.6 Hz, 1H), 3.05 (p, *J* = 6.9 Hz, 2H), 1.22 (d, *J* = 8.1 Hz, 2H), 1.08 (d, *J* = 7.6 Hz, 2H), 0.74 (t, *J* = 7.3 Hz, 3H). ^{13}C NMR (101 MHz, DMSO-*d*$_6$) δ 198.04, 197.82, 166.62, 166.01, 153.14, 151.37, 149.99, 149.69, 149.63, 149.55, 145.37, 140.07, 138.18, 138.01, 136.16, 136.07, 132.15, 130.77, 129.88, 124.53, 124.48, 123.95, 123.87, 122.29, 121.96, 121.79, 121.34, 120.78, 120.41, 115.66, 111.17, 40.40, 30.33, 26.47, 26.38, 19.20, 13.54. HMRS [ESI+] ion $[C_{38}H_{37}IrN_7O_2]^+$ m/z calculated: 816.2633. Found: 816.2633 [M+].

Ligand 4.7 (2-Phenylbenzothiazole): 2-Bromobenzothiazole (0.56 g, 2.62 mmol), phenyl boronic acid (0.47 g, 3.40 mmol), potassium carbonate (1.80 g, 13.08 mmol) and $Pd(PPh_3)_4$ (1% catalyst loading) were added to a sealed microwave tube along with 15 mL of 1,4-dioxane/water (3:1). The reaction vessel was heated to 160 °C for 21 minutes, then cooled to room temperature. The crude was extracted with DCM (3 × 20 mL) and was then washed with water (20 mL), then saturated ammonium chloride solution (20 mL) and then brine (20 mL). The combined organic was then dried under reduced

pressure and was purified via column chromatography on silica gel with an eluent of DCM (100%), product is a white crystalline solid, yield (0.43 g, 77%). ^{1}H NMR (400 MHz, DMSO-d_6) δ 8.16 (dd, *J = 8.0, 2.1* Hz, 1H), 8.13 – 8.05 (m, 3H), 7.64 – 7.53 (m, 4H), 7.48 (ddd, *J = 8.4, 7.2, 1.3* Hz, 1H). ^{13}C NMR (101 MHz, DMSO-d_6) δ 167.29, 153.55, 134.44, 132.85, 131.43, 129.42, 127.20, 126.68, 125.57, 122.89, 122.38.

Ligand 4.8 (2-(4-Dimethylaminophenyl)benzothiazole): 2- Bromobenzothiazole (0.5 g, 2.34 mmol), 4-dimethylaminophenylboronic acid (0.5 g, 3.04 mmol), potassium carbonate (1.6 g, 11.68 mmol) and $Pd(PPh_3)_4$ (1% catalyst loading) were added to a sealed microwave tube along with 15 mL of 1,4-dioxane/water (1:1). The reaction vessel was heated to 160 °C for 21 minutes, then cooled to room temperature. Upon cooling to room temperature, the product crashed out of solution as a crystalline yellow solid. These crystals were collected via vacuum filtration and were then purified through washing thoroughly with water (≈100 mL), yield (0.40 g, 68%). ^{1}H NMR (400 MHz, $CDCl_3$) δ 8.00 – 7.94 (m, 3H), 7.84 (ddd, *J = 7.9, 1.3, 0.6* Hz, 1H), 7.43 (ddd, *J = 8.3, 7.3, 1.3* Hz, 1H), 7.30 (ddd, *J = 8.4, 7.3, 1.2* Hz, 1H), 6.77 – 6.73 (m, 2H), 3.06 (s, 6H). ^{13}C NMR (101 MHz, $CDCl_3$) δ 168.96, 154.57, 152.34, 134.70, 129.01, 126.12, 124.33, 122.43, 121.49, 111.84, 40.34.

ligand 4.9 (2-(2-thienyl)pyridine): 2-Bromopyridine (0.59 mL, 6.2 mmol), 2-thienylboronic acid (0.793 g, 6.2 mmol), K_2CO_3 (3.43 g, 24.8 mmol), and $Pd(PPh_3)_4$ (1% catalyst loading) were added to a microwave tube along with 16 mL of degassed 1,4-dioxane/water (3:1). The reaction vessel was heated to 160 °C for 21 minutes, then

cooled to room temperature. The post-reaction mixture was extracted with ethyl acetate (3 × 20 mL) and the organic layer dried over $MgSO_4$ before concentrating under reduced pressure. The resulting crude product was purified by column chromatography on silica gel with hexanes/ethyl acetate (9:1) as eluent. Yield (0.60 g, 60%). ^{1}H NMR (400 MHz, $CDCl_3$) δ 8.57 (dt, *J* = 4.9, 1.6 Hz, 1H), 7.73 – 7.62 (m, 2H), 7.59 (dd, *J* = 3.7, 1.2 Hz, 1H), 7.40 (dd, *J* = 5.1, 1.2 Hz, 1H), 7.21 – 7.08 (m, 2H). ^{13}C NMR (101 MHz, $CDCl_3$, 298 K) δ 152.61, 149.58, 144.90, 136.67, 128.07, 127.60, 124.55, 121.93, 118.80.

Ligand 4.10 (1-[4-(pyridin-2-yl)phenyl]ethan-1-one): 2-Bromopyridine (0.54 mL, 5.07 mmol), 4-acetylphenylboronic acid (0.83 g, 5.07 mmol), K_2CO_3 (2.80 g, 20.28 mmol), and $Pd(PPh_3)_4$ (1% catalyst loading) were added to a microwave tube along with 16 mL of degassed 1,4-dioxane/water (3:1). The reaction vessel was heated to 160 °C for 21 minutes, then cooled to room temperature. The post-reaction mixture was extracted with ethyl acetate (3 × 20 mL) and the organic layer dried over $MgSO_4$ before concentrating under reduced pressure. The resulting crude product was purified by column chromatography on silica gel with hexanes/ethyl acetate (9:1) as eluent. Yield (0.81 g, 81%). ^{1}H NMR (400 MHz, DMSO-*d*$_6$) δ 8.73 (d, *J* = 4.8 Hz, 1H), 8.28 – 8.20 (m, 4H), 8.12 – 8.04 (m, 4H), 7.96 (t, *J* = 7.6 Hz, 1H), 7.45 (dd, *J* = 7.4, 4.8 Hz, 2H), 2.63 (s, 7H). ^{13}C NMR (101 MHz, DMSO-*d*$_6$) δ 197.61, 154.34, 149.18, 142.03, 138.21, 137.04, 128.70, 126.86, 123.66, 121.42, 26.87.

A4.3: ^{1}H and ^{13}C NMR Spectra and Mass spectra

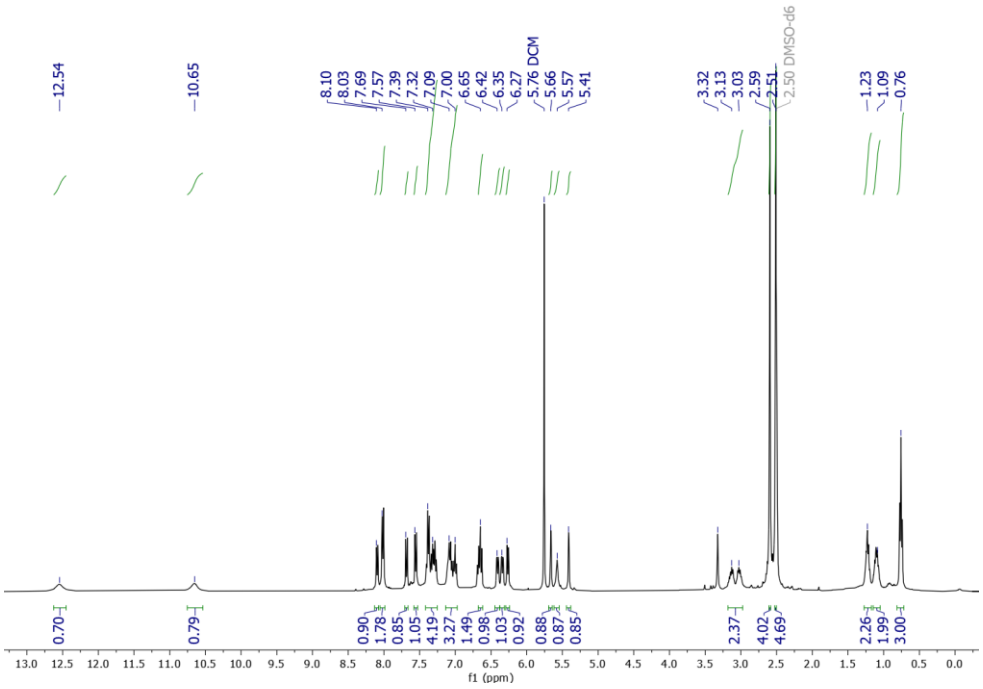


Figure A.4.1 ^{1}H NMR spectrum of iridium complex **4.1**, DMSO-d_6, 400 MHz, 298 K.

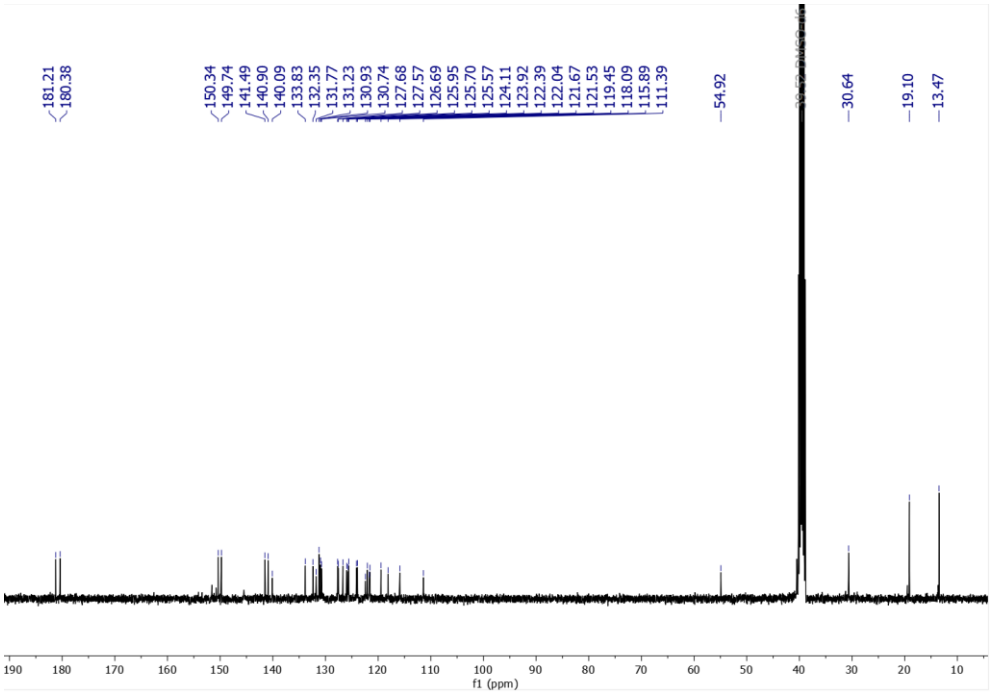


Figure A.4.2 ^{13}C NMR spectrum of iridium complex **4.1,** DMSO-d_6, 101 MHz, 298 K.

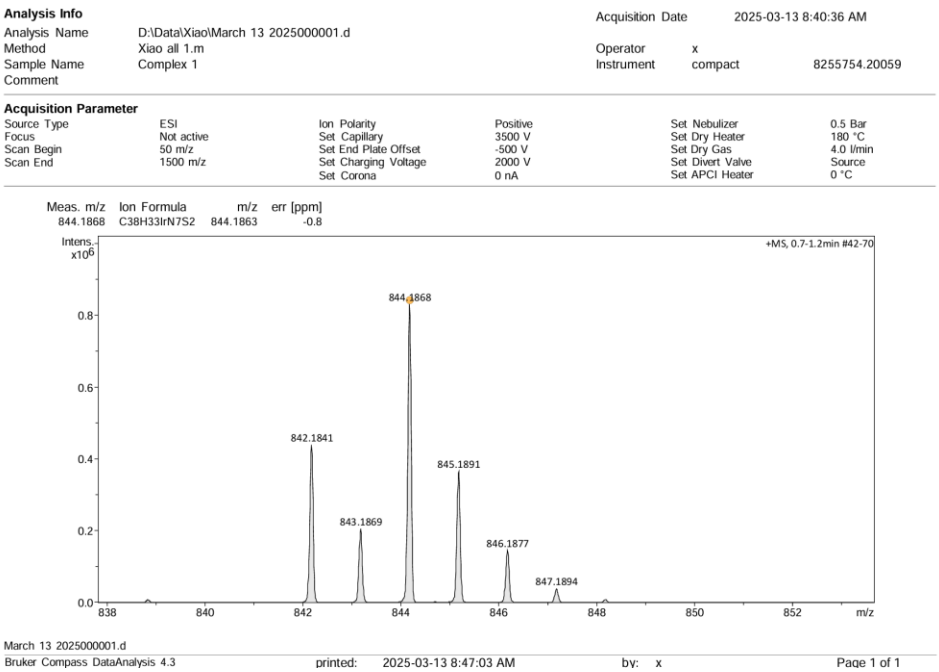


Figure A.4.3 Mass spectrum of iridium complex **4.1**. HMRS [ESI+] ion $[C_{38}H_{33}IrN_7S_2]^+$ m/z calculated: 844.1863 Found: 844.1868 [M+].

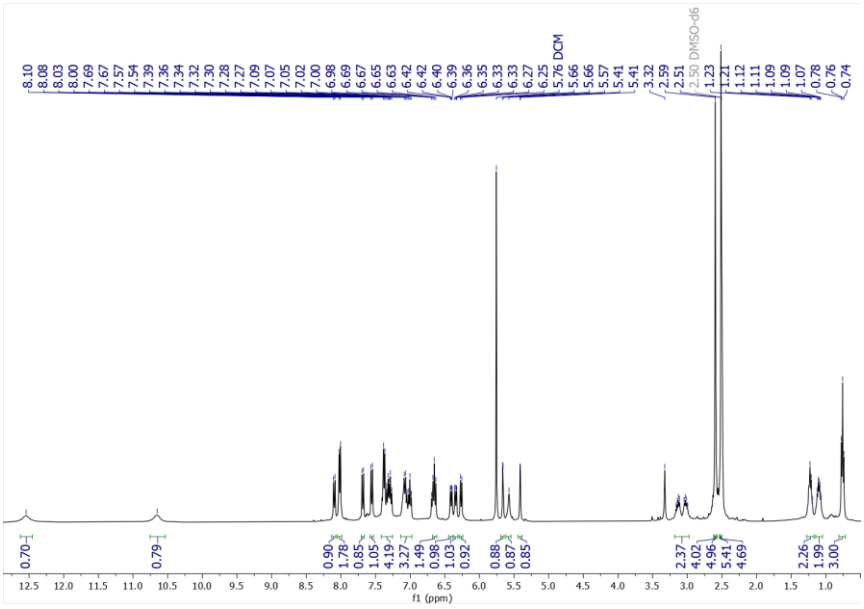


Figure A.4.4 ^{1}H NMR spectrum of iridium complex **4.2**, DMSO-d_6, 400 MHz, 298 K.

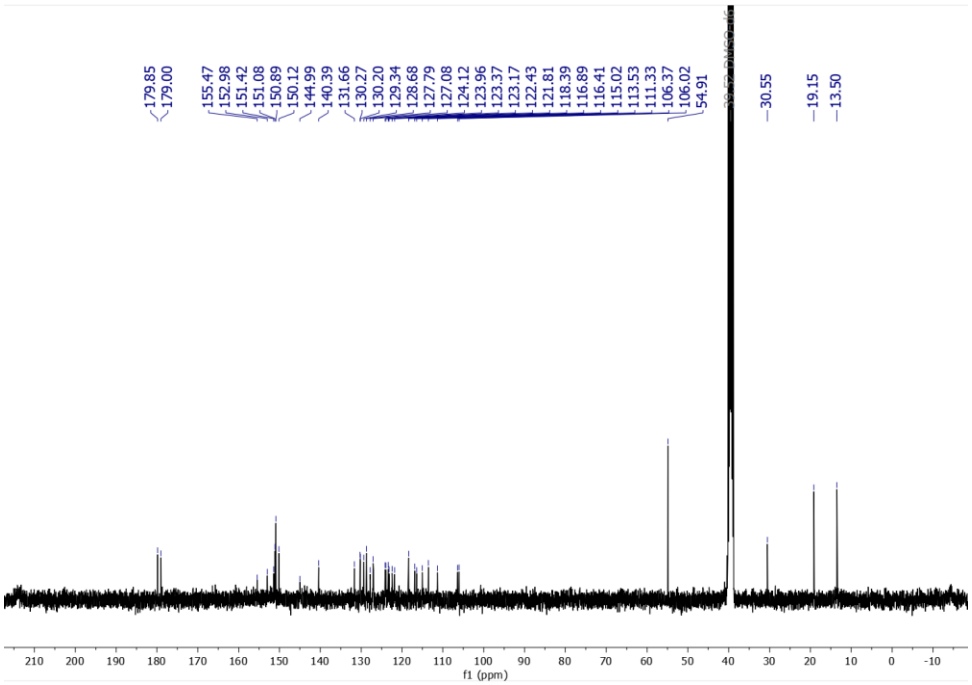


Figure A.4.5 ^{13}C NMR spectrum of iridium complex **4.2**, DMSO-d_6, 101 MHz, 298 K.

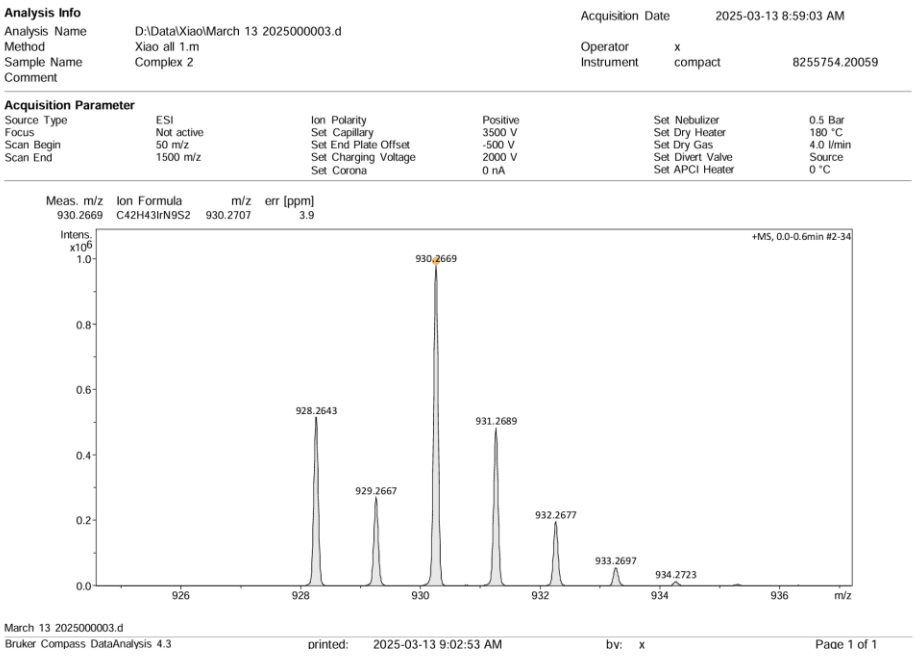


Figure A.4.6 Mass spectrum of iridium complex **4.2**. HMRS [ESI+] ion $[C_{42}H_{43}IrN_9S_2]^+$ m/z calculated: 930.2707 Found: 930.2669 [M+].

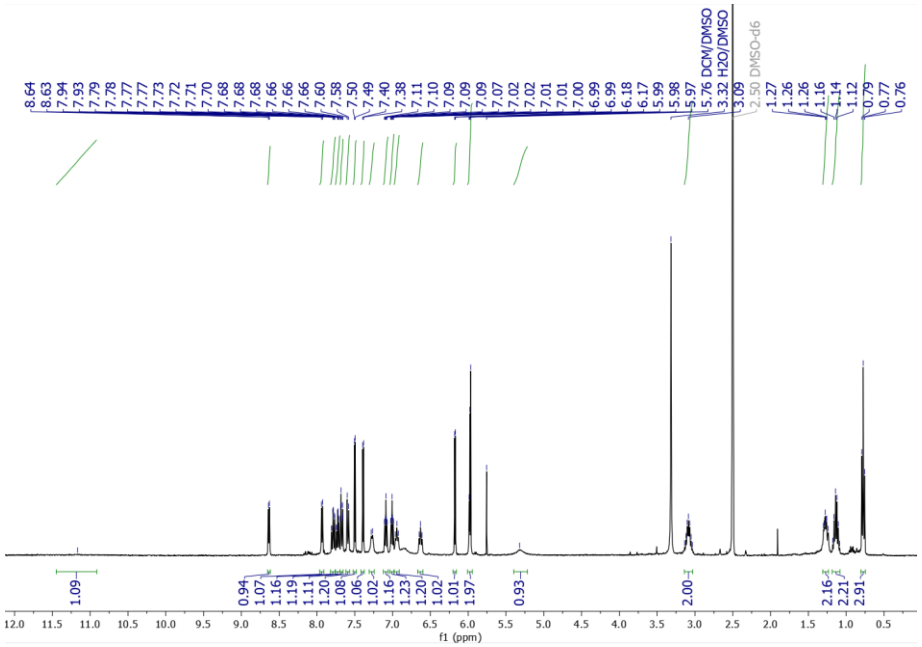


Figure A.4.7 ^{1}H NMR spectrum of iridium complex **4.3**, DMSO-d_6, 400 MHz, 298 K.

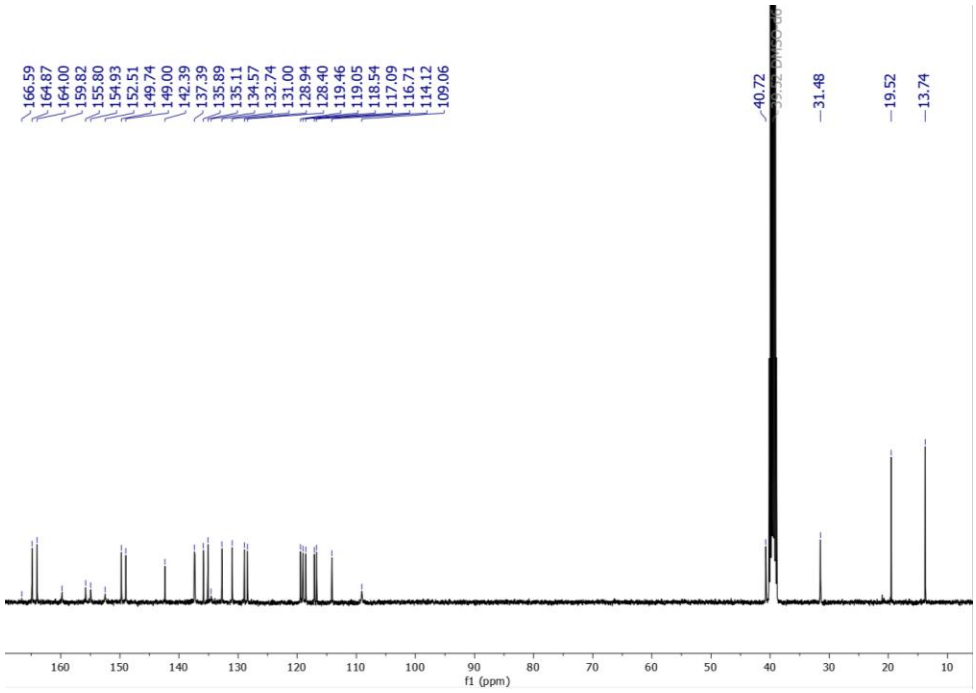


Figure A.4.8 ^{13}C NMR spectrum of iridium complex **4.3**, DMSO-d_6, 101 MHz, 298 K.

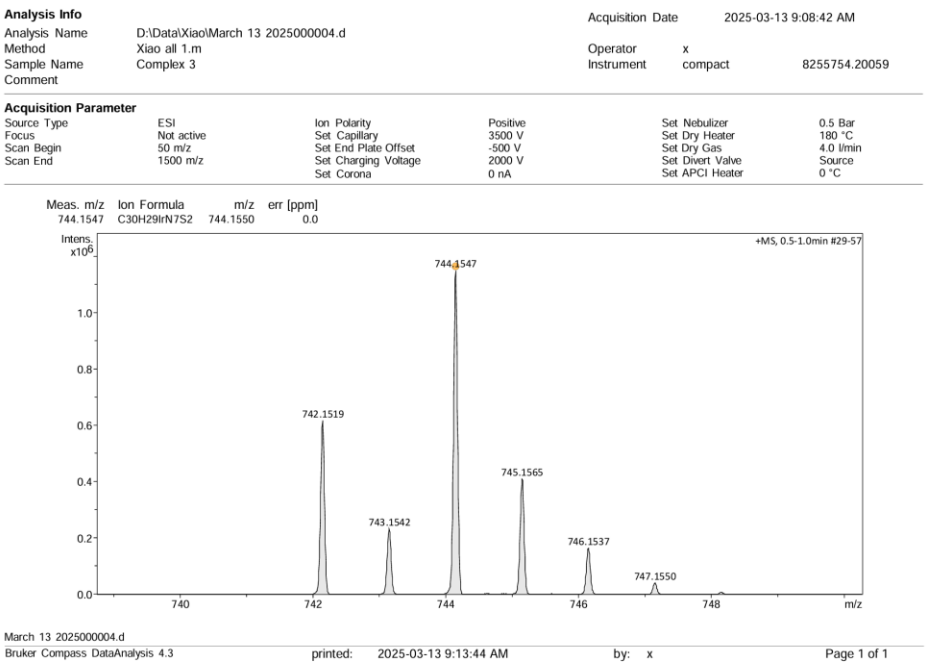


Figure A.4.9 Mass spectrum of iridium complex **4.3**. HMRS [ESI+] ion $[C_{30}H_{29}IrN_7S_2]^+$ m/z calculated: 744.1550. Found: 744.1547 [M+].

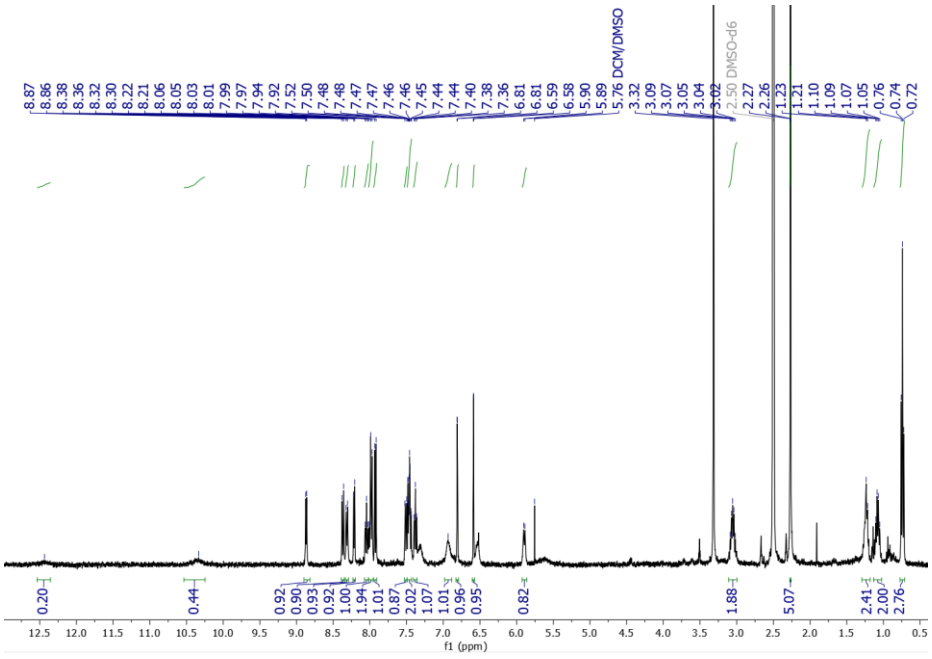


Figure A.4.10 ^{1}H NMR spectrum of iridium complex **4.4**, DMSO-d_6, 400 MHz, 298 K.

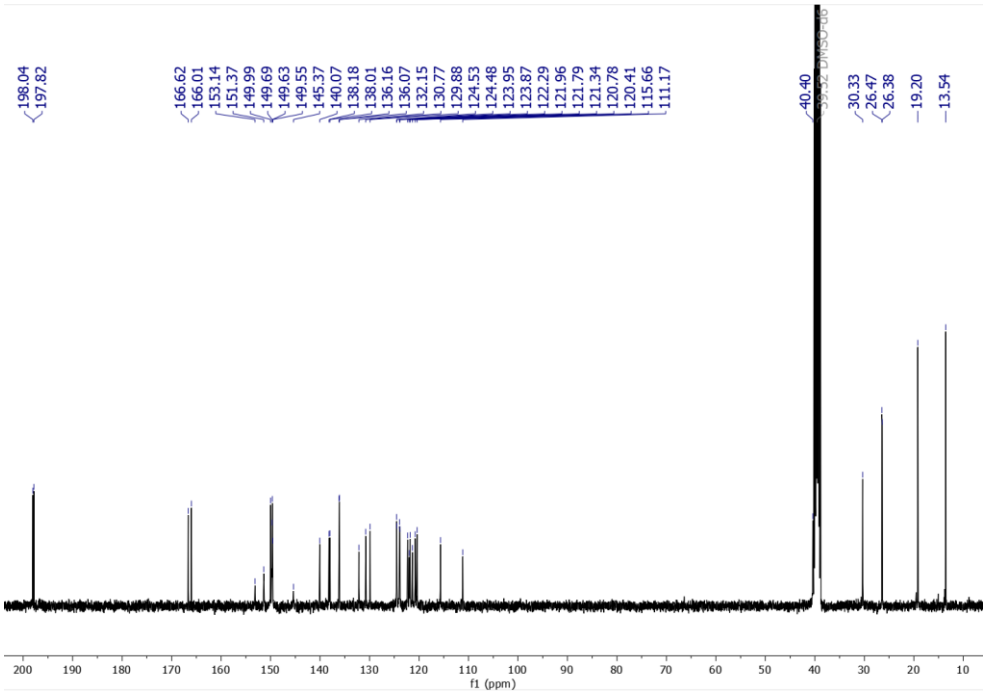


Figure A.4.11 ^{13}C NMR spectrum of iridium complex **4.4**, DMSO-d_6, 101 MHz, 298 K.

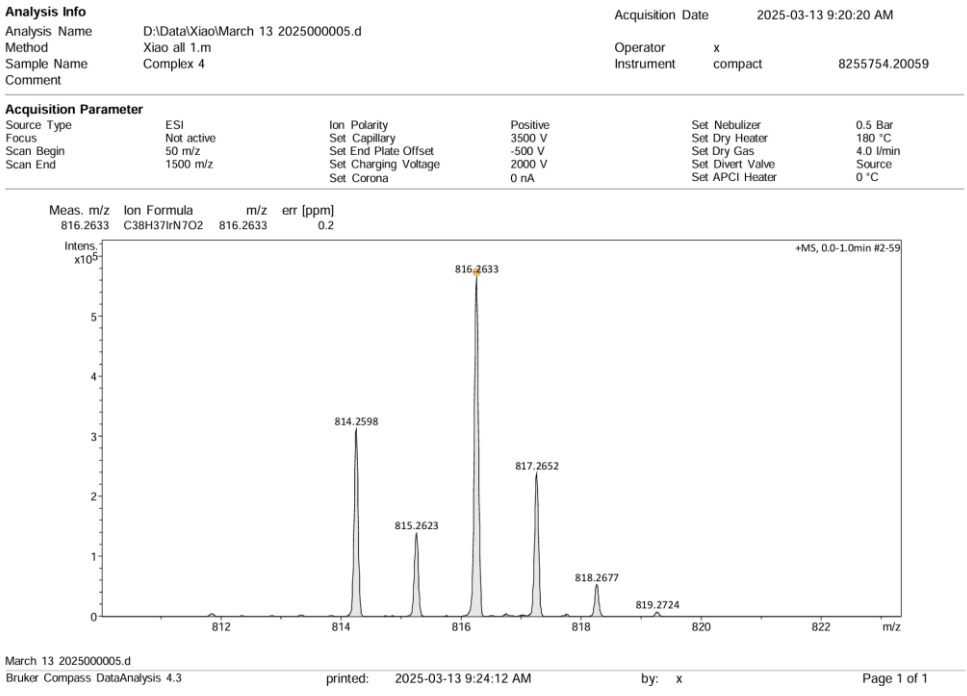


Figure A.4.12 Mass spectrum of iridium complex **4.4**. HMRS [ESI+] ion $[C_{38}H_{37}IrN_7O_2]^+$ m/z calculated: 816.2633. Found: 816.2633 [M+].

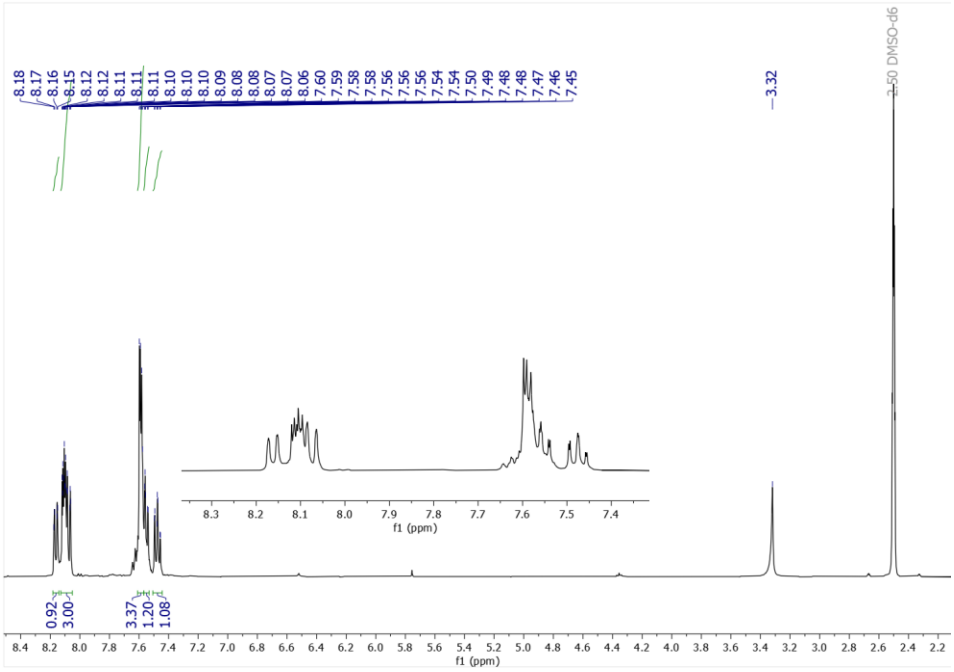


Figure A.4.13 ^{1}H NMR spectrum of ligand **4.7**, DMSO-d_6, 400 MHz, 298 K.

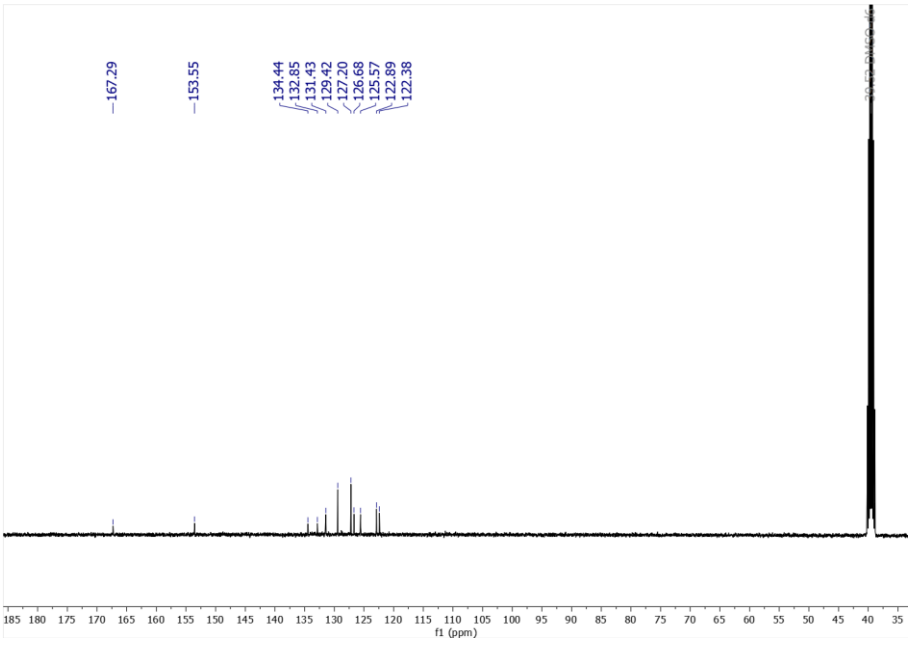


Figure A.4.14 ^{13}C NMR spectrum of ligand **4.7**, DMSO-d_6, 101 MHz, 298 K.

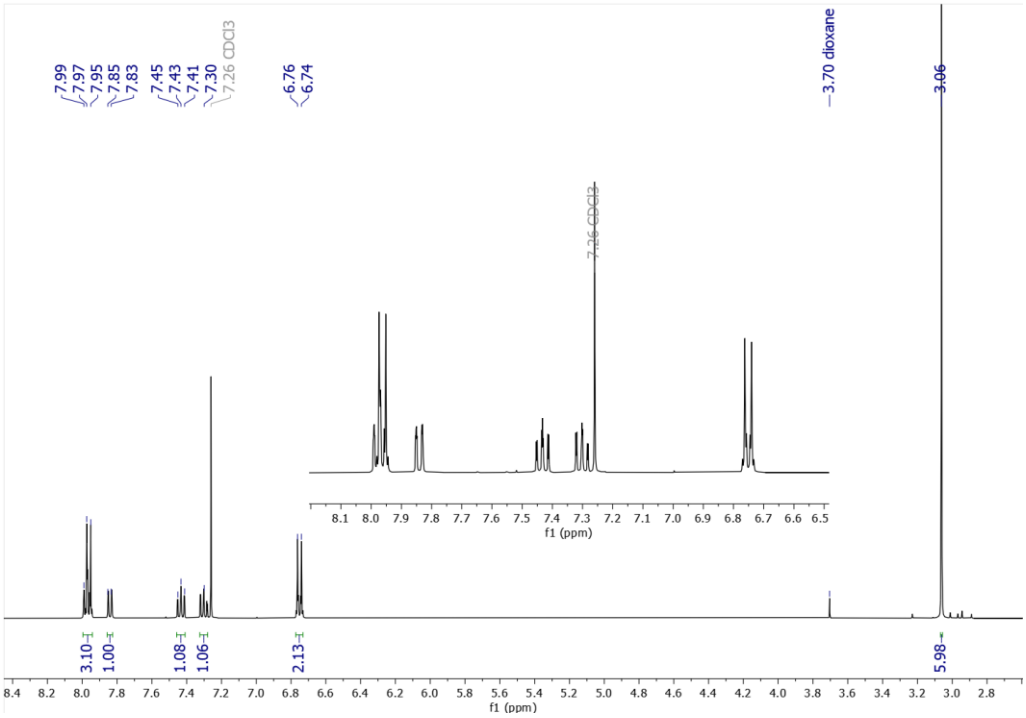


Figure A.4.15 ^{1}H NMR spectrum of ligand **4.8**, $CDCl_3$, 400 MHz, 298 K.

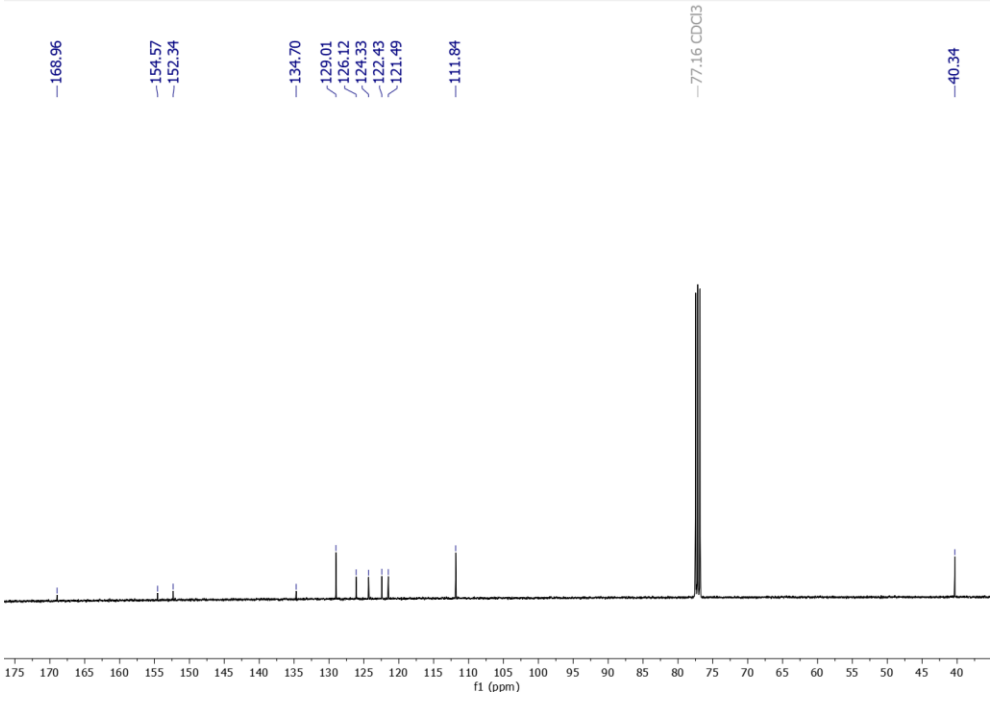


Figure A.4.16 ^{13}C NMR spectrum of ligand **4.8**, $CDCl_3$, 101 MHz, 298 K.

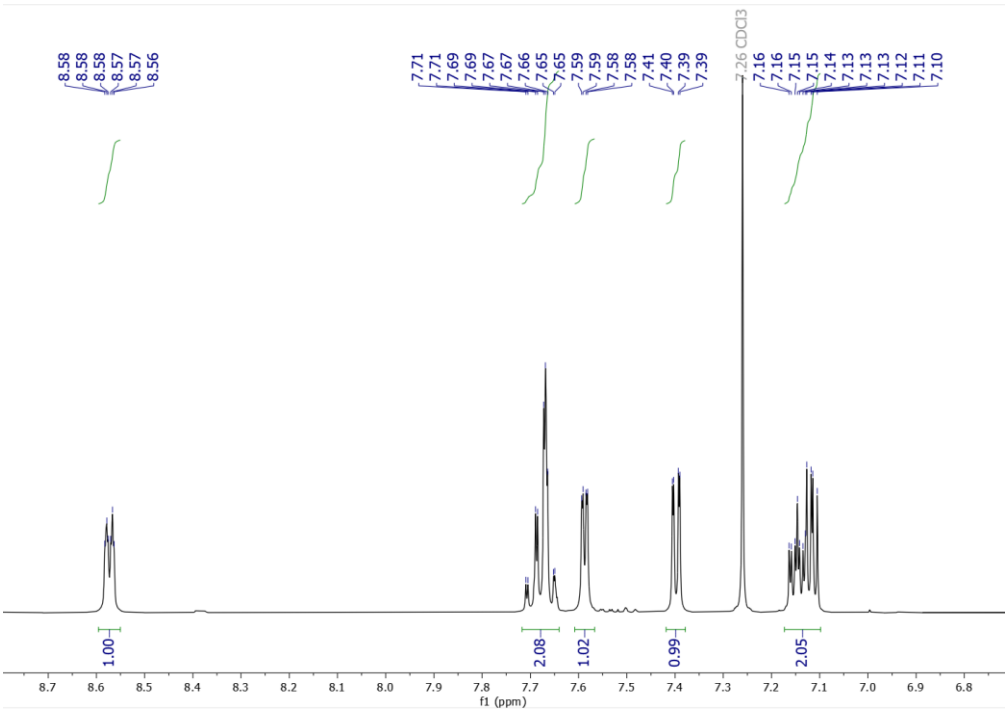


Figure A.4.17 ^{1}H NMR spectrum of ligand **4.9**, $CDCl_3$, 400 MHz, 298 K.

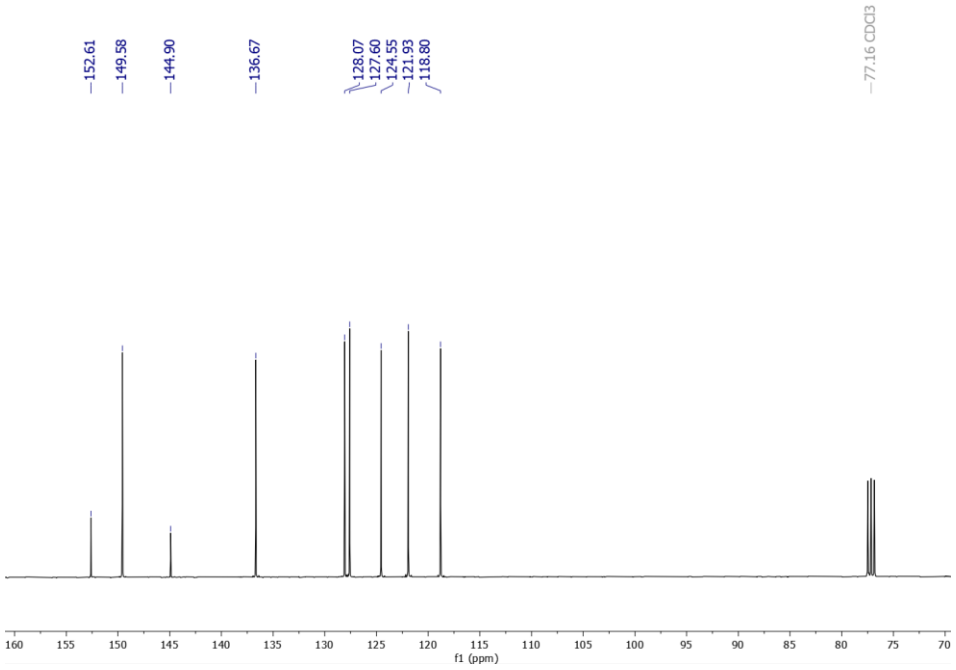


Figure A.4.18 ^{13}C NMR spectrum of ligand **4.9**, $CDCl_3$, 101 MHz, 298 K.

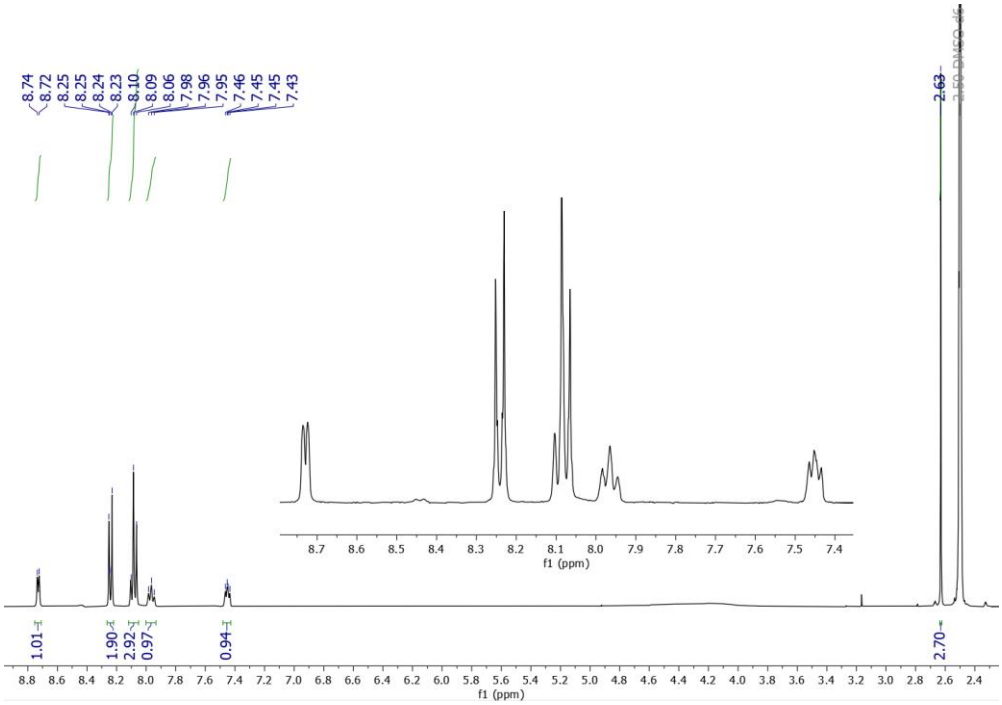


Figure A.4.19 ^{1}H NMR spectrum of ligand **4.10**, DMSO-d_6, 400 MHz, 298 K.

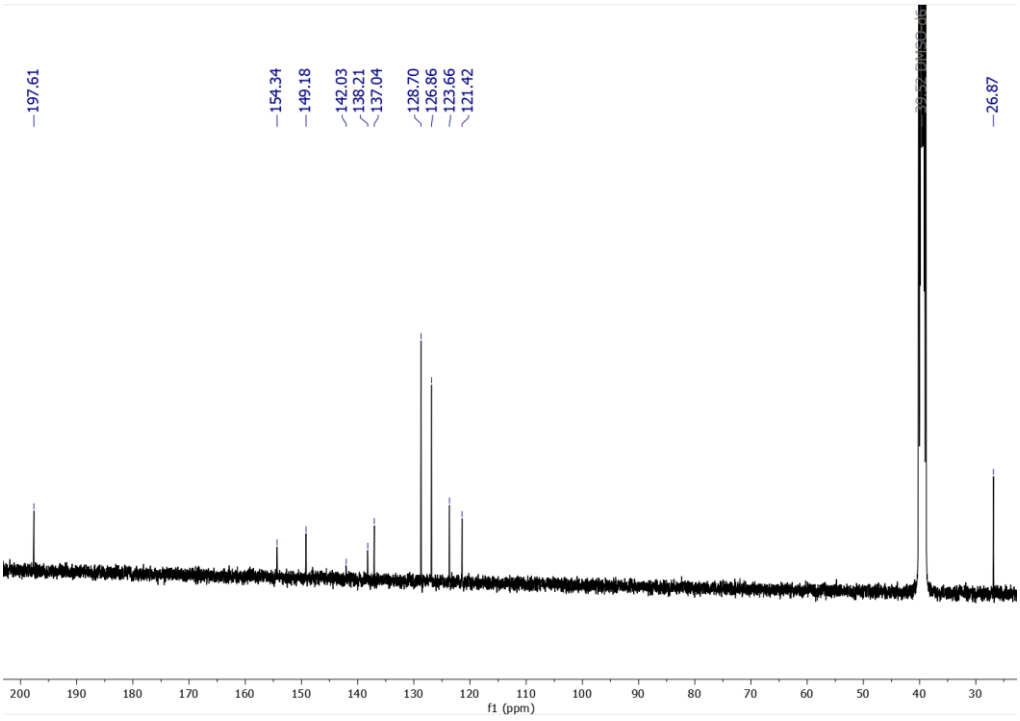


Figure A.4.20 ^{13}C NMR spectrum of ligand **4.10**, DMSO-d_6, 101 MHz, 298 K.

A4.4: UV-vis, Excitation and Emission Data

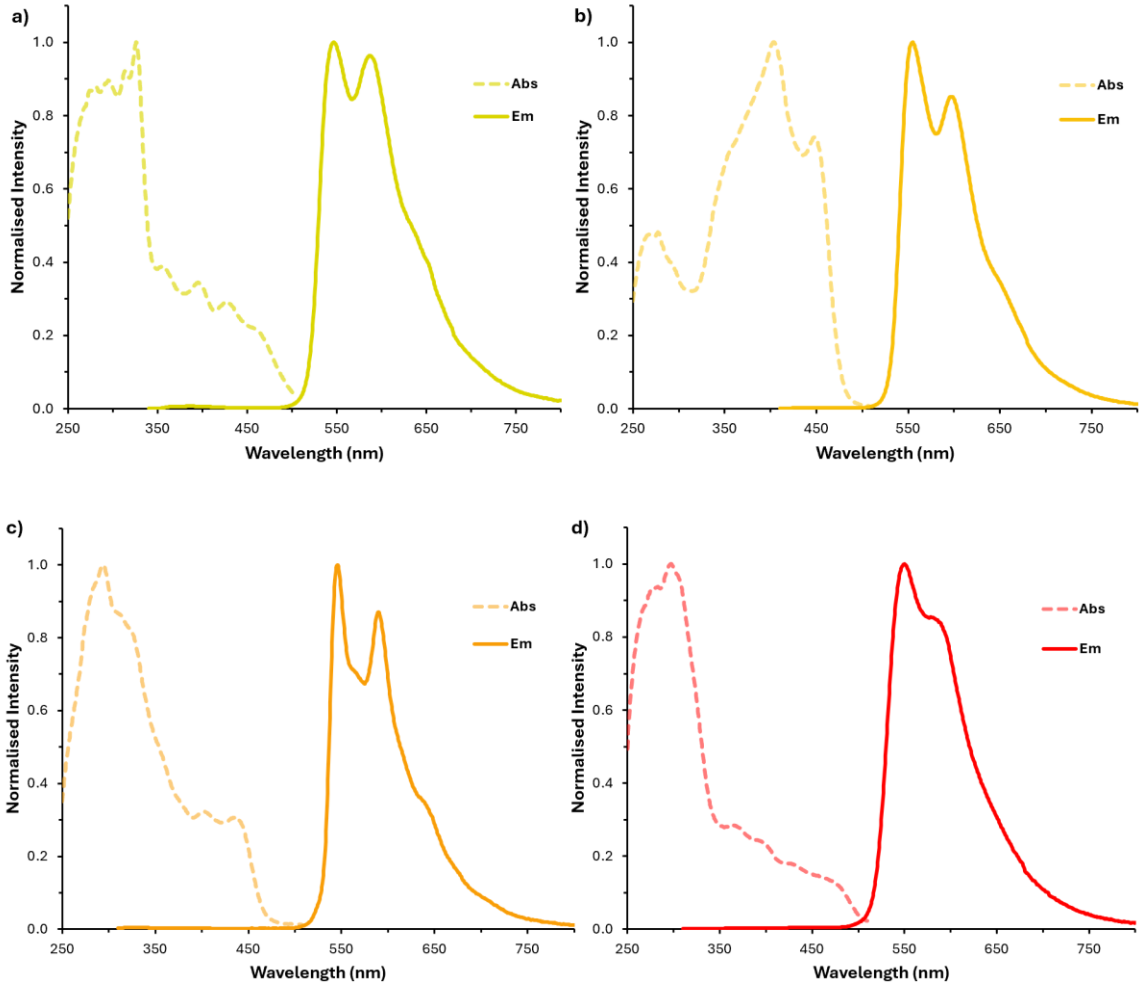


Figure A.4.21 Normalised emission and excitation spectra of iridium complexes **4.1-4.4** ($c = 1\times10^{-5}$ M) measured in $CHCl_3$ solution. **a)** Complex **4.1**, **b)** complex **4.2**, **c)** complex **4.3**, **d)** complex **4.4**.

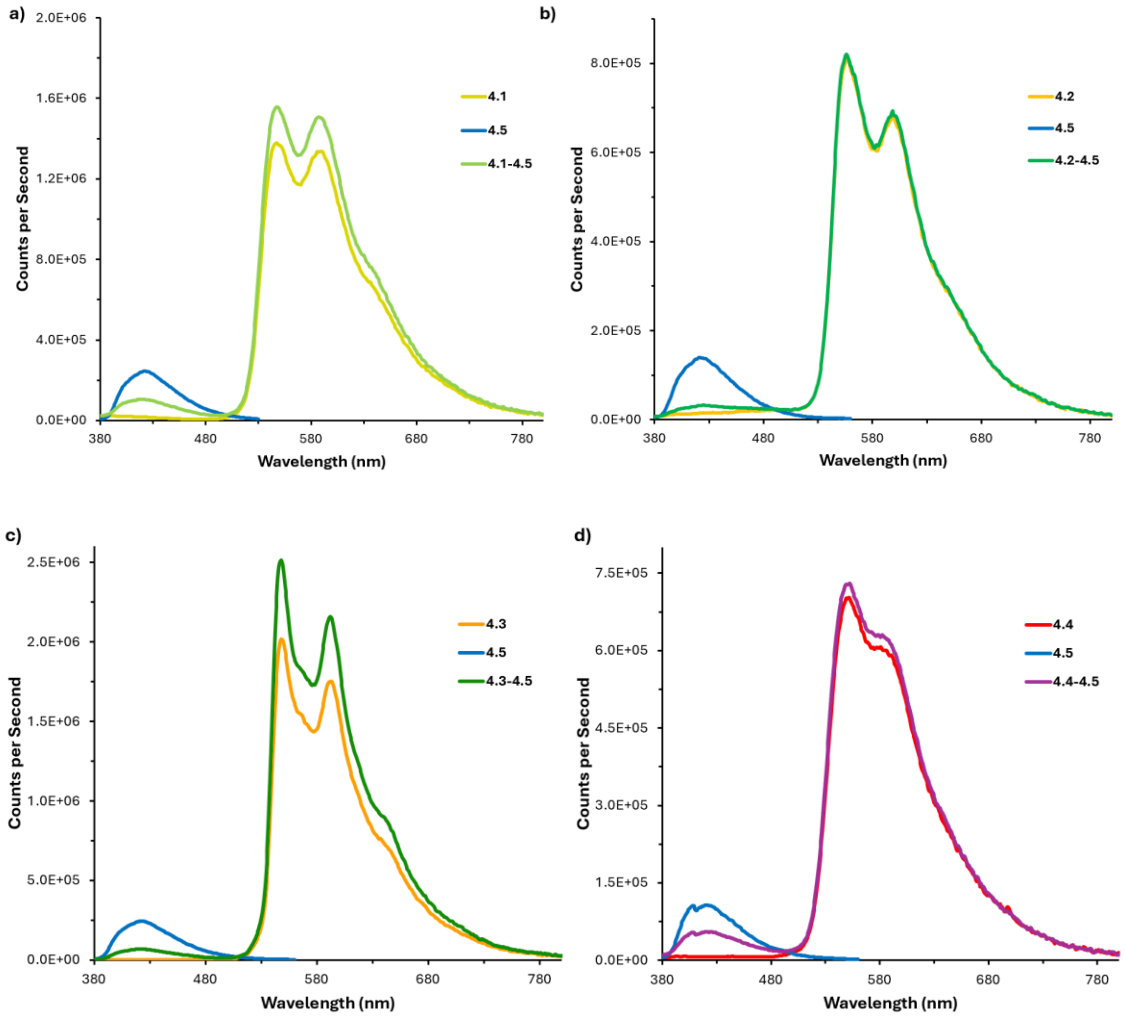


Figure A.4.22 Overlaid emission spectra of complexes **4.1** with deep blue emitter compound **4.5** (blue) and co-systems **4.1•4.5-4.1•4.5** from FRET experiments in $CHCl_3$ solution. All samples excited at λ_{ex} = 350 nm. **a)** Complex **4.1** and co-system **4.1•4.5**, **b)** complex **4.2** and co-system **4.2•4.5**, **c)** complex **4.3** and co-system **4.3•4.5**, **d)** complex **4.4** and co-system **4.4•4.5**.

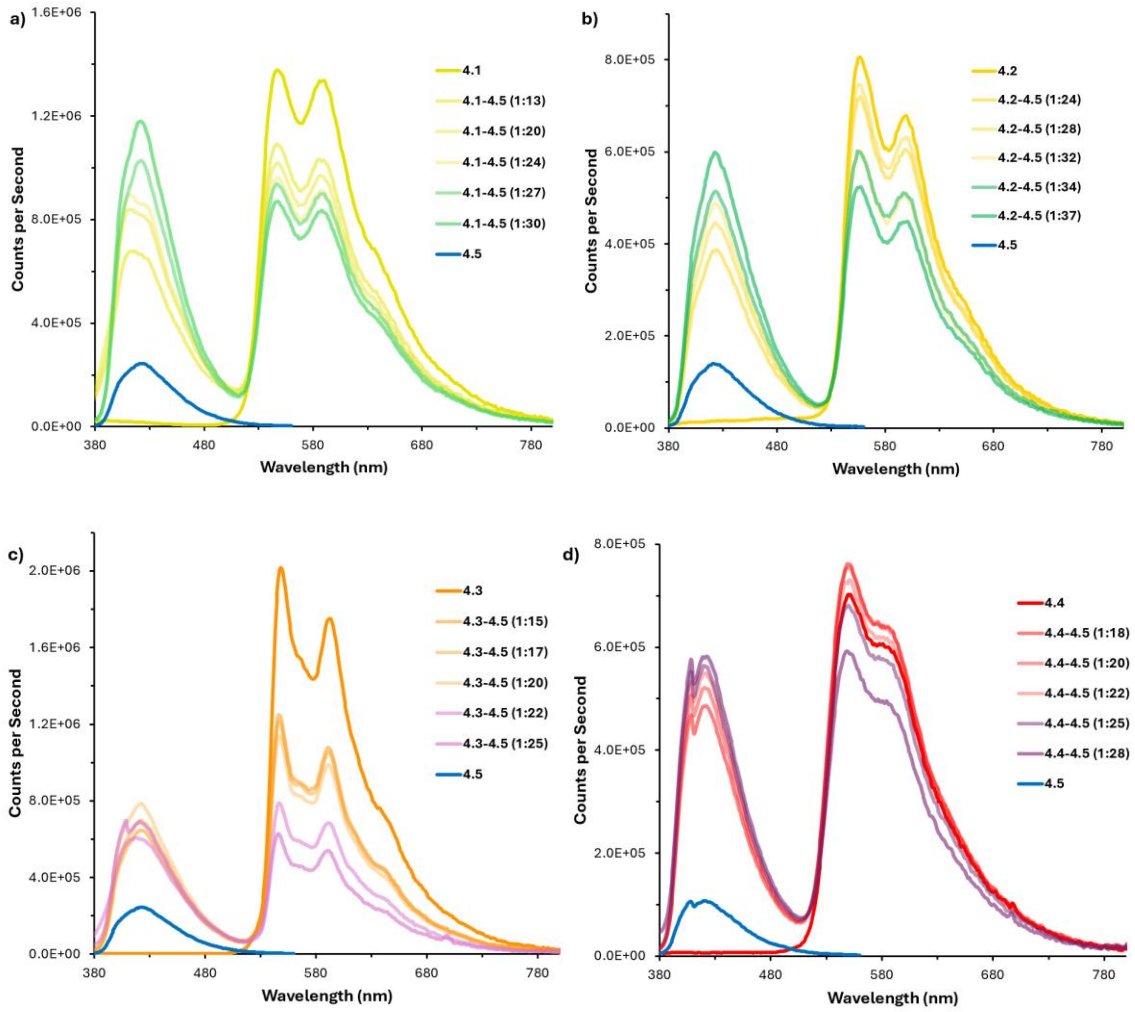


Figure A.4.23 Emission titrations of complexes **4.1-4.4** with deep blue emitter **4.5** used to create CIE plots in figure **4.6**. Equivalents added are indicated in the legend of each graph; **a)** complex **4.1** with **4.5**, **b)** complex **4.2** with **4.5**, **c)** complex **4.3** with **4.5** and **d)** complex **4.4** with **4.5**.

A4.5: K_a Binding Studies

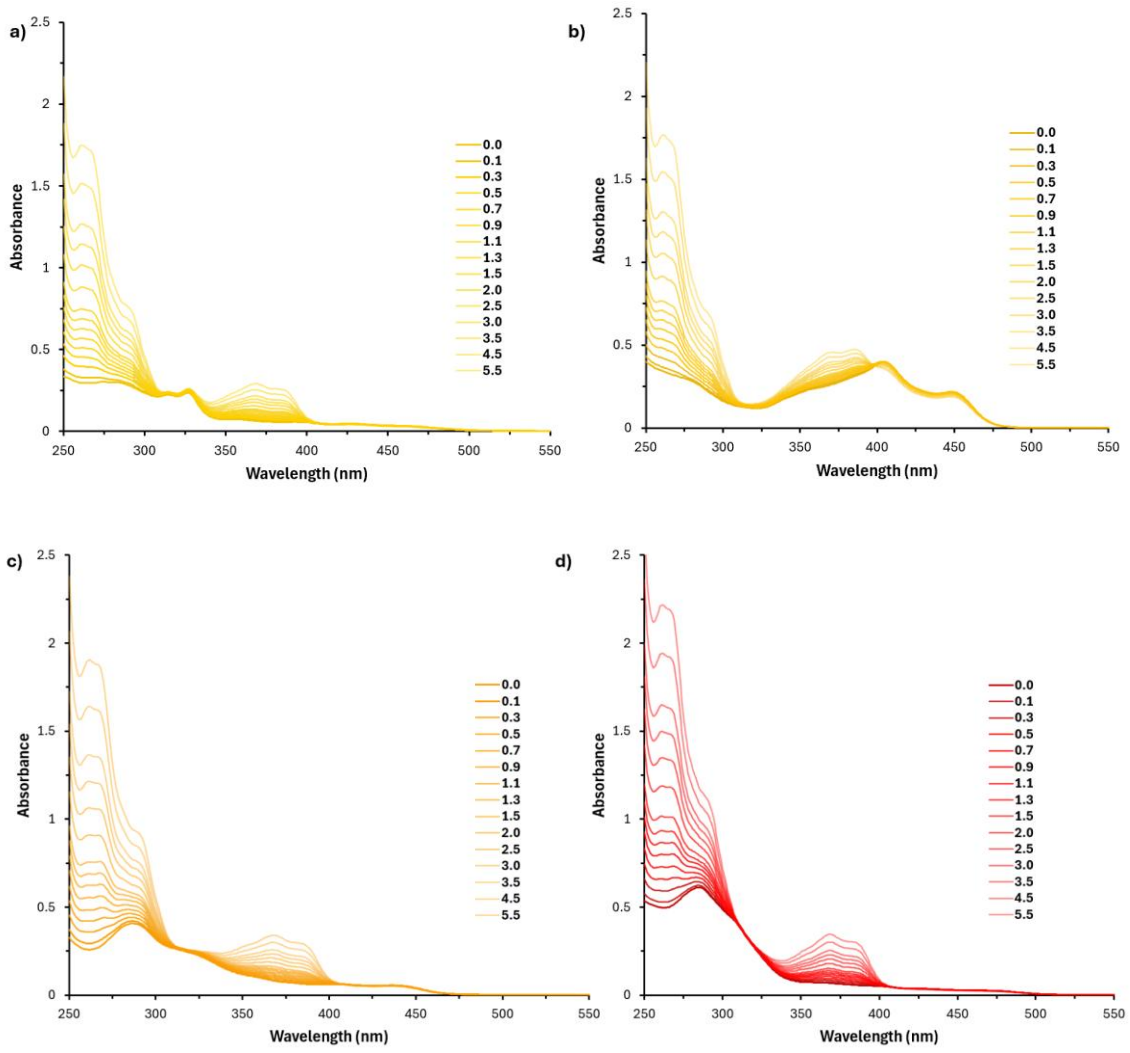


Figure A.4.24 UV-vis titration of complexes **4.1-4.4** with additions of compound **4.5** in $CHCl_3$ at 298 K. Initial concentration of complexes **4.1-4.4** is 1×10^{-5} M, the legend indicates molar equivalents of compound **4.5** added. **a)** complex **4.1** with **4.5**, **b)** complex **4.2** with **4.5**, **c)** complex **4.3** with **4.5** and **d)** complex **4.4** with **4.5**.

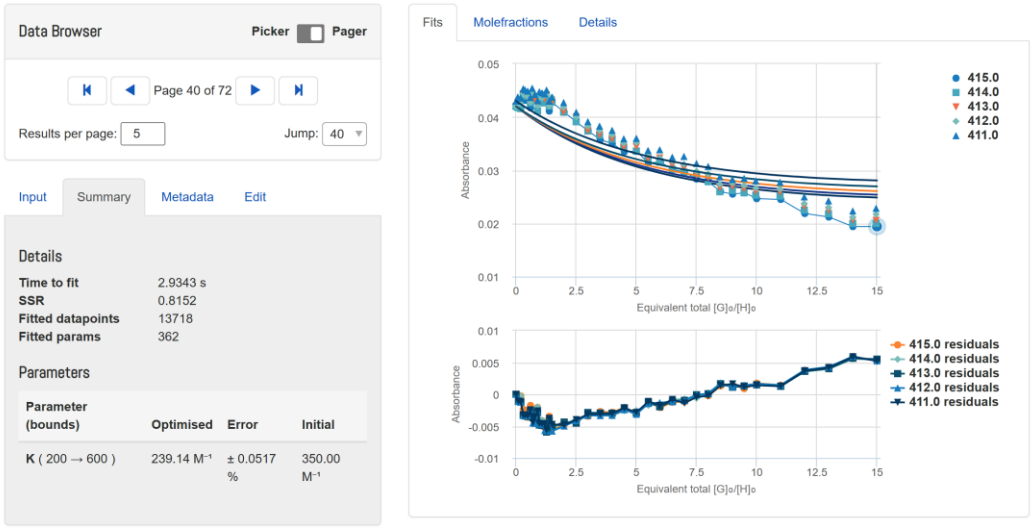


Figure A.4.25 Screengrab of linear regression bindfit calculation data of co-system **4.1•4.5**. Links to open-source calculations of titration runs presented below.

http://app.supramolecular.org/bindfit/view/87063b0c-1b52-4ba3-ade7-a6fba2bfc02a

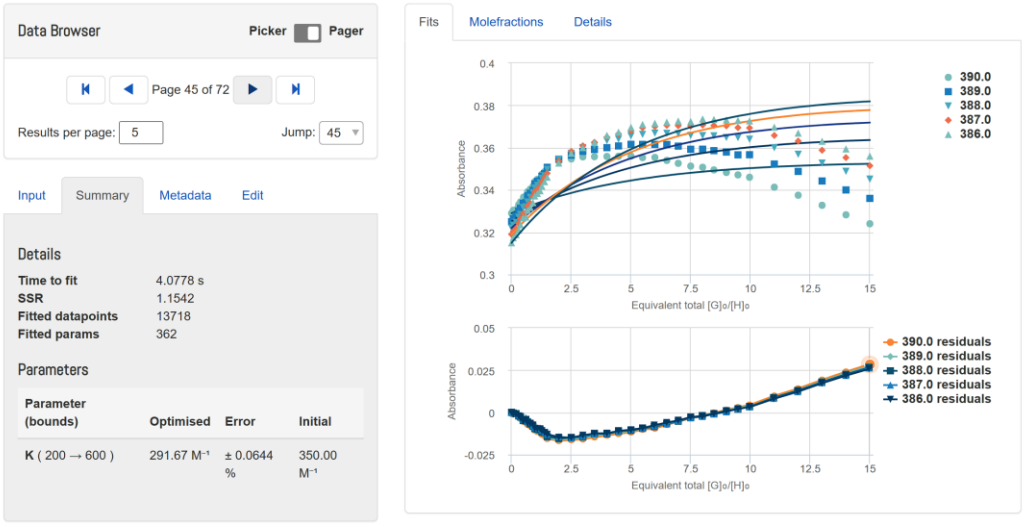


Figure A.4.26 Screengrab of linear regression bindfit calculation data of co-system **4.2•4.5**. Links to open-source calculations of titration runs presented below.

http://app.supramolecular.org/bindfit/view/2b4334a9-d013-4407-9155-27ca3cd78ed4

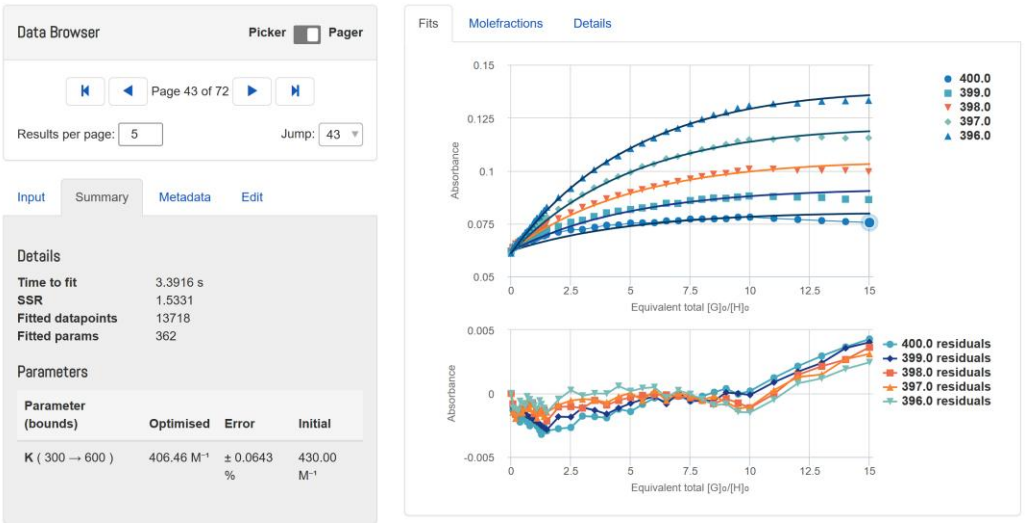


Figure A.4.27 Screengrab of linear regression bindfit calculation data of co-system **4.3•4.5**. Links to open-source calculations of titration runs presented below.

http://app.supramolecular.org/bindfit/view/f2104784-5bba-4ca3-a5e6-b0bd910c5b8d

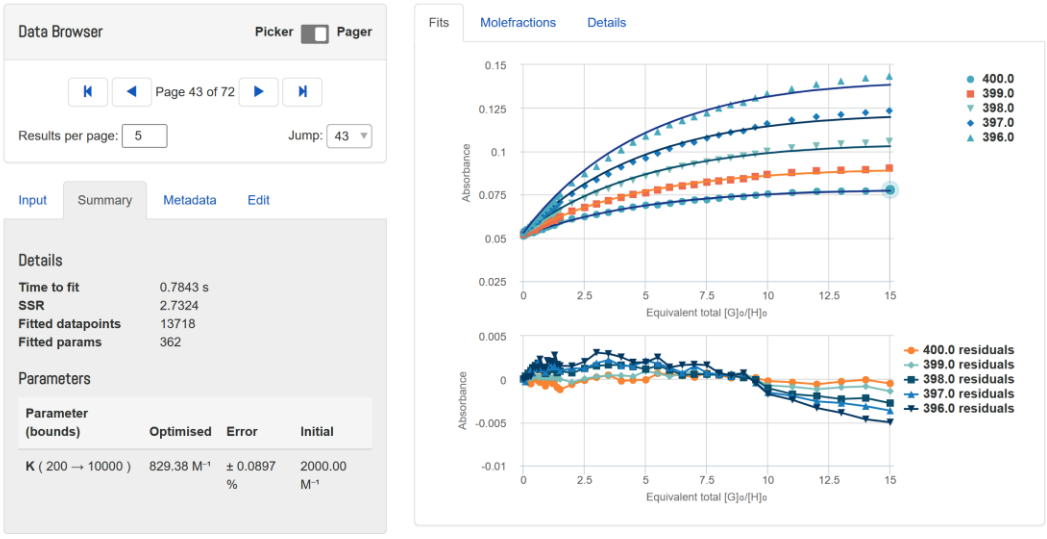


Figure A.4.28 Screengrab of linear regression bindfit calculation data of co-system **4.4•4.5**. Links to open-source calculations of titration runs presented below.

http://app.supramolecular.org/bindfit/view/aded41ec-1b4b-45b3-936d-b0f291e33620

A4.6: PLQYs and Decay Lifetimes

Decay Lifetime Measurement of Ir(III) complex 4.1

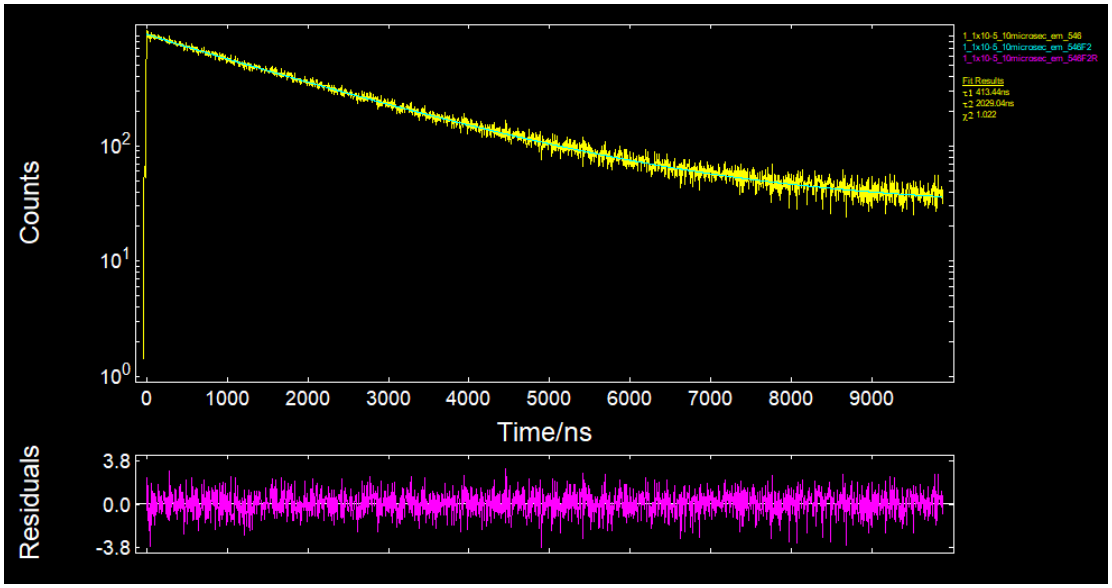


Figure A.4.29 Biexponential lifetime decay of Ir(III) complex **4.1**, ~$1 \cdot 10^{-5}$ M in $CHCl_3$ degassed for 20 mins (Ar) at 298 K after excitation at 365 nm. Data collected at λ_{max} = 470 nm.

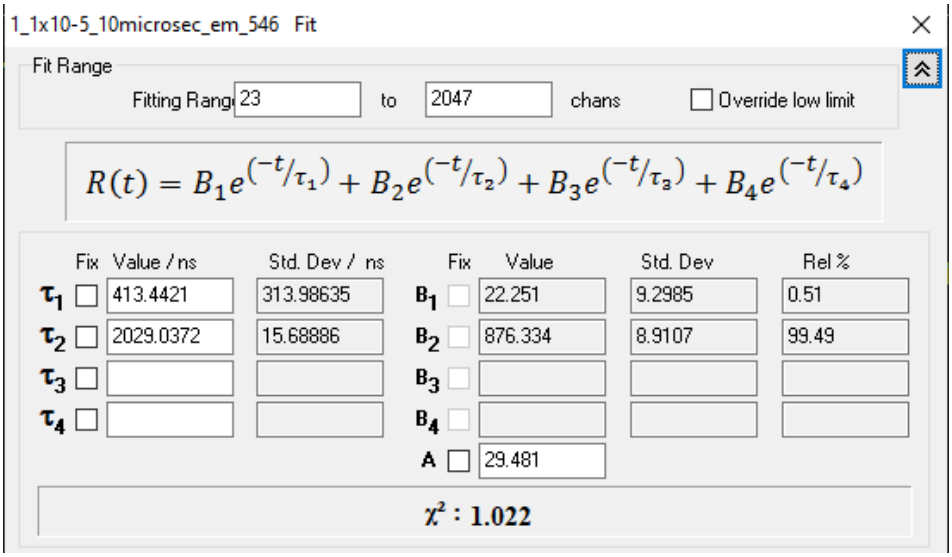


Figure A.4.30 Fit result of Ir(III) complex **4.1**, ~$1 \cdot 10^{-5}$ M in $CHCl_3$ degassed for 20 mins (Ar) at 298 K after excitation at 365 nm. Data collected at λ_{max} = 470 nm.

Decay Lifetime Measurement of Ir(III) complex 4.1•4.5 (white light)

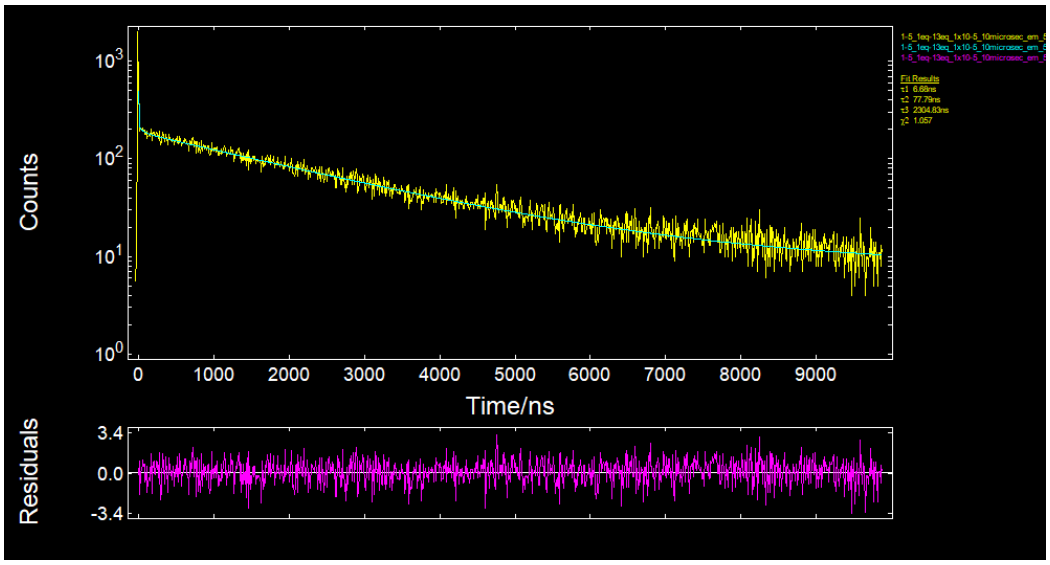


Figure A.4.31 Biexponential lifetime decay of Ir(III) complex **4.1•4.5,** (1:24) ~$1 \cdot 10^{-5}$ M in $CHCl_3$ degassed for 20 mins (Ar) at 298 K after excitation at 365 nm. Data collected at λ_{max} = 540 nm.

Fit Range

Fitting Rang 12 to 1023 chans Override low limit

$$R(t) = B_1 e^{(-t/\tau_1)} + B_2 e^{(-t/\tau_2)} + B_3 e^{(-t/\tau_3)} + B_4 e^{(-t/\tau_4)}$$

	Fix	Value / ns	Std. Dev / ns		Fix	Value	Std. Dev	Rel %
τ_1	☐	6.6781	1.46467	B_1	☐	1228.554	377.4719	1.94
τ_2	☐	77.7900	73.03773	B_2	☐	23.829	22.2698	0.44
τ_3	☐	2304.8298	32.87692	B_3	☐	179.532	1.8917	97.63
τ_4	☐			B_4	☐			
				A	☐	7.951		

χ^2 : 1.057

Figure A.4.32 Fit result of Ir(III) complex **4.1•4.5,** (1:24) ~$1 \cdot 10^{-5}$ M in $CHCl_3$ degassed for 20 mins (Ar) at 298 K after excitation at 365 nm. Data collected at λ_{max} = 540 nm.

Decay Lifetime Measurement of Ir(III) complex 4.2

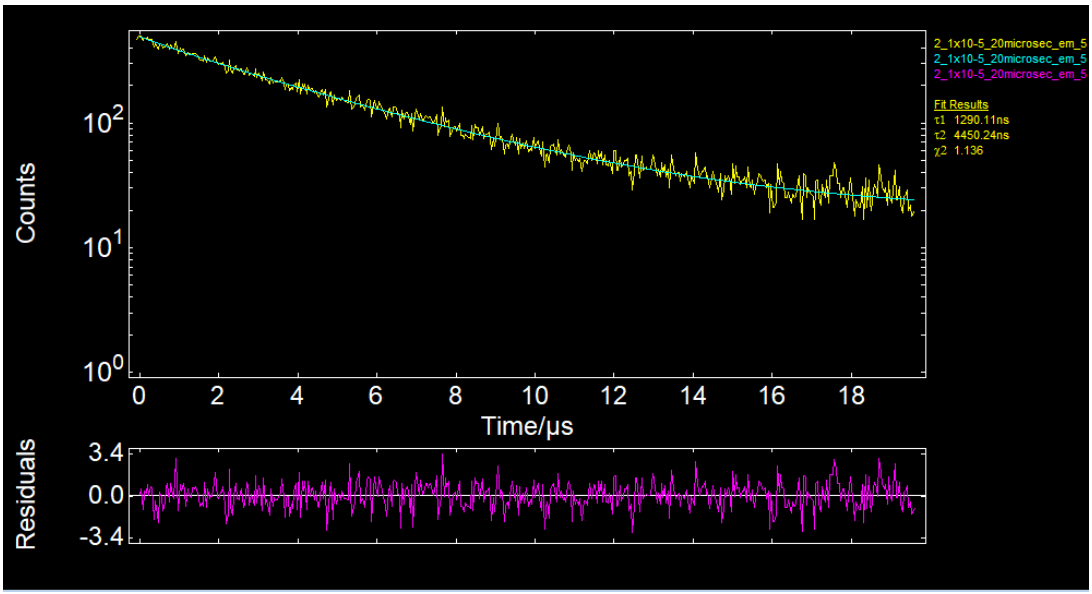


Figure A.4.33 Biexponential lifetime decay of Ir(III) complex **4.2**, ~$1 \cdot 10^{-5}$ M in $CHCl_3$ degassed for 20 mins (Ar) at 298 K after excitation at 365 nm. Data collected at Λ_{max} = 470 nm.

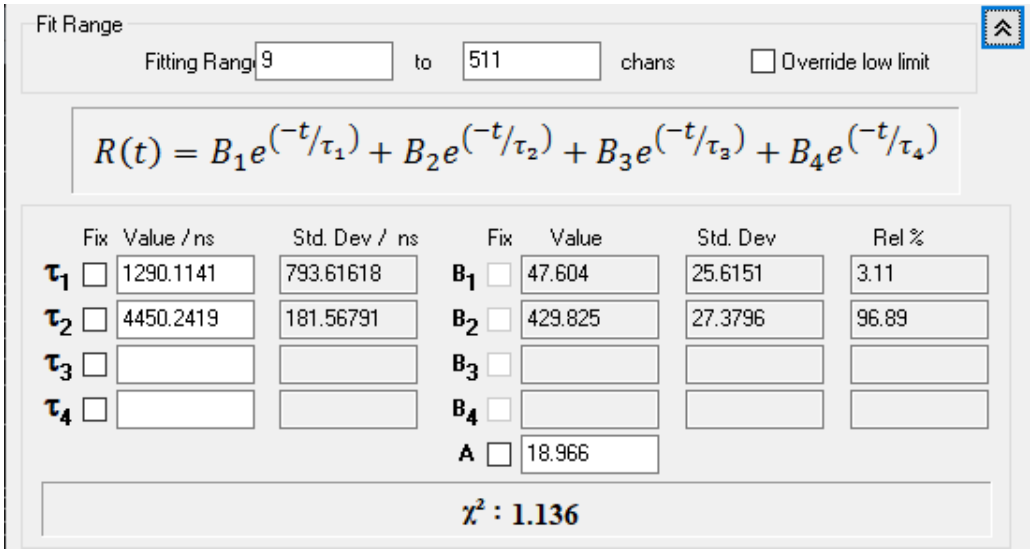


Figure A.4.34 Fit result of Ir(III) complex **4.2**, ~$1 \cdot 10^{-5}$ M in $CHCl_3$ degassed for 20 mins (Ar) at 298 K after excitation at 365 nm. Data collected at Λ_{max} = 470 nm.

Decay Lifetime Measurement of Ir(III) complex 4.2•4.5 (almost white light)

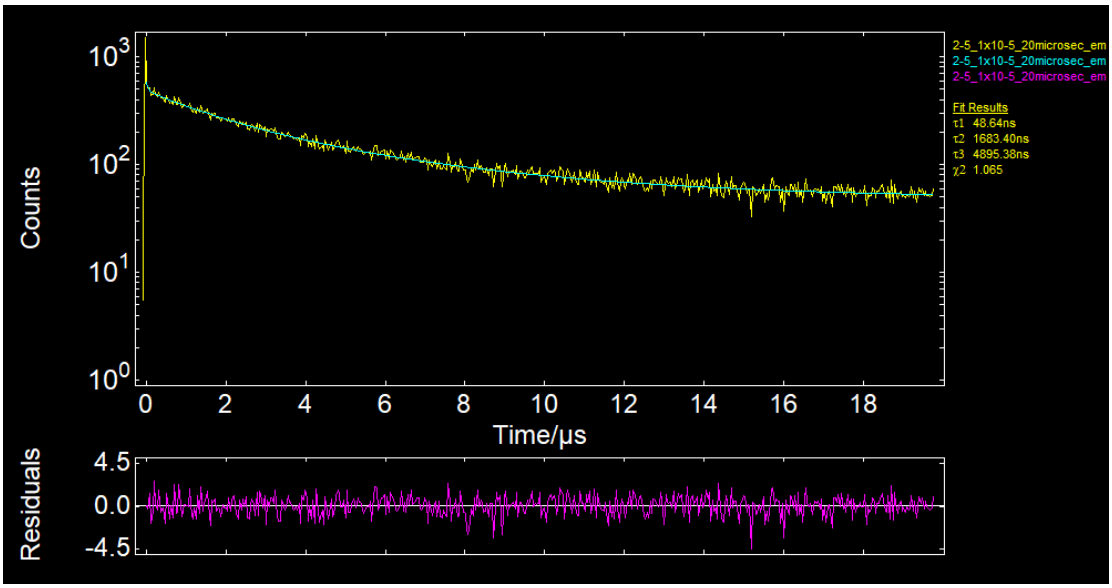


Figure A.4.35 Biexponential lifetime decay of Ir(III) complex **4.2•4.5,** (1:32) ~$1 \cdot 10^{-5}$ M in $CHCl_3$ degassed for 20 mins (Ar) at 298 K after excitation at 365 nm. Data collected at λ_{max} = 540 nm.

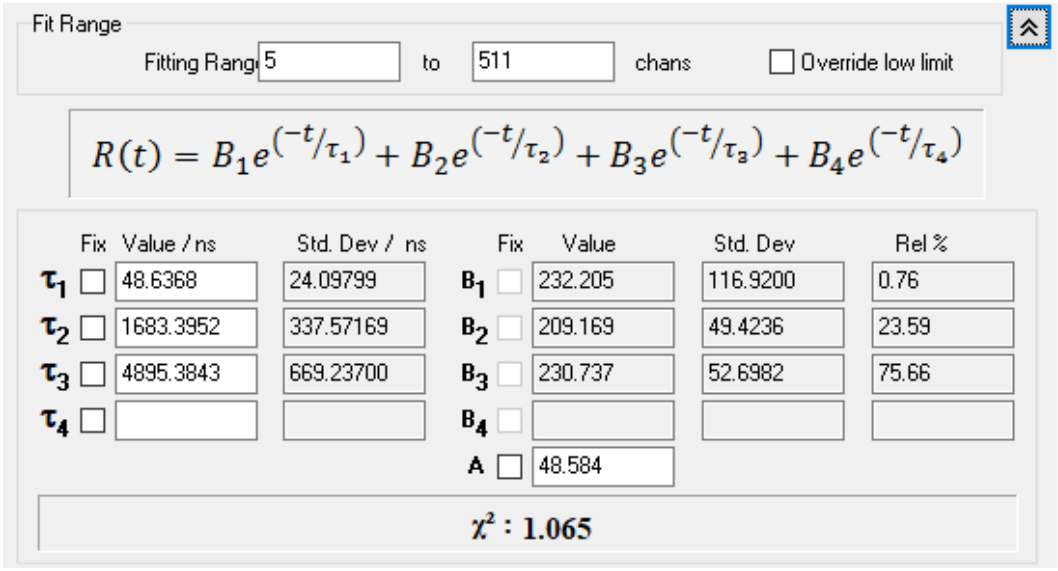


Figure A.4.36 Fit result of Ir(III) complex **4.2•4.5,** (1:32) ~$1 \cdot 10^{-5}$ M in $CHCl_3$ degassed for 20 mins (Ar) at 298 K after excitation at 365 nm. Data collected at λ_{max} = 540 nm.

Decay Lifetime Measurement of Ir(III) complex 4.3

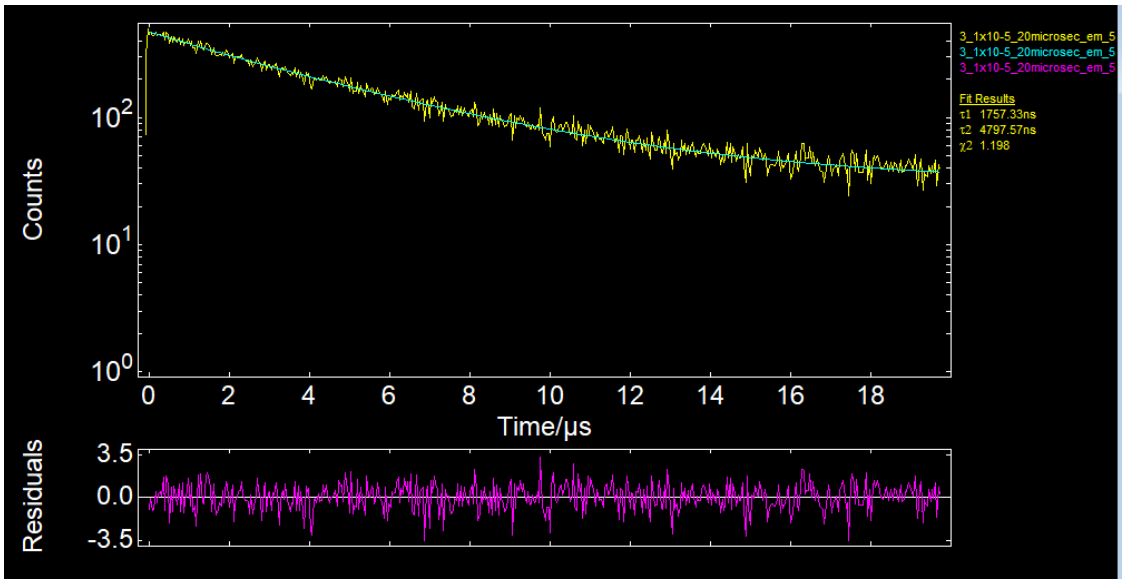


Figure A.4.37 Biexponential lifetime decay of Ir(III) complex **4.3**, ~$1 \cdot 10^{-5}$ M in $CHCl_3$ degassed for 20 mins (Ar) at 298 K after excitation at 365 nm. Data collected at λ_{max} = 470 nm.

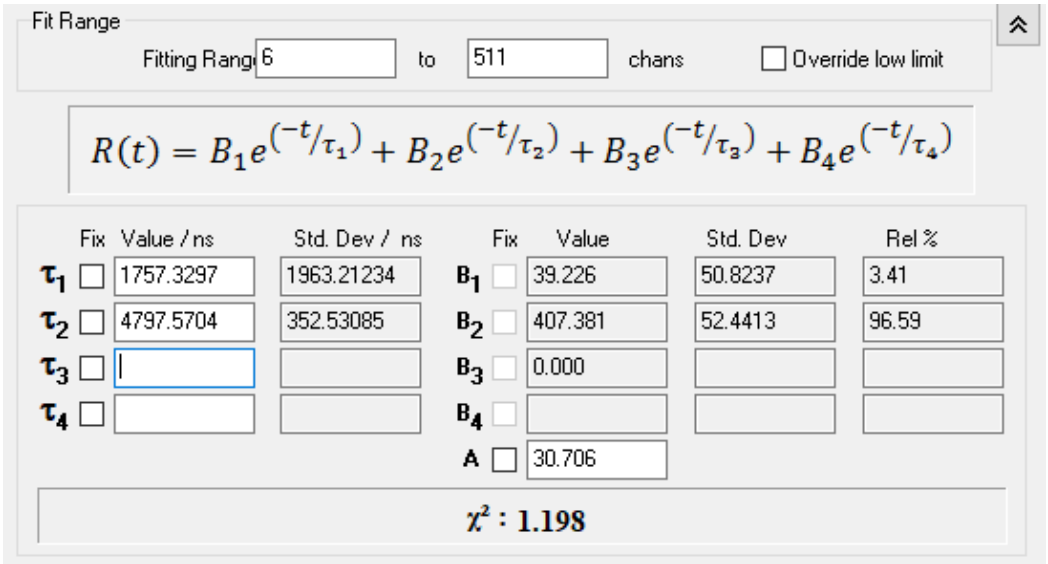


Figure A.4.38 Fit result of Ir(III) complex **4.3**, ~$1 \cdot 10^{-5}$ M in $CHCl_3$ degassed for 20 mins (Ar) at 298 K after excitation at 365 nm. Data collected at λ_{max} = 470 nm.

Decay Lifetime Measurement of Ir(III) complex 4.3•4.5 (white light)

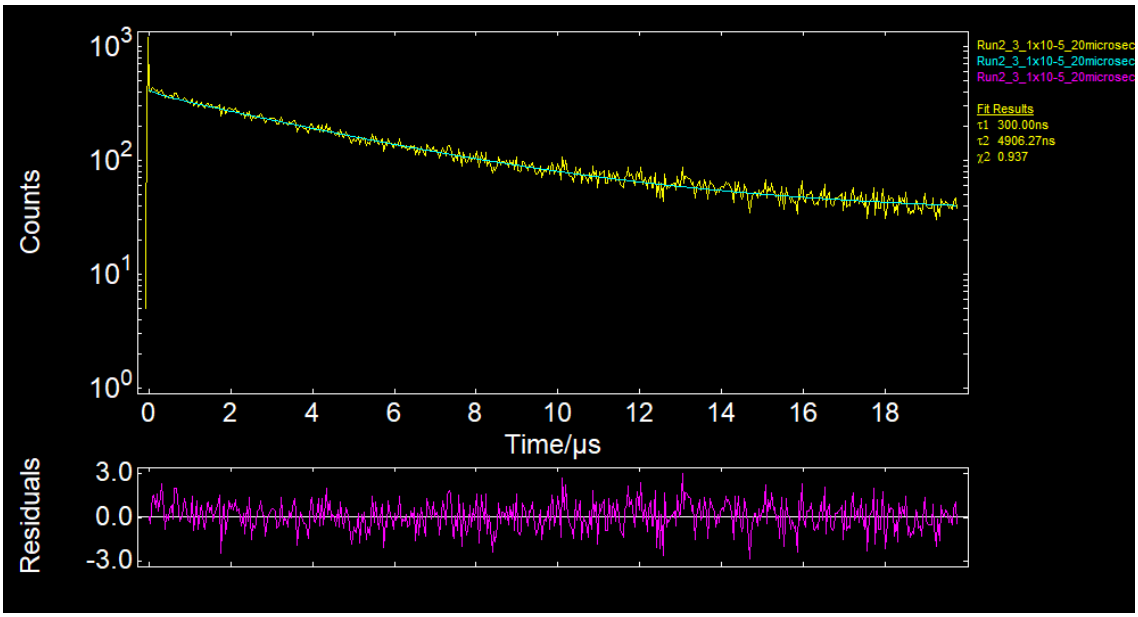


Figure A.4.39 Biexponential lifetime decay of Ir(III) complex **4.3•4.5,** (1:20) ~$1 \cdot 10^{-5}$ M in $CHCl_3$ degassed for 20 mins (Ar) at 298 K after excitation at 365 nm. Data collected at λ_{max} = 540 nm.

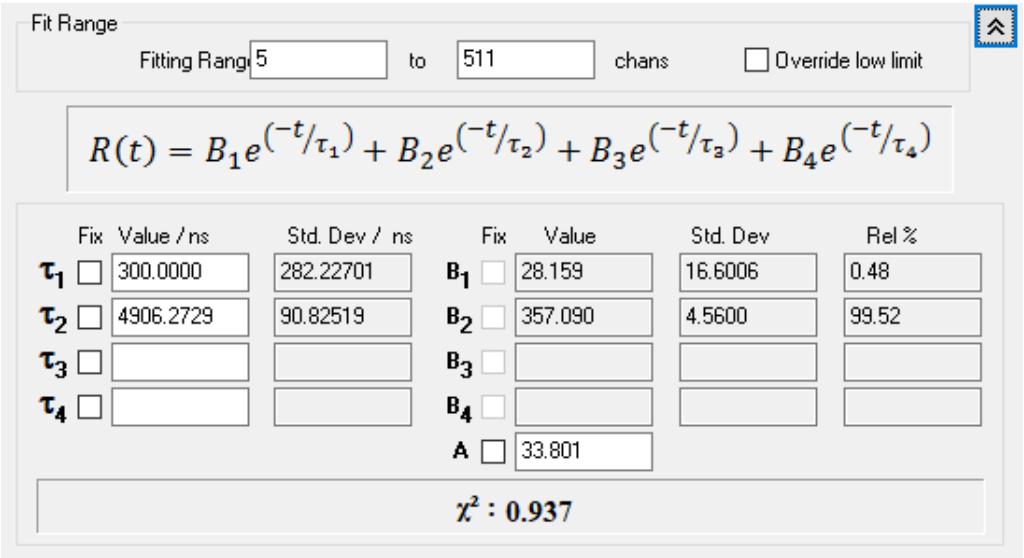


Figure A.4.40 Fit result of Ir(III) complex **4.3•4.5,** (1:20) ~$1 \cdot 10^{-5}$ M in $CHCl_3$ degassed for 20 mins (Ar) at 298 K after excitation at 365 nm. Data collected at λ_{max} = 540 nm.

Decay Lifetime Measurement of Ir(III) complex 4.4

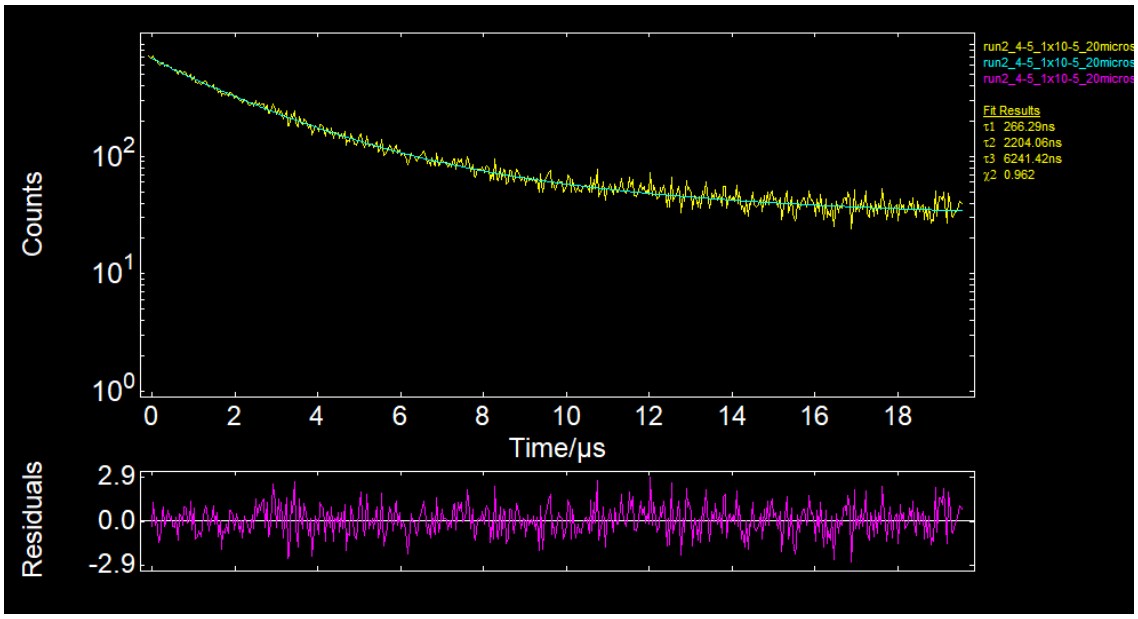


Figure A.4.41 Biexponential lifetime decay of Ir(III) complex **4.4**, ~$1 \cdot 10^{-5}$ M in $CHCl_3$ degassed for 20 mins (Ar) at 298 K after excitation at 365 nm. Data collected at λ_{max} = 470 nm.

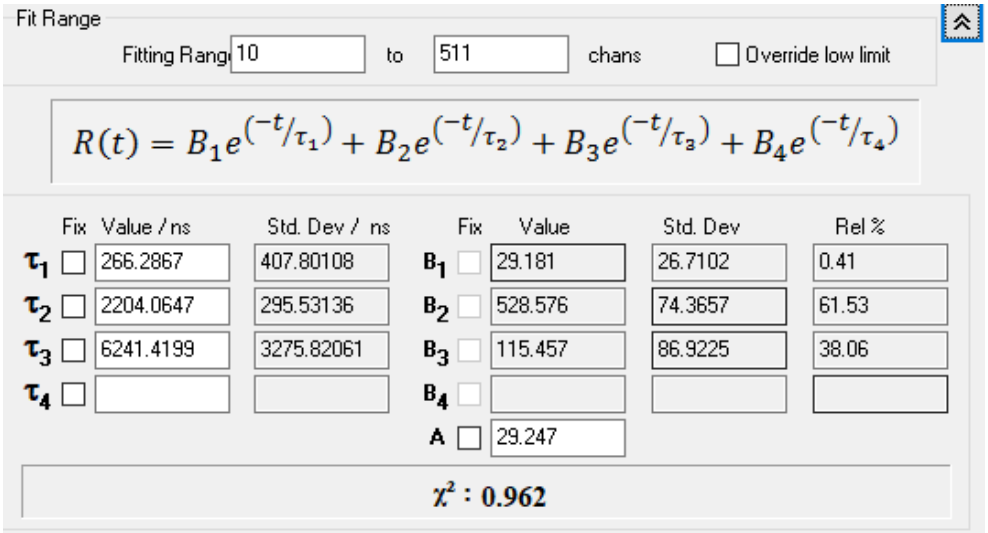


Figure A.4.42 Fit result of Ir(III) complex **4.4**, ~$1 \cdot 10^{-5}$ M in $CHCl_3$ degassed for 20 mins (Ar) at 298 K after excitation at 365 nm. Data collected at λ_{max} = 470 nm.

Decay Lifetime Measurement of Ir(III) complex 4.4•4.5 (white light)

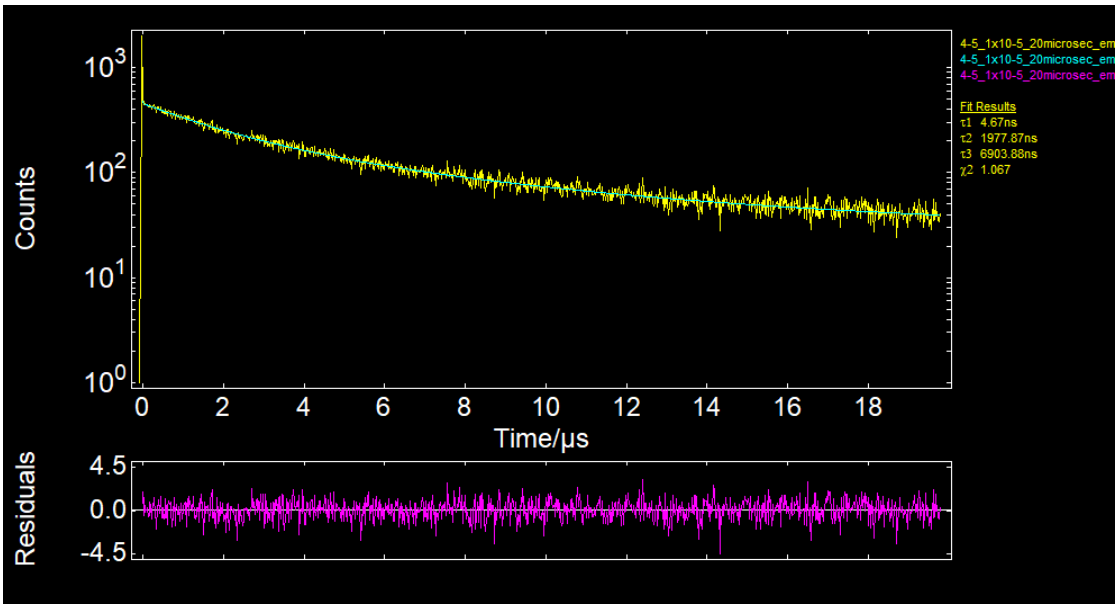


Figure A.4.43 Biexponential lifetime decay of Ir(III) complex **4.4•4.5**, (1:25) ~$1 \cdot 10^{-5}$ M (Absorbance of 0.082 from UV-Vis) in $CHCl_3$ degassed for 20 mins (Ar) at 298 K after excitation at 365 nm. Data collected at λ_{max} = 540 nm.

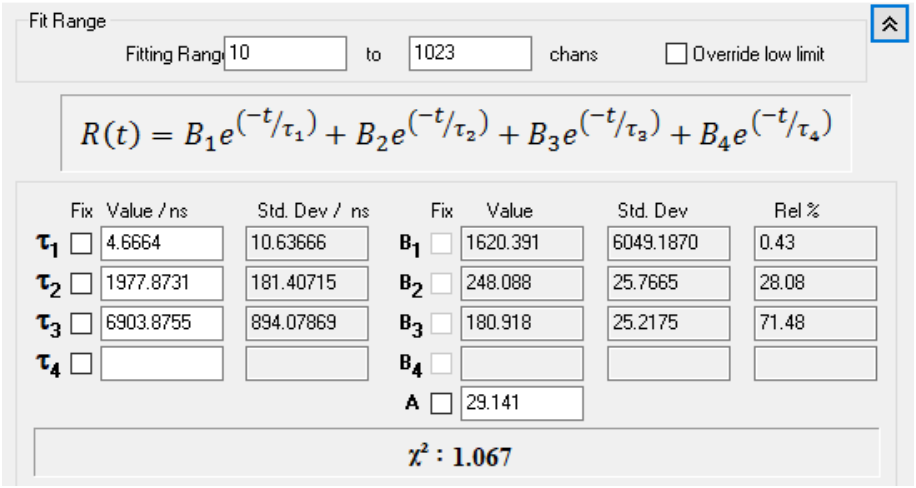


Figure A.4.44 Fit result of Ir(III) complex **4.4•4.5,** (1:25) ~$1 \cdot 10^{-5}$ M (Absorbance of 0.082 from UV-Vis) in $CHCl_3$ degassed for 20 mins (Ar) at 298 K after excitation at 365 nm. Data collected at λ_{max} = 540 nm.

A4.7: Cyclic Voltammetry

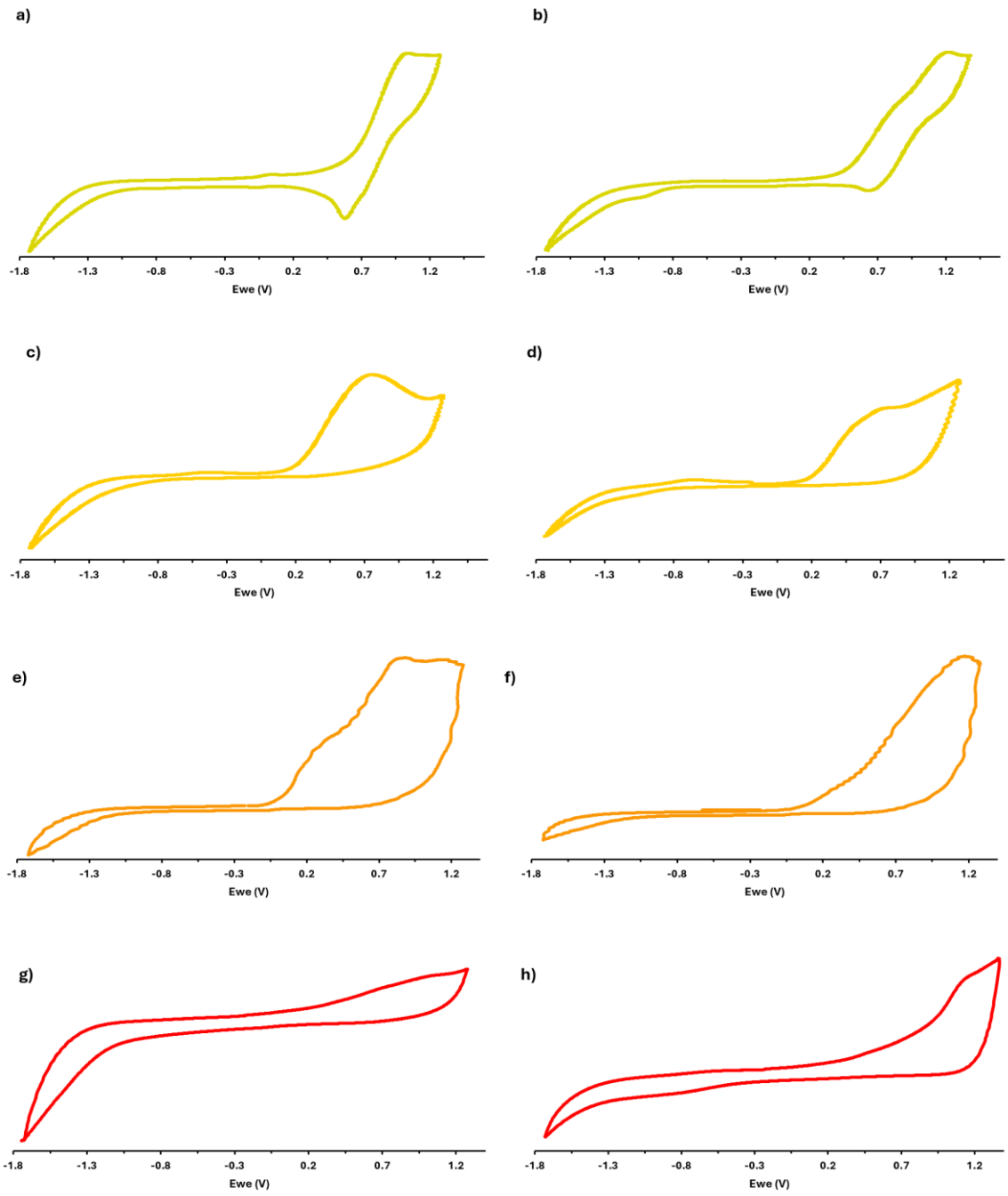


Figure A.4.45 Cyclic voltammetry of complexes **4.1-4.4** and co-systems **4.1•4.5-4.4•4.5** 2 mM in dry degassed $CHCl_3$ normalised to a ferrocene standard. **a)** complex **4.1**, **b)** co-system **4.1•4.5**, **c)** complex **4.2**, **d)** co-system **4.2•4.5**, **e)** complex **4.3**, **f)** co-system **4.3•4.5**, **g)** complex **4.4** and **h)** co-system **4.4•4.5**.

Curriculum Vitae

Trystan Harri Jones

Education

2021-2025 **PhD Chemistry** – Properties and Applications of Hydrogen-Bond Rich Iridium (III) Complexes

University of New Brunswick, Canada

2016-2021 **Master of Chemistry 1st Class with Honours** – Developing New Boryl-Amido Chelating Ligands

University of Edinburgh, Scotland

Research Experience

2021-2025 **PhD Researcher** – University of New Brunswick, Canada

Supervisor: Prof. Barry Blight

2024 **Associate Researcher** – University of Liverpool, UK

Supervisor: Dr. John Ward

2020-2021 **MChem Research Assistant** – University of Edinburgh, Scotland

Supervisor: Prof. Michael Ingleson

2019-2020 **Associate Researcher** – University of Edinburgh

Supervisor: Prof. Fabio Nudelman

Teaching Experience

2024-2025 **Lecturer** – University of New Brunswick, Canada

Introduction to Organic Chemistry

2021-2025 **Teaching Assistant** – University of New Brunswick, Canada

Organic Chemistry lab II

Organic Chemistry lab I

Publications

[4] – Automation Accelerated screening of H-Bond-Rich Iridium Photosensitisers for Hydrogen Generation

T. Harri Jones, Christopher F. Bradshaw, John W. Ward, Barry A. Blight., RSC Catalysis Science & Technology, 2025, 15, 2459-2465

[3] – Deep Colour Tuneability of Heteroleptic Ir(III) Complexes Through Second-Sphere Coordination

T. Harri Jones, Barbora Balónová, Allison E. True, Sydney Hetherington, Barry A. Blight., RSC Advances, 2024, 14, 34288-34297

(Featured article: RSC Advances Inorganic Chemistry year in review 2024 and 2024 RSC Advances Popular Advances Collection)

[2] – Amides as Modifiable Directing Groups in Electrophilic Borylation

Iqbal, S. A., Uzelac, M., Nawaz, I., Wang, Z., **Jones, T. H.**, Gary Stephen Nichol, Yuan, K.; Millet, C., Ghayoor Abbas Chotana, Michael James Ingleson., Chemical Science, 2023, 14 (14), 3865-3872

[1] – Synthesis and Characterization of New Co(II), Rh(III), and Pt(II) Complexes

Da, W., **Jones, T. H.**, Lin, J. B., Blight, B. A., Canadian Journal of Chemistry, 2022, 101 (3), 177-185

Awards and Professional Memberships

2022-2025 Associate Member of the **Canadian Society of Chemistry**

2022-2025 Associate Member of the **Royal Society of Chemistry**

2021-2025 International Tuition and Stipend Award **UNB**

2025	MaGee-Corke Graduate Scholarship **UNB**
2024	Johnson-Matthey Precious Metal Award **JM**
2024	Frank and J Norah Toole Graduate Scholarship **UNB**
2023-2024	Conference Travel Award **UNB**
2023	Karel Wiesner Postgraduate Award **UNB**

Conferences and Meetings

2025	CSC, Canadian Society of Chemistry Annual Conference, Ottawa, ON. Talk: Colour Tuning Iridium Emitters Through Hydrogen-Bonding
2025	CANUK, International Meeting for Canada-UK Chemistry Partners, Québec City, QC. Poster: Automation Accelerated Screening of H-Bond-Rich Iridium Photosensitisers for Hydrogen Generation (CANUK poster prize)
2024	MASC, RSC Supramolecular Chemistry Meeting, York, UK. Poster: Colour Tuning Iridium Complexes Through Second-Sphere Coordination
2023	MASC, RSC Supramolecular Chemistry Meeting, Birmingham, UK. Poster: Development of an Iridium-Centred Rotaxane
2023	ComSciCan, Canadian Conference for Science Communication, Hamilton, ON.
2023	R3 Environmental Technologies Meeting, Fredericton, NB. Poster: Development of an Iridium-Centred Rotaxane